Transactions of the ASME® Journal of Heat Transfer

Published Bimonthly by The American Society of Mechanical Engineers

VOLUME 125 • NUMBER 4 • AUGUST 2003

PHOTOGALLERY

2001 MAX JACOB MEMORIAL AWARD LECTURE

TECHNICAL PAPERS

Conduction Heat Transfer

Forced Convection

(Contents continued on inside back cover)

Transactions of the ASME, Journal of Heat Transfer (ISSN 0022-1481) is published bi-monthly (Feb., Apr., June, Aug., Oct., Dec.) by The American Society of Mechanical Engineers, Three Park Avenue, New York, NY 10016. Periodicals postage paid at New York, NY and additional mailing offices. POSTMASTER: Send address changes to Transactions of the ASME, Journal of Heat Transfer, c/o THE AMERICAN SOCIETY OF MECHANICAL ENGINEERS, 22 Law Drive, Box 2300, Fairfield, NJ 07007-2300. **CHANGES OF ADDRESS** must be received at Society headquarters seven weeks before they are to be effective. Please send old label and new address. **STATEMENT from By-Laws.** The Society shall not be responsible for statements or opinions advanced in papers or ... printed in its publications (B7.1, Para. 3), **COPYRIGHT © 2003** by The American Society of Mechanical Engineers. For authorization to photocopy material for internal or personal use under those circumstances not falling within the fair use provisions of the Copyright Act, contact the Copyright Clearance Center (CCC), 222 Rosewood Drive, Danvers, MA 01923, tel: 978-750-8400, *www.copyright.com*. Request for special permission or bulk copying should be addressed to Reprints/Permission Department. **INDEXED** by Applied Mechanics Reviews and Engineering Information, Inc. Canadian Goods & Services Tax Registration #126148048.

(**Contents continued**)

Journal of Heat Transfer **Volume 125, Number 4** **AUGUST 2003**

Natural and Mixed Convection

Radiative Heat Transfer

Evaporation, Boiling, and Condensation

Melting and Solidification

Combustion and Gas Turbine Heat Transfer

Bubbles, Particles, and Droplets

Porous Media

Heat and Mass Transfer

TECHNICAL NOTES

ANNOUNCEMENT

The ASME Journal of Heat Transfer is abstracted and indexed in the following:

Applied Science and Technology Index, AMR Abstracts Database, Chemical Abstracts, Chemical Engineering and Biotechnology Abstracts (Electronic equivalent of Process and Chemical Engineering), Civil Engineering Abstracts, Compendex (The electronic equivalent of Engineering Index), Corrosion Abstracts, Current Contents, E & P Health, Safety, and Environment, Ei EncompassLit, Engineered Materials Abstracts, Engineering Index, Enviroline (The electronic equivalent of Environment Abstracts), Environment Abstracts, Environmental Engineering Abstracts, Environmental Science and Pollution Management, Fluidex, Fuel and Energy Abstracts, Index to Scientific Reviews, INSPEC, International Building Services Abstracts, Mechanical & Transportation Engineering Abstracts, Mechanical Engineering Abstracts, METADEX (The electronic equivalent of Metals Abstracts and Alloys Index), Petroleum Abstracts, Process and Chemical Engineering, Referativnyi Zhurnal, Science Citation Index, SciSearch (The electronic equivalent of Science Citation Index), Theoretical Chemical Engineering

Journal of Heat Transfer

Photogallery

The seventh ‘‘Heat Transfer Photogallery’’ was sponsored by the K-22 Heat Transfer Visualization Committee for the 2002 International Mechanical Engineering Congress and Exhibition (IMECE) in New Orleans, Louisiana, held November 17–22, 2002. Out of the total 13 presented entries, the peer-reviewed selection process identified the top seven for publication in the ASME *Journal of Heat Transfer* August issue of 2003. Ballots to choose up to best eight entries were solicited for those who participated and visited the Photogallery session at 2002 IMECE. The total twenty-six ballots were returned and the order of the presentation in this publication is consistent with the rankings of the final seven based on the ballot.

The purpose of publishing these photographs is to draw attention to the innovative features of optical diagnostic techniques and aesthetic qualities of thermal processes. To focus on visualization, the text is kept to a minimum and further details should be found through the listed references or directly from the authors. The photographs include: (1) Optically-sectioned μ-PIV measurements using CLSM [1], (2) Behavior of aqueous lithium-bromide drops in horizontal tube banks [2], (3) Low Bond number two-phase flow regime transition from slug to annular wavy flow in a microchannel, (4) Microscale bubble nucleation from an artificial cavity in single microchannel, (5) Thermal transport during nanoscale machining by field emission of electrons from carbon nanotubes [3], (6) Visualization of ebullient dynamics in surfactant solutions [4], and (7) Heat and mass transfer in a peristaltic micro mixer [5].

My wish is that the journal readers enjoy viewing these collections, acquire knowledge of the state-of-the-art features potentially applicable for their own research, and also promote their participation in 2003-IMECE Photogallery session presentation (refer to the Call for Photogallery for 2003-IMECE announced in this volume).

References

[1] Park, J. S., Kihm, K. D., and Allen, J. S., 2002, ‘‘Three-Dimensional Microfluidic Measurements Using Optical Sectioning By Confocal Microscopy: Flow Around a Moving Bubble in a Micro-Channel,’’ IMECE Paper No. 2002-32790.

[2] Killion, J. D., and Garimella, S., 2003, ‘‘Gravity-Driven Flow of Liquid Films and Droplets in Horizontal Tube Banks,’’ Int. J. Refrig., in press (accepted).

[3] Wong, B. T., Mengüç, M. P., Vallance, R. R., and Rao, A., 2003, ‘‘Modeling of Energy Transfer for Carbon Nanotube-Based Precision Machining,’’ Proceedings of the Annual Meeting American Physical Society (APS) March Meeting 2003, Austin, TX, March 3–7, 2003.

[4] Zhang, J., and Manglik, R. M., 2003, ‘‘Pool Boiling Heat Transfer in Aqueous Solutions of Cationic Surfactants,’’ Paper No. TED-AJ03-248.

[5] Beskok, A., and Warburton, T. C., 2001, ‘‘An Unstructured H/P Finite Element Scheme for Fluid Flow and Heat Transfer in Moving Domains,’’ J. Comput. Phys., **174**, pp. 492–509.

K. D. Kihm
Department of Mechanical Engineering,
Texas A&M University,
College Station, TX 77843-3123

Theory of Confocal Pinhole

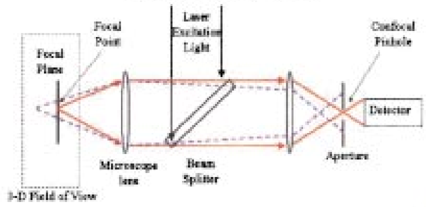

High-Speed Confocal Microscope, Yokogawa CSU-10

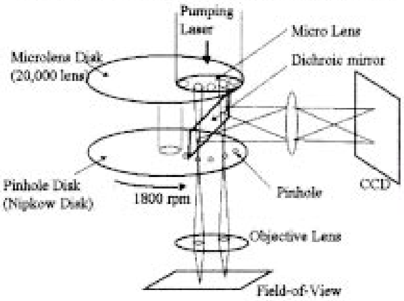

Confocal Laser Scanning Microscope

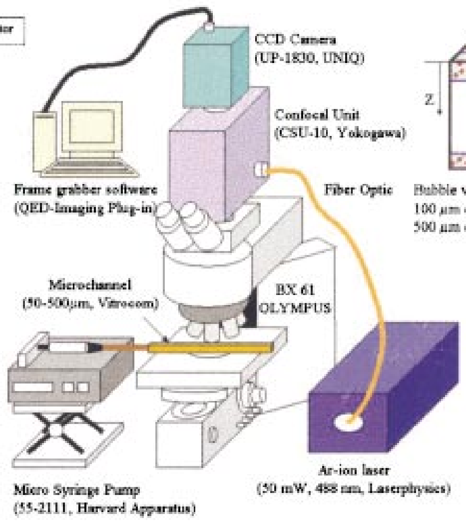

Optical Sectioned Micro-Focal Plane

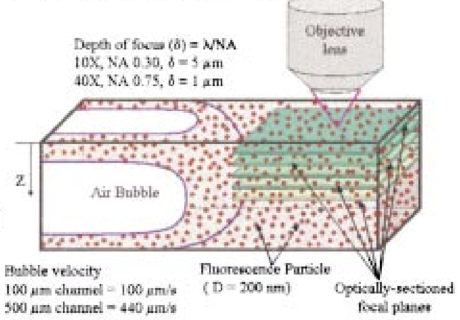

Capillary Number

$Ca = \mu U/\sigma$

500 μm channel: $Ca = 6.11\times10^{-6}$

100 μm channel: $Ca = 1.39\times10^{-6}$

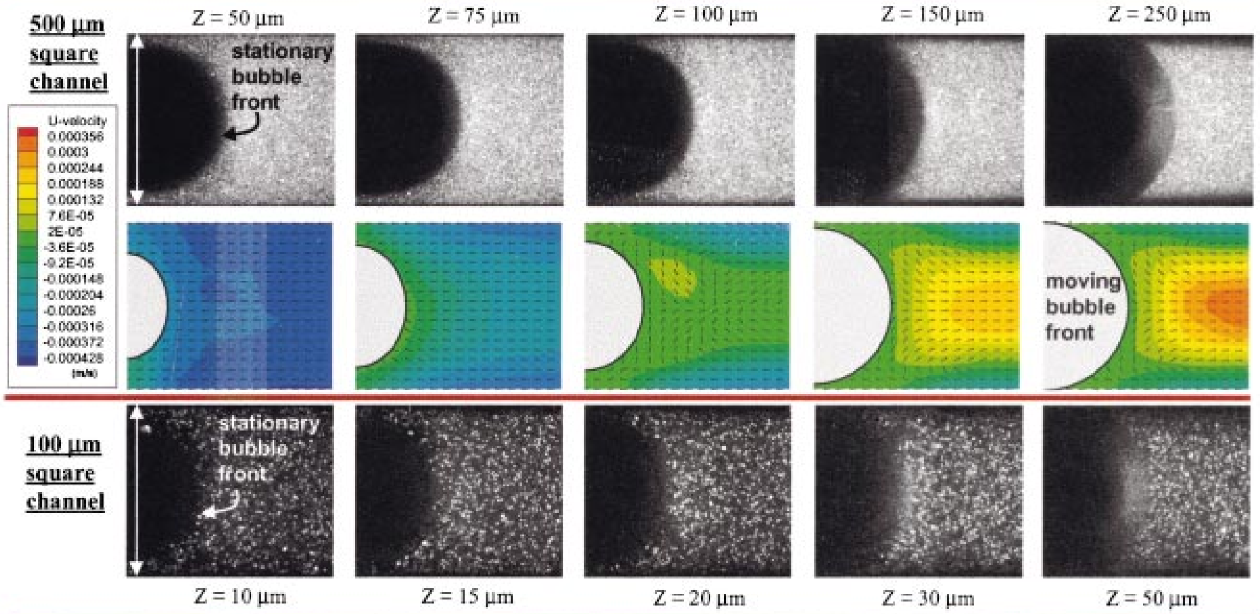

Optically–Sectioned Micro PIV Measurements Using CLSM*

- Full-field flow mapping at the bubble front advancing in a rectangular cross-sectioned microchannel -

J. S. Park, C. K. Choi and K. D. Kihm
Texas A&M University, College Station, Texas

J. S. Allen
NASA Glenn Research Center, Cleveland, Ohio

The Confocal Laser Scanning Microscope* (CLSM) enables optically sectioned μ-PIV measurements with extremely shallow field-of-depth of 1.0-μm and a lateral resolution better than 0.5-μm. Hollow sphere, 200-nm fluorescent particles are used as tracers to achieve a full-field, optically sectioned flow velocity vector mapping, for the region at the gas bubble front, advancing in two different microchannels of 500-μm by 500-μm (Capillary number = 6.11×10^{-6}), and 100-μm by 100-μm ($Ca = 1.39\times10^{-6}$) square cross-sections. This work is supported by the NASA OBPR-Fluid Physics Research Grant (NAG3-2712) and the CLSM was purchased by the Permanent University Facility Award from Texas A&M University.

Aqueous Lithium Bromide (55 wt%) Falling Over 15.9 mm OD Copper Tube Bank

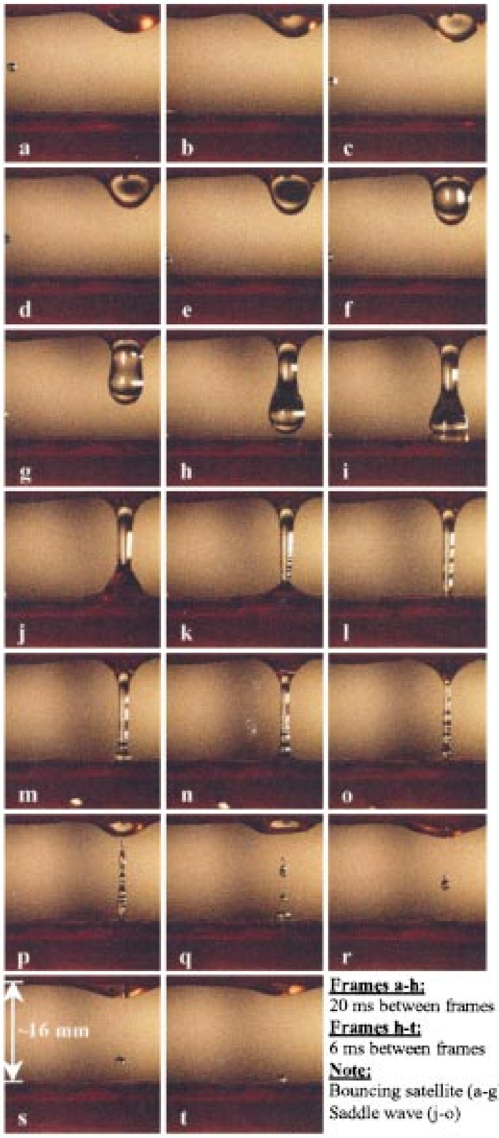

Frames a-h:
20 ms between frames
Frames h-t:
6 ms between frames
Note:
Bouncing satellite (a-g)
Saddle wave (j-o)

Water Falling Over 12.7 mm OD Brass Tube Bank (25.4 mm between tubes)

Droplet Formation

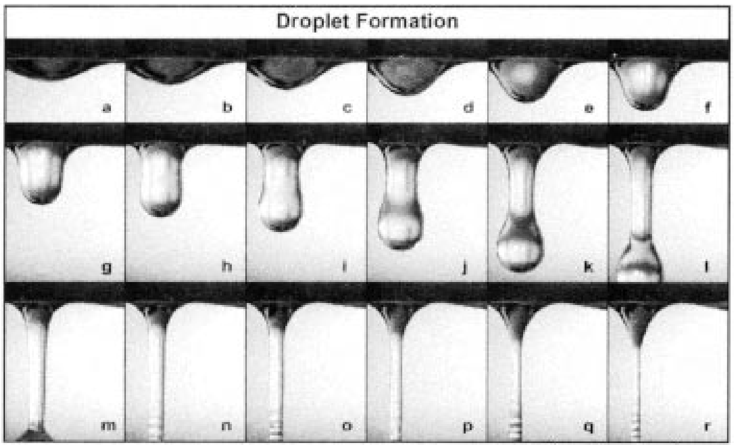

10 ms between frames

Droplet Detachment and Impact – View from End of Tubes

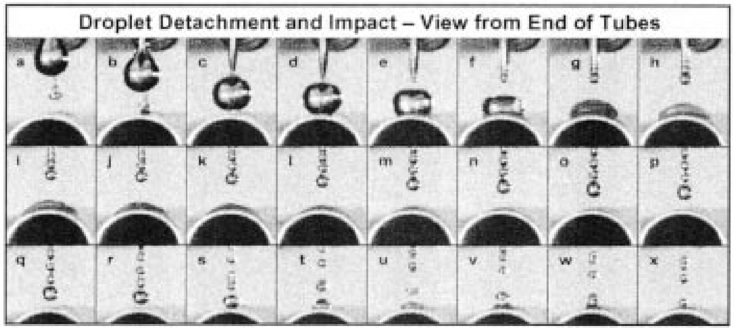

10 ms between frames a-c, 2 ms between frames c-x

Droplet Impact and Saddle-Wave Propagation

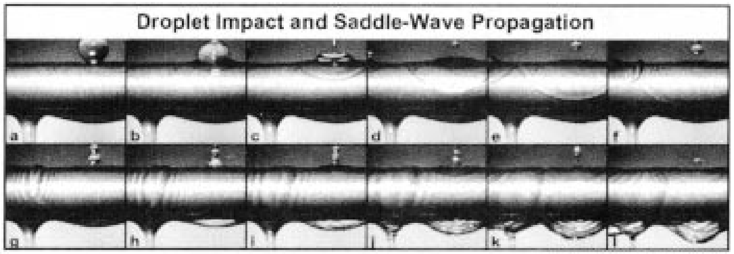

4 ms between frames

BEHAVIOR OF AQUEOUS LITHIUM-BROMIDE DROPS IN HORIZONTAL TUBE BANKS

Jesse D. Killion and Srinivas Garimella
Iowa State University, Ames, Iowa

Liquid films falling over banks of internally cooled horizontal tubes are frequently used to absorb a surrounding vapor, particularly when the heat of absorption is high and when high transfer rates and low pressure drops are required, as in absorption heat pump systems. Recent studies have shown that, in systems utilizing water/lithium-bromide, the droplets contribute significantly to the total absorption rate. It is thought that the droplets can affect absorption rates both directly, by absorption on their continuously evolving surface, and indirectly, by waves on the liquid film caused by droplet formation, detachment, and impact. The video frames presented here illustrate the complex details of the droplet flow modes have been previously unaccounted for in mathematical models. By revealing the surface shape evolution and flow features, these images provide a basis for more accurately predicting the coupled heat and mass transfer rates.

The tube bank shown comprises 9 copper tubes (15.9 mm OD, 15.9 mm tube-to-tube gap). LiBr solution (55%-wt) flowed at $Re_f = 4\Gamma/\mu = 120$, where Γ = mass-flow-rate/(2×tube length) and μ = viscosity. The system was at 24 °C and 1 atm with no vapor flow and no surfactant. The images were captured with 1024x1024 pixel resolution at 500 frames per second. Similar flow phenomena for the flow of water over a bank of 6 tubes (OD 12.7 mm, 25.4 mm tube-to-tube gap) are also shown.

(a) Schematic of Microchannels' Configuration for Visualization

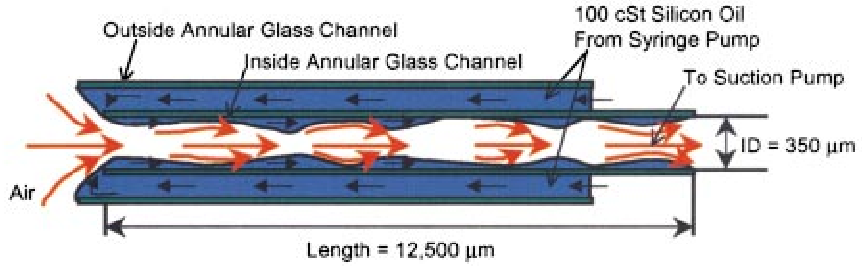

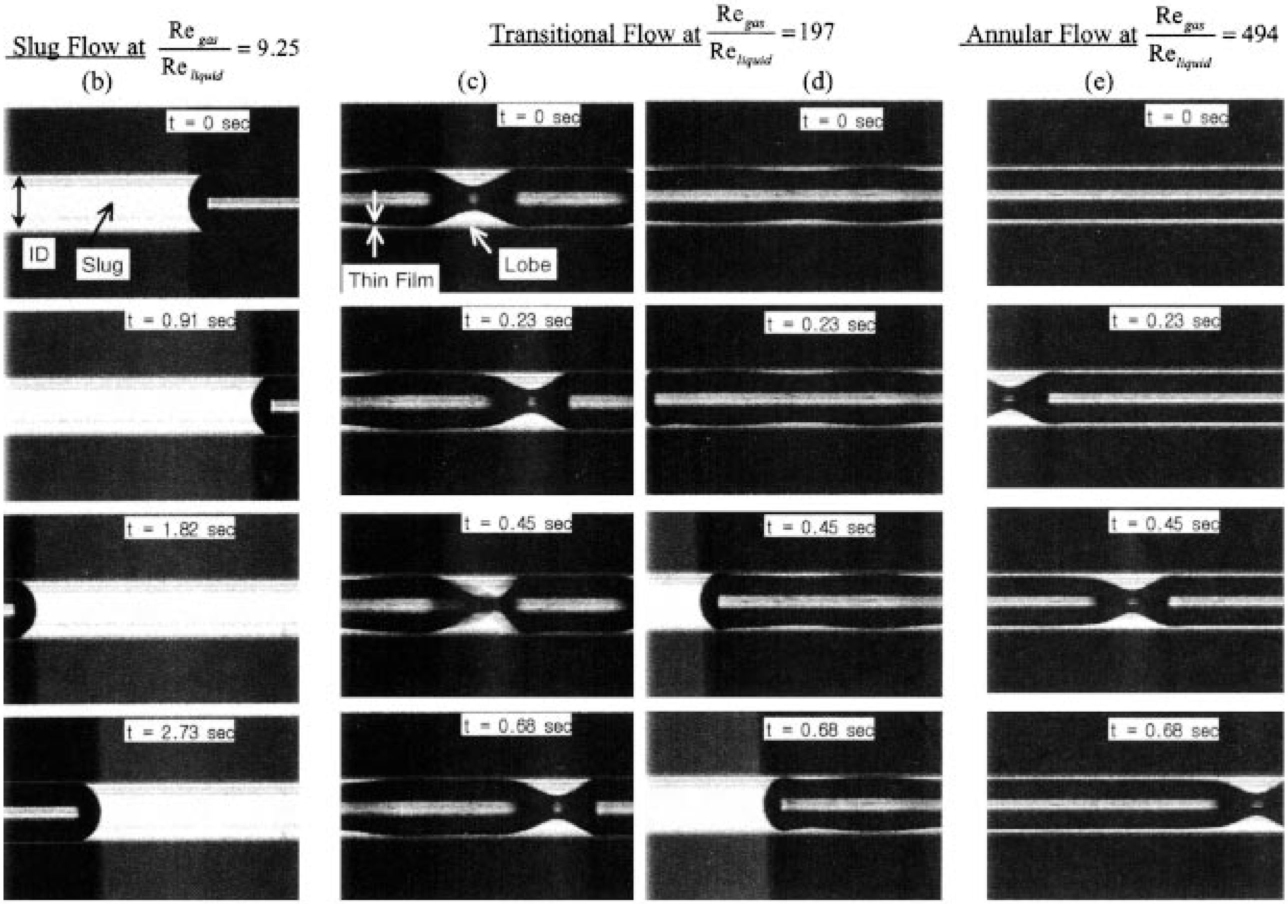

Low Bond Number Two-Phase Flow Regime Transition from Slug to Annular Wavy Flow in a Microchannel

Sang Young Son and Jeffrey S. Allen
National Center for Microgravity Research, Cleveland, OH
Kenneth D. Kihm
Texas A&M University, College Station, TX

The low Bond number flow ($Bo = 0.055$) regime transition from slug to core-annular flow is visualized. Visualization uses an annular microchannel with a length of 12,500 μm and inside diameter (ID) of 350 μm. An experimental set-up (a) is designed and applied for the visualization. The test configuration minimizes the entrance effect on the flow and maintains a constant mass flow rate of the liquid phase (100 cSt silicon oil). The flow regimes ((b), (c), (d), and (e)) are changing with respect to increasing the ratio of Reynolds numbers (Re_{gas}/Re_{liquid}). (b) is slug flow. (c) and (d) show two transitional modes of regime changing from core-annular to slug flow. In (c), the liquid film wave is amplified until liquid pinch-off occurs. (d) shows that the slug flow, which is generated upstream, penetrates the downstream liquid film wave. The conventional mode of transition such as churn flow or bubbly flow is not observed in this experimental conditions.

(a) SEM Image of fabricated artificial cavity

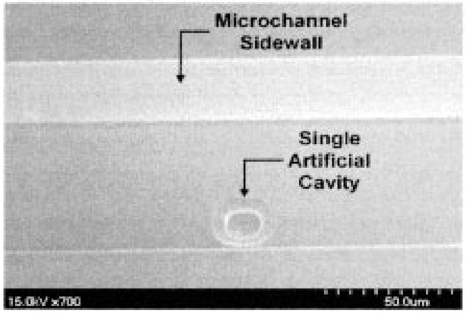

(b) Sequential images of bubble nucleation in flow boiling

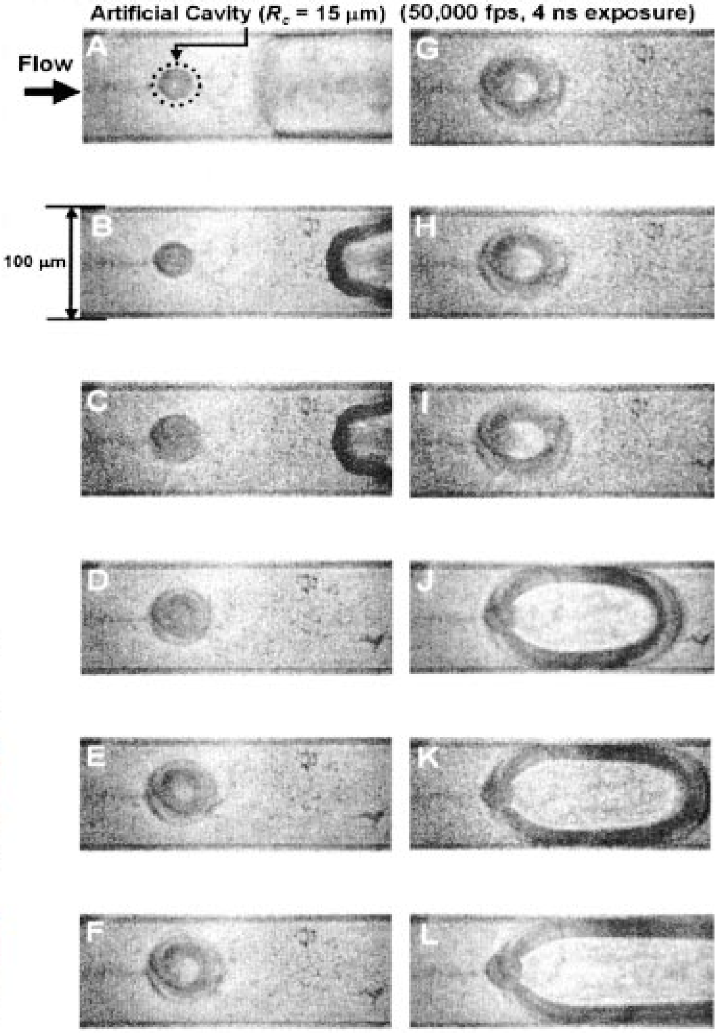

(c) Bubble growth rate in flow boiling

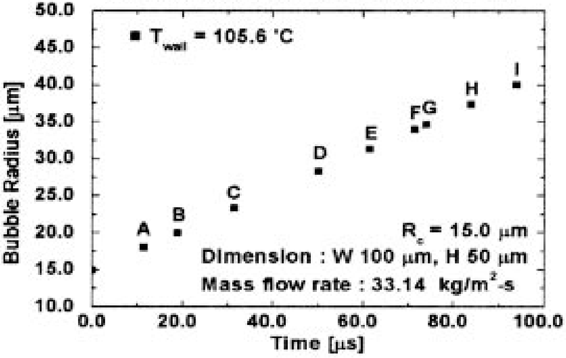

(d) Schematics of flow regime in flow boiling

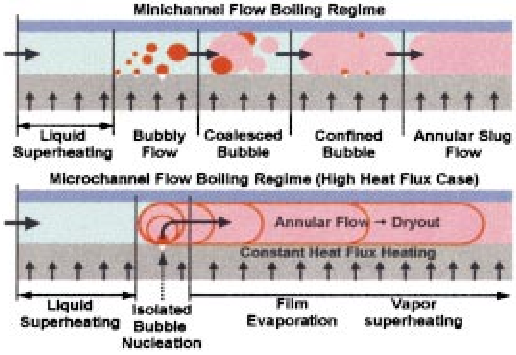

Microscale bubble nucleation from an artificial cavity in single microchannel

JaeYong Lee[*,***], KyungIl Cho[*], InSeob Song[*], ChongBo Kim[**], Sang Young Son[*,***]
[*] MEMS Lab, Samsung Advanced Institute of Technology, Korea
[**] Department of Mechanical Engineering, INHA University, Korea
[***]Corresponding Author, National Center for Microgravity Research, NASA Glenn Research Center, Cleveland OHIO

Bubble nucleation of flow boiling from a single artificial cavity has been visualized in a microchannel. Visualization uses 4ns pulse light at 532nm wavelength from two resonance Nd:YAG lasers for the illumination. And in order to take two sequential images, a progressive scan digital CCD camera with straddling technique at 50,000 frame per second. An integrated MEMS device is fabricated for the investigation. The device is composed with a single microchannel (D_h = 67μm), a single artificial cavity (Radius of Cavity (R_c) = 15μm) (**a**), visualization window, Pt-line heater for constant heat flux condition, and Pt-RTD temperature sensors on both sides. The visualized sequential images (**b**) are applied to map the bubble growth (**c**). The map (**c**) shows that the bubble growth rate is quite linear ((**b**), A-I) until the bubble forms as an annular flow ((**b**), K and L). A single bubble from a cavity explosively grows and fills whole downstream of channel without coalescence and confinement with other bubbles ((**b**), K and L). (**d**) schematically shows the difference in the flow regime development between meso- and micro-scale flow boiling.

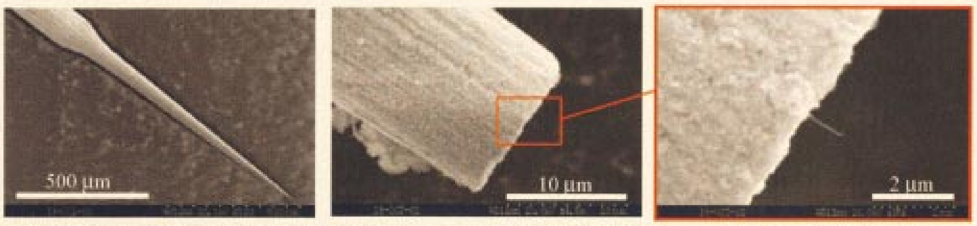

Fig. 1: Structure of probe tips and mounted carbon nanotubes (CNTs) for demonstrating the feasibility of nanoscale machining. (a) Tungsten probe fabricated using electro-chemical etching; (b) Tungsten probe with mounted single CNT; (c) Enlarged view of the mounted CNT on the probe.

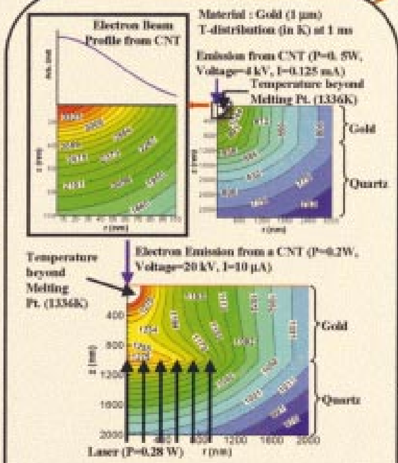

Fig. 2: Numerical modeling of the heat transport using a Monte Carlo method for electron transport, Fresnel equations and heat conduction equation.

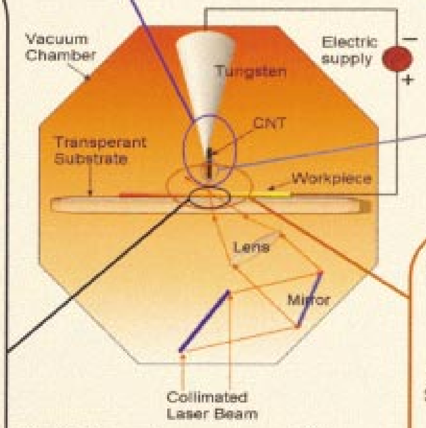

Fig. 3: Proposed nanoscale machining uses energy delivered by an electron beam emitted from CNTs and a collimated laser beam.

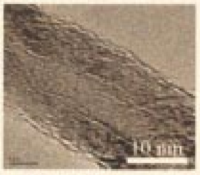

Fig. 4: Concentric walls in a MWNT

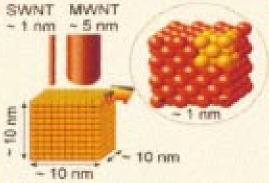

Fig. 5: The size comparison between CNTs and workpiece

Thermal Transport During Nanoscale Machining by Field Emission of Electrons from Carbon Nanotubes

C. Trinkle, Dr. P. Kichambare, and Prof. R. R. Vallance
Precision Systems Laboratory
Department of Mechanical Engineering
University of Kentucky
Lexington, KY 40506

B. Wong and Prof. M. P. Mengüç
Radiative Transfer Laboratory
Department of Mechanical Engineering
University of Kentucky
Lexington, KY 40506

B. Sadanadan and Prof. A. M. Rao
Department of Physics and Astronomy
Clemson University
Clemson, SC 29634

A. Bah and Prof. K. Javed
Chemistry Department
Kentucky State University
Frankfort, KY 40601

We are investigating a new process for nanoscale machining called Threshold Heating and Emission from Nanotubes (THEN). THEN is a hybrid process in which the total thermal energy necessary to remove atoms from a workpiece surface will be applied from two sources: (1) localized energy from a laser beam focused to a micron-scale spot and (2) a high-precision electron beam emitted from the tips of carbon nanotubes. Computational simulations of the process suggest that the thermal energy is sufficient to elevate the temperature of nanoscale regions on a gold film to well above melting "temperature." To experimentally validate the process and simulations, we are fabricating nanotools, similar to those used in scanning tunneling microscopy, that consist of multi-walled nanotubes (MWNTs) deposited by chemical vapor deposition on etched tungsten probe tips. This work is supported by an NSF Nanoscale Interdisciplinary Research Team (NIRT) award from the Nano Manufacturing program in Design, Manufacturing, and Industrial Innovation (DMI-0210559).

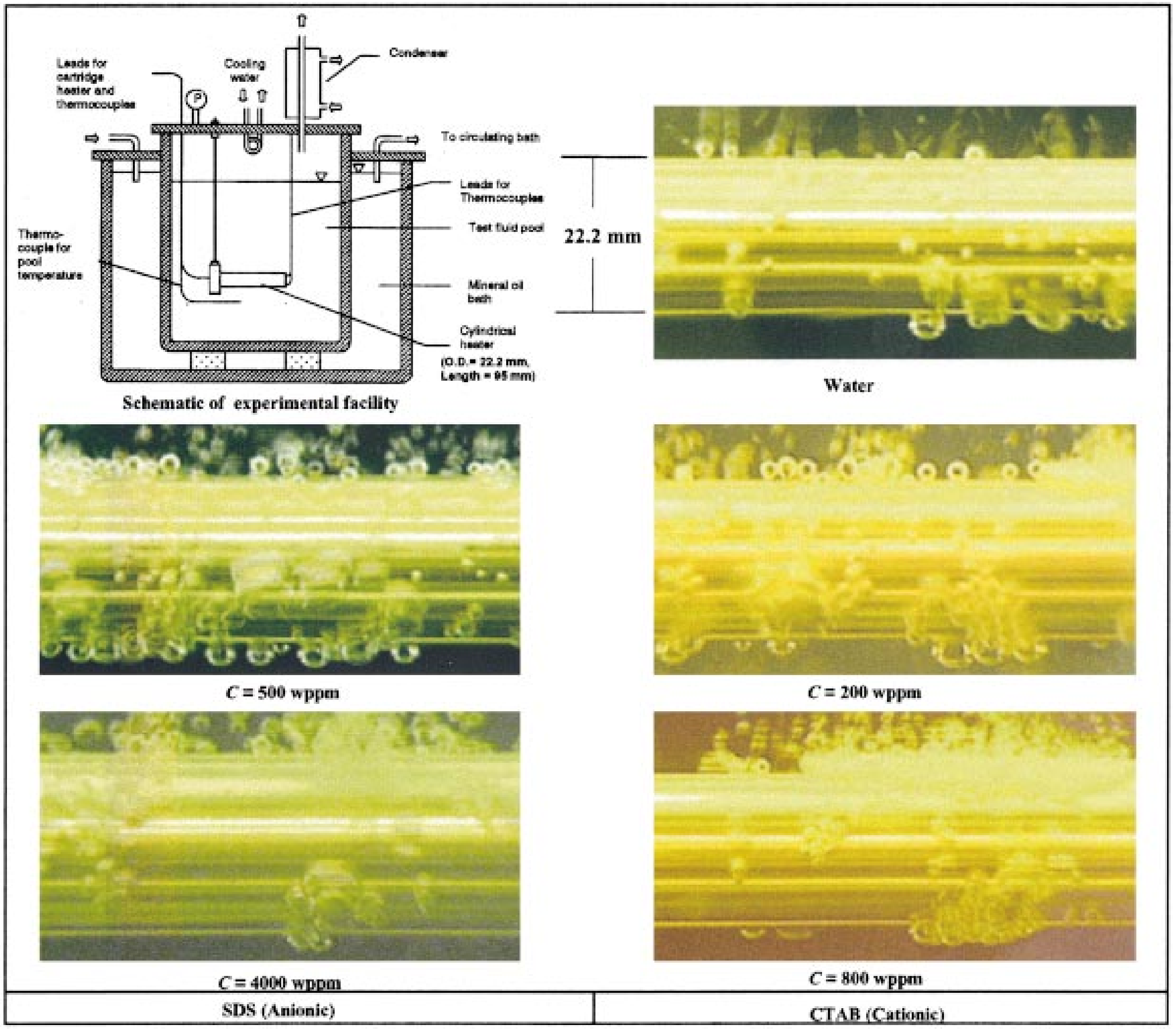

Fig. 1 Boiling behavior for distilled water, and aqueous SDS and CTAB Solutions at $q''_w = 20$ kW/m^2

VISUALIZATION OF EBULLIENT DYNAMICS IN SURFACTANT SOLUTIONS

Juntao Zhang and Raj M. Manglik
University of Cincinnati, Cincinnati, Ohio

Saturated, nucleate pool boiling behavior of aqueous surfactant solutions on a horizontal, cylindrical heater and the associated bubble dynamics has been experimentally observed. Two surfactants of different ionic nature, molecular weight, and critical micelle concentration, SDS (anionic, M = 288.3, c.m.c ≅ 2500 wppm) and CTAB (cationic, M = 365.4, c.m.c. ≅ 400 wppm) are employed, and the bubbling activity is recorded at different concentration levels. The growth of nucleating vapor bubbles and their motion near the cylindrical heater surface were recorded by a PULNiX TMC-7 high-speed color CCD camera with shutter speeds of up to 1/10,000 second. This is interfaced with a PC through a FLASHBUS MV pro image capture kit that has high-speed PCI-based bus mastering capabilities (up to 132 Mbytes/s). A FUJI 12.5 – 75 mm micro lens was used on the CCD camera to facilitate high quality close-up photography. The bubbling dynamics for SDS and CATB solutions of different concentrations and that of deionized distilled water are presented. Boiling in surfactant solutions is seen to be more vigorous in comparison to that in water, and is characterized by clusters of smaller-sized and more regularly shaped bubbles. With a significantly higher bubble departure frequency, there is virtually no coalescence of either the neighboring bubbles or sliding bubbles that come in contact with others around the heater's periphery when the surfactant concentration is smaller than c.m.c. However, in post-c.m.c. boiling, increased coalescence between vapor bubbles with considerable surface foaming is observed. Furthermore, the difference in bubble clusters and number of active nucleation sites in the ebullient behavior of SDS and CTAB, are reflective of their different ionic nature, molecular weight, and interfacial diffusion characteristics.

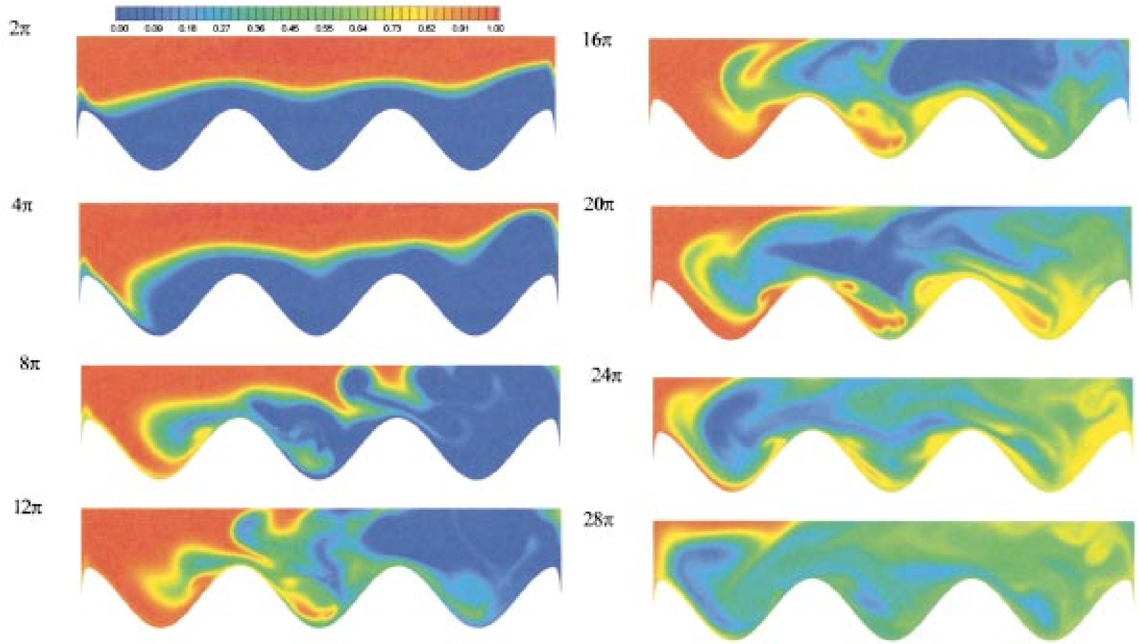

Fig 1. Time evolution of concentration contours for α=77.5, Pe=6,000 and ε/H=0.3

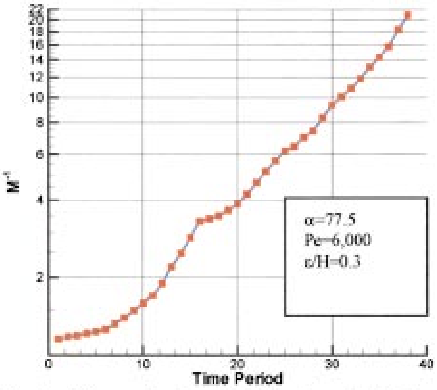

Fig 2. Time variation of M^{-1} for Pe=6,000 flow.

Mixing Index:

$$M = \frac{\sqrt{\sum_{i=1}^{N}\left(\frac{\theta_i}{\theta_o}-1\right)^2}}{(N-1)}$$

θ_i : Concentration at point *i*.

θ_o : Mean Concentration

N : Number of discrete points
(N=300,000)

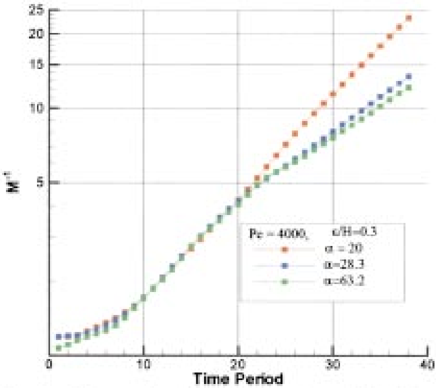

Fig 3. Time variation of M^{-1} for Pe=4,000 flow.

HEAT AND MASS TRANSFER IN A PERISTALTIC MICRO MIXER

S. Kumar and A. Beskok,
Texas A&M University, College Station, Texas

We present numerical simulation results of heat and mass transfer in a peristaltic micro-mixer. The device consists of a rectangular box with a traveling wave motion imposed on its flexible bottom surface. Parametric studies are performed as a function of the Stokes (α) and Peclet (Pe) numbers, and the normalized wave amplitude (ε^*). Due to the similarities between the heat and species transport equations, and the adiabatic thermal boundary conditions, the results are equally applicable to the species mixing and heat transfer analyses. Fig. 1 shows temperature contours for $\alpha=77.5$, $Pe=6{,}000$, $\varepsilon^*=0.3$ conditions, obtained at various times. Although the velocity and pressure fields are time-periodic with a normalized period of $T=\pi$, the heat and mass transport are unsteady. Initial conditions are chosen such that the final temperature of perfect mixture should reach $\theta_o=0.5$. At early times ($T<4\pi$), transport is diffusion dominated, since the flow field is also developing from quiescent conditions. For later times ($4\pi<T<40\pi$), we identify strong convective mixing, as shown in the temperature contours. Mixing efficiency is characterized using the Mixing index (M), which reaches zero for a perfect mixture. In Fig. 2, we present variation of the inverse Mixing Index (M^{-1}) as a function of the period. The semi-logarithmic plot shows almost exponential increase in M^{-1} for $20\pi<T$. In Fig. 3, we present time variation of M^{-1} for Pe=4,000 flows at various Stokes numbers.

2001 Max Jacob Memorial Award Lecture

John C. Chen
Carl R. Anderson Professor of Engineering,
Lehigh University,
Bethlehem, PA 18015

Surface Contact—Its Significance for Multiphase Heat Transfer: Diverse Examples

The nature and dynamics of surface contacts often govern heat transfer in multiphase systems. Physical scale, time scale, and intermolecular forces all affect basic mechanisms of transport between the multiphase medium and a submerged surface. Parameters in one or more of these domains can be the determining factor for transfer rate and efficiency, depending on the specific application. Research results for systems as diverse as fluidized particles and condensing liquids are examined to illustrate this significance. Specifically, it is shown that for heat transfer to/from surfaces submerged in bubbling fluidized beds, parameters in time domain are most important. In the case of condensation, it is shown that substantial enhancement of heat transfer coefficient can be obtained by controlling parameters in the domain of surface free energies. [DOI: 10.1115/1.1566050]

1 Introduction

Heat transfer between multiphase media and solid surfaces are encountered in applications as diverse as power generation, chemical processing, and biological systems. Examples are steam generators, vapor condensers, two-phase heat exchangers, distillation reboilers, fluidized bed reactors and combustors, and many others. In contrast to single-phase systems where basic transport mechanisms are mostly understood, the mechanisms for transport in multiphase systems still are mostly being developed. One reason for this is the complexity of interfacial contact at the surface, which is affected by intermolecular forces, varies with specific phases, influenced by dimensional scale, and is often of transient (dynamic) nature. One common cause of this complexity is the self-determining nature of phasic distribution found in multiphase media. Whether it's solid/gas distribution in fluidized media, or vapor/liquid distribution in two-phase flows, the local concentration and morphology of individual phases usually are not known a priori. The hundreds of research papers that are published each year in leading journals and conference proceedings attest to the importance of this subject, as well as to its unfinished state of development.

To design transport systems, engineers use a variety of approaches ranging over the spectrum from the purely empirical to the deterministic. From the viewpoint of applications, any approach (or combination of approaches) is acceptable if it promotes sound engineering design. Some well-known approaches can be located along this spectrum, as illustrated in Fig. 1. The placement of any single approach is a matter of judgment and subject to personal opinion. For example, one could argue that Fourier's law of conduction is a basic principle and should be placed toward the deterministic end of the spectrum. However, we note that when Josef Fourier published his treatise in 1822, he described the proportionality between conductive heat flux and temperature gradient as just an empirical relationship (see Lienhardt [1]). With better understanding of single-phase transport phenomena, more deterministic approaches are available for such systems, e.g., the Graetz solution for laminar convection. In contrast, design of multiphase transport systems currently rely heavily on heuristic experience, e.g., correlations for boiling curves. Fortunately, if one can identify the domain of governing parameters for surface contacts in a specific multiphase system, the difficulty of engineering design is much lessened. Whether it's parameters in spatial, time, energy, or other domains, once recognized we can utilize a combination of heuristic knowledge and phenomenological models for engineering design and/or to improve the transport process. This paper seeks to illustrate this point with examples from two diverse systems—heat transfer in fluidized beds and dropwise condensation.

2 Heat Transfer in Fluidized Beds, Significance of Parameters in Time Domain

2.1 Background. Fluidized bed is a unit operation in which gas flows upward through a bed of solid particles, suspending the particles against gravitational body force. The particles may remain suspended in the bed for a long residence time (dense-bubbling fluidized bed) or be transported through the bed with a short residence time (fast fluidized bed). In either case, the solid-gas contact is utilized to promote either physical processes such as heating/cooling, or chemical processes such as combustion or catalytic cracking (Kunii and Levenspiel [2]). In spite of its commercial success, the technology of fluidization still relies heavily

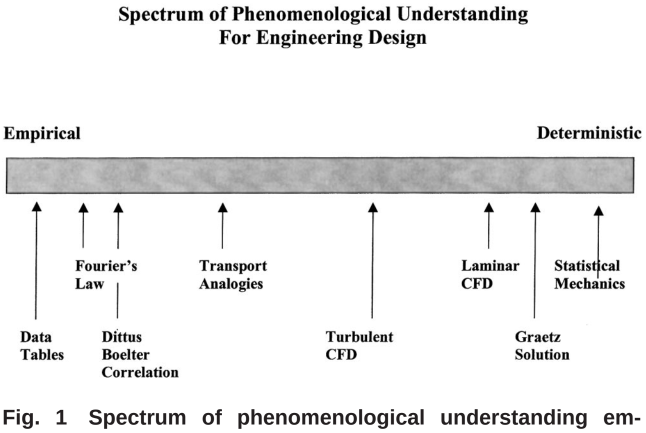

Fig. 1 Spectrum of phenomenological understanding employed in engineering design

---

Contributed by the Heat Transfer Division for publication in the JOURNAL OF HEAT TRANSFER. Manuscript received by the Heat Transfer Division August 16, 2002; revision received January 20, 2003. Associate Editor: V. Dhir.

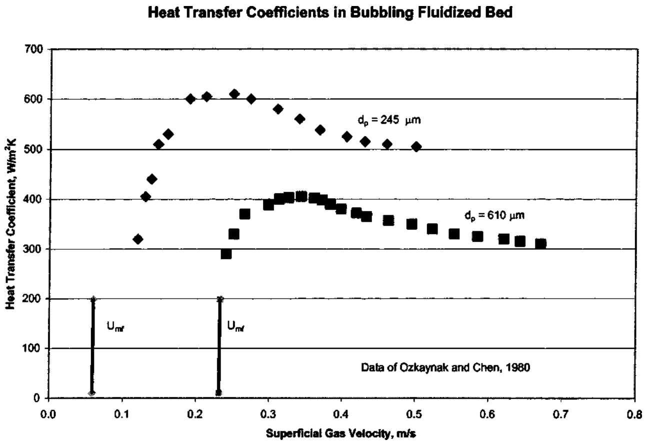

Fig. 2 Example of heat transfer coefficients at surface of vertical tube in bubbling fluidized bed

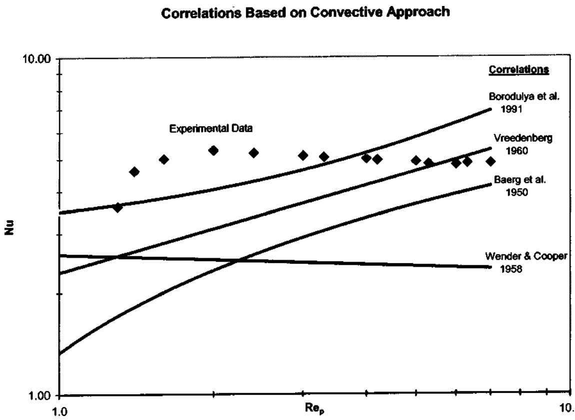

Fig. 3 Comparison of correlations to experimental data for heat transfer in bubbling fluidized beds

on heuristic knowledge with little in way of unifying theories. Merrow [3] estimates that manufacturing processes that involve solid particles often reach no more than 60% of their design capacity, far inferior to processes that deal with single-phase gases or liquids.

Many fluidized bed applications require thermal control by extraction or addition of thermal energy (e.g., heat removal in fluidized combustors). For this purpose, tubes carrying cooling/heating fluids are often immersed in the fluidized bed, hence requiring knowledge of the heat transfer coefficient (h) at the immersed (tube) surfaces for engineering design. Most applications rely on experimental measurements, which have been reported by various authors [4–10]. Typical results are illustrated by the sample data of Ozkaynak and Chen [4] for spherical glass particles fluidized in ambient air, replotted in Fig. 2. Significant characteristics are:

- Heat transfer coefficient (h) increases steeply as gas velocity exceeds minimum fluidization velocity (U_{mf}).
- The heat transfer coefficient attains maximum magnitude at some specific velocity that varies with particle size.
- Beyond the maximum point, h declines slightly with further increase of gas velocity.
- Absolute magnitude of h is several fold greater than obtained by single-phase gas convection at similar velocities.
- The heat transfer coefficient decreases with increasing particle size.

Heat transfer tubes located vertically in the fluidized bed, as the case for data of Fig. 2, have axial symmetry due to alignment with gravitational body force. Tubes located horizontally do not have such axial symmetry and one finds significant variations of the local coefficient around the tube circumference. Chandran et al. [5] reported variations up to 500% in h at different positions on the tube surface, for a given operating condition.

2.2 Models. To date, there is no universally accepted theory for the mechanisms of heat transfer in fluidized beds. It is generally recognized that gaseous convection, conduction through contacting particles, and thermal radiation can all contribute to heat transfer between the fluidized medium and immersed surfaces. For most applications, the combined "convection" due to gas and particles is the major contributor and has been the objective of predictive models.

A common approach assumes similarity to gaseous convection and assigns thermal resistance to a boundary layer at the heat transfer surface [6,8,9–11]. The enhancement found at gas velocities greater than U_{mf} is attributed to "scouring by solid particles, decreasing the effective film thickness." Models following this approach attempt to correlate a Nusselt number with the fluid Prandtl number, a modified Reynolds number and the Archimedes number, using either the particle diameter (d_p) or the tube diameter (d_t) as the characteristic length dimension. This approach has led to dozens of empirical correlations, an example being the correlation of Borodulya et al. [11],

$$\mathrm{Nu}=0.74(\mathrm{Ar})^{0.1}\left(\frac{\rho_s}{\rho_g}\right)^{0.14}\left(\frac{c_{ps}}{c_{pg}}\right)^{0.24}(1-\varepsilon)^{0.67}+0.46(\mathrm{Re}_p\mathrm{Pr}_g)\frac{(1-\varepsilon)^{0.67}}{\varepsilon} \tag{1}$$

where,

$$\mathrm{Nu}\equiv\frac{hd_p}{k_g}$$

$$\mathrm{Re}_p\equiv\frac{d_p\rho_g U}{\mu_g}$$

$$\mathrm{Ar}\equiv\frac{gd_p^3(\rho_s-\rho_g)}{\rho_g\nu^2}$$

ε = void fraction, volume fraction gas.

Figure 3, modified from Chen [12], compares several different correlations against each other and against a set of experimental data, for ambient-pressure fluidization of 240-micrometer glass beads. It is seen that there is very little agreement between the various correlations and with data, with deviations of order 100%. A fairly recent model suggested by Molerus and Schweinzer [13] considers gas convection through the matrix of particles in vicinity of the heat transfer surface. This model resulted in a dimensionless correlation for the Nusselt number in terms of the Archimedes number and the fluid Prandtl number, at velocities above U_{mf}. This correlation was limited to large particles (i.e., Geldart group D particles) and would significantly under-predict the data of Fig. 3. While all such empirical, convective correlations are easy to use, their generality is questionable.

A variation of the convective model is that of Martin [14–16] who proposed an analogy between particle motion in fluidized beds and random motion of gaseous molecules. Utilizing kinetic theory of gases, Martin developed a model with just one empirical parameter to predict heat transfer coefficients in fluidized beds. Good results were reported when the model was compared with experimental data from several sources (Martin [16]). Despite this success, the kinetic theory analogy has been challenged by investigators who note that the nature of alternating contacts between particle emulsion and gas bubbles in fluidized beds is qualitatively different than that of contact by particles in random motion.

For "large" particles, typically with diameters greater than 1 mm, whose thermal response time is long, a contact resistance approach has been suggested. Such models assume that the average temperature of particles does not change while in contact with the heat transfer surface, and thus utilize pseudo-steady-state conduction analysis. Adams and Welty [17] analyzed gas convection enhanced conduction in the interstitial channels between the surface and particles, resulting in numerical solutions for distribution of Nusselt numbers around horizontal tubes. In a similar vein, Decker and Glicksman [18] utilized empirical correlations for convective heat transfer of packed beds to estimate the convective/conductive transfer of particles on surfaces submerged in fluidized beds. Clearly, such approaches are unlikely to be valid for fluidization of small or medium size particles as encountered in many chemical and combustion applications.

2.3 Mechanisms and Time Domain Effect. Mechanistically speaking, it is questionable if steady-state convection is an accurate analogy for heat transfer in fluidized beds. Visual observations in actively bubbling beds indicate that the particle emulsion actually remains fairly static, until disturbed by discrete gas bubbles rising through the bed. Phenomenologically, the best model for fluidized bed heat transfer may well be the "packet model" suggested by Mickley and Fairbanks [19] nearly half a century ago in 1955. They considered the heat transfer surface to be alternately contacted by gas bubbles and an emulsion of closely packed particles (packets). This leads to a surface renewal process whereby heat transfer occurs primarily by transient conduction between the emulsion packets and the surface during periods when the particle packets reside at the heat transfer surface. One then would need to know the distribution of packet residence times and the fraction of total time with packet contact—hence attention is focused on parameters in the time domain.

Three decades after Mickley and Fairbank's paper, this basic concept was experimentally confirmed by researchers who were able to measure transient variations of particle concentration at heat transfer surfaces. Surface capacitance sensors with flush mounted electrodes of the type shown in Fig. 4, redrawn from Ozkaynak and Chen [20], utilized the difference of dielectric constants between gas and solids to obtain real-time measurements of fluctuating particle concentration at surfaces immersed in fluidized beds. With appropriate electronic circuits operating in range of several hundred kilohertz, such sensors had response times several orders of magnitude faster than the characteristic time scale of particle dynamics.

Figure 5 shows a sample trace obtained by Chandra and Chen [21], indicating the transient variation of particle concentration at sides of a horizontal tube immersed in a fluidized bed of glass beads (mean diameter of 245 micrometers), operating at superficial air velocity of 0.63 m/s (12 times minimum fluidization velocity). It is seen that the particle concentration is highly dynamic, varying dramatically over time. It is also seen that the instantaneous concentration mostly alternated between almost pure gas (bubble phase) and high concentration approaching that of packed beds (emulsion packet phase). This is the behavior hypothesized by Mickley and Fairbanks. Such evidence of highly transient contacts lends support to the surface renewal model, where the time average heat transfer coefficient (h) has proportional contributions from the bubble phase coefficient (h_b) and packet phase coefficient (h_p),

$$h=(1-f_p)h_b+(f_p)h_p \tag{2}$$

where f_p is the fraction of time when surface is in contact with the dense packet phase. Treating the particle packet as a pseudo-homogeneous medium of solid volume concentration $(1-\varepsilon)_p$ Mickley and Fairbanks' transient conduction analysis yielded the following equation for average packet coefficient,

$$h_p=2\left[\frac{k_p\rho_s c_{ps}(1-\varepsilon)_p}{\pi\tau_p}\right]^{1/2} \tag{3}$$

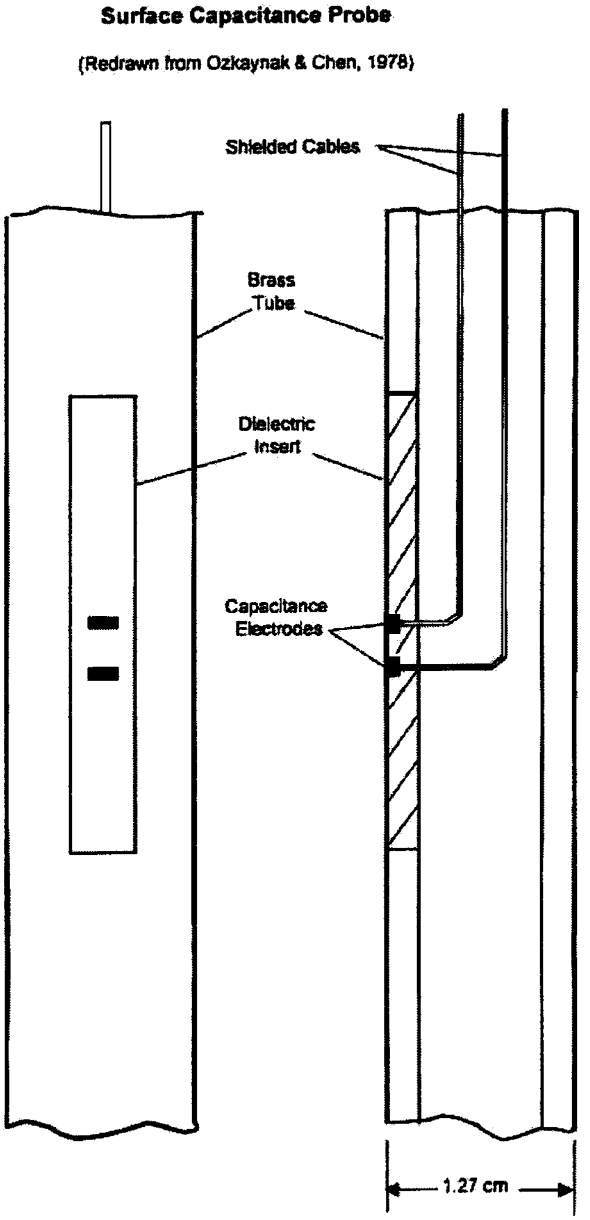

Fig. 4 Probe for measurement of solid volume fraction at surface of heat transfer tube in fluidized beds

where τ_p is the root-mean residence time of packets at the heat transfer surface,

$$\tau_p\equiv\left[\frac{\sum_{i=1}^{i=n}(\tau_p)_i}{\sum_{i=1}^{i=n}\sqrt{(\tau_p)_i}}\right]^2 \quad \text{for stochastic number of } n \text{ packets.} \tag{4}$$

If one accepts the fact that h_b is small in comparison to h_p, then the Mickley-Fairbank model reduces to the following equation for effective heat transfer coefficient in bubbling fluidized beds,

$$h\cong f_p h_p=2\,f_p\left[\frac{k_p\rho_s c_{ps}(1-\varepsilon)_p}{\pi\tau_p}\right]^{1/2} \tag{5}$$

All parameters in Eq. (5) can be evaluated from properties of the solid particles and gas, with the exception of the two time-domain parameters f_p and τ_p. Therein lies the difficulty. These two im-

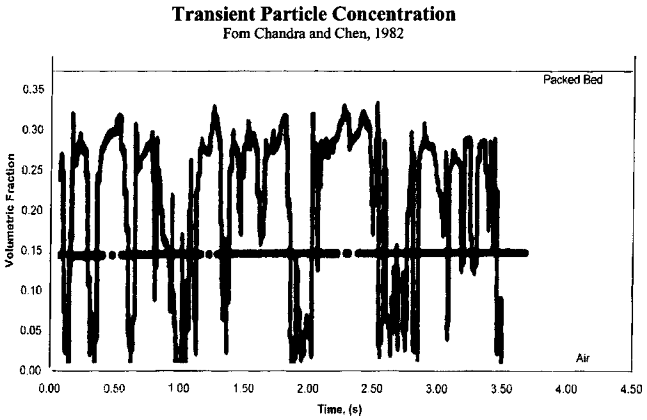

Fig. 5 Capacitance signal of particle concentrations at heat transfer surface in bubbling fluidized bed

portant parameters in the time domain depend on the multiphase fluid dynamics of the fluidized bed and to a large extent are not known a priori.

Some limited information on these time parameters were obtained using the capacitance-sensors and have been reported in the open literature. For the case of vertical tubes in bubbling beds, Ozkanak and Chen [4] found that the probability distribution of residence times for particle packets is log normal. The root-mean residence times vary with particle density, particle size, gas properties, gas velocity and bed geometry. Figure 6 plots some of their experimental results, showing that the mean residence time (τ_p) increases with particle diameter (d_p). These data also indicate exponential decrease of the mean residence time with increasing excess gas velocity above minimum fluidization velocity, $U\text{-}U_{mf}$. The latter characteristic is consistent with observations that excess gas velocity increases bubble frequency, so that packets residing on the heat transfer surface are more frequently displaced. In a similar vein, Ozkaynak and Chen [4] reported measurements of the time fraction when the heat transfer surface is covered by particle packets (f_p), as replotted in Fig. 7. The time fraction is seen also to increase with particle size, and decrease with excess gas velocity.

The situation for heat transfer tubes placed horizontally in fluidized beds is even more complex and unknown. Measurements of parameters in the time domain reported by Chandran and Chen [21] indicate that the absence of axial symmetry causes large variations in both time-fraction (f_p) and residence-time (τ_p) around the tube circumference, with resultant variations in the heat transfer coefficient (h). These authors attempted correlations for f_p and τ_p, but recognized that much more data are required before any general correlations could be realized.

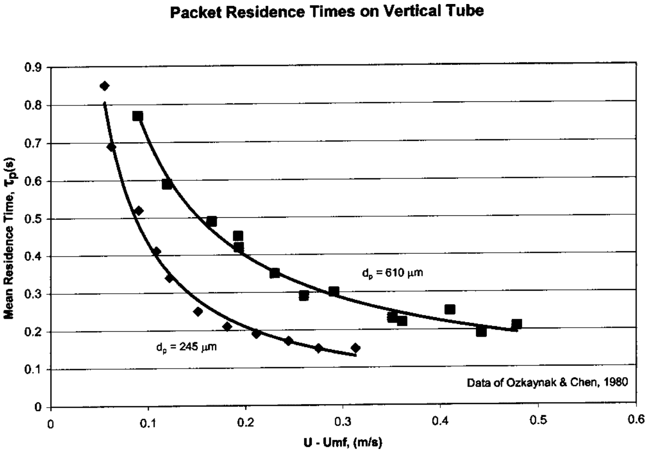

Fig. 6 Residence times of particle packets at surface of heat transfer tube in bubbling fluidized bed

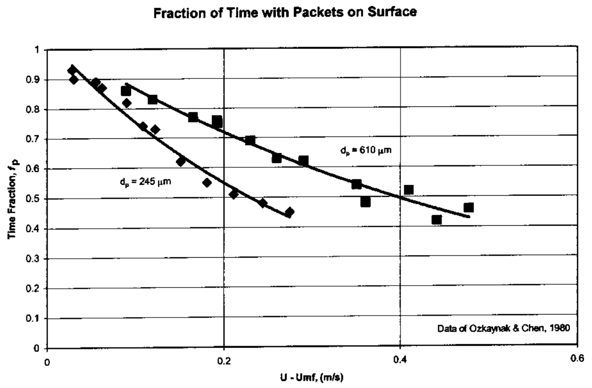

Fig. 7 Fraction of time with particle packets at local position on heat transfer surface in bubbling fluidized bed

The data of Fig. 6 implies an added complication in the time domain. With residence times of order <1s, the Fourier modulus for transient conduction in the particle packets would be of order,

$$Fo \equiv \frac{k_p \tau_p}{\rho_s c_{ps}(1-\varepsilon)_p d_p^2} \leq O[10] \tag{6}$$

This magnitude of the Fourier modulus implies that the conduction waves in the emulsion packets may penetrate distances of only a few particle diameters during the residence period, τ_p. Since packing density of particles is reduced in the first layer of particles at a solid wall, one should account for the corresponding reduction of effective thermal conductivity in this near-surface region. It is therefore desirable to modify the Mickley-Fairbanks' packet model, originally proposed for emulsion packets with uniform voidage and properties. Chandran and Chen [22] obtained numerical solutions of the transient conduction problem, resulting in a correction factor (C_k) to account for this variation of thermal conductivity in the first layer of particles at a surface. An easier approach is to use effective packet properties, taken at one-half the penetration depth of the temperature wave for the given operating condition.

From solution of the transient conduction equation, we find the penetration depth (ξ), defined as the distance into the packet emulsion where 90% of the temperature change is obtained in residence time τ_p, to be given by

$$\operatorname{erf}\left(\frac{\xi}{2}\sqrt{\alpha_p \tau_p}\right) = 0.9$$

$$\xi \cong 2.32\sqrt{\alpha_p \tau_p} \tag{7}$$

where

$$\alpha_p \equiv \frac{k_p}{\rho_s c_{ps}(1-\varepsilon_p)}. \tag{8}$$

At positions within one particle diameter of the heat transfer surface, we can use an approximation of the local void fraction by fit to the results of Kubie and Broughton [23],

$$\varepsilon_x = 1 - 2.04(1-\varepsilon_p)\left(\frac{x}{d_p}\right)\left(1 - 0.51\left(\frac{x}{d_p}\right)\right). \tag{9}$$

At positions greater than one d_p from the surface, the local void fraction and packet properties are equal to the values at bulk emulsion voidage, ε_p. It is suggested that the packet model of Mickley and Fairbanks be modified for cases where $\xi/2 < d_p$ by taking effective thermal conductivity of the emulsion packet at

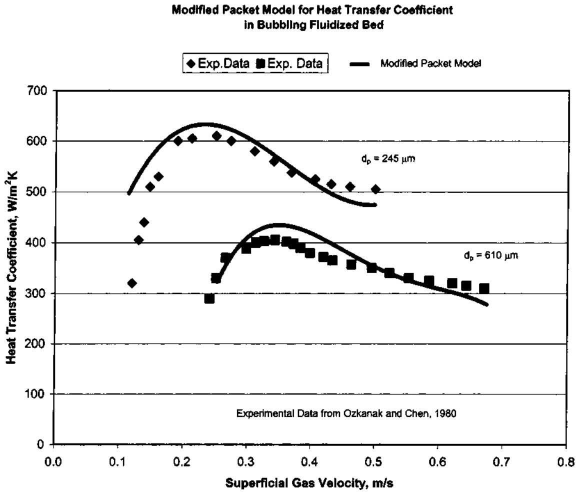

Fig. 8 Comparison of modified packet model, using time domain parameters, with experimental data for heat transfer in bubbling fluidized beds

position of $\xi/2$. By correlation of results presented by Kunii and Smith [24] for packed media with stationary fluid, in the range of interest,

$$k_p = a k_g \left(\frac{k_s}{k_g} \right)^b$$

$$a = 3.5 - 2.5\varepsilon \tag{10}$$

$$b = 0.46 - 0.46\varepsilon$$

where, for $\xi/2 \geqslant d_p$,

$$\varepsilon = \varepsilon_p, \quad \text{the bulk void fraction in emulsion packet,} \tag{11}$$

$$\text{approximately equal to } \varepsilon \text{ at } U_{mf},$$

and for $\xi/2 < d_p$,

$$\varepsilon = 1 - 2.04(1 - \varepsilon_p)\left(\frac{\xi/2}{d_p} \right)\left(1 - 0.51\left(\frac{\xi/2}{d_p} \right) \right). \tag{12}$$

The modified "packet model" is then given by Eqs. (5, 10, 11, or 12).

At present time, there are insufficient measurements of the key time parameters f_p and τ_p to fully test this model. However, it is appropriate to ask the question: for cases where the time-domain parameters are known, can the packet theory accurately predict heat transfer coefficients? Equation (5) indicates that decreasing f_p and τ_p has opposite effects on magnitude of *h*. Would the trends indicated in Figs. 6 and 7, when applied to Eqs. (5, 10, 11, 12), give correct magnitude and trend for the effective heat transfer coefficient, *h*? To test this issue, we can use the data for τ_p and f_p shown in Figs. 6 and 7 in equations (5, 10, 11, 12) and compare the calculated values of *h* to the experimentally measured heat transfer coefficients of Fig. 2. This was done, based on the mean curves for τ_p and f_p shown in Figs. 6 and 7, respectively. These values of the time parameters were then utilized in the modified packet model, equations (5, 10, 11, 12), to calculate predicted values for the heat transfer coefficient, *h*. Results are compared to experimental values of *h* in Fig. 8, over a range of gas velocities and for two different sizes of particles. While the agreement is not perfect, the comparison is quite satisfactory. The modified packet model gives good representation of the magnitudes of *h*, as well as the trends for parametric variations with gas velocity and particle size. For both size particles, the modified model calculated increasing *h* as gas velocity exceeded U_{mf}, reaching a maximum at some intermediate velocity, and then decreasing slowly with further increases of gas velocity. Comparing Fig. 8 and 3, it is seen that this modified packet model is substantially better than the empirical convective models in its ability to calculate effective heat transfer coefficients for fluidized beds. Of course, additional comparisons with more extended data would be very desirable.

Based on this limited assessment, we suggest the following conclusion: Heat transfer to surfaces submerged in bubbling fluidized beds is governed by parameters in the time domain, namely the mean residence time (τ_p) and the time-fraction of residence (f_p) of emulsion packets at the surface. With information on these two parameters, the modified packet model can provide predictions of the heat transfer coefficient, *h*.

2.4 Further Developments.

Further development of this approach depends on the acquisition of knowledge about the two time-domain parameters, τ_p and f_p. Lacking such, it is still impossible to calculate heat transfer coefficients a priori, for engineering design. The goal is to obtain sufficient knowledge for prediction of τ_p and f_p for process conditions (e.g., solid and gas properties, system geometry, gas velocity) in any application. This author suggests that this goal can be attained by a combination of two tasks.

First, the technical community can collect an extended database of experimental measurements of τ_p and f_p, over wide range of operating conditions. Empirical correlations can then be developed for these two time-domain parameters, and utilized in the modified packet model for calculation of heat transfer coefficients. The capacitance sensing technique, as referenced above, is one means for achieving such measurements. Other techniques, e.g., optical probes, may also prove to be useful. The range of experimental conditions needs to cover conditions of anticipated applications, including variations in gas pressure and temperature, as well as different type/size of particles and different bed geometries.

A second, complimentary task is to develop deterministic models for the dynamics of particle movement in fluidized beds. Such models must correctly represent particle-fluid, particle-particle, and particle-wall interactions. In recent years, promising progress has been made with two types of multi-phase models. Firstly, continuum models using local averaging at the scale of the computational cell have treated the gas and solid phases as interpenetrating continuum media. The resulting Navier-Stokes equation is then solved by computational fluid dynamic (CFD) techniques. Examples of this type of models are the works of Anderson and Jackson [25] Gidaspow [26], Hrenya and Sinclair [27]. These CFD models have been able to determine bed pressure drop and average bed porosity. The main difficulty with this continuum approach is the need for constitutive relations to describe the interfacial transfer of mass/momentum/energy between the interpenetrating media. These constitutive relations, mostly of empirical nature, are required to obtain closure of the problem. Van Wachem et al. [28] concluded that the selection of specific constitutive relationships could alter the model predictions significantly. Quoting these authors,"—we have shown how the hybrid drag model proposed by Gidaspow [26] produces a discontinuity in the drag coefficient, how an order-of-magnitude difference in the normal stress is predicted by the various frictional stress models—." Another difficulty for the present objective, is the length scale—the local averaging at scale of computational cell is usually too coarse to follow dynamic variations of particle emulsion at heat transfer surfaces. Excellent reviews of the potentials and limitations of such CFD models are given by van Wachem, J. C. Schouten et al. [28] and by Arastoopour [29].

An alternate to the continuum model is the discrete particle model (DPM) using Lagrangian formulation. Introduced by Cundall and Strack [30] for granular flow, DPM tracks the motion of particles by direct application of Newton's second law of motion to the collision process of individual particles. This approach provides deterministic representation of particle-particle and particle-wall interactions. In the recent decade, researchers have extended the DPM approach to account for fluid-particle interactions, concentrating initially on the drag force exerted by the fluid upon particles (see for example Tsuji et al. [31], Drake and Walton [32], Langston et al. [33]). More recently, several researchers further extended DPM models to account for effects of mutual momentum transfer between the fluid and particle phases, thus making this approach useful for fluidized beds where such interaction is important. The simultaneous tracking of particle collisions and gas motion calls for the direct integration of the Lagrangian discrete particle model with the Eulerian CFD continuum model. With various simplifying approximations, Tsuji et al. [34] and Hoomans et al. [35] have successfully applied this approach to model bubbling fluidized beds, with some limitations. Xu and Yu [36] and Xu et al. [37] were able to relax some of these limitations with more rigorous combination of CFD with DPM, using a collision dynamic model that better represents stiff particles. These researchers also introduced Newton's third law of motion to obtain a rigorous coupling between the particle scale of DPM and the larger cell-scale of CFD. Van Wachem, J. van der Schaaf et al. [38] compared Lagrangian-Eulerian simulations with experiments and concluded that two-dimensional simulations are in fair agreement with experiments but that three-dimensional simulation is required to capture more precisely the behavior of fluidized beds. While a detailed review of such Lagrangian-Eulerian models is beyond the scope of the present paper, a brief synopsis is warranted, in view of the promise of this approach for advancing the state of art toward prediction of heat transfer in fluidized beds.

The essence of discrete particle model (DPM) is the conservation of linear and rotational momentum of the particles as they undergo particle-particle, particle-wall and particle-gas interactions. Following Xu and Yu, [36], this can be expressed by Newton's 2nd law of motion for a particle,

$$m_i \frac{d\nu_i}{dt} = m_i g + f_{gi} + \sum_{j=1}^{k} (f_{cij} + f_{dij}) \tag{13}$$

$$I_i \frac{d\omega_i}{dt} = \sum_{j=1}^{k_i} T_{ij} \tag{14}$$

where m_i, υ_i, I_i, ω_i are the mass, linear velocity, moment of inertia, and rotational velocity of particle *i*, respectively. Forces acting upon particle *i* are the gas drag force (f_{gi}), the contact force between particles *i* and *j* (f_{cij}), and the contact damping force between particles *i* and *j* (f_{dij}). T_{ij} is the torque generated by interparticle contact, as measured to the mass center of particle *i*. On the fluid side, using local mean variables over a computational cell, computational fluid dynamics (CFD) are based on the continuity and Navier-Stokes equations,

$$\frac{\partial \varepsilon}{\partial t} + \nabla \cdot (\varepsilon u) = 0 \tag{15}$$

$$\frac{\partial(\rho_g \varepsilon u)}{\partial t} + \nabla \cdot (\rho_g \varepsilon u u) = -\nabla p - F + \nabla \cdot (\varepsilon \tau) + \rho_g \varepsilon g \tag{16}$$

where ρ_g, ε, *u*, *p* are the gas density, void fraction, velocity and pressure, respectively. *F* is the volumetric interaction force between gas and particles, and τ is the viscous stress tensor. To obtain closure of this problem, one needs specific descriptions (constitutive relations) for the various terms in Eqs. (13–16). Much of the science and art for these combined Lagrangian-Eulerian models lies in the formulation of these constitutive relations, and the reader is referred to the works of Xu and Yu [36], Hoomans et al. [35], and Xu et al. [39].

Numerical simulation of bubbling fluidized beds requires significant computing power, and this is on the horizon as larger parallel computing systems become available. At the time of this writing, researchers have successfully achieved two-dimensional simulations with $O[10^4]$ number of particles. While this level is not quite sufficient for our purpose of predicting heat transfer coefficients on submerged surfaces, the qualitative results show good promise. Figure 9 presents simulation results obtained by Xu and Yu [36] for a two-dimensional bed (15 cm width) of 4.0 mm diameter particles, fluidized at superficial gas velocity of 2.8 m/s by a single gas jet. It is seen that characteristic bubbling behavior is obtained. Figure 10 shows dynamic variations of void fraction, obtained by simulation for a two-dimensional bed of particles fluidized by atmospheric air. The gradations of color and shade indicate instantaneous voidages in the bed. One can expect that if a heat transfer tube were submerged in this bed, the simulation would predict the dynamics of alternating contact with gas bubbles and packets of particle emulsion. While this figure presents only 0.09 seconds of the transient dynamics, it is obvious that simulation for longer time duration would give stochastic information on the time-domain variables of interest, τ_p and f_p, for any Eulerian control volume at the heat transfer surface. While such simulation results would need to be confirmed by comparison to experimental data, one hopes that success can be achieved with ever improving models.

In conclusion, we can anticipate in the future that the accumulation of experimental measurements and numerical simulation results for the time-domain parameters, mean residence time τ_p and time fraction f_p, will enable the engineering community to utilize the modified packet model to obtain a priori predictions of heat transfer coefficients in bubbling fluidized beds.

3 Dropwise Condensation, Significance of Parameters in Surface Energy Domain

3.1 Background. It is known that vapor in contact with a cold surface of temperature below saturation dew point can condense on that surface as a liquid film, as liquid drops, or as a mix of the two patterns. Filmwise condensation occurs when the condensate liquid wets the solid surface, most likely on surfaces with high free energies. Dropwise condensation occurs when the solid surface has low free energy and is poorly wetted by the condensate liquid. Observations of dropwise condensation indicate a highly transient, cyclic process—the condensate nucleating as small droplets on the cold surface, which then grow and coalesce into larger drops. When the large drops reach a size sufficient to be removed from the surface by external forces (e.g., gravity or vapor shear), they tend to sweep over the surface, absorbing and wiping small droplets in their path. New droplets then form and grow on the wiped surface, repeating the cyclic process. Figure 11 shows a normal-view photograph of dropwise condensation, from Lienhard [1]. It is seen that at a given moment, drops of various sizes exist on the solid surface. In Fig. 11, one can particularly note the region above the large central drop, showing a path that was wiped by passage of that large drop in which smaller drops are nucleating and starting to grow. On dimensional scale of drops, the heat transfer process is highly transient over time and variable over space. However, on the system scale, a large number of drops and droplets would exist on the solid surface at any one time, each in its own history of nucleation, growth and removal. Over a sufficiently large surface, one can thus anticipate an average heat transfer behavior that is essentially at steady state for a given set of process conditions.

A condensation heat transfer coefficient is commonly defined as the ratio of surface heat flux to the degree of subcooling temperature on the surface,

$$h_c \equiv \frac{q}{\Delta T_s} \tag{17}$$

where $\Delta T_s \equiv T_s - T_w$. In filmwise condensation, the heat flux is controlled by the thermal resistance of the liquid film and therefore the mechanism of film removal directly affects the heat transfer coefficient. In case of film condensation on a vertical wall, where gravitational body force causes film removal, the classic

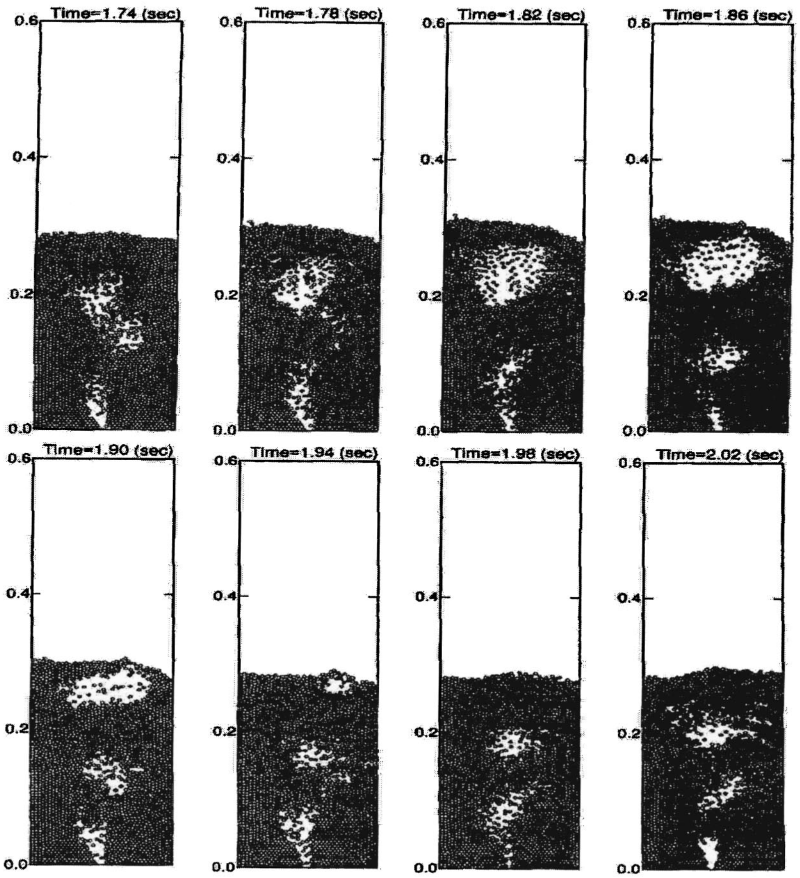

Fig. 9 Numerical simulation of fluidized bed by combined Eulerian-Lagrangian model [36]

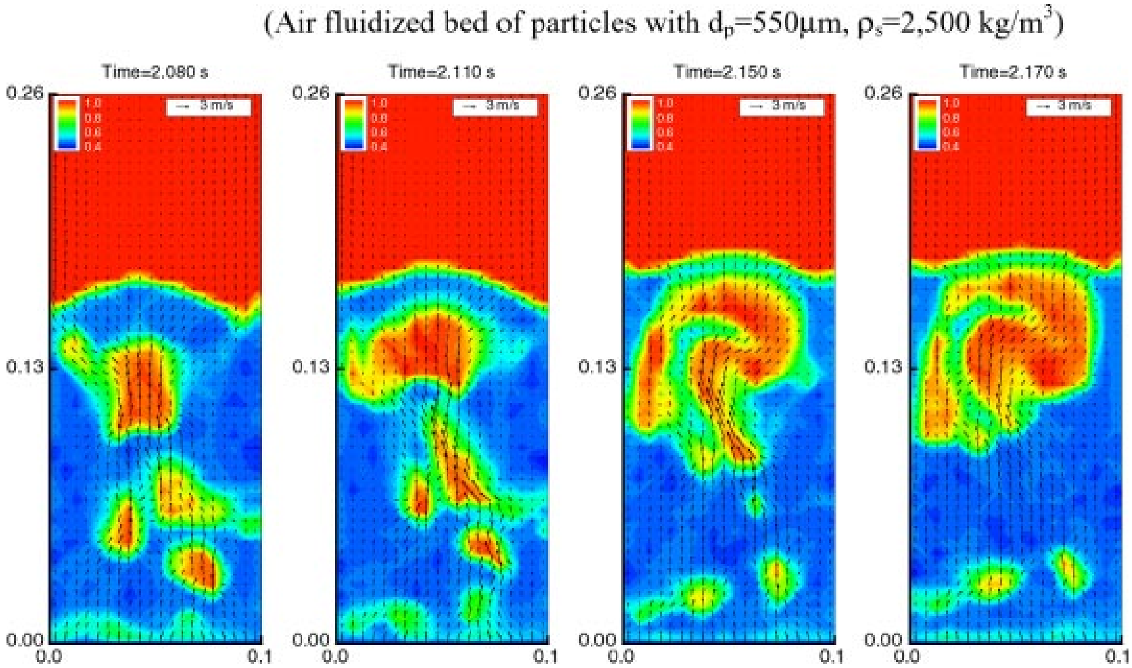

Fig. 10 Void fractions obtained from combined Eulerian/Lagrangian simulation model for a bubbling fluidized bed [39]

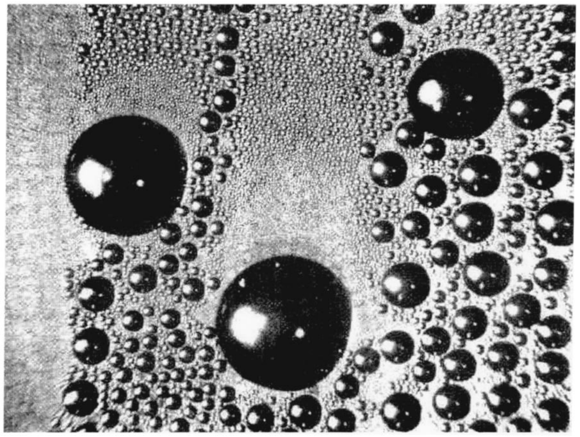

Fig. 11 Dropwise condensation on vertical surface, photo from Lienhard [1]

Nusselt analysis (1916) [40] gives good predictions for laminar films. In the case of external condensation on a horizontal tube, the average Nusselt number is given by,

$$\mathrm{Nu}_c \equiv \frac{h_c D}{k_l} = 0.729\left[\frac{\rho_l(\rho_l-\rho_v)h_{lv}}{\mu_l k_l}\left(\frac{gD^3}{\Delta T_s}\right)\right]^{1/4} \tag{18}$$

The reader is referred to various heat transfer textbooks for extensions of the Nusselt analysis to turbulent films and other wall geometries, e.g. Lienhard, [1].

The dropwise condensing coefficient can be significantly greater than corresponding filmwise coefficient, as illustrated in Fig. 12 by data of Marto et al. [41] for horizontal tubes. In their experiments, Marto et al. achieved dropwise condensation by coating the metal tube surface with a thin layer of fluoroacrylic. It is seen from Fig. 12 that dropwise condensation attained heat transfer coefficients over three times greater than those in filmwise condensation. It is also notable that these results indicate h_c for dropwise condensation to be essentially constant, independent of heat flux q, and therefore of the subcooling ΔT_s.

3.2 Models. The mechanism for heat transfer in dropwise condensation is still in debate. One premise is that there actually exists a liquid microfilm, of order <1 μm thickness, on the solid surface. As the thickness increases due to condensation, a critical thickness is reached at which surface tension of the liquid causes rupture of this microfilm, and formation/coalescence of drops. A new microfilm is presumed to quickly form over the uncovered wall surface. Condensation then continues on the growing drops and on the microfilm between drops. This model, here termed the "micro-film model," was initially proposed by Jakob in 1936 [42] and followed-up by several researchers in subsequent decades, e.g., Welch and Westwater [43], Sugawara and Katusuta [44].

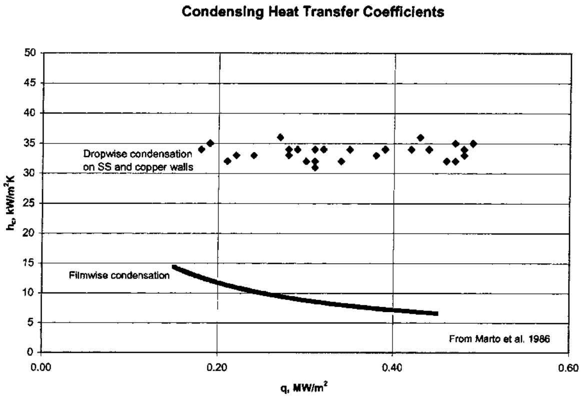

Fig. 12 Example of heat transfer coefficients for film wise and drop wise condensation

A different model starts with the premise that when the subcooled surface is poorly wetted by the liquid phase, micro-drops of condensate nucleate heterogeneously at selected sites on the solid surface. This concept is analogous to the premise for heterogeneous nucleation of vapor bubbles on superheated surfaces in boiling, and has gained support in recent years. The experimental evidence of Umur and Griffith [45] confirmed that the surface area between condensate drops remains dry with no indication of a microfilm. Thus, this model presumes a cyclic process of droplet nucleation at active sites, growth by mass addition due to condensation, coalescence due to surface tension effects, and finally removal by body force or shear drag. Since its early proposal by Eucken [46], this "nucleation model" has been further developed by a number of authors in recent years, e.g. Graham and Griffith [47], Rose and Glicksman [48], Tanaka [49], Rose [50], Wu et al. [51].

Following the concept of the nucleation model, heat transfer during dropwise condensation would occur by conduction through the drops and by vapor convection on the bare solid surface. The first path generally dominates and has been the focus of attention for most models. As described by Graham and Griffith [47], vapor condensing on a drop surface releases latent heat, which is conducted through the liquid drop to the solid surface, to be then dispersed through the substrate. For condensation of pure vapor on an isothermal surface, and neglecting the minor subcooling energy of liquid in the drop, the overall temperature driving force (ΔT_t) is comprised of the temperature drops associated with three resistances,

$$\Delta T_s = \Delta T_k + \Delta T_{ic} + \Delta T_i \tag{19}$$

where ΔT_k is the temperature drop due to conductive resistance in the liquid drop, ΔT_{ic} is the depression of saturation temperature associated with curvature of the vapor/liquid interface, and ΔT_i is the temperature drop associated with mass transfer resistance at the interface. From thermodynamic and heat flow principles, the following expressions have been derived for the three temperature differences for a hemispherical drop of diameter D (see Graham and Griffith, [47], Carey, [52]):

$$\Delta T_k = Q_d/(2\pi D k_l) \tag{20}$$

$$\Delta T_{ic} = \left(\frac{D_m}{D}\right)\Delta T_s \tag{21}$$

$$\Delta T_i = 2Q_d/(\pi D^2 h_i) \tag{22}$$

where Q_d is the rate of heat transfer to the hemispherical drop, D_m is the diameter of the minimum stable drop, given by

$$D_m = \frac{4\sigma T_s}{\rho_l h_{lv}\Delta T_s}. \tag{23}$$

In Eq. (22) h_i is the heat transfer coefficient at the liquid/vapor interface, derived to be

$$h_i \cong \frac{\rho_v h_{lv}^2}{T_v}\left(\frac{2\alpha}{2-\alpha}\right)\left(\frac{M}{2\pi R T_v}\right)^{1/2} \tag{24}$$

where α, M, and R are the accommodation coefficient at interface, molecular weight, and universal gas constant, respectively. Combining Eqs. (19–22), we obtain the following equation for rate of heat transfer to the drop of diameter D,

$$Q_d = \pi D^2\left[\frac{1-\dfrac{D_m}{D}}{\dfrac{D}{2k_l}+\dfrac{2}{h_i}}\right]\Delta T_s. \tag{25}$$

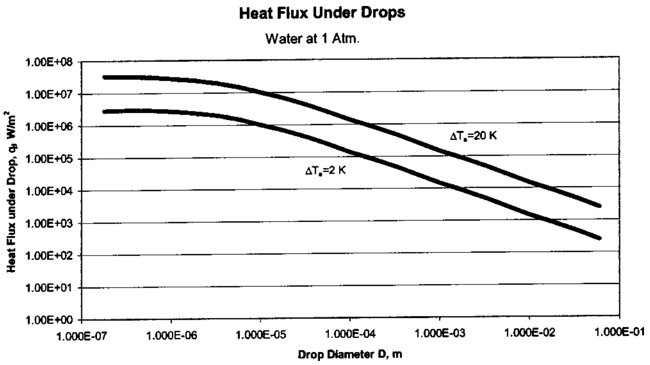

Fig. 13 Heat flux under drops of varying sizes for drop-wise condensation

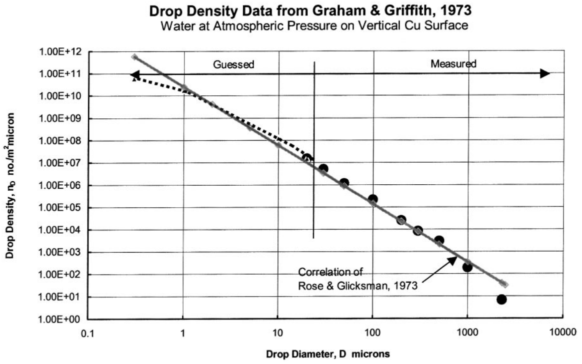

Fig. 14 Number density of condensate drops as function of drop diameter during dropwise condensation

The wall heat flux under the footprint of a drop with diameter D is then,

$$q_d = \frac{4Q_d}{\pi D^2} = 4\left[\frac{1-\dfrac{D_m}{D}}{\dfrac{D}{2k_l}+\dfrac{2}{h_i}}\right]\Delta T_s\,. \tag{26}$$

From Eqs. (26) and (23), one can determine the relative effectiveness of various size drops for condensation heat transfer. Figure 13 shows the sensitivity of q_d to drop size D, for water vapor condensing at atmospheric pressure. It is seen that the smaller drops are much more effective, with a decrease of two orders of magnitude in q_d, as D increases from 0.01 mm to 1 mm. The reason is attributable to the shorter path length for heat conduction in the condensate liquid in the case of smaller drops. Further implications of this behavior will be examined below.

The heat flux due to n_D drops of diameter between D and $D+dD$ per unit wall surface area is,

$$dq = n_D Q_d dD \tag{27}$$

and the total heat flux on the wall surface would be the integral over the entire range of drop sizes,

$$q = \int_{D_m}^{D_x} n_D Q_d dD \tag{28}$$

Neglecting the heat transfer to dry areas on the surface (usually small), the dropwise condensation heat transfer coefficient is thus obtained as,

$$h_c = \pi \int_{D_m}^{D_x} n_D D^2 \left[\frac{1-\dfrac{D_m}{D}}{\dfrac{D}{2k_l}+\dfrac{2}{h_i}}\right] dD \tag{29}$$

This model is formulated for a wall of isothermal temperature T_w, a reasonable approximation for solids of high thermal conductivity and reasonable thickness. For thin walls or walls with low thermal conductivity, there may be significant constriction resistance associated with lateral conduction resistance in the wall material, (see Mikic [53]).

To apply this model of dropwise condensation, Eq. (29), one needs information on n_D, the distribution of drop density by drop size. Graham and Griffith [47] used a microscope camera to measure the population density by drop size, for condensation of steam on a vertical copper surface. Some of their data, for water at atmospheric pressure, are recalculated in terms of the density n_D and plotted in Fig. 14. Unfortunately, physical constraints of the equipment limited measurements to drops of $D > 10\ \mu$m. For smaller drops, with diameters less than 10 μm, the investigators "guessed" a distribution to match measured heat fluxes, as indicated on Fig. 14. These authors further determined that the small drops are extremely important, with over 50% of the heat transfer being associated with drops of D less than 10 microns, beyond the range of experimentally measured drop densities.

Other authors have attempted to develop models for the drop density. LeFevre and Rose [54] suggested an empirical function to represent the distribution in terms of the fraction of wall surface area covered by drops of diameter between D and D_x,

$$f_D = 1 - \left(\frac{D}{D_x}\right)^b \tag{30}$$

where D_x is the diameter of largest drop on the surface, and b is an empirical constant assigned value of 0.33 by these authors. This function gives the following expression for drop density distribution,

$$n_D = \frac{4b}{\pi D_x D^2}\left(\frac{D}{D_x}\right)^{b-1}. \tag{31}$$

Rose and Glicksman [48] proposed a model for the cyclic growth history of drops, thence obtaining estimates of n_D and concluding that their results can be approximated by using a value of 0.382 for b in Eq. (30 and 31). Their correlation is shown as the solid line on Fig. 14, indicating reasonable agreement with the data of Graham and Griffith for water condensing on vertical surface. Most recently, Wu et al. [51] used a random fractal model to obtain drop size distribution, matching their results by numerical simulation to heat transfer data reported in literature.

Mechanistically, it is self-evident that the steady-state distribution of drop sizes results from a balance of the transient dynamics for drop nucleation, growth, coalescence, and removal. Many, many parameters would affect this balance, including properties of the fluid and surface, as well as geometric and operational conditions. For example, any mechanism that increases retention of large drops on the surface, e.g., surface tension effects, would increase the fraction of larger drops. Conversely, mechanisms that aid removal of drops, e.g., external body force or shear force, would increase the frequency of drop removal and increase the fraction of smaller drops on the surface at any moment. The interaction of these parameters is highly complex and would be dependent of system variations. As Graham and Griffith concluded in 1973 [47], "It is a disappointment in that a simple, universal dropwise condensation heat transfer correlation appears to be out of reach. Separate drop distribution curves will be needed for high and low pressure and for each fluid-material combination." This view is especially valid for any dropwise condensation under "non-typical" conditions, where all empirical models of n_D obtained for "typical" conditions would be inapplicable.

One class of nontypical conditions is where drop formation is deliberately promoted by specific modification of material properties. Indeed, motivated by the promise for high heat transfer coefficients, many researchers have attempted to promote dropwise condensation. Almost all such efforts utilize the sensitivity of drop formation on ‘‘wetting’’ behavior of the fluid-solid interface, i.e., on surface tensions and surface energies. This leads us to consider the significance of parameters in the domain of surface energies.

3.3 Effects in Domain of Surface Energies. The fundamental basis for surface energies arises from intermolecular forces. In review of basic concepts, recall that intermolecular forces are considered to consist of a short range repulsive force and longer range electrostatic, inductive and dispersive attractive forces, commonly referred to as the van der Waal forces. The well known Lennard-Jones potential (Hirschfelder [55]) represents the summation of these forces by the equation,

$$\phi_{LJ}=4\varepsilon\left[\left(\frac{r_o}{r}\right)^{12}-\left(\frac{r_o}{r}\right)^{6}\right] \tag{32}$$

where r is the intermolecular spacing and the parameters r_o, ε vary with molecular specie. In the liquid near a vapor interface, the molecules are space slightly further apart than in the bulk liquid. This has little effect on the longer-range attractive forces, but significantly reduces the short-range repulsive force. With the discontinuity at the interphase, there results a net force on liquid molecules in direction normal to the interface, that tends to pull toward the bulk liquid volume. In directions parallel to the interface, symmetry exists about each molecule so that there is no net force vector parallel to the interface. Instead, there results a net tension force on the molecules, equal in all directions parallel to the interface—hence, ‘‘surface tension’’ of the liquid in contact with its vapor (σ_{lv}). Thermodynamic considerations show that σ_{lv} is equal to the change in Helmholtz free energy of the surface, per unit increase of interfacial surface area.

The shape of a liquid-vapor interface can be strongly affected by surface tension. The Laplace equation can be derived by force balance on the interface, and for liquid drops where the interface is characterized by two radii of curvature (r_1 and r_2), results in the following expression relating pressure difference across the interface with the surface tension σ_{lv},

$$P_l-P_v=\sigma_{lv}\left(\frac{1}{r_1}+\frac{1}{r_2}\right) \tag{33}$$

When spherical symmetry exists, $r_1=r_2=r$, and the interfacial pressure difference is,

$$P_l-P_v=\frac{2\sigma_{lv}}{r} \tag{34}$$

The Laplace equation relates interfacial pressure difference, surface tension, and interfacial geometry and therefore can be utilized in conjunction with equations of hydrodynamics to determine the shape of liquid-vapor interfaces. Alternatively, in an equilibrium situation with negligible hydrostatic pressure, the Laplace equation directly gives the pressure difference between the two phases. Thus, we find that for spherical droplets of water (e.g., condensation drops in fog), the liquid pressure can be as much as 2–5 atmospheres greater than the surrounding air pressure (for drop diameters of 1–2 μm).

Our interest here is in dropwise condensation on solid surfaces, wherein liquid drops exist on solid surface in presence of the vapor phase. Zisman [56] and de Gennes [57] give good reviews of the fundamental physics for such 3-phase systems. A macroscopic view of the contact line, where the three phases are in contact, can be expressed in terms of the free energy per unit area of each interface, i.e., the interfacial tensions σ_{lv}, σ_{sl}, σ_{sv}, for liquid/vapor, solid/liquid, solid/vapor, respectively. Young’s equation, derived from equilibrium force balance, relates the contact angle θ to the three surface tensions (interfacial energies),

$$\sigma_{lv}\cos\theta=\sigma_{sv}-\sigma_{sl} \tag{35}$$

where the contact angle θ is traditionally taken to be the angle between the tangent to the liquid/vapor interface and the solid surface, measured on the liquid side. From thermodynamic considerations, it can be shown (see Carey [52]) that the net change of total system free energy per unit increase of solid/liquid interface area, for constant liquid volume and temperature, is

$$\partial F=[\sigma_{lv}\cos\theta-\sigma_{sv}+\sigma_{sl}]\partial A_{sl} \tag{36}$$

and at equilibrium, total free energy is at minimum,

$$\frac{\partial F}{\partial A_{sl}}=[\sigma_{lv}\cos\theta-\sigma_{sv}+\sigma_{sl}]=0 \tag{37}$$

which gives us Eq. (35) again.

It should be noted that Young’s equation is an approximation that neglects:

- adsorption of fluid molecules on the solid surface
- variation of interfacial tension in local vicinity of the contact line
- dynamic effects in nonequilibrium situations.

The reader is referred to Johnson [58] for a detailed discussion of Young’s equation and its limitations. Wayner [59] also gives an excellent review of this topic, with special attention on physics of the contact line region.

In spite of its approximate nature, Young’s equation is a useful concept as we consider the phenomenon of wetting. A liquid is said to be wetting if it tends to spread as a film along the solid surface, and conversely to be nonwetting if it tends to retract and form ‘‘beads’’ on that surface. Force balance shows that if,

$$\frac{\sigma_{sv}-\sigma_{sl}}{\sigma_{lv}}>1 \tag{38}$$

the contact line tends to pull away from the liquid bulk, thus spreading the liquid on the solid surface. Conversely, force balance tends to pull the contact line inward toward the liquid bulk (beading) when,

$$\frac{\sigma_{sv}-\sigma_{sl}}{\sigma_{lv}}<1. \tag{39}$$

Thus, Eq. (35) shows that wetting cases correspond to $0\leqslant\theta<\pi/2$. Conversely, nonwetting cases correspond to $\pi/2<\theta\leqslant\pi$. A spreading coefficient may be defined as,

$$S_p\equiv\sigma_{sv}-\sigma_{sl}-\sigma_{lv}. \tag{40}$$

A positive value of S_p corresponds to a net decrease of free energy per unit increase of solid/liquid interfacial area, necessary for spontaneous spreading of the liquid on the solid as clearly seen from Eq. (36) for case of $\theta=0$.

Equation (40) indicates that solids with high surface energies ($\sigma_{sv}>100$ ergs/cm^2) tend to be more easily wetted. Indeed, most molecular liquids achieve good wetting on high-energy surfaces. Low energy surfaces ($\sigma_{sv}<100$ ergs/cm^2) can be wetted, partially wetted, or nonwetted, depending on the liquid specie (see de Gennes [57]). Figure 15 illustrates how the equilibrium contact angle θ varies on a smooth Teflon (polytetrafluoroethylene) surface with the interfacial free energy (σ_{lv}) of *n*-alkane liquids. Clearly, the specific pairing of a liquid with a solid defines the balance between surface energies and thus the degree of wetting that can be obtained. For condensation, this balance governs whether filmwise or dropwise condensation is obtained. At the conditions represented by data points of Fig. 15, partial wetting is indicated and it is likely that condensation of these *n*-alkanes on the Teflon surface would occur in filmwise fashion, with some minimum film thickness, below which droplet/rivulet formation occurs. The situation is notably different for water with its high interfacial energy (59×10^{-3} N/m at normal boiling point); the spreading coefficient S_p would be negative and one expects condensation to occur in dropwise fashion on this Teflon surface.

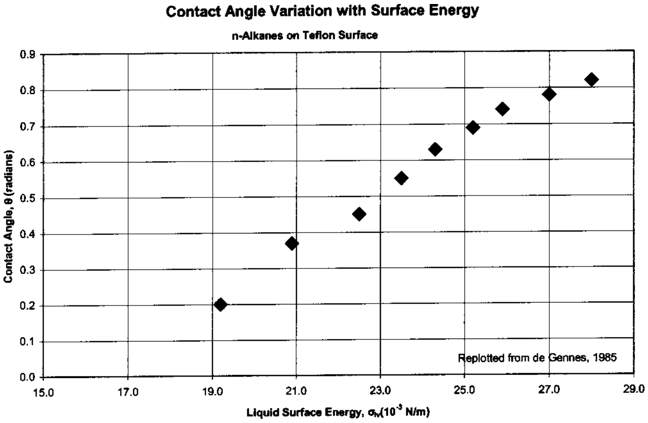

Fig. 15 Effect of surface energy on equilibrium contact angle, from de Gennes [52]

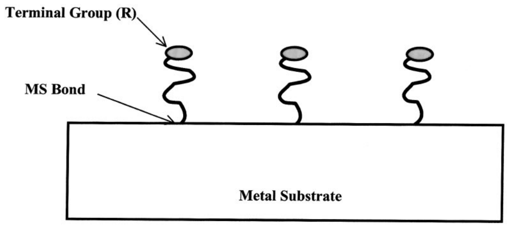

Example: alkylthiol monolayer self-assembled onto metal substrate

$$HS(CH_2)_n R + M \rightarrow MS(CH_2)_n R$$

Fig. 16 Self assembled monolayer (SAM) on metal surface

From the above, it is clear that the possibility for dropwise versus filmwise condensation is governed by the three surface tensions that determine the spreading coefficient, as indicated in Eq. (40). All attempts to promote dropwise condensation have revolved around the adjustment of these parameters in the domain of surface energies. Tanasawa [60] classified the methods that have been employed for such purpose as,

1. Adsorption of a nonwetting agent (i.e., organic molecules) on condensing surface prior to operation.
2. Intermittent injection of nonwetting agent into the condensing vapor, for adsorption onto the condensing surface.
3. Plating the condensing surface with noble metal.
4. Coating the condensing surface with layer of organic polymer.

All these methods utilize reduction of the solid surface energy σ_{sv} to obtain negative spreading coefficient S_p. It may seem that the plating of noble metals is an exception, in view of the high energies of pure metal surfaces. However, since electroplated surfaces of noble metals (e.g., gold, silver) are known to be highly active in adsorption of trace organic compounds, it has been suggested that it is the adsorbed organics that actually cause lowering of surface energy on the noble metal plating and promote dropwise condensation (see Wilkins et al. [61], Woodruff and Westwater [62]).

The use of coatings on the condensing surface must overcome three potentially detrimental problems. The additional thermal resistance through the thickness of the coating may negate any potential gain from dropwise condensation. This is of importance for coatings of low thermal conductivity, the case for most organic materials. In practice this limits the thickness of organic coatings to a few microns or less. Second, the bond between coating and substrate must be intimate so as to avoid a contact resistance for conduction across the bonding interface. Finally, for practical operation over long times, it is necessary for the coating to be robust mechanically and stable chemically. Marto et al. [41] evaluated several different coatings for sustained dropwise condensation of steam and found that the durability of organic coatings depended not only on the molecular structure and thickness of the organic material, but was also affected by the chemical activity and surface roughness of the solid substrate. These investigators reported organic coatings of fluoroacrylic on Ti/Au surface and of parylene-D on Cu/Ni surface that sustained dropwise condensation for periods exceeding 12,000 hours. An example of their data is shown in Fig. 12, indicating dropwise condensation coefficients of order 3×10^4 W/m^2 K. Low energy coatings can be applied by various techniques, with varying degrees of success in achieving low thickness, durability, and good bonding to substrate. One intriguing technique, using ion implantation, has been reported by D. C. Zhang et al. [63], and Q. Zhao et al. [64]. As described by Zhao et al., a copper substrate surface was deoxidized and then cleaned by sputtering in an Ar$^+$ beam. To develop a nonwetting surface, the clean Cu surface was then plated successively by ion implantation of Cr and N. Spectroscopic examination of the resulting surface showed an alloy layer with approximately 12% and 9% Cr and N content, respectively, along with noticeable amounts of C and O. Metalographic examination of the layer showed that the normal crystalline structure of Cu had been transformed into an amorphous state, with accompanying reduction of ~30% in elasticity. Since surface energy varies directly with modulus of elasticity, the new surface was of reduced surface energy. Because the low-energy layer thus obtained had thickness of $<10^4$ Angstroms (<1 μm), its conduction resistance was negligible and the investigators were able to achieve dropwise condensation coefficients up to 3×10^5 W/m^2 K on a vertical surface. In tests with steam condensing on treated copper tubes (vertical placement), the authors reported sustained operation for over a year. Ma et al. [65] subsequently coated polymers (polyhexafluoropropene and polytetrafluoroethylene) on brass surfaces by both ion-beam implantation and by plasma polymerization. While dropwise condensation was achieved with high heat transfer coefficients, these investigators concluded that the properties and durability of these coatings were sensitive to deposition process conditions (e.g., energy level of ion beam), and further study was recommended.

The current status for dropwise condensation may be characterized as a general acknowledgment that surface energy parameters are the governing keys, and that the ability to manipulate these parameter will determine successful applications of this mode of multiphase heat transfer in the future.

3.4 Further Developments. We next examine two fairly recent developments in manipulation of surface energies that are intriguing for dropwise condensation. Both developments are based on chemosorption, the modification of the solid surface energy, by use of self-assembled monolayers (SAMs) of organic molecules.

Certain organic compounds have terminal groups at the two ends of the molecule with very different chemical characteristics. For example, alkylthiol molecules have one end terminating with a HS group, the other end terminating with a CH$_n$ group. The HS group can strongly bond with metal atoms of the solid surfaces, permitting good adherence of the organic molecule to the surface. The attached molecules then self assemble into a monolayer with the CH$_n$ group sticking up over the surface, as illustrated in Fig. 16. By judicious choice of the terminal hydrocarbon group, different levels of surface energy can be obtained, hence controlling wetting characteristic of the solid surface. Because the self-assembled monolayers have thickness of order 10 angstroms, they present negligible resistance to heat conduction. Thus, the use of self assembled monolayers promises to overcome the three potentially detrimental problems mentioned above.

Kumar and Whitesides [66] used SAMs of functionalized al-

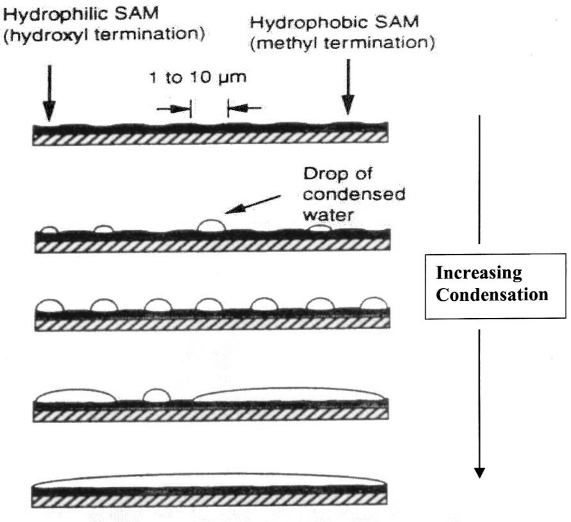

Condensation on Patterned SAM Surface
Redrawn from Kumar and Whitesides, 1994

Fig. 17 Dropwise condensation on gold plated Si surface with patterned self assembled monolayer coating

Test Section for Measurement of Condensing Heat Transfer Coefficients by Wilson Plot Method
(Das et al., 2000)

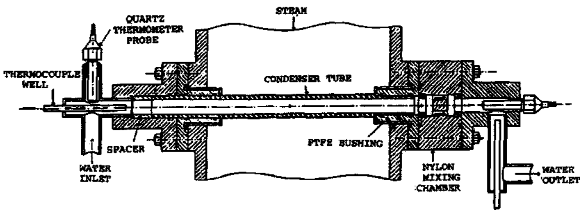

Fig. 18 Test section used by Das et al. [67] for measurement of condensing heat transfer coefficients on horizontal tubes

kanethiolates to control the pattern for dropwise condensation. Using lithographic stamping, these investigators fabricated patterned surfaces on gold plated Silicon with well-defined hydrophobic and hydrophilic regions. Hexadecanethiol [$HS(CH_2)_{15}CH_3$], with methyl termination, formed hydrophobic SAM regions, while 11-mercaptoundecanol [$HS(CH_2)_{11}OH$], with hydroxyl termination, formed hydrophilic SAM regions. Condensation of water then occurred preferentially on the hydrophilic regions, generating diffraction patterns as desired by these investigators. Figure 17 (modified from their paper) illustrates the process of dropwise condensation progressing from a bare SAM covered surface, to initial formation of a few drops on some of the hydrophilic regions, to many uniform drops over all the hydrophilic regions, before eventually obtaining large drops that bridged over the hydrophobic regions to cover the entire surface. For the purpose of these investigators, it was particularly meaningful that micro-patterns of only micron length scale could be fabricated with such distinct regions of surface energies.

Das et al. [67] used an organic self-assembled monolayer coating to promote dropwise condensation of steam on a horizontal tube. SAM coatings of hexadecanethiol [$HS(CH_2)_{15}CH_3$] were formed on copper, copper-nickel, and gold-coated aluminum tubes to obtained hydrophobic surfaces. The investigators reported that the coated surfaces had large advancing contact angles of 110–112 deg, reflecting their very low surface energies. The tubes were individually mounted in the apparatus shown in Fig. 18, and condensing heat transfer coefficients obtained by the Wilson plot technique. Some of their results for condensation of steam at subatmospheric pressure (10 kPA) are replotted in Fig. 19, along with the corresponding values for condensation on a bare tube (without SAM coating). It is seen that the heat transfer coefficients for SAM coated tubes were all greater than those for the bare, uncoated tube of gold covered aluminum. Filmwise condensation coefficients, represented by the Nusselt theory (Eq. 18), are the smallest of all, being a factor or ~3 less than the coefficients for the bare tube. This implied that the gold-on-aluminum surface of the bare tube did obtain at least partial dropwise condensation. For the three SAM coated surfaces, the authors noted that thermal conductivity of the substrate material apparently had significant effect on the condensing heat transfer coefficient. This is contrary to the earlier results of Marto et al. [41], reproduced in Fig. 12, which indicated insensitivity to substrate material. Thus, the importance of constrictive thermal impedance in the substrate material remains an unsettled issue. For our purpose, the significant finding by Das et al. [67] is proof that self-assembled monolayers of organic compounds can be used to effectively promote dropwise condensation.

The second development of interest addresses the question, "can manipulation of parameters in the domain of surface energies not only promote dropwise condensation, but further enhance the heat transfer coefficient during dropwise condensation?" In seeking enhancement, one objective to explore is the control of drop size distribution and population density. As noted above and illustrated in Fig. 13, small drops are more effective than large drops in dropwise condensation. Graham and Griffith [47] estimated the fraction of heat flux due to drops of different diameters, plotting their results for various population distributions. Figure 20, reproduced from their paper (distribution numbers represent various assumed population distributions), indicates that the cumulative heat flux due to drops with diameter greater than 10 microns account for less than 35% of the total heat flux. This same indication of the importance of small drops is seen from the empirical correlation obtained by Tanasawa [60], reproduced here in Fig. 21. This plot shows a remarkably consistent correlation between average heat transfer coefficient and the diameter of departing drops during dropwise condensation. Since drops grow to largest size before departure, it is significant that reducing the diameter of departing drops from 2 mm to 0.2 mm increases the average heat transfer coefficient by almost 100%. Tanasawa's plot further indicates that this enhancement is independent of the method for drop removal. The data of Fig. 21 included experi-

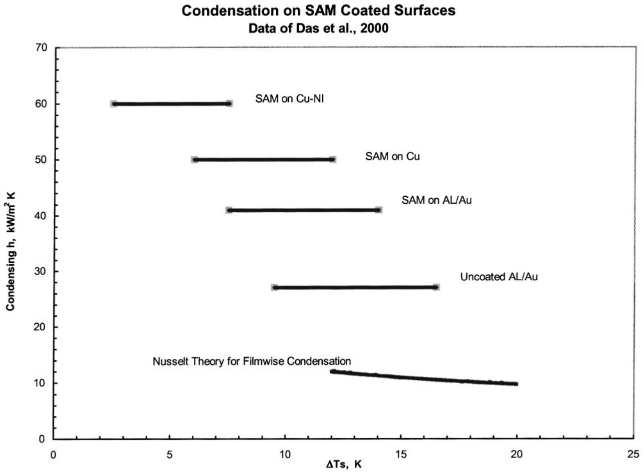

Fig. 19 Condensation coefficients for horizontal tubes coated with self assembled monolayers of organic compound to promote dropwise condensation

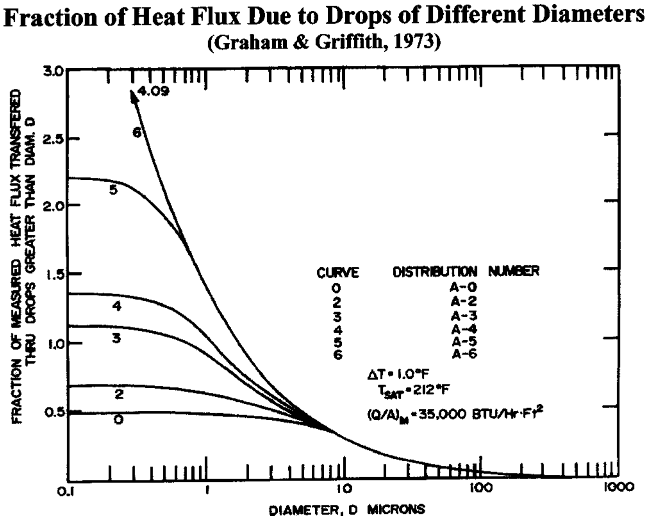

Fig. 20 The dominant contribution of small drops to total heat flux during dropwise condensation, from Graham and Griffith [47]

ments using vertical gravitational force, inclined gravitational force, centrifugal force, and vapor shear to induce drop removal. It appears that the primary need is to remove drops from the condensing surface as early as possible during the drops' growth cycle, by any means possible.

The work of Chaudhury and Whiteside [68] promises a novel development for promoting drop movement. They were able to induce drop movement uphill along a 15° incline by application of surface forces. Specifically, these investigators modified a method developed by Elwing et al. [69] to create a gradient of surface energy on the solid surface. A silicone wafer was exposed to a diffusing vapor of decyltrichlorosilane ($Cl_3Si(CH_2)_9CH_3$), which then chemically bonded to the silicone surface as a self assembled monolayer. Due to the concentration gradient associated with the diffusion process, the resulting SAM varied in concentration along the wafer, as illustrated in Fig. 22. Since the selected SAM had a hydrophobic terminal group, the free energy of the resulting surface varied with concentration, with lower values of σ_{sv} where SAM is more concentrated. These investigators reported that their SAM layer had a thickness of ~6 Angstroms at the hydrophobic end, decreasing at rate of ~1 Angstroms per mm toward the hydrophilic end. As illustrated in Fig. 22, the resulting surface had a gradient of surface energy, increasing along the wafer surface with increasing distance from the original source of silane. Figure 23, copied from Chaudhury and Whiteside [68], showed the static contact angle obtained for water drops at various positions along this gradient surface, varying over a range of almost 100 degrees.

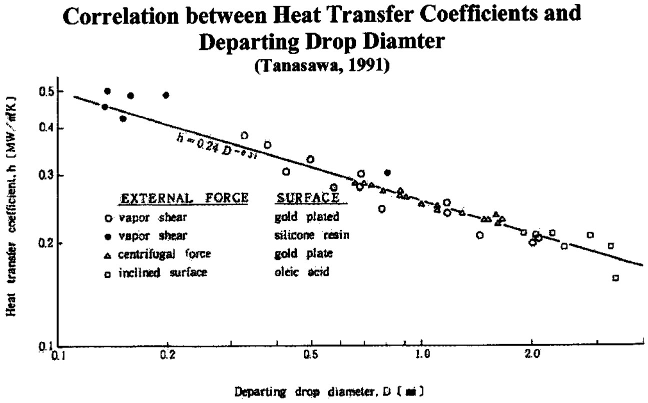

Fig. 21 Dependence of heat transfer coefficients on diameter of departing drops for drop wise condensation, from Tanasawa [60]

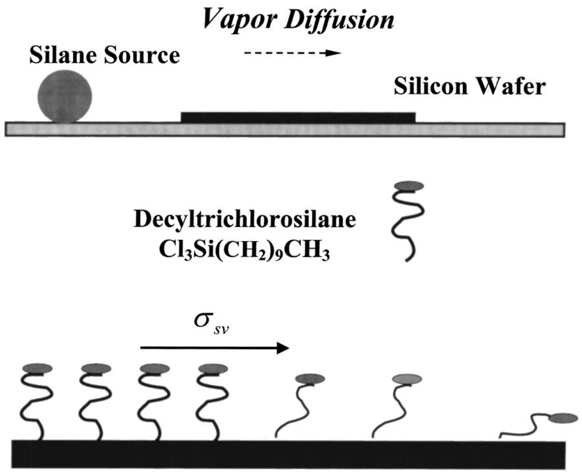

Fig. 22 Creation of gradient surface with self assembled monolayer

A drop of liquid on a surface that has a spatial gradient of surface free energy would be subjected to unbalanced Young's force. As illustrated in Fig. 24, for a cross-sectional slice of the drop of thickness dy, the unbalanced Young's forces is,

$$dF_x = [(\sigma_{sv} + \sigma_{sl})_a - (\sigma_{sv} + \sigma_{sl})_b]dy$$

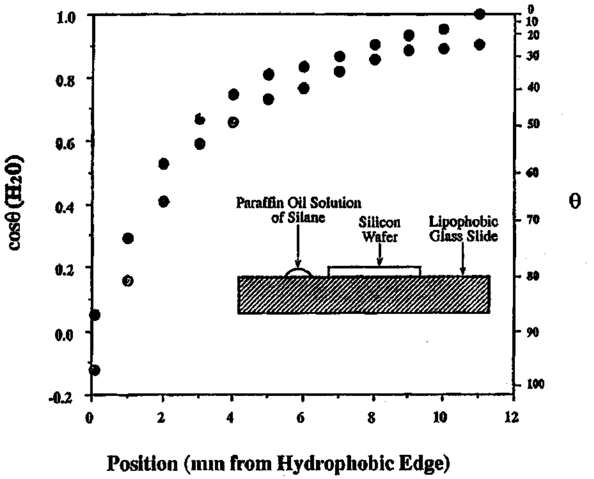

Fig. 23 Variation of static contact angle along a gradient surface, from Chaudhury and Whiteside [68]

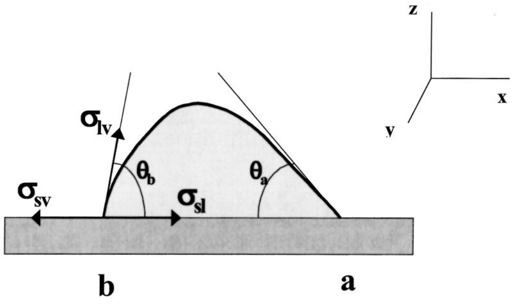

Fig. 24 Forces on liquid drop located on surface with gradient in surface free energy

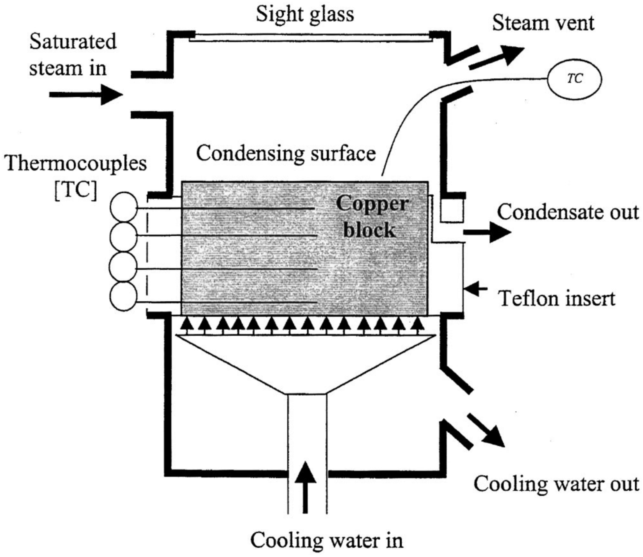

Fig. 25 Test apparatus for condensation on gradient surfaces, Daniel, Chaudhury and Chen [71]

$$dF_x = \sigma_{lv}(\cos\theta_a - \cos\theta_b)dy \tag{41}$$

The net force on the drop is the integral of Eq. (41) over the thickness of the drop. This force can induce drop translation along the surface toward the region of higher surface energy. If the liquid/surface system has significant hysteresis, the net force would need to overcome the difference between advancing and receding contact angles to sustain drop motion. It is worth noting that such motion is not caused by classic Marangoni effect associated with concentration or temperature gradients in the liquid, but is strictly due to the unbalanced Young's forces resulting from gradient in surface free energy. Chaudhury and Whiteside were able to obtain movement of 1–2 μl water drops, with average speed of 1 to 2 mm/s., upward on a surface inclined 15° from horizontal.

Leveraging from above finding, a project was initiated to determine if this phenomenon of unbalanced Young's forces can be utilized to promote drop removal on condensing surfaces and thereby increase the condensation heat transfer coefficient. Figure 25 shows the test apparatus built for this experiment. A copper block of 5.0 cm diameter was sealed into a stainless steel vessel in such a manner as to create two separate chambers, each encompassing one surface of the copper block. Saturated steam was supplied to one chamber at controlled pressure and flow rate. Cooling water was sprayed onto the block surface in the second chamber. In operation, condensation occurs on the block surface in the steam chamber, the latent heat being conducted through the copper block to the water-cooled surface. The rate of condensation was adjusted by varying the rate of cooling water flow. During experiments, steam flow and cooling water flow would be maintained till steady state thermal conditions were obtained before taking measurements. To minimize non-condensable gases in the steam chamber, a continuous venting of excess steam was maintained during experiments. In selected tests, video records were obtained of the condensing surface to characterize the condensate removal process. Four microthermocouples were imbedded in the copper block to measure its temperature gradient, thus obtaining the heat flux through the block. Thermal insulation at sides of the block assured essentially one-dimensional conduction in the block, so that the heat flux obtained in the block represented the condensing heat flux (q) on the block surface. Extrapolation of the temperature profile to the condensing surface provided the surface temperature (T_w), while measurements of steam pressure and temperature provided the saturation steam temperature (T_s).

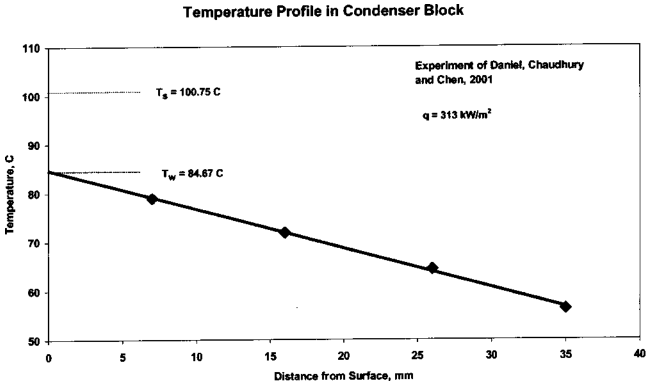

Fig. 26 Sample measurements from experiment of Daniel, Chaudhury and Chen [71]

These measurements enabled direct calculation of the condensation coefficient as defined by Eq. (17), averaged over the circular condensing area of the block surface. Figure 26 shows an example of the temperature profiles measured in the copper block during condensation. The point plotted at each distance represents average temperature obtained in 16 measurements over an hour or more of operation. It is seen that a linear temperature profile was obtained, the correlation coefficient typically being greater than 0.99 (0.998 in case of the example in Fig. 26). Extrapolation of the temperature profile to surface of the condenser block and gradient of the profile provided quantitative values for wall surface temperature and heat flux, respectively, as indicated in the figure. This experimental apparatus was supported on a swivel such that tests could be performed with the condensing surface at various inclinations, from horizontal to vertical.

Using this apparatus, experiments were conducted in filmwise condensation, normal dropwise condensation and enhanced dropwise condensation (gradient surface). These different conditions were obtained by appropriate treatment of the condensing surface. In this paper, we will examine the results for filmwise and enhanced-dropwise condensation. For filmwise condensation, the copper surface was prepared by polishing to mirror finish, and then coated with a thin film ($\sim 10^2$ Angstrom thickness) of silicon by vacuum deposition. The silicon was then oxidized by exposure to a high temperature air, and plasma treated to remove all traces of adsorbed organic compounds. This resulted in a uniformly hydrophilic surface, upon which condensation occurred in filmwise fashion. For enhanced dropwise condensation, the silicon surface was subjected to a controlled silanization reaction by vapor diffusion, as illustrated in Fig. 22. Specifically, the silicon surface was first oxidized to SiO_2, which was then reacted with a vapor of chlorosilane (Cl_3SiR), where the R group was a hydrocarbon chain of various molecular lengths. In presence of atmospheric water, the chlorosilane reacts with the SiO_2 to form a series of silicon-oxygen bonds, thus creating a robust self-assembled monolayer film. Such SAM films have thickness of O[10 Angstroms], and thus are of negligible thermal resistance. As noted above, the vapor diffusion process causes higher molecular concentration of the SAM on the regions of the surface in proximity to the chlorosilane source. By judicious placement of the source relative to the surface, we were able to produce various patterns of gradient energy on the condensing surface.

One pattern of particular interest was radial-centrosymmetric, with highest SAM concentration at the center of the circular condensing surface. This was produced by suspending the chlorosilane source at a point 2 mm above the Si surface, directly over the center point. The resulting SAM film had highest concentration at the center, the concentration decreasing with radial distance. To characterize the surface-energy landscape on this surface, static contact angles (with water) were measured at various radial posi-

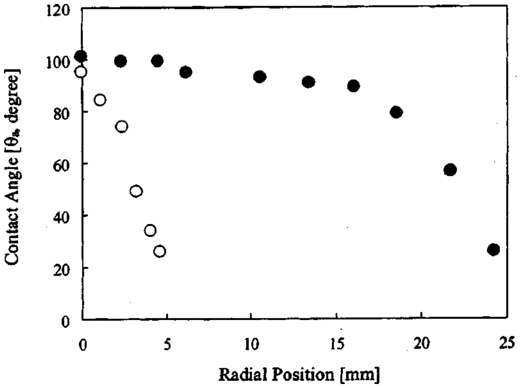

Fig. 27 Static contact angles on a circular surface with radial gradient of surface free energies, from Daniel [70]: ● SAM with octyltrichlorosilane; and ○ SAM with dodecyltrichlorosilane.

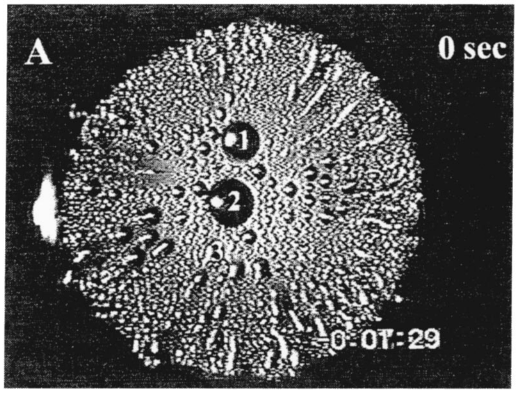

Fig. 28 Drop removal pattern during condensation on SAM surface with radial gradient in surface free energies, from Daniel, Chaudhury and Chen [71]

tions. Figure 27 (Daniel [70]) shows the radial distribution of contact angles on two versions of the test surfaces, fabricated with octyl ($R=8$) and dodecyl ($R=10$) chlorosilanes, respectively. It is seen that these surfaces indeed had gradients of surface free energy, with minimum energy (maximum contact angle) at the hydrophobic center and maximum energy (minimum contact angle) at the hydrophilic rim of the circular surface. Our intention was to promote drop removal radially from the surface by induced flow toward the rim edge of the surface.

Condensation tests were performed with these SAM coated surfaces having radial gradients of surface energy. For comparison, condensation tests under comparable conditions were also performed on the uncoated, uniformly high-energy (hydrophilic) surface, and on uniformly low-energy (hydrophobic) surface. Both sets of experiments were carried out with the surface in upfacing, horizontal position. Video recordings of the condensation process showed distinctly different behavior of the liquid condensate in these different experiments. In the case of the uniform hydrophilic surface, filmwise condensation was obtained. The condensate collected as a film on the horizontal surface, reaching a steady-state thickness when overflow drainage at the rim edge balanced the rate of condensate formation. In contrast, condensation on the SAM coated surface was of dropwise fashion. As commonly observed in dropwise condensation, droplets nucleated on the subcooled surface, growing by mass addition from condensation until occurrence of drop removal. The unique feature recorded for dropwise condensation on our gradient surfaces was the nature of drop removal. In as much as the condensing surface was horizontal, there was no gravitational force to trigger drop removal. Also, with minimal steam flow over the condensing surface, there was negligible shear force to cause drop movement. The video records showed that drop removal on the gradient surfaces did indeed occur very efficiently, and that the flow pattern for the drops followed the radial pattern of the gradients in surface energy. This result provided qualitative verification of the starting premise—that unbalanced Young's forces on surfaces with gradients in free energy can promote drop motion and removal during condensation.

The visual impression of this process can best be obtained from the video movies. Figure 28 presents a single frame extracted from a video sequence, showing the condensate pattern on the SAM coated gradient surface. While such a snapshot does not adequately document the motion of drops, it does indicate the radial pattern of drops flow. Clearly, this pattern of radial flow paths was a result of the radial pattern of surface energies laid down in the SAM coating process. Magnified observations from such snapshots indicated a relative increase in population of small to midsize drops with a perceivable decrease in population of larger drops, when compared to dropwise condensation on uniform surface with gravity induced drop removal (comparing Figs. 28 and 11). At least qualitatively, the gradient in surface energy appears to have induced early drop removal, as desired.

One result of these experiments was surprising, namely the speed with which drops moved on the gradient surfaces. Pretest expectation was for drops of ~0.5–1.0 mm diameter to translate on the gradient surface with velocity of $O[1\text{ mm/s}]$, as reported by Chaudhury and Whiteside [68]. Video records in the present experiment enabled measurement of drop velocity. Figure 29 shows two frames of the video taken 1 millisecond apart. On these magnified images, it was possible to track individual drops. In Fig. 29, the drop identified with number (1) had a diameter of 0.5 mm, and translated a distance of 0.15 cm in this time span. Thus, the effective velocity for this drop was 1.5 m/s. Similar results

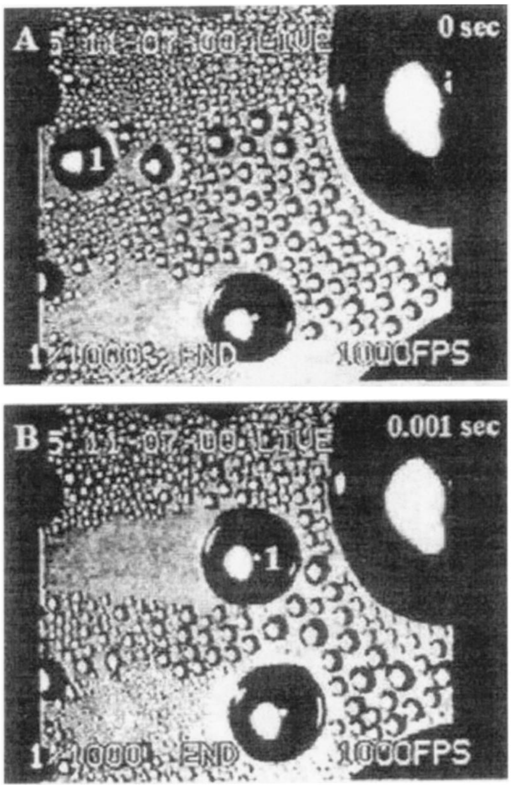

Fig. 29 Video sequence of drop movement on gradent surface in time span of 1 millisecond, from Daniel [70]

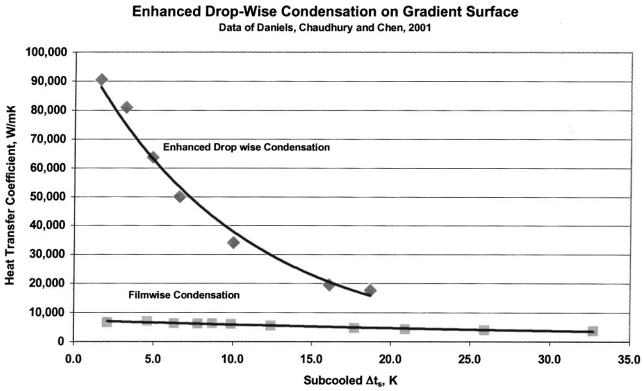

Fig. 30 Enhanced heat transfer for drop-wise condensation on surface with gradient in free energy, results of Daniel, Chaudhury and Chen [71]

were obtained for other drops tracked by the videos. This thousand-fold increase in drop velocity over expectation was startling. It suggests greater promise for enhancement of condensation heat transfer than originally anticipated. It also raises an intriguing question—what is the mechanism that would induce drop motion of such velocity? A hint was found in the fact that this accelerated drop motion occurred only during active condensation. In a series of tests, it was observed that the accelerated drop motion slowed significantly when the source of steam was cut off, resuming when the steam source to the condenser was restarted. It appears that the mechanism for accelerated drop movement derives from interaction between the condensation process and the unbalanced Young's forces, requiring simultaneous presence of both.

One possible mechanism postulated by the co-investigators is the interaction of drop-coalescence process with the unbalanced Young's forces. Daniel et al. [71] point out that drops grow during dropwise condensation, and coalescence occurs when neighboring drops grow into contact. When two drops coalesce, the resulting final drop has center of mass located between the centers of the two original drops, which represent a net displacement of the original drops. On a surface with gradient of surface energy, the growth of a condensate drop favors the circumferential edge that is in contact with higher energy (more wettable) surface. The resulting coalescence process would preferentially favor that direction, thus accelerating the net movement in that direction. This postulated mechanism may be correct, but in opinion of the present author it needs further investigation before complete acceptance. The occurrence of rapid drop movement during condensation on a gradient surface is an open and intriguing phenomenological issue.

Without fully resolving the mechanism for rapid drop movement, the experiments of Daniel et al. [71] did provide the first direct proof of principle, that engineering of surface energy gradients can enhance the heat transfer coefficient in dropwise condensation. The most telling evidence is found in comparison of data for dropwise condensation on a gradient surface with data for filmwise condensation on a uniformly hydrophilic surface. Figure 30 plots the heat transfer coefficients for these two cases, both obtained for condensation of saturated steam at ~1 atmosphere pressure on horizontal, up-facing surfaces. Measurements were obtained over ranges of subcooled surface temperatures, 2 to 18°K for dropwise condensation and 2 to 33°K for filmwise condensation. A very obvious enhancement was obtained in the case of dropwise condensation on the gradient surface. At the lowest surface subcooling of 2°K, typical for many applications, the heat transfer coefficient on the gradient surface attained a magnitude of 90,000 W/mK—approximately 14 times the coefficient for filmwise condensation. In contrast, normal dropwise condensation on a uniformly hydrophobic surface would see enhancements of approximately 2–3 times at such subcoolings. The results shown in Fig. 30 indicate that the enhancement on gradient surfaces diminished at higher subcoolings, presumably caused by limits in drop-flow capacity relative to increasing heat flux and condensate formation rate. Nevertheless, even at a surface subcooling of 18°K, there was a 4-fold enhancement in the heat transfer coefficient.

We concluded that for dropwise condensation, the parameter domain of surface free energy is critical. The experiments described above take advantage of parameters in this domain, creating engineered surfaces with gradients in surface energy which were observed to promote drop removal at velocities of $O[1\ \mathrm{m/s}]$, even on horizontal surfaces. While the mechanism for this high-velocity drop movement is an open phenomenological question, the results indicate very substantial enhancement of condensation heat transfer coefficient.

4 Conclusion

The complexities of multiphase heat transfer often can be isolated for engineering purposes by judicious recognition of surface contact parameters in selected domains. The two diverse examples presented above illustrate this point. One showed that heuristic knowledge of time-domain parameters for surface contacts can significantly improve predictions of heat transfer coefficients for surfaces immersed in bubbling fluidized beds. The second showed that manipulation of parameters in domain of surface free energies can be utilized to gain many-fold enhancements of heat transfer coefficients in dropwise condensation.

Nomenclature

Ar = Archimedes number
C_k = Correction factor for small Fo
c_p = heat capacity
D = diameter of tube or bed
D = diameter of drop
d_p = diameter of particle
F = Volumetric interaction force between gas and particles
Fo = Fourier modulus
f = fraction of time in residence at surface
g = gravitational acceleration
h = heat transfer coefficient
h_{lv} = latent heat of condensation/vaporization
I_i = moment of inertia of particle i
k = thermal conductivity
M = molecular weight
m_i = mass of particle i
n_D = distribution of drop sizes
Nu = Nusselt number
P = pressure
q = heat flux
r_o = parameter in Lennard-Jones potential
Re_p = Reynolds number based on particle diameter
P = pressure
Pr = Prandtl number
Q_d = heat transfer rate to drop
R = Universal gas constant
r = radius of curvature
S_p = spreading coefficient
T = temperature
U = superficial gas velocity
U_{mf} = superficial gas velocity at minimum fluidization
u = local velocity
v_i = linear velocity of particle i
x = distance from heat transfer surface

Greek Notton

α = thermal diffusivity
α = accommodation coefficient
ε = void fraction
ε = parameter in Lennard-Jones potential

ϕ_{LJ} = Lennard-Jones potential
π = Pi
μ = viscosity
ν = kinematic viscosity
ρ = density
σ = surface tension, or interfacial free energy per unit area
τ = viscous stress tensor
τ_p = residence time of packets
ω_i = rotational velocity of particle i
ξ = penetration depth

Subscripts

b = bubble
c = condensation
g = gas
i = interface transfer resistance
ic = interface curvature effect
k = conductive resistance in liquid drop
l = liquid
m = minimum diameter drop
p = particle packets
s = solid particles
s = saturation state
v = vapor
w = wall surface
x = maximum diameter drop

References

[1] Lienhard, J. H., 1981, *A Heat Transfer Textbook*, Prentice-Hall, Inc., Englewood Cliffs, NJ.
[2] Kunii, D., and Levenspiel, O., 1991, *Fluidization Engineering*, 2nd Ed., Butterworth-Heinemann, Boston.
[3] Merrow, E. W., 1985, ‘‘Linking R&D to Problems Experienced in Solids Processing,’’ Chem. Eng. Prog., **81**(5), pp. 14–22.
[4] Ozkaynak, T. F., and Chen, J. C., 1980, ‘‘Emulsion Phase Residence Time and Its Use in Heat Transfer Models in Fluidized Beds,’’ AIChE J., **26**(4), pp. 544–550.
[5] Chandran, R., Chen, J. C., and Staub, F. W., 1980, ‘‘Local Heat Transfer Coefficients Around Horizontal Tubes in Fluidized Beds,’’ ASME J. Heat Transfer, **102**(2), pp. 152–157.
[6] A. Baerg, A., Klasson, J., and Gishler, P. E., 1950, ‘‘Heat Transfer in a Fluidized Solids Bed,’’ Can. J. Res., **28**(8), p. 287.
[7] Borodulya, V. A., Yu, S., Teplitsky, A. P., Sorokin, V. V., Markevich, I. I., and Kovenskiy, V. I., 1989, ‘‘External Heat Transfer in Polydispersed Fluidized Beds at Increased Temperatures,’’ J. Eng. Phys., **56**(5), pp. 767–773.
[8] Chen, J. C., and Tuzla, K., 1955, ‘‘Heat Transfer to Immersed Surfaces in Bubbling Fluidized Beds,’’ *Annual Review of Heat Transfer*, **7**, C. Tien, ed., Begel House Pub., Washington, D. C., pp. 1–38.
[9] Vreedenberg, H. A., 1960, ‘‘Heat Transfer Between a Fluidized Bed and a Vertical Tube,’’ Chem. Eng. Sci., **11**(4), pp. 274–285.
[10] Wender, L., and Cooper, G. T., 1958, ‘‘Heat Transfer Between Fluidized Solids Beds and Boundary Surfaces—Correlation of Data,’’ AIChE J., **4**(1), pp. 15–23.
[11] Borodulya, V. A., Yu, S., Teplitsky, A. P., Markevich, I. I., Hassan, A. F., and Yeryomenko, T. P., 1991, ‘‘Heat Transfer Between a Surface and a Fluidized Bed: Consideration of Pressure and Temperature Effects,’’ Int. J. Heat Mass Transf., **34**(1), pp. 47–53.
[12] Chen, J. C., 1976, ‘‘Heat Transfer to Tubes in Fluidized Beds,’’ Invited Lecture, Paper No. 76-HT-75, *National Heat Transfer Conference*, St. Louis, MO, ASME.
[13] Molerus, O., and Schweinzer, J., 1989, ‘‘Prediction of Gas Convective Part of the Heat Transfer to Fluidized Beds.’’ *Fluidization IV*, Engineering Foundation, New York, pp. 685–693.
[14] Martin, H., 1981, ‘‘Fluid-Bed Heat Exchangers—A New Model for Particle Convective Energy Transfer,’’ Chem. Eng. Commun., **13**, pp. 1–16.
[15] Martin, H., 1984, ‘‘Heat Transfer Between Gas Fluidized Beds of Solid Particles and the Surfaces of Immersed Heat Exchanger Elements I,’’ Chem. Eng. Process., **18**, pp. 157–169.
[16] Martin, H., 1984, ‘‘Heat Transfer Between Gas Fluidized Beds of Solid Particles and the Surfaces of Immersed Heat Exchanger Elements II,’’ Chem. Eng. Process., **18**, pp. 199–223.
[17] Adams, R. L., and Welty, J. R., 1979, ‘‘A Gas Convection Model of Heat Transfer in Large Particle Fluidized Beds,’’ AIChE J., **25**(3), pp. 395–405.
[18] Decker, N., and Glicksman, L. R., 1983, ‘‘Heat Transfer in Large Particle Fluidized Beds,’’ Int. J. Heat Mass Transf., **26**(9), pp. 1307–1320.
[19] Mickley, H. S., and Fairbanks, D. F., 1955, ‘‘Mechanism of Heat Transfer to Fluidized Beds,’’ AIChE J., **1**(3), pp. 374–385.
[20] Ozkaynak, T. F., and Chen, J. C., 1978, ‘‘Average Residence Times of Emulsion and Void Phases at the Surface of Heat Transfer Tubes in Fluidized Beds,’’ AIChE Symp. Ser., **74**, pp. c1–c9.
[21] Chandran, R., and Chen, J. C., 1982, ‘‘Bed-Surface Contact Dynamics for Horizontal Tubes in Fluidized Beds,’’ AIChE J., **28**(6), pp. 907–913.
[22] Chandran, R., and Chen, J. C., 1985, ‘‘Influence of the Wall on Transient Convection Into Packed Media,’’ AIChE J., **31**(1), pp. 168–170.
[23] Kubie, J., and Broughton, J., 1975, Int. J. Heat Mass Transf., **18**, p. 289.
[24] Kunii, D., and Smith, J. M., 1960, AIChE J., **6**, pp. 71–78.
[25] Anderson, T. B., and Jackson, R., 1967, ‘‘A Fluid Mechanical Description of Fluidized Beds,’’ Ind. Eng. Chem. Fundam., **6**, pp. 527–539.
[26] Gidaspow, D., 1994, *Multiphase Flow and Fluidization*, Academic Press, San Diego, CA.
[27] Hrenya, C. M., and Sinclair, J. L., 1997, ‘‘Effects of Particle-Phase Turbulence in Gas-Solid Flows,’’ AIChE J., **43**, p. 853.
[28] van Wachem, B. G. M., Schouten, J. C., van den Bleek, C. M., Krishna, R., and Sinclair, J. L., 2002, ‘‘Comparative Analysis of CFD Models of Dense Gas-solid Systems,’’ AIChE J., **47**(5), pp. 1035–1051.
[29] Arastoopour, H., 2002, ‘‘Numerical Simulation and Experimental Analysis of Gas/Solid Flow Systems: 1999 Flour-Daniel Plenary Lecture,’’ Powder Technol., **119**(2–3), pp. 59–67.
[30] Cundall, P. A., and Strack, O. D. L., 1979, ‘‘A Discrete Numerical Model for Granular Assemblies,’’ Geotechnique, **29**, pp. 47–65.
[31] Tsuji, Y., Tanaka, T., and Ishida, T., 1992, ‘‘Lagrangian Numerical Simulation of Plug Flow of Cohesionless Particles in a Horizontal Pipe,’’ Powder Technol., **71**, pp. 239–250.
[32] Drake, T. G., and Walton, Ol. R., 1995, ‘‘Comparison of Experimental and Simulated Grain Flows,’’ ASME J. Appl. Mech., **62**, pp. 131–135.
[33] Langston, P. A., Tuzun, U., and Heyes, D. M., 1996, ‘‘Distinct Element Simulation of Interstitial Air Effects in Axially Symmetric Granular Flows in Hoppers,’’ Chem. Eng. Sci., **51**, pp. 873–891.
[34] Tsuji, Y., Kawaguchi, T., and Tanaka, T., 1993, ‘‘Discrete Particle Simulation of Two-dimensional Fluidized Bed,’’ Powder Technol., **77**, pp. 79–87.
[35] Hoomans, B. P. B., Kuipers, J. A. M., Briels, W. J., and Van Swaaij, W. P. M., 1996, ‘‘Discrete Particle Simulation of Bubble and Slug Formation in a Two-dimensional Gas-Fluidized Bed: A Hard Sphere Approach,’’ Chem. Eng. Sci., **51**, pp. 99–118.
[36] Xu, B. H., and Yu, A. B., 1997, ‘‘Numerical Simulation of the Gas-Solid Flow in a Fluidized Bed by Combining Discrete Particle Method with Computational Fluid Dynamics,’’ Chem. Eng. Sci., **52**(16), pp. 2785–2806.
[37] Xu, B. H., Yu, A. B., Chew, S. J., and Zulli, P., 2000, ‘‘Numerical Simulation of the Gas-Solid Flow in a Bed with Lateral Gas Blasting,’’ Powder Technol., **109**, pp. 13–26.
[38] van Wachem, B. G. M., van der Schaaf, J., Schouten, J. C., Krishna, R., and van den Bleek, C. M., 2001, ‘‘Experimental Validation of Lagrangian-Eulerian Simulations of Fluidized Beds,’’ Powder Technol., **116**(2–3), pp. 155–165.
[39] Xu, B. H., Yu, A. B., Zulli, P., and Chen, J. C., 2000, ‘‘A Study of Bubble Dynamics in a Gas Fluidized Bed,’’ *Fluidization 2000 Science and Technology*, 7th China-Japan Symposium, October 20–22, 2000, D. Xu and S. Mori, eds, Xi’an, China, pp. 125–130.
[40] Nusselt, W., 1916, *Die Oberflachenkondensation des Wasser dampfes*, Z. Vereins deutscher Ininuere, **60**, pp. 541–575.
[41] Marto, P. J., Looney, D. J., Rose, J. W., and Wanniarachchi, A. S., 1986, ‘‘Evaluation of Organic Coatings for the Promotion of Dropwise Condensation of Steam,’’ Int. J. Heat Mass Transf., **29**(8), pp. 1109–1117.
[42] Jakob, M., 1936, Mech. Eng. (Am. Soc. Mech. Eng.), **58**, p. 729.
[43] Welch, J. F., and Westwater, J. W., 1961, ‘‘Microscopic Study of Dropwise Condensation,’’ *International Developments in Heat Transfer*, Part 2, ASME, New York, pp. 302–309.
[44] Sugawara, S., and Katusuta, K., 1966, ‘‘Fundamental Study on Dropwise Condensation,’’ *Proc. 3rd International Heat Transfer Conference*, **2**, ASME, New York, pp. 354–361.
[45] Umur, A., and Griffith, P., 1965, ‘‘Mechanism of Dropwise Condensation,’’ ASME J. Heat Transfer, **87**, pp. 275–282.
[46] Eucken, A., 1937, Naturwissenschaften, **25**, p. 209.
[47] Graham, C., and Griffith, P., 1973, ‘‘Drop Size Distribution and Heat Transfer in Dropwise Condensation,’’ Int. J. Heat Mass Transf., **16**, pp. 337–346.
[48] Rose, J. W., and Glicksman, L. R., 1973, ‘‘Dropwise Condensation—The Distribution of Drop Sizes,’’ Int. J. Heat Mass Transf., **16**, pp. 411–425.
[49] Tanaka, H., 1975, ‘‘A Theoretical Study of Dropwise Condensation,’’ ASME J. Heat Transfer, **97**(1), pp. 72–78.
[50] Rose, J. W., 1981, ‘‘Dropwise Condensation Theory,’’ Int. J. Heat Mass Transf., **24**, pp. 191–194.
[51] Wu, Y. T., Yang, C. X., and Yuan, X. G., 2002, ‘‘Drop Distribution and Numerical Simulation of Dropwise Condensation Heat Transfer,’’ Int. J. Heat Mass Transf., **44**, pp. 4455–4464.
[52] Carey, V. P., 1992, *Liquid-Vapor Phase Change Phenomena*, Hemisphere Publishing Corp., Washington.
[53] Mikic, B. B., 1969, ‘‘On Mechanism of Dropwise Condensation,’’ Int. J. Heat Mass Transf., **12**, pp. 1311–1323.
[54] LeFevre, E. J., and Rose, J. W., 1966, ‘‘A Theory of Heat Transfer by Dropwise Condensation,’’ *Proc. 3rd Intern. Heat Transfer Conf., AIChE*, **2**, p. 362.
[55] Hirschfelder, J. O., Curtiss, C. F., and Bird, R. B., 1954, *Molecular Theory of Gases and Liquids*, John Wiley, New York.
[56] Zisman, W., 1964, *Contact Angle, Wettability and Adhesion*, Adv. In Chem. Series, no. 43, F. M. Fowkes, ed., Amer. Chem. Soc., Washington, DC.
[57] de Gennes, P. G., 1985, ‘‘Wetting: Statics and Dynamics,’’ Rev. Mod. Phys., **57**(3), Part 1, pp. 827–863.

[58] Johnson, R. E., Jr., 1959, ‘‘Conflicts Between Gibbsian Thermodynamics and Recent Treatments of Interfacial Energies in Solid-Liquid-Vapor Systems,’’ J. Phys. Chem., **63**, pp. 1655–1658.
[59] Wayner, P. C., Jr., 1999, ‘‘Intermolecular Forces in Phase-Change Heat Transfer: 1998 Kern Award Review,’’ AIChE J., **45**(10), pp. 2055–2068.
[60] Tanasawa, I., 1991, *Advances in Condensation Heat Transfer*, **21**, Adv. In Heat Transfer, Academic Press, New York, pp. 55–140.
[61] Wilkins, D. G., Bromley, L. A., and Read, S. M., 1973, ‘‘Dropwise and Filmwise Condensation of Water Vapor on Gold,’’ AIChE J., **19**, p. 119.
[62] Woodruff, D. W., and Westwater, J. W., 1979, ‘‘Steam Condensation on Electroplated Gold: Effect of Plating Thickness,’’ Int. J. Heat Mass Transf., **22**, p. 629.
[63] Zhang, D. C., Lin, Z. Q., and Lin, J. F., 1986, ‘‘New Surface Materials for Dropwise Condensation,’’ *Proc. 8th International Heat Transfer Conference*, San Francisco, **4**, pp. 1677–1682.
[64] Zhao, Q., Zhang, D. C., Zhu, X. B., Xu, D. W., Lin, Z. Q., and Lin, J. F., 1990, ‘‘Industrial Application of Dropwise Condensation,’’ *Proc. 9th Intern. Heat Transfer Conf.*, Jerusalem, **4**, pp. 391–394.
[65] Ma, X. H., Xu, D. Q., and Lin, J. F., 1994, ‘‘A Study of Dropwise Condensation on the Ultra-thin Polymer Surfaces,’’ *Proc. 10th Intern. Heat Transfer Conference*, Brighton, UK, **3**, pp. 356–364.
[66] Kumar, A., and Whitesides, G. M., 1994, ‘‘Patterned Condensation Figures as Optical Diffraction Gratings,’’ Science, **263**, pp. 60–62.
[67] Das, A. K., Kilty, H. P., Marto, P. J., Andeen, G. B., and Kumar, A., 2000, ‘‘The Use of an Organic Self-Assembled Monolayer Coating to Promote Dropwise Condensation of Steam on Horizontal Tubes,’’ ASME J. Heat Transfer, **122**, pp. 278–286.
[68] Chaudhury, M. K., and Whitesides, G. M., 1992, ‘‘How to Make Water Run Uphill,’’ Science, **256**, pp. 1539–1541.
[69] Elwing, S., Welin, A., Askendal, A., Nilsson, U., and Lundstrom, I., 1987, ‘‘A Wettability Gradient Method for Studies of Macromolecular Interactions at the Liquid Solid Interface,’’ J. Colloid Interface Sci., **119**, p. 203.
[70] Daniel, S., 2001, ‘‘Fast Drop Movement During Condensation on a Surface Possessing a Wettability Gradient,’’ M.S. thesis, Dept. of Chemical Engineering, Lehigh University.
[71] S. Daniel, S., Chaudhury, M. K., and Chen, J. C., 2001, ‘‘Fast Drop Movements Resulting from the Phase Change on a Gradient Surface,’’ Science, **291**, pp. 633–636.

Sarit Kumar Das
Heat Transfer and Thermal Power Lab,
Mechanical Engineering Department,
Indian Institute of Technology,
Madras, India 600036

Nandy Putra

Peter Thiesen

Wilfried Roetzel

Institut für Thermodynamik,
Universität der Bundeswehr Hamburg,
D-22039 Germany

Temperature Dependence of Thermal Conductivity Enhancement for Nanofluids

Usual heat transfer fluids with suspended ultra fine particles of nanometer size are named as nanofluids, which have opened a new dimension in heat transfer processes. The recent investigations confirm the potential of nanofluids in enhancing heat transfer required for present age technology. The present investigation goes detailed into investigating the increase of thermal conductivity with temperature for nano fluids with water as base fluid and particles of Al_2O_3 or CuO as suspension material. A temperature oscillation technique is utilized for the measurement of thermal diffusivity and thermal conductivity is calculated from it. The results indicate an increase of enhancement characteristics with temperature, which makes the nanofluids even more attractive for applications with high energy density than usual room temperature measurements reported earlier.
[DOI: 10.1115/1.1571080]

Keywords: *Conduction, Heat Transfer, Suspensions, Thermal, Thermophysical*

Introduction

Heat transfer technology stands at the cross roads of miniaturization on one hand and astronomical increase in heat flux on the other. The usual enhancement techniques for heat transfer can hardly meet the challenge of ever increasing demand of heat removal in processes involving electronic chips, laser applications or similar high energy devices. The factors which limit the usual techniques are many folded. One major limitation is the poor thermal characteristics of usual heat transfer fluids. They are about two orders of magnitude less efficient in conducting heat compared to metals. This inherent inadequacy of these fluids makes the heat removal mechanism less effective even with the best utilization of their flow properties.

The idea of increasing thermal conductivity of fluids with conducting particles suspended on them is not new. Ahuja [1] and Liu et al. [2] carried out the studies on practical implication of hydrodynamics and heat transfer of slurries. However, the usual slurries with suspended particles of the order of micro to millimeters suffer from a number of drawbacks. The abrasive action of the particles causes erosion of components, clogging becomes a major problem in small flow passages and their requirement of momentum transfer increases the pressure drop considerably. In addition to these the tendency of micro/millimeter size particles to settle under gravity brings fouling and related problems. Thus eventhough the slurries have higher conductivities, they are hardly useable as heat transfer fluids from other technological considerations.

The above bottleneck of slurries with micron or bigger size particles can be removed by using particles of nanometer dimensions. The concept was first materialised by series of research works at the Argonne National Laboratory and probably Choi [3] was the first to call the fluids with particles of nanometer dimension suspended in them as ‘‘nano-fluids,’’ which has gained popularity.

The subsequent study by Lee et al. [4] was a detail measurement of thermal conductivity of two types of nano particles Al_2O_3 and CuO. The average weighted particle diameter they used were 23.6 nm for CuO and 38.4 nm for Al_2O_3. These particles were used with two different base fluids—water and ethylene glycol to get four combinations of nanofluids. Using transient hot wire method, the thermal conductivities of the fluids were measured which showed significant improvement. The phenomenal increase in the thermal conductivities of the liquids with the addition of small volume of nano particles has created tremendous interest in this technique of heat transfer enhancement. The reason for this lies in the fact that due to small particle size and their small volume fraction problems such as clogging and increase in pressure drop become insignificant. The large surface area of the nano particles not only reduces the non equilibrium effect between fluid and solid but also increases the stability of the particles and sedimentation problem is greatly reduced. A more recent study by Xuan and Li [5] has shown that even with particles as large as 100 nm (which is rather sub-micron particles rather than nano particles) the stability can be achieved by using very meagre amount of laurate salt.

Thus the problems of traditional slurries can be eliminated by reducing the particles to nanometer dimensions. It must be kept in mind that the enhancement that is talked about in the above studies is only that of thermal conductivity. The real enhancement of heat transfer capability of these fluids when used under convective condition is expected to be much higher as the studies of Ahuja [1], Sohn and Chen [6] for laminar flow and that of Liu et al. [2] for turbulent flow indicate. This makes nanofluids a prospective candidate for cooling application such as energy intensive laser and X-ray applications, super conducting magnets, high speed computing systems, fibre manufacturing processes and high-speed lubrication applications.

The need of explaining the results observed above can be fulfilled by theorising them or fitting them to existing theories. The classical theory of thermal conductivity of fluid with suspended solid particles is from Maxwell [7] more than a century back which assumes the shape of particles to be spherical. This theory was subsequently modified for non-spherical particles by Hamilton and Crosser [8] for solid to liquid thermal conductivity ratio of more than 100. This formula was further confirmed by Wasp [9] for spherical particles. However measurement of Lee et al. [4] confirmed that even though the model of Hamilton and Crosser [8] agrees well with Al_2O_3-water or ethylene glycol nanofluid, it fails in the case of nanofluids containing CuO nanoparticles. Thus, it can be said that simple model using the concept of suspensions of millimeters to micrometer dimensions are doubtful for application to nanofluids. The reason for the failure of Hamilton and

---

Contributed by the Heat Transfer Division for publication in the JOURNAL OF HEAT TRANSFER. Manuscript received by the Heat Transfer Division July 31, 2001; revision received January 21, 2003. Associate Editor: S. S. Sadhal.

Crosser [8] model to CuO nanofluid may lie in the fact that the particles of Al_2O_3 used in the experiment were of 38.4 nm size while that of CuO was 23.6 nm. It is well known that the oxides of metals are thermally insulators when compared to pure metals. Hence even though difficult to produce, the recent efforts are towards using pure metal nano powders such as Cu-ethylene glycol or Cu-transformer oil nanofluids. Xuan and Li [5] could enhance the thermal conductivity of water by using Cu particles of comparatively large size (100 nm) to the same extent as has been done by oxide particles of Cu of much smaller dimension (36 nm). The more recent breakthrough was again from Argonne National Laboratory by Eastmann et al. [10] which brought out the astonishing finding that by using pure Cu nanoparticles of less than 10 nm size a phenomenal 40% increase in thermal conductivity can be attained with only 0.3% volume fraction of the solid. This indicates very clearly that Maxwell [7] or Hamilton Crosser [8] model breaks down completely with decreasing particles size in the nanometer range. Thus as has been felt by Eastman et al. [10] that the ‘‘anomalously increased’’ effective thermal conductivity of nanofluids with smaller particles cannot be explained by existing theories because they do not take into account the phenomenal increase of surface to volume ratio of particles with decreasing size.

All the investigation mentioned above measured thermal conductivity at room temperature and hence failed to have an insight to probable enhancement mechanism. Apart from this in all the cases above measurements were made by a particular variation of transient hot-wire method. Even though it has been claimed that this method is suitable for electrically conducting fluids, no discussion has been presented on the possible concentration of ions of conducting fluids around the hot wire due to the electrical field there. Thus, the present study aims at throwing some light on the enhancement mechanism of heat transfer by experimentally evaluating the temperature effect on thermal conductivity. The experimental method used here is based on the oscillation method proposed by Roetzel [11] and further developed by Czarnetski [12]. The method is purely thermal and the electrical components of the apparatus are away from the test sample which does not influence the ion movements. Finally the enhancements of conductivity of Al_2O_3 and CuO based water nano fluids at higher temperature will give more clear idea about the behavior of nano fluids at the practical range of application since all the single phase cooling application uses temperatures between room and saturation temperature.

Preparation and Characterization of Nanofluids

The preparation of nanofluid must ensure proper dispersion of nanoparticles in the liquid and proper mechanism such as control of pH value or addition of surface activators to attain the stability of the suspension against sedimentation. In the present experiment ultrasonic vibration is used for dispersing the particles. The nano particles were produced (by Nanophase Technologies Corporation) using physical vapor synthesis method. Under atmospheric condition these particles form loose agglomerates, which are of the order of micrometers as can be seen in the TEM photographs shown in Fig. 1. However they can be dispersed in the fluid quite successfully which results in breaking of the agglomerates to some extent giving particles of nanometer range as shown in Fig. 2. The particles of the nano powder show a lognormal size distribution. The size distribution of a typical sample is given in Fig. 3. The volume weighted average values of particle diameter for Al_2O_3 was 38.4 nm while that for CuO was 28.6 nm. As can be seen from Fig. 2 the agglomerates of nanoparticles after dispersion are much smaller compared to that for the power, which confirms a good dispersion in the liquid. However to compare the results with Lee et al. [4] no effort has been made to further break up the smaller agglomerates.

The dispersion of the particles was done by first mixing the required volume of the powder in the chemical measuring flask with distilled water and then using Ultrasonic vibration to disperse it. It may be mentioned here that the true density of particles are more than 50 times the apparent density. Hence the volume of the solid was determined by calculating the equivalent weight the solid using the true density (neglecting the weight of air trapped inside) and using that weight the suspension was made. After making the proper mixture the flask was kept under ultrasonic vibration for 12 hours. After this no sedimentation was observed for the fluids for about next 12 hours and thereafter minor sedimentation were observed for 3% and 4% (volume) suspensions and none for 1% and 2% (volume) suspensions. Even though in practical applications it is expected to stabilize the particles with suitable third agent such as oleic acid or laurate salts, in the present case this has not been done. This is because of the fact that the time required for the experiments were much less than that required for the first sedimentation to occur and the addition of the third agent may influence the thermal conductivity of base fluid itself and thus the real enhancement by using nanoparticles may be over shadowed. To keep consistency with this, for each experiment freshly vibrated fluid was used so that the experimental time of 1.5 to 2 hours does not bring out sedimentation. As a cross check, the density of nanofluids was measured and was also calculated from the weight of powder alone and the volume of the suspension assuming the rest of the volume to be of water. The two calculations agreed excellently excluding any possibility of agglomerates with non wetted space in between. Thus nano fluids were prepared which are usable for conductivity measurement without any stabilising agent.

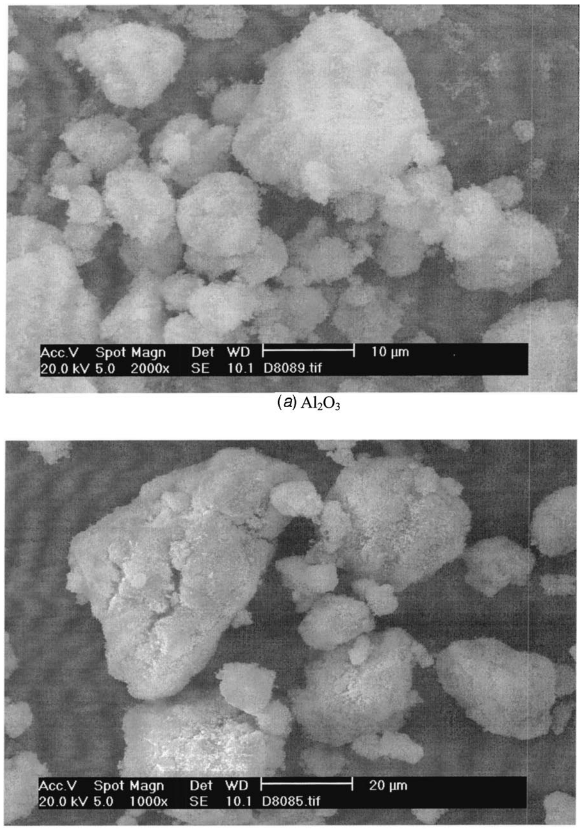

(a) Al_2O_3

(b) CuO

Fig. 1 TEM photographs of agglomerated powder of nano particles

Measurement of Thermal Conductivity

Principle of Measurement. The measurement of thermal diffusivity and the thermal conductivity is based on the energy equation for conduction given by

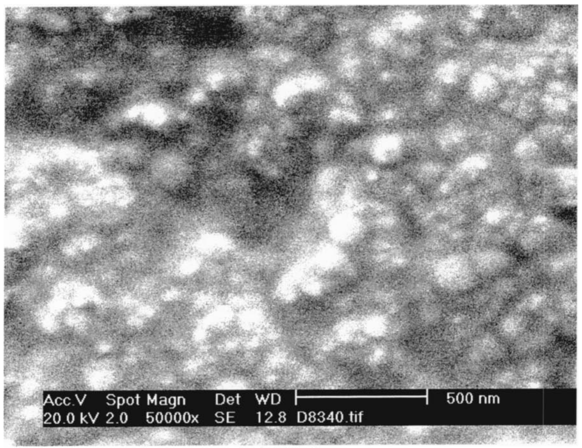

(*a*) Al_2O_3

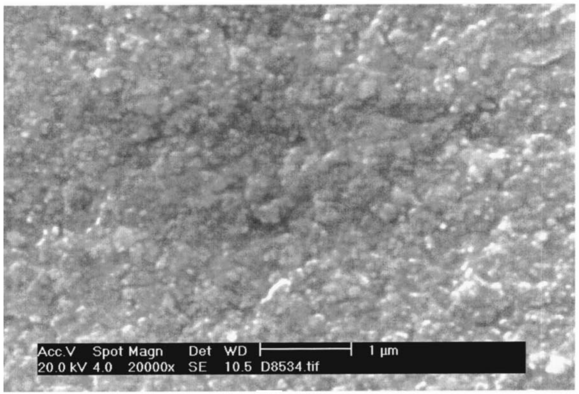

(*b*) CuO

Fig. 2 TEM photographs of dispersed nano particles

$$\frac{1}{\alpha}\frac{\partial T}{\partial t}=\nabla^2 T \tag{1}$$

In the present case this equation is applied with the assumption that the test fluid is isotropic and the thermophysical properties are uniform and constant with time throughout the entire specimen volume. The cylindrical fluid volume considered for analysis with its boundaries is shown in Fig. 4. At the surfaces *A* and *B*, periodic temperature oscillations are generated with an angular velocity given by

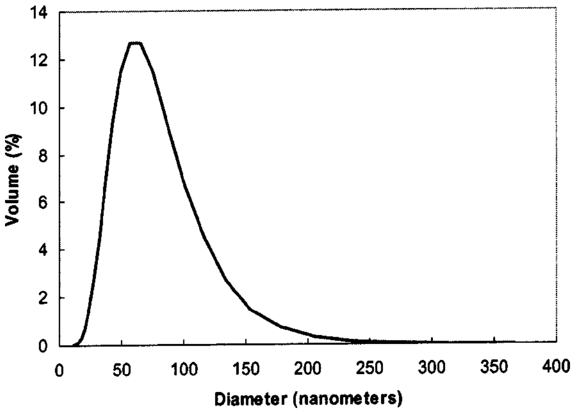

Fig. 3 Volume weighted particle size distribution for Al_2O_3 particles

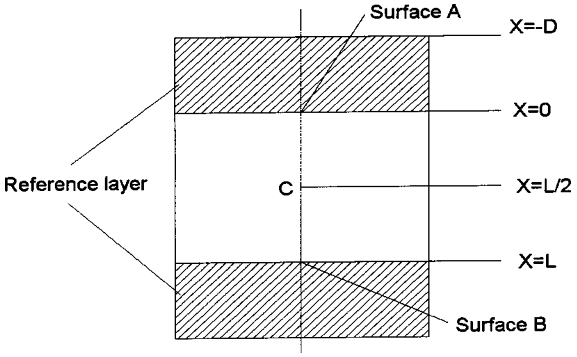

Fig. 4 The fluid volume for analysis

$$\omega=\frac{2\pi}{t_p} \tag{2}$$

Thus with the nondimensional space and time co-ordinates

$$\xi=x\sqrt{\frac{\omega}{\alpha}} \tag{3}$$

$$\tau=\omega\cdot t \tag{4}$$

the governing Eq. (1) in its one dimensional form can be reduced to

$$\frac{\partial^2 T}{\partial \xi^2}=\frac{\partial T}{\partial \tau} \tag{5}$$

For the general case of input oscillations with same main frequency but different amplitude and phase at surfaces *A* and *B*, the boundary conditions are given by

$$T(\xi_0=0,\tau)=T_m+u_0\cos(\tau+G_0) \tag{6}$$

$$T(\xi_L=L\sqrt{\omega/a},\tau)=T_m+u_L\cos(\tau+G_L) \tag{7}$$

Under steady periodic conditions the solution of the differential Eq. (5) with boundary condition given by Eqs. (6) and (7) can be obtained by using method of Laplace transform. The solution can be written in complex form as

$$T(\xi,\tau)=T_m+\frac{u_L e^{iG_L}\sinh(\xi\sqrt{i})-u_0 e^{iG_0}\sinh(\sqrt{i}(\xi-\xi_L))}{\sinh(\xi_L\sqrt{i})}e^{i\tau} \tag{8}$$

The complex amplitude ratio between the mid point of the specimen and the surface can be given by

$$B^*=\frac{2u_L e^{iG_L}}{u_L e^{iG_L}+u_0 e^{iG_0}}\cosh\left[\frac{L}{2}\left(\frac{i\omega}{\alpha}\right)^{1/2}\right] \tag{9}$$

The real measurable phase shift and amplitude ratio can be expressed as

$$\Delta G=\arctan\left(\frac{\mathrm{Im}(B^*)}{\mathrm{Re}(B^*)}\right) \tag{10}$$

And

$$\frac{u_L}{u_{L/2}}=\sqrt{\mathrm{Re}(B_R^*)^2+\mathrm{Im}(B_R^*)^2} \tag{11}$$

By measuring phase and amplitude of temperature oscillation at the two surfaces as well as at the center (point C), the thermal diffusivity can be determined either from Eq. (10) or from Eq. (11). To measure the thermal conductivity directly from experiment, we must consider the temperature oscillation in the reference layer at the two boundaries of the test fluid. The frequency of temperature oscillation in this layer is also same as the frequency generated in the Peltier element (described later) and that in the test fluid. The one dimensional heat conduction in the reference layer is given by

$$\frac{\partial^2 T_R}{\partial \zeta^2} = \frac{\partial T_R}{\partial \tau} \tag{12}$$

$$\text{where} \quad \zeta = x\sqrt{\frac{\omega}{\alpha_R}}. \tag{13}$$

The boundary conditions for the reference layer are

$$T_R(\zeta=0,\tau) = T(\xi=0,\tau) \tag{14}$$

Interface temperature balance,

$$\lambda_R \sqrt{\frac{\omega}{\alpha_R}} \frac{\partial T_R}{\partial \zeta}\bigg|_{\zeta=0} = \lambda \sqrt{\frac{\omega}{\alpha}} \frac{\partial T}{\partial \xi}\bigg|_{\xi=0} \tag{15}$$

Interface flux balance.

The solution of Eq. (12) along with boundary condition (14) and (15) is given by

$$T_R^*(\zeta,\tau,\xi_L) = T_m + u_0 e^{i(\tau+G_0)} \cosh(\zeta\sqrt{i}) + C[u_R e^{i(\tau+G_R)} - u_0 e^{i(\tau+G_0)} \cosh(\xi_L\sqrt{i})] \frac{\sinh(\zeta\sqrt{i})}{\sinh(\xi_L\sqrt{i})} \tag{16}$$

Where

$$C = \frac{\lambda}{\lambda_R} \sqrt{\frac{\alpha_R}{\alpha}} \tag{17}$$

The complex amplitude ratio in this case between $x=-D$ (D being the thickness of reference layer) and $x=0$ is given by

$$B_R^* = \cosh(\zeta_D\sqrt{i}) - C\sinh(\zeta_D\sqrt{i}) \times \left[\frac{(u_L/u_0)e^{i(G_L-G_0)} - \cosh(\xi_L\sqrt{i})}{\sinh(\xi_L\sqrt{i})}\right] \tag{18}$$

The real phase shift and amplitude attenuation is giving by

$$\Delta G_R = \arctan\left(\frac{\mathrm{Im}(B_R^*)}{\mathrm{Re}(B_R^*)}\right) \tag{19}$$

and

$$\frac{u_D}{u_0} = \sqrt{\mathrm{Re}(B_R^*)^2 + \mathrm{Im}(B_R^*)^2} \tag{20}$$

the thermal diffusivity of the test fluid has already been measured as described earlier and that of the reference layer being known, the thermal conductivity of the specimen can be evaluated from above formula.

Data Reduction

The temperature oscillation generated by the Peltier element requires to be strictly periodic. The shape of the oscillation is immaterial since any periodic oscillation can be expanded by Fourier series in the form

$$T(\tau) = \frac{a_0}{2} + \sum_{k=1}^{\infty} A_k \sin(k\tau + \theta_k) \tag{21}$$

where

$$a_k = \frac{1}{\pi}\int_0^{2\pi} T(\tau)\cos(k\tau)\,d\tau, \quad k=1,2,3,\ldots \tag{22}$$

$$b_k = \frac{1}{\pi}\int_0^{2\pi} T(\tau)\sin(k\tau)\,d\tau, \quad k=0,1,2,3,\ldots \tag{23}$$

and

$$A_k = \sqrt{(a_k^2 + a_k^2)}, \quad \tan G_k = \frac{a_k}{b_k} \tag{24}$$

In the solution presented for fluid as well as the reference layer earlier the fundamental oscillation is considered and the coefficients a_k and b_k are evaluated by numerical integration at the appropriate location to yield the corresponding amplitude attenuation and phase shift.

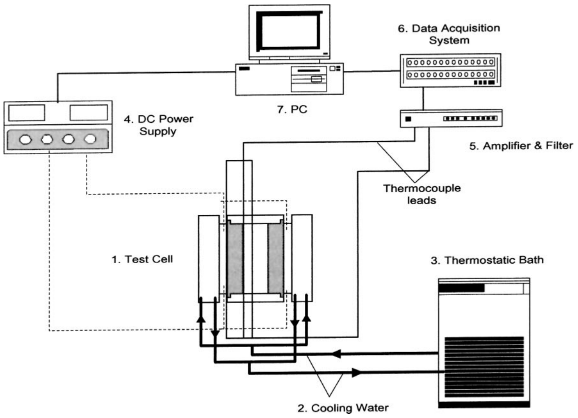

Fig. 5 Schematic of the experimental setup

The Experimental Set-up and Procedure

The experimental setup has been shown schematically in Fig. 5. As has been stated earlier a temperature oscillation technique which is a modification of that used by Czarnetzky and Roetzel [12] has been used. This technique required a specially fabricated test cell (1) which is cooled by cooling water (2) on both of the ends coming from a thermostatic bath (3). Electrical connection provides power to the Peltier element which is a DC power obtained through a converter (4). The temperatures are measured in the test section (discussed later) through a number of thermocouples and these responses are amplified with amplifier (5) followed by a filter which is finally fed to the data acquisition system (6) comprising of a card for logging the measured data. The data logger is in turn connected to a computer with proper software (7) for online display which is required to assess the steady oscillation and for recording data. Since in the present experiments the prime objective is to observe the effect of temperature on the enhancement of thermal conductivity, the control of temperature of the fluid is important which is effected by proper adjustment of the cooling water from the thermostatic bath. However for higher temperatures it is sometimes necessary to increase the input voltage to attain the required temperature level which is then fine tuned to the required temperature by control of cooling water temperature.

The test section is a flat cylindrical cell as shown in Fig. 6. The cell is mounted with its axis in horizontal position. The frame of the cell is made of POM (Polyoxymethylene), which can be machined accurately and simultaneously acts as the first layer of insulation. The frame consists of the main part with a 40 mm hole in it which makes the cavity to hold the test fluid, as well as the two end plates which sandwiches the water cooler and the Peltier element at both ends. The hole in the main frame is closed from both sides with disc type reference material of 40 mm diameter and 15 mm thickness. Thus the space for the test fluid is formed which has a dimension of 40 mm dia and 8 mm thickness. The fluid is filled through a small hole in the body of the cell. The measurement of temperatures are made at three locations—at the interface of the Peltier element and the reference layer, at the interface of the reference layer and test fluid and the central axial plane of the test fluid. For this purpose Ni-CrNi thermocouples of 0.1 mm diameter were used at the interfaces and 0.5 mm diameter

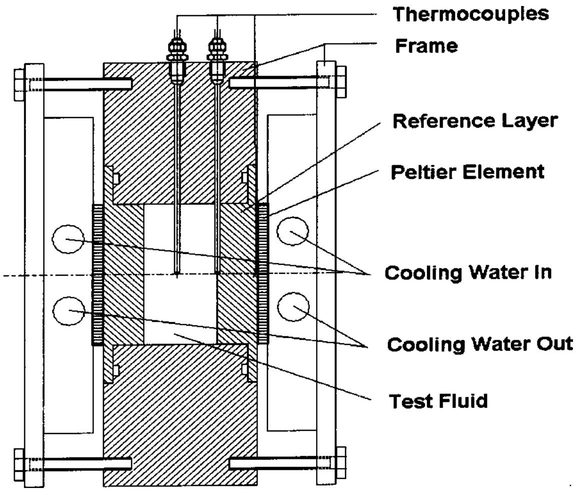

Fig. 6 The test cell construction

at the central plane from its stability consideration. The thermocouples at the interfaces are put in small groove and welded at the tip while that at the center hangs from the wall. Before putting the end reference plates, the central position of the thermocouple was ensured through a precision measurement. The entire cell was insulated further. The temperature of reference material was given periodic oscillation by two Peltier elements (40 mm×40 mm square) from two ends. The temperature oscillation in this element are controlled to obtained two objectives:

1) The oscillation amplitude is adjusted to be kept small enough (of the order of 1.5 K) within the test fluid to retain constant fluid properties and to avoid natural convection on one hand and on the other it is not allowed to decrease too much so that the accuracy of the measurement is affected. The Grashof number was calculated to be 850, which is below the asymptotic limit for onset of natural convection. The measurement with pure water of known conductivity reconfirmed that no natural convection was present.

2) The smaller amplitude and accurate adjustment of the mean temperature of oscillation ensures that for the conducting fluid, test is made at the sought temperature.

For example a typical temperature oscillation recorded at the locations after steady oscillation are reached is shown in Fig. 7. It can be seen that the amplitude of the temperature oscillation produced by the Peltier element gets attenuated and its phase gets shifted as it crossed the reference material. It is further attenuated and shifted as it reaches the center of the test fluid. The theoretical principle presented earlier reveals that it is possible to evaluate the thermal diffusivity of the fluid very accurately by considering amplitude attenuating of thermal oscillation from the boundary (fluid reference material interface) to the center of the fluid. However for direct measurement of thermal conductivity one has to consider the attenuation at the reference material as well. Since the reference material has been worked upon and the microcracks and inhomogenity of material brings out uncertainty in its thermal conductivity value, direct evaluation of thermal conductivity of fluid is less accurate. Hence, in the present measurement the value of thermal diffusivity for the nanofluid is evaluated from experiment. Subsequently the density has been measured and specific heat is calculated from handbook, as

$$C_{p,nf}=\frac{m_s C_{p,s}+m_w C_{p,w}}{m_s+m_w} \tag{25}$$

Finally the thermal conductivity is calculated from

$$\lambda_{nf}=\alpha_{nf}\rho_{nf}C_{p,nf} \tag{26}$$

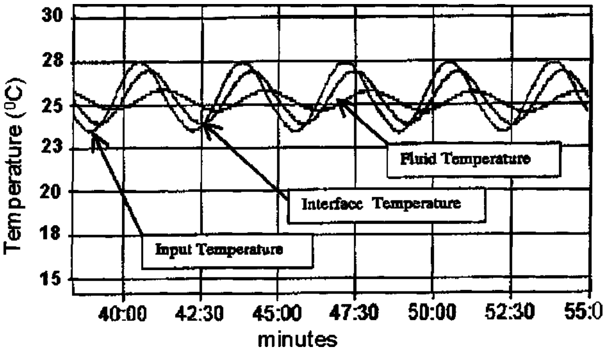

Fig. 7 Amplitude attenuation of source temperature oscillation in reference layer and in test fluid

Error Estimates

For measurement of thermal diffusivity, the main sources of experimental uncertainty are the accuracy of thermocouples and the location of temperature measurement. In the present measurement thermocouples with an accuracy of 0.1 K were used and location was determined with an accuracy 1.25%. Over the measured temperature range the accuracy of temperature measurement came out to be 3.4%. This limits the combined uncertainty of measurement within an acceptable limit of 5%. It was observed that for using method to determine thermal conductivity directly one has to take care of uncertainty of the thermal conductivity of the reference layer, which is more than 5%. This makes the measurement more inaccurate and hence has not been used here. As a safeguard against experimental error the experimental setup described above was first calibrated by measuring thermal diffusivity of demineralised and distilled water over a wide range of temperature. It was found that over the temperature range of 20°C to 50°C the average deviation of thermal diffusivity from the standard values of handbook (VDI Wärmeatlas [13]) was 2.7%. Over the range from 20 to 30°C the maximum error was found to be limited to 2.11%. The maximum error was limited to 7% up to temperature 50°C. This gave an indication about the accuracy of the measurement and showed that over the entire range of measurement an acceptable range of accuracy existed. The values of error in thermal conductivity calculated from error analysis in the previous section also matches well with the observed values. The enhancement thermal conductivity values of nano fluids are moderate increase of 2% to 36% over the base value of water and hence the present ranges of accuracy is acceptable for the present case.

Results and Discussion

To begin with measurements were done at room temperature for Al_2O_3 and CuO nanofluids of water at various particles volume concentrations. The results presented in Fig. 8 show an excellent agreement with the measurement of Lee et al. [4] considering the fact that minor differences in particles size existed between them. The room temperatures were also not identical in the two cases, still the present measurements confirm the same level of enhancement of thermal conductivity as observed by the Argonne group using an entirely different measurement technique.

Subsequently measurements were made for the nano fluids of Al_2O_3-water and CuO-water with different particles concentration and most importantly at different temperatures, which is the main objective of the present work. Figure 9 shows the enhancement of thermal conductivity of Al_2O_3 based nanofluids with temperature. It is interesting to see both for 1% and 4% (volume) particle concentrations there is a considerable increase in the enhancement from 21°C to 51°C. With 1% particles at room temperature (21°C)

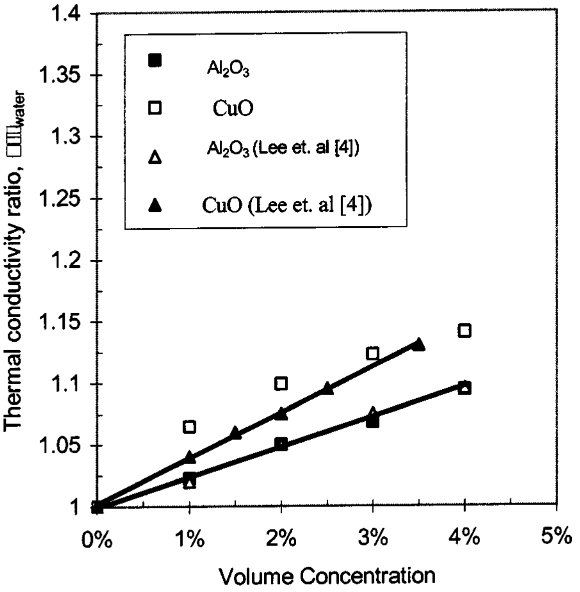

Fig. 8 Enhancement of thermal conductivity at room temperature

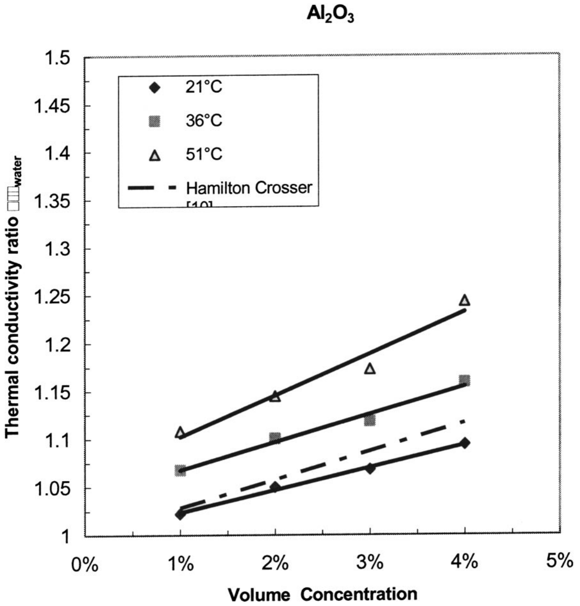

Fig. 10 Enhancement of thermal conductivity of water—Al_2O_3 nanofluids against particles concentration and temperature and comparison with Hamilton-Crosser [8] model

the enhancement in only about 2%, but at 51°C this value increases to about 10.8%. Thus the present measurement shows that in practical heat transfer application the enhancement achieved by adding small volume of nano particles is considerably higher compared to that believed at present [4]. The measurement with 4% concentration shown in the same figure (Fig. 9) shows one more interesting feature. Here the enhancement goes from 9.4% to 24.3% with temperature rising from 21°C to 51°C. The average rate of increase of enhancement in this case in much higher compared to that of the 1% nanofluids, which can be observed from the increased slope of the fitted line of the two nano fluids shown. Thus it can be said that the enhancement of thermal conductivity shows a dramatic increase with temperature and the rate of this increase depends on the concentration of nano particles. As has been expressed by Lee et al. [4], the Hamilton−Crosser [8] model given by effective conductivity in the form

$$\frac{\lambda}{\lambda_w}=\frac{\lambda_s+(n-1)\lambda_w-(n-1)\phi(\lambda_w-\lambda_s)}{\lambda_a+(n-1)\lambda_w+\phi(\lambda_w-\lambda_s)} \tag{27}$$

is agreed upon by Al_2O_3 based nano fluids at room temperature. This is somewhat contrary to the results of CuO based nanofluid which did not agree with the model. Figure 10 shows that this agreement for Al_2O_3-water is somewhat accidental because the agreement is only good at room temperature. At elevated temperature even Al_2O_3-water nanofluid disagree with Hamilton−Crosser model [8] because this model hardly changes the effective conductivity with temperature (the change in λ/λ_w curve with temperature for this model [8] cannot be distinguished). This brings out some insight to the mechanism for thermal conductivity enhancement in nanofluids. In ordinary slurries the thermal conductivity is increased due to higher thermal conductivity of the solid particles and hence the combine effective conductivity is some kind of average of the liquid and solid conductivity. The Hamilton−Crosser [8] is a kind of such average, weighted according to the particles shape.

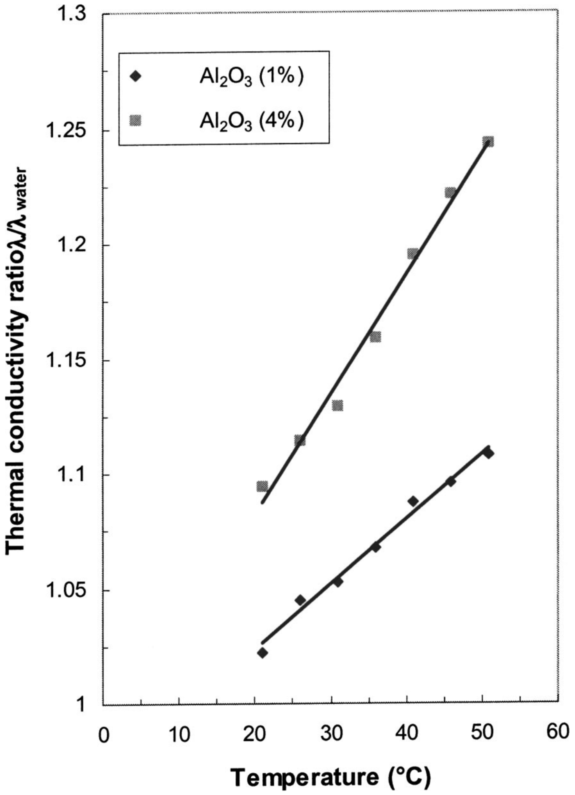

Fig. 9 Temperature dependence of thermal conductivity enhancement for water—Al_2O_3 nanofluids

In nanofluid the main mechanism of thermal conductivity enhancement can be thought as the stochastic motion of the nano particles. Presumable this Brownian like motion will be dependent on fluid temperature and so this amount of enhancement with temperature is quite explicable for Al_2O_3 since the particles size (both for Lee et al. [4] and present study) was bigger. At low temperature this motion was less significant giving the characteristics of normal slurries which rapidly changed at elevated temperature bringing more nanoeffect in the conducting behavior of the fluid. This explanation also indicates the reason for the "anomalously increased" conductivity of nano fluid containing Cu particles of less than 10 nm as observed by Eastman et al. [10]. The main mechanism of enhancement of thermal conductivity there is the increased stochastic motion of the nanoparticles

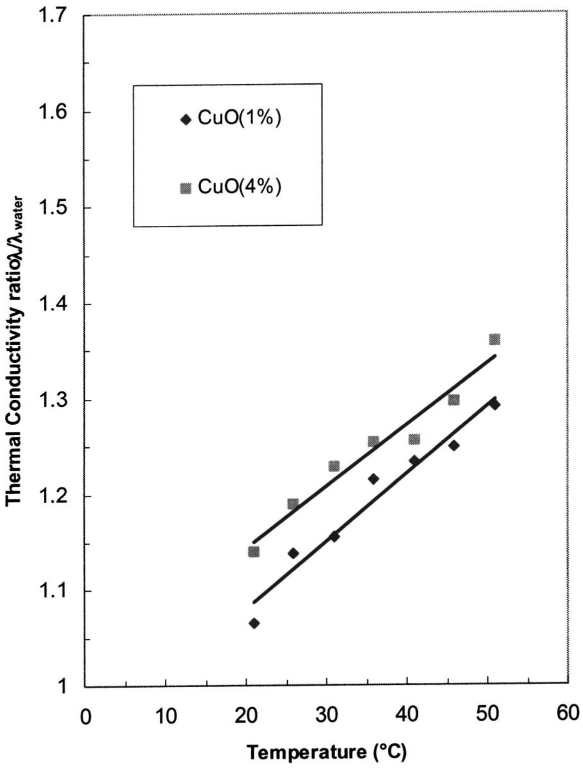

Fig. 11 Temperature dependence of thermal conductivity enhancement for water—CuO nanofluids

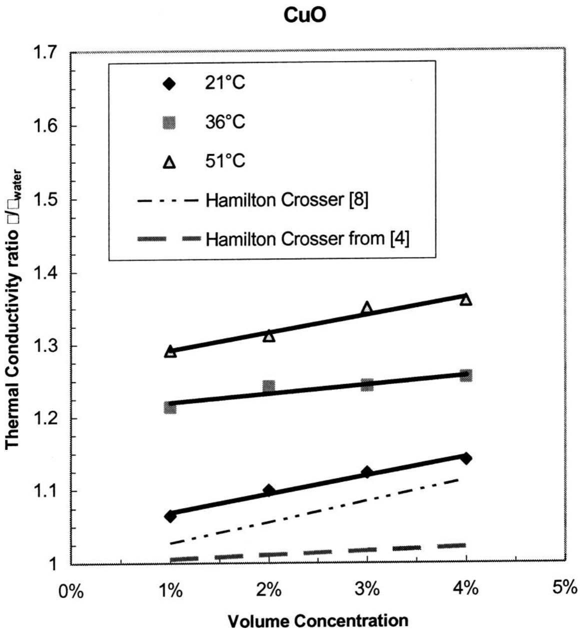

Fig. 12 Effect of particle concentration on the thermal conductivity enhancement of water-CuO nanofluids at different temperature and comparison with Hamilton-Crosser [8] models of [4] and calculated by us

rather than the thermal conductivity of Cu because the volume fraction used (0.5%) was too small to bring about such an effect by any kind weighted average. Thus the present results indicate that it is possible to have a threshold temperature corresponding to each particle size at which the effective thermal conductivity of nanofluids starts deviating from that of usual slurries and the enhancement through stochastic motion of the particles start dominating. The measurements with CuO-water nanofluid show nano effect even at room temperature and in this case the enhancement of the conductivity is much higher as shown in Fig. 11. The Hamilton-Crosser [8] model gives a value less than that measured at room temperature. The measurement of enhancement of conductivity with particle concentration at different temperature presented in Fig. 12 confirms this and indicates the necessity for better theoretical model for these for the entire range of temperature. In this case the effect of temperature on thermal conductivity enhancement is even more dramatic as it climbs from 6.5% to 29% (for 1% particle concentration) and from 14% to 36% (for 4% particle concentration). However, in the case of CuO water nanofluid the rate of change of enhancement with temperature did not change as much with concentration as that observed for Al_2O_3-water nanofluid in the present measurements. At this point, we would like to express that the Hamilton Crosser model for CuO as calculated by Lee et al. [4] seems to be incorrect since the curve given by them corresponds to a particle conductivity of less than 2 W/m K which is much smaller than value in literature (~17.65 W/m K) [14]. For convenience we have indicated both the curves in Fig. 12.

In general, the effect of particle concentration was found to be less for CuO water nanofluid compared to Al_2O_3-water nanofluids which can be attributed to the larger particle size of Al_2O_3. On the other hand the effect of temperature was found to be more predominant in CuO water fluid which is due to the stochastic motion of the particles which arguably will be more mobile with smaller particle size.

Conclusion

The temperature effect of thermal conductivity enhancement in nanofluids has been presented through an experimental investigation. A purely thermal method consisting of temperature oscillations at the fluid sample has been used for this purpose. The method has been found to be appropriate for nano fluids both from accuracy and prevention of natural convection point of view. The measurement confirmed the level of thermal conductivity enhancement at room temperature as observed by others. It was further observed that a dramatic increase in the enhancement of conductivity takes place with temperature. It is observed that a 2 to 4 fold increase in thermal conductivity enhancement of nanofluids can take place over a temperature range of 21°C to 51°C. This finding makes nanofluids even more attractive as cooling fluid for devices with high energy density where the cooling fluid is likely to work at a temperature higher than the room temperature. It has been observed that nanofluids containing smaller CuO particles show more enhancement of conductivity with temperature. However the enhancement is considerably increased for nanofluids with Al_2O_3 as well. The effect of particle concentration was observed to be more for the Al_2O_3-water system. The measurements indicate that particle size is an important parameter for the observed behavior and the usual weighted average type of model for effective thermal conductivity is a poor approximation of the actual enhancement particularly at the higher temperature range. The results indicate that a stochastic motion of nano particles can be a probable explanation if future theoretical studies can confirm it.

The main limitation of the previous and the present experiments is the non-availability of nano particles of different sizes for same material which can conclusively indicate the effect of particle size. However the present study brings out the important aspect of temperature dependence of conductivity enhancement which can be used as an important source for a comprehensive theoretical treatment in the future.

Acknowledgment

This research work has been carried out during a research stay of the first author at the Institut für Thermodynamik (Institute of Thermodynamics) of the Universität der Bundeswehr Hamburg (University of the Federal Armed Forces, Hamburg) under the research fellowship granted by the Alexander von Humboldt Foundation which is greatly appreciated. Thanks are also due to the Deutsche Akademischer Austauschdienst (German Academic Exchange Service) who financed the research stay of Mr. Nandy Putra in Hamburg.

Nomenclature

B = the amplitude ratio
B^* = complex amplitude ratio
C = constant
C_p = specific heat, kJ/kg.K
D = thickness of reference layer, m
G = the phase shift
L = thickness of fluid sample, m
m = mass, kg
n = shape factor
T = temperature, K
t = time, s
t_p = period, s
u = amplitude, K
x = space coordinate, m

Greek Symbols

α = thermal diffusivity, m^2/s
Δ = difference
ξ, ζ = dimensionless space coordinates
λ = thermal conductivity, W/(m K)
ω = the constant angular frequency, 1/s
ρ = the density, kg/m^3
τ = dimensionless time (angle)

Subscripts

m = mean
nf = nanofluids
R = reference layer
s = solid (particle)
w = water (base fluid)

References

[1] Ahuja, A. S., 1975, ''Augmentation of Heat Transport in Laminar Flow of Polystyrene Suspension: Experiments and Results,'' J. Appl. Phys., **46**(8), pp. 3408–3416.
[2] Liu, K. V., Choi, U. S., and Kasza, K. E., 1988, ''Measurement of Pressure Drop and Heat Transfer in Turbulent Pipe Flows of Particulate Slurries,'' Argonne National Laboratory Report, ANL-88-15.
[3] Choi, U. S., 1995, ''Enhancing Thermal Conductivity of Fluids With Nanoparticles,'' *Developments and Applications of Non-Newtonian Flows*, D. A. Siginer and H. P. Wang, eds., FED-vol. 231/MD-Vol. 66, ASME, New York, pp. 99–105.
[4] Lee, S., Choi, U. S., Li, S., and Eastman, J. A., 1999, ''Measuring Thermal Conductivity of Fluids Containing Oxide Nanoparticles,'' ASME J. Heat Transfer, **121**, pp. 280–289.
[5] Xuan, Y., and Li, Q., 2000, ''Heat Transfer Enhancement of Nanofluids,'' Int. J. Heat Fluid Flow, **21**, pp. 58–64.
[6] Sohn, C. W., and Chen, M. M., 1981, ''Microconvective Thermal Conductivity in Disperse Two Phase Mixture as Observed in a Low Velocity Couette Flow Experiment,'' ASME J. Heat Transfer , **103**, pp. 47–51.
[7] Maxwell, J. C., 1881, *A Treatise on Electricity and Magnetism*, 2nd Ed., **1**, Clarendon Press, Oxford, U.K., p. 435.
[8] Hamilton, R. L., and Crosser, O. K., 1962, ''Thermal Conductivity of Heterogeneous Two Component Systems,'' I & EC Fundamentals, **1**(3), pp. 187–191.
[9] Wasp, F. J., 1977, ''Solid-Liquid Slurry Pipeline Transportation,'' Trans. Tech., Berlin.
[10] Eastman, J. A., Choi, U. S., Li, S., Yu, W., and Thompson, L. J., 2001, ''Anomalously Increased Effective Thermal Conductivities of Ethylene Glycol-Based Nanofluids Containing Copper Nanoparticles,'' Appl. Phys. Lett., **78**(6), pp. 718–720.
[11] Roetzel, W., Prinzen, S., and Xuan, Y., 1990, ''Measurement of Thermal Diffusivity Using Temperature Oscillations,'' *Thermal Conductivity 21*, C. Y, Cremers and H. A. Fine, eds., Plenum Press, New York and London, pp. 201–207.
[12] Czarnetzki, W., and Roetzel, W., 1995, ''Temperature Oscillation Techniques for Simultaneous Measurement of Thermal Diffusivity and Conductivity,'' Int. J. Thermophys., **16**(2), pp. 413–422.
[13] *VDI-Wärmeatlas*, 1997, 8th Ed. VDI Verlag GmbH, Düsseldorf.
[14] Bolz, R., and Tuve, G., 1970, *Handbook of Tables for Applied Engineering Science*, The Chemical Rubber Co.

Dual Pulsating or Steady Slot Jet Cooling of a Constant Heat Flux Surface

A. K. Chaniotis

D. Poulikakos
e-mail: dimos.poulikakos@ethz.ch

Y. Ventikos

Institute of Energy Technology,
Laboratory of Thermodynamics
in Emerging Technologies,
ETH, Zurich, Switzerland

The work presented in this paper focuses on the effect of jet pulsation on the heat transfer and fluid dynamics characteristics of single and double jet impingement on a constant heat flux heated surface. Specifically, the influence of frequency, amplitude and in particular, of the phase difference of the two jets on the temperature distribution of the heated surface is examined. The simulations are conducted using a novel, remeshed Smooth Particle Hydrodynamics (SPH) methodology that is based on particle discretization of the governing compressible Navier-Stokes equations. It was found that the strong aerodynamic and thermal interaction that exists between the gaseous jets and the impingement surface leads to non-linear system responses; with serious heat transfer implications. Dynamical systems analysis leads to the identification of intermittent periodic/chaotic behavior above a threshold value of the Reynolds number. As a result, a reduction in the maximum plate temperature in a window of periodic behavior was discovered.
[DOI: 10.1115/1.1571093]

Keywords: *Convection, Electronics, Heat Transfer, Impingement, Numerical Methods*

1 Introduction

Jet impingement is a technique for enhancing heat transfer that is employed in a variety of applications ranging from drying of textiles and films, to metal sheet manufacturing and to gas turbine and electronic equipment cooling. Due to its importance, jet impingement heat transfer has been the topic of numerous investigations in recent years (see for example [1–4]). Most of the previous studies have focused on optimizing transport processes associated with steady jet impingement. Configurations that have received attention include impingement of axisymmetric (circular) and slot (two dimensional) jets, with different spacing between the jet(s) and the impingement surface, or different inlet velocity profiles (flat, developed, or inclined), and with or without confinement [1–3,5–11].

More recently, researchers started pursuing experimentally and numerically heat transfer enhancement via flow pulsation [12–22]. Some investigations involving jet pulsation show no enhancement or even deterioration of heat transfer due to pulsation [15,17], because the pulsation energy in these studies affects mainly the large scales of the flow and not the small structures which can enhance the mixing [15] or because the non-linear dynamic responses of the hydrodynamic and thermal boundary layers [17]. Others reported a marginal beneficial effect of pulsation [23,24]. There are also some studies which reported significant enhancement [13,19,20,25], because of either the interaction of large scale structures with the boundary layer (periodic formation of vortical structures which impinge upon the heat transfer surface), or because of the secondary flow structures (vortex rings) [18,19,22]. In summary due to a host of physical reasons explained in [17–19,22] a variety of heat transfer scenarios are possible.

The present basic research work considers a pair of slot air jets, impinging on a heated solid wall at constant heat flux. This jet impingement arrangement is attractive due to its simplicity and to the high convective heat transfer coefficients it yields, corresponding to low wall temperatures. Most of the studies of jet impingement with pulsation presented until now focus on single jet configurations (Fig. 1(*a*)). An early investigation of two-dimensional jet array impingement on an isothermal plate [5] showed heat transfer reduction but improved heat flux uniformity compared to the single jet geometry. Recently, Sheriff and Zumbrunnen in [21] investigated experimentally the effect of flow pulsation on the cooling performance of jet arrays and reported improved heat transfer uniformity as well as presence of coherent structures, but no significant enhancement, with respect to the heat transfer characteristics.

The focus and the main novel feature of the present work is the investigation of a pair of pulsed slot jet impingement, in an absolute sense, as well as in comparison with single pulsed jet impingement at the same flow rate (Fig. 1(*b*)).

2 Governing Equations and SPH Methodology

2.1 Basic Equations. The fundamental system of differential equations governing the motion of a viscous, heat conducting, compressible medium consists of the continuity, momentum and energy equations. The conservation equations for a calorically perfect gas without an energy source in nondimensional form are:

$$\frac{D\rho}{Dt}=-\rho\frac{\partial u_i}{\partial x_i} \tag{1}$$

$$\rho\frac{Du_i}{Dt}=-\frac{1}{M^2\gamma}\frac{\partial p}{\partial x_i}+\frac{1}{\mathrm{Re}}\frac{\partial \tau_{ij}}{\partial x_j} \tag{2}$$

with

$$\tau_{ij}=\mu\left(\frac{\partial u_i}{\partial x_j}+\frac{\partial u_j}{\partial x_i}-\frac{2}{3}\delta_{ij}\frac{\partial u_k}{\partial x_k}\right) \tag{3}$$

$$\rho c_v\frac{DT}{Dt}=\frac{\gamma}{\mathrm{Re}\,\mathrm{Pr}}\frac{\partial}{\partial x_i}\left(k\frac{\partial T}{\partial x_i}\right)-(\gamma-1)p\frac{\partial u_i}{\partial x_i}+\frac{M^2\gamma(\gamma-1)}{\mathrm{Re}}\tau_{ij}\frac{\partial u_i}{\partial x_j} \tag{4}$$

The dimensionless numbers that appear in the equations are:

$$\mathrm{Re}=\frac{\rho_0U_0L_0}{\mu_0},\quad M^2=\frac{U_0^2}{\gamma RT_0},\quad \mathrm{Pr}=\frac{\mu_0c_{p0}}{k_0} \tag{5}$$

Contributed by the Heat Transfer Division for publication in the JOURNAL OF HEAT TRANSFER. Manuscript received by the Heat Transfer Division July 15, 2002; revision received February 14, 2003. Associate Editor: S. P. Vanka.

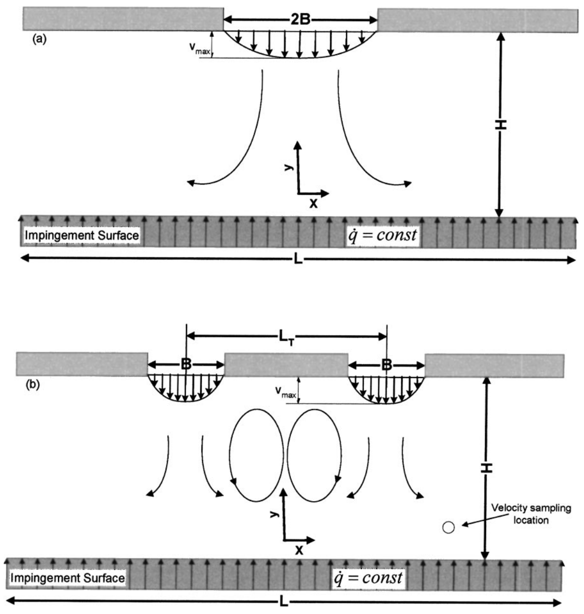

Fig. 1 Schematic representation of: (*a*) a single slot jet impingement on a heated surface; and (*b*) a pair of planar air jets impingement on a heated surface

where Re denotes the Reynolds number, M the Mach number and Pr the Prandtl number and ρ is the nondimensional density, u_i the nondimensional velocity components, p the nondimensional pressure, T the non-dimensional temperature, μ the nondimensional viscosity, k the nondimensional thermal conductivity, and c_v the nondimensional specific heat at constant volume. The dimensionless quantities are defined as:

$$x_i = \frac{x_i^*}{L_0}, \quad \rho = \frac{\rho^*}{\rho_0}, \quad t = \frac{t^* U_0}{L_0}, \quad u_i = \frac{u_i^*}{U_0}, \quad T = \frac{T^*}{T_0}, \tag{6}$$

$$p = \frac{p^*}{\rho_0 R T_0}, \quad \mu = \frac{\mu^*}{\mu_0}, \quad k = \frac{k^*}{k_0} \quad c_v = \frac{c_v^*}{c_{v0}}$$

where ρ^* is the density, u_i^* the velocity components, p^* the pressure, T^* the temperature, μ^* the viscosity, k^* the thermal conductivity, R is the gas constant, and c_v^* the specific heat at constant volume.

The quantities L_0, ρ_0, U_0, T_0, μ_0, c_{p0}, and k_0 denote the characteristic length, density, velocity, temperature, dynamic viscosity, specific gravity, specific heat and thermal conductivity, respectively, and γ is the ratio of the specific heat capacities.

The system of the differential equations (1–4) is closed with the nondimensional equation of state for an ideal gas:

$$p = \rho T \tag{7}$$

All the thermodynamic (c_v) and transport (μ,k) properties are dependent on the temperature [26,27].

In principle, a particular flow problem may be solved by integrating the mass, momentum and energy equations, which are described above, and additionally the equation of state. The initial conditions are usually prescribed functions that describe the velocity field and the two of the three scalar intensive properties (density, temperature and pressure) of the flow.

The computational domains used in the present study are shown in Figs. 1(*a*,*b*). The inflow conditions are parabolic velocity profile at constant (ambient) temperature.

Single Jet.

$$u = 0 \quad v = v_{\max}\left(1 - \frac{x^2}{B^2}\right), \quad T_{\text{inlet}} = 1 \tag{8}$$

where $v_{\max}$ is the time dependent maximum velocity of the jet (at the centerline)

$$v_{\max} = V_{\max}(1 + A\sin(\omega t)) \tag{9}$$

Pair of Jets.

$$u = 0 \quad v = v_{\max}\left(1 - \frac{\left(x - \frac{L_T}{2}\right)^2}{\left(\frac{B}{2}\right)^2}\right), \quad T_{\text{inlet}} = 1 \tag{10}$$

As in the case of a single jet,

$$v_{\max} = V_{\max}\left(1 + A\sin\left(\omega t \pm \frac{\varphi}{2}\right)\right) \tag{11}$$

where A and ω denote the amplitude and the frequency of the jet pulse, $V_{\max}$ denotes the jet time averaged maximum velocity (at the centerline) and φ denotes the phase angle between the two jets.

The average jet velocity $\overline{V}$ of the parabolic profile is

$$\overline{V} = \frac{2V_{\max}}{3} \tag{12}$$

The Reynolds number is defined as

$$\text{Re} = \frac{\overline{V}\rho D_h}{\mu} \tag{13}$$

where D_h is the slot hydraulic diameter, $D_h = 4B$ for the single jet and $D_h = 2B$ for the jet pair configurations, respectively.

The top plate is defined as an adiabatic wall (no-slip, no penetration, $dT/dy = 0$), the side outflow conditions are those of zero gradient ($du/dx = dv/dx = dT/dx = 0$) and ambient pressure boundary. The impingement plate is defined as a solid wall (no-slip, no penetration) heated with constant heat flux. In dimensionless form this heat flux reads:

$$Q = -\frac{q''_{\text{wall}} L_o}{k_0 T_0} \tag{14}$$

In order to be able to compare the heat transfer performance between the single jet and the jet pair configurations Fig. 1 we need an equivalency criterion. The criterion is that the same flow rate is issued from the two configurations. As a result, and based on the definitions above, the cooling performance of the single jet configuration for a certain Reynolds number will be compared to the cooling performance of the jet pair configuration, for a Reynolds number half as large.

A commonly examined configuration, [5], i.e., $H/B = 5$, $L_T/B = 5$ and $L/B = 20$ and $Q = 2$ (the value of Q allows for a visible rise in the temperature but at the same time the buoyancy effects are negligible) is adopted in all computations unless otherwise noted.

Additionally, a numerical simulation of compressible flow requires an accurate control of wave reflections from the computational domain. For accurate predictions, it is necessary to eliminate the acoustic waves by a mechanism as non-reflecting or absorbing boundary conditions [28,29].

2.2 Numerical Method. A Lagrangian particle method (Smooth Particle Hydrodynamics, SPH) is used in the present study for the discretization and numerical solution of the governing equations. SPH is a Lagrangian solver of the compressible Navier-Stokes equations [30,31]. The SPH equations are obtained

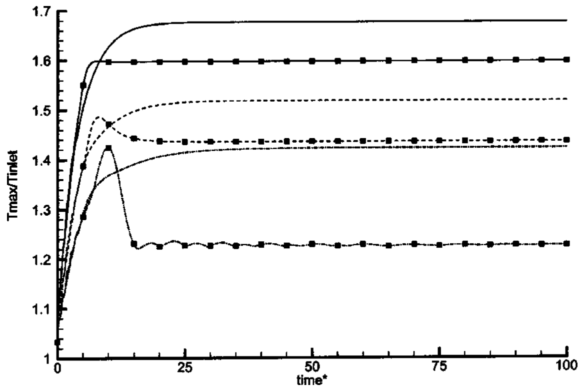

Fig. 2 Maximum surface temperature as a function of time (nondimensional): (–■–) Single jet Re=133.3, (-■-) Single jet Re=266.6, (-·-■-·-) Single jet Re=533.3, (——) Pair jet Re=66.6, (- -) Pair jet Re=133.3, and (-·-) Pair jet Re=266.6

from continuum equations of fluid dynamics by interpolating a set of points. The flow quantities are discretized into particles, where each particle α is associated with a mass m_a, density ρ_a, velocity u_a, viscosity μ_a, pressure p_a and position r_a. The key idea of the method is the representation of the physical quantities as a linear superposition of kernel functions centered on the particle locations using an interpolation operator (for more details concerning SPH and applications of the method Refs. [30–36] are recommended). Using the standard SPH formulation [31] and ideas outlined in previous works [24,37], the governing equations (1–7) can be discretized as:

$$\frac{D\rho_a}{Dt} = -\rho_a \sum_b V_b(\vec{u}_b - \vec{u}_a)\cdot\nabla_a W(r_a - r_b, h) \qquad (15)$$

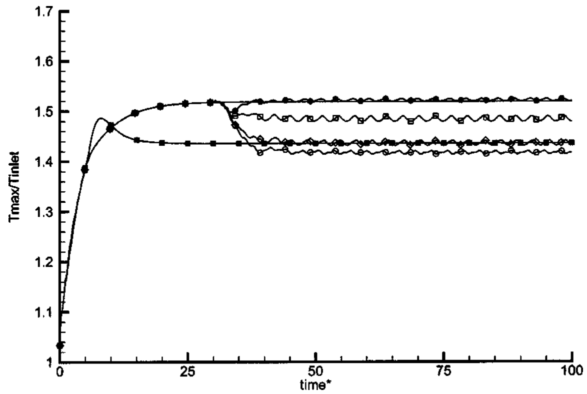

Fig. 4 Maximum surface temperature as a function of time (nondimensional): (–■–) Steady single jet for Re=266.6, (——) Steady pair jet for Re=133.3, (–●–) Pulsating pair jet *A*=0.5, ω=2, φ=0 for Re=133.3, (–□–) Pulsating pair jet *A*=0.5, ω=2, φ=1 rad for Re=133.3, (–◇–) Pulsating pair jet *A*=0.5, ω=2, φ=2 rad for Re=133.3, and (–○–) Pulsating pair jet *A*=0.5, ω=2, φ=3.14 rad for Re=133.3

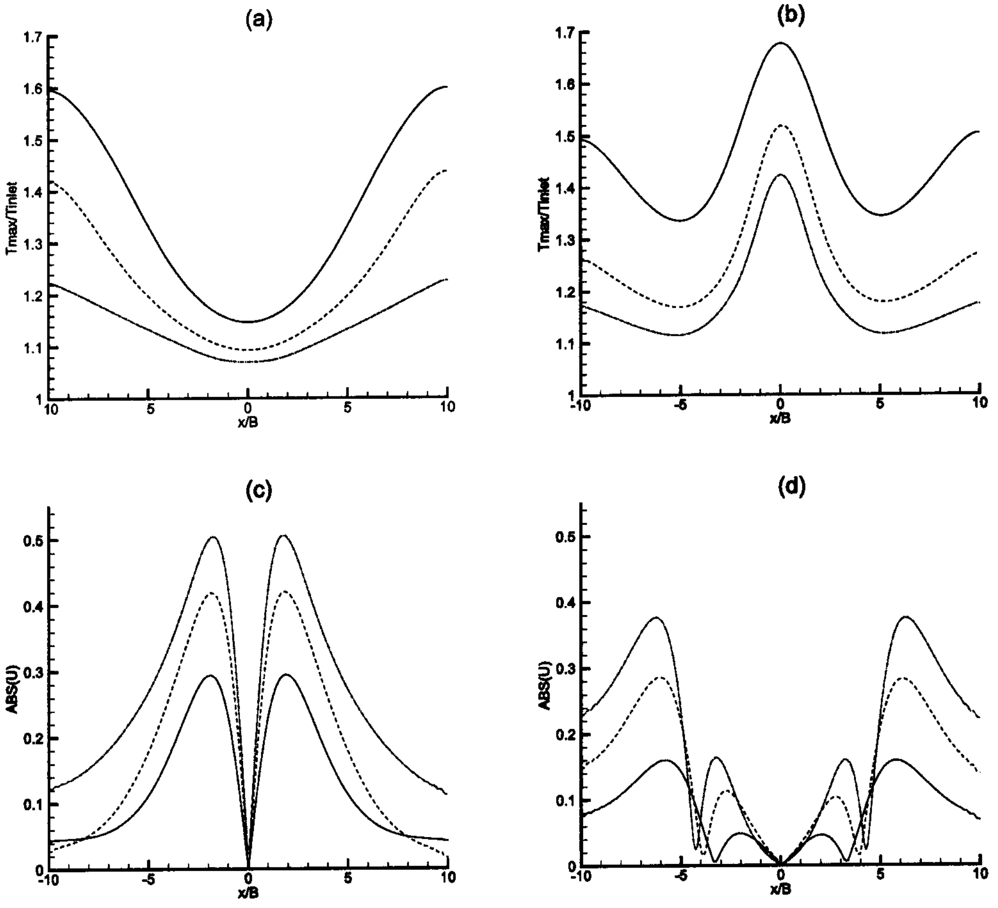

Fig. 3 Variation of the surface temperature as a function of the plate position: (*a*) single jet, (—) Re=133.3, (- -) Re=266.6, (-·-) Re=533.3; (*b*) pair jet, (——) Re=66.6, (- -) Re=133.3, (-·-) Re=266.6; (and variation of the velocity near the wall as a function of the plate position) (*c*) single jet, (——) Re=133.3, (- -) Re=266.6, (-·-) Re=533.3; and (*d*) pair jet, (——) Re=66.6, (- -) Re=133.3, (-·-) Re=266.6

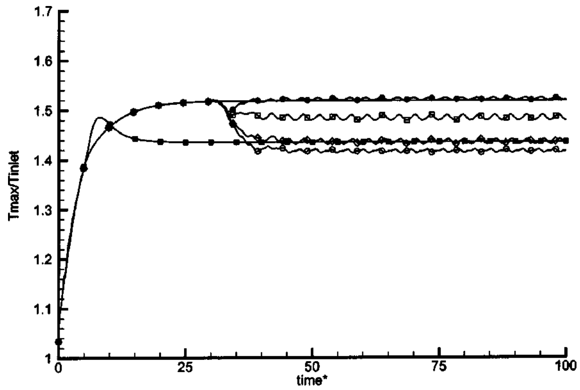

Fig. 5 Maximum surface temperature as a function of time (nondimensional): (–■–) Steady single jet for Re=266.6, (——) Steady pair jets for Re=133.3, (–●–) Pulsating pair jets $A=0.5$, $\omega=1$, $\varphi=3.14$ rad for Re=133.3, (–□–) Pulsating pair jets $A=0.5$, $\omega=2$, $\varphi=3.14$ rad for Re=133.3, and (–◇–) Pulsating pair jets $A=0.5$, $\omega=4$, $\varphi=3.14$ rad for Re=133.3

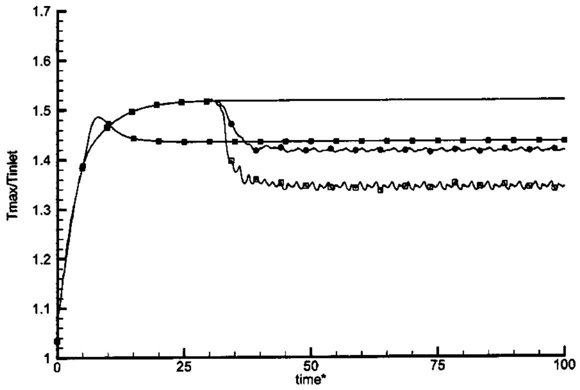

Fig. 7 Maximum surface temperature as function of time (nondimensional): (–■–) Steady single jet for Re=266.6, (——) Steady pair jets for Re=133.3, (–●–) Pulsating pair jets $A=0.5$, $\omega=2$, $\varphi=3.14$ rad for Re=133.3, and (–◇–) Pulsating pair jets $A=1.0$, $\omega=2$, $\varphi=3.14$ rad for Re=133.3

where $\vec{u}=(u,v)$.

$$\left\langle \rho\frac{Du}{Dt}\right\rangle_a = -\frac{1}{M^2\gamma}\left\langle\frac{\partial p}{\partial x}\right\rangle_a + \frac{1}{\mathrm{Re}}\left\{\frac{4}{3}\left\langle\frac{\partial}{\partial x}\mu\frac{\partial u}{\partial x}\right\rangle_a - \frac{2}{3}\left\langle\frac{\partial}{\partial x}\mu\frac{\partial v}{\partial y}\right\rangle_a + \left\langle\frac{\partial}{\partial y}\mu\frac{\partial u}{\partial y}\right\rangle_a + \left\langle\frac{\partial}{\partial y}\mu\frac{\partial v}{\partial x}\right\rangle_a\right\} \tag{16}$$

$$\left\langle \rho\frac{Dv}{Dt}\right\rangle_a = -\frac{1}{M^2\gamma}\left\langle\frac{\partial p}{\partial y}\right\rangle_a + \frac{1}{\mathrm{Re}}\left\{\frac{4}{3}\left\langle\frac{\partial}{\partial y}\mu\frac{\partial v}{\partial y}\right\rangle_a - \frac{2}{3}\left\langle\frac{\partial}{\partial y}\mu\frac{\partial u}{\partial x}\right\rangle_a + \left\langle\frac{\partial}{\partial x}\mu\frac{\partial u}{\partial y}\right\rangle_a + \left\langle\frac{\partial}{\partial x}\mu\frac{\partial v}{\partial x}\right\rangle_a\right\} \tag{17}$$

where the bracket means discretized quantity with respect to the particle a.

A general formulation is adopted for the derivation of the viscous terms of the Eqs. (16) and (17) which accounts for variable viscosity μ (viscosity is a function of temperature):

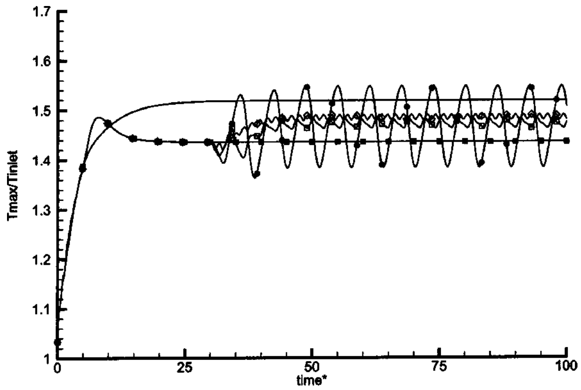

Fig. 6 Maximum surface temperature as function of time (nondimensional): (–■–) Steady single jet for Re=266.6, (——) Steady pair jets for Re=133.3, (–●–) Pulsating single jets $A=0.5$, $\omega=1$ for Re=133.3, (–□–) Pulsating single jets $A=0.5$, $\omega=2$ for Re=133.3, and (–◇–) Pulsating single jets $A=0.5$, $\omega=4$ for Re=133.3

$$\left\langle\frac{\partial}{\partial x_i}\mu\frac{\partial u^k}{\partial x_j}\right\rangle_a = \mu_a\sum_b V_b(u_b^k-u_a^k)\cdot\frac{\partial^2}{\partial x_i x_j}W(r_a-r_b,h) + \left(\sum_b V_b(\mu_b-\mu_a)\cdot\frac{\partial}{\partial x_i}W(r_a-r_b,h)\right)\left(\sum_b V_b(u_b^k-u_a^k)\cdot\frac{\partial}{\partial x_j}W(r_a-r_b,h)\right) \tag{18}$$

The energy equation reads

$$\left\langle\rho c_v\frac{DT}{Dt}\right\rangle_a = \frac{\gamma}{\mathrm{Re\ Pr}}\left\{\left\langle\frac{\partial}{\partial x}k\frac{\partial T}{\partial x}\right\rangle_a + \left\langle\frac{\partial}{\partial y}k\frac{\partial T}{\partial y}\right\rangle_a\right\} - (\gamma-1)\left\langle p\left(\frac{\partial u}{\partial x}+\frac{\partial v}{\partial y}\right)\right\rangle_a + \frac{M^2\gamma(\gamma-1)}{\mathrm{Re}}\left\{\left\langle\frac{2}{3}\mu\left[\left(\frac{\partial u}{\partial x}-\frac{\partial v}{\partial y}\right)^2+\left(\frac{\partial u}{\partial x}\right)^2+\left(\frac{\partial v}{\partial y}\right)^2\right]\right\rangle_a + \left\langle\mu\left[\left(\frac{\partial v}{\partial x}-\frac{\partial u}{\partial y}\right)^2\right]\right\rangle_a\right\} \tag{19}$$

where

$$\left\langle\frac{\partial}{\partial x_i}\left(k\frac{\partial T}{\partial x_i}\right)\right\rangle_a = k_a\sum_b V_b(T_b-T_a)\cdot\frac{\partial^2}{\partial x_i^2}W(r_a-r_b,h) + \left(\sum_b V_b(k_b-k_a)\cdot\frac{\partial}{\partial x_i}W(r_a-r_b,h)\right)\left(\sum_b V_b(T_b-T_a)\cdot\frac{\partial}{\partial x_i}W(r_a-r_b,h)\right) \tag{20}$$

The particles are moved in a Lagrangian frame, following the flow paths

$$\left\langle\frac{d\vec{x}}{dt}\right\rangle_a = \vec{u}_a \tag{21}$$

Lagrangian numerical methods enjoy the advantage of automatic adaptivity for their computational elements. However, the flow strain can cluster particles in some regions of the flow field and spread them apart in another. A novel feature of the present approach, correcting this deficiency, is the periodic re-meshing

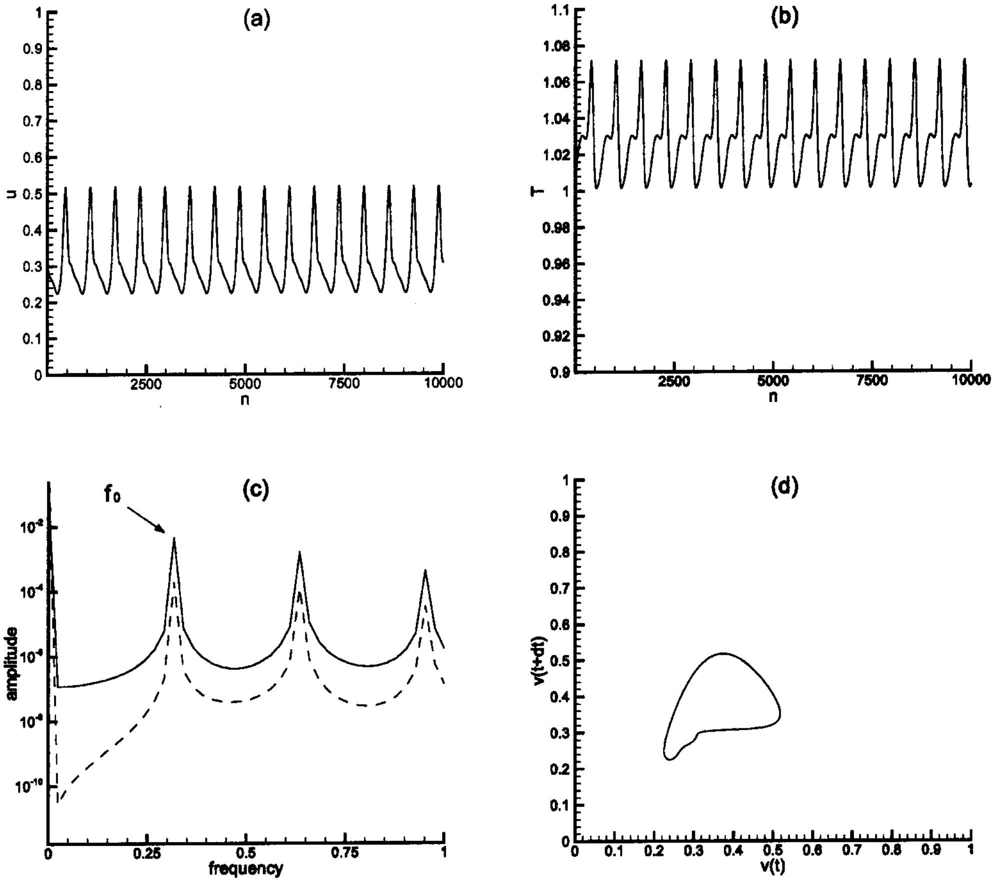

Fig. 8 Pulsating pair jets $A=1.0$, $\omega=2$, $\varphi=3.14$ rad for Re$=133.3$: (*a*) velocity time series, (*b*) temperature time series, (*c*) frequency (——) of the velocity and (– –) temperature, and (*d*) two-dimensional time delay reconstruction of the phase space

and re-initialization of the particle locations that are being distorted by the flow map by high order moment conserving kernels (remeshed SPH) [37].

All the boundary conditions are modeled by boundary particles (imaginary particles), which have similar physical properties to those of the particles that represent the flow field. The boundary particles interact with the interior particles in such a way that the necessary boundary conditions are satisfied. More detailed information for the implementation of boundary conditions in the SPH method can be found in [24,32,35]. More detailed information for the discretization, and the particle remeshing can be found in [30,31,37–40]. For the time integration, an ordinary differential equation integrator [41,42] is used, which can handle stiff and non-stiff systems accurately and with optimum computational cost. In all simulations the thermodynamic and transport properties are dependent on the temperature [26,27]. For the sake of generality, in all simulations we took into account many effects (viscous dissipation and variable properties) since we believe that this led to more accurate and more realistic modeling (DNS quality). Of course the effect of the viscous dissipation term is small.

3 Results and Discussion

The local heat transfer coefficient can be expressed as

$$h=\frac{1}{T_{\text{wall}}-T_{\text{inlet}}}q''_{\text{wall}} \tag{22}$$

where T_{inlet} is the jet inlet temperature and T_{wall} is the wall temperature. The unknown in the above equation is the wall temperature. The corresponding local Nusselt number reads $Nu=hL/k$. It is clear from Eq. (22) that the maximum wall temperature corresponds to a minimum Nusselt number. Additionally, the maximum temperature is a critical design parameter for a cooling process, exemplified by the reliable performance of electronic equipment. For this reason, the maximum wall temperature will be the basic monitoring quantity in our investigation.

Simulations are performed for $66.6<\text{Re}<533.3$ for the single jet case, which corresponds to fully laminar jets. The Prandtl number is 0.72 and the Mach number is 0.1. A Mach number less than 0.3 corresponds to a practically incompressible flow [43]. For the SPH simulations, 10,000–80,000 particles are used, depending on the Reynolds number, and always produced fully resolved solutions for all the cases [24,37].

Out of the extensive set of cases that have been simulated, we have selected a representative group that we shall utilize for quantitative comparisons. In Fig. 2 the maximum temperature of the surface is shown as a function of time for the single and pair jets for steady jet inflow. It is clear that the jet pair configuration always features higher maximum temperature when compared to a single jet of an equivalent (twice as large) Reynolds number. This difference in the maximum temperature between the single jet and the jet pair can be explained from the variation of the temperature along the plate (Fig. 3). The convection in the middle of the plate is very weak for the jet pair configuration (Fig. 3(*b*)) in contrast to the single jet (Fig. 3(*a*)) where it is in this region that the maximum convective heat transfer occurs. On the other hand, the temperature variation along the surface is smaller for the jets pair configuration (Fig. 3). It is also of interest to note that the maximum temperature difference between equivalent Reynolds numbers for single and double-jet configurations is increasing, with the increase of the Reynolds number. This means that the

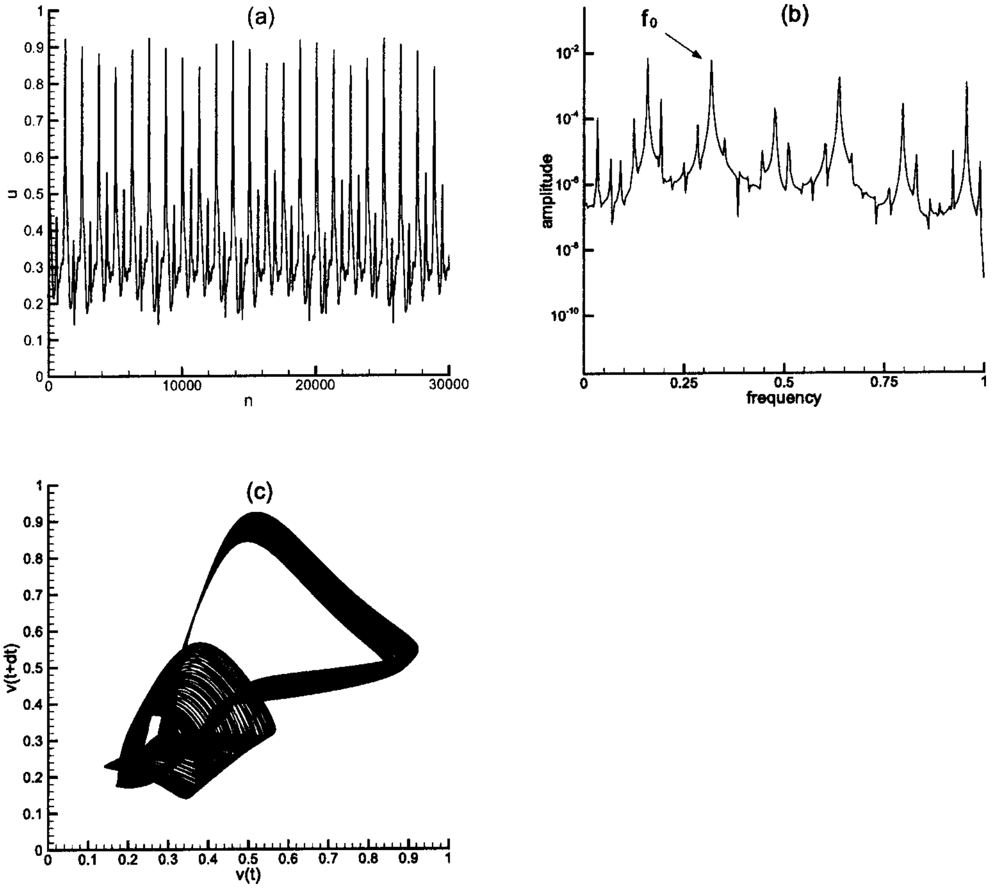

Fig. 9 Pulsating pair jets $A=1.0$, $\omega=2$, $\varphi=3.14$ rad for Re=266.6: (*a*) velocity time series, (*b*) frequency of the velocity, and (*c*) two-dimensional time delay reconstruction of the phase space

relative efficiency of the double-jet configuration is decreasing, when compared with the single-jet one, as the Reynolds number increases.

In Fig. 4 the maximum temperature is shown as a function of time for different phase angle differences of the pulsating jet pair. This figure shows that the pulsation of the two jets with amplitude $A=0.5$ and angular velocity $\omega=2$ in phase ($\varphi=0$), increases the maximum temperature by 0.4% (negligibly) and possibly within the limits of the modeling accuracy. Increasing the phase difference between the two jets, for example to $\varphi=1$ rad, the maximum temperature decreases by 2% compared to the steady jet pair case but it is still higher than that of the single steady jet.

For an even larger phase angle difference ($\varphi=2$ rad) the temperature is reduced more (5% compared with the steady jet pair) and it is comparable to the single steady jet. For the maximum possible phase angle difference ($\varphi=3.14$ rad) the temperature is reduced even more (6% compared with the steady pair) and is now smaller than that of the single steady jet.

The effect of the frequency (or angular velocity) for the jet pair and a comparison to a single jet is shown in Fig. 5. Interestingly, the maximum temperature is not a monotonic function of the frequency, which is also experimentally observed [17]. It is also shown that when the frequency is low, the maximum temperature is higher than the one reached in the steady state case. This is obviously the effect of the prevalence of lower air velocities for a relatively long period of time. Fig. 6 shows the effect of the frequency variation on the maximum temperature for the case of single jet impingement. The pulsation increases the maximum temperature compared to the steady case (a not beneficial effect for the stand point of temperature control).

One crucial parameter for heat transfer enhancement is the amplitude of the pulse. In Fig. 7, the maximum surface temperature is shown as a function of time for two different amplitudes, compared always with the steady single jet and jet pair cases. An important thermal design finding is that marked decrease of the maximum temperature can be achieved by varying the amplitude: For $A=1.0$, an 11% decrease in maximum temperature is found compared to the steady jet pair case and a decrease of about 6% compared to the steady single jet.

The importance of the effect of the amplitude is reported in [16,18,19,21,24] where a major increase of the average heat transfer coefficient is found compared with the steady-jet results. As the amplitude of the pulse increases the generated vortices penetrate more in the wall jet region and boost the heat transfer.

For Re=133, a portion of the velocity and temperature time series is shown in Fig. 8(*a*), (*b*), where the unit of "*n*" represents 5 time steps of the computation. The velocity and temperature sampling location in this and subsequent figures is designated with a circle in Fig. 1(*b*). This location is arbitrarily selected, but we have verified that the nature of the results presented is not affected by this selection. The power spectrum of the signals obtained from longer time series is shown in Fig. 8(*c*), where the peak in $f_0=0.31831$ corresponds to the frequency imposed from the pulsation. (The frequency f_0 is related to the angular velocity of the pulse ω, ($f_0=\omega/2\pi=2\text{ rad}/2\pi$)).

The two-dimensional time delay reconstruction [44] of the velocity signal is shown in Fig. 8(*c*) where the time delay used is about one tenth of the period. It is obvious that the system is characterized by a limit cycle behavior, obeying the forcing frequency of the two jets.

For higher Reynolds number ($\mathrm{Re}_{\mathrm{single}}=533.3$, $\mathrm{Re}_{\mathrm{pair}}=266.6$) the increase of the pulsation amplitude decreases the maximum plate

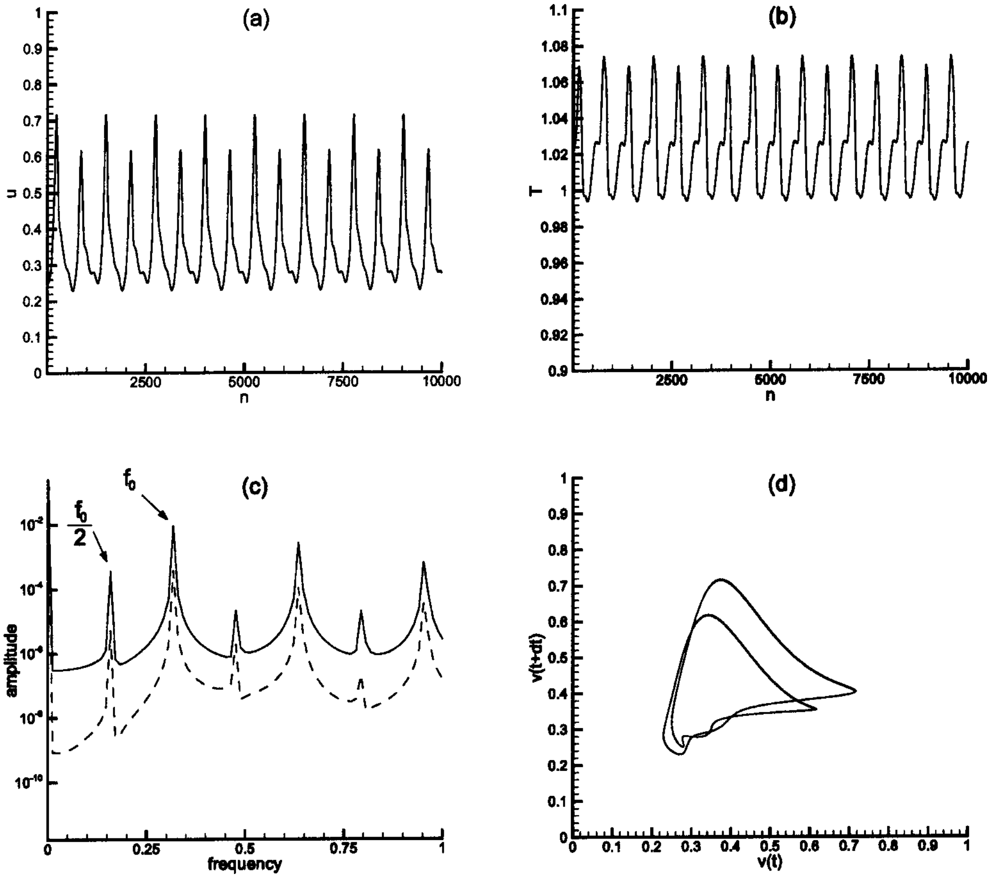

Fig. 10 Pulsating pair jets $A=1.0$, $\omega=2$, $\varphi=3.14$ rad for Re=218.6: (*a*) velocity time series, (*b*) temperature time series, (*c*) frequency (——) of the velocity and (– –) temperature, and (*d*) two-dimensional time delay reconstruction of the phase space

temperature (not shown here for brevity) an observation similar to that of Fig. 7. The difference between the steady single jet and the steady jet pair is smaller for smaller Reynolds numbers ($\mathrm{Re}_{\mathrm{single}}=266.6, \mathrm{Re}_{\mathrm{pair}}=133.3$). For the maximum amplitude of the pulsation $A=1.0$, the maximum temperature decrease is approximately 12%, compared to the steady jet pair.

For the Reynolds number Re=266.6 the signal is not periodic any more (Fig. 9(*a*)). In the frequency spectra of the velocity signal, many sub-harmonics appear, Fig. 9(*b*). The two-dimensional time delay reconstruction of the signal is presented in Fig. 9(*c*) where the time delay used is about one tenth of the period. The calculated maximum Lyapunov exponent [44] is $\lambda=0.0075$ bits/orbit. This small value of the computed Lyapunov exponent is however within the numerical error margin, for this Reynolds number, and thus inconclusive. The frequency spectrum and the emergence of subharmonics, on the other hand, hint towards a rich dynamical behavior and the possibility of a period doubling scenario [45]. This observation guides us in exploring the evolution of the system as the parameter (i.e., Reynolds number) increases from 133.3 (Fig. 8) to 266.6 (Fig. 9).

In Fig. 10(*a*), a part of the velocity signal for Re=218.6 is shown (Fig. 10(*b*) depicts a similar time series for temperature). The emergence of a second frequency, 1/2 of the main forcing frequency of the system, is observed (Fig. 10(*c*)). The attractor (Fig. 10(*d*)), shows also that the period of the velocity signal is twice the period of the pulse. The delay is again about one tenth of the period and the embedding dimension is again two.

An exhaustive set of simulations has been conducted, in order to pinpoint the exact Reynolds number that this first period doubling bifurcation takes place. It was found that this occurs at Re =208, between the two cases presented in Fig. 8 and Fig. 10, with accuracy better than 1 in the Reynolds number scale. Further increasing the Reynolds number leads to an increase of the amplitude of the first sub-harmonic, $f=f_0/2$. At the same time, the trajectories in the time delay reconstruction start to separate in two cycles as shown in Fig. 10(*d*) [45–47].

As the Reynolds number increases further, the amplitude of the sub-harmonic frequency $f=f_0/2$ becomes dominant and in the attractor the two cycles become unequal. Further increase of the Reynolds number (Re=258.6) leads to an even smaller sub-harmonic (Fig. 11 and Fig. 11(*b*)), which has frequency $f=f_0/8$. The attractor (Fig. 11(*c*) and Fig. 11(*d*)) shows likewise the existence of that sub-harmonic, as the smaller cycle of the attractor Fig. 10(*d*) splits into four trajectories Fig. 11(*d*). The minimal sufficient embedding dimension is $m=3$ (all attractor depictions in the present work are two-dimensional, however wherever quantitative phase-space computations are performed, like in the case of Lyapunov exponents, higher embedding dimensions are utilized as necessary). It is clear that the system is not following the usual period doubling bifurcation (period-2⇒period-4⇒period-8⇒etc) [47]. Such incomplete sequences have been observed in fluid dynamic systems (usually coupled with heat transfer) [48–50].

For even higher Reynolds numbers, (Re=533.3), the signal is fully non-periodic, as hinted by the time series in Fig. 12(*a*) and by the filling up of the spectrum in Fig. 12(*b*). The calculated maximum Lyapunov exponent is, in this case, $\lambda=0.37\pm0.01$ bits/orbit, which allows for a confident characterization of this case as fully chaotic.

The existence of intermittent intervals of periodicity, within the overall chaotic time series, can be deduced from Fig. 12(*a*) [51] (the same behavior is evident in the temperature time series also).

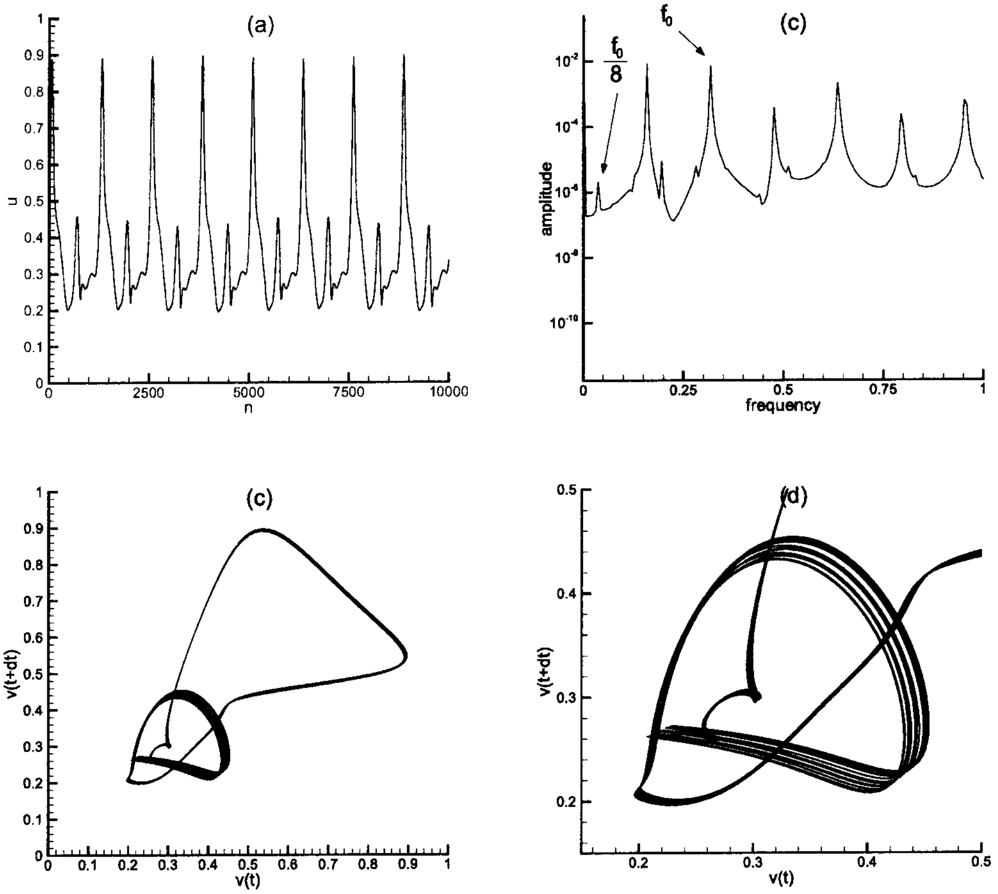

Fig. 11 Pulsating pair jets $A=1.0$, $\omega=2$, $\varphi=3.14$ rad for Re=258.6, (*a*) velocity time series, (*b*) frequency spectrum of the velocity, (*c*) two-dimensional time delay reconstruction of the phase space n, and (*d*) focus of the two-dimensional time delay reconstruction of the phase space

We can verify that the apparently periodic portions of the signal in Fig. 12(*a*) are indeed periodic, by examining the relative segments of the time series, Fig. 12(*d*) and the corresponding frequency domain signatures, Fig. 12(*e*). This switching from fully aperiodic to periodic behavior, for this Reynolds number, has implications in the observed maximum temperatures: for the aperiodic intervals, the maximum temperature presents us with significantly larger values and a much more intense oscillatory behavior than those observed during the periodic intervals (Fig. 13(*a*)). There is a predictable relationship between the operating temperature of electronic parts and reliability. Materials employed in the manufacture of electronic devices have finite temperature limits; when these limits are exceeded, the physical properties are altered and the device ceases to perform its intended function. Failure also can occur gradually as a result of sustained operation at intermediate temperatures, producing slow but persistent deterioration of materials and finally ending in failure of the device. The performance of such components is affected by high temperatures for "finite time" (Fig. 13(*b*)) and not just instantaneous single picks.

The prevalence of a period doubling bifurcation scenario, (see Fig. 10 and Fig. 11 and discussion for transition from $f_0/2$ to $f_0/8$), which moreover presents us with intermittent behavior for particular values of the Reynolds number, dictates a scrutinized investigation of the parameter space of interest, guided by engineering design considerations: Dynamical systems theory, when applied to systems of the nature described herewith, introduces universal behavior laws, when bifurcation and state diagrams are concerned. More specifically, it can be observed from a typical bifurcation diagram for period-doubling systems, that the possibility for "discontinuous" behavior for parameter intervals, embedded within the chaotic regime is possible. After the accumulation of bifurcations has occurred (Feigenbaum [45]), and the transition to chaotic states has been realized, the possibility exists that a further increase in the Reynolds number may lead to periodic or quasiperiodic behavior, the famous windows of periodicity in bifurcation theory. By investigating the temporal behavior of the system for a series of states within the chaotic regime, we identify a region of such non-monotonic behavior:

Fig. 14(*A*) shows that from Reynolds number 273.33 until Reynolds number 346.66, the system presents us with a significant drop in maximum temperature, and a accompanying decrease in the temperature fluctuation, signatures of periodic behavior, as we have seen from Fig. 13. A much more pronounced drop in temperature can be observed if we focus at our control point (shown in Fig. 1(*b*)) in the flow field, (Fig. 14(*B*)). Dynamical systems theory predictions are indeed confirmed, if we investigate dynamic behavior for the four Reynolds numbers identified in Fig. 14(*B*) as (*a*), (*b*), (*c*), and (*d*):

Figure 15 shows time histories, frequency spectra and attractors for the last chaotic state (Re=273.33, (*a*), the first periodic state of the identified window (Re=280.0, (*b*), the last periodic state of the identified window (Re=333.33, (*c*) and the first chaotic state of the new chaotic regime (Re=346.66, (*d*), after the window in periodicity has been surpassed. The condition represented by state (*c*), has an apparently complex attractor shape Fig. 15(*c*), but examination of the corresponding frequency spectrum reveals a series of distinct peaks, and not the fuller broad spectrum, characteristic of chaos, that we see for example for states (*a*) and (*d*), Fig. 15(*a*), (*d*).

A Lyapunov exponent computation for this case (*c*) gives a

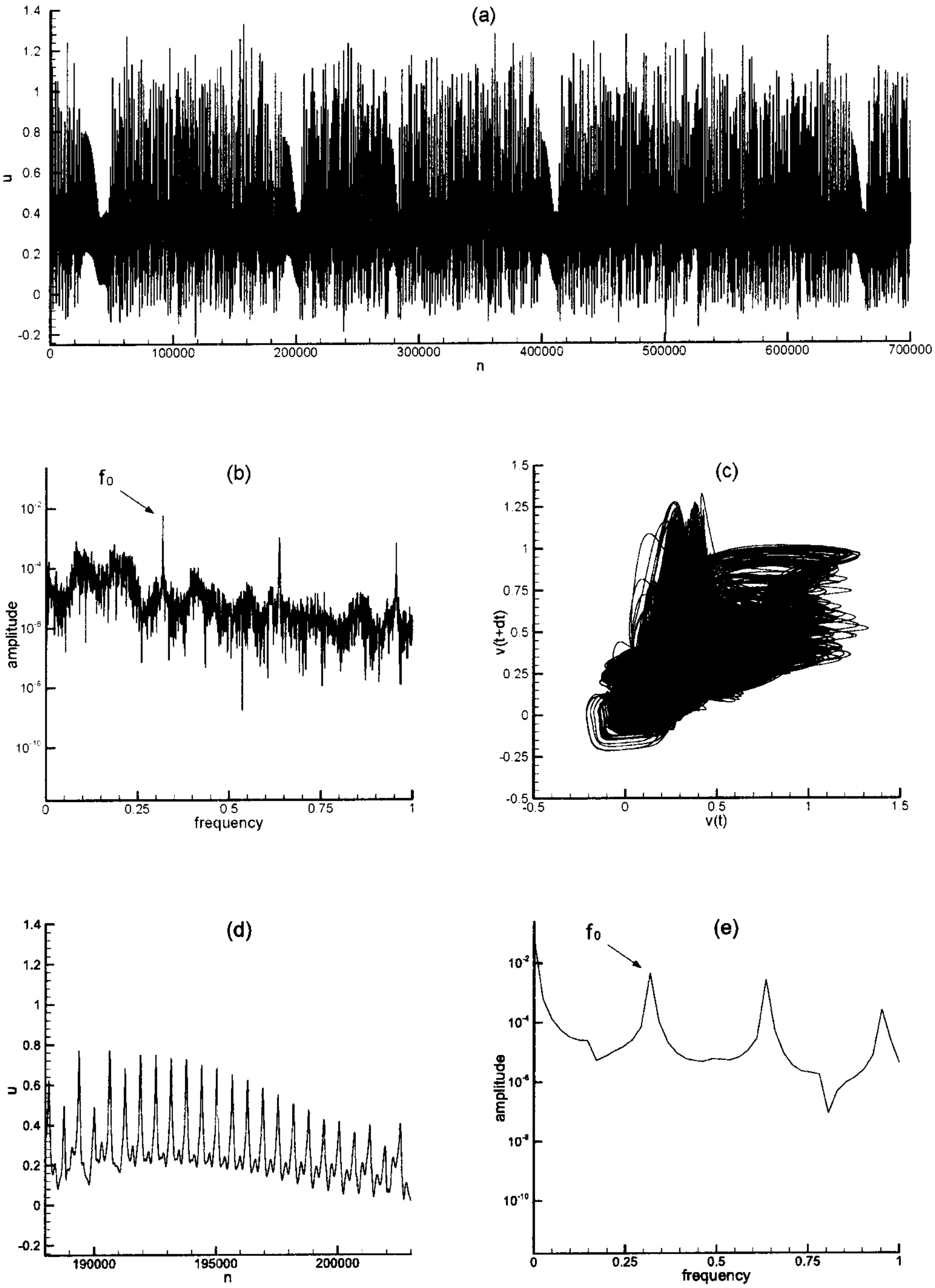

Fig. 12 Pulsating pair jets $A=1.0$, $\omega=2$, $\varphi=3.14$ rad for Re=533.3, (*a*) velocity time series, (*b*) frequency spectra of the velocity signal (*a*), (*c*) phase space reconstruction of (*a*) with time delay about one fifth of the period, (*d*) portion of (*a*), and (*e*) frequency spectra of the velocity signal (*b*)

value that fluctuates around zero, confirming our observations. What this set of observations tell us is that there exists an optimal Reynolds number (which corresponds to Fig. 14(*B*), (*c*)), where the flow rate is the maximum allowing periodic behavior along with the corresponding desirable decrease for the maximum temperature. From a design point of view, this last condition would correspond to a very favorable operating point for the configuration, since it combines the controlled behavior of periodic flow, (that allows for avoidance of sustained maximum temperature peaks), with the highest flow rate that such a periodic state is possible. We must note that dynamical systems theory provides for the existence of additional periodic windows, further down the parameter scale, however these windows are of significantly smaller width in the Reynolds number scale, and for the system under investigation, non-exploitable practically.

4 Conclusions

A detailed set of two-dimensional resolved simulations for the flow and heat transfer characteristics of single and pair slot pulsating jets impinging on a hot, constant heat flux surface, has been conducted. We have investigated the performance of these configurations, using the maximum temperature of the impingement surface as the principal design criterion. By varying systemati-

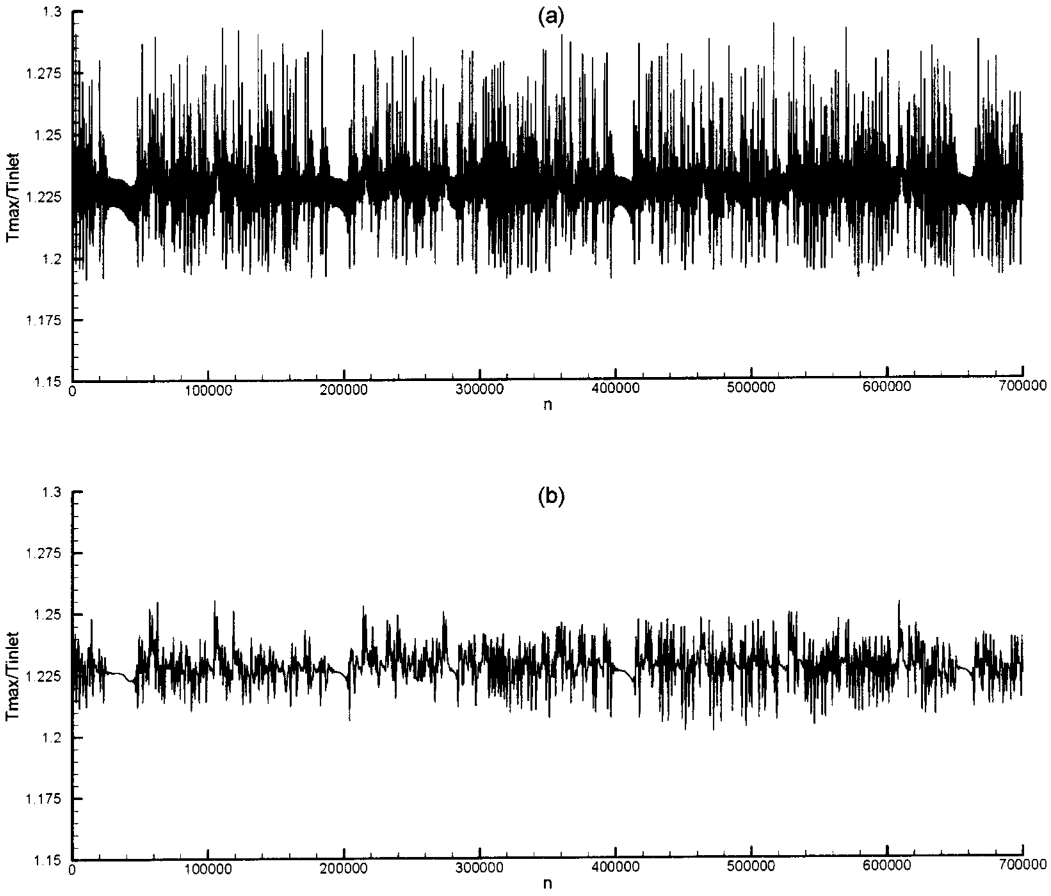

Fig. 13 Pulsating pair jets $A=1.0$, $\omega=2$, $\varphi=3.14$ rad for Re=533.3: (*a*) maximum temperature; and (*b*) maximum temperature using a low pass filter (1-period)

cally the pulsation characteristics (frequency, amplitude and phase angle) as well as the Reynolds number, we have identified optimum operating regimes. For the case of Re=133.33 $A=1.0$, $\omega=2$ and $\varphi=3.14$ rad, we have found an improvement of 6% when compared to the single non-pulsating jet. Enhancement in performance is observed when the jets are pulsating out of phase. Moreover, guided by dynamical systems theory, we have identified both intermittent behavior of the system (periodic/chaotic) for particular Reynolds numbers, and more importantly, windows of pure periodicity at post-chaotic values of the Reynolds number. This latter observation can assist in the selection of particularly favorable design regimes, since it allows for all the beneficial features of periodic behavior (i.e., quiescent behavior of the maximum temperature with lower average values as well), at higher than intuitively accessible flow rates. The improvement in the maximum temperature is not very large in an absolute sense but it may still be important when it comes to sensitive electronics.

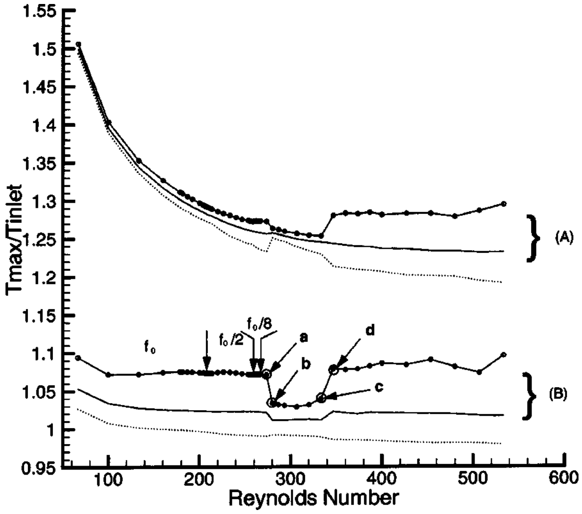

Fig. 14 (*A*) Maximum temperature of the plate, (*B*) Temperature of a control point as a function of Reynolds number: (——) Average temperature (*A*) and (*B*), (–○–) Maximum temperature, and (· · · ·) Minimum temperature

Acknowledgment

The Rechenzentrum of the ETHZ and T. Racic are kindly acknowledged for providing support and computer time. We thank Professor D. Zumbrunnen for his many useful and clarifying remarks that helped us to improve the paper.

Nomenclature

Roman Symbols

A = amplitude of the pulse
B = width of the slot jet
c_v = specific heat at constant Volume
D = hydraulic diameter, $D=2B$
f = frequency
f_0 = pulsation frequency $f_0=\omega/2\pi$
H = distance between jet exit and Impingement Plate
h = local heat transfer coefficient

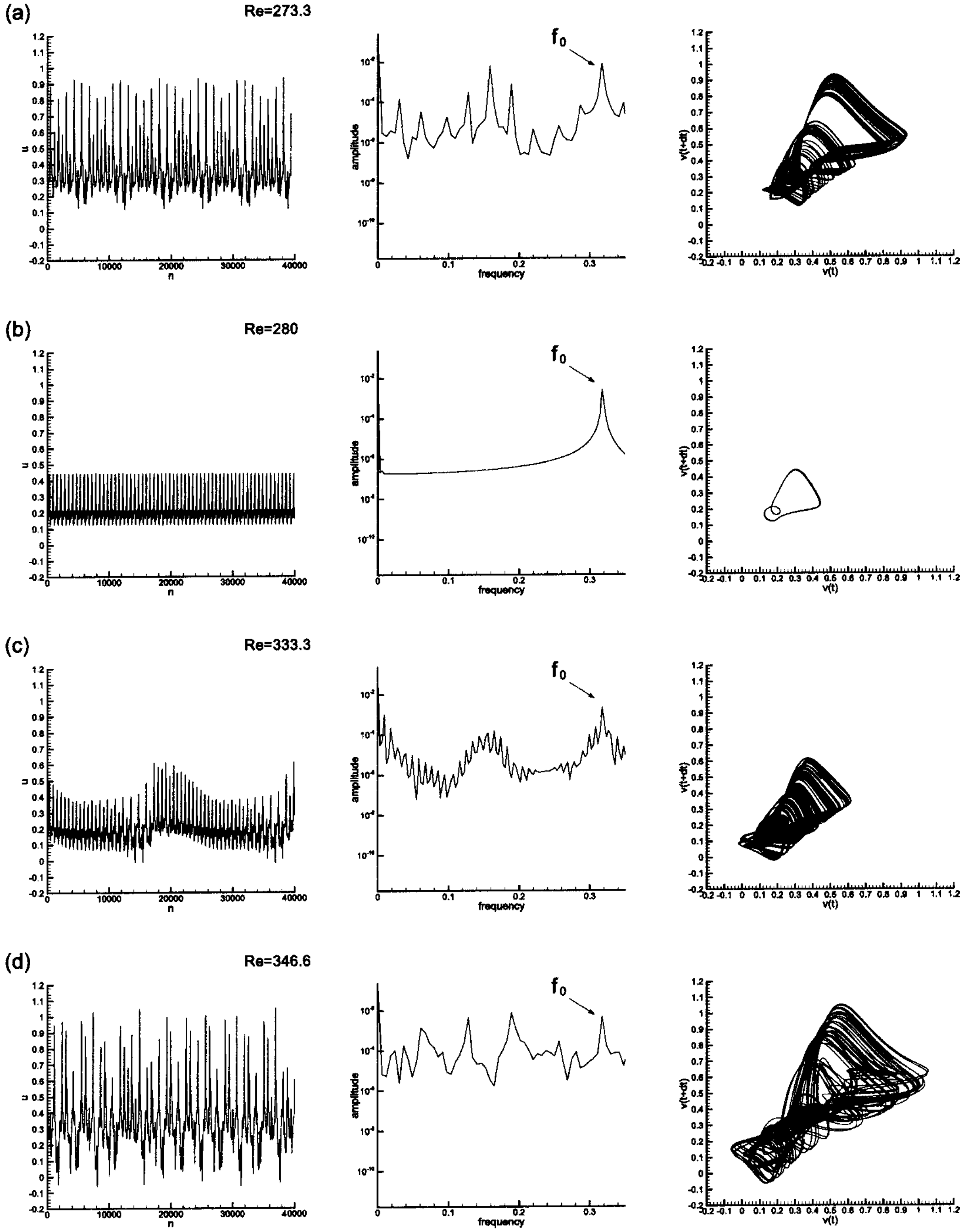

Fig. 15 Dynamic behavior for the four states identified in Fig. 14: First column: Velocity time series; Second column: Frequency spectrum of the velocity; and Third column: two-dimensional time delay reconstruction of the phase space.

k = thermal conductivity of air
L = length of the impingement Plate
LT = slot spacing
M = Mach number
m = mass
Pr = Prandtl number
p = pressure
Q = dimensionless heat flux
q''_{wall} = wall heat flux
r = position vector
Re = Reynolds number at slot exit,
Re = $\bar{V}\rho D/\mu$
Nu = local Nusselt number hL/k
T = temperature
u_i = velocity component
$V_{\underline{\mathrm{max}}}$ = time averaged maximum Velocity of the Jet
V = averaged jet velocity
v_{max} = time dependent maximum Velocity of the Jet
x_i = location vector

Greek Symbols

γ = ratio of specific heat capacities
μ = viscosity of air
ρ = density of air
φ = phase angle difference between The Two Jets
ω = nondimensional angular velocity of the pulse

Subscripts

α = particle α
b = particle b
pair = pair slot jet
single = single slot jet

References

[1] Martin, H., 1977, ''Heat and Mass Transfer between Impinging Gas Jets and Solid Surfaces,'' Adv. Heat Transfer, **13**, pp. 1–60.
[2] Polat, S., Huang, B., Mujumdar, A. S., and Douglas, W. J. M., 1989, ''Numerical Flow and Heat Transfer under Impinging Jets: A Review,'' Annu. Rev. Numer. Fluid Mech. Heat Transfer, **2**, pp. 157–197.
[3] Viskanta, R., 1993, ''Heat-Transfer to Impinging Isothermal Gas and Flame Jets,'' Exp. Therm. Fluid Sci., **6**(2), pp. 111–134.
[4] Lienhard, V. J. H., 1995, ''Liquid Jet Impingement,'' Annu. Rev. Heat Transfer, **6**, pp. 199–270.
[5] Gardon, R., and Akfirat, J. C., 1966, ''Heat Transfer Characteristics of Impinging Two-Dimensional Air Jets,'' J. Heat Transfer, **88**, pp. 101–108.
[6] Donaldso, C. D., Snedeker, R. S., and Margolis, D. P., 1971, ''Study of Free Jet Impingement: 2. Free Jet Turbulent Structure and Impingement Heat Transfer,'' J. Fluid Mech., **45**, pp. 477–512.
[7] Metzger, D. E., and Korstad, R. J., 1972, ''Effects of Crossflow on Impingement Heat-Transfer,'' Journal of Engineering for Power-Transactions of the ASME, **94**(1), pp. 35.
[8] Sparrow, E. M., and Wong, T. C., 1975, ''Impingement Transfer Coefficients Due to Initially Laminar Slot Jets,'' Int. J. Heat Mass Transf., **18**, pp. 597–605.
[9] Sparrow, E. M., and Lee, L., 1975, ''Analysis of Flow Field and Impingement Heat-Mass Transfer Due to a Nonuniform Slot Jet,'' Journal of Heat Transfer transactions of the ASME , **97**(2), pp. 191–197.
[10] Saad, N. R., Douglas, W. J. M., and Mujumdar, A. S., 1977, ''Prediction of Heat-Transfer Under an Axisymmetric Laminar Impinging Jet,'' Ind. Eng. Chem. Fundam., **16**(1), pp. 148–154.
[11] Hollworth, B. R., and Berry, R. D., 1978, ''Heat-Transfer From Arrays of Impinging Jets With Large Jet-to-Jet Spacing,'' Journal of Heat Transfer-Transactions of the ASME , **100**(2), pp. 352–357.
[12] Kataoka, K., Ase, H., and Sako, N., 1988, ''Unsteady Aspects of Large-Scale Coherent Structures and Impingement Heat-Transfer in Round Air Jets With and Without Controlled Excitation,'' International Journal of Engineering Fluid Mechanics, **1**(3), pp. 365–382.
[13] Eibeck, P. A., Keller, J. O., Bramlette, T. T., and Sailor, D. J., 1993, ''Pulse Combustion—Impinging Jet Heat-Transfer Enhancement,'' Combust. Sci. Technol., **94**(1–6), pp. 147–165.
[14] Zumbrunnen, D. A., and Aziz, M., 1993, ''Convective Heat Transfer Enhancement Due to Intermittency in an Impinging Jet,'' Journal of Heat Transfer-Transactions of the ASME , **115**(1), pp. 91–98.
[15] Azevedo, L. F. A., Webb, B. W., and Queiroz, M., 1994, ''Pulsed Air-Jet Impingement Heat-Transfer,'' Exp. Therm. Fluid Sci., **8**(3), pp. 206–213.
[16] Mladin, E. C., and Zumbrunnen, D. A., 1994, ''Nonlinear Dynamics of Laminar Boundary-Layers in Pulsatile Stagnation Flows,'' J. Thermophys. Heat Transfer, **8**(3), pp. 514–523.
[17] Sheriff, H. S., and Zumbrunnen, D. A., 1994, ''Effect of Flow Pulsations on the Cooling Effectiveness of an Impinging Jet,'' Journal of Heat Transfer-Transactions of the ASME , **116**(4), pp. 886–895.
[18] Mladin, E. C., and Zumbrunnen, D. A., 1995, ''Dependence of Heat-Transfer to a Pulsating Stagnation Flow on Pulse Characteristics,'' J. Thermophys. Heat Transfer, **9**,(1), pp. 181–192.
[19] Mladin, E. C., and Zumbrunnen, D. A., 1997, ''Local Convective Heat Transfer to Submerged Pulsating Jets,'' Int. J. Heat Mass Transf., **40**(14), pp. 3305–3321.
[20] Sailor, D. J., Rohli, D. J., and Fu, Q. L., 1999, ''Effect of Variable Duty Cycle Flow Pulsations on Heat Transfer Enhancement for an Impinging Air Jet,'' Int. J. Heat Mass Transf., **20**(6), pp. 574–580.
[21] Sheriff, H. S., and Zumbrunnen, D. A., 1999, ''Local and Instantaneous Heat Transfer Characteristics of Arrays of Pulsating Jets,'' Journal of Heat Transfer-Transactions of the ASME , **121**(2), pp. 341–348.
[22] Mladin, E. C., and Zumbrunnen, D. A., 2000, ''Alterations to Coherent Flow Structures and Heat Transfer Due to Pulsations in an Impinging Air-Jet,'' Int. J. Therm. Sci., **39**(2), pp. 236–248.
[23] Haneda, Y., Tsuchiya, Y., Nakabe, K., and Suzuki, K., 1998, ''Enhancement of Impinging Jet Heat Transfer by Making Use of Mechano-Fluid Interactive Flow Oscillation,'' Int. J. Heat Fluid Flow, **19**(2), pp. 115–124.
[24] Chaniotis, A. K., and Poulikakos, D., 2001, ''Modeling of Continuous and Intermitent Gas Jet Impingement and Heat Transfer on a Solid Surface,'' Proc of ASME International Mechanical Engineering Congress and Exposition, New York.
[25] Zumbrunnen, D. A., and Balasubramanian, M., 1995, ''Convective Heat Transfer Enhancement Due to Gas Injection into an Impinging Liquid Jet,'' Journal of Heat Transfer-Transactions of the ASME , **117**(4), pp. 1011–1017.
[26] Kee, R. J., Rupley, F. M., Meeks, E., and Miller, J. A., 1996, ''Chemkin-Iii: A Fortran Chemical Kinetics Package for the Analysis of Gas-Phase Chemical and Plasma Kinetics,'' Sandia Report SAND96-8216, Sandia National Laboratories, Livermore, CA.
[27] Kee, R. J., Dixon-Lewis, G., Warnatz, J., Coltrin, M. E., and Miller, J. A., 1986, ''A Fortran Computer Package for the Evaluation of Gas-Phase, Multicomponent Transport Properties,'' Sandia Report SAND86-8246, Sandia National Laboratories, Livermore, CA.
[28] Thompson, K. W., 1987, ''Time-Dependent Boundary-Conditions for Hyperbolic Systems,'' J. Comput. Phys., **68**(1), pp. 1–24.
[29] Poinsot, T. J., and Lele, S. K., 1992, ''Boundary-Conditions for Direct Simulations of Compressible Viscous Flows,'' J. Comput. Phys., **101**(1), pp. 104–129.
[30] Monaghan, J. J., 1985, ''Particle Methods for Hydrodynamics,'' Comput. Phys. Rep., **3**(2), pp. 71–124.
[31] Monaghan, J. J., 1992, ''Smoothed Particle Hydrodynamics,'' Annu. Rev. Astron. Astrophys., **30**, pp. 543–574.
[32] Morris, J. P., Fox, P. J., and Zhu, Y., 1997, ''Modeling Low Reynolds Number Incompressible Flows Using Sph,'' J. Comput. Phys., **136**(1), pp. 214–226.
[33] Bicknell, G. V., 1991, ''The Equations of Motion of Particles in Smoothed Particle Hydrodynamics,'' SIAM J. Sci. Comput. (USA), **12**(5), pp. 1198–1206.
[34] Monaghan, J. J., 1988, ''An Introduction to Sph,'' Comput. Phys. Commun., **48**(1), pp. 89–96.
[35] Takeda, H., Miyama, S. M., and Sekiya, M., 1994, ''Numerical-Simulation of Viscous-Flow by Smoothed Particle Hydrodynamics,'' Prog. Theor. Phys., **92**(5), pp. 939–960.
[36] Monaghan, J. J., and Kocharyan, A., 1995, ''Sph Simulation of Multiphase Flow,'' Comput. Phys. Commun., **87**(1–2), pp. 225–235.
[37] Chaniotis, A. K., Poulikakos, D., and Koumoutsakos, P., 2002, ''Remeshed Smoothed Particle Hydrodynamics for the Simulation of Viscous and Heat Conducting Flows,'' J. Comput. Phys., **182**(1), pp. 67–90.
[38] Hockney, R. W., and Eastwood, J. W., 1988, *Computer Simulation Using Particles*, Institute of Physics Publishing, Bristol.
[39] Koumoutsakos, P., 1997, ''Inviscid Axisymmetrization of an Elliptical Vortex,'' J. Comput. Phys., **138**(2), pp. 821–857.
[40] Cottet, G. H., and Koumoutsakos, P. D., 2000, *Vortex Methods*, Cambridge University Press, London.
[41] Byrne, G. D., 1992, *Pragmatic Experiments with Krylov Methods in the Stiff Ode Setting*, Oxford Univ. Press.
[42] Brown, P. N., Byrne, G. D., and Hindmarsh, A. C., 1989, ''Vode—A Variable-Coefficient Ode Solver,'' SIAM J. Sci. Comput. (USA), **10**(5), pp. 1038–1051.
[43] Panton, R. L., 1984, *Incompressible Flow*, Wiley, New York.
[44] Kantz, H., and Schreiber, T., 1997, *Nonlinear Time Series Analysis*, Cambridge University Press, Cambridge.
[45] Feigenbaum, M. J., 1983, ''Universal Behavior in Non-Linear Systems,'' Physica D, **7**(1–3), pp. 16–39.
[46] Libchaber, A., Laroche, C., and Fauve, S., 1982, ''Period Doubling Cascade in Mercury, a Quantitative Measurement,'' J. Phys. (France), Lett., **43**(7), pp. L211–L216.
[47] Pulliam, T. H., and Vastano, J. A., 1993, ''Transition to Choas in an Open Unforced 2-D Flow,'' J. Comput. Phys., **105**(1), pp. 133–149.
[48] Thompson, J. M. T., and Steward, H. B., 1986, *Nonlinear Dynamics and Chaos: Geometrical Methods for Engineers and Scientists*, John Wiley and Sons, Chichester.
[49] Arneodo, A., Coullet, P., Tresser, C., Libchaber, A., Maurer, J., and Dhumieres, D., 1983, ''On the Observation of an Uncompleted Cascade in a Rayleigh-Benard Experiment,'' Physica D, **6**(3), pp. 385–392.
[50] Yoo, J. S., and Han, S. M., 2000, ''Transitions and Chaos in Natural Convection of a Fluid with Pr$=$0.1 in a Horizontal Annulus,'' Fluid Dyn. Res., **27**(4), pp. 231–245.
[51] Pomeau, Y., and Manneville, P., 1980, ''Intermittent Transition to Turbulence in Dissipative Dynamical-Systems,'' Commun. Math. Phys., **74**(2), pp. 189–197.

Heat Transfer Between Blockages With Holes in a Rectangular Channel

S. W. Moon

S. C. Lau

Department of Mechanical Engineering,
Texas A&M University,
College Station, TX 77843-3123

Experiments have been conducted to study steady heat transfer between two blockages with holes and pressure drop across the blockages, for turbulent flow in a rectangular channel. Average heat transfer coefficient and local heat transfer distribution on one of the channel walls between two blockages, and overall pressure drop across the blockages were obtained, for nine different staggered arrays of holes in the blockages and Reynolds numbers of 10,000 and 30,000. For the hole configurations studied, the blockages enhanced heat transfer by 4.6 to 8.1 times, but significantly increased the pressure drop. Smaller holes in the blockages caused higher heat transfer enhancement, but larger increase of the pressure drop than larger holes. The heat transfer enhancement was lower in the higher Reynolds number cases. Because of the large pressure drop, the heat transfer per unit pumping power was lower with the blockages than without the blockages. The local heat transfer was lower nearer the upstream blockage, the highest near the downstream blockage, and also relatively high in regions of reattachment of the jets leaving the upstream holes. The local heat transfer distribution was strongly dependent on the configuration of the hole array in the blockages. A third upstream blockage lowered both the heat transfer and the pressure drop, and significantly changed the local heat transfer distribution. [DOI: 10.1115/1.1576812]

Keywords: Experimental, Forced Convection, Blockages With Holes, Turbines, Turbulent

Introduction

Various methods have been used to protect turbine airfoils from the hostile environments in the hot gas paths: film cooling, transpiration cooling, enhanced internal cooling, impingement cooling, and the use of thermal barrier coatings. Han et al. [1] and Lau [2] surveyed published literature on turbine airfoil heat transfer and cooling technology. For internal cooling of turbine airfoils, ribs, pin fins, and impinging jets are often used to enhance the heat transfer by convection between the surfaces of internal passages and the cooling air. Another internal cooling channel configuration is being considered for the region of an airfoil near the trailing edge. Cooling air is forced to flow past staggered holes along two or more internal partitions near the trailing edge before exiting the airfoil through an array of slots along the trailing edge. The cooling airflow through these holes is expected to enhance the heat transfer on the two opposite walls between the partitions with the holes.

There has not been any study of heat transfer for flows through staggered hole arrays in channels with the geometry described above. Ekkad et al. [3] and Pamula et al. [4] used liquid crystals and smoke for visualization to study the heat transfer in a two-pass channel with the two straight passes separated by a dividing wall with an array of holes. Their results showed that flow impingement and cross flow induced swirls increased the heat transfer in the second pass of the channel. Kukreja and Lau [5] conducted experiments to measure the local heat transfer for turbulent flows through a long, straight, square channel with ribs of various configurations, including perforated ribs, on two opposite walls, using transient liquid crystal thermometry. The rib height-to-hydraulic diameter ratio and the rib pitch-to-height ratio were 0.125 and 10, respectively, and the Reynolds number ranged from 15,000 to 50,000. Perforated ribs were found to be not as good as solid ribs in enhancing heat transfer. Although perforated ribs caused lower pressure drop, they did not improve thermal performance. Increasing the size of the holes, the number of holes, or the total hole area did not increase the overall heat transfer.

Buchlin [6] studied the effects of the configuration and the pitch of perforated ribs, the ratio of the open area to the total frontal area of the ribs (open area ratio), and the Reynolds number on heat transfer on a surface with periodic perforated ribs in a wind tunnel. Five types of perforated ribs were tested: bottom hole type, tilted hole type, arch type, column type, and chevron type. An increase of the local heat transfer of up to a factor of 3.0 was observed immediately downstream of the perforated ribs, when compared with corresponding local heat transfer for solid ribs. An optimal design was recommended: chevron type perforated ribs with a rib pitch-to-height ratio of 5.0 and an open area ratio of 0.53, and Reynolds numbers between 30,000 and 60,000. Among other studies of perforated ribs and partial blockages are Hwang et al. [7] and Liou and Chen [8].

The main objective of this study is to examine, for turbulent airflow through blockages with staggered holes in a wide rectangular channel, the heat transfer on the channel walls between blockages. The local heat transfer distribution and the average heat transfer on one of the channel walls between two blockages are measured, along with the overall pressure drop across the blockages, for different staggered arrays of holes in the blockages and Reynolds numbers of 10,000 and 30,000, typical for internal cooling of turbine airfoils. Designers of turbine engines should find the results of this fundamental study very useful.

Experimental Apparatus and Procedure

Experiments were conducted to determine, for turbulent airflow through blockages with holes in a rectangular channel, the steady heat transfer on the channel walls between blockages. Two geometrically identical test sections were used in this study. The first test section was a 35.6-cm long rectangular channel with a flow cross section of 17.8 cm (width) by 3.05 cm (height). The channel

---

Contributed by the Heat Transfer Division for publication in the JOURNAL OF HEAT TRANSFER. Manuscript received by the Heat Transfer Division August 15, 2002; revision received March 7, 2003. Associate Editor: K. S. Ball.

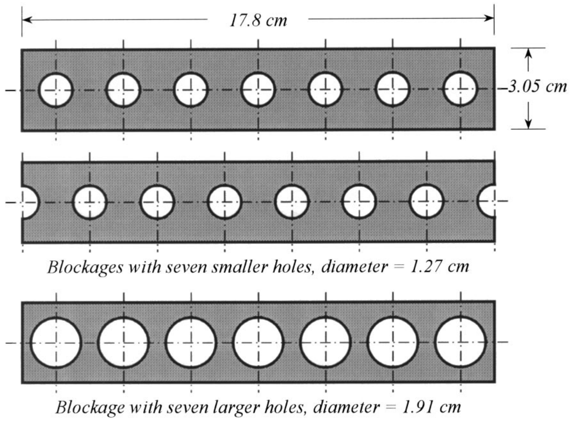

Blockages with seven smaller holes, diameter = 1.27 cm

Blockage with seven larger holes, diameter = 1.91 cm

Fig. 1 Blockages with holes in this experimental study

was constructed of plywood with a smooth birch inner surface. Inside the channel there were two or three acrylic blockages, each with a cross section that was the same as the channel cross section and a thickness of 1.91 cm. The distance separating consecutive blockages was 6.35 cm, and the last blockage was installed at a distance of 7.62 cm from the exit of the channel. Each blockage had a row of seven equally spaced holes to allow air to flow through (Fig. 1). The distance between adjacent holes in a blockage was 2.54 cm, and the array of holes in a blockage was staggered with respect to that in the next blockage.

During an experiment, air was drawn into the test channel from the air-conditioned laboratory with a blower. After the air passed through the staggered array of holes in the blockages in the test channel, it flowed into a large plenum. A gate valve and a calibrated orifice flow meter, connected in series to the plenum with PVC pipes and fittings along an open flow loop, controlled and measured the mass flow rate, respectively. Figure 2 shows the test flow loop with the first test section.

To measure the average heat transfer coefficient on the exposed surface of one of the channel walls between two blockages as air passed through the test channel, the portion of the bottom wall between the last two blockages was replaced with a 1.27 cm thick copper plate. The copper plate measured 6.35 cm by 17.8 cm, which was exactly the same as the dimensions of the exposed surface between two blockages. During an experiment, the block was heated by passing electric current through a 6.35 cm by 17.8 cm flexible heater that was attached with silicone adhesive to the outer surface of the copper plate. Fiberglass and Styrofoam insulation on the outer surface of the heater minimized extraneous heat losses.

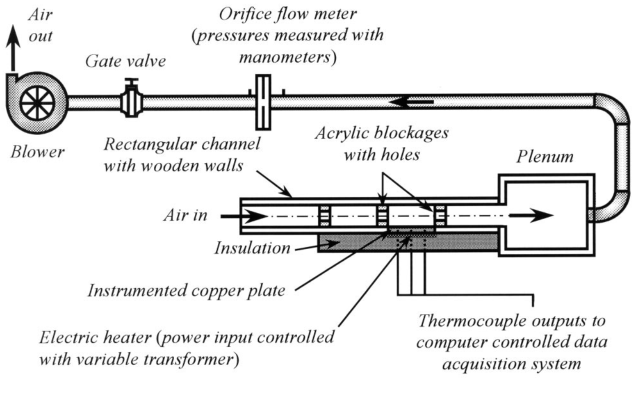

Fig. 2 Schematic of test apparatus for average heat transfer measurements

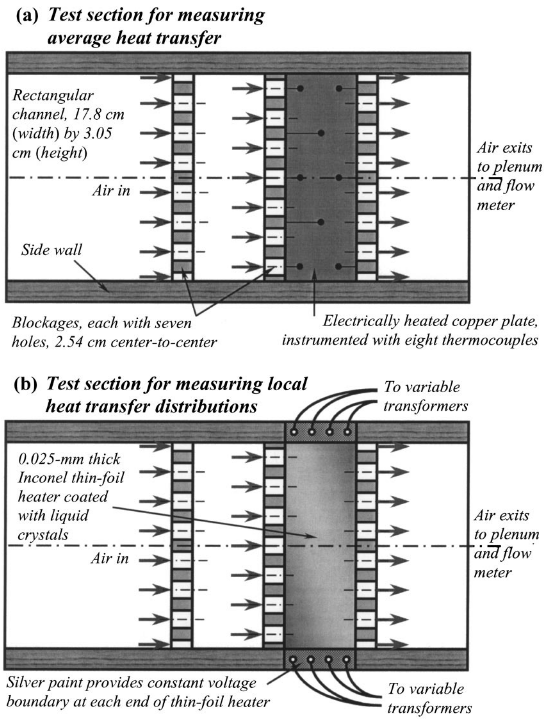

Fig. 3 Schematics of test sections for average and local heat transfer measurements (not to scale)

The copper plate was instrumented with eight small gage T-type (copper-constantan) thermocouples. The thermocouples were installed in deep holes that were drilled into the copper plate in a direction parallel to the top and bottom surfaces of the block. Figure 3(a) shows the locations of the junctions of these thermocouples that were distributed over the 6.35 cm by 17.8 cm area between the two blockages with holes. Silver paint was used to ensure good contact between each thermocouple junction and a copper plate. An ohmmeter was used to check for good contact between each thermocouple and the copper plate. Two thermocouples were used to record the inlet air temperature.

A computer-controlled data acquisition system recorded the thermocouple outputs during an experiment. Each thermocouple, along with the data acquisition system, was calibrated with a constant temperature bath and an NIST-calibrated mercury thermometer.

Two digital TRMS multimeters and a current clamp were used to measure the voltage and current supplied to the heater. An inclined oil manometer and a U-tube water manometer were used to measure the pressure drop across the orifice and the pressure upstream of the orifice, respectively.

During an experiment, the overall pressure drop across the last two blockages was also measured. The difference between the static pressures at two taps, located at a distance of 1.27 cm upstream of the second to last blockage and 1.27 cm downstream of the last blockage, was measured with a U-tube manometer or an inclined manometer, depending on the range of measurement.

Experiments were conducted to determine the average heat transfer coefficient on one of the channel walls between two blockages, for nine different staggered arrays of holes in the blockages and two airflow rates, with corresponding Reynolds numbers, based on the hydraulic diameter of the test channel, of 10,000 and 30,000.

Table 1 gives the configurations and dimensions of the nine staggered hole arrays. In seven of the nine cases, the diameter of the holes was 1.27 cm, and in the other two cases, the diameter of the holes was 1.91 cm. The center of the holes was located along

Table 1 Configurations and dimensions of staggered hole arrays in the blockages in this study

Case	1	2	3	4	5	6	7	8	9
Number of Blockages	2	2	2	2	2	3	3	2	3
Diameter of Holes in Blockages (cm)	1.27	1.27	1.27	1.27	1.27	1.27	1.27	1.91	1.91
Distance from Center of Holes in First Blockage to Heated Wall (cm)	⋯	⋯	⋯	⋯	⋯	1.52	1.52	⋯	1.52
Distance from Center of Holes in Second Blockage to Heated Wall (cm)	1.52	1.14	1.14	1.91	1.91	1.52	1.14	1.52	1.52
Distance from Center of Holes in Third Blockage to Heated Wall (cm)	1.52	1.14	1.91	1.91	1.14	1.52	1.91	1.52	1.52
Symbol for Identifying Location and Size of Holes	MM	LL	LU	UU	UL	MMM	MLU	$\underline{\text{MM}}$	$\underline{\text{MMM}}$

the mid plane of the test channel in cases 1, 6, 8, and 9, and was above or below the mid plane of the test channel in the other cases. Symbols have been assigned to identify the locations of the holes in each blockage relative to the mid plane of the test channel: "M" for the center of holes located in the mid plane of the test channel, "U" for "above the mid plane," and "L" for "below the mid plane."

The second test section was for determining the local, steady distribution of the heat transfer coefficient on the exposed surface of one of the channel walls between two blockages as air passed through the test channel. The test section had the same dimensions as the first test section, except that the top wall was a 5.0 mm thick clear acrylic plate and the portion of the bottom wall between the last two blockages was covered with a 0.025 mm thick Inconel thin-foil heater. The thin-foil heater was attached to the bottom wall with a double-sided adhesive sheet that was cut to the same width as the thin-foil heater. Figure 3(b) shows the top view of the second test section.

The power input to the thin-foil heater was controlled with two variable transformers connected in parallel, and two digital TRMS multimeters and a current clamp were used to measure the voltage and current supplied to the heater.

Thermochromic liquid crystals (over a thin base layer of black paint) were sprayed onto the exposed top surface of the thin-foil heater to indicate the temperature distribution when electrical current was allowed to pass through the thin-foil heater during an experiment. The narrow-band liquid crystals, with a sensitivity of 1.0°C, turned yellow when the temperature was 35.2°C. A digital camera recorded the contours on the liquid crystal-coated surface for five different power inputs, and a computer software was used to analyze the pictures and to prepare a contour map to indicate the distribution of the local heat transfer coefficient.

Experiments were conducted to determine the local distribution of the heat transfer coefficient on the bottom channel wall between two blockages, for the same nine staggered arrays of holes in the blockages and the same Reynolds numbers as for the average heat transfer experiments. Separate experiments were performed to calibrate the liquid crystals. There were 18 test runs each for measuring average heat transfer, local heat transfer distribution, and overall pressure drop. Each test run was repeated at least once, and during each test run, data were recorded multiple times so that there were sufficient data for statistical uncertainty analysis of the measured quantities.

Data Reduction

The Reynolds number for the flow of air through the test section is based on the hydraulic diameter of the test section, D_h, and is calculated as

$$\mathrm{Re}_{Dh}=\frac{\rho\overline{u}D_h}{\mu}=\frac{2\dot{m}}{\mu(W+H)} \tag{1}$$

where $\overline{u}$ is the average velocity, ρ and μ are the density and dynamic viscosity, $\dot{m}$ is the mass flow rate, and W and H are the width and the height of the test channel.

The overall and local heat transfer coefficients are evaluated, respectively, as

$$\overline{h}=\frac{q_c}{A_s(\overline{T}_w-\overline{T}_m)}=\frac{VI-q_{\mathrm{loss}}}{A_s(\overline{T}_w-\overline{T}_m)} \tag{2}$$

$$h=\frac{q_c}{A_s(T_w-\overline{T}_m)}=\frac{VI-q_{\mathrm{loss}}}{A_s(T_w-\overline{T}_m)} \tag{3}$$

where V and I are the applied voltage and current, A_s is the area of the heated surface, and $\overline{T}_m$ is the average of the inlet bulk temperature and the bulk temperature at the downstream edge of the copper plate or the thin-foil heater. The latter bulk temperature is determined based on an energy balance as $T_{m,o}=T_{m,i}+(VI-q_{\mathrm{loss}})/(\dot{m}c_p)$.

The average and local Nusselt numbers are defined as

$$\overline{\mathrm{Nu}}_{Dh}=\frac{\overline{h}D_h}{k} \tag{4}$$

$$\mathrm{Nu}_{Dh}=\frac{hD_h}{k} \tag{5}$$

The Nusselt numbers are normalized with the Nusselt number for fully developed turbulent flow in a smooth channel with the same hydraulic diameter as the test channel (p. 492, Incropera and DeWitt [9]).

$$\mathrm{Nu}_{Dh,0}=\frac{(f_0/8)(\mathrm{Re}_{Dh}-1000)\mathrm{Pr}}{[1+12.7(f_0/8)^{1/2}(\mathrm{Pr}^{2/3}-1)]} \tag{6}$$

where f_0 is the friction factor for fully developed turbulent flow in the smooth channel, and is given by (p. 470, Incropera and DeWitt [9])

$$f_0=[0.79\ln(\mathrm{Re}_{Dh})-1.64]^{-2} \tag{7}$$

Based on the measured overall pressure drop across two blockages with holes, the friction factor is determined as

$$f=\frac{(\Delta p/\Delta x)D_h}{\rho\overline{u}^2/2} \tag{8}$$

where $\overline{u}$ may be calculated from $\dot{m}$. The friction factor is normalized with f_0 given in Eq. (7).

The relative thermal performance is

$$TP=\left(\frac{\mathrm{Nu}_{Dh}}{\mathrm{Nu}_{Dh,0}}\right)\cdot\left(\frac{f}{f_0}\right)^{-1/3} \tag{9}$$

Table 2 Average heat transfer and overall pressure drop results of this study

	Case	1	2	3	4	5	6	7	8	9
Re_{Dh}	Hole Location and Size Symbol	MM	LL	LU	UU	UL	MMM	MLU	$\underline{\text{MM}}$	$\underline{\text{MMM}}$
10,000	$\overline{\mathrm{Nu}}_{Dh}$	214.02	244.75	236.40	214.44	205.57	208.46	224.01	157.03	155.79
	$\overline{\mathrm{Nu}}_{Dh}/\mathrm{Nu}_{Dh,0}$	7.06	8.10	7.84	7.10	6.83	6.91	7.43	5.20	5.16
	f	42.79	36.81	39.57	35.89	39.57	40.49	35.25	5.89	5.34
	f/f_0	1,365.2	1,172.8	1,259.9	1,143.4	1,259.1	1,289.1	1,122.0	187.56	169.98
	TP	0.64	0.77	0.73	0.68	0.63	0.64	0.72	0.91	0.93
30,000	$\overline{\mathrm{Nu}}_{Dh}$	420.65	501.39	482.27	436.84	413.44	399.98	438.76	326.17	320.08
	$\overline{\mathrm{Nu}}_{Dh}/\mathrm{Nu}_{Dh,0}$	6.01	7.08	6.86	6.18	5.86	5.66	6.44	4.68	4.57
	f	47.26	42.83	43.30	40.03	44.55	42.83	35.50	5.92	5.08
	f/f_0	1,993.6	1,813.1	1,828.6	1,693.5	1,883.9	1,811.9	1,484.1	249.50	214.19
	TP	0.48	0.58	0.56	0.52	0.47	0.46	0.57	0.74	0.76

This ratio compares the heat transfer per unit pumping power for the test channel, with blockages, with that for a smooth channel with the same hydraulic diameter as the test channel.

The maximum uncertainty of the mass flow rate is estimated to be ±3.79%. The variation of the pressure drop across the orifice flow meter, measured with a manometer, is the dominating term in the calculation of the uncertainty of the mass flow rate. Using uncertainties of 1.6 mm for all dimensions of the test section and 1.0% for all properties of air, the maximum uncertainties of the Reynolds number is calculated to be ±4.07% (Coleman and Steele [10]). For all the test runs, the Re_{Dh} values are within ±1.5% of the nominal value of 10,000 or 30,000.

For the average heat transfer measurements, the maximum uncertainties of the temperature difference, the voltage, and the current are ±4.90%, ±0.23%, and ±1.89%, respectively. With these values, the maximum uncertainty of the heat transfer coefficient is calculated to be ±5.27%. Using uncertainties of 1.6 mm for the hydraulic diameter and 1.0% for the thermal conductivity of air, the corresponding maximum uncertainty of the Nusselt number is determined to be ±6.18%. For the local heat transfer measurements, the maximum uncertainties of the heat transfer coefficient and the Nusselt number are ±6.86% and ±7.59%, respectively.

The maximum uncertainty of the friction factor is determined to be ±8.53%.

Presentation and Discussion of Experimental Results

Average Heat Transfer and Overall Pressure Drop. Experimental average heat transfer and overall pressure drop results have been obtained for nine different staggered arrays of holes in the blockages and two airflow rates, with corresponding Reynolds numbers, Re_{Dh}, of 10,000 and 30,000. These results are presented in Table 2 as average Nusselt numbers and friction factors, $\overline{\mathrm{Nu}}_{Dh}$ and f, and average Nusselt number and friction factor ratios, $\overline{\mathrm{Nu}}_{Dh}/\mathrm{Nu}_{Dh,0}$ and f/f_0.

Both the average Nusselt number and the friction factor are higher when the Reynolds number is higher. However, $\overline{\mathrm{Nu}}_{Dh}/\mathrm{Nu}_{Dh,0}$ decreases and f/f_0 increases as the Reynolds is increased from 10,000 to 30,000. The smaller holes (with diameter of 1.27 cm) in the blockages cause higher heat transfer enhancement than the larger holes (with diameter of 1.91 cm), with values of $\overline{\mathrm{Nu}}_{Dh}/\mathrm{Nu}_{Dh,0}$ between 5.66 and 8.10 compared with values between 4.57 and 5.20. The smaller holes also cause significantly larger increase of the pressure drop than the larger holes. The f/f_0 values in the smaller hole cases are at least six times of those in the larger hole cases.

Among the smaller hole cases, the heat transfer enhancement is the highest in Case 2 (LL), with the holes in both the upstream and downstream blockages offset toward the heated surface (below the mid plane of the test channel, with the heated copper plate in the bottom wall of the channel). The heat transfer enhancement is also quite high in Case 3 (LU), with the holes in the upstream blockage below the mid plane of the test channel and the holes in the downstream blockage above the mid plane of the test channel. In both cases, there are only two blockages with holes. The heat transfer enhancement is lower in the other three cases with only two blockages: Case 1 (MM), Case 4 (UU), and Case 5 (UL). The values of $\overline{\mathrm{Nu}}_{Dh}/\mathrm{Nu}_{Dh,0}$ do not differ significantly in these cases.

Adding a third blockage with holes upstream of the two blockages lowers the heat transfer enhancement. This is evident when the values of $\overline{\mathrm{Nu}}_{Dh}/\mathrm{Nu}_{Dh,0}$ for Case 3 (LU) and Case 7 (MLU) are compared, and when the values for Case 1 (MM) and Case 6 (MMM) are compared. The extra upstream blockage, with holes that are staggered with respect to those in the blockage upstream of the heated wall, prevents the air from the open channel from flowing straight toward the holes in the blockage upstream of the heated wall. A portion of the flow probably impinges on the upstream surface of the blockage upstream of the heated wall, and gets drawn into recirculating zones, before turning downstream and passing through the holes in the blockage. The local heat transfer distributions, to be presented later, will show that the extra upstream blockage significantly changes the flow field, and thus, the heat transfer on the walls, between the two downstream blockages. The results for Case 1 (MM) and Case 6 (MMM) also show that, in the case in which the holes in all three blockages are located in the mid plane of the channel, the heat transfer is higher on the walls between the two upstream blockages than on the walls between the two downstream blockages.

The $\overline{\mathrm{Nu}}_{Dh}/\mathrm{Nu}_{Dh,0}$ values in the two cases with larger holes in the blockages, Case 8 ($\underline{\text{MM}}$) and Case 9 ($\underline{\text{MMM}}$), are much lower than those in the other cases with smaller holes, with values between 17% and 36% lower. Adding a blockage with large holes upstream of the two blockages with large holes again lowers the heat transfer enhancement.

The blockages with the smaller holes in the mid plane of the channel in Case 1 (MM) cause the highest overall pressure drop. The friction factor ratio is lower in Case 6 (MMM) and Case 7 (MLU) than in Case 1 (MM) and Case 3 (LU), respectively, indicating that adding a third upstream blockage lowers the pressure drop across the two downstream blockages. A comparison of the f/f_0 values for Case 8 ($\underline{\text{MM}}$) and Case 9 ($\underline{\text{MMM}}$) shows the same trend.

Because of the very large pressure drops caused by the blockages with holes, the values of the thermal performance ratio in all cases with various hole configurations are less than 1.0. That is, the heat transfer per unit pumping power is actually lower with the blockages than without the blockages. In the cases with the smaller holes, the TP value ranges from 0.63 to 0.77 for $\mathrm{Re}_{Dh}=10{,}000$, and from 0.46 to 0.58 for $\mathrm{Re}_{Dh}=30{,}000$. In the two cases with the larger holes, the TP values are about 0.92 and 0.75, respectively, for $\mathrm{Re}_{Dh}=10{,}000$ and 30,000. Adding a third blockage upstream of the two blockages does not significantly affect the thermal performance ratio.

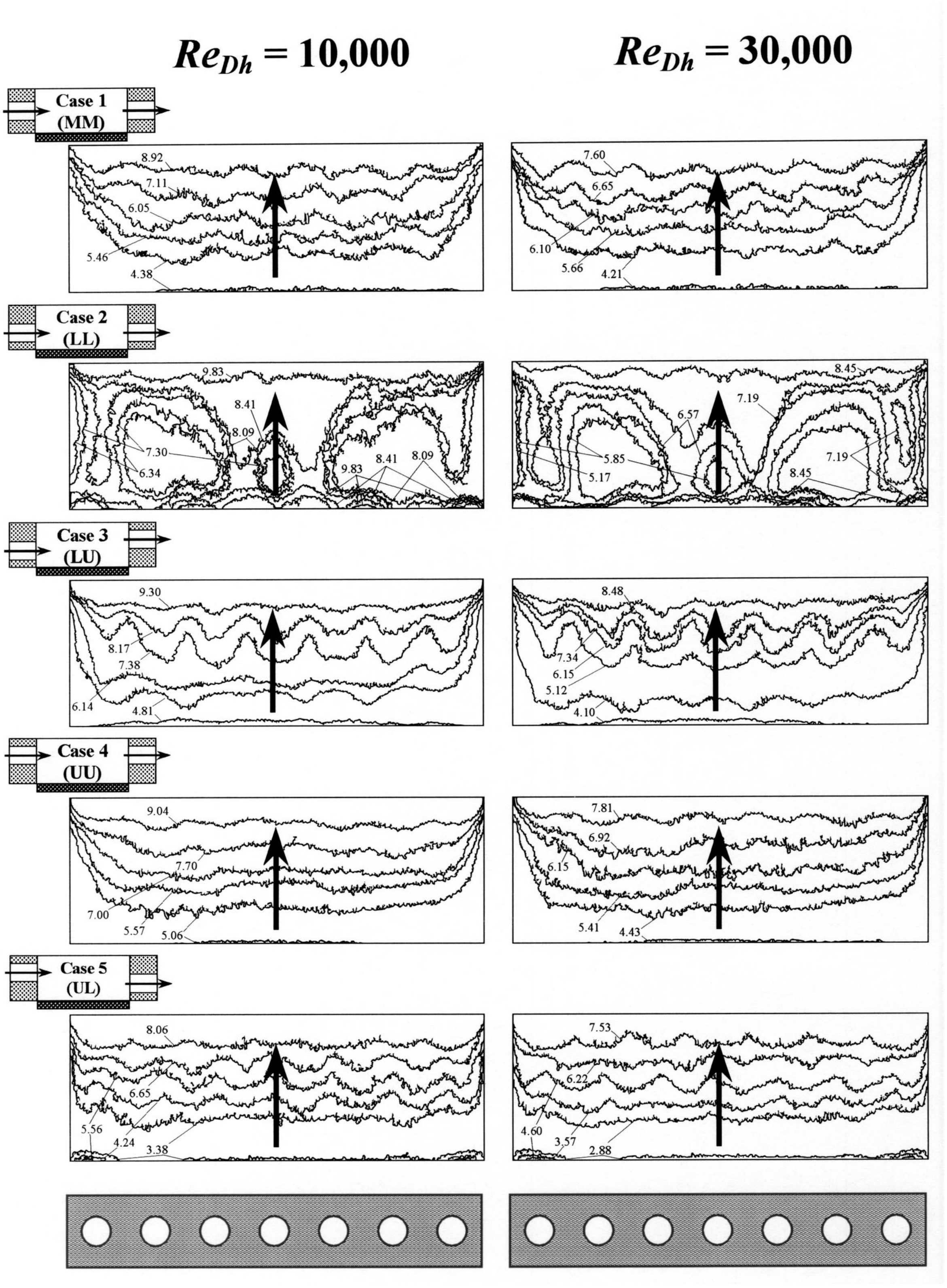

Fig. 4 Local steady heat transfer distributions ($Nu_{Dh}/Nu_{Dh,0}$) on heated bottom wall between two blockages with holes in a rectangular channel for nine different hole arrays. Arrows show direction of main flow.

Local Heat Transfer Distribution. Attention is now focused on local heat transfer distributions. In Fig. 4, the local distributions of $\mathrm{Nu}_{Dh}/\mathrm{Nu}_{Dh,0}$ on the heated bottom wall between two blockages with holes are presented, for the nine different hole configurations, and for $\mathrm{Re}_{Dh}=10{,}000$ and 30,000. The heat transfer is generally lower nearer the upstream blockage, and in most cases, the heat transfer is the highest near the base of the downstream blockage. The $\mathrm{Nu}_{Dh}/\mathrm{Nu}_{Dh,0}$ distributions have higher values in the lower Re_{Dh} cases. The trend is consistent with that based on the average heat transfer results. In all of the cases

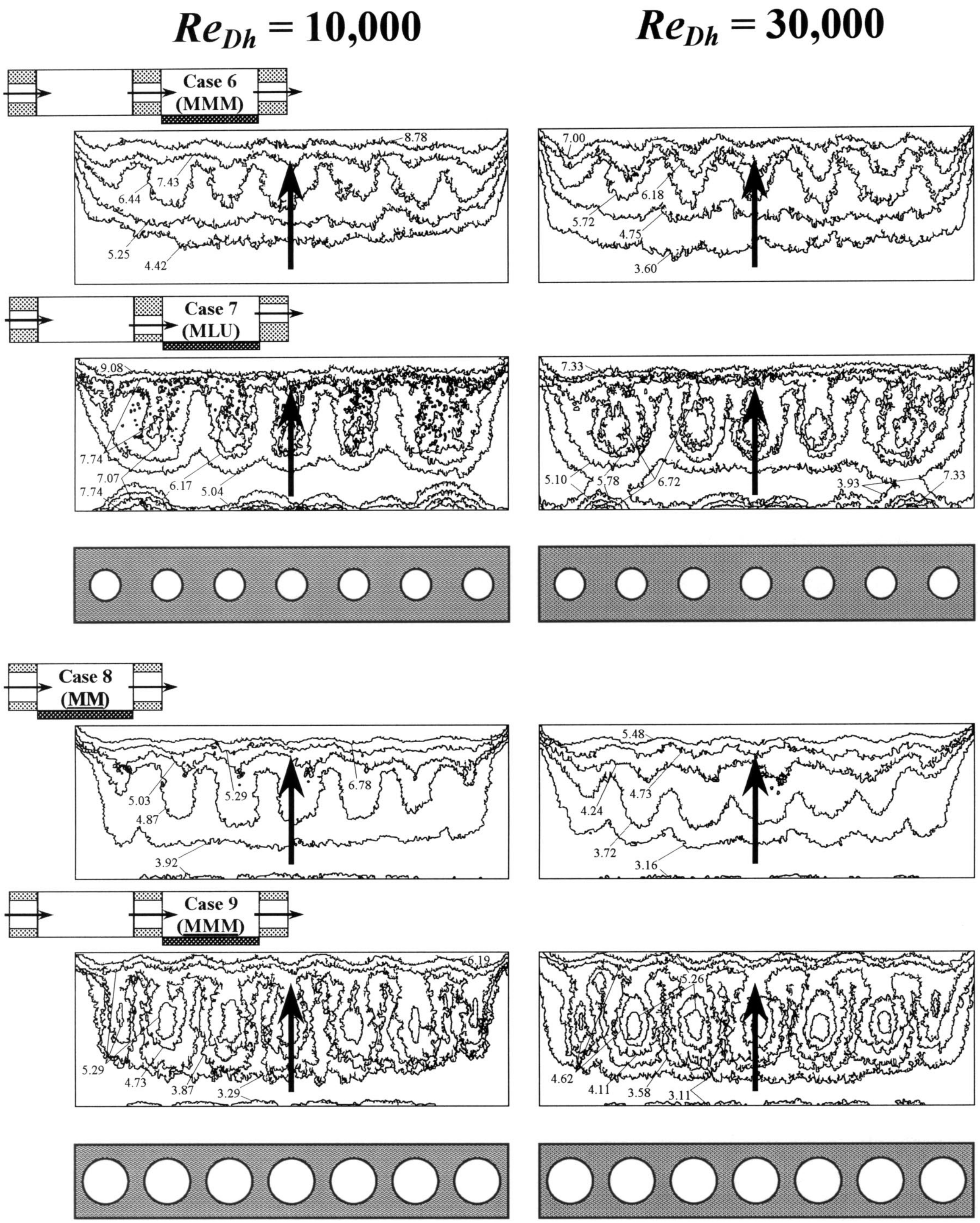

Fig. 4 (***continued***)

studied, the ranges of the $\mathrm{Nu}_{Dh}/\mathrm{Nu}_{Dh,0}$ values presented in Fig. 4 are comparable to the $\overline{\mathrm{Nu}}_{Dh}/\mathrm{Nu}_{Dh,0}$ values presented in Table 2.

The $\mathrm{Nu}_{Dh}/\mathrm{Nu}_{Dh,0}$ distribution is strongly dependent on the configuration of the hole array in the blockages. The shapes of the $\mathrm{Nu}_{Dh}/\mathrm{Nu}_{Dh,0}$ contours are similar for $\mathrm{Re}_{Dh}=10{,}000$ and 30,000, while the magnitudes of $\mathrm{Nu}_{Dh}/\mathrm{Nu}_{Dh,0}$ are different for the two distributions (as stated earlier, higher in the lower Re_{Dh} case). There are larger spanwise variations of the Nusselt number ratio in some cases than in other cases. The addition of a third blockage upstream also significantly changes the $\mathrm{Nu}_{Dh}/\mathrm{Nu}_{Dh,0}$ distribution.

The heat transfer is generally very high near the downstream blockage. As air passes through the holes in the upstream blockage, a portion of the air escapes immediately through the staggered holes in the downstream blockage. The remaining portion of the airflow impinges on the region of the upstream surface of the downstream blockage between the staggered holes. The air turns toward the top and bottom walls along the upstream surface of the downstream blockage, causing the high heat transfer near the downstream edge of the heated bottom wall. If the jets through the holes in the upstream blockage do not reattach on the heated bottom wall, a large recirculating region may dominate the space below the jets. The air eventually continues downstream through the holes in the downstream blockage. The decreasing heat transfer toward the upstream blockage and the relatively low heat transfer near the upstream blockage may be caused by the recirculating flow below the jets through the upstream holes.

In Case 4 (UU), the smaller holes in both the upstream and downstream blockages are high above the bottom wall. There appears to be no reattachment of the jets from the upstream holes on the bottom wall. The decreasing heat transfer toward the upstream blockage appears to indicate that there is an uninterrupted backflow along the bottom wall. There is very little spanwise variation of the heat transfer distribution, except that the heat transfer is lower near the side walls.

The shapes of the $\mathrm{Nu}_{Dh}/\mathrm{Nu}_{Dh,0}$ distributions for Case 1 (MM) and Case 5 (UL) are similar to those of the distributions for Case 4 (UU). Moving the holes in both the upstream and downstream blockages to the mid plane of the channel or staggering the holes vertically by moving the holes in the downstream blockage to below the mid plane of the channel do not significantly change the $\mathrm{Nu}_{Dh}/\mathrm{Nu}_{Dh,0}$ distributions. The contours in Case 1 (MM) and Case 5 (UL) are ‘‘wavier’’ than those in Case 4 (UU). There appears to be no reattachment of the jets (or only weak reattachment of a portion of the airflow) from the upstream holes on the bottom walls. In Case 5 (UL), with the holes in the downstream blockage closer to the heated bottom wall, more of the airflow may pass directly through these holes and be deflected toward the unheated upper wall, and a smaller portion of the airflow may turn toward the heated bottom wall. The result is the slightly lower heat transfer distribution compared with those in the other two cases. The average heat transfer results also indicate slightly lower $\overline{\mathrm{Nu}}_{Dh}/\mathrm{Nu}_{Dh,0}$ values in Case 5 (UL) than in Case 1 (MM) and Case 4 (UU).

In Case 3 (LU), with the holes in the upstream blockage below the mid plane of the channel and those in the downstream blockage above the mid plane, the local heat transfer distributions are higher than those in the previous three cases. Because the holes in the downstream blockage are above those in the upstream blockage, the flow of air passing through the upstream holes may be drawn toward the higher downstream holes, weakening the reattachment of the flow on the bottom wall. Since the upstream holes are located close to the bottom wall, the recirculating flow may be affected by the jets leaving the holes. Both the possible reattachment of the jets on the bottom wall and the smaller recirculating region below the upstream holes may contribute to the higher local heat transfer over the entire heated bottom wall and the ‘‘wavier’’ contours, compared with those in the previous cases. The average heat transfer results show that the $\overline{\mathrm{Nu}}_{Dh}/\mathrm{Nu}_{Dh,0}$ values are the second highest among all nine cases studied.

The $\mathrm{Nu}_{Dh}/\mathrm{Nu}_{Dh,0}$ distributions for Case 2 (LL) are very different from those in the previous cases. The heat transfer is the highest among all nine cases studied. Although the holes in both the upstream and downstream blockages are close to the heated bottom wall, there are no isolated high transfer regions to indicate reattachment of the jets leaving the upstream holes on the bottom wall. It is believed that, because both the upstream and downstream holes are close to the bottom wall, there is a strong backflow along the bottom wall. This backflow prevents the reattachment of the jets. The interaction between the jets and the backflow may result in vigorous mixing immediately over the heated bottom wall and the high heat transfer on much of the surface of the bottom wall.

The addition of a third upstream blockage changes the $\mathrm{Nu}_{Dh}/\mathrm{Nu}_{Dh,0}$ distribution on the wall between the two downstream blockages. The $\mathrm{Nu}_{Dh}/\mathrm{Nu}_{Dh,0}$ contours are ‘‘wavier’’ in Case 6 (MMM) than in Case 1 (MM). The shapes of the $\mathrm{Nu}_{Dh}/\mathrm{Nu}_{Dh,0}$ distributions in Case 6 (MMM) are similar to those in Case 3 (LU). The additional third upstream blockage may increase the mixing of the flow before it passes through the holes in the blockage upstream of the heated bottom wall, and may cause the jets leaving the holes to spread more than in Case 1 (MM) without the third blockage. A portion of the airflow through the upstream holes may reattach on the bottom wall, increasing the waviness of the $\mathrm{Nu}_{Dh}/\mathrm{Nu}_{Dh,0}$ contours. In Case 7 (MLU), there is clearly reattachment of the jets leaving the holes. The side walls may contribute to the merging of the two reattaching jets on each side of the bottom wall.

The larger holes in the blockages in Case 8 ($\underline{\mathrm{MM}}$) and Case 9 ($\underline{\mathrm{MMM}}$) cause lower heat transfer than the smaller holes in the other cases. The lower heat transfer is the result of the lower average velocity through the larger holes than the smaller holes (for the same Re_{Dh}) and the larger open area ratio (ratio of the total cross-sectional area of the holes to the channel cross-sectional area). The larger total cross-sectional area of the holes allows the flow to pass the blockage more readily with less deflection of the flow off the upstream surface of the downstream blockage. With the addition of a third upstream blockage, the $\mathrm{Nu}_{Dh}/\mathrm{Nu}_{Dh,0}$ distributions for Case 9 ($\underline{\mathrm{MMM}}$) show seven distinctive zones of high heat transfer on the heated bottom wall when the jets leaving the upstream holes reattach on the bottom wall.

Conclusions

Separate experiments have been conducted to determine the average heat transfer coefficient and the local heat transfer distribution on one of the channel walls between two blockages with holes in a rectangular channel, and the overall pressure drop across the blockages. For the hole configurations studied, smaller holes cause higher heat transfer enhancement, but also significantly larger increase of the pressure drop than larger holes. Because the blockages with holes cause very large pressure drops, the heat transfer per unit pumping power is lower with the blockages than without the blockages. The local heat transfer distribution is strongly dependent on the configuration of the hole array in the blockages. The addition of a third upstream blockage also significantly changes the local heat transfer distribution between the two downstream blockages. Further studies are needed to measure, or to determine numerically, the detailed flow fields and heat transfer distributions for flows through blockages with holes in channels to better understand heat transfer enhancement with these blockages.

Acknowledgments

The Texas Advanced Research Program/Advanced Technology Program sponsored this research.

Nomenclature

A_s = surface area, m^2
c_p = specific heat of air, J/(kg·K)
D_h = hydraulic diameter, m
f = friction factor
h = local heat transfer coefficient, W/(m^2·K)
$\overline{h}$ = average heat transfer coefficient, W/(m^2·K)
H = height of test channel, m
I = current, A
k = thermal conductivity of air, W/(m·K)
$\dot{m}$ = mass flow rate, kg/s
Nu_{Dh} = Nusselt number
$\overline{\mathrm{Nu}}_{Dh}$ = average Nusselt number
Δp = pressure drop, N/m^2
Pr = Prandtl number
q_c = rate of convective heat transfer, W
q_{loss} = extraneous heat losses, W
Re_{Dh} = Reynolds number
$\overline{T}_m$ = average bulk mean temperature, K
$T_{m,i}$ = inlet bulk mean temperature, K

$T_{m,o}$ = bulk mean temperature at downstream edge of heated surface, K

T_w = local temperature on surface of thin-foil heater, K

$\overline{T}_w$ = average surface temperature of heated copper plate, K

TP = thermal performance ratio

$\overline{u}$ = mean velocity, m/s

V = voltage drop across heater or thin-foil heater, V

W = width of test channel, m

Δx = distance between two pressure taps for measuring pressure drop across two blockages with holes, m

Greek Symbols

μ = dynamic viscosity of air, $N \cdot s/m^2$

ρ = density of air, kg/m^3

Subscripts

0 = reference, fully developed turbulent flow in smooth channel with the same hydraulic diameter as test channel

References

[1] Han, J. C., Dutta, S., and Ekkad, S. V., 2001, *Gas Turbine Heat Transfer and Cooling Technology*, Taylor and Francis, New York, NY.

[2] Lau, S. C., 2002, ‘‘Enhanced Internal Cooling of Gas Turbine Airfoils,’’ in *Heat Transfer in Gas Turbines*, B. Sundén, and M. Faghri, eds., WIT Press, Southampton, UK.

[3] Ekkad, S. V., Pamula, G., and Acharya, S., 2000, ‘‘Influence of Crossflow-Induced Swirl and Impingement on Heat Transfer in an Internal Coolant Passage of a Turbine Airfoil,’’ ASME J. Heat Transfer, **122**, pp. 587–597.

[4] Pamula, G., Ekkad, S. V., and Acharya, S., 2000, ‘‘Influence of Crossflow-Induced Swirl and Impingement on Heat Transfer in a Two-Pass Channel Connected by Two Rows of Holes,’’ ASME Paper No. 2000-GT-0235.

[5] Kukreja, R. T., and Lau, S. C., 1998, ‘‘Distributions of Local Heat Transfer Coefficient on Surfaces With Solid and Perforated Ribs,’’ J. Enhanced Heat Transfer, **5**(1), pp. 9–21.

[6] Buchlin, J.-M., 2002, ‘‘Convective Heat Transfer in a Channel With Perforated Ribs,’’ Int. J. Therm. Sci., **41**, pp. 332–340.

[7] Hwang, J. J., Lia, T. Y., and Liou, T. M., 1998, ‘‘Effect of Fence Thickness on Pressure Drop and Heat Transfer in a Perforated-Fenced Channel,’’ Int. J. Heat Mass Transfer, **41**, pp. 811–816.

[8] Liou, T. M., and Chen, S. H., 1998, ‘‘Turbulent Heat and Fluid Flow in a Passage Distributed by Detached Perforated Ribs of Different Heights,’’ Int. J. Heat Mass Transfer, **41**, pp. 1795–1806.

[9] Incropera, F. P., and DeWitt, D. P., 2002, *Fundamentals of Heat and Mass Transfer*, 5th ed., John Wiley & Sons, New York, NY.

[10] Coleman, H. W., and Steele, W. G., 1989, *Experimentation and Uncertainty Analysis for Engineers*, John Wiley & Sons, New York, NY.

Jun-Mei Shi*

Michael Breuer
e-mail: breuer@lstm.uni-erlangen.de

Franz Durst

e-mail: durst@lstm.uni-erlangen.de
Lehrstuhl für Strömungsmechanik,
Universität Erlangen-Nürnberg,
Cauerstr. 4, D-91058 Erlangen,
Germany

Michael Schäfer
e-mail: schaefer@fnb.tu-darmstadt.de
Numerische Berechnungsverfahren im
Maschinenbau,
Technische Universität Darmstadt,
Petersenstraße 30, D-64287 Darmstadt,
Germany

An Improved Numerical Study of the Wall Effect on Hot-Wire Measurements

Numerical investigations of the heat transfer from hot wires in near-wall measurements were carried out. Special attention was paid to the effect of the wall thickness, the flow conditions below the wall and the shear velocity connected to different wall materials. Compared with previous studies, an improved physical model taking into account the flow region below the wall in the computational domain was applied. The results obtained agree well with experimental data in the literature for walls consisting of both highly and poorly conducting materials. The investigation showed that the shear velocity U_τ has a significant influence on hot-wire measurements in the vicinity of a wall. Nevertheless, discernible effects of the wall thickness and the flow condition below the wall were found only in the case of a poorly conducting wall. In addition, the results also suggest a weak effect of the overheat ratio for a wire with an infinitely large aspect ratio.
[DOI: 10.1115/1.1571848]

Keywords: Conjugate, Convection, Heat Transfer, Hot-Wire, Measurement Techniques, Modeling, Shear Flows, Temperature

1 Introduction

Hot-wire anemometry (HWA) is an important measurement technique, widely applied to investigations of both laminar and turbulent flows. The technique is well developed for standard flow situations. Nevertheless, large deviations occur when measurements are conducted in the proximity of a wall, e.g., in the viscous sublayer of a boundary layer, since the heat transfer from the wire is modified due to the additional influence of the wall. Hence a correction procedure has to be applied for HWA near-wall measurements.

Considering a wire of constant temperature arranged normal to the flow direction, its heat transfer coefficient h (see Eq. (7)) in a free stream depends on the local flow velocity U_0, the physical properties of the fluid, the temperature of the wire T_W and of the ambient fluid T_∞ (or the overheat ratio $\tau = T_W/T_\infty$, T in $[K]$), the length L and the diameter D of the wire probe, and the state of the flow (laminar or turbulent). Additional influencing parameters such as the wire-to-wall distance Y and the thermal condition at the fluid-wall interface are introduced in a near-wall flow. The latter is a final effect of the conjugate heat transfer consisting of the heat convection in the flow region and the heat conduction in the solid wall. In a theoretical model of the wall region, a Neumann condition $\partial T/\partial x = 0$ can be assumed at the downstream lateral boundary, whereas the upstream lateral end of the wall can be assumed to take the ambient temperature considering that the wall temperature decays at a power rate in this direction (see, e.g., [1]). Hence only the thermal conductivity of the wall material k_w, the wall thickness H, and the boundary condition at the bottom of the wall remain as the main influencing parameters of the wall region.

It was confirmed experimentally by Janke [2] that the state of the global flow is irrelevant for HWA measurements very close to a wall, namely within the dimensions of the viscous sublayer of a boundary layer flow, where the local flow is dominated by the molecular transport and thus is laminar in nature. Hence without loss of generality, only the laminar state of the flow needs to be considered. The natural convection and the viscous heating effect are negligible under the usual operating conditions of HWA near-wall measurements (small overheat ratio) in an air flow [3,4]. The dependence on the probe length L can also be neglected if the end effect, i.e., additional heat loss to the prongs, can be reduced to a negligible level by using a very large aspect ratio L/D. As a result, the problem can be treated in a two-dimensional frame by considering a perfectly aligned probe in the limit of $L/D \rightarrow \infty$ [5]. Although the above simplifications can be introduced, the physics of the problem are still complex. Introducing the Nusselt number Nu (Eqs. (7) and (8)) for characterizing the heat transfer from the wire, within the validity of continuum mechanics this quantity depends on the Reynolds number $\mathrm{Re} = U_0 D/\nu_\infty$, the distance-to-diameter ratio Y/D, the overheat ratio τ, the Prandtl number $\mathrm{Pr} = \mu_\infty c_{p,\infty}/k_\infty$ at ambient temperature, the variation of the fluid properties with the temperature, the thermal conductivity ratio between the wall material and the fluid medium $k_w^* = k_w/k_\infty$, combined with the boundary condition at the bottom of the solid wall. Here the quantities with the suffix ∞ are fluid properties evaluated at ambient temperature. In the literature, the dimensionless groups, $Y^+ = YU_\tau/\nu$ and $D^+ = DU_\tau/\nu$ rather than Re and Y/D are usually employed as the influencing parameters. They are related to each other in a linear shear flow, i.e., $Y^+ = \sqrt{\mathrm{Re}(Y/D)}$ and $D^+ = \sqrt{\mathrm{Re}/(Y/D)}$, as shown by Shi et al. [6].

Numerous investigations have been carried out in recent decades devoted to establishing a generic correction procedure for the near-wall application of hot-wire anemometry. However, the problem is still not fully resolved in several respects. Durst and Zanoun [7] noted that the data from HWA measurements in the proximity of poorly conducting walls [2,7–9] show much larger scatter than the highly conducting case. One of the reasons might be the difference in the thermal conductivity of the wall material employed in these experiments. This difference can result in large deviations in the measured velocities according to the experimental study of Gibbings et al. [10] and our previous numerical results [6,11]. The differences in experimental setups and configurations might also be responsible for the discrepancies among different measurements. For example, some measurements were carried out in the proximity of the bottom wall of a channel [8,9], i.e., without flow convection below the wall, whereas others were performed over a thin flat plate mounted in the middle of a chan-

---

*Present address: Institut für Sicherheitsforschung, Forschungszentrum Rossendorf, Bautzner Landstr. 128, D-01328 Dresden, Germany, Tel: +49-351-2602503, Fax: +49-351-2602383, Email: j.shi@fz-rossendorf.de

Contributed by the Heat Transfer Division for publication in the JOURNAL OF HEAT TRANSFER. Manuscript received by the Heat Transfer Division September 11, 2002; revision received March 3, 2003. Associate Editor: M. Faghri.

nel [2,12], i.e., with fluid flow below the wall. Since the conjugate heat transfer problem consisting of the heat convection from a hot-wire in cross-flow and the heat conduction in the solid wall has to be considered in the study, the flow on the underside of the wall and the wall thickness are likely to have an important influence on the heat transfer from the wire. Few investigations have dealt with these effects except for that of Durst and Zanoun [7]. Nevertheless, the thermal conductivity of the wall material is not clear in their study and hence their conclusion might deserve a re-examination.

It is also inconclusive in the literature whether the dimensionless wire diameter $D^+=DU_\tau/\nu$ is a suitable independent variable for the velocity correction needed for HWA near-wall measurements. The effect of the wire diameter D has so far been well confirmed in the literature [9,12–15]. Nevertheless, a number of investigations [9,15–17] reported that the velocity measured by a hot-wire at a given dimensionless distance Y^+ from a wall is independent of the shear velocity U_τ, although the measurements of Wills [18] and Gibbings et al. [10] show this dependence. At present, D rather than D^+ is usually suggested as a dependent variable in the velocity correction procedures commonly adopted in practical applications. Therefore, this issue still has to be clarified by a systematic investigation of the shear velocity effect.

The situation described above also indicates that the understanding of the physics behind the wall effect on hot-wire measurements is still inadequate. This is due to the limitations of the available studies. Most of the experimental investigations carried out so far were simply intended to establish a correction procedure, with little attention being paid to the physics of the problem. The information regarding the wall thermal conductivity, the wall thickness, the shear velocity of the local flow or even the overheat ratio of the wire was often not reported. Hence it is usually difficult to deduce a clear physical understanding of the wall influence from the experimental data available. Obviously, the numerical simulation technique has good advantages in resolving this problem, considering that all the parameters are clearly defined and that the field solutions obtained are useful for a deep insight into the mechanisms involved. The limitations of numerical investigations carried out so far are mainly due to their oversimplified physical models. For example, the heat conduction in a solid wall was not taken into account in some studies [15,17,19]. Instead, the Dirichlet condition $T_w=T_\infty$ was applied at the fluid-wall interface for the case of highly conducting walls and the adiabatic (Neumann) condition was employed to model the effect of poorly conducting walls. Such a model was shown to be inappropriate in the latter case [6,11] by taking the conjugate heat conduction in the wall into account. Nevertheless, in these studies the adiabatic condition was adopted at the underside of the wall, which might be not an appropriate approximation to physical reality. Probably for this reason, the results for poorly conducting walls indicated a relatively weaker wall effect than many experimental data [2,7,9]. This drawback can be overcome by extending the computational domain to include the flow region below the wall. As a result, the thermal conditions at both fluid-wall interfaces are parts of the numerical solution, rather than being prescribed as a priori boundary conditions as before. Such a model is expected to produce more realistic numerical results and thus to resolve the deviations between simulation and measurement.

The considerations described above motivated the work reported in this paper. In contrast to our previous investigations [6,11] the present study is concerned with the conjugate heat transfer consisting of the heat convection on both sides of the wall and the heat conduction in the solid wall (see Fig. 1). Consequently, the physical model considered is strongly improved. Two wall materials, highly and poorly conducting, i.e., aluminum ($k_w^*=9186$) and mirror glass ($k_w^*=29.6$), were used for the investigation. This enhanced model enabled us to systematically examine the influence of the wall thickness H, the flow on the underside of the wall (varied by a factor S), the shear velocity (U_τ) and the overheat ratio of the wire τ and therefore goes far beyond the investigations in [6,11]. The results indicate an important influence of the shear velocity for both wall materials and a discernible effect of the experimental setup in the case of a poorly conducting wall. In addition, the effect of the overheat ratio was found to be very weak. Compared with our previous studies [6,11], the agreement with the experimental data was significantly improved due to adopting a much more realistic theoretical model. Moreover, the present results are also useful for improving the understanding of the physics related to hot-wire near-wall measurements.

The paper is organized as follows. First, we give a detailed description of the theoretical model and the numerical methods. Then the results of the numerical calibration for the hot wire are reported. Thereafter, the effect of various influencing factors are discussed separately. Finally, a summary of the results is provided.

2 Theoretical Formulation and Numerical Method

2.1 Theoretical Model. The model configuration employed is illustrated schematically in Fig. 1. An infinitely long and heated circular cylinder with a diameter $D=5\ \mu$m was mounted horizontally above the plate to represent the hot-wire probe. Two wire temperatures, $T_W=100$ and 166.5°C were used, which correspond to an overheat ratio $\tau=1.27$ and 1.5, respectively. The fluid considered was air. To simulate the heat transfer from the wire in the viscous sublayer of the boundary layer, inflows with linear velocity profiles and with ambient temperature $T_\infty=20°$C were prescribed for the flow regions on both sides of the plate. The conjugate heat transfer problem consisting of two flow regions on both sides of the wall and the heat conduction in the solid wall was considered. The flow was assumed to be undisturbed at the top and bottom boundaries. A zero gradient boundary condition for a fully developed flow was assigned at the outflow boundary. No-slip and impermeability conditions, namely $U=0$ and $V=0$, were defined at all solid surfaces. A Dirichlet condition $T_w=T_\infty$ was applied at the upstream lateral boundary of the wall ($x=-L_1$) considering the power-rate decay of the wall temperature in this direction [1]. Similarly to the outflow boundary conditions of the flow region, a Neumann condition $\partial T/\partial x=0$ was used for the downstream lateral boundary of the wall ($x=L_2$). Tests were carried out with the Dirichlet condition $T_w=T_\infty$. The resulting difference in the Nusselt number of the wire (see Eq. (8)) was found to be negligible when the computational domain was extended in the x-direction to $L_1/D=8000-10{,}000$ upstream and to $L_2/D=10{,}000-12{,}000$ downstream of the cylinder. The height of the computational domain was chosen so that $H_a^+=H_aU_{\tau,a}/\nu_\infty>10$ and $H_b^+=H_bU_{\tau,b}/\nu_\infty>5$. Such a domain size was proved to be sufficiently large to obtain reliable numerical results [11].

The continuum condition was assumed to be satisfied. The fluid was treated as being incompressible (the fluid density was independent of the pressure). However, the variation of the fluid properties (density ρ, dynamic viscosity μ, thermal conductivity k and specific heat at constant pressure c_p) at different temperatures was taken into account by expressing these quantities as quadratic polynomial functions of the temperature T [6], based on data from the *VDI-Wärmeatlas* [20]. The natural convection and viscous dissipation were neglected owing to the dimensions and temperature values involved. Detailed discussions of the physics and justifications for these assumptions and simplifications can be found in [3,4].

Introducing U_0 for the normalization of the velocity components, D for the coordinates, the simplified governing equations for the flow regions can be expressed in a Cartesian coordinate system in nondimensional form as follows:

$$\frac{\partial(\rho^*U_i^*)}{\partial x_i^*}=0 \tag{1}$$

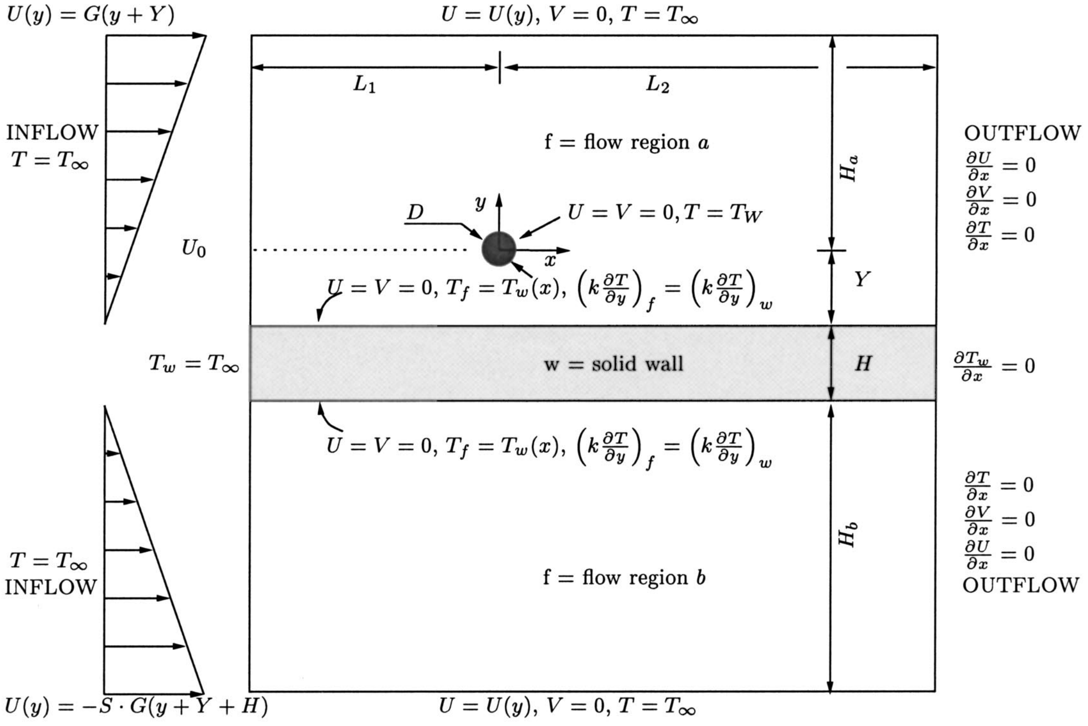

Fig. 1 Sketch of the physical model for the investigation of HWA near-wall measurements

$$\frac{\partial(\rho^* U_i^* U_j^*)}{\partial x_i^*} = -\frac{\partial P^*}{\partial x_j^*} + \frac{1}{\mathrm{Re}}\frac{\partial}{\partial x_i^*}\left[\mu^*\left(\frac{\partial U_j^*}{\partial x_i^*} + \frac{\partial U_i^*}{\partial x_j^*}\right)\right] \tag{2}$$

$$c_p^*\frac{\partial(\rho^* U_i^* T^*)}{\partial x_i^*} = \frac{1}{\mathrm{Re\,Pr}}\frac{\partial}{\partial x_i^*}\left(k^*\frac{\partial T^*}{\partial x_i^*}\right) \tag{3}$$

where $i, j = 1, 2$ are the coordinate indices for the x, y components, respectively. The quantities ρ^*, μ^*, k^*, and c_p^* are dimensionless properties normalized by the corresponding values evaluated at the ambient temperature T_∞, namely ρ_∞, μ_∞, k_∞, and $c_{p,\infty}$, respectively. $T^* = (T - T_\infty)/(T_W - T_\infty)$ is the dimensionless temperature. The dimensionless groups appearing in the governing equations are the Prandtl number and the Reynolds number, defined as

$$\mathrm{Pr} = \frac{\mu_\infty c_{p\infty}}{k_\infty} = \mathrm{const} \quad \text{and} \quad \mathrm{Re} = \frac{U_0 D}{\nu_\infty}, \tag{4}$$

respectively.

Only the energy equation is relevant in the solid wall. It reduces to a Laplace equation governing the heat conduction, since constant physical properties can be assumed in view of the small temperature difference in the wall region. The energy equation of the fluid and wall regions is coupled by means of the temperature continuity and the heat flux conservation at their interfaces, namely

$$T_f^* = T_w^* \quad \text{and} \quad \left(k\frac{\partial T^*}{\partial y^*}\right)_f = \left(k\frac{\partial T^*}{\partial y^*}\right)_w. \tag{5}$$

The Reynolds numbers involved were in the range $0.001 \leqslant \mathrm{Re} \leqslant 2$ and the resulting wall distance in wall units covered the range $0.32 \leqslant Y^+ \leqslant 8$. In order to examine the effect of the flow conditions below the plate (region b) on the heat transfer from the hot wire, the shear rate below the wall was varied with a factor of $S = 1$, 0.1 and 0.025 (see Fig. 1). In the case of $\tau = 1.27$, numerical results were obtained for two wall thicknesses, namely $H = 3$ and 8 mm, and for three distance-to-diameter ratios, $Y/D = 10$, 20, and 100, respectively. Suitable combinations of Re and Y/D allow us to vary the dimensionless wire diameter $D^+ = U_\tau D/\nu$ (or the shear velocity U_τ since $D = 5\ \mu\mathrm{m}$ is given) for a fixed value of Y^+ with reference to the relations $D^+ = \sqrt{\mathrm{Re}/(Y/D)}$ and $Y^+ = \sqrt{\mathrm{Re}(Y/D)}$. Hence, both the influence of experimental model configurations and the shear velocity (U_τ) effect on HWA near-wall measurements can be investigated in detail. It is worth pointing out that the present study could not produce data sets where Y^+ varies systematically in a defined range for each constant value of D^+. In contrast, measurements are usually conducted in a given flow (U_τ fixed) by changing the wire-to-wall distance Y in experimental investigations, yielding a data set for a constant D^+ but varying Y^+. Hence experimental studies of the D^+ effect are usually realized by repeating the measurements in different flows (different U_τ) or with different wire diameters (D). Nevertheless, with the present method we have the relation $D^+ = Y^+/(Y/D)$. Hence at each Y^+ numerical results for three different values of D^+ are available, which is sufficient to reveal the influence of D^+ owing to variations of U_τ.

To characterize the heat transfer from the hot wire, the Nusselt number of the wire was evaluated. The local Nusselt number $\mathrm{Nu}(\theta)$ is defined based on the local heat transfer rate of unit area at the wire surface:

$$\dot{q}(\theta) = h(\theta)(T_W - T_\infty) = -k(T_W)\left.\frac{\partial T(r,\theta)}{\partial r}\right|_{r=D/2} \tag{6}$$

where r and θ are the polar coordinates originated at the wire center, and $h(\theta)$ is the local heat transfer coefficient at the wire surface. Normalizing $\dot{q}(\theta)$ with a reference value, $\dot{q}_c = k_c(T_W - T_\infty)/D$, one obtains

$$\mathrm{Nu}(\theta) = \frac{\dot{q}(\theta)}{\dot{q}_c} = \frac{h(\theta)D}{k_c} = -\frac{k(T_W)}{k_c}\left.\frac{\partial T^*(r^*,\theta^*)}{\partial r^*}\right|_{(r^*=0.5)}. \tag{7}$$

The mean Nusselt number can be calculated by averaging the local value over the cylinder surface:

$$\mathrm{Nu}=\int_0^1 \mathrm{Nu}(\theta^*)\,\mathrm{d}\theta^* \tag{8}$$

where $\theta^*=\theta/(2\pi)$. Choosing $k_c=k(T_W)$ for the definition in Eq. (7), the Nusselt number $\mathrm{Nu}(\theta)$ reduces to the dimensionless temperature gradient at the wire surface. It is worth mentioning that the fluid properties are usually assumed to be constant in many theoretical studies. In this case, the Nusselt number is denoted by Nu_∞ in the present study.

For a clear understanding of the wall effect on the heat transfer from the hot wire, the distribution of the dimensionless temperature $T_w^*=(T_w-T_\infty)/(T_W-T_\infty)$ and the dimensionless heat flux at the fluid-plate interfaces $(y^*=-Y/D,-(Y+H)/D)$,

$$D_y=\frac{\left(k\,\dfrac{\partial T}{\partial y}\right)_w}{k_\infty\dfrac{T_W-T_\infty}{\ell_c}}=\frac{k_w^*}{\mathrm{Re\,Pr}}\left(\frac{\partial T^*}{\partial y^*}\right)_w, \tag{9}$$

was analyzed. Here $\ell_c=D/(\mathrm{Re\,Pr})$ is used. Consequently, D_y is equivalent to the diffusion integral of the energy Eq. (3) and thus reflects directly the wall influence on the heat transfer from the wire. In addition, a quantity called the modified Biot number, Bi, was introduced. The definition is as follows. Expressing the heat flux at the fluid-plate interface as

$$\dot{q}_w=\left(k_w\frac{\partial T}{\partial y}\right)_w=h_w(T_w-T_\infty), \tag{10}$$

one has

$$\mathrm{Bi}=\frac{h_w\ell_c}{k_w}=\frac{1}{\mathrm{Re\,Pr}}\,\frac{(\partial T^*/\partial y^*)_w}{T_w^*}. \tag{11}$$

Physically, this quantity characterizes the ratio of the conductive thermal resistance inside the solid material to the convective thermal resistance in the fluid and thus is useful for understanding the effect of the experimental condition on HWA near-wall measurements.

2.2 Numerical Method. The numerical solution was based on the finite-volume flow solver, FASTEST2D [21]. A brief description of the numerical features of the code could be found in Shi et al. [6]. In order to accelerate the information propagation during the solution procedure, the data dependence of the energy equation between the fluid and solid wall regions, i.e., the exchange of the conjugate temperature and heat flux at the plate (interface) was implemented at each inner iteration. Convergence was assumed to be satisfied when the maximum sum of the normalized absolute residuals in all equations was reduced by six orders of magnitude.

A local grid refinement technique (for details, see Lange et al. [22]) was employed to achieve high local resolution near the hot wire. In the computations 512 grid points at the cylinder surface ($D=5\ \mu$m) and about 2.2×10^5 grid points for the total computational domain were applied on the fifth (finest) multigrid level. The grid convergence rate and the grid independence of the numerical results are similar to a previous study [11]. Richardson extrapolation [23] was applied to reduce the discretization error. These measures ensure high accuracy of the present results. Detailed information is provided in Shi [24].

3 Numerical Calibration

For the purpose of numerical calibration, the heat transfer from the hot wire in free stream was first investigated. Since the ambient temperature and the fluid properties are known *a priori*, the Nusselt number of the wire depends on the wire Reynolds number and the overheat ratio, namely $\mathrm{Nu}=f(\mathrm{Re},\tau)$. Densely distributed numerical results were obtained in the range $0.001\leqslant\mathrm{Re}\leqslant2$ for $\tau=1.27$ and $0.01\leqslant\mathrm{Re}\leqslant1$ for $\tau=1.5$ in order to establish a precise calibration relationship at each overheat ratio. Comparisons of the present results with classical results available in the literature are presented in Fig. 2. The correlation method for the overheat ratio due to Collis and Williams [25] was applied for those results obtained for temperature-dependent fluid properties (including the present results and the experimental data of Collis and Williams [25]), namely they are presented in the form $\mathrm{Nu}_m(T_m/T_\infty)^{-0.17}=f(\mathrm{Re}_m)$, where $\mathrm{Nu}_m=(k_W/k_m)\mathrm{Nu}$ and $\mathrm{Re}_m=(U_0D/\nu_m)$ are the Nusselt and Reynolds number, respectively, defined based on the properties evaluated at the film (mean) temperature $T_m=0.5(T_\infty+T_W)$ (T in [K]). No correlation is necessary for other theoretical results Nu_∞ [5,26–29] obtained by assuming constant fluid properties, since the correlation function turns out to be the same as $\mathrm{Nu}_\infty=f(\mathrm{Re})$ in this case. As shown in Fig. 2, the present data agree well with the numerical results of Dennis et al. [30] and the experimental data of Collis and Williams [25]. Excellent agreements are also observed with the higher-order analytical results [27,28] in the low Reynolds number range and with the lower-order analytical solutions [5,26,29] at the limit Re→0. Hence the above comparisons confirm that the present numerical calibration is highly precise.

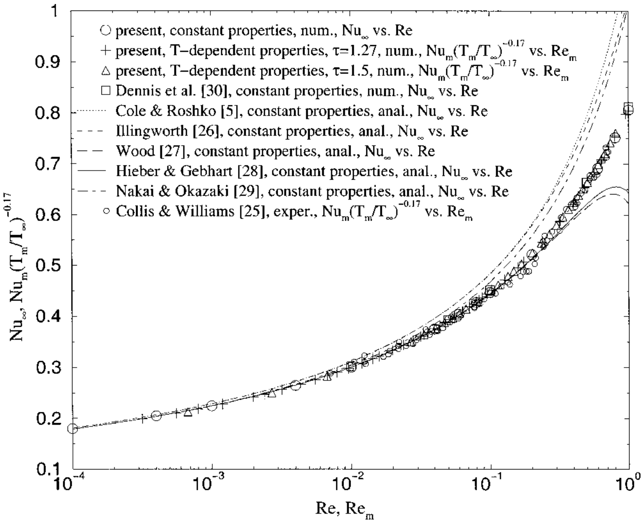

Fig. 2 Comparison of the present results at very small Reynolds numbers with classical results from the literature

4 Effect of the Physical Model Configuration

In order to examine the effect of the physical model configuration on HWA near-wall measurements, numerical simulations were carried out for two values of the wall thickness, namely $H=3$ and 8 mm, and for various inflow velocities below the wall, namely $U=-S\cdot G\cdot(y+Y+H)$ where $S=1$, 0.1 and 0.025. The investigations were performed both for an aluminum ($k_w^*=9186$) and a mirror glass ($k_w^*=29.6$) wall using a distance-to-diameter ratio $Y/D=100$ and an overheat ratio $\tau=1.27$.

4.1 Highly Conducting Walls. No discernible difference was predicted in the Nusselt number and thus in the converted velocity reading of the wire U^+_{appa} for an aluminum wall regardless of varying wall thicknesses and inflow velocities below the wall. Moreover, as shown in Fig. 3, the present numerical results almost coincide with our previous data [6,11], which were obtained based on $H=1.5$ mm and the simplifying adiabatic boundary condition at the bottom of the wall. The physical cause is due to the small thermal conductive resistance inside an aluminum wall according to the analysis of the Biot number (not shown here; detailed information is provided in Shi [24]). Hence it can be concluded that the model configuration (the wall thickness and the flow condition

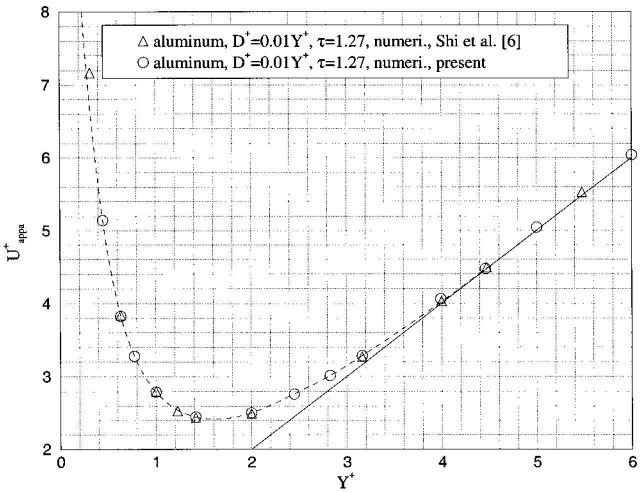

Fig. 3 Comparison of the present results for the apparent velocity U^{+}_{appa} in the case of an aluminum wall with those of Shi et al. [6]; $k^{*}_{w}=9186$, $Y/D=100$, $D=5\ \mu$m

below the wall) does not have an discernible influence on HWA measurements in the vicinity of highly conducting walls.

4.2 Poorly Conducting Walls. In contrast to highly conducting walls, the effect of the wall thickness H and the flow condition below the wall (varied by S) was found to be not negligible in the case of a mirror glass wall ($k^{*}_{w}=29.6$). This is demonstrated by the numerical results presented in Fig. 4. The data obtained in previous investigations [6,11] based on a different physical model are also displayed for comparison. It can be observed that the wire measures a larger apparent velocity U^{+}_{appa} in the case of an increasing flow velocity (larger S) below the wall or a thicker wall. The influence of these parameters is more evident at small wire-to-wall distances, i.e., $Y^{+}\leqslant 2$. Therefore, it is necessary to take these influencing factors into account in the velocity correction procedure for poorly conducting walls. It is worth pointing out that the present results are in contradiction with the measurements of Durst and Zanoun [7], which indicate a stronger wall effect in the case of a 3 mm thick glass wall compared with an 8 mm wall. Their conclusion is difficult to justify since one cannot expect the strongest wall effect for the case of an infinitely thin wall. This issue as well as the effect of the flow on the underside of the wall can be better understood by an examination of the distribution of temperature T^{*}, heat flux $\mathcal{D}_{y}$ (Eq. (9)) and modified Biot number Bi (Eq. (11)) at the fluid-plate interfaces ($y=-Y$ and $y=-(Y+H)$) (for details refer to Shi [24]). In addition, it was not possible to measure the thermal conductivities of the glass walls used in the experiments of Durst and Zanoun [7]. Therefore, there is no evidence that the two different walls used had the same thermal conductivity, which might explain the controversy.

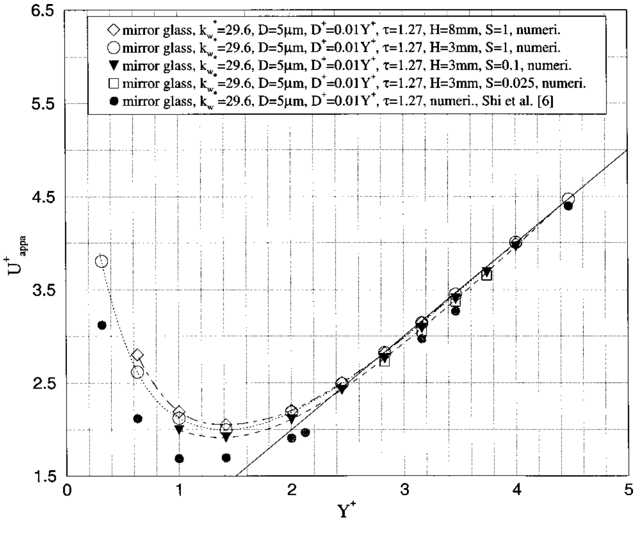

Fig. 4 Comparison of the numerical results of the velocity reading U^{+}_{appa} of the hot wire close to mirror glass walls ($k^{*}_{w}=29.6$) obtained by using different model configurations

Compared with the present results, the previous study [6] significantly under-predicted the velocity reading of the wire owing to the inappropriate adiabatic boundary condition applied at the bottom of the wall and also due to the small wall thickness ($H=1.5$ mm). Nevertheless, this drawback has no consequence for our conclusion concerning the effect of the wall material in the case of poorly conducting walls. Moreover, the present results for U^{+}_{appa} are found to be about 1.5–3.5% lower than the corresponding true value U^{+}_{0} in a certain range of wire-to-wall distances ($2.5<Y^{+}<4$) when the flow convection below the plate is reduced ($S=0.1$ and 0.025). A similar phenomenon was predicted by Shi et al. [6] and can also be recognized from the experimental data of Ligrani and Bradshaw [8] and Chew et al. [9], which were obtained from measurements directly above the bottom wall of a channel, corresponding to the case $S=0$. Nevertheless, one might suspect that they are unphysical results caused by the limitation of our previous physical model [6] or due to the measurement error of the experimental investigations mentioned above. Now this observation ($U^{+}_{\text{appa}}<U^{+}_{0}$) can be confirmed. In contrast to the cases $S=0.1$ and 0.025, this phenomenon was not observed in the case of the same shear rate on both sides of the wall ($S=1$), where the heat transfer from the wire was enhanced by the stronger flow convection below the wall.

5 Effect of the Shear Velocity U_{τ}

In order to examine whether the shear velocity U_{τ} has an important effect on HWA near-wall measurements, simulations were carried out for various distance-to-diameter ratios, $Y/D=10$, 20, and 100. This allowed the dimensionless diameter $D^{+}=DU_{\tau}/\nu_{\infty}$ or the shear velocity U_{τ} ($D=5\ \mu$m fixed) to be varied 10 times for the same value of Y^{+}. The investigation was performed for the case of an overheat ratio $\tau=1.27$, a wall thickness $H=3$ mm, the same inflow velocity on both sides of the wall ($S=1$) and for both wall materials, namely an aluminum wall ($k^{*}_{w}=9186$) and a mirror glass wall ($k^{*}_{w}=29.6$). In addition, the study was concentrated on the case of small dimensionless distances $Y^{+}<5$. Outside this range, the effect of U_{τ} is negligible [6].

5.1 Nusselt Number. The results for the Nusselt number are displayed in Fig. 5. It is observed that with both wall materials, the heat loss from a hot wire at a given Re increases significantly with decreasing Y/D in the case of small flow convection (i.e., small Re). As expected, a stronger wall effect is observed in the case of an aluminum wall. Moreover, for a given Re, the influence of the wall material is more evident in the case of a smaller Y/D. On the other hand, with increasing Re all curves for various values of Y/D asymptotically approach the calibration results obtained for a hot wire in a free stream, indicating a vanishing wall influence.

5.2 Apparent Velocity Measured by a Hot Wire. It was shown in Shi et al. [6] that the shear velocity U_{τ} has no effect on the average Nusselt number of a hot wire and thus on HWA measurements if the hot wire is located outside the wall influence, e.g., $Y^{+}\geqslant 5$. However, this conclusion is no longer true when Y^{+} decreases, as demonstrated in Fig. 6. The numerical results show that at the same Y^{+}, the apparent velocity U^{+}_{appa} increases with

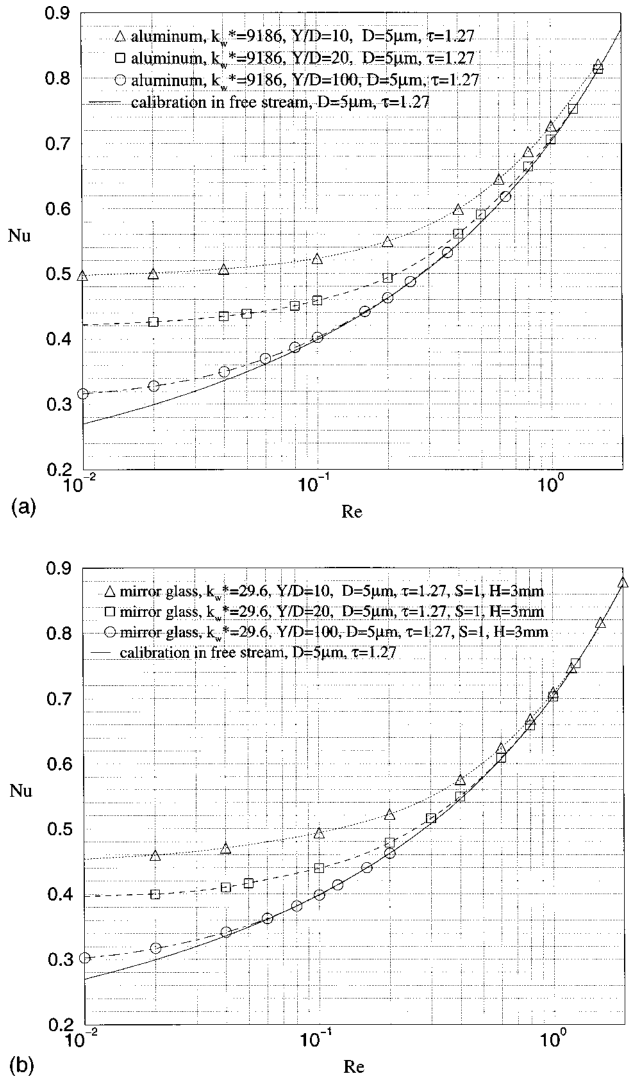

Fig. 5 The average Nusselt number Nu of a hot wire in near-wall cross-flow for various Y/D, $D=5$ μm, $\tau=1.27$: (a) aluminum wall ($k_w^*=9186$); and (b) mirror glass wall ($k_w^*=29.6$).

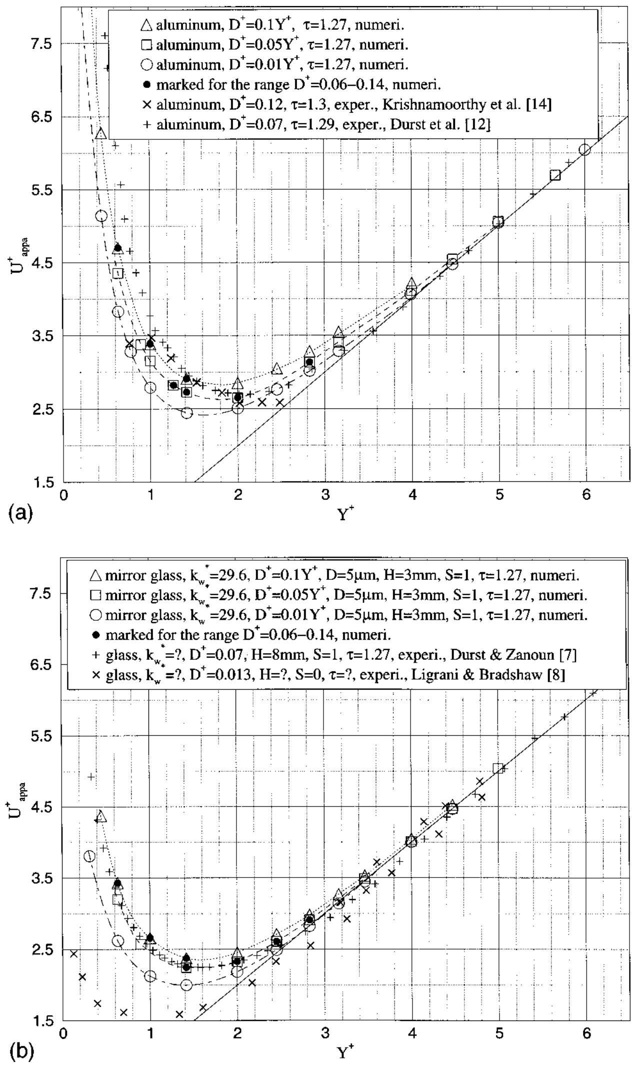

Fig. 6 Velocity reading of the wire, comparison between various $D^+(=U_\tau D/\nu_\infty)$ varied by the shear velocity U_τ or Y/D, where $D^+(=Y^+/(Y/D))$, $D=5$ μm and $\tau=1.27$. H and S are irrelevant in the case of an aluminum wall: (a) aluminum wall ($k_w^*=9186$); and (b) mirror glass wall ($k_w^*=29.6$).

increasing D^+ (increasing U_τ or decreasing Y/D) at $Y^+\leqslant 4$ for an aluminum wall ($k_w^*=9186$) and $Y^+\leqslant 3$ for a mirror glass wall ($k_w^*=29.6$). Hence, the present results are in accordance with the experimental data of Wills [18] and Gibbings et al. [10], which also indicate a U_τ influence, but nevertheless contradict those studies rejecting the U_τ effect [2,9,15–17].

The present results might be more reliable for several reasons. First, the numerical results have been carefully validated for the calibration curve (Section 3). Moreover, there is an analytical solution in the literature [31,32] for the heat conduction from a two-dimensional cylinder close to a perfectly conducting wall (in a semi-infinite space under the boundary condition $T_w=T_\infty$), which for $(Y/D)^2\gg 1$ can be simplified to

$$\mathrm{Nu}_\infty(0)\approx\frac{2}{\ln(4Y/D)} \tag{12}$$

This solution can be used as a reference value of the numerical results at the lower limit ($\mathrm{Re}_{D,\infty}\to 0$) for the aluminum wall (Fig. 5(a)), despite that this relation was obtained based on constant fluid properties and Nu_∞ is defined based on $k_c=k_\infty$. Equation (12) can be considered as the Nusselt number of a hot wire at $Y^+=0$ from a perfectly conducting wall, which is a function of Y/D. As a result, it is expected that the asymptotic value for the velocity reading at $Y^+=0$, denoted by $U^+_{\mathrm{appa},Y^+=0}$, also depends on Y/D. Bearing in mind that diffusion is the dominant mechanism for the heat transfer from a hot wire at small Y^+, the effect of Y/D or equivalently U_τ on HWA near-wall measurements can be theoretically justified. In contrast, the numerical results of Bhatia et al. [17] and Chew et al. [15] for the adiabatic boundary condition might be insufficiently precise[1] according to other numerical studies [19,32]. The grid independence of their numerical results was also not reported. Therefore, the conclusions from these studies need to be re-examined. In fact, the influence of U_τ is noticeable from the results of Chew et al. [15], which seems to be at least as strong as that of the wire diameter D for $Y^+<2$ in the case of an adiabatic wall (refer to Figs. 4 and 6 of Chew et al. [15]). Concerning the experimental investigations[2], only Janke [2] has presented results for varying U_τ systematically obtained at the same values of Y^+, which is necessary for a precise evaluation. A

---

[1] Both failed to predict a reduced Nusselt number for a hot wire close to an adiabatic wall compared with the corresponding free-stream result.

[2] Refer to Fig. 8 of Janke [2], Fig. 13 of Chew et al. [9], Fig. 4 of Kostić and Oka [16], and Fig. 8 of Bhatia et al. [17].-

weak effect of U_τ with the same trend as the present results is discernible in his data. In addition, the experimental study of Bhatia et al. [17] was limited to $Y^+>3$ (refer to Fig. 8 of their paper), where the U_τ effect is already very weak according to the present numerical results.

The influence of Y/D or U_τ predicted in the present numerical study is similar to that of the wire diameter reported in the literature. This supports the dimensional analysis of Shi et al. [6] and also the similarity implied in it. Therefore, it is necessary to take both influences of wire diameter and shear velocity into account. As an approximation, the parameter $D^+=(DU_\tau/\nu)$ might be used for the representation of these influences. However, strictly, the present results cannot confirm this similarity. Further investigations with various D need to be carried out to examine how well U^+_{appa} can be described as a function of Y^+ and D^+ for a fixed overheat ratio τ and experimental setup. Additionally, in view of Eq. (12) and the small Peclet number involved in HWA near-wall measurements, it is worth mentioning that the influence of U_τ or Y/D is mainly due to the diffusion effect of the wall rather than the change of convection corresponding to different shear rates of the flow.

As another evaluation of the numerical results, the experimental data[3] of Durst et al. [12] and Krishnamoorthy et al. [14] obtained with an aluminum wall are plotted in Fig. 6(a) for comparison. The conditions in these experiments are very close to those of the present study, i.e., the same wire diameter and a similar overheat ratio. The dimensionless diameter is $D^+=0.12$ and $D^+=0.07$, respectively. For convenience of comparison, the numerical results obtained with $0.06\leqslant D^+\leqslant 0.14$ are marked. These results are found to agree very well with the experimental data. Therefore, one might be allowed to conclude that the two-dimensional model adopted in the present study is acceptable for the investigation of HWA near-wall measurements. On the other hand, the apparent velocities predicted for $Y/D=100$ are obviously smaller than the experimental data in the case of $Y^+<2$ owing to the small values of D^+ ($D^+=0.01Y^+$ in this case). In addition, it is noted that a direct comparison of the two sets of experimental data does not support the U_τ effect. Nevertheless, this is not a reason to reject the numerical results considering the small difference in U_τ between them and the possible experimental errors.

In the case of a mirror glass wall (Fig. 6(b)), the marked numerical results ($0.06\leqslant D^+\leqslant 0.14$, $\tau=1.27$ and $H=3$ mm) also agree very well with the experimental data of Durst et al. [7] ($D^+=0.07$, $\tau=1.29$ and $H=8$ mm). Nevertheless, the thermal conductivity of the wall material (k^*_w) in their experiment is not known. The results of Ligrani and Bradshaw [8] extracted from their paper are much smaller than the other results. This may be due to a number of causes, such as the small $D^+(=0.013)$ and no flow convection below the wall $(S=0)$, etc. in their study. In addition, the thermal conductivity and thickness of the wall and the overheat ratio were not given by the authors. Although both experiments were conducted by employing a glass wall, their thermal conductivity could be different, which has been shown to have a significant effect on HWA near-wall measurements [6,10].

6 Effect of the Overheat Ratio τ

The effect of the overheat ratio τ on HWA near-wall measurements was first reported by Krishnamoorthy et al. [14] and was confirmed by Chew et al. [9] and Durst et al. [12]. At the same time, Chew et al. [9] also reported that this effect vanishes for a hot wire with a large aspect ratio $(L/D\geqslant 250)$. This is in favor of the two-dimensional numerical results of Chew et al. [15], which also indicate no overheat ratio effect. Hence Chew et al. [9] proposed that the effect of the overheat ratio is physically due to the end effect, namely the additional heat loss in the axial direction of a hot wire. This interpretation is surely plausible. However, as mentioned above, the results of Chew et al. [15] for an adiabatic wall seem to be insufficiently accurate. Therefore, it was useful to repeat the numerical investigation in order to verify the interpretation of Chew et al. [9].

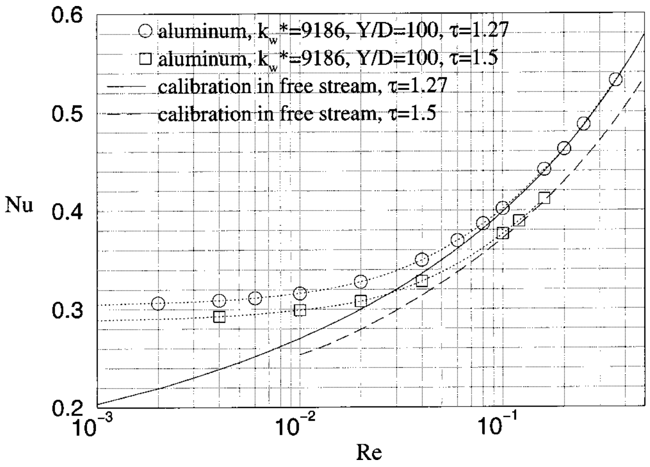

Fig. 7 Comparison of the average Nusselt number *Nu* of a hot wire in cross-flow of a free stream, close to an aluminum wall and at different overheat ratios, τ=1.27 and 1.5; k^*_w=9186, Y/D=100, D=5 μm

Without loss of generality, the investigation was restricted to an aluminum wall and $Y/D=100$. Simulations were carried out for τ=1.27 and 1.5. The results for the Nusselt number together with the calibration results are presented in Fig. 7. The corresponding results for the apparent velocity U^+_{appa} versus Y^+ are displayed in Fig. 8. These results show a slight increase in U^+_{appa} in the case of a higher overheat ratio (τ=1.5). This is in accordance with the measurements of Krishnamoorthy et al. [14] and Durst et al. [12] (not shown here). Nevertheless, the overheat ratio effect predicted in the present study $(L/D=\infty)$ is much weaker than that observed in the experimental data. This suggests that the effect of the overheat ratio can be substantially reduced by using a large aspect ratio. Hence the conclusion of Chew et al. [9] might be largely

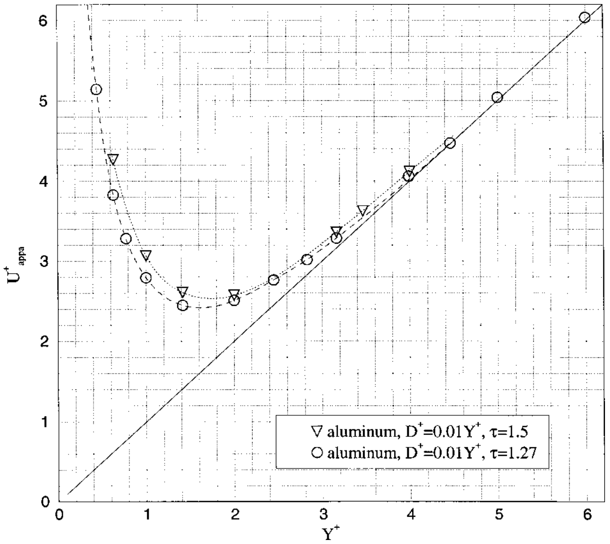

Fig. 8 Effect of the overheat ratio τ (=1.27 and 1.5) on HWA near-wall measurements close to an aluminum wall, k^*_w=9186, Y/D=100, D=5 μm

---

[3] The data of Durst et al. [12] were provided by the authors and those of Krishnamoorthy et al. [14] were extracted from their paper.

acceptable. However, according to the present results, this effect seems not to completely vanish even for a hot wire with an infinitely large aspect ratio.

7 Conclusions

Numerical simulations of the forced convection from a hot wire in cross-flow of both free stream and wall-bounded flow were carried out in order to investigate the wall effect on HWA near-wall measurements. Special interest was paid to the influence of the wall thickness H, the flow conditions below the wall (varied by the factor S), the shear velocity U_τ and the overheat ratio τ. Compared with previous studies, an improved physical model that takes the flow region below the wall into account in the computational domain was employed. Based on the present numerical investigation, the following conclusions can be drawn:

- The experimental setup and model configuration do not have a meaningful influence on HWA measurements in the case of highly conducting walls. In contrast, their influences cannot be neglected in the case when a thin poorly conducting wall (e.g., mirror glass, $H=3$ mm) is involved in the experiment.
- The results indicate that within the influencing range of the wall, the shear velocity U_τ or equivalently the distance-to-diameter ratio Y/D has a significant effect on HWA near-wall measurements. This finding is a new proof to object to the universal velocity correction procedure, which suggests a single dependence on Y^+, proposed in the literature.
- The effect of the overheat ratio τ was found to be very weak for a wire with an infinitely large aspect ratio.
- The present results also confirmed the observations of Shi et al. [6] concerning the negative velocity corrections needed for HWA measurements close to poorly conducting walls.
- The numerical study leads to a deeper insight into the physics of the problem, which is not available from experimental investigations.

Acknowledgments

This work was supported by a fellowship from the German Academic Exchange Service (DAAD) to J.-M. Shi, which is gratefully acknowledged. The authors also thank Prof. G. Biswas of the Indian Institute of Technology, Kanpur, for valuable discussions.

Nomenclature

Bi = modified Biot number, Eq. (11)
c_p = specific heat at constant pressure
D = hot-wire diameter
D_y = diffusion flux at fluid-wall interfaces, Eq. (9)
G = shear rate of the flow, $\partial U/\partial y$
H = wall thickness
H_a, H_b = heights of the computational domain
h = heat transfer coefficient
k = thermal conductivity
L = length of the wire probe
L_1, L_2 = lengths of the computational domain
Nu = Nusselt number, Eqs. (7)–(8) with $k_c=k_W$
Nu_m = Nusselt number, with $k_c=k_m$
Nu_∞ = Nusselt number, with $k_c=k_\infty$
P = pressure
Pr = Prandtl number, Eq. (4)
$\dot{q}$ = local heat transfer rate of unit area, Eq. (6)
Re = Reynolds number, Eq. (4)
Re_m = Reynolds number at the film temperature, $=U_0D/\nu_m$
r = radial component of a polar coordinate system
S = shear coefficient below the wall, see Fig. 1
T = temperature
U_τ = friction velocity, $=\sqrt{\tau_w/\rho_\infty}$
U, V = Cartesian velocity components
x, y = Cartesian coordinates
Y = wire-to-wall distance

Greek Symbols

μ = dynamic viscosity
ν = kinematic viscosity
ρ = fluid density
τ = overheat ratio, $=T_W[K]/T_\infty[K]$
τ_w = wall shear stress, $\mu_\infty(\partial U/\partial y)_w$
θ = tangential component of a polar coordinate system

Indices:

0 = actual value or free-stream case
appa = apparent value
a = above the plate
b = below the plate
c = characteristic quantities
f = flow region
∞ = values at ambient temperature T_∞
m = values at the film (mean) temperature, $T_m=(T_W+T_\infty)/2$
W = at the wire surface or at wire temperature
w = solid wall
$*$ = nondimensional quantity
$+$ = in wall units, $\phi^+=\phi U_\tau/\nu_\infty$

References

[1] Carslaw, H. S., and Jaeger, J. C., 1959, *Conduction of Heat in Solids*, 2nd edition, Clarendon Press, Oxford.
[2] Janke, G., 1987, ''Hot Wire in Wall Proximity,'' in *Advances in Turbulence*, G. Comte-Bellot and J. Mathieu, eds., Springer, Berlin, pages 488–498.
[3] Bradshaw, P., 1971, *An Introduction to Turbulence and Its Measurement*, Pergamon Press, Oxford.
[4] Lange, C. F., 1997, ''Numerical Predictions of Heat and Momentum Transfer from a Cylinder in Crossflow With Implications to Hot-Wire Anemometry,'' Ph.D. thesis, Inst. Fluid Mech., Friedrich-Alexander University of Erlangen-Nuremberg.
[5] Cole, J., and Roshko, A., 1954, ''Heat Transfer From Wires at Reynolds Numbers in the Oseen Range,'' *Proc. Heat Transfer and Fluid Mech. Inst.*, University of California, Berkeley, CA, **6**, pp. 357–384.
[6] Shi, J.-M., Breuer, M., and Durst, F., 2002, ''Wall Effect on Heat Transfer From a Micro Cylinder in Near-Wall Shear Flow,'' Int. J. Heat Mass Transf., **45**, pp. 1309–1320.
[7] Durst, F., and Zanoun, E. S., 2002, ''Experimental Investigation of Near-Wall Effects on Hot-Wire Measurements,'' Exp. Fluids, **33**, pp. 210–218.
[8] Ligrani, P. M., and Bradshaw, P., 1987, ''Subminiature Hot-Wire Sensors: Development and Use,'' J. Phys. E, **20**, pp. 323–332.
[9] Chew, Y. T., Khoo, B. C., and Li, B. C., 1998, ''An Investigation of Wall Effects on Hot-Wire Measurements Using a Bent Sublayer Probe,'' Meas. Sci. Technol., **9**, pp. 67–85.
[10] Gibbings, J. C., Madadnia, J., and Yousif, A. H., 1995, ''The Wall Correction of the Hot-Wire Anemometer,'' Flow Meas. Instrum., **6**, pp. 127–136.
[11] Durst, F., Shi, J.-M., and Breuer, M., 2002, ''Numerical Prediction of Hot-Wire Corrections Near Walls,'' ASME J. Fluids Eng., **124**, pp. 241–250.
[12] Durst, F., Zanoun, E.-S., and Pashtrapanska, M., 2001, ''In Situ Calibration of Hot Wires Close to Highly Heat-Conducting Walls,'' Exp. Fluids, **31**, pp. 103–110.
[13] Zemskaya, A. S., Levitskiy, V. N., Repik, Y. U., and Sosedko, Y. P., 1979, ''Effect of the Proximity of the Wall on Hot-Wire Readings in Laminar and Turbulent Boundary Layers,'' Fluid Mech.-Sov. Res., **8**, pp. 133–141.
[14] Krishnamoorthy, L. V., Wood, D. H., Antonia, R. A., and Chambers, H. J., 1985, ''Effect of Wire Diameter and Overheat Ratio Near a Conducting Wall,'' Exp. Fluids, **3**, pp. 121–127.
[15] Chew, Y. T., Shi, S. X., and Khoo, B. C., 1995, ''On the Numerical Near-Wall Corrections of Single Hot-Wire Measurements,'' Int. J. Heat Fluid Flow, **16**, pp. 471–476.
[16] Kostić, Z., and Oka, S., 1972, ''Influence of Wall Proximity on Hot-Wire Velocity Measurements,'' DISA Information, **13**, pp. 29–33.
[17] Bhatia, J. C., Durst, F., and Jovanović, J., 1982, ''Corrections of Hot-Wire Anemometer Measurements Near Walls,'' J. Fluid Mech., **122**, pp. 411–431.
[18] Wills, J. A. B., 1962, ''The Correction of Hot-Wire Readings for Proximity to a Solid Boundary,'' J. Fluid Mech., **12**, pp. 388–396.
[19] Lange, C. F., Durst, F., and Breuer, M., 1999, ''Wall Effects on Heat Losses From Hot-Wires,'' Int. J. Heat Fluid Flow, **20**, pp. 34–47.
[20] Verein Deutscher Ingenieure, 1994, *VDI-Wärmeatlas*, 7th edition, VDI, Düsseldorf.
[21] Durst, F., and Schäfer, M., 1996, ''A Parallel Blockstructured Multigrid Method for the Prediction of Incompressible Flows,'' Int. J. Numer. Methods Fluids, **22**, pp. 549–565.

[22] Lange, C. F., Schäfer, M., and Durst, F., 2002, ''Local Block Refinement With a Multigrid Flow Solver,'' Int. J. Numer. Methods Fluids, **38**, pp. 21–41.

[23] Ferziger, J. H., and Perić, M., 1999, *Computational Methods for Fluid Dynamics*, Springer, Berlin.

[24] Shi, J.-M., 2002, ''Numerical Study of Classical Low Reynolds Number Flow Problems: Leading Edge Singularity of a Semi-Infinite Plate and Hot-Wire Near-Wall Corrections,'' Ph.D. thesis, Inst. Fluid Mech., Friedrich-Alexander University of Erlangen-Nuremberg, Shaker Verlag, Aachen.

[25] Collis, D. C., and Williams, M. J., 1959, ''Two-Dimensional Convection From Heated Wires at Low Reynolds Numbers,'' J. Fluid Mech., **6**, pp. 357–384.

[26] Illingworth, C. R., 1963, ''Flow at small Reynolds number,'' In *Laminar Boundary Layers*, L. Rosenhead, ed., Oxford, Clarendon Press, p. 197.

[27] Wood, W. W., 1968, ''Calculation for Anemometry With Fine Hot Wires,'' J. Fluid Mech., **32**, pp. 9–19.

[28] Hieber, C. A., and Gebhart, B., 1968, ''Low Reynolds Number Heat Transfer From a Circular Cylinder,'' J. Fluid Mech., **32**, pp. 21–28.

[29] Nakai, S., and Okazaki, T., 1975, ''Heat Transfer From a Horizontal Circular Wire at Small Reynolds and Grashof Numbers—II: Mixed Convection,'' Int. J. Heat Mass Transf., **18**, pp. 397–413.

[30] Dennis, S. C. R., Hudson, J. D., and Smith, N., 1968, ''Steady Laminar Forced Convection From a Circular Cylinder at Low Reynolds Numbers,'' Phys. Fluids, **11**, pp. 933–940.

[31] Rohsenow, W. M., 1973, *Handbook of Heat Transfer*, McGraw-Hill, New York.

[32] Wacker, D., 1985, ''Die numerische Lösung der Navier-Stokesschen Gleichungen für einen beheizten Zylinder in Wandnähe mit Berücksichtigung des Wärmeübergangs,'' Ph.D. thesis, Technische Universität Berlin.

Swirling Effect on Thermal-Fluid Transport Phenomena in a Strongly Heated Concentric Annulus

Shuichi Torii
e-mail: torii@mech.kagoshima-u.ac.jp
Associate Professor,
Mem. ASME
Department of Mechanical Engineering,
Kagoshima University,
1-21-40, Korimoto, Kagoshima 890-0065,
Japan

Wen-Jei Yang
e-mail: wjyang@engin.umich.edu
Professor,
Fellow ASME
Mechanical Engineering and Applied Mechanics,
University of Michigan,
Ann Arbor, Michigan 48109

A numerical study is performed to investigate thermal transport phenomena in circular Couette flow in a concentric annulus, in which an axially rotating inner cylinder and stationary outer cylinder are strongly heated under the same heat flux condition. The anisotropic $\overline{t^2}$-ε_t *heat-transfer model together with the anisotropic k-ε turbulence model is employed to determine thermal eddy diffusivity. When the inner cylinder is at rest, the turbulent kinetic energy and temperature variance substantially diminish over the whole annular cross-section along the flow, resulting in laminarization, i.e., a deterioration in heat-transfer performance at the inner and outer cylinder walls. In contrast, a substantial reduction in the turbulent kinetic energy and temperature variance in the laminarizing flow is suppressed in the presence of inner core rotation. In other words, inner core rotation contributes to the suppression of laminarization in a strongly heated gas flow. These characteristics in thermal fluid flow with temperature-dependent thermal property are summarized in the form of dimensionless heat flux parameter versus inlet Reynolds number with the Taylor number, as the parameter.* [DOI: 10.1115/1.1571086]

Keywords: *Annular Flow, Computational, Forced Convection, Heat Transfer, Turbulence*

Introduction

An effect of promoting the turbulent transport of heat and momentum by the centrifugal force occurs in a concentric annulus with an inner cylinder rotating around the axis, in which Taylor vortices appear [1–4]. Such swirl flow is referred to as circular Couette flow, which implies a flow with one surface rotating and the other stationary (or both surfaces rotating in the same direction at different angular velocities). However, little information is available on heat and fluid flow in a strongly heated annulus with a stationary outer surface and a rotating inner core. This reflects the difficulty in measuring turbulent quantities in strongly heated flows in a rotating annulus. Although numerical simulations can produce detailed information on transport phenomena, existing theoretical studies have suffered from assuming constant properties in the governing equations. Consequently, few useful results have been retrieved on thermal and fluid flow transport characteristics inside an intensely heated annulus with a rotating inner surface, though a coolant in rotating machinery, such as high-temperature gas mixing devices, is normally subjected to high flux heating.

Dalle Donne and Meerwald [5,6] measured local heat-transfer and friction coefficients in subsonic turbulent flow through annuli with large temperature differences between wall and coolant and obtained the corresponding experimental correlations. Nemira et al. [7] derived heat transfer correlation based on experimental data on local heat transfer coefficients from outer and inner cylinders of one-and both-side heated annuli to gas with variable physical thermal properties. Numerical analysis on heat and fluid flow transport phenomena in concentric annuli with a stationary inner surface under high heat flux heating were carried out by Torii et al. [8]. They disclosed that (i) when the gas flow is strongly heated with the same heat flux level at the inner and outer tube walls, the local heat transfer coefficients on both walls approach laminar values along the flow, that is, laminarization takes place; (ii) the existing criteria for laminarization in circular tube flows can be applied to annular flows as well if the occurrence of laminarization is estimated using a dimensionless heat flux parameter q_w^+; but (iii) annular flows heated strongly from only one side are less vulnerable to laminarization even if the usual criteria are satisfied. A similar study has been reported by Fujii et al. [9]. Recently, McEligot et al. [10] carried out an assessment of several turbulence models in internal gas flows under strong heating. They reported that a turbulence model capable of reproducing the correct near-wall limiting behavior of turbulent quantities is recommended to calculate strongly heated turbulent or laminarizing gas flows.

The present study treats the thermal and fluid flow transport phenomena in a concentric annulus, in which an axially rotating inner cylinder and an stationary outer cylinder are heated under uniform high heat flux. In order to shed light on the mechanism of the transport phenomena, the anisotropic $\overline{t^2}$-ε_t heat transfer model of Torii and Yang [11] is employed in the analysis, because the model satisfies the requirement for near-wall limiting behavior. Turbulent thermal conductivity λ_t is determined using the temperature variance, $\overline{t^2}$, and the dissipation rate of temperature fluctuation, ε_t, together with the turbulent kinetic energy, k, and its dissipation rate, ε. Emphasis is placed on the effects of heat flux level and inner surface rotation on turbulent kinetic energy, temperature variance, turbulent heat flux, and velocity profiles. Note that no verification and validation of these results are performed here, because swirl introduces major flow-physical complications and there is simply no quantitative evidence, i.e., no experimental data as to the validation of the predictions.

Governing Equations and Numerical Scheme

Consider a forced flow through a concentric annulus consisting of a rotating inner cylinder and a stationary outer cylinder under a uniform high flux heating condition. The physical configuration

---

Contributed by the Heat Transfer Division for publication in the JOURNAL OF HEAT TRANSFER. Manuscript received by the Heat Transfer Division March 13, 2002; revision received February 5, 2003. Associate Editor: S. P. Vanka.

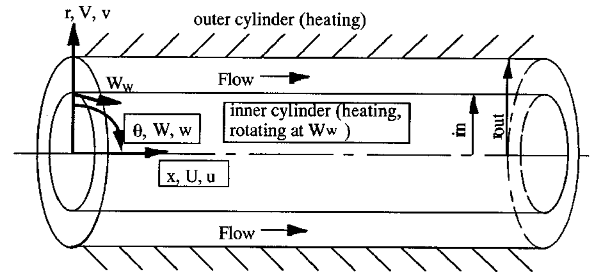

Fig. 1 A schematic of the physical system and coordinates

Table 1 Empirical constants and model functions used in the anisotropic $\overline{t^2}$-ε_t heat-transfer model

C_{P1}	1.20	C_{P2}	0.51	C_{P3}	0.52	C_s	0.11
f_{P1}	1.0	f_{P2}	1.0	f_{P3}	1.0	C_{st}	0.11
C_λ	0.078	B_λ	3.4	A_λ	35.6		
C_{d1}	2.0	C_{d2}	0.8	α_1	0.056	α_2	0.014
R_h	$(k/\nu)(k/\varepsilon)^{-1}(\overline{t^2}/\varepsilon_t)^2$						
f_{d1}	$1-\exp\left(-\sqrt{\frac{R_h}{10}}\right)$						
f_{d2}	$\left\{1-\exp\left(-\frac{y^+}{8}\right)\right\}^2$						
f_λ	$\left\{1-\exp\left(-\frac{y^+}{A_\lambda}\right)\right\}^2\left(1+\frac{B_\lambda}{R_h^{3/4}}\right)$						

and the cylindrical coordinate system are schematically shown in Fig. 1. In analyzing the strongly heated gas flow, dependence of the gas properties on temperature, as well as the change in gas density, needs to be taken into account [12]. Based on this idea, to predict the strongly heated circular pipe flow, Torii and Yang [13] employed the governing equations, which are taken temperature dependence of thermal properties into account. As for the similar analysis, Ezato et al. [14] assumed that the fluctuations of the thermal properties are sufficiently small than their mean values and neglected the terms including the fluctuations of the thermal properties. That is, the turbulent fluctuations of λ, μ, and c_p through temperature fluctuation are neglected. Since the buoyancy parameter $\mathrm{Gr}/\mathrm{Re}_{\mathrm{inlet}}^2$ is less than 0.1, forced convection dominates. Hence, the continuity, momentum, and energy equations for an incompressible fluid, with neglect of the buoyancy force, read as

Continuity Equation:

$$\frac{\partial \rho U_i}{\partial x_i}=0 \tag{1}$$

Momentum Equations:

$$\frac{\partial(\rho U_j U_i)}{\partial x_j}=\frac{\partial P}{\partial x_i}+\frac{\partial}{\partial x_j}\left[\mu\left(\frac{\partial U_i}{\partial x_j}+\frac{\partial U_j}{\partial x_i}\right)-\rho\overline{u_i u_j}\right] \tag{2}$$

Energy Equation:

$$\frac{\partial(c_p\rho U_i T)}{\partial x_i}=\frac{\partial}{\partial x_i}\left(\lambda\frac{\partial T}{\partial x_i}-c_p\rho\overline{u_i t}\right) \tag{3}$$

The turbulent heat flux $-c_p\rho\overline{u_i t}$ in Eq. (3) can be given by an anisotropic eddy-diffusivity representation [11] as:

$$\begin{aligned}-c_p\rho\overline{u_i t}=&\,C_\lambda f_\lambda c_p\rho k\left(\frac{k}{\varepsilon}\right)^{-1}\left(\frac{\overline{t^2}}{\varepsilon_t}\right)^2\frac{\partial T}{\partial x_i}\\&-f_\lambda c_p\rho k\left(\frac{k}{\varepsilon}\right)^{-2}\left(\frac{\overline{t^2}}{\varepsilon_t}\right)^4\left[\alpha_1\left(\frac{\partial U_i}{\partial x_j}+\frac{\partial U_j}{\partial x_i}\right)\right.\\&\left.+\alpha_2\left(\frac{\partial U_i}{\partial x_j}-\frac{\partial U_j}{\partial x_i}\right)\right]\frac{\partial T}{\partial x_j},\end{aligned} \tag{4}$$

where C_λ is a model constant and f_λ is a model function. The transport equations for $\overline{t^2}$ and ε_t in Eq. (4) are expressed in the tensor form as:

$$\frac{\partial(\rho U_j\overline{t^2})}{\partial x_j}=\frac{\partial}{\partial x_j}\left[\left(\frac{\lambda}{c_p}+C_s\frac{k}{\varepsilon}\rho\overline{u_i u_j}\right)\frac{\partial\overline{t^2}}{\partial x_j}\right]-2\rho\overline{u_j t}\frac{\partial T}{\partial x_j}-2\rho\varepsilon_t \tag{5}$$

and

$$\begin{aligned}\frac{\partial(\rho U_j\varepsilon_t)}{\partial x_j}=&\,\frac{\partial}{\partial x_j}\left[\left(\frac{\lambda}{c_p}+C_{st}\frac{k}{\varepsilon}\rho\overline{u_i u_j}\right)\frac{\partial\varepsilon_t}{\partial x_j}\right]-C_{p1}f_{p1}\rho\frac{\varepsilon_t}{\overline{t^2}}\overline{u_j t}\frac{\partial T}{\partial x_j}\\&-C_{p2}f_{p2}\rho\frac{\epsilon}{k}\overline{u_i u_j}\frac{\partial U}{\partial x_j}-C_{p3}f_{p3}\rho\frac{\varepsilon_t}{k}\overline{u_i u_j}\frac{\partial U}{\partial x_j}\\&-C_{d1}f_{d1}\rho\frac{\varepsilon_t^2}{\overline{t^2}}-C_{d2}f_{d2}\rho\frac{\varepsilon\varepsilon_t}{k},\end{aligned} \tag{6}$$

respectively. The empirical constants and model functions in Eqs. (4–6) are summarized in Table 1.

The Reynolds stress, $-\rho\overline{u_i u_j}$, in Eqs. (2), (5), and (6) is determined using the anisotropic eddy diffusivity representation [15]:

$$\begin{aligned}-\rho\overline{u_i u_j}=&-\frac{2}{3}\delta_{ij}\rho k-\mu_t\left(\frac{\partial U_i}{\partial x_j}+\frac{\partial U_j}{\partial x_i}\right)+\frac{k}{\varepsilon}\mu_t\\&\times\sum_{\beta=1}^{3}C_\beta\left(S_{\beta ij}-\frac{1}{3}S_{\beta pp}\delta_{ij}\right)+\frac{2}{3}\mu_t\frac{k}{\varepsilon}(-\delta_{ij}-\delta_{in}\delta_{jn}\\&+4\delta_{im}\delta_{jm})\left(\frac{\partial\sqrt{k}}{\partial x_n}\right)^2,\end{aligned} \tag{7}$$

where,

$$S_{1ij}=\frac{\partial U_i}{\partial x_\gamma}\frac{\partial U_j}{\partial x_\gamma}$$

$$S_{2ij}=\frac{1}{2}\left(\frac{\partial U_\gamma}{\partial x_i}\frac{\partial U_j}{\partial x_\gamma}+\frac{\partial U_\gamma}{\partial x_j}\frac{\partial U_i}{\partial x_\gamma}\right)$$

$$S_{3ij}=\frac{\partial U_\gamma}{\partial x_i}\frac{\partial U_\gamma}{\partial x_j}$$

Here, the turbulent viscosity μ_t can be expressed in terms of turbulent kinetic energy k and its dissipation rate ε, referred to as the Kolmogorov-Prandtl's relation [16]:

$$\mu_t=C_\mu f_\mu\rho\frac{k^2}{\varepsilon}. \tag{8}$$

C_μ and f_μ are a model constant and a model function, respectively. The turbulent quantities k and ε in Eqs. (4)–(7) are determined using equations [15] in Cartesian tensor form:

$$\frac{\partial(\rho U_j k)}{\partial x_j}=\frac{\partial}{\partial x_j}\left[\left(\mu+\frac{\mu_t}{\sigma_k}\right)\frac{\partial k}{\partial x_j}\right]-\rho\overline{u_i u_j}\frac{\partial U_i}{\partial x_j}-\rho\varepsilon \tag{9}$$

$$\begin{aligned}\frac{\partial(\rho U_j\varepsilon)}{\partial x_j}=&\,\frac{\partial}{\partial x_j}\left[\left(\mu+\frac{\mu_t}{\sigma_\varepsilon}\right)\frac{\partial\varepsilon}{\partial x_j}\right]-C_{\varepsilon 1}f_{\varepsilon 1}\rho\frac{\varepsilon}{k}\overline{u_i u_j}\frac{\partial U_i}{\partial x_j}\\&-C_{\varepsilon 2}f_{\varepsilon 2}\rho\frac{\varepsilon^2}{k}\end{aligned} \tag{10}$$

Table 2 Empirical constants and model functions in the anisotropic k-ε turbulence model

$C\mu$	σ_k	σ_ε	$C_{\varepsilon 1}$	$C_{\varepsilon 2}$	C_1	C_3
0.09	1.4	1.3	1.39	1.8	0.8	-0.15
f_μ	$\left(1+\frac{3.45}{\sqrt{Rt}}\right)\left\{1-\exp\left(-\frac{y^+}{70}\right)\right\}$					
$f_{\varepsilon 1}$	$1+0.25\exp\left(\frac{-Rt}{25}\right)$					
$f_{\varepsilon 2}$	$\left[1-\frac{2}{9}\exp\left\{-\left(\frac{Rt}{6}\right)^2\right\}\right]\left\{1-\exp\left(-\frac{y^+}{5}\right)\right\}^2$					

The empirical constants and model functions in Eqs. (8–10) are listed in Table 2. Notice that the original model function is slightly modified so as to simulate the transition from turbulent to laminar flows, whose modification process is described in reference [17].

A set of the governing equations is solved using the control-volume-based formulation of Patankar [18]. In this procedure, the domain is discretized by a series of control volumes, with each control volume containing a grid point. Each differential equation is expressed in an integral manner over the control volume, and profile approximations are made in each coordinate direction, leading to a system of algebraic equations that can be solved in an iterative manner. The SIMPLE (Semi-Implicit Method for Pressure-Linked Equations) algorithm is employed to couple the pressure and velocity fields [18]. A staggered grid is considered such that the velocity components are located at the control volume faces, whereas pressure and temperature are located at the centers of control volumes to avoid the velocity-pressure decoupling. A power law interpolation scheme is used to evaluate the values of variables at the control volume interfaces. The discretized equations are solved with a line-by-line and the TDMA (tridiagonal-matrix algorithm). The convergence criteria of the residuals of all equations are assumed to be less than 10^{-5} of total inflow rates. Since all turbulent quantities, as well as the time-averaged streamwise velocity, vary rapidly in the near-wall region, the size of nonuniform cross-stream grids is increased, with a geometric ratio from the wall toward the center region of the annulus. The maximum control volume size near the center regime is always kept at less than 3 percent of the hydrodynamic tube radius. In order to ensure the accuracy and validity of calculated results, at least two control volumes are positioned in the viscous sublayer, i.e., $y^+<5$. A length of 180 diameters is employed and their volumes in the streamwise direction are distributed uniformly. At each axial location, the thermal properties for each control volume are determined at the axial pressure and temperature, using a numerical code of reference [19]. This is because the effects of temperature on properties such as viscosity and thermal conductivity have to be taken into account.

A hydrodynamically fully-developed isothermal annular flow in the absence of the inner core rotation is assumed at the inlet location, i.e., at the onset of heating. The boundary conditions are no slip at the inner and outer wall surfaces for velocities and turbulent kinetic energy, except W and ε which are given by Ww and $\varepsilon=2\nu(\partial\sqrt{k}/\partial r)^2$, respectively. The thermal boundary condition is constant wall heat flux. As for $\overline{t^2}$ and ε_t, the wall boundary conditions are $\partial\overline{t^2}/\partial r=0$ and $\varepsilon_t=\partial^2(\overline{t^2}/2)/\partial r^2$. At the exit, the boundary conditions for the dependent variables are obtained by setting the first derivatives in the axial direction equal to zero, though its second partial derivative, for T, is zero. The above boundary condition at the exit is strictly valid only when the flow and temperature profiles are fully developed, because the computational domain is sufficiently large, as mentioned in the following.

The nondimensional heat flux parameter q_w^+ is employed to represent wall heat flux. It is defined [7] as

$$q_w^+=\frac{d_{\rm in}q_{\rm in}+d_{\rm out}q_{\rm out}}{(d_{\rm in}+d_{\rm out})(G_{\rm inlet}c_{p\rm inlet}T_{\rm inlet})}, \tag{11}$$

where $d_{\rm in}$ and $d_{\rm out}$ denote the inner and outer diameters of the annulus, respectively, and $q_{\rm in}$ and $q_{\rm out}$ correspond to their respective wall heat fluxes. For annular flows with a rotating inner surface, the axial and tangential flow fields are also governed by dimensionless parameters including radius ratio, r^*, inlet Reynolds number (i.e., Reynolds number at the onset of heating), $\mathrm{Re}_{\rm inlet}$, and Taylor number, Ta. $\mathrm{Re}_{\rm inlet}$ and Ta are defined as

$$\mathrm{Re}_{\rm inlet}=\frac{2u_m(r_{\rm out}-r_{\rm in})}{\nu}\quad\text{and}\quad \mathrm{Ta}=\frac{W_w(r_{\rm out}-r_{\rm in})}{\nu}\sqrt{\frac{r_{\rm out}-r_{\rm in}}{r_{\rm in}}} \tag{12}$$

The dimensionless parameters are $r^*=0.8$; $q_w^+<0.01$; $\mathrm{Re}_{\rm inlet}=8000-10000$; $\mathrm{Ta}=0\sim10000$; inlet gas (nitrogen) temperature $T_{\rm inlet}=173$ K. In calculation, maximum temperature of the fluid at the exit was about 1000 K.

Simulations with grids of various degrees of coarseness are conducted to determine the required resolution for grid-independent solutions. Throughout the numerical calculations, the number of control volumes is properly selected between 72 and 144 over the cross-section of the concentric annulus and the corresponding number in the streamwise direction is changed with 1000 and 2000. Consequently, the maximum relative error was estimated to be about 2% by comparing the solutions on regular and fine grids with twice the grid points in the streamwise direction, while there was only a slightly appreciable differences, 0.8%, between numerical results with different radial grid spacing. In the following figures, the predictions obtained at 72×1000 and 144×2000 are shown for the turbulent kinetic energy and the temperature variance.

In order to verify the turbulence model and to determine the reliability of the computer code, numerical predictions are compared with some existing experimental results in the isothermal flow field. The model is applied to the turbulent flow in an annulus in the presence of the axially rotating inner cylinder. Numerical results are obtained at a location of 220 times the tube diameter downstream from the inlet where the hydrodynamically fully-developed condition prevails. Figure 2 depicts the predicted time-averaged velocity profile. For comparison, the experimental data of Hirai et al. [3] at Re=10000 and $r^*=0.55$, for Ta=0 and 10000, are superimposed in Fig. 2. Here, Figs. 2(*a*) and (*b*) correspond to the streamwise and tangential distributions, respectively. The calculation result agrees with the experimental results. In Fig. 3, the calculated turbulent kinetic energy is compared with the experimental data of Brighton and Jones [20] at Re=46000, $r^*=0.56$, $T=0$. The predicted results are normalized by the square of the friction velocity on the outer wall, $(u^*_{\rm out})^2$. The turbulence model reproduces well the turbulent kinetic energy distribution over the whole cross-section of the annulus. The reliability of the computer code and the validity of the turbulence model are borne out through the above comparisons.

Results and Discussion

The effect of inner surface rotation on heat transfer performance in a strongly heated gas flow is illustrated in Fig. 4 for $\mathrm{Re}_{\rm inlet}=8000$ and $q_w^+=0.0041$ in the form of Nusselt number Nu versus Reynolds number Re, with Ta as the parameter. For comparison, the experimental data (at $q_w^+=0.00465$) of Torii et al. [8] are superimposed in Fig. 4 as open circles. Figures 4(*a*) and (*b*) refer to the performances of the inner and outer cylinder walls, respectively. $q_w^+=0.0041$ corresponds to the criterion for occurrence of flow laminarization in a stationary annulus with both the inner and outer tube walls [8] being strongly heated with the same

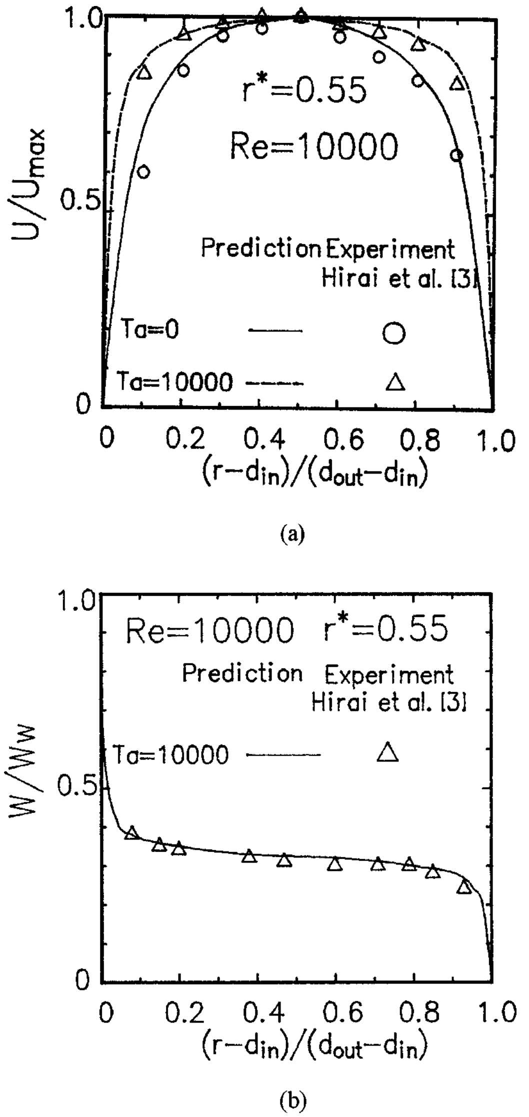

Fig. 2 Distribution of predicted time-averaged velocity in concentric annulus for Re=10000 and $r^*=0.55$: (*a*) streamwise velocity, and (*b*) tangential velocity

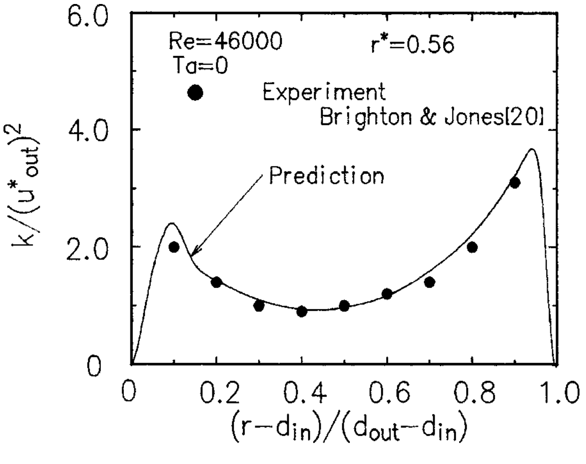

Fig. 3 Distribution of predicted turbulent kinetic energy in stationary concentric annulus for Re=46000, $r^*=0.56$

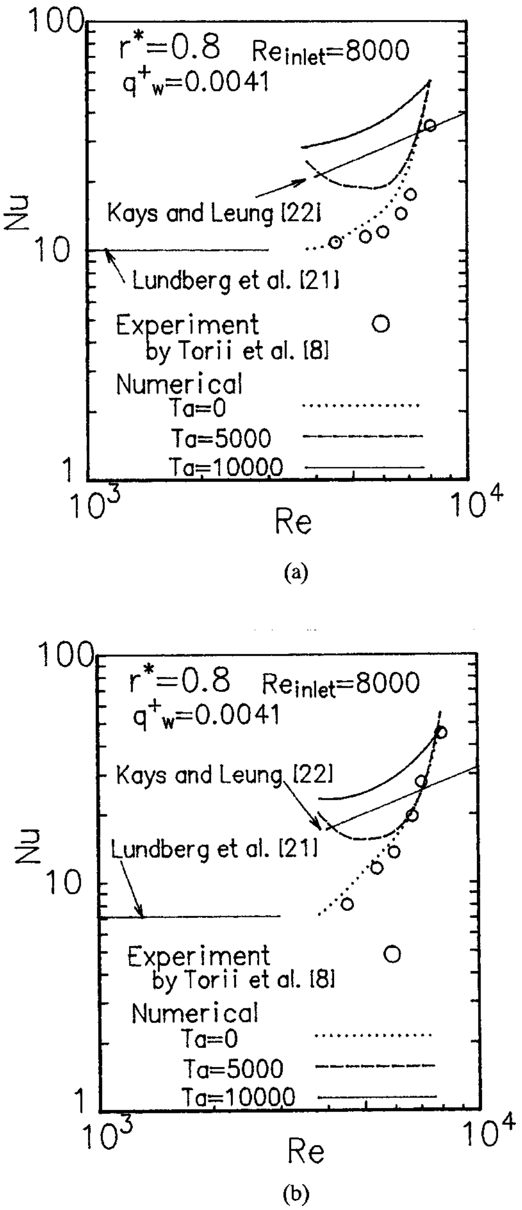

Fig. 4 Variations of local Nusslet number with Reynolds number Re as a function of Taylor number at $q_w^+=0.0041$ for (*a*) inner wall side and (*b*) outer wall side

heat flux under the condition of $\mathrm{Re}_{\mathrm{inlet}}=8000$. In Fig. 4, the two solid straight lines for defining the end of the laminar regime and the beginning of the turbulent one are the theoretical results for stationary concentric annuli obtained by Lundberg et al. [21] and Kays and Leung [22], respectively. Note that at a fixed $\mathrm{Re}_{\mathrm{inlet}}$, the heat transfer rates in the thermal and hydrodynamically fully-developed region are different at the inner and outer cylinder walls. A reduction in the Reynolds number in Fig. 4 signifies a change in the streamwise location, because the Reynolds number decreases with the axial distance, resulting from an increase in the molecular viscosity through heating. As for the experiment, the uncertainty in the heat transfer coefficients strongly depends on the accuracy of local heat flux and inner and outer cylinder wall temperatures. That is, each test section for outer cylinder was individually calibrated by determining the local electrical resistivity of the cylinder material and the local effective heat-exchange coefficient between the outer wall of the cylinder and the environment. The inside wall temperature of the out cylinder was calculated using measured outside wall temperature, in which the uncertainty was reduced by taking into account radial and axial conductions (including the effects of temperature-dependent thermal conductivity, electrical resistivity and the diameter of the outer cylinder) and radiation from the outside surface of the outer cylinder. The outside wall temperature of the inner cylinder was calculated using measured outside wall temperature, in which the uncertainty was reduced by taking into account radial and axial conductions in the same manner as the outer cylinder case. These effects were also taken into account to determine local heat flux. For $\mathrm{Ta}=0$ in Fig. 4, the Nusselt numbers at the inner and outer cylinder walls decrease first in the inlet region due to the thermal entrance effect, followed by an upturn, and finally approaching asymptotically the laminar correlation further downstream. The substantial reduction in Nu along the flow is attributed to the occurrence of laminarization. A substantial reduction of the heat transfer performance due to high heat flux heating is in good agreement with the experimental data, as seen in Fig. 4 and is also predicted by numerical analysis of Torii et al. [8] and Fujii et al. [9]. It is observed for that when the inner surface rotates axially at $\mathrm{Ta}=5000$, the Nusslet number does not approach the laminar correlation in the downstream region, but Nu in the entrance region departs from the turbulent correlation, as seen in Fig. 4. This implies that as the flow goes downstream, a significant reduction in the Nusselt number is suppressed by the presence of the inner surface rotation. When the fluid flow is imposed with a further increase in the inner surface rotation to $\mathrm{Ta}=10000$, heat transfer performance is amplified than the annular channel flow case at a constant thermal property, as observed in the circular Couette flow in the concentric annulus [4]. In other words, even with application of high heat flux at both the inner and outer cylinder surface walls, the presence of the inner cylinder surface rotation can suppress a deterioration of heat transfer performance in the annular flow, thus preventing an occurrence of the flow laminarization.

Additional numerical results are obtained at $q_w^+=0.0041$ and $\mathrm{Re}_{\mathrm{inlet}}=8000$ to determine the effect of inner surface rotation on the thermal flow fields, i.e., the turbulent kinetic energy, velocity, temperature variance, and turbulent heat flux. The distribution of turbulent kinetic energy in the annular flow is illustrated in Figs. 5(*a*) and (*b*) for $\mathrm{Ta}=0$ and 5000, respectively. The calculation is carried out for the grid sizes of 72×1000 and 144×2000. Here, the turbulent kinetic energy k is normalized by dividing it by a square of the outer cylinder-wall friction velocity at the onset of heating, $(u^*_{\mathrm{out}})^2_{\mathrm{inlet}}$ and the dimensionless distances of 0 and 1 in the abscissa correspond to the inner and outer cylinder side-walls, respectively. One observes that the similar profiles are predicted for two different grids. It is seen in Fig. 5(*a*) that the turbulent kinetic energy in the absence of inner surface rotation ($\mathrm{Ta}=0$) is substantially attenuated over the entire flow cross-section and eventually disappears downstream (for example, at $x/D=150$). This behavior is in accordance with the prediction by means of the k-ε turbulence model [8]. In contrast, one observes in Fig. 5(*b*) at $\mathrm{Ta}=5000$ that the inner surface rotation contributes to an enhancement of the turbulent kinetic energy in the vicinity of the rotating inner wall in the downstream region. This results in suppressing the reduction of turbulent kinetic energy on the outer cylinder wall side by rapid flow acceleration due to gas expansion, because of production of k on the inner cylinder wall side. The corresponding streamwise variation in the time-averaged velocity profile is depicted in Figs. 6(*a*) and (*b*) for $\mathrm{Ta}=0$ and 5000, respectively. The laminar flow profile is superimposed for comparison. The velocity is normalized using the maximum value at each respective relative velocity. It is observed in Fig. 6(*a*) that with a stationary inner surface, the velocity gradients at both side walls are substantially attenuated, forming a velocity profile for a laminar flow case. On the other hand, the substantial reduction in the velocity gradient near both side walls is suppressed in the presence of inner surface rotation, while the velocity profiles at different axial locations deviate from the laminar one, resulting in an increase in the velocity gradients at both side walls, as seen in Fig. 6(*b*). Furthermore, the inner core rotation causes the tangential velocity W, which is depicted in Fig. 7 and is normalized by the tangential velocity at the inner cylinder wall W_w. The tangential velocity at $\mathrm{Ta}=0$ is zero over the flow cross section. One observes that the tangential velocity W/W_w decreases steeply near the rotating inner cylinder but becomes almost flat until near the outer cylinder where it diminishes sharply to zero. It is found that even if the annular flow with a rotating inner surface is heated from both side walls at a heat flux high enough to cause laminarization of flow in a stationary annulus, the inner surface rotation induces an enhancement in the turbulent kinetic energy, particularly in the inner wall region, as shown in Fig. 5(*b*). This is because an increase in streamwise and tangential velocity gradients in the vicinity of the rotating wall contributes to the production of the turbulent kinetic energy in Eq. (9).

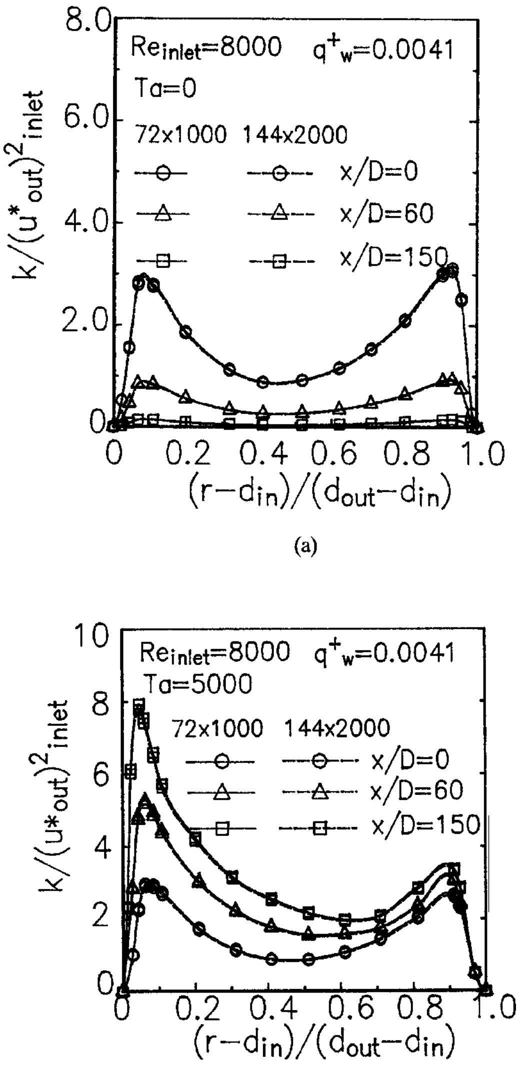

(a)

(b)

Fig. 5 Streamwise variation of turbulent kinetic energy profile in annular flows at Re=8000 and $q_w^+=0.0041$ for (*a*) stationary (Ta=0) and (*b*) rotating inner surface (Ta=5000)

Figures 8(*a*) and (*b*) show radial distributions of the temperature variance, $\overline{t^2}$, in the thermal field at different axial locations for $\mathrm{Ta}=0$ (the laminarization case) and 5000 (the nonlaminarization case), respectively. The calculation is carried out for the grid sizes of 72×1000 and 144×2000. Here the temperature variance is divided by the square of the local friction temperature at the

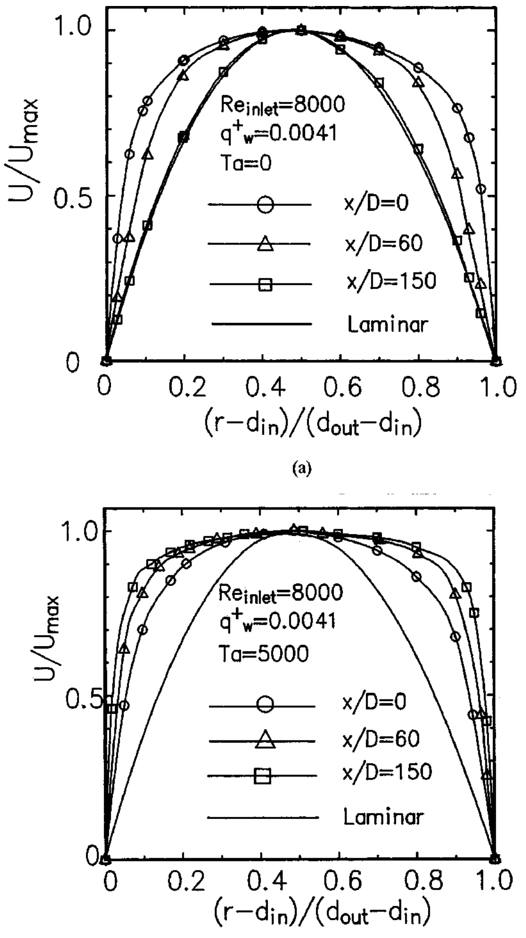

(a)

(b)

Fig. 6 Streamwise variation of time-averaged velocity profile in annular flows at Re=8000 and $q_w^+=0.0041$ for (*a*) stationary (Ta=0) and (*b*) rotating inner surface (Ta=5000)

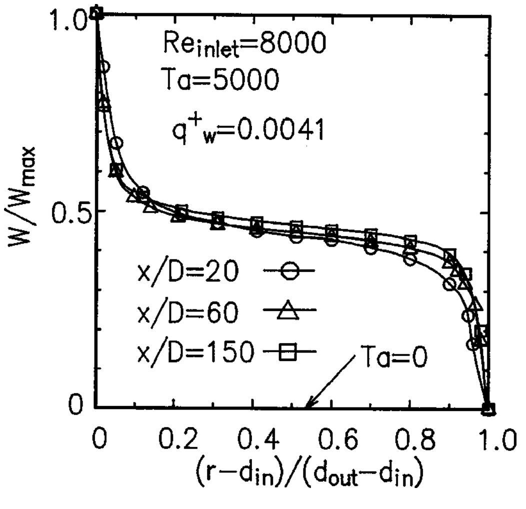

Fig. 7 Streamwise variation of tangential velocity profile in annular flow at Re=8000 and $q_w^+=0.0041$

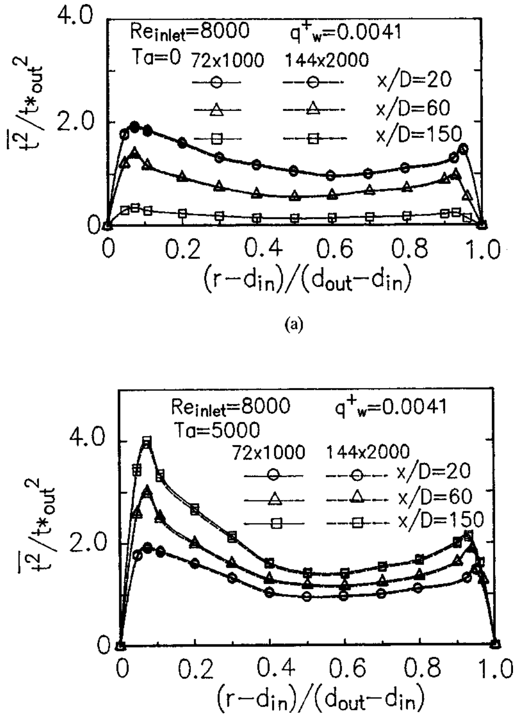

(a)

(b)

Fig. 8 Streamwise variation of temperature variance profile in annular flows at Re=8000 and $q_w^+=0.0041$ for (*a*) stationary (Ta=0) and (*b*) rotating inner surface (Ta=5000)

outer cylinder wall, t_{out}^*, to be in dimensionless form. It is seen that no substantial deterioration is detected for two different grids. In a laminarizing flow, it rapidly diminishes over the entire cross section along the flow, as seen in Fig. 8(*a*), signifying a fast deterioration of temperature fluctuations in the thermal field. A similar behavior appears in laminarizing flows through a pipe heated at a very high wall heat flux [13,23]. In contrast, Fig. 8(*b*) indicates that (i) when the inner surface rotates around the axis, attenuation in the temperature variance is suppressed near the inner and outer walls, and (ii) the temperature variance is intensified over the whole flow cross section in the flow direction, but a substantial amplification of the temperature variance yields at inner cylinder side. The streamwise change in turbulent heat flux profiles is depicted in Fig. 9. Here, the turbulent heat flux $-\overline{vt}$ is divided by the product of the friction temperature, t_{out}^*, and the friction velocity, u_{out}^*, on the stationary outer cylinder wall at each streamwise location. One observes that the normal turbulent heat flux level in the laminarizing flow, $-\overline{vt}$, is substantially reduced along the flow (Fig. 9(*a*)). In contrast, in the nonlaminarizing flow case (Fig. 9(*b*)), the normal turbulent heat flux near the rotating inner surface is followed by a substantial increase in the downstream region, while that near the outer cylinder wall is slightly increased. Meanwhile, the streamwise turbulent heat flux, $\overline{ut}$, is not presented here, since it has no direct effect on heat transfer. Since the eddy diffusivity concept in Eq. (4) is employed to determine the normal turbulent heat flux, $-c_p\bar{\rho}\overline{vt}$, in Eq. (3), turbulent heat flux is expressed using ε, $\overline{t^2}$, T, and ε_t, whose transport equations are directly related to k. Hence, reductions in the temperature variance and turbulent kinetic energy cause attenuation in the turbulent heat flux, resulting in the deterioration of heat transfer performance in a stationary annulus, as seen in Fig. 4. However, this trend is suppressed in the presence of inner surface rotation. It is found, therefore, that the occurrence of laminarization in the annular flow is affected by heat flux level and inner core rotation.

Next is to determine the criterion for the laminarization of flow in a concentric annulus heated under uniform wall heat flux from both cylinder sidewalls. First of all, conditions should be specified under which the flow is certainly laminarized. Torii and Yang [17] and Torii et al. [24] established the criterion for the laminarizing

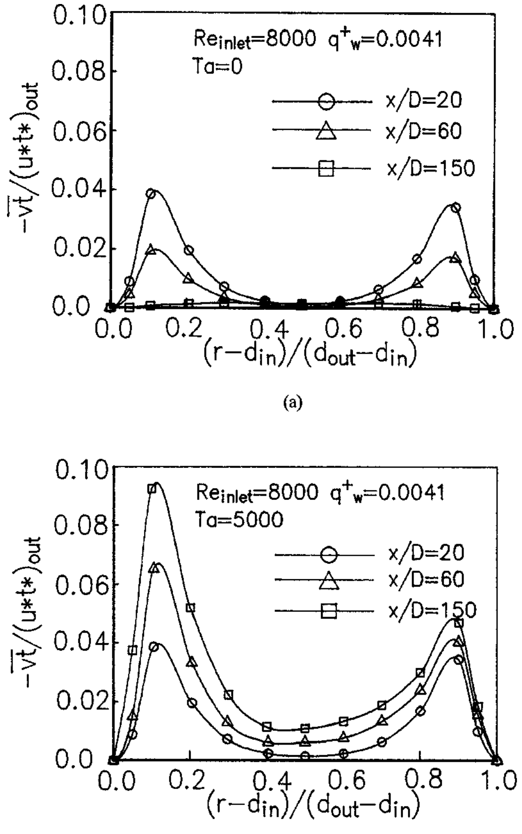

(a)

(b)

Fig. 9 Streamwise variation of turbulent heat flux profile in annular flows at Re=8000 and q^+_w=0.0041 for (*a*) stationary (Ta=0) and (*b*) rotating inner surface (Ta=5000)

flow in a tube and a two-dimensional channel with high heat flux using the k-ε and k-ε-$\overline{t^2}$-ε_t models, respectively. That is, laminarization occurs when the calculated turbulent kinetic energy at the location 150 diameters downstream from the inlet becomes lower than one-tenth of the inlet value. The same idea, in which the criterion is for the turbulent kinetic energy at $x/D=150$ to be lower than one-tenth of its inlet value, is adopted in the present study. This is because the streamwise variation of a turbulent kinetic energy in the laminarizing flow, as depicted in Fig. 5(*a*), is similar to that in the strongly heated tube case [24]. The predicted criterion is depicted in Fig. 10 in the form of inlet Reynolds number $\mathrm{Re}_{\mathrm{inlet}}$ versus nondimensional heat flux q_w^+ with the Taylor number, as the parameter, in which the predicted criterion for the annular tube flow [8] is superimposed for comparison. It is observed that the criterion in the nonrotation case is similar to that in the annular flow over a range of Reynolds numbers considered here, while it is increased with an increase in the Taylor number. One may thus conclude that if the inner core in the concentric annulus is rotated around the axis, the occurrence of laminarization is not predicted by the criteria in the annular flow in the absence of inner core rotation. In other words, when an annular flow with an axially rotating inner core is laminarized due to high flux heating, an extremely high heat flux must be imposed in the flow beyond the criterion for the laminarizing flow without the inner core rotation. This trend becomes larger in the lower Reynolds number region.

Summary

The anisotropic $\overline{t^2}$-ε_t heat transfer model has been employed to numerically investigate fluid flow and heat transfer in a strongly heated annular cylinder in the presence of inner surface rotation. Consideration was given to the influence of rotating speed on the thermal and flow fields. The study has concluded that:

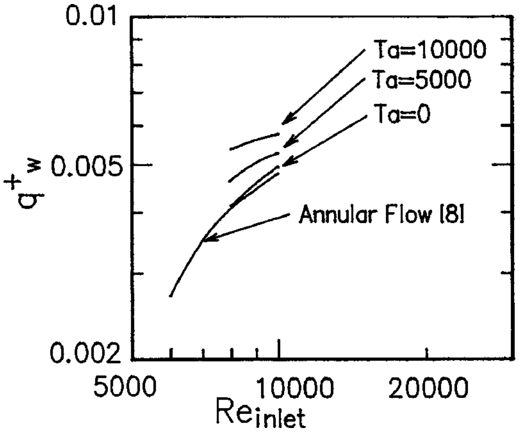

Fig. 10 A comparison of criteria for the occurrence of flow laminarization

1. With application of heating high enough to cause laminarization of the flow inside an annulus with a stationary inner surface, both surfaces cause a substantial reduction in local Nusselt number. The deterioration of heat transfer performance in the laminarizing flow is suppressed with an increase in the rotational speed.
2. When laminarization takes place, the velocity gradient in the vicinity of the rotating wall is diminished along the flow, resulting in a substantial attenuation in turbulent kinetic energy over the entire flow cross-section. In addition, both the temperature variance and turbulent heat flux are attenuated over the whole flow cross-section in the streamwise direction, causing deterioration in heat transfer performance.
3. In contrast, a substantial reduction in turbulent kinetic energy and temperature variance, which takes place in the laminarizing flow, is suppressed by inner surface rotation, resulting in suppression of the laminarization of flow process.
4. As the rotation speed of inner core in the annulus is increased, the criterion for the laminarizing flow is intensified. This trend becomes larger in the lower region of the inlet Reynolds number.

Nomenclature

c_p = specific heat under constant pressure, J/(kgK)
$C_\mu, C_1, C_3, C_{\varepsilon 1}, C_{\varepsilon 2}$ = turbulence model constants for velocity field
$C_\lambda, C_{p1}, C_{p2}, C_{p3}$ = turbulence model constants for temperature field
$C_s, C_{st}, C_{d1}, C_{d2}$ = turbulence model constants for temperature field
$d_{\mathrm{in}}, d_{\mathrm{out}}$ = inner and outer diameters of the annulus, respectively
D = hydraulic diameter of the annulus, $(d_{\mathrm{out}}-d_{\mathrm{in}})$, m
h = heat transfer coefficient, W/m^{2}K
$f_\mu, f_{\varepsilon 1}, f_{\varepsilon 2}$ = turbulence model functions for temperature field
$f_\lambda, f_{p1}, f_{p2}, f_{p3}, f_{d1}, f_{d2}$ = turbulence model functions for temperature field
g = gravitational acceleration, m/s^2
G = mass flux of gas flow, kg/(m^{2}s)
Gr = Grashof number, $g\beta q_w D^4/(\nu^2\lambda)$
k = turbulent kinetic energy, m^2/s^2

Nu = Nusselt number, hD/λ
P = time-averaged pressure, Pa
Pr = Prandtl number
q = heat flux, $\mathrm{W/m^2}$
q_w^+ = dimensionless heat flux parameter, Eq. (11)
Re = Reynolds number, DG/μ
$\mathrm{Re}_{\mathrm{inlet}}$ = inlet Reynolds number, Eq. (12)
R_t = turbulent Reynolds number, $k^2/(\varepsilon\nu)$
$R\tau$ = dimensionless distance, y^+
r = radial coordinate, m
r^* = radius ratio, $r_{\mathrm{in}}/r_{\mathrm{out}}$
$r_{\mathrm{in}}, r_{\mathrm{out}}$ = inner and outer radius of the annulus, respectively, m
T = time-averaged temperature, K
Ta = Taylor number, Eq. (12)
t = fluctuating temperature component, K
t^* = friction temperature, $qw/(\rho c_p u^*)$, K
$\overline{t^2}$ = temperature variance, K^2
U, V, W = time-averaged velocity components in axial, normal-wall, and tangential direction, respectively, m/s
U_i, u_i = time-averaged and fluctuating velocity components in the x_i directions, m/s
u_{inlet} = inlet velocity, m/s
u_m = mean velocity over channel cross section
u, v, w = fluctuating velocity components in axial, wall-normal and tangential directions, respectively, m/s
u^* = friction velocity, m/s
u^+ = dimensionless velocity, U/u^*
$\overline{-u_i u_j}$ = Reynolds stress, $\mathrm{m^2/s^2}$
$\overline{-u_i t}$ = turbulent heat flux, mK/s
W_w = tangential velocity at the inner cylinder wall, m/s
x = axial coordinate, m
x_i = coordinates, m
y = wall-normal coordinate, m
y^+ = dimensionless distance, $u^*\delta/\nu$

Greek Letters

α = thermal diffusivity, $\mathrm{m^2/s}$
α_1, α_2 = turbulence model constants for temperature field
ρ = density, $\mathrm{kg/m^3}$
δ = distance from wall, m
ε = turbulent energy dissipation rate, $\mathrm{m^2/s^3}$, $\varepsilon = \nu\overline{\partial_{u_i}/\partial_{x_j}\partial_{u_j}/\partial_{x_i}}$
ε_t = dissipation rate of temperature variance, $\mathrm{K^2/s}$, $\varepsilon_t = \alpha\overline{\partial t/\partial_{x_i}\partial t/\partial_{x_i}}$
λ, λ_t = molecular and turbulent thermal conductivities, respectively, W/(Km)
μ, μ_t = molecular and turbulent viscosities, respectively, Pa s
ν = fluid kinematic viscosity, $\mathrm{m^2/s}$
$\sigma_k, \sigma_\varepsilon, \sigma_h, \sigma_\phi$ = turbulence model constants for diffusion of k, ε, $\overline{t^2}$, and ε_t, respectively
θ = tangential direction

Subscripts

b = bulk
c = center or insulated wall
in = inner wall
inlet = inlet
max = maximum
out = outer wall
w = wall

Superscripts

= time-averaged value

References

[1] Kuzay, T. M., and Scott, C. J., 1975, "Turbulent Heat Transfer Studies in Annulus with Inner Cylinder Rotation," *Proceedings of the ASME Winter Annual Meeting*, 75-WA/HT-55, pp. 1–11.

[2] Kuzay, T. M., and Scott, C. J., 1976, "Turbulent Prandtl Numbers for Fully Developed Rotating Annular Axial Flow of Air," *Proceedings of the ASME-AIChE Heat Transfer Conference*, 76-HT-36, pp. 1–13.

[3] Hirai, S., Takagi, T., and Matumoto, M., 1997, "Prediction of the Laminarization Phenomena in Turbulent Swirling Flows," Trans. Jpn. Soc. Mech. Eng., **52**, pp. 1608–1616.

[4] Torii, S., and Yang, W.-J., 1994, "Numerical Study on Turbulent Couette Flow and Heat Transfer in Concentric Annuli," Numer. Heat Transfer, Part A, **26**, pp. 321–336.

[5] Dalle Donne, M., and Meerwald, E., 1966, "Experimental Local Heat-Transfer and Average Friction Coefficients for Subsonic Turbulent Flow of Air in an Annulus at High Temperatures," Int. J. Heat Mass Transf., **9**, pp. 1361–1376.

[6] Dalle Donne, M., and Meerwald, E., 1973, "Heat Transfer and Friction Coefficients for Turbulent Flow of Air in Smooth Annuli at High Temperatures," Int. J. Heat Mass Transf., **16**, pp. 787–809.

[7] Nemira, M. A., Vilemas, J. V., and Simonis, V. M., 1980, "Heat Transfer to Turbulent Flow of Gases with Various Physical Properties in Annuli (Correlation of Experimental Reuslts)," Heat Transfer-Sov. Res., **12**, pp. 104–112.

[8] Torii, S., Shimizu, A., Hasegawa, S., and Kusama, N., 1991, "Laminarization of Strongly Heated Annular Gas Flows," JSME Int. J., Ser. B, **34**(2), pp. 157–168.

[9] Fujii, S., Akino, N., Hishida, M., Kawamura, H., and Sanokawa, K., 1991, "Numerical Studies on Laminarization of Heated Turbulent Gas Flow in Annular Duct," J. Atomic Energy Soc. Jpn., (in Japanese), **33**(12), pp. 1180–1190.

[10] McEligot, D. M., Shehata A. M., and Kunugi, T., 1998, "Prediction of Strongly-Heated Internal Gas Flows," *Proc. 2nd International Conference in Turbulent Heat Transfer*, **I**, pp. 1–15.

[11] S. Torii, and W.-J. Yang, 1996, "A New Near-Wall Two-Equation Model for Turbulent Heat Transport," Numer. Heat Transfer, Part A, **29**, pp. 417–440.

[12] Schlichting, H., 1985, *Boundary Layer Theory*, 2nd ed., McGraw-Hill, New York.

[13] Torii, S., and Yang, W.-J., 1997, "Laminarization of Turbulent Gas Flows inside a Strongly Heated Tube," Int. J. Heat Mass Transf., **40**(13), pp. 3105–3118.

[14] Ezato, K., Shehata, A. M., Kunugi, T., and McEligot, D. M., 1999, "Numerical Prediction of Transitional Features of Turbulent Forced Gas Flows in Circular Tubes with Strongly Heating," J. Heat Transfer, **121**, pp. 546–555.

[15] Myong, H. K., and Kasagi, N., 1990, "A New Approach to the Improvement of *k-ε* Turbulence Model for Wall-Bounded Shear Flows," JSME Int. J., Ser. B, **33**(1), pp. 63–72.

[16] Rodi, W., 1982, "Examples of Turbulence Models for Incompressible Flows," AIAA J., **20**, pp. 872–879.

[17] Torii, S., and Yang, W.-J., 2000, "Thermal-Fluid Transport Phenomena in Strongly Heated Channel Flows," Int. J. Numer. Methods Heat Fluid Flow, **10**, pp. 802–823.

[18] Patankar, S. V., 1980, *Numerical Heat Transfer and Fluid Flow*, Hemisphere Pub., New York.

[19] Propath Group, 1987, "Propath: a Program Package for Thermophysical Property," Version 4.1, Propath Group, http://www.rccm.co.jp./seihin/propath/

[20] Brighton, J. A., and Jones, J. B., 1964, "Fully Developed Turbulent Flow in Annuli," Trans. ASME, D, pp. 835–844.

[21] Lundberg, R. E., McCuen, P. A., and Reynolds, W. C., 1963, "Heat Transfer in Annular Passages: Hydrodynamically Developed Laminar Flow with Arbitrarily Prescribed Wall Temperatures or Heat Fluxes," Int. J. Heat Mass Transf., **6**, pp. 495–529.

[22] Kays, W. M., and Leung, E. Y., 1963, "Heat Transfer in Annular Passages: Hydrodynamically Developed Turbulent Flow with Arbitrarily Prescribed Heat Flux," Int. J. Heat Mass Transf., **6**, pp. 537–557.

[23] Ogawa, M., Kawamura, H., Takizuka, T., and Akino, H., 1982, "Experiment on Laminarization of Strongly Heated Gas Flow in Vertical Circular Tube," J. Atomic Energy Soc. Jpn., (in Japanese) **24**, pp. 60–67.

[24] Torii, S., Shimizu, A., Hasegawa, S., and Higasa, M., 1990, "Laminarization of Strongly Heated Gas Flows in a Circular Tube (Numerical Analysis by Means of a Modified $k-\varepsilon$ Model)," JSME Int. J., Ser. B, **33**(3), pp. 538–547.

Spatial and Temporal Stabilities of Flow in a Natural Circulation Loop: Influences of Thermal Boundary Condition

Y. Y. Jiang

M. Shoji

Department of Mechanical Engineering,
School of Engineering,
The University of Tokyo,
7-3-1 Hongo, Bunkyo-ku, Tokyo 113-8656,
Japan

In a natural circular loop, the thermal convection demonstrates various spatial patterns and temporal instabilities. Problem consists in determining them with respects to thermal boundary conditions. To this end a multiple scales analysis is applied which resembles the inherent characteristic of the pattern formation in the Rayleigh-Bénard convection. A three-dimensional nonlinear model is proposed by incorporating the flow modes derived along the analysis. The differences of thermal boundary condition are reflected by a coefficient δ. For small δ, numerical solution to the model shows that only temporal instability exists and Lorenz chaos is possible, otherwise, for large values both spatial and temporal instabilities occur leading to cellular flow and intermittency chaos. The model predicted some additional phenomena opening for experimental observation. It seems significant that this study proposes an algorithm for the control of flow stability and distribution by varying the thermal boundary condition. [DOI: 10.1115/1.1571846]

Keywords: Enclosure Flows, Heat Transfer, Instability, Natural Convection, Nuclear, Thermosyphons

1 Introduction

Natural circulation loops have been widely studied in the last several decades, because of their applications in solar water systems, nuclear reactors and geothermal energy systems, etc. [1,2]. Another driving force for the wide studies has been its special situation in nonlinear dynamics, i.e., it is a typical pedagogical example of Lorenz chaos [3]. Figure 1 shows the schematic imagine of the simplest configuration of the loop, which is fabricated from a circular tube. The tube is heated from below and cooled from above. Thermal convection (Rayleigh-Bénard convection) occurs when buoyancy is accumulated large enough.

Engineering applications ask for stable operation state, but it is early noted that the instability may caused by dynamical reasons [4–6]. For example, in glass loops, of which the bottom half was wholly heated and the top one was wholly cooled, many observed the Lorenz chaos, i.e., a one-dimensional unstable flow with repetitive direction reversals between clockwise and anticlockwise [7–9]. The phenomenon is well described and hence named by the Lorenz model [8–10].

However the flow was found to be dependent on the thermal boundary condition (heating-cooling mode) and the tube wall property. Jiang et al. [11], as an instance, observed no unstable flow in a loop made of copper tube under the same boundary conditions as [7]. The reason is that the high thermal conductivity of the copper tube stabilized the flow. Wang et al. [12] and Yuen and Bau [13,14] etc. tried to shift the threshold point of the occurrence of the Lorenz flow by changing the heating-cooling modes and obtained satisfactory results in their experiments.

In some other experiments, it is found that the boundary conditions can even change the flow structure. Sano [15] built a glass loop; unlike the aforementioned experiments, his loop was only heated in the bottom quarter and cooled in the top one. As a result, he observed a three-dimensional cellular flow structure instead of the one-dimensional flow. At larger heating powers, the cellular flow bifurcates into intermittency chaos, i.e., a three-dimensional unstable flow stemming from the intermittent period locking of local flow modes. Sano suggested that his heating-cooling mode avoids sharp changes of tube wall temperature. This condition seems particularly important for generating three-dimensional flow because the transverse velocity components, originated by local temperature disturbance, could develop into global three-dimensional structures unaffectedly, otherwise, the heated and cooled fluid elements are likely to collide head-on keeping the flow one-dimensional.

Since the thermal boundary condition (or say the heating-cooling mode) originates such important discrepancies on flow structure and temporal stabilities, it is significant to formulate theoretically the effects; this makes the topic of our study. The effects have not been well modeled partially due to the methodology reasons, i.e., it is challenging to determine the real flow structure with respect to a specific boundary condition. In fact, the usual way is to obtain a model from the original governing equations by assuming a priori the flow pattern. In [8–14] the Lorenz model was found with a presumption of one-dimensional Poiseuille flow. Sano [16] proposed a three-dimensional model in a similar way. He assumed that the flow is three-dimensional at first and then selected, according to his experimental observation, flow modes to composite the cellular flow. However, both experimental observation and numerical simulation [17–19] found that the four flow modes also prevail, more or less, in a loop demonstrating one-dimensional Lorenz chaos. That is, in this usual way no matter what should be the real flow, we could arrive at as many fictional flow patterns and instabilities as we want. It is also difficult to say how many modes are enough to describe a real flow and whether other kinds of flow mode appear at a boundary condition different from the above ones. Therefore, it is necessary to find a theoretical method to predict the real flow structure for a given thermal boundary condition instead of experimental observation or numerical simulation.

This difficulty is overcome by a Multiple Scales Analysis [20]. The method was originally developed to analyze the critical behavior of the non-equilibrium phase transition [21–23] (in [21], it

---

Contributed by the Heat Transfer Division for publication in the JOURNAL OF HEAT TRANSFER. Manuscript received by the Heat Transfer Division April 29, 2002; revision received March 5, 2003. Associate Editor: H. Bau.

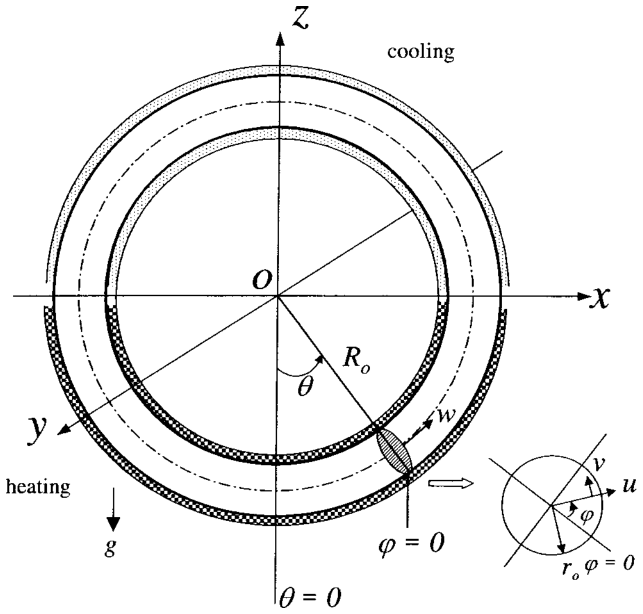

Fig. 1 Schematic configuration of a natural circulation loop and its coordinate system (r,φ,θ)

is called as synergetic analysis), which resembles the common perturbation analysis. As well known, Rayleigh-Bénard convection (RBC in brief) is also a typical non-equilibrium phase transition; the resultant flow pattern (called as dissipative structure [24]) is produced in a process of 'forming structure through fluctuation', i.e., it is a result of the competition and self-organization between the fluctuations of many scales in the fluid. The method, among other similar ones, is a way to demonstrate this process mathematically. Around the threshold point of the phase transition, variables are expanded with respect to a control parameter (e.g., the excess Rayleigh number $\mathrm{Ra}-\mathrm{Ra}_0$ in RBC); each order corresponds to a fluctuation in that scale. Time is also divided into fast and slow scales. The fast and slow fluctuations can be separated via the multiple scales analysis [25–28] or the use of mode projection techniques [22]. From particular microscopic equations, this analysis derives a macro equation for finite amplitude of flow field perturbations, which represents the final dissipative structure. The method has an additional advantage that the insignificant fluctuations in smaller scales are automatically neglected.

In a comprehensive review, Cross and Hohenberg [20] classified the stability problems of nonlinear systems into three types, i.e., Type I_s of a spatial instability, Type III_o of a temporal instability and Type I_o of both. The loop system falls into the Type I_o system where both the spatial and temporal behaviors of the flow are concerned. The following synergetic analysis includes five steps: (1) obtaining a solution for motionless state before the onset of convection; (2) getting the governing equations for the perturbed field about the motionless state; (3) around the threshold point of flow onset, casting the equations with respect to $\mathrm{Ra}-\mathrm{Ra}_0$ into a series of linear equations, each denotes a fluctuation in that scale; (4) solving the linear equations for flow modes possibly existent; (5) deriving an amplitude equation for the fluctuation in the basic scale, which determines the velocity of the convection slightly above the threshold point. The influences of thermal boundary condition are then discussed in Section 6 in a framework of a multi-dimensional model. The model integrates basic flow modes of the two categories derived above. The process of forming pattern is demonstrated by numerical data; as time goes on some modes survive to form the final structure and the others are damped off. This process depends highly on the thermal boundary condition.

2 Fundamental Equations

When we study the flow and heat transfer in the loop, it is by no means to propose a model or analysis applicable in whatever case. In this work the simplifying assumptions are that: (1) the torus radius is much larger than the pipe radius, that is, $R_0 \gg r_0$ (in most of the experiments $R=R_0/r_0\approx 33$), (2) the flow is a laminar Newtonian one and incompressible, (3) the fluid has constant properties (except for the use of the Boussinesq approximation for the density), (4) there are negligible Coriolis acceleration, centrifugal force and viscous dissipation, (5) the thermal boundary condition is symmetric about the central vertical axis and is independent of φ, (6) the tube wall has insignificant axial heat conduction and thermal expansion. These assumptions do not violate the actual conditions of the experiments in [[7–9,15], etc.]

The governing equations expressed in Cartesian coordinate in Fig. 1, are as follows,

$$\nabla\cdot\mathbf{v}^*=0 \tag{2.1a}$$

$$\rho_0\mathrm{D}\mathbf{v}^*/\mathrm{D}t^*=-\nabla p^*+\mu\nabla^2\mathbf{v}^*-\rho_0[1-\beta(T^*-T_0^*)]g\cdot\mathbf{e}_z \tag{2.1b}$$

$$\mathrm{D}T^*/\mathrm{D}t^*=a\nabla^2T^* \tag{2.1c}$$

Here we let $\rho=\rho_0[1-\beta(T^*-T_0^*)]$ in the gravity term and $\rho=\rho_0$ in the others in accordance with the Boussinesq approximation. $e_z(0,0,1)$ is the unit vector in vertical direction.

3 Solution for Motionless State

Before the occurrence of RBC, the fluid is in a motionless state (mentioned afterwards as $\mathbf{V}^{(0)}$), where energy is transported by heat conduction. Since $R_0/r_0 \gg 1$ and the thermal boundary condition is independent of φ, it is reasonable to average the temperature filed in (r,φ) plane by a bulk value $T_s^*(\theta)=\int_{r_0}^{0}\pi r^*T_s^*(r,\varphi,\theta)dr^*/\pi r_0^2$. Any boundary condition can be expressed as an axially distributed heat flux $q_{\mathrm{in}}(\theta)$, the governing equation for the bulk temperature $T_s^*(\theta)$ becomes,

$$\lambda_f\frac{\mathrm{d}^2T_s^*}{R_0^2\mathrm{d}\theta^2}=2q_{\mathrm{in}}/r^0 \tag{3.1}$$

Since the thermal boundary condition is symmetric about the vertical axis, we cast T_s^* into a Fourier series as,

$$T_s^*=T_{s,0}^*+\sum_{n=1}^{\infty}T_{s,n}^*\cos n\theta \tag{3.2}$$

We then derive the solution T_s^* by substituting the series for Eq. (3.1) and determining the expressions of $T_{s,n}^*$ for a specific boundary condition. As instances, we obtained the values of $T_{s,n}^*$ for the cases of [7–9,15]. In [9], the bottom half of the loop is heated at $T_w^*=T_h^*$ and the upper half is cooled at $T_w^*=T_c^*$ (referred as BC-TT). T_s^* reads,

$$\begin{aligned}T_s^*&=0.5(T_h^*+T_c^*)+\sum_{n=0}^{\infty}\frac{(-1)^nR^2\mathrm{Nu}(T_h^*-T_c^*)}{\pi(2n+1)[(2n+1)^2+R^2\mathrm{Nu}]}\\&\quad\times\cos(2n+1)\theta\\&\approx 0.5(T_h^*+T_c^*)+0.318(T_h^*-T_c^*)\cos\theta\quad\text{for } R\gg 1\end{aligned} \tag{3.3}$$

In the deduction h is supposed to be independent of θ. In [7,8] the bottom half is heated with uniform heat flux $q_{\mathrm{in}}=q_0$ and the upper half is cooled at $T_w^*=T_c^*$ (referred as BC-QT), T_s^* becomes,

$$T_s^* = (q_0/h + T_c^*) + \sum_{n=0}^{\infty} \frac{(-1)^n 4R^2 \mathrm{Nu} \cdot q_0/h}{\pi(2n+1)[(2n+1)^2 + R^2 \mathrm{Nu}]} \times \cos(2n+1)\theta$$
$$\approx (q_0/h + T_c^*) + 1.273(q_0/h)\cos\theta \quad \text{for } R \gg 1 \tag{3.4}$$

In Sano [15], the heating-cooling modes (referred as BC-Sano) were to form a uniform vertical temperature gradient in motionless state. That is,

$$T_s^* = 0.5(T_h^* + T_c^*) + 0.5(T_h^* - T_c^*)\cos\theta \tag{3.5}$$

This ideal condition is named a standard boundary condition, and those with non-zero high modes in Eq. (3.2) can be considered as deformations to it.

The consistent pressure field p_s^* is

$$p_s^* \approx p_0^* + R_0\rho_0 g \cos\theta - R_0\rho_0 g\beta \times \Delta T(1/3 \cos 2\theta + 1/24 \cos 4\theta - 3/8) \tag{3.6}$$

where ΔT equals $0.318(T_h^* - T_c^*)$ for BC-TT, $0.5(T_h^* - T_c^*)$ for BC-Sano and $1.273 q_0/h$ for BC-QT.

4 Expressions of the Perturbed Field About $\mathbf{V}^{(0)}$

The perturbation fields of $\mathbf{v}' = \mathbf{v}^* - 0$, $T' = T^* - T_s^*$ and $p' = p^* - p_s^*$ about $\mathbf{V}^{(0)}$ satisfy the following equations,

$$\nabla \cdot \mathbf{v}' = 0 \tag{4.1a}$$

$$\rho_0 \mathrm{D}\mathbf{v}'/\mathrm{D}t^* = -\nabla p' + \mu\nabla^2\mathbf{v}' + \rho_0 g\beta \cdot T' \cdot \mathbf{e}_z \tag{4.1b}$$

$$\mathrm{D}T'/\mathrm{D}t^* + \mathbf{v}' \cdot \nabla(T_s^* + T') = a\nabla^2 T' \tag{4.1c}$$

The boundary conditions are

$$\mathbf{v}' = T' = 0 \quad \text{at } r^* = r_0 \tag{4.2}$$

Introducing non-dimensional quantities,

$$r = r^*/r_0, \quad t = t^*/(r_0^2/a), \quad \mathbf{v} = \mathbf{v}'/(a/r_0),$$
$$T = T'/(\Delta T/R), \quad p = p'/(\rho_0 a^2/r_0^2) \tag{4.3}$$

Equations (4.1) and (4.2) are expressed in terms of the coordinated system (r,φ,θ) as follows (Keep in mind that $R \gg 1$ and hence small terms $O(R^{-1})$ are omitted.):

$$\frac{\partial u}{\partial r} + \frac{u}{r} + \frac{1}{r}\frac{\partial v}{\partial \varphi} + \frac{1}{R}\frac{\partial w}{\partial \theta} = 0 \tag{4.4a}$$

$$\frac{\partial u}{\partial t} + \mathbf{v} \cdot \nabla u - \frac{v^2}{r} - \frac{w^2 \cos\varphi}{R} = -\frac{\partial p}{\partial r} - \mathrm{RaPr}T \cos\varphi \cos\theta + \mathrm{Pr}\left(\nabla^2 u - \frac{u}{r^2} - \frac{2}{r^2}\frac{\partial v}{\partial \varphi}\right) \tag{4.4b}$$

$$\frac{\partial v}{\partial t} + \mathbf{v} \cdot \nabla v + \frac{uv}{r} + \frac{w^2 \sin\varphi}{R} = -\frac{\partial p}{r\partial \varphi} + \mathrm{RaPr}T \sin\varphi \cos\theta + \mathrm{Pr}\left(\nabla^2 v - \frac{v}{r^2} + \frac{2}{r^2}\frac{\partial u}{\partial \varphi}\right) \tag{4.4c}$$

$$\frac{\partial w}{\partial t} + \mathbf{v} \cdot \nabla w + \frac{w}{R}(u \cos\varphi - v \sin\varphi) = -\frac{\partial p}{R\partial \theta} + \mathrm{RaPr}T \sin\theta + \mathrm{Pr}\nabla^2 w \tag{4.4d}$$

$$\frac{\partial T}{\partial t} + \mathbf{v} \cdot \nabla T - w\left[\sin\theta + \sum_{n=2}^{\infty} C_n \sin n\theta\right] = \nabla^2 T \tag{4.4e}$$

$$T = u = v = w = 0 \quad \text{at } r = 1 \tag{4.5}$$

where

$$\mathbf{v} \cdot \nabla = u\frac{\partial}{\partial r} + v\frac{1}{r}\frac{\partial}{\partial \varphi} + w\frac{1}{R}\frac{\partial}{\partial \theta} \tag{4.6}$$

is the convection term,

$$\nabla^2 = \frac{\partial^2}{\partial r^2} + \frac{1}{r}\frac{\partial}{\partial r} + \frac{1}{r^2}\frac{\partial^2}{\partial \varphi^2} + O(R^{-2}) \tag{4.7}$$

is the Laplacian. The differences of thermal boundary condition are designated here by C_n; their values depend on T_s^*, or,

$$C_n = n \cdot T_{s,n}^*/\Delta T \tag{4.8}$$

For example, we have at $2n+1 \ll R$,

$$C_{2n} = 0, \quad C_{2n+1} = (-1)^n \frac{R^2 \mathrm{Nu}}{(2n+1)^2 + R^2 \mathrm{Nu}} \approx (-1)^n, \tag{4.9}$$

for BC-QT and BC-TT and

$$C_n = 0, \quad \text{at } n \geqslant 2 \tag{4.10}$$

for BC-Sano.

5 Multiple Scales Analysis of the Steady Flow

As mentioned in the introduction, the onset of Rayleigh-Bénard Convection at the critical Rayleigh number Ra_0 is a typical continuous phase transition. Theories and experiments [[8,15,29], etc.] have shown firstly that the flow velocity is proportional to $(\mathrm{Ra} - \mathrm{Ra}_0)^{0.5}$ near the threshold point Ra_0. In order to carry on the dynamical analysis, we expand $(\mathrm{Ra} - \mathrm{Ra}_0)$ as a power series in ε, or,

$$[(\mathrm{Ra} - \mathrm{Ra}_0)/\mathrm{Ra}_0] = \varepsilon^2 + \varepsilon^4 + \varepsilon^6 + \ldots, \quad \varepsilon \ll 1 \tag{5.1}$$

This expansion will be validated in Eq. 5.20 and the numerical data in Section 6.2 as well. Accordingly the dependent variables are expressed around their steady values as:

$$\Theta = \varepsilon\Theta^{(1)} + \varepsilon^2\Theta^{(2)} + \varepsilon^3\Theta^{(3)} + \ldots, \quad \Theta = (u,v,w,T,p) \tag{5.2}$$

where $\Theta^{(i)}$ denotes the fluctuations in different scales. And secondly at $\mathrm{Ra} = \mathrm{Ra}_0$ the linear problem is asymptotically time independent, i.e. the marginally stable mode survives and all other modes decay. Slow time dependence must be restored to eliminate secular terms and thereby extend the range of validity in time to times $t = O(\varepsilon^{-2})$. The time variable t must therefore be rescaled to timescale $\tau = \varepsilon^2 t$.

Substituting Eqs. (5.1) and (5.2) into the governing Eqs. (4.4) and (4.5), we decompose the resultant equations into separate groups with respect to the ε orders, which are simply expressed in the following form:

$$\mathbf{L}\mathbf{V}^{(i)} - \partial\mathbf{P}^{(i)} = \dot{\mathbf{V}}^{(i)} + \mathbf{N}(\mathbf{V},\mathbf{V})^{(i)} \quad i = 1,2,3,\ldots \tag{5.3}$$

Here $\mathbf{V} = [T,u,v,w]$ and $\partial\mathbf{P} = [0,\nabla p/\mathrm{Pr}]$ are four-dimensional vectors. $\mathbf{L}$ is a linear matrix operator. Before discussing the boundary condition effects, we make $C_n = 0$ for $n \geqslant 2$ to simply the analysis. The time derivatives $\dot{\mathbf{V}}^{(i)}$ are $\partial\mathbf{V}^{(i)}/\partial\tau$, which are zeros at order ε and ε^2, and $\dot{\mathbf{V}}^{(3)} = [\dot{T}, \dot{\mathbf{v}}/\mathrm{Pr}]$ at order ε^3. $\mathbf{N}(\mathbf{V},\mathbf{V})^{(i)}$ represent the nonlinear terms. The expressions of $\mathbf{L}$ and $\mathbf{N}(\mathbf{V},\mathbf{V})^{(i)}$ are listed in Appendix A.

5.1 Onset of Convection. In order to express the steady flow at $\mathrm{Ra} = \mathrm{Ra}_0$, we solve the linear equations

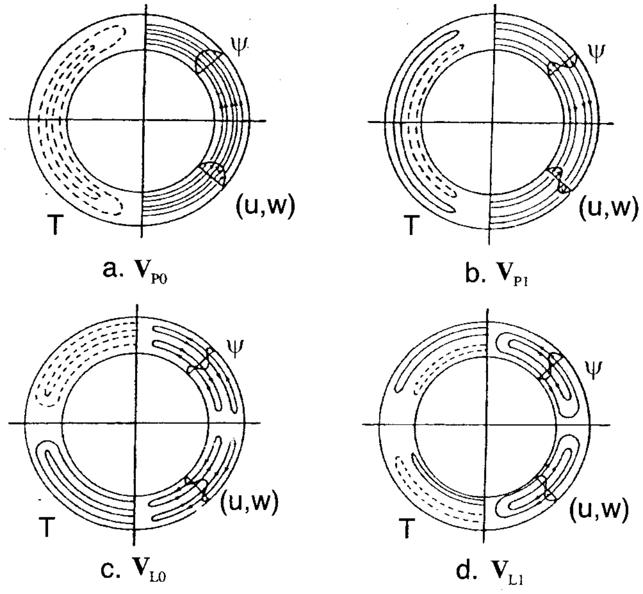

a. $\mathbf{V}_{\mathrm{P0}}$ b. $\mathbf{V}_{\mathrm{P1}}$

c. $\mathbf{V}_{\mathrm{L0}}$ d. $\mathbf{V}_{\mathrm{L1}}$

Fig. 2 Velocity and temperature fields of the basic flow; In each graph the right half shows streamlines ψ, and velocity components (u,w), while the left one shows isotherms (solid and broken lines correspond to positive and negative values, respectively)

$$\nabla\cdot\mathbf{v}^{(1)}=0 \tag{5.4a}$$

$$\mathbf{L}\mathbf{V}^{(1)}-\partial\mathbf{P}^{(1)}=0 \tag{5.4b}$$

to find a convective solution appearing at the lowest critical Ra number. On expanding all quantities in terms of the double Fourier series in φ and θ, the solution is found to be in a form of (see Appendix B for detail):

$$\mathbf{V}_{\mathrm{P0}}^{(1)}=\left[\sum_{n=0}^{\infty}T_{\mathrm{P0,2n+1}}^{(1)}\sin(2n+1)\theta,\right.$$
$$\left.\sum_{n=1}^{\infty}U_{\mathrm{P0,2n}}^{(1)}\sin 2n\theta,0,\sum_{n=0}^{\infty}W_{\mathrm{P0,2n}}^{(1)}\cos 2n\theta\right] \tag{5.5}$$

with a consistent pressure $\Sigma_{n=1}^{\infty}P_{\mathrm{P0,2n}}^{(1)}\sin 2n\theta$. We truncate, without losing the generality, the Fourier series as follows:

$$\mathbf{V}_{\mathrm{P0}}^{(1)}=[T_{\mathrm{P0,1}}^{(1)}\sin\theta,0,0,W_{\mathrm{P0,0}}^{(1)}] \tag{5.6}$$

with denotations of,

$$T_{\mathrm{P0,1}}^{(1)}=AJ_0(k_0r),\quad W_{\mathrm{P0,1}}^{(1)}=Ak_0^2J_0(k_0r) \tag{5.7}$$

where A is the amplitude of flow motion, $J_i(x)$ is the first kind Bessel function of order i, and k_i the first zero points of $J_i(x)$. The vector $\mathbf{V}_{\mathrm{P0}}^{(1)}$ describes a Poiseuille-like flow along the loop. Figure 2(a) shows its structure where positive A represents a flow in anti-clockwise. It corresponds to the A_∞ mode in Sano [16]. The stability analysis shows that a pitchfork bifurcation takes place at:

$$\mathrm{Ra}_0=k_0^4=33.445 \tag{5.8}$$

at which the $\mathbf{V}^{(0)}$ state gives way to $\mathbf{V}_{\mathrm{P0}}^{(1)}$. The value agrees well with the experimental results of Sano [15].

5.2 Fluctuations at High ε Orders. At $\mathrm{Ra}>\mathrm{Ra}_0$, the amplitude of the Poiseuille-like flow is really time dependent that is $A=A(\tau)$. According to the solution of $\mathbf{V}_{\mathrm{P0}}^{(1)}$, the nonlinear term $\mathbf{N}(\mathbf{V},\mathbf{V})^{(i)}$ gets the form of Eq. (A4). The solution of the nonhomogeneous equations,

$$\nabla\cdot\mathbf{v}^{(2)}=0 \tag{5.9a}$$

$$\mathbf{L}\mathbf{V}^{(2)}-\partial\mathbf{P}^{(2)}/\mathrm{Pr}=\mathbf{N}(\mathbf{V},\mathbf{V})^{(i)} \tag{5.9b}$$

is composed by a general solution and two coupling particular solutions, or

$$\mathbf{V}^{(2)}=\mathbf{V}_{\mathrm{P0}}^{(2)}+\mathbf{V}_{\mathrm{L0}}^{(2)}+\mathbf{V}_{\mathrm{L1}}^{(2)} \tag{5.10}$$

The general solution $\mathbf{V}_{\mathrm{P0}}^{(2)}$ is a Poiseuille flow at order ε^2, i.e., it has the same flow pattern as $\mathbf{V}_{\mathrm{P0}}^{(1)}$ but an amplitude an order smaller than $A(\tau)$. Following Eq. (A4), the particular solution $\mathbf{V}_{\mathrm{L0}}^{(2)}$ reads:

$$\mathbf{V}_{\mathrm{L0}}^{(2)}=[T_{\mathrm{L0,1}}^{(2)}\cos\theta,U_{\mathrm{L0,2}}^{(2)}\cos 2\theta,0,W_{\mathrm{L0,2}}^{(2)}\sin 2\theta] \tag{5.11}$$

with a conservation pressure $P_{\mathrm{L0,2}}^{(2)}\cos 2\theta$ (see Appendix C for detail). This solution corresponds to the flow mode S_{02} in [16]. The mode has 4 localized flow cells in the four quarters (see Fig. 2(c)); the circling of the fluid in each cell enhances local convective heat transfer between tube inner surface and main flow. The second particular solution $\mathbf{V}_{\mathrm{L1}}^{(2)}$ takes a form of:

$$\mathbf{V}_{\mathrm{L1}}^{(2)}=[T_{\mathrm{L1,1}}^{(2)}\cos\theta\cos\varphi,(U_{\mathrm{L1,0}}^{(2)}+U_{\mathrm{L1,2}}^{(2)}\cos 2\theta)\cos\varphi,$$
$$(V_{\mathrm{L1,0}}^{(2)}+V_{\mathrm{L1,2}}^{(2)}\cos 2\theta)\cos 2\theta\sin\varphi,W_{\mathrm{L1,2}}^{(2)}\sin 2\theta\cos\varphi] \tag{5.12}$$

with its conservation pressure $(P_{\mathrm{L1,0}}^{(2)}+P_{\mathrm{L1,2}}^{(2)}\cos 2\theta)\cos\varphi$ (see Eq. (C1)). This solution (see Fig. 2(d)) describes another kind of local flow cells in the 4 quarters that commonly observed by experiments [17,19] or predicted by numerical simulation [18] (they named it local flow re-circulations). The mode $\mathbf{V}_{\mathrm{L1}}^{(2)}$ corresponds to the S_{12} in Sano [16]. The two particular solutions $\mathbf{V}_{\mathrm{L0}}^{(2)}$ and $\mathbf{V}_{\mathrm{L1}}^{(2)}$ can be approximated by a power series of the radius r for the sake of the difficulty in obtaining their analytic expressions.

Similarly in the nonlinear equations,

$$\nabla\cdot\mathbf{v}^{(3)}=0 \tag{5.13a}$$

$$\mathbf{L}\mathbf{V}^{(3)}-\partial\mathbf{P}^{(3)}/\mathrm{Pr}=\mathbf{N}(\mathbf{V},\mathbf{V})^{(i)} \tag{5.13b}$$

at order ε^3. According to the solutions of $\mathbf{V}^{(1)}$ and $\mathbf{V}^{(2)}$, **?**$(\mathbf{V},\mathbf{V})^{(3)}$ is expressed in Eq. (A6), where the expressions of functions d_i and e_i were omitted because they have nothing to do with the following contents. The time derivative becomes,

$$\dot{\mathbf{V}}^{(3)}=[0.346\dot{A}(\tau)J_0(k_0r)\sin\theta,0,0,\dot{A}(\tau)(k_0r)\mathrm{Pr}^{-1}J_0] \tag{5.14}$$

Although we are not bothered to solve $\mathbf{V}^{(3)}$, its form is of interest, which is,

$$\mathbf{V}^{(3)}=\mathbf{V}_{\mathrm{P0}}^{(3)}+\mathbf{V}_{\mathrm{L0}}^{(3)}+\mathbf{V}_{\mathrm{L1}}^{(3)}+\hat{\mathbf{V}}_{\mathrm{P0}}^{(3)}+\mathbf{V}_{\mathrm{P1}}^{(3)}+\mathbf{V}_{\mathrm{P2}}^{(3)} \tag{5.15}$$

$\mathbf{V}_{\mathrm{P0}}^{(3)}$ is the general solution. $\mathbf{V}_{\mathrm{L0}}^{(3)}$ and $\mathbf{V}_{\mathrm{L1}}^{(3)}$ are two particular solutions stemming from e_i. The modes $\hat{\mathbf{V}}_{\mathrm{P0}}^{(3)}$, $\mathbf{V}_{\mathrm{P1}}^{(3)}$ and $\mathbf{V}_{\mathrm{P2}}^{(3)}$ originate from d_i; they represent different Poiseuille-type flows. Among them $\hat{\mathbf{V}}_{\mathrm{P0}}^{(3)}$ is really in the form of $\mathbf{V}_{\mathrm{P0}}^{(3)}$, but we write them separately to avoid confusion because $\hat{\mathbf{V}}_{\mathrm{P0}}^{(3)}$ is a particular solution different from $\mathbf{V}_{\mathrm{P0}}^{(3)}$. $\mathbf{V}_{\mathrm{P1}}^{(3)}$ describes an anti-parallel Poiseuille-type flow shown in Fig. 2(b).

5.3 Amplitude Equation for $\mathbf{V}_{\mathrm{P0}}^{(1)}$. It turns out that $\mathbf{V}_{\mathrm{P0}}^{(1)}$, the flow at order ε, must satisfy a solvability condition if the nonlinear Eqs. (5.13) are solvable, i.e., the Fredholm theorem [20] states that the vector of the right hand side of Eqs. (5.13) must be orthogonal to the zero eigenvector $\mathbf{V}_{\mathrm{P0}}^{(1)}$. This is because

$$(\mathbf{V}_{\mathrm{P0}}^{(1)},\dot{\mathbf{V}}^{(3)}+\mathbf{N}(\mathbf{V},\mathbf{V})^{(i)})=(\mathbf{V}_{\mathrm{P0}}^{(1)},\mathbf{L}\mathbf{V}^{(3)})=(\mathbf{L}\mathbf{V}_{\mathrm{P0}}^{(1)},\mathbf{V}^{(3)})=0 \tag{5.16}$$

where for any two variables $\mathbf{V}_1$ and $\mathbf{V}_2$, the inner product $(\mathbf{V}_1,\mathbf{V}_2)$ is defined as

$$(\mathrm{Ra}T_1T_2+\mathbf{v}_1\cdot\mathbf{v}_2)_\Omega \tag{5.17}$$

with $(\ )_\Omega$ signifying an integration over the whole body. Equation (5.16) thus finally results in a solvability condition for the amplitude $A(t)=A(\tau/\varepsilon^2)$, that is,

$$\eta \mathrm{d}A/\mathrm{d}t=\varepsilon^2A-\xi\cdot A^3 \tag{5.18}$$

with

$$\eta=0.173(2+\mathrm{Pr}^{-1}),$$

$$\xi=(0.036\mathrm{Pr}^2+7.47\times10^{-4}\mathrm{Pr}-0.035)/(\mathrm{Pr}R)^2 \tag{5.19}$$

Equation (5.18) is the simplest amplitude equation (or say order-parameter equation) having the general form of those derived by [[24–27,30], etc.] for Rayleigh-Bénard convection.

Equation (5.18) resembles a Van der Pol oscillator. At $\varepsilon^2,\ \xi>0$, the oscillator drives the flow to the final state, reading

$$A=\pm|\varepsilon^2/\xi|^{0.5} \tag{5.20}$$

At this time the motionless state $\mathbf{V}^{(0)}$ gives way to the steady flow $\mathbf{V}^{(1)}_{\mathrm{P}0}$ through a pitchfork bifurcation. From Eq. (5.20) we see that the amplitude A is proportional to $(\mathrm{Ra}-\mathrm{Ra}_0)^{0.5}$ in the neighborhood of Ra_0. The result agrees with the experimental fact [8,15] and the common scaling law of the continuous phase transition.

The amplitude equation implies that this steady flow seems to be stable all along. But this is not true since the actions of the flow modes at higher ε orders become significant at large ε. As soon as the other flow modes were introduced, we will find afterward that further bifurcations occur on the flow structure and temporal stability. The routes of the bifurcations depend on the thermal boundary condition as well.

6 Modeling the Spatial and Temporal Stabilities

This section is devoted to model the influence of thermal boundary condition on flow distribution and temporal behavior. In Section 5 we derived two categories of flow mode. The first is signified as $\mathbf{V}_{\mathrm{P}m}$, $m=0,1,2,\ldots$ and summarized in Eq. (B4). The flow modes $\mathbf{V}^{(i)}_{\mathrm{P}0}$, $i=1,2,3$, and $\hat{\mathbf{V}}^{(3)}_{\mathrm{P}0}$, $\mathbf{V}^{(3)}_{\mathrm{P}1}$, $\mathbf{V}^{(3)}_{\mathrm{P}2}$ belong to this category, which signifies the parallel or anti-parallel global convections in the loop. The second is termed $\mathbf{V}_{\mathrm{L}m}$, $m=0,1,2,\ldots$ and generalized in Eq. (C1). The flow modes $\mathbf{V}^{(i)}_{\mathrm{L}0}$ and $\mathbf{V}^{(i)}_{\mathrm{L}1}$, $i=2,3$ lie in this category, which represents quadruple flow cells. Furthermore, it is argued that only these two kinds of flow mode are possible for the present study because of two reasons. First, it is found that preserving more high θ modes of the series of $\mathbf{V}^{(1)}_{\mathrm{P}0}$ in Eq. (5.5) produces no new flow modes out of $\mathbf{V}_{\mathrm{P}m}$ and $\mathbf{V}_{\mathrm{L}m}$. Second, if we continue the similar deduction process in Section 5 to higher ε orders, we also find no new flow mode appearing. It seems reasonable to formulate the flow by incorporating these two categories of flow mode.

6.1 Model Formulation. To propose a qualitative model, we select the first two flow modes from each category and term them as $\mathbf{V}^{(1)}_{\mathrm{P}0}$, $\mathbf{V}^{(1)}_{\mathrm{L}0}$, $\mathbf{V}^{(1)}_{\mathrm{P}1}$, and $\mathbf{V}^{(1)}_{\mathrm{L}1}$. Their expressions and solutions are listed in Eqs. (B10–14) and (C12–15). Two points should be noted that firstly those four modes are solutions of the homogeneous Eqs. (5.4), as differs from the deductions of such as $\mathbf{V}^{(2)}_{\mathrm{L}0}$, $\mathbf{V}^{(2)}_{\mathrm{L}1}$ and $\mathbf{V}^{(3)}_{\mathrm{P}1}$; the later are particular solutions. And secondly, an important coefficient δ appears in the solutions of $\mathbf{V}^{(1)}_{\mathrm{L}0}$ and $\mathbf{V}^{(1)}_{\mathrm{L}1}$. The coefficient accounts for the boundary condition effects. From Eq. (C9) or (C10), we find its direct relation with C_n, i.e., simply,

$$\delta=(1-C_3) \tag{6.1}$$

It has been shown in Section 3 that the thermal boundary condition determines the axial distribution of fluid temperature at motionless state T^*_s. If we expand T^*_s in Fourier series (see Eq. (3.2)), the difference lies in the expressions at the high modes $T^*_{s,n}$, which is consequently reflected in Eq. (4.4e) by C_n. Since the boundary condition at $\delta=1$ (BC-Sano) is named standard, from the unit value the discrepancy of δ represents the irregularity of the axial distribution of T^*_s.

Since in unsteady flow, all the flow modes should be functions of time, a real flow pattern is expressed as,

$$\begin{aligned} w=&X(t)W^{(1)}_{\mathrm{P}0,0}+X_a(t)W^{(1)}_{\mathrm{L}0,2}\sin 2\theta+X_b(t)W^{(1)}_{\mathrm{L}1,2}\cos\varphi\sin 2\theta\\ &+X_c(t)W^{(1)}_{\mathrm{P}1,0}\cos\varphi \end{aligned} \tag{6.2a}$$

$$\begin{aligned} T=&Y(t)T^{(1)}_{\mathrm{P}0,1}\sin\theta+Z(t)T^{(1)}_{\mathrm{L}0,1}\cos\theta+Z_b(t)T^{(1)}_{\mathrm{L}1,1}\cos\varphi\cos\theta\\ &+Y_c(t)T^{(1)}_{\mathrm{P}1,1}\cos\varphi\sin\theta \end{aligned} \tag{6.2b}$$

$$u=X_a(t)U^{(1)}_{\mathrm{L}0,2}\cos 2\theta+X_b(t)U^{(1)}_{\mathrm{L}1,2}\cos\varphi\cos 2\theta \tag{6.2c}$$

$$v=X_b(t)V^{(1)}_{\mathrm{L}1,2}\sin\varphi\cos 2\theta \tag{6.2d}$$

$$p/\mathrm{Pr}=X_a(t)P^{(1)}_{\mathrm{L}0,2}\cos 2\theta+X_b(t)P^{(1)}_{\mathrm{L}1,2}\cos\varphi\cos 2\theta \tag{6.2e}$$

By substituting these expressions for Eqs. (4.4), and equating like terms, we have at $r=0.2$,

$$\dot{X}=-5.7832\mathrm{Pr}X+0.086458\mathrm{Pr}Y \tag{6.3a}$$

$$\dot{X}_a=-(15.265+20.291\mathrm{Pr})X_a+0.019666\delta\mathrm{Pr}Z \tag{6.3b}$$

$$\dot{X}_b=-14.682\mathrm{Pr}X_b+0.017028\delta\mathrm{Pr}Z_b \tag{6.3c}$$

$$\dot{X}_c=-14.682\mathrm{Pr}X_c+0.034055\mathrm{Pr}Y_c \tag{6.3d}$$

$$\begin{aligned} \dot{Y}=&5.7832(\mathrm{Ra}X-Y)+(7.9025\delta XZ-15.055X_aY\\ &+0.98507\delta X_cZ_b+12.641X_bY_c)/R \end{aligned} \tag{6.3f}$$

$$\begin{aligned} \dot{Y}_c=&14.682(\mathrm{Ra}X_c-Y_c)+(5.4535\delta XZ_b-33.883X_aY_c\\ &+20.062\delta X_cZ+8.7237\delta X_bZ_b-25.831X_bY)/R \end{aligned} \tag{6.3g}$$

$$\begin{aligned} \dot{Z}=&12.714(\mathrm{Ra}X_a-Z)+(-3.7635\delta^{-1}XY+11.841X_aZ\\ &-0.67980\delta^{-1}X_cY_c-8.7237X_bZ_b)/R \end{aligned} \tag{6.3h}$$

$$\begin{aligned} \dot{Z}_b=&14.682(\mathrm{Ra}X_b-Z_b)+(-5.4535\delta^{-1}XY_c+33.883X_aZ_b\\ &-13.845\delta^{-1}X_cY+61.536X_bZ)/R \end{aligned} \tag{6.3i}$$

For $\delta=1$ the model resembles the ELM8 model in [16] with a few differences. Equations (6.3) reduce to the Lorenz model when only the terms X, Y, and Z are retained:

$$\dot{X}=-\mathrm{Pr}X+\mathrm{Pr}Y,\quad \dot{Y}=(\mathrm{Ra}/\mathrm{Ra}_0)X-Y+XZ,\quad \dot{Z}=-bZ-XY \tag{6.4}$$

where b is a geometrical parameter.

6.2 Discussion on Numerical Results. We solved the model via a fourth-order Runge-Kutta method with a time step of $\Delta t=10^{-4}$. The following discussion was based on the results for $R=33$ and $\mathrm{Pr}=5$; the parameters agree approximately with those of the experiments in [7–9,15]. With increases in Rayleigh number Ra, the simulation predicted various flows as functions of the coefficient δ. Figure 3 summarizes the transitions of them, where each curve designates the border of the two neighboring flow states, which are fitted by the points numerically calculated. Although we only calculated the model at $\delta=0.01\sim1.5$, it is possible to get a solution at still larger values.

Regardless of the variation in δ, the thermal convection starts always at $\mathrm{Ra}_{\hat{0}}=66.89$. Note that we truncated $\mathbf{V}^{(1)}_{\mathrm{P}0}$ at the leading order of the Fourier series (see Eqs. (B8) and (B11)), which leads to a critical Rayleigh number twice as much as the theoretical one $\mathrm{Ra}_0=k_0^4$.

The convection is steady until further bifurcation occurs. In the steady flow, the relation $w\propto(\mathrm{Ra}-\mathrm{Ra}_{\hat{0}})^{0.5}$ predicted in Eq. (5.20)

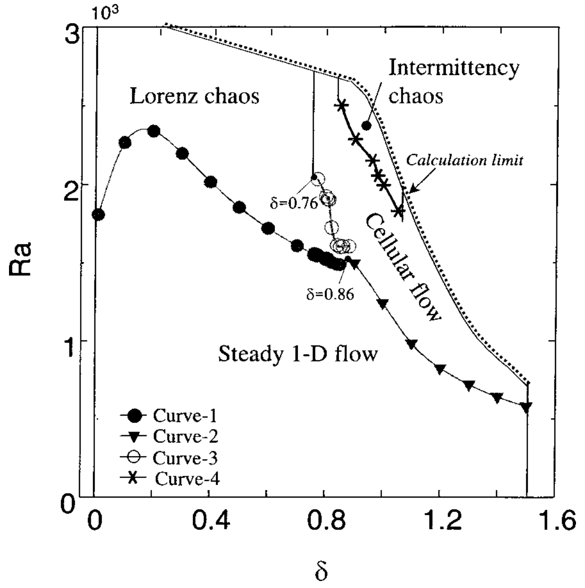

Fig. 3 Transitions of flow behavior as functions of δ and Ra. The curves are fitted by numerical data; each designates a margin of its two neighboring domains.

is well fitted up to Ra$\approx$300. The steady flow is always one-dimensional. All the steady flows are δ unrelated as well. Along converging to the steady state from a fictional original one, the decaying process of the perturbation is direct below Ra$\approx$105 and oscillatory above it. A supercritical Hopf bifurcation occurs at that point. In non-linear dynamics, the former steady state is a node and the later a focus. As instances, Fig. 4 shows the trajectories of the two convergence processes.

(1) Flow at Small δ. With increasing in Ra, the flow behavior continues to bifurcate in different routes at different δ. We discuss at first the case for small δ (δ=0$\sim$0.76), which is the condition of BC-TT and BC-QT.

Figure 5(a) shows, as a non-trivial instance, the transitions of flow with Rayleigh number for δ=0.5. The corresponding trajectory at each state is shown in Fig. 6. The damping process of perturbations to the flow changes again at Ra=925. Above it, Fig. 6a shows that the flow direction reverses once time before converging to the steady state. As a result, the final steady flow is in a direction opposite to the original. If Ra>1793, the flow reverses many times during the decaying process (see Fig. 6(b)). This resembles the transient Lorenz chaos that was experimentally observed by Gorman et al. [8].

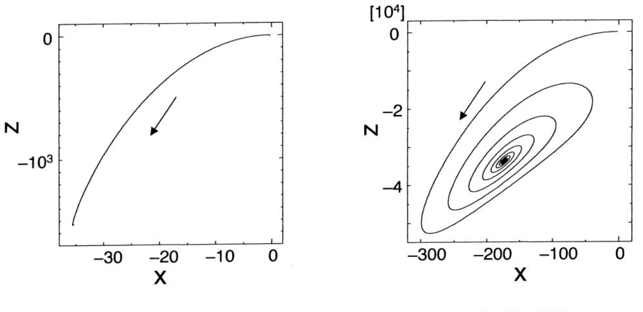

a. Ra=100

b. Ra=800

Fig. 4 Typical decaying processes of perturbation about the steady flow (a) toward a node (b) toward a focus

The convergence becomes slower and slower with increasing in the Rayleigh number until the occurrence of the second Hopf bifurcation at a threshold value $\mathrm{Ra}_c\approx$1850. This second Hopf is a subcritical (catastrophic) one, after which a perturbation to the flow begins to increase with time and makes the flow chaotic. Figure 6(c) shows the trajectory of x versus z in the chaotic flow, which has the typical butterfly structure of the Lorenz chaos. Figure 7(a) shows a return map plotted by the maxima of time series of z. In the map the fractional λ structure suggests that the flow behavior inherits from the characteristic of the Lorenz chaos. In fact, the Lorenz chaos was experimentally observed in loops under BC-QT and BC-TT. The critical Ra for the occurrence of Lorenz chaos depends on δ as well; the Curve-1 of Fig. 3 shows that a maximum exists at about δ=0.2. The Lorenz chaos is replaced by a multi-periodic flow at still larger Rayleigh number. Figure 6d shows the trajectory of the periodic flow for δ=0.5, which appears at Ra>2305. Its return map shown in Fig. 7(b) consists in four fixed points rather than the fractional structure.

It is also shown that in converged solutions the flow modes $\mathbf{V}_{\mathrm{P0}}^{(1)}$ and $\mathbf{V}_{\mathrm{L0}}^{(1)}$ survive while $\mathbf{V}_{\mathrm{P1}}^{(1)}$ and $\mathbf{V}_{\mathrm{L1}}^{(1)}$ are damped off. In other words the spatial bifurcation of the cross-sectional distribution (in (r,φ) plane) is prohibited. To summary the result for small δ, our model predicts no three-dimensional dimensional flow but a one-dimensional Lorenz chaos. The conclusion agrees with the experimental results in [7–9].

(2) Flow at Large δ. For δ>0.86 (see the Curve-2 in Fig. 3) the flow behavior bifurcates in a different route as Rayleigh number increases. We take a non-trivial example of the standard boundary condition of δ=1, for which the transitions of flow with increasing in Ra are shown in Fig. 5(b). Figure 8 shows typical result at every state.

This is the case of BC-Sano (δ=1). The aforementioned steady flow exists until Ra$\approx$1240. Above this value a periodic flow appears whose unique frequency is detected by the power spectrum, referred as f_1 (see Fig. 8(a)). The numerical data show that at this time the two flow modes $\mathbf{V}_{\mathrm{P1}}^{(1)}$ and $\mathbf{V}_{\mathrm{L1}}^{(1)}$ appear simultaneously making the flow structure no more one-dimensional. It is to say that the one-dimensional flow is replaced by a three-dimensional structure. This periodic flow is just the so-called cellular flow observed in [15]. The Curve-2 in Fig. 3 suggests that the cellular flow appears at smaller Ra for larger δ.

At Ra$\approx$1845 a Neimark bifurcation occurs in the orbit of the periodic flow, making the flow multi-periodic (see Fig. 8(b)) The Neimark bifurcation is a Hopf bifurcation for periodic orbit [31]. In a Poincare section, the trajectory of the orbit is a point before the Neimark and a circle after it. The secondary oscillation frequency f_2 appears in the multi-periodic flow. With further increase in the Rayleigh numbers, the oscillation of multi-periodic flow becomes complicated, but all its frequencies shown in the power spectrum can be interpreted of the combination of two frequencies f_1 and f_2 in the form $l_1 f_1 + l_2 f_2$ where l_1 and l_2 are integers. But at some particular values of Ra, frequency locking occurs and a quasi-periodic flow is predicted (Fig. 8(c)); in these cases some frequencies are no longer of $l_1 f_1 + l_2 f_2$.

At $\mathrm{Ra}_c\approx$2002 the spectrum becomes broad and the orbit chaotic (see Fig. 8(d)). We have mentioned that this is the intermittency chaos. The critical Ra for the occurrence of intermittency chaos is very sensitive to the value of δ (see Curve-4, Fig. 3). At large δ, the flow becomes chaotic at very small Ra. The model failed to predict Curve-4 for very large δ due to the divergence of the numerical calculation.

In summary, the three-dimensional cellular flow and intermittency chaos are possible for large δ. The conclusion agrees with the experimental results in [15]. As was mentioned in the introduction, the discrepancies between the flow in a loop at BC-QT or BC-TT and that at BC-Sano are due to an intuitional physical mechanism. In the former case, sharp changes of tube temperature are formed at both cooling-heating connections. They promote the

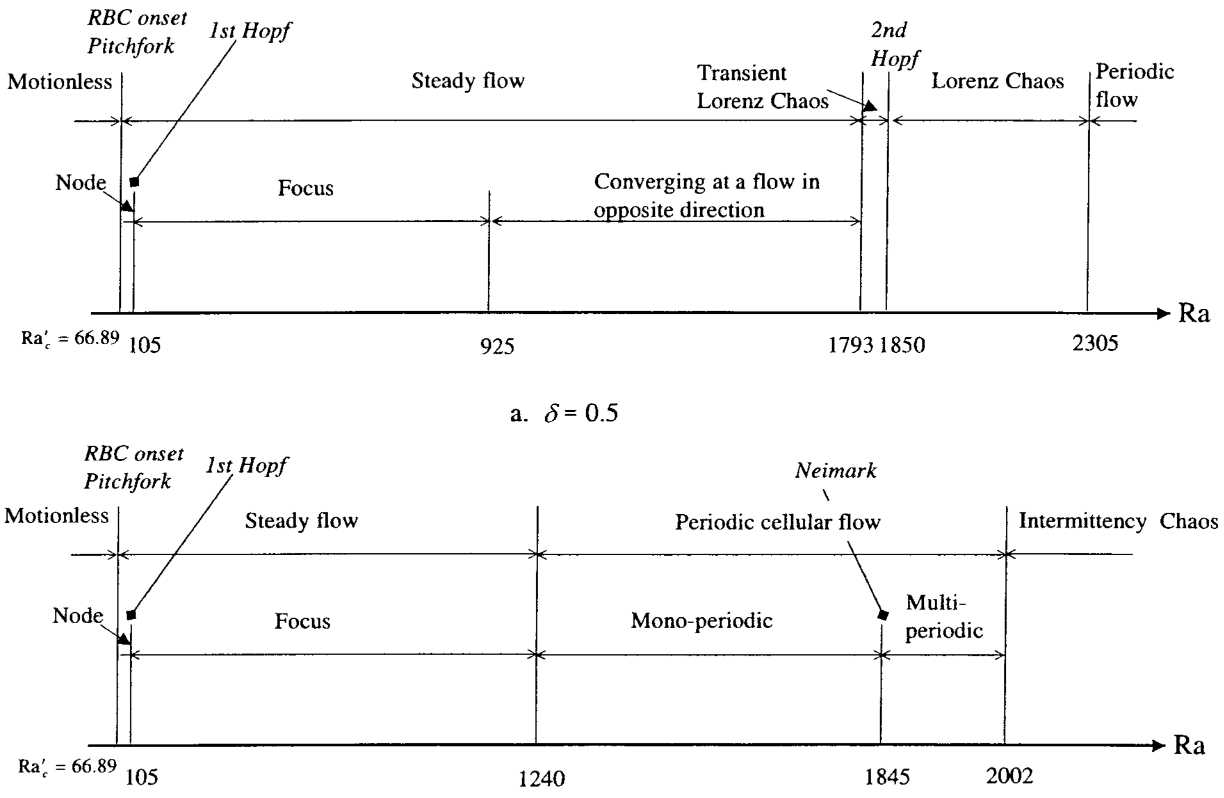

a. $\delta = 0.5$

b. $\delta = 1$

Fig. 5 Two typical bifurcation routes predicted the model

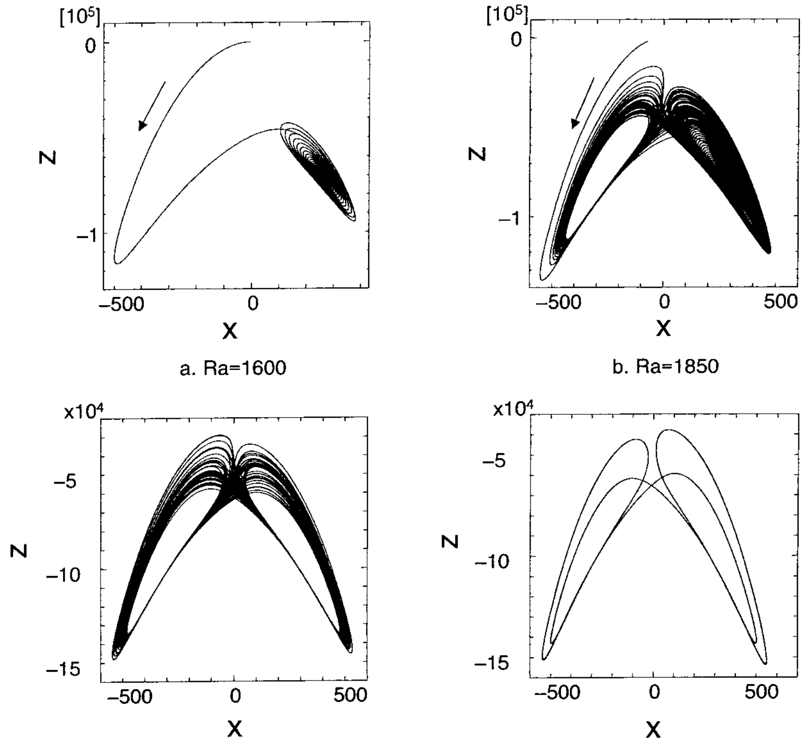

a. Ra=1600

b. Ra=1850

c. Ra=2200

d. Ra=2330

Fig. 6 Trajectories of the flow at different Rayleigh number for δ=0.5

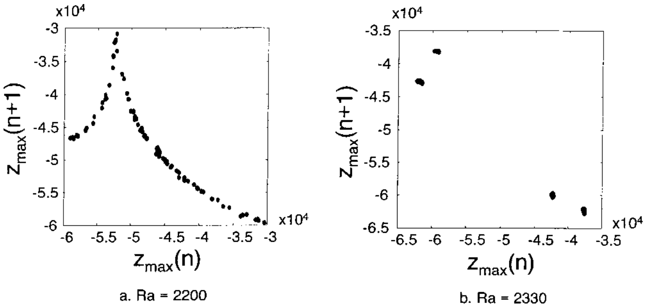

Fig. 7 Typical return maps of *z* in flows for δ=0.5: (a) Lorenz chaos, (b) periodic flow

intensive mixture of flow elements and hence prohibit the spatial bifurcation in the (r,φ) plane. Only in this case, the feasibility of one-dimensional formulation is ensured and the assumptions made by Yorke et al. [10] are reasonable. The later case is entirely opposite where the sharp changes of tube temperature are removed and the evolutions of the bi-directional flow and local flow cells are not influenced. In other words the presence of the high order modes of T_s^* affects the evolution of the spatial bifurcation in the flow.

(3) Transition From Lorenz Chaos to Cellular Periodic Flow. Figure 3 also shows another interesting transition, i.e., for δ=0.76~0.86 a transition from Lorenz chaos to cellular periodic flow occurs at Curve-3. Figure 9 shows a typical trajectory demonstrating this transition. As time goes on, the original one-

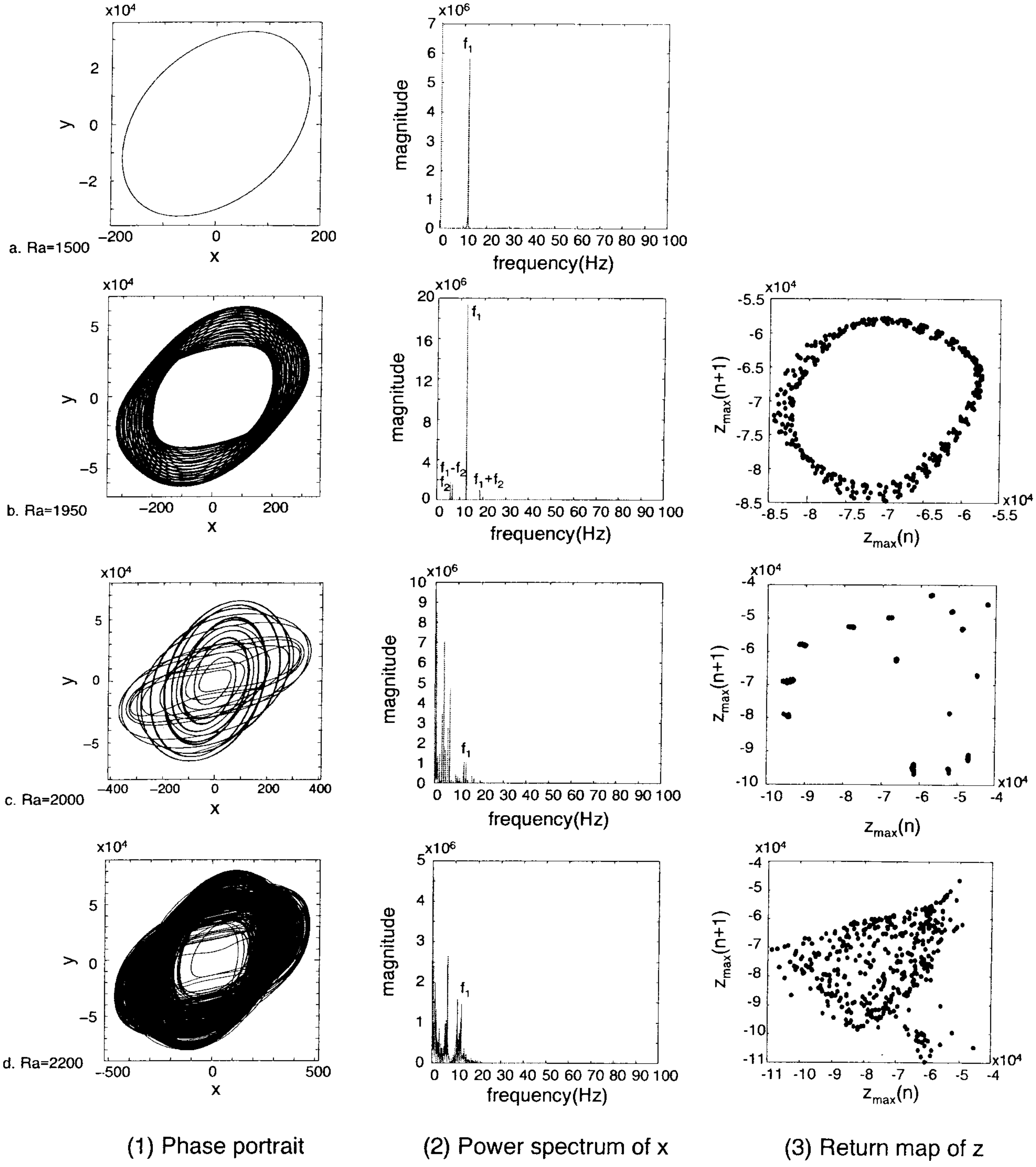

Fig. 8 Trajectories of the flow at different Rayleigh number for δ=1

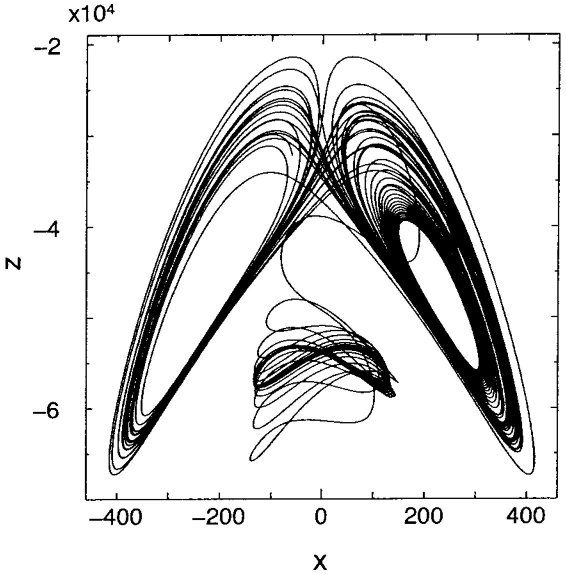

Fig. 9 Transition from Lorenz chaos to periodic cellular flow (Ra=1630, δ=0.86)

dimensional flow demonstrates the Lorenz-like oscillation for a while and then is replaced by a periodic cellular one. The numerical data discovered that the Lorenz flow disappears due to the appearing of the two flow modes $\mathbf{V}_{\mathrm{P1}}^{(1)}$ and $\mathbf{V}_{\mathrm{L1}}^{(1)}$. This phenomenon helps to demonstrate the interaction between the spatial stability and the temporal one although its existence needs experimental examination. At still larger Ra the cellular flow continues to demonstrate the aforementioned bifurcations. This scope can be considered as the margin of the two flow bifurcation routes.

7 Conclusions and Remarks

In this article, we applied a Multiple Scales Analysis to study the fluctuation and self-organization in the flow in a natural circulation loop. The analysis picked up two categories of flow modes. The study focuses on the influences of thermal boundary condition on the spatial and temporal stabilities of the flow, as is discussed in a framework of a three-dimensional model. Main conclusions are summarized as follows.

1. The multiple scale analysis alleviates the difficulty in determining the flow modes that are possibly existent. An amplitude equation for the basic Poiseuille flow is obtained from a solvability condition. The velocity of the steady flow increases with the Rayleigh number; their relation agrees with general scaling law of the continuous phase transition, i.e., there is $A \propto (\mathrm{Ra}-\mathrm{Ra}_0)^{0.5}$ slightly above Ra_0.
2. In the model a coefficient δ is proposed to measure the difference of thermal boundary condition from the standard one. The numerical solution of the model depends on the value of δ. For $\delta<0.76$, no spatial bifurcation appears in the cross-section, and the flow demonstrates one-dimensional character. The Lorenz chaos appears at large Rayleigh numbers. For $\delta>0.86$, spatial instability occurs prior to temporal one, making the flow structure three-dimensional, The flow bifurcates to intermittency chaos afterwards. For $0.86>\delta>0.76$, the model predicts a transition from Lorenz chaos to cellular flow, which calls for experimental verification.

It is remarkable to apply the Multiple Scales Analysis to the thermosyphon study, although the detailed mathematic process is quite complicate, as could be remedied by numerically solving the linear equations for a specific problem. In fact, this method is widely used in the study of fluid pattern formation, and we applied it to non-rectangular coordinate system. It seems also significant that we can vary both the spatial and temporal behaviors by changing the boundary conditions, i.e., following the reverse approach one can design a heating-cooling mode in accordance with δ to obtain a wanted flow. If the presumptions in Section 2 are relaxed flow modes out of the two categories are expected. Besides proposing methods to shift the occurrence of the Lorenz chaos the present work indicates a wider prospect of the stability and pattern controlling of natural convection.

Nomenclature

A = amplitude of flow oscillation
a = thermal diffusivity, m^2/s
C_n = coefficient, $Cn = nT_{s,n}^*/\Delta T$
g = gravity accelerator, kg·m/s^2
h = heat transfer coefficient, $h = q_{in}/(T_w^* - T_s^*)$, W/(m^2·K)
$J_i(x)$ = first kind Bessel function of order i
k_i = the first zero point of $J_i(x)$
$\mathbf{L}$ = linear operator
$\mathbf{N}(\mathbf{V},\mathbf{V})$ = nonlinear operator
Nu = Nusselt number, $2r_0h/\lambda_f$
p, p^* = Pressure, $p = (p^* - p_s^*)/(\rho_0 a^2/r_0^2)$, Pa
Pr = Prandtl number, ν/a
q = heat flux, W/m^2
r, r^* = radial coordinate, $r = r^*/r_0$, m
r_0 = pipe section radius, m
R_0, R = loop radius of curvature, $R = R_0/r_0$, m
Ra = Rayleigh number, $(g\beta\Delta T r_0^3)/(R\upsilon a)$
T, T^* = temperature, $T = (T^* - T_s^*)/(\Delta T/R)$, K
t, t^* = time, $t = t^*/(r_0^2/a)$, s
ΔT = temperature difference, K
u,v,w = velocities in r, φ and θ directions, respectively, m/s
$\mathbf{V}$ = state vector, (T,u,v,w)
$\mathbf{v}$, $\mathbf{v}^*$ = velocity vector, (u,v,w), $\mathbf{v} = \mathbf{v}^*/(a/r_0)$
x, y, z, x_a, x_b, x_c, y_c, z_b = variables defined in Eq. (6.2)

Greek Symbols

β = thermal expansion coefficient, K^{-1}
δ = thermal boundary condition coefficient
ε = expansion of $(\mathrm{Ra}-\mathrm{Ra}_0)/\mathrm{Ra}_0$, See Eq. (5.1)
η, ξ = coefficients defined in Eq. (5.19)
φ = pipe circumferential angle
θ = loop axial angle
λ = thermal conductivity, W/(m·K)
μ = dynamic viscosity of fluid, kg/(m·s)
υ = kinematical viscosity of fluid, m^2/s
ρ = density of the fluid, kg/m^3
τ = slow time scale, $\varepsilon^2 t$

Superscripts

$*$ = variable with dimension
$'$ = perturbed field for the static heat conduction state
(i) = variables at $\varepsilon^{(i)}$ order

Subscripts

0 = reference value, threshold point for flow onset
c = cooling, critical point for flow instability
f = fluid
h = heating
L = Localized cellular flow modes
m = order of Fourier series for φ
n = order of Fourier series for θ
P = parallel Poiseuille-type flow modes
s = motionless state
w = tube wall

Appendix A

At the Multiple Scales Analysis, we make $C_n=0$ for $n\geqslant 2$ so as to simply the process, the linear operator is,

$$\mathbf{L}=\begin{bmatrix} \nabla^2, & 0, & 0, & \sin\theta^{\#} \\ -\mathrm{Ra}\cos\varphi\cos\theta, & \nabla^2-\dfrac{1}{r^2}, & -\dfrac{2}{r^2},\dfrac{\partial}{\partial\varphi}, & 0 \\ \mathrm{Ra}\sin\varphi\cos\theta, & \dfrac{2}{r^2},\dfrac{\partial}{\partial\varphi}, & \nabla^2-\dfrac{1}{r^2}, & 0 \\ \mathrm{Ra}\sin\theta, & 0 & 0, & \nabla^2 \end{bmatrix}. \tag{A1}$$

Note that in section 6, the linear problem was also solved in its full form when the influences of thermal boundary condition are concerned. At this moment, the term with super mark #, i.e., $\sin\theta$ should be replaces by $[\sin\theta+\Sigma_{n=2}^{\infty}C_n\sin n\theta]$.

The nonlinear term $\mathbf{N}(\mathbf{V},\mathbf{V})^{(i)}$ is different at each ε order; for ε order it reads

$$\mathbf{N}(\mathbf{V},\mathbf{V})^{(i)}=[0], \tag{A2}$$

and for ε^2 order, it is

$$\mathbf{N}(\mathbf{V},\mathbf{V})^{(i)}$$

$$=\begin{bmatrix} \mathbf{v}^{(1)}\cdot\nabla T^{(1)} \\ \left(\mathbf{v}^{(1)}\cdot\nabla u^{(1)}-\dfrac{v^{(1)^2}}{r}-\dfrac{\cos\varphi}{R}w^{(1)^2}\right)\Big/\mathrm{Pr} \\ \left(\mathbf{v}^{(1)}\cdot\nabla v^{(1)}+\dfrac{u^{(1)^2}}{r}+\dfrac{\sin\varphi}{R}w^{(1)^2}\right)\Big/\mathrm{Pr} \\ \left(\mathbf{v}^{(1)}\cdot\nabla w^{(1)}+\dfrac{w^{(1)}}{R}(u^{(1)}\cos\varphi-v^{(1)}\sin\varphi)\right)\Big/\mathrm{Pr} \end{bmatrix} \tag{A3}$$

After knowing the solution of $\mathbf{V}_0^{(1)}$, this nonlinear term $\mathbf{N}(\mathbf{V},\mathbf{V})^{(i)}$ becomes:

$$\mathbf{N}(\mathbf{V},\mathbf{V})^{(i)}=\begin{bmatrix} 0.346[A(\tau)J_0(k_0r)]^2R^{-1}\cos\theta \\ -[A(\tau)J_0(k_0r)]^2R^{-1}\mathrm{Pr}^{-1}\cos\varphi \\ [A(\tau)J_0(k_0r)]^2R^{-1}\mathrm{Pr}^{-1}\sin\varphi \\ 0 \end{bmatrix} \tag{A4}$$

For ε^3 order, we have:

$$\mathbf{N}(\mathbf{V},\mathbf{V})^{(i)}=\begin{bmatrix} \mathbf{v}^{(1)}\cdot\nabla T^{(2)}+\mathbf{v}^{(2)}\cdot\nabla T^{(1)} \\ \left[\mathbf{v}^{(1)}\cdot\nabla u^{(2)}+\mathbf{v}^{(2)}\cdot\nabla u^{(1)}-\dfrac{2v^{(1)}v^{(2)}}{r}-\dfrac{2w^{(1)}w^{(2)}}{R}\cos\varphi\right]/\mathrm{Pr} \\ \left[\mathbf{v}^{(1)}\cdot\nabla v^{(2)}+\mathbf{v}^{(2)}\cdot\nabla v^{(1)}+\dfrac{2u^{(1)}u^{(2)}}{r}+\dfrac{2w^{(1)}w^{(2)}}{R}\sin\varphi\right]/\mathrm{Pr} \\ \left[\mathbf{v}^{(1)}\cdot\nabla w^{(2)}+\mathbf{v}^{(2)}\cdot\nabla w^{(1)}+\dfrac{w^{(1)}}{R}(u^{(2)}\cos\varphi-v^{(2)}\sin\varphi)+\dfrac{w^{(2)}}{R}(u^{(1)}\cos\varphi-v^{(1)}\sin\varphi)-Ra_cT^{(1)}\sin\theta\right]/\mathrm{Pr} \end{bmatrix} \tag{A5}$$

and for this study, it is in a form of,

$$\mathbf{N}(\mathbf{V},\mathbf{V})^{(i)}=\begin{bmatrix} [U_a^{(2)}T^{(1)}+(W_a^{(2)}T^{(1)}-w^{(1)}T_a^{(2)})R^{-1}]\sin\theta+A(\tau)^3d_1(r,\cos m\varphi,\sin(2n+1)\theta)+A(\tau)^2A^{(2)}e_1(r,\cos m\varphi)\cos\theta \\ [A(\tau)^3d_2(r,\cos l\varphi)\sin 2\theta+A(\tau)^2A^{(2)}e_2(r)\cos\varphi]/\mathrm{Pr} \\ [A(\tau)^3d_3(r,\sin l\varphi)\sin 2\theta+A(\tau)^2A^{(2)}e_3(r)\sin\varphi]/\mathrm{Pr} \\ [0.5[w^{(1)}(U_{b,0}^{(2)}-V_{b,0}^{(2)})R^{-1}-\mathrm{Ra}T^{(1)}]+A(\tau)^3d_4(r,\cos 2n\theta,\cos l\varphi)+A(\tau)^2A^{(2)}e_4(r,\cos 2n\theta,\cos l\varphi)]/\mathrm{Pr} \end{bmatrix}, \tag{A6}$$

$$l=0,1,2 \qquad m,n=0,1$$

Appendix B

Consider the linear marginal problem,

$$\nabla\cdot\mathbf{v}=0 \tag{B1a}$$

$$\mathbf{LV}-\partial\mathbf{P}=0 \tag{B1b}$$

where Eq. ($B2a$) implies that W and T are an order of R larger than U, V and P. Since it is difficult to precisely solve the ordinary equations, we obtain an estimation by firstly solving W and T at order $O(1)$ from

$$\mathrm{RaPr}T\sin\theta+\mathrm{Pr}\nabla^2w=0 \tag{B2a}$$

$$\nabla^2T+w\sin\theta=0 \tag{B2b}$$

and secondly deriving U, V and P at order $O(R^{-1})$ from

$$\frac{\partial u}{\partial r}+\frac{u}{r}+\frac{1}{r}\frac{\partial v}{\partial\varphi}+\frac{1}{R}\frac{\partial w}{\partial\theta}=0 \tag{B3a}$$

$$-\frac{\partial p}{\partial r}-\mathrm{RaPr}T\cos\varphi\cos\theta+\mathrm{Pr}\left(\nabla^2u-\frac{u}{r^2}-\frac{2}{r^2}\frac{\partial v}{\partial\varphi}\right)=0 \tag{B3b}$$

$$-\frac{\partial p}{r\partial\varphi}+\mathrm{RaPr}T\sin\varphi\cos\theta+\mathrm{Pr}\left(\nabla^2v-\frac{v}{r^2}+\frac{2}{r^2}\frac{\partial u}{\partial\varphi}\right)=0 \tag{B3c}$$

For the parallel Poiseuille-type flow modes with the form,

$$\mathbf{V}_{\mathrm{P}m}=\left[\sum_{n=0}^{\infty}T_{\mathrm{P}m,2\mathrm{n}+1}\sin(2n+1)\theta\cos m\varphi,\sum_{n=1}^{\infty}U_{\mathrm{P}m,2\mathrm{n}}\sin 2n\theta\cos m\varphi,\sum_{n=1}^{\infty}V_{\mathrm{P}m,2\mathrm{n}}\sin 2n\theta\sin m\varphi,\sum_{n=0}^{\infty}W_{\mathrm{P}m,2\mathrm{n}}\cos 2n\theta\cos m\varphi\right]$$

$$m=0,1,2\ \ldots \tag{B4}$$

and the conservation pressure $\Sigma_{n=1}^{\infty}P_{\mathrm{P}m,2n}\sin 2n\theta\cos m\varphi$, we have an infinite set of ordinary differential equations from Eqs. ($B2$):

$$\nabla_m^2 W_{\mathrm{P}m,0}+\mathrm{Ra}T_{\mathrm{P}m,1}/2=0,\quad \nabla_m^2 T_{\mathrm{P}m,1}+W_{\mathrm{P}m,0}-W_{\mathrm{P}m,2}/2=0,$$
$$\nabla_m^2 W_{\mathrm{P}m,2n}+\mathrm{Ra}(T_{\mathrm{P}m,2n+1}-T_{\mathrm{P}m,2n-1})/2=0, \tag{B5}$$
$$\nabla_{m,0}^2 T_{\mathrm{P}m,2n+1}-(W_{\mathrm{P}m,2n+2}-W_{\mathrm{P}m,2n})/2=0,\quad n=1,2,3,\ldots$$

where $\nabla_m^2=\mathrm{d}^2/\mathrm{d}r^2+(1/r)\mathrm{d}/\mathrm{d}r-m^2/r^2-O(R^{-2})$. Assuming the solution to be of the form,

$$W_{\mathrm{P}m,2n}^{(1)}=a_{2n}J_m(k_m r),\quad T_{\mathrm{P}m,2n+1}^{(1)}=b_{2n+1}J_m(k_m r),$$
$$n=0,1,2,\ldots \tag{B6}$$

we obtain the recursive relations:

$$b_1=(2k_m^2/\mathrm{Ra})a_0,$$
$$a_{2n}=a_{2n-2}-2k_m^2 b_{2n-1},\quad b_{2n+1}=b_{2n-1}+(2k_m^2/\mathrm{Ra})a_{2n}, \tag{B7}$$
$$n=1,2,3,\ldots$$

where a_0 is to be determined.

The threshold value of Ra for flow occurrence is derived by re-adding the time derivatives to the equation group of $W_{\mathrm{P}m,2n}$ and $T_{\mathrm{P}m,2n+1}$, or

$$-k_m^2 a+\mathrm{Ra}\cdot b=\mathrm{d}a/\mathrm{d}t$$
$$-k_m^2 b+a=\mathrm{d}b/\mathrm{d}t \tag{B8}$$

where $a=\Sigma_{n=0}^{\infty}a_{2n}$ and $b=\Sigma_{n=0}^{\infty}b_{2n+1}$. (Note that $\nabla_m^2 J_m(k_m r)=-k_m^2$.) As soon as the eigenvalues of the coefficient matrix of Eq. ($B8$) with respect to (a,b) have negative real parts, the no-zero solution is stable, as requires:

$$\mathrm{Ra}\geqslant k_m^4 \tag{B9}$$

As instances we list the solutions for the flow modes at $m=0$ and 1, which are truncated at $n=0$ of θ modes, denoting

$$\mathbf{V}_{\mathrm{P}0}^{(1)}=[T_{\mathrm{P}0,1}^{(1)}\sin\theta,0,0,W_{\mathrm{P}0,0}^{(1)}] \tag{B10}$$

with

$$T_{\mathrm{P}0,1}^{(1)}=AJ_0(k_0 r),\quad W_{\mathrm{P}0,0}^{(1)}=Ak_0^2 J_0(k_0 r)1 \tag{B11}$$

and

$$\mathbf{V}_{\mathrm{P}1}^{(1)}=[T_{\mathrm{P}1,1}^{(1)}\sin\theta\cos\varphi,0,0,W_{\mathrm{P}1,0}^{(1)}\cos\varphi] \tag{B12}$$

with

$$T_{\mathrm{P}1,1}^{(1)}=AJ_1(k_1 r),\quad W_{\mathrm{P}1,0}^{(1)}=Ak_1^2 J_1(k_1 r) \tag{B13}$$

Among all the flow modes, $\mathbf{V}_{\mathrm{P}0}^{(1)}$ appears at the smallest Rayleigh number that

$$\mathrm{Ra}_0=k_0^4=33.445 \tag{B14}$$

Physically speaking only $\mathbf{V}_{\mathrm{P}0}^{(1)}$ is true at the threshold point of flow onset, and we name it the marginally stable flow mode. The corresponding Ra_0 is just the point for flow onset and the variable a_0 is the amplitude $A(\tau)$.

As the difference of thermal boundary condition is concerned, Eq. ($B2b$) should be replaced by,

$$\nabla^2 T+w\left[\sin\theta+\sum_{n=2}^{\infty}C_n\sin n\theta\right]=0 \tag{B15}$$

although this deformation does not change the expressions of $\mathbf{V}_{\mathrm{P}0}^{(1)}$ and $\mathbf{V}_{\mathrm{P}1}^{(1)}$.

Appendix C

For the localized cellular flow modes with the form,

$$\mathbf{V}_{\mathrm{L}m}=\left[\sum_{n=0}^{\infty}T_{\mathrm{L}m,2n+1}\cos(2n+1)\theta\cos m\varphi,\right.$$
$$\sum_{n=1}^{\infty}U_{\mathrm{L}m,2n}\cos 2n\theta\cos m\varphi,\sum_{n=1}^{\infty}V_{\mathrm{L}m,2n}\cos 2n\theta\sin m\varphi,$$
$$\left.\sum_{n=1}^{\infty}W_{\mathrm{L}m,2n}\sin 2n\theta\cos m\varphi\right]m=0,1,2\ \ldots \tag{C1}$$

and the corresponding pressure $\Sigma_{n=0}^{\infty}P_{\mathrm{L}m,2n}\cos 2n\theta\cos m\varphi$ we have an infinite set of ordinary differential equations from Eqs. ($B2$):

$$\nabla_m^2 T_{\mathrm{L}m,1}+W_{\mathrm{L}m,2}/2=0,$$
$$\nabla_m^2 T_{\mathrm{L}m,2n+1}+(W_{\mathrm{L}m,2n+2}-W_{\mathrm{L}m,2n})/2=0, \tag{C2}$$
$$\nabla_m^2 W_{\mathrm{L}m,2n}-\mathrm{Ra}(T_{\mathrm{L}m,2n+1}-T_{\mathrm{L}m,2n-1})/2=0,$$
$$n=1,2,3,\ldots$$

Assuming the solution to be of the form,

$$W_{\mathrm{L}m,2n}=a_{2n}J_m(k_m r),\quad T_{\mathrm{L}m,2n+1}=b_{2n+1}J_m(k_m r),$$
$$n=1,2,3\ \ldots \tag{C3}$$

we obtain the recursive relations:

$$a_2=2k_m^2 b_1,$$
$$a_{2n+2}=a_{2n}+2k_m^2 b_{2n-1},\quad b_{2n+1}=b_{2n-1}-(2k_m^2/\mathrm{Ra})a_{2n}, \tag{C4}$$
$$n=1,2,3,\ldots$$

where b_1 is need to be determined.

On considering the differences of thermal boundary condition, we substitute the series for Eqs. ($B2a$) and ($B15$) instead. As a result Eq. ($C2$) becomes,

$$\nabla_m^2 T_{\mathrm{L}m,1}+\sum_{n=1}^{\infty}W_{\mathrm{Lm},2n}(C_{2n+1}+C_{2n-1})/2=0 \tag{C5}$$

$$\nabla_m^2 T_{\mathrm{L}m,2n+1}+\sum_{n=1}^{\infty}C_{2n-1}(W_{\mathrm{L}m,2n+1+2n-1}-W_{\mathrm{L}m,2n+1-(2n-1)})/2$$
$$=0 \tag{C6}$$

$$\nabla_m^2 W_{\mathrm{L}m,2n}-\mathrm{Ra}(T_{\mathrm{L}m,2n+1}-T_{\mathrm{L}m,2n-1})/2=0,\quad n=1,2,3,\ldots \tag{C7}$$

If Eq. ($C5$) is written in a form of,

$$\nabla_m^2 T_{\mathrm{L}m,1}-\frac{\delta}{2}W_{\mathrm{L}m,2}=0 \tag{C8}$$

the following relation is thus obtained,

$$\delta=\sum_{n=1}^{\infty}(C_{2n-1}-C_{2n+1})W_{\mathrm{L}m,4}/W_{\mathrm{L}m,2} \tag{C9}$$

Here $W_{\mathrm{L}m,2n}$ are also functions of C_n; they can be derived in a similar way to Eq. ($C4$). Then the value of δ should be determined. For the simplest case, we truncate Eq. ($C9$) at the second order, or,

$$\delta=(1-C_3) \tag{C10}$$

For the boundary conditions BC-QT and BC-TT, Eq. (4.9) suggests that,

$$C_{2n+1}\approx(-1)^n, \tag{C11}$$

so there is $\delta \approx 0$. For the standard boundary condition (BC-Sano) we have $\delta = 1$.

Additionally we solve the flow modes for $m = 1$ and 2, which are truncated at the basic θ modes, denoting

$$\mathbf{V}_{\mathrm{L}0} = [T_{\mathrm{L}0,1} \cos \theta, U_{\mathrm{L}0,2} \cos 2\theta, 0, W_{\mathrm{L}0,2} \sin 2\theta] \tag{C12}$$

with

$$\begin{aligned} T_{\mathrm{L}0,1} &= \delta[J_0(k_I r) + cI_0(k_I r) - 2J_0(k_I)], \\ W_{\mathrm{L}0,2} &= -2k_I^2[J_0(k_I r) - cI_0(k_I r)] \\ U_{\mathrm{L}0,2} &= -4k_I R^{-1}[J_1(k_I r) - cI_1(k_I r)], \\ P_{\mathrm{L}0,2}/\mathrm{Pr} &= 2k_I^4 J_0(k_I) R^{-1}, \quad c = J_0(k_I)/I_0(k_I) \end{aligned} \tag{C13}$$

and

$$\begin{aligned} \mathbf{V}_{\mathrm{L}1} = [&T_{\mathrm{L}1,1} \cos \theta \cos \varphi, (U_{\mathrm{L}1,0} + U_{\mathrm{L}1,2} \cos 2\theta) \cos \varphi, \\ &(V_{\mathrm{L}1,0} + V_{\mathrm{L}1,2} \cos 2\theta) \cos 2\theta \sin \varphi, W_{\mathrm{L}1,2} \sin 2\theta \cos \varphi] \end{aligned} \tag{C14}$$

with

$$\begin{aligned} U_{\mathrm{L}1,0} &= V_{\mathrm{L}1,0} = P_{\mathrm{L}1,0} = 0, \quad T_{\mathrm{L}1,1} = -\delta J_1(k_1 r), \\ W_{\mathrm{L}1,2} &= -2k_1^2 J_1(k_1 r) \\ U_{\mathrm{L}1,2} &= R^{-1}\{2k_1 J_0(k_1)(1 - r^2) \\ &\quad + 4J_1(k_1 r)/r - 4k_1[J_0(k_1 r) - J_0(k_1)]\}, \\ V_{\mathrm{L}1,2} &= R^{-1}[-6k_1 J_0(k_1)(1 - r^2) + 4J_1(k_1 r)/r], \\ P_{\mathrm{L}1,2}/\mathrm{Pr} &= R^{-1}[-16k_1 J_0(k_1 r) + 4k_1^2 J_1(k_1 r)] \end{aligned} \tag{C15}$$

where $I_0(x)$ is the first kind modified Bessel function and $k_I \approx 4.611$ satisfies $I_0(k_I)J_1(k_I) - J_0(k_I)I_1(k_I) = 0$. In practice it is recommended to estimate the values of these flow modes by direct numerical calculation of Eqs. ($B1$).

References

[1] Greif, R., 1988, ''Natural Circulation Loops,'' ASME J. Heat Transfer, **110**, pp. 1243–1258.

[2] Zvirin, Y., 1981, ''A Review of Natural Circulation Loops in Pressurized Water Reactors and Other Systems,'' Nucl. Eng. Des., **67**, pp. 203–225.

[3] Lorenz, E. N., 1963, ''Deterministic Nonperiodic Flow,'' J. Atmos. Sci., **20**, pp. 130–141.

[4] Keller, J. B., 1966, ''Periodic Oscillations in a Model of Thermal Convection,'' J. Fluid Mech., **26**, pp. 599–606.

[5] Welander, P., 1967, ''On the Oscillatory Instability of a Differentially Heated Fluid Loop,'' J. Fluid Mech., **29**, pp. 17–30.

[6] Malkus, W. R. V., 1972, ''Non-Periodic Convection at High and Low Prandtl Number,'' mem. Soc. R. Sci. Liege., 4kk, pp. 125–128.

[7] Creveling, H. F., Depaz, J. F., Baladi, J. Y., and Schoenhals, R. J., 1975, ''Stability Characteristics of a Single-Phase Convection Loop,'' J. Fluid Mech., **67**, pp. 65–84.

[8] Gorman, M., Widmann, P. J., and Robbins, K. A., 1986, ''Nonlinear Dynamics of Convection Loop: A Quantitative Comparison of Experiment With Theory,'' Physica D, **19D**, pp. 255–267.

[9] Ehrhard, P., and Muller, U., 1990, ''Dynamical Behavior of Natural Convection in a Single-Phase Loop,'' J. Fluid Mech., **217**, pp. 487–518.

[10] Yorke, J. A., Yorke, E. D., and Mallet-Paret, J., 1987, ''Lorenz-Like Chaos in a Partial Differential Equation for a Heated Fluid Loop,'' Physica D, **24D**, pp. 279–292.

[11] Jiang, Y. Y., Shoji, M., and Naruse, M., 2002, ''Boundary Condition Effects on Flow Stability in a Toroidal Thermosyphon,'' Int. J. Heat Fluid Flow, **23**(1), pp. 81–91.

[12] Wang, Y., Singer, J., and Bau, H. H., 1992, ''Controlling Chaos in a Thermal Convection Loop,'' J. Fluid Mech., **237**, pp. 479–498.

[13] Yuen, P. K., and Bau, H. H., 1996, ''Rendering a Subcritical Hopf Bifurcation Supercritical,'' J. Fluid Mech., **317**, pp. 91–109.

[14] Yuen, P. K., and Bau, H. H., 1999, ''Optimal and Adaptive Control of Chaotic Convection-Theory and Experiments,'' Phys. Fluids, **11**(6), pp. 1435–1448.

[15] Sano, O., 1991, ''Cellular Structure in a Natural Convection Loop and Its Chaotic Behavior, I. Experiment,'' Fluid Dyn. Res., **8**, pp. 189–204.

[16] Sano, O., 1991, ''Cellular Structure in a Natural Convection Loop and Its Chaotic Behavior, II. Theory,'' Fluid Dyn. Res., **8**, pp. 205–220.

[17] Damerell, P. S., and Schoenhals, R. J., 1979, ''Flow in a Toroidal Thermosyphon With Angular Displancement of Heated and Cooled Sections,'' ASME J. Heat Transfer, **101**, pp. 672–676.

[18] Lavine, A. S., Grief, R., and Humphrey, J. A. C., 1986, ''Three-Dimensional Analysis of Natural Convection in a Toroidal Loop: Effect of Tilt Angle,'' ASME J. Heat Transfer, **108**, pp. 796–805.

[19] Stern, C. H., Greif, R., and Humphrey, J., 1988, ''An Experimental-Study of Natural-Convection in a Toroidal Loop,'' ASME J. Heat Transfer, **107**, pp. 877–884.

[20] Cross, M. C., and Hohenberg, P. C., 1993, ''Pattern Formation out of Equilibrium,'' Rev. Mod. Phys., **65**(3), pp. 851–1112.

[21] Haken, H., 1983, *Synergetics, An Introduction. Nonequilibrium Phase Transitions and Self-Organization in Physics, Chemistry and Biology*, Springer-Verlag, Berlin, Chap. 5.

[22] Landau, L. D., and Lifshitz, E. M., 1958, *Statistical Physics*, Addison Wesley, Reading, MA, Chap. XIV.

[23] Newell, A. L., Passot, T., and Lega, J., 1993, ''Order Parameter Equations for Patterns,'' Annu. Rev. Fluid Mech., **25**, pp. 399–453.

[24] Nicolis, G., and Prigogine, I., 1977, *Self-Organization in Nonequilibrium Systems: from Dissipative Structures to Order through Fluctuations*, Wiley, New York.

[25] Newell, A. L., and Whitehead, J. A., 1969, ''Finite Bandwidth, Finite Amplitude Convection,'' J. Fluid Mech., **38**, pp. 279–303.

[26] Segel, L. A., 1969, ''Distant Side-Walls Cause Slow Amplitude Modulation of Cellular Convection,'' J. Fluid Mech., **38**, pp. 203–224.

[27] Pomeau, Y., and Manneville, P., 1979, ''Stability and Fluctuations of a Spatially Periodic Convective Flow,'' J. Phys. Lett., **40**, pp. 609–612.

[28] Newell, A. L., Passot, T., and Souli, M., 1990, ''The Phase Diffusion and Mean Drift Equations for Convection at Finite Rayleigh Numbers in Large Containers,'' J. Fluid Mech., **220**, pp. 187–252.

[29] Cross, M. C., 1980, ''Derivation of the Amplitude Equation at the Rayleigh-Benard Instability,'' Phys. Fluids, **23**(9), pp. 1727–1731.

[30] Swift, J., and Hohenberg, P. C., 1977, ''Hydrodynamic Fluctuations at the Convective Instability,'' Phys. Rev. A, **15**(1), pp. 319–328.

[31] Thompson, J. M. T., and Stewart, H. B., 1993, *Nonlinear Dynamics and Chaos*, John Wiley and Sons Ltd., New York, pp. 212–227.

Laminar Natural Convection Heat Transfer in a Differentially Heated Square Cavity Due to a Thin Fin on the Hot Wall

Xundan Shi
Graduate Student

J. M. Khodadadi
Professor
e-mail: khodajm@auburn.edu

Mechanical Engineering Department,
Auburn University,
201 Ross Hall,
Auburn, AL 36849-5341

A finite-volume-based computational study of steady laminar natural convection (using Boussinesq approximation) within a differentially heated square cavity due to the presence of a single thin fin is presented. Attachment of highly conductive thin fins with lengths equal to 20, 35 and 50 percent of the side, positioned at 7 locations on the hot left wall were examined for Ra$=10^4$, 10^5, 10^6, *and* 10^7 *and* $Pr=0.707$ *(total of 84 cases). Placing a fin on the hot left wall generally alters the clockwise rotating vortex that is established due to buoyancy-induced convection. Two competing mechanisms that are responsible for flow and thermal modifications are identified. One is due to the blockage effect of the fin, whereas the other is due to extra heating of the fluid that is accommodated by the fin. The degree of flow modification due to blockage is enhanced by increasing the length of the fin. Under certain conditions, smaller vortices are formed between the fin and the top insulated wall. Viewing the minimum value of the stream function field as a measure of the strength of flow modification, it is shown that for high Rayleigh numbers the flow field is enhanced regardless of the fin's length and position. This suggests that the extra heating mechanism outweighs the blockage effect for high Rayleigh numbers. By introducing a fin, the heat transfer capacity on the anchoring wall is always degraded, however heat transfer on the cold wall without the fin can be promoted for high Rayleigh numbers and with the fins placed closer to the insulated walls. A correlation among the mean Nu, Ra, fin's length and its position is proposed.*
[DOI: 10.1115/1.1571847]

Keywords: *Cavities, Finned Surfaces, Heat Transfer, Natural Convection, Vortex*

Introduction

Buoyancy-driven convection in a sealed cavity with vertical sides that are cooled and heated is a prototype of many industrial applications, such as reactor insulation, cooling of radioactive waste containers, ventilation of rooms, fire prevention, solar energy collection and dispersion of waste heat in estuaries [1,2]. It is generally known that fluid flow in this system is characterized by a single large recirculating cell. The lighter fluid ascends along the hot wall. The fluid then descends along the cold wall as it gets heavier. For small Grashof numbers, the flow is weak and the isotherms are parallel to the vertical walls, indicating that heat is transferred by conduction across the fluid. For large Grashof numbers, the flow becomes strong and the isotherms are no longer parallel to the vertical walls. This indicates that heat is transferred by convection and conduction.

In a great number of studies, square, rectangular, inclined, slender and shallow cavities with various wall conditions have been extensively considered by researchers. Modification of heat transfer in cavities due to introduction of obstacles and fins attached to the wall(s) has received some consideration in recent years [3–10]. Laminar natural convection next to a heated wall with single and repeated two-dimensional rectangular roughness elements was studied numerically and experimentally [3]. Natural convection in an air-filled differentially heated inclined square cavity with a diathermal thin partition placed at the middle of its cold wall was numerically studied [4] for Rayleigh numbers 10^3–10^5. It was observed that due to suppression of convection, heat transfer reductions of up to 47 percent in comparison to the cavity with no partition was observed. Natural convection in a square cavity with a conducting partition positioned at the middle of its hot wall and with perfectly conducting horizontal walls was numerically studied [5]. For low values of the partition-to-fluid thermal conductivity ratio, reductions in heat transfer relative to the case of cavity with no partition was observed for Rayleigh numbers 10^4–10^5. Natural convection in a differentially heated slender rectangular cavity (aspect ratio of 20) with multiple conducting fins on the cold wall was reported by Scozia and Frederick [6] for Rayleigh numbers of 10^3–10^5. As the inter-fin aspect ratio was varied from 20 to 0.25, the flow patterns evolved considerably and the average Nusselt number exhibited maximum and minimum values whose locations depended on the value of Ra. Facas [7] reported results of a computational study of natural convection (Grashof number range of 9×10^3–10^5) inside an air-filled slender cavity (aspect ratio of 15) with fins/baffles—0.1, 0.3 and 0.5 of the cavity width—attached along both the heated and cooled sides of the cavity. For the fin length of 0.1, multicellular flow structure was observed. However, for longer fin lengths, the flow broke down into secondary recirculations, in addition to the primary recirculation. As a result, higher heat transfer rates across the two sides of the cavity were observed. Nag et al. [8] studied the effect of a horizontal thin partition (both infinite thermal conductivity and insulated) placed on the hot (left) wall of a differentially heated square cavity. The range of the Rayleigh number was 10^3–10^6 and three partition lengths placed at three positions were studied. It was concluded that for a partition of infinitely high thermal conductivity, the Nusselt number on the cold wall was greater than the case with no fin irrespective of the position of the partition on the hot wall. Natural convection in inclined rect-

---

Contributed by the Heat Transfer Division for publication in the JOURNAL OF HEAT TRANSFER. Manuscript received by the Heat Transfer Division August 12, 2002; revision received March 5, 2003. Associate Editor: H. Bau.

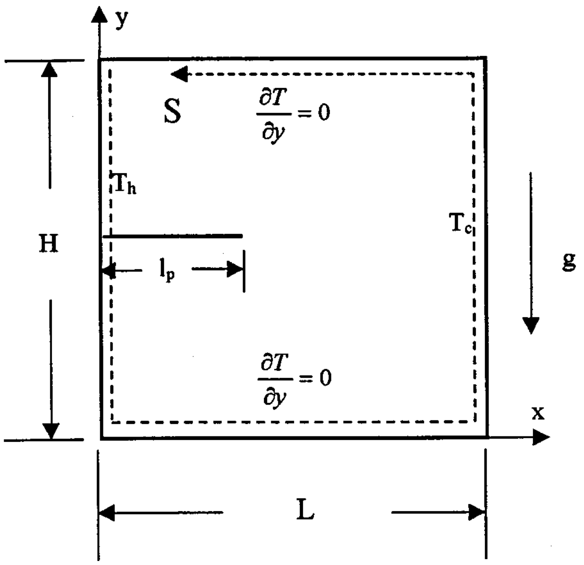

Fig. 1 Natural convection in a square cavity with a thin fin

angular enclosures (aspect ratio of 2.5 and higher) with perfectly conducting fins attached on the heated wall was numerically studied by Lakhal et al. [9]. Recently, Bilgen [10] reported numerical results of laminar and turbulent natural convection (Ra numbers 10^4-10^{11}) in enclosures with partitions attached on the insulated horizontal walls. Practical heat transfer correlations for design of similar systems were derived.

There are many industrial applications that can be simplified into models of fins/partitions in sealed cavities. Examples can be found in designing an air-conditioned room in which a partition is installed. Other examples can be found where the heat transfer through a fluid layer contained in an enclosure needs to be controlled via attaching fins on the walls. These applications can be found in solar collectors, nuclear reactors, heat exchangers and electronic equipment. Upon proper placing of the fins on the walls of an enclosure, the heat transfer rate through the enclosure may be enhanced or reduced. Hence, studying how the position of the fin, length of the fin and the Rayleigh number affect the heat transfer rate of the enclosure has great value from practical as well as theoretical point of views. As for the difference between this study and that of Nag et al. [8], a higher range of the Rayleigh number is studied in this paper along with longer lengths of the fin and the number of fin positions are seven as compared to three [8]. In addition, the present study is a logical extension of the recent work of the authors [11] who reported a detailed parametric study of flow and heat transfer in a lid-driven cavity due to the presence of thin fin. A major objective of this study (similar to [11]) is to determine the critical locations where attachment of fins bring about marked changes in the thermal fields.

Problem Formulation

The schematic drawing of the system and the coordinates are shown in Fig. 1. The height and the width of the enclosure are denoted by H and L, respectively. In this study, only a square enclosure is considered ($H=L$). The depth of the enclosure perpendicular to the plane of the diagram is assumed to be long. Hence, the problem can be considered to be two-dimensional. The top and bottom walls are insulated, whereas the left wall is maintained at a high temperature (T_h) and the right wall is maintained at a lower temperature (T_c), with $T_h>T_c$. A horizontal fin with length l_p can be attached to different positions on the left or the right walls. A dimensionless variable L_p for the length of the fin is defined as $L_p=l_p/L$. A special coordinate system (s) along the walls is adopted with its origin at $x=0$ and $y=H$, as identified by the dashed lines in Fig. 1. The coordinate of the fin (s_p) indicates the position of the fin, i.e., $s_p=0$ to H (left wall) and $s_p=H+L$ to $2H+L$ (right wall). A dimensionless variable is defined as follows: $S_p=s_p/L$.

The fin is made of highly conductive materials and the temperature of the fin is maintained at the same temperature of the wall to which it is attached ($\mathrm{Bi}\ll 1$). This represents a limiting case for the thermal conductivity, whereas an insulated fin represents the other extreme of thermal conductivity. A fin with a finite thermal conductivity will behave somewhere between these two limiting cases. It is assumed that the effect of the temperature on density is confined only to the body force term of the momentum equation and all other fluid properties are independent of temperature and pressure. The flow field is considered to be steady and the fluid is incompressible.

Dimensionless Form of the Governing Equations. Dimensionless form of the governing equations can be obtained via introducing dimensionless variables. These are defined as follows:

$$X=\frac{x}{L} \quad Y=\frac{y}{L} \quad U=\frac{uL}{\alpha} \quad V=\frac{\nu L}{\alpha}$$

$$P=\frac{pL^2}{\rho\alpha^2} \quad \theta=\frac{T-T_c}{T_h-T_c}. \tag{1}$$

Variables u, v, and T are the velocity components in the x, y-direction and temperature, respectively. The pressure (p) in the above equation is the "reduced" pressure wherein the hydrostatic pressure has been removed from the total pressure. Quantities ρ and α are the density and thermal diffusivity of the fluid, respectively. Based on the dimensionless variables above, the dimensionless equations for the conservation of mass, momentum and energy incorporating natural convection via the Boussinesq approximation are:

$$\frac{\partial U}{\partial X}+\frac{\partial V}{\partial Y}=0, \tag{2}$$

$$U\frac{\partial U}{\partial X}+V\frac{\partial U}{\partial Y}=-\frac{\partial P}{\partial X}+\mathrm{Pr}\left(\frac{\partial^2 U}{\partial X^2}+\frac{\partial^2 U}{\partial Y^2}\right), \tag{3}$$

$$U\frac{\partial V}{\partial X}+V\frac{\partial V}{\partial Y}=-\frac{\partial P}{\partial Y}+\mathrm{Pr}\left(\frac{\partial^2 V}{\partial X^2}+\frac{\partial^2 V}{\partial Y^2}\right)+\mathrm{Ra}\cdot\mathrm{Pr}\cdot\theta, \tag{4}$$

$$U\frac{\partial \theta}{\partial X}+V\frac{\partial \theta}{\partial Y}=\frac{\partial^2 \theta}{\partial X^2}+\frac{\partial^2 \theta}{\partial Y^2}. \tag{5}$$

In the energy equation, the viscous dissipation terms are neglected and the reference temperature in the buoyancy term was taken to be equal to T_c. Parameters Ra and Pr are the Rayleigh and Prandtl numbers, respectively. These are defined as,

$$\mathrm{Ra}=\frac{g\beta(T_h-T_c)L^3}{\nu\alpha}, \quad \mathrm{Pr}=\frac{\nu}{\alpha}. \tag{6}$$

Quantities ν and β are the kinematic viscosity and thermal expansion coefficient of the fluid, respectively. The dimensionless form of the boundary conditions are:

$$\begin{aligned}
&\text{On the left wall}(X=0): \quad U=V=0, \theta=1,\\
&\text{On the right wall}(X=1): \quad U=V=0, \theta=0,\\
&\text{On the bottom wall}(Y=0): \quad U=V=0, \frac{\partial\theta}{\partial Y}=0,\\
&\text{On the top wall}(Y=1): \quad U=V=0, \frac{\partial\theta}{\partial Y}=0,\\
&\text{On the fin:} \quad U=V=0, \theta=\theta_w.
\end{aligned} \tag{7}$$

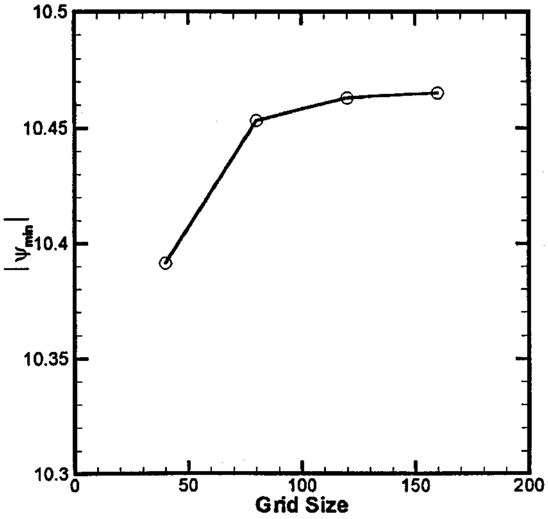

Fig. 2 The absolute value of the stream function at the center of primary vortex, ψ_{min}, as a function of the grid size (Ra $=10^5$, $S_p=0.5$, and $L_p=0.5$)

Here θ_w is the θ value of the wall the fin is attached to (0 or 1). From the equations above, we can see that the dimensionless parameters governing this problem are Ra, Pr, L_p, and S_p. In this study, the Prandtl number of the fluid is fixed to 0.707. The Rayleigh numbers considered are 10^4, 10^5, 10^6, and 10^7.

Computational Details

The solution of the governing equations can lead to a complete understanding of the velocity and temperature fields for natural convection in a square cavity with a thin fin. Consequently, the effect of the fin on the flow and thermal fields can be evaluated. The steady-state governing equations were iteratively solved by the finite-volume-method using Patankar's SIMPLE algorithm [12]. A two-dimensional uniformly-spaced staggered grid system was used. Hayase et al.'s [13] QUICK scheme was utilized for the convective terms, whereas the central difference scheme was used for the diffusive terms. In order to keep consistent accuracy over the entire computational domain, a third-order-accurate boundary condition treatment suggested by Hayase et al. [13] was adopted.

Grid Independence Study and Benchmarking of the Code. In order to determine the proper grid size for this study, a grid independence test was conducted for the Rayleigh number of 10^5 in a square cavity with a fin positioned at the middle of the left wall. The length of the fin was set to be 50 percent of L. Four different grid densities were used for the grid independence study. These grid densities were $40^x\times40^y$, $80^x\times80^y$, $120^x\times120^y$, and $160^x\times160^y$. The minimum value of the stream function of the primary vortex (ψ_{min}) is commonly used as a sensitivity measure of the accuracy of the solution. Quantity ψ_{min} is selected as the monitoring variable for the grid independence study. Figure 2 shows the dependence of quantity ψ_{min} on the grid size. Comparison of the predicated ψ_{min} values among four different cases suggests that the two grid distributions of $120^x\times120^y$ and $160^x\times160^y$ give nearly identical results. Considering both the accuracy and the computational time, the following calculations were all performed with a $120^x\times120^y$ uniformly-spaced grid system.

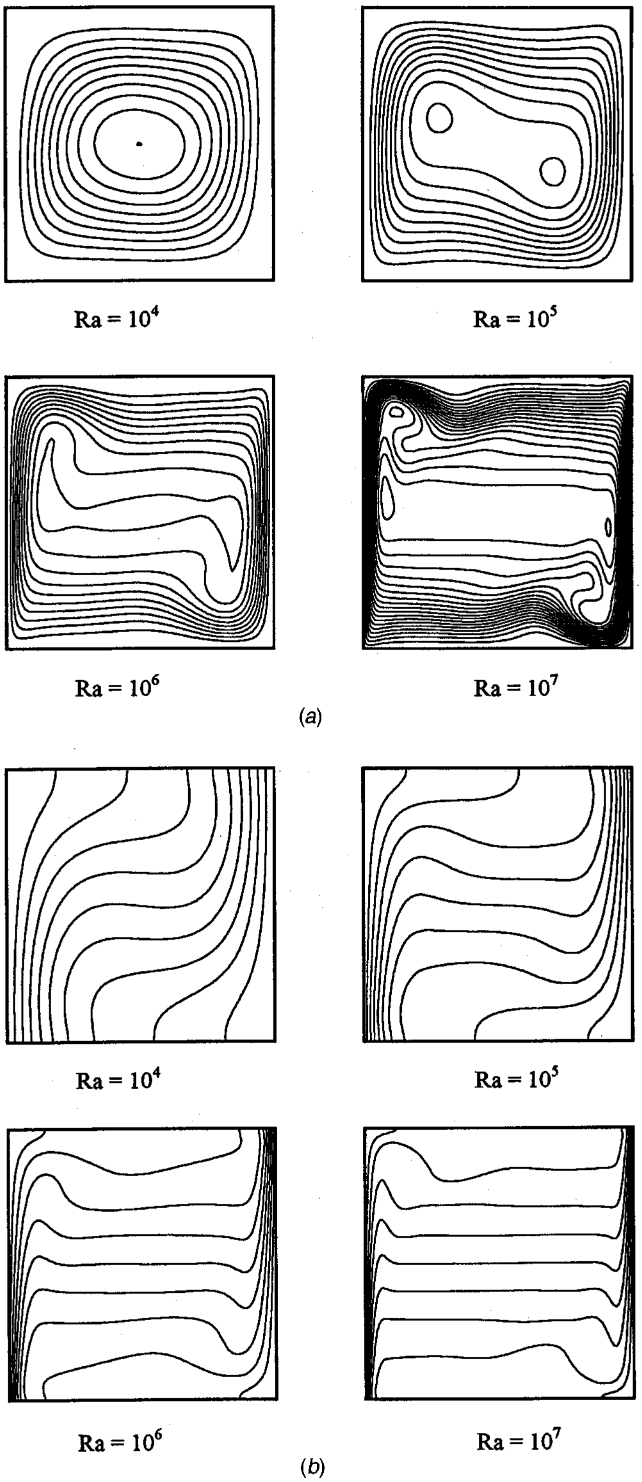

Fig. 3 Natural convection in a square cavity: (*a*) streamlines and (*b*) temperature contours [contour level increment of 0.1]

The code was tested and verified extensively via comparing the results with the benchmark problems [14,15]. Figure 3(*a*) shows the streamlines in a square cavity for Ra$=10^4$, 10^5, 10^6 and 10^7, respectively. The rise of the fluid due to heating on the left wall and consequent falling of the fluid on the right cold wall creates a clockwise-rotating vortex. Another feature of these streamline patterns is that the streamlines become more packed next to the side walls as the Rayleigh number increases. This suggests that the flow moves faster as natural convection is intensified. Figure 3(*b*) shows the dimensionless temperature contours for Rayleigh numbers ranging from 10^4 to 10^7. The contour level increments for each case are kept constant at 0.1. As natural convection is strengthened, temperature contours show slight deviation from the pure conduction case with the contour lines becoming skewed. Under high Rayleigh number conditions, the degree of distortion from the pure conduction case is very marked and the contour

Table 1 Comparison of the predicted mean Nusselt number $\overline{Nu}$ on the left or right walls of a cavity without a fin with references [8,14,15]

Ra	10^4	10^5	10^6	10^7
De Vahl Davis [14,15]	2.243	4.519	8.800	-
Nag et al. [8]	2.24	4.51	8.82	-
Present Study	2.247	4.532	8.893	16.935

lines become almost horizontal lines around the center of the enclosure. Table 1 gives the values of the mean Nusselt number for the left or right walls for $Ra=10^4$, 10^5, 10^6, and 10^7 for a square cavity without a fin. These values were in excellent agreement with those reported earlier [8,14,15]. Further details of code verification can be found elsewhere [16].

Parameters for Numerical Simulations. Tolerance of the normalized residuals upon convergence is set to 10^{-6} for every calculation case. The under-relaxation parameters for u, v, and T are all set to 0.6, whereas under-relaxation parameter for pressure correction is set to 0.3. However, converged solutions can not be obtained for 2 cases with $Ra=10^6$ ($L_p=0.35$, 0.5, and $S_p=0.5$) and 15 cases with $Ra=10^7$ ($L_p=0.2$, 0.35, 0.5, and $S_p=0.375$, 0.5, 0.625, 0.75, 0.875). To achieve converged solutions for these cases, it was necessary to retain the unsteady terms in the momentum and energy equations. This approach is called the false transient method. The temporal terms were approximated using a second-order implicit difference scheme, namely the three-time-level scheme. The success of the time-dependent method over the stationary one suggests that for these parameters a turning point in the parameter space is being approach.

Results and Discussion

In order to understand the flow field and heat transfer characteristics of this problem, a total of 84 cases were considered. This involved studying the effect of a fin attached at 7 evenly-spaced positions on the left wall. The Rayleigh numbers are 10^4, 10^5, 10^6, and 10^7. The fin's length can be 20 percent, 35 percent, and 50 percent of the width of the cavity. The typical number of iterations needed to converge was 10,000~12,000. All the calculations were performed on a Cray SV1 of the Alabama Supercomputer Center (Huntsville, Alabama).

Flow Fields in a Square Cavity With a Thin Fin. Figure 4(*a*) to 4(*c*) show the flow fields for a square cavity ($Ra=10^4$) with a fin at three representative positions for different lengths of the fin, $L_p=0.2$, 0.35, and 0.5, respectively. The plots are arranged going from left to right with the ascending of the S_p value. For

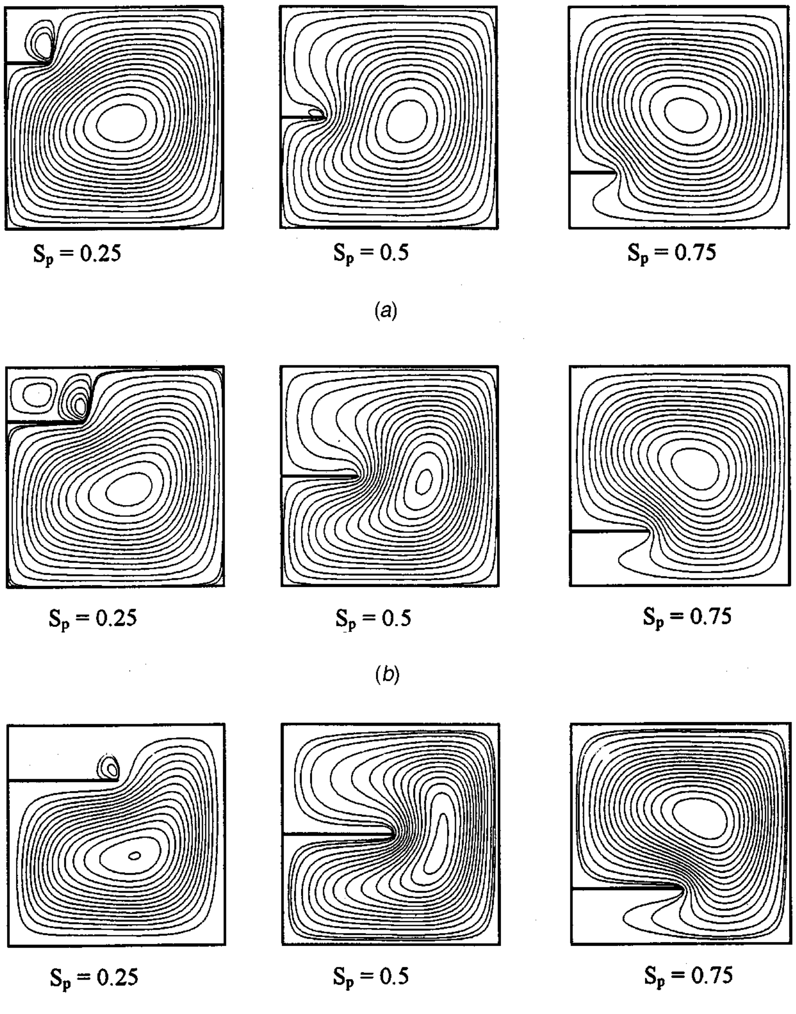

Fig. 4 Flow fields for $Ra=10^4$ with fins at different positions: (*a*) $L_p=0.2$, (*b*) $L_p=0.35$, and (*c*) $L_p=0.5$

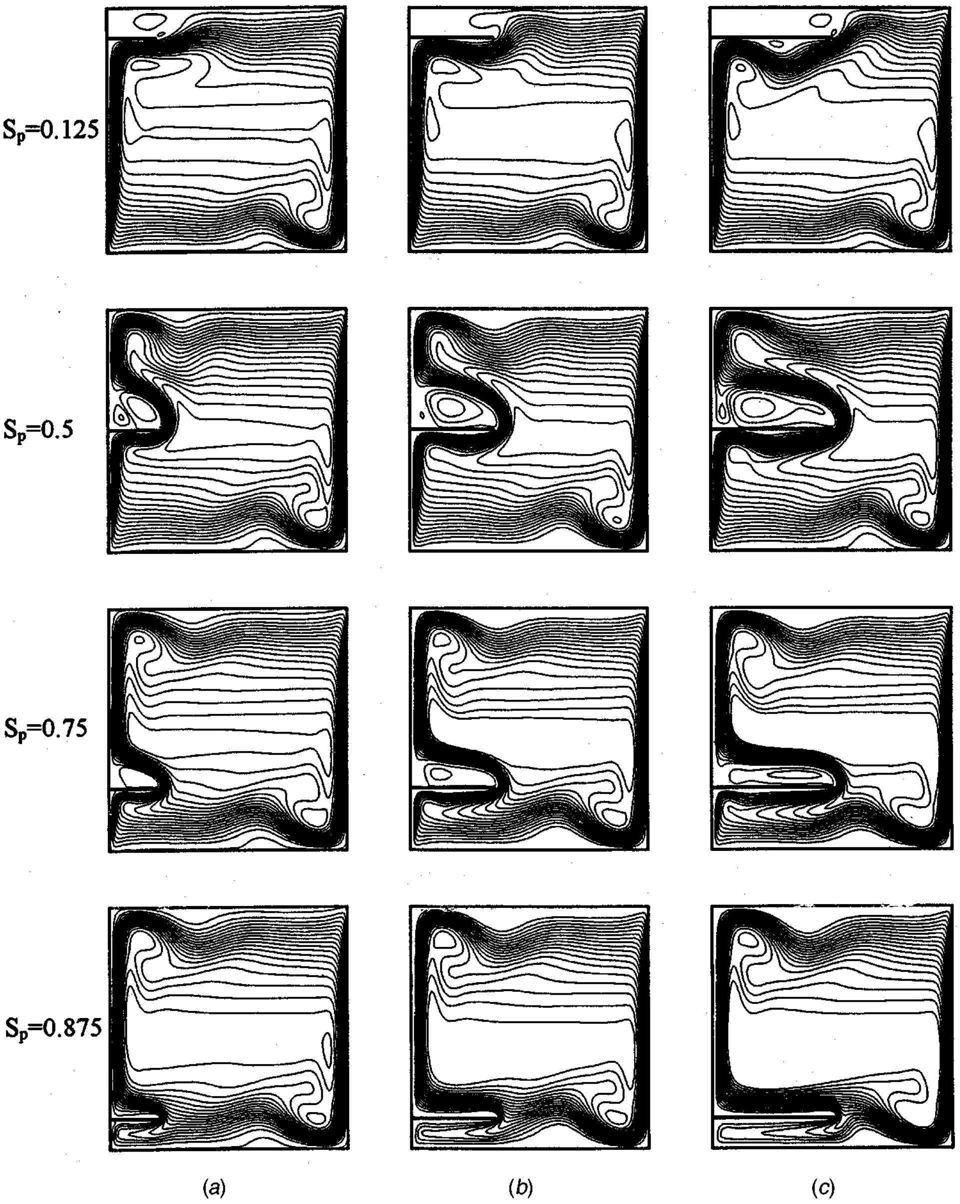

Fig. 5 Flow fields for Ra=10^7 with fins at different positions: (*a*) L_p=0.2, (*b*) L_p=0.35, and (*c*) L_p=0.5

Ra$=10^4$ with the shortest fin ($L_p=0.2$), a large clockwise (CW) rotating cell was observed for all fin positions. The fluid that is heated next to the hot wall (left wall) rises and replaces the cooled fluid next to the cold wall (right wall) that is falling, thus giving rise to a CW rotating vortex (also called the primary vortex). It was observed that placing a 0.2 thin fin at various positions not only changes the flow fields near the fin, but also the strength of the primary vortex. This is because the fin blocks the movement of the fluid and weakens the primary vortex. The effect of the length of the fin and its position on the strength of the primary vortex will be discussed later. By comparing all the cases in Figure 4(*a*), one can see that a fin attached to the middle of the wall has the most remarkable effect on the fluid flow in the cavity. A fin redirects the movement of the fluid and weakens the fluid motion within the area above the fin for $S_p \leqslant 0.5$, whereas it weakens the fluid motion within the area under the fin while $S_p > 0.5$. A counter clockwise (CCW) rotating vortex that is driven by the primary vortex can be found above the fin for $S_p \leqslant 0.5$. Figures 4(*b*) and 4(*c*) show the selected streamline patterns for $L_p=0.35$ and 0.5, respectively, for the Rayleigh number of 10^4. In general, the presence and the character of the primary CW rotating vortex is unaltered, with a longer fin bringing about more changes to the flow compared to a shorter fin. It was noticed that for $S_p \leqslant 0.375$, as many as two recirculating vortices are found above the fin and under the top insulated wall.

For Ra$=10^5$, the streamlines near the fin exhibit similar trends as those for Ra$=10^4$, and in some instances, the stream function field exhibits two local minima that was also observed for the cases with no fin (Fig. 3(*a*)). The flow fields for natural convection in a square cavity (Ra$=10^7$) with a fin at four representative positions for different lengths of the fin, $L_p=0.2$, 0.35, and 0.5, are shown in Fig. 5(*a*) to 5(*c*), respectively. The more packed stream function contours indicate that the fluid moves faster as the Rayleigh number increases. A CCW rotating vortex was observed above the fin for most cases with its intensity being more pronounced compared to the corresponding cases with Ra$=10^6$. The longer fin has more remarkable effects on the flow fields. Upon

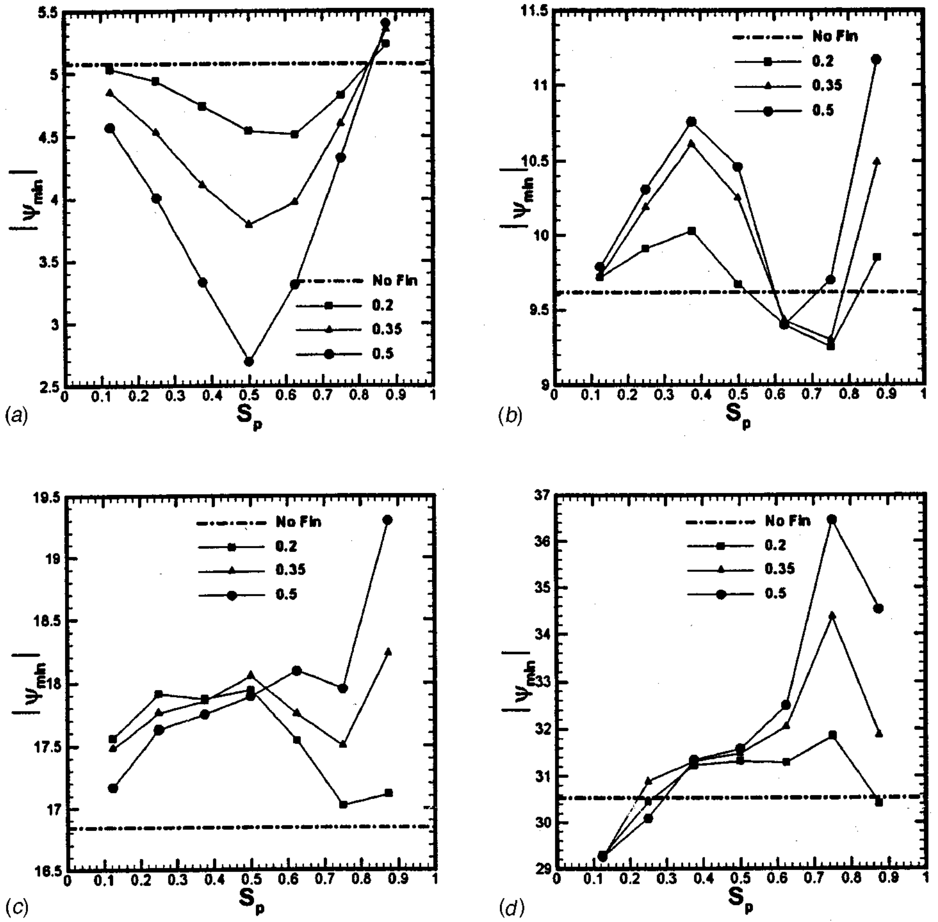

Fig. 6 Variation of the absolute value of $\psi_{\min}$ with the position of the fin: (*a*) Ra=10^4, (*b*) Ra=10^5, (*c*) Ra=10^6, and (*d*) Ra=10^7

comparing to Fig. 3(*a*) placing a fin at the middle of the left wall has marked effect on the flow in the cavity. For many of the cases, the stream function field exhibits two, three or even four local minima that was also observed for the cases with no fin (Fig. 3(*a*)).

Variation of the Minimum Stream Function Value of the Primary Vortex. For a differentially heated square cavity, as the Rayleigh number increases, the difference between the stream function value on the wall (generally taken to be zero) and the extreme value of the stream function field (minimum or maximum, depending on the usage by the researcher) widens monotonically. Therefore, the absolute value of $\psi_{\min}$ (minimum value of the stream function field) can be viewed as a measure of the intensity of natural convection. So it is necessary to study how the length and the position of the fin affects the absolute value of the $\psi_{\min}$. Figure 6 shows the variation of the absolute value of $\psi_{\min}$ with the position of the fin. The dash-dotted lines in the figures are the absolute value of $\psi_{\min}$ in the cavity without a fin. For Ra $=10^4$ (Fig. 6(*a*)), placing a fin at the middle of the left wall lowers the absolute value of $\psi_{\min}$ dramatically for all different lengths of the fins. This is because for the case of Ra$=10^4$ (convection not being strong compared to conduction), the fin's presence brings about resistance to the motion of the primary vortex and it has the most remarkable effects on the flow field when it is placed at the middle of the left wall. For a given position of the fin, the deviation of the absolute value of $\psi_{\min}$ compared to the case with no fin becomes more marked with the increase of the length of the fin. Except for the fins of different lengths positioned at $S_p=0.875$, introduction of a fin on the left wall weakens the intensity of the primary vortex. Placing a fin near the left bottom corner can enhance the primary vortex somewhat. This is because the fluid moves slowly in this area and a hot fin placed at $S_p>0.8$ heats the cold fluid coming toward it from the right wall.

For Ra$=10^5$ (Fig. 6(*b*)) placing a fin over most of the left wall can enhance the primary vortex. But placing a fin over $0.5<S_p<0.8$ for $L_p=0.2$, $0.6<S_p<0.8$ for $L_p=0.35$ and $0.6<S_p<0.7$ for $L_p=0.5$ can weaken the primary vortex. This weakening range becomes smaller with the increase of the fin's length. The absolute value of $\psi_{\min}$ attains its maximum for $S_p=0.375$ if placing a fin in the top half of the left wall. Also placing a fin near the left bottom corner can enhance the primary vortex. For such a situation, a longer fin results in a stronger primary vortex. Interestingly, the absolute value of $\psi_{\min}$ does not change with the length of the fin for $S_p=0.625$. It is observed that for the case of Ra$=10^5$ (convection dominating conduction), a fin can block the flow, thus weakening the primary vortex, but at the same time a long enough hot fin can heat the fluid and make it lighter resulting in enhancement of the primary vortex. These two mechanisms certainly counter balance each other for $S_p=0.625$, regardless of the fin's length.

Figure 6(*c*) shows the variation of the absolute value of $\psi_{\min}$ with the position of the fin when Ra$=10^6$. One can observe that all the computed $\psi_{\min}$ values are above the dash-dotted line. Given the strong effect of natural convection, this means that placing a fin of any length can always enhance the primary vortex regardless of its position. Placing a fin on the top half of the left wall can weaken the primary vortex somewhat with the increase

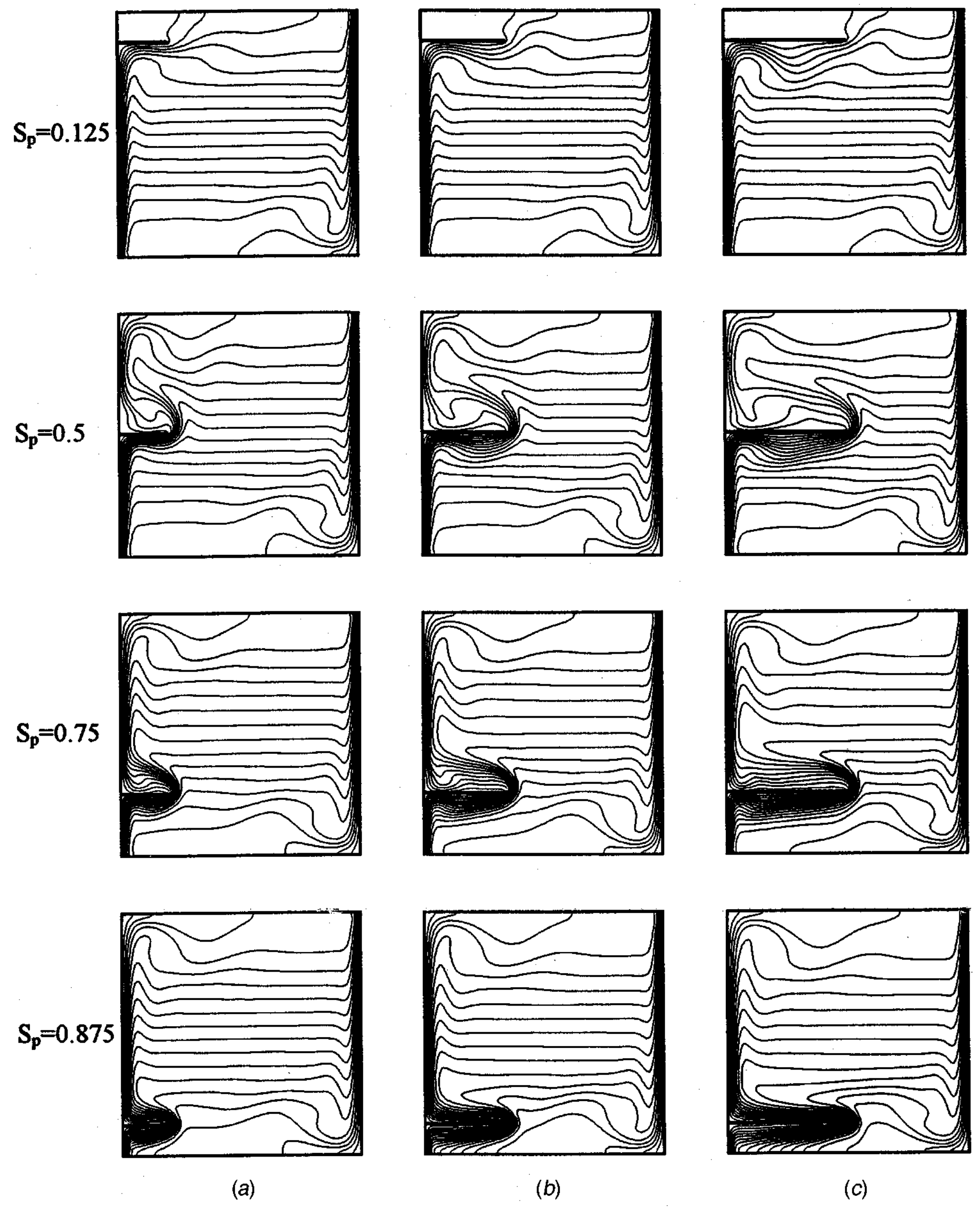

Fig. 7 Temperature fields for Ra=10^7 with fins at different positions: (*a*) L_p=0.2, (*b*) L_p=0.35, and (*c*) L_p=0.5 [contour level increment of 0.05]

of the fin's length, whereas placing a fin on the lower half of the left wall can enhance the primary vortex with the increase of the fin's length.

Figure 6(*d*) shows the variation of the absolute value of $\psi_{\min}$ with the position of the fin when Ra$=10^7$. Placing a fin near the top corner of the left wall does not enhance the primary vortex. This is because the fluid is being heated after traveling from the bottom to the top of the left wall. The hot fin's effect of blocking the fluid motion is more dominant than the effect of heating the fluid to enhance the primary vortex in this case. Another interesting case is that of placing a fin at $S_p=0.75$. For lower Ra numbers, the computed $\psi_{\min}$ reached its maximum value when a fin was placed at $S_p=0.875$. But for Ra$=10^7$, it reaches its maximum value when $S_p=0.75$, instead of $S_p=0.875$. To summarize, one can observe that most computed absolute values of $\psi_{\min}$ are smaller than those with no fin for Ra$=10^4$, whereas most computed absolute values of $\psi_{\min}$ are greater than those with no fin for Ra$=10^5$, 10^6 and 10^7. This implies that the effect of the hot fin heating the flow and enhancing the primary vortex becomes more marked with the rise of the Rayleigh number.

Temperature Fields in a Square Cavity with a Thin Fin. Figures 7(*a*) to 7(*c*) show the contours of dimensionless temperature (θ) for natural convection in a square cavity (Ra$=10^7$) with a fin at four representative positions for $L_p=0.2$, 0.35, and 0.5, respectively. The value of θ on the left wall and the fin is 1, whereas the value of θ on the right wall is zero, and the contour levels are incremented by 0.05. Since the Boussinesq approximation was adopted in this study, the energy equation does affect the momentum equation. Comparing Figures 7(*a*) and 3(*b*), a 0.2 L long fin at most positions only changes the temperature distribution locally and the rest of the cavity remains unaffected. This is because the primary vortex has not altered too much upon introduction of a 0.2 L long fin and the fin only changes the velocity distribution locally. As mentioned before, a fin at $S_p \leqslant 0.5$ can weaken the fluid motion in the area above the fin and thus decreased heat transfer capability is expected. The diminished temperature gradient indicated by the marked separation of the temperature contours above the fin is clearly seen for the fins of different lengths positioned at $S_p = 0.125$. The size of this zone of decreased heat transfer activity expands with the increase of the length of the fin. The temperature contours under the fin are more packed than those above the fin. This implies better heat transfer on the bottom surface of the fin than on the top surface when $S_p \leqslant 0.625$. When $S_p > 0.625$, the packed temperature contours are observed above the fin, whereas the separated temperature contours are now observed under the fin. This indicates that there is better heat transfer on the top surface of the fin compared to the bottom surface when $S_p > 0.625$. For longer fins, the temperature contours to the right of the fin are also affected by the introduction of the fin. Higher temperature gradients next to the right wall are observed while placing the fin close to two ends of the left wall compared to placing a fin at the middle of the left wall.

Variation of the Local Nusselt Number on the Walls of the Cavity. In order to evaluate how the presence of the fin affects the heat transfer rate along the hot (left) and cold (right) walls, it is necessary to observe the variations of the local Nusselt numbers on these walls. These are defined as:

$$\mathrm{Nu}_l = -\left.\frac{\partial \theta}{\partial X}\right|_{X=0}, \tag{8}$$

$$\mathrm{Nu}_r = -\left.\frac{\partial \theta}{\partial X}\right|_{X=1}, \tag{9}$$

with the subscripts l and r referring to the left and right walls, respectively.

In order to present the local Nusselt number variation, the use of the S coordinate system was adopted. For example, variation of the Nu_l with Y is plotted in graphical form as Nu_l versus $S(0 \sim 1)$. The variation of Nu_r with Y can be treated similarly as Nu_r versus $S(2 \sim 3)$, going from the bottom to top on the right wall. Figure 8 shows the variation of the local Nusselt numbers along the left and right walls of the cavity with fins at different positions for $\mathrm{Ra} = 10^4$. The variation of the local Nusselt numbers along the left and right walls without a fin are also plotted as the thickest solid lines and denoted by the symbol NP (that stands for no partition). The variation of the local Nusselt numbers on the left and right walls for the case with no fin are nearly identical.

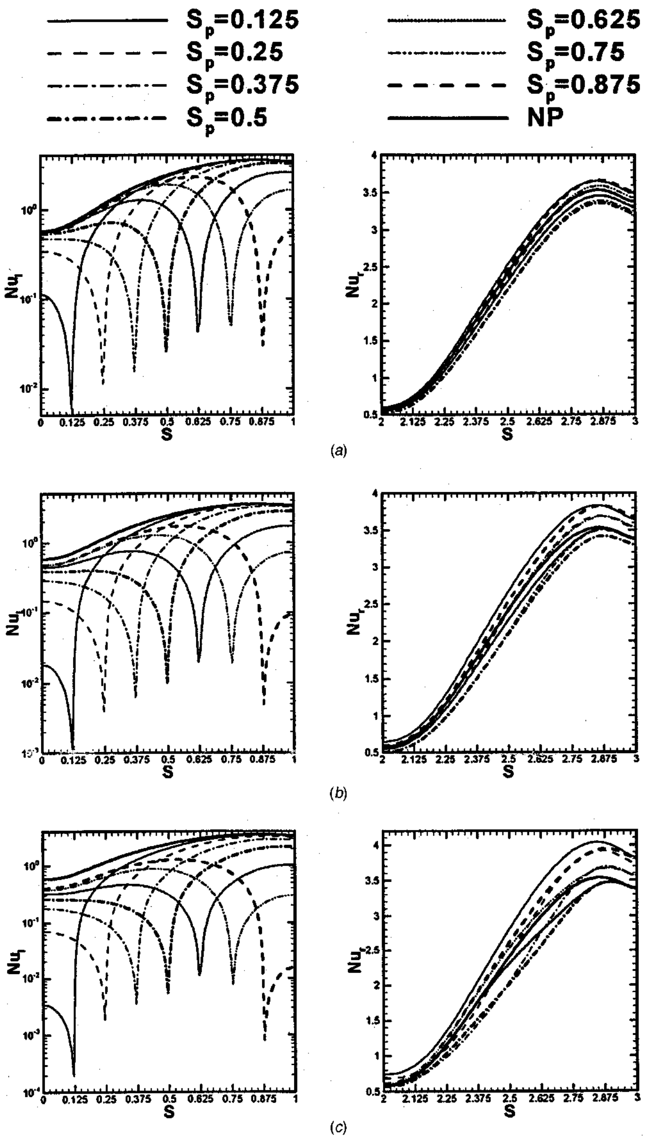

Fig. 8 Variation of the local Nusselt number along the left and right walls of the cavity with fins at different positions ($\mathrm{Ra} = 10^4$): (*a*) $L_p = 0.2$, (*b*) $L_p = 0.35$, and (*c*) $L_p = 0.5$

From Fig. 8, one can observe that placing a fin on the left hot wall always reduces the local Nusselt number on that wall appreciably. This is because the fin blocks the flow near it, thus giving rise to varied flow patterns on the top and bottom of the fin depending on the length and position of the fin. For the case of a fin placed at the middle of the left wall, the streamlines on its both sides appear fairly symmetric (middle column of Fig. 4) and the local Nusselt numbers on the left wall both above and below the fin are nearly identical. If a fin is placed near the top insulated wall (left column of Fig. 4), the development of the boundary layer on the left wall below the fin is unaltered, however a significant separated region (low velocity zone) is observed between the fin and the top insulated wall. The variation of the local Nusselt numbers on these two parts of the left wall in Fig. 8 are directly linked to the two distinct flow patterns causing significant heat transfer reduction above the fin and less marked or negligible heat transfer reduction below the fin. For a fin placed near the bottom insulated wall (right column of Fig. 4), a separated region is observed under the fin, however the development of the boundary layer on the left wall above the fin resumes after the fluid travels over the fin. The variation of the local Nusselt numbers above and under the fin (Fig. 8) are directly linked to these two distinct flow patterns causing significant heat transfer reduction under the fin and less marked or negligible heat transfer reduction above the fin. It is observed that for a fin placed at a fixed position, the local Nusselt number near the fin decreases with the increase of the fin's length. For shorter fins, the fin has very little influence on the area that is far from the fin. For example, for a fin at $S_p = 0.125$, the local Nusselt number distribution at the bottom of the left wall is very close to the case without a fin. Even though a fin attached on the left hot wall always reduces the heat transfer on the left wall, this does not mean that the heat flux brought into the cavity will be reduced because the thermally conductive fin can also transfer heat into the cavity. When comparing all the plots in the right column of Fig. 8, one can see that placing a fin on the left hot wall has most remarkable effects on the local Nusselt number on the right cold wall with the increase of the fin's length. This is directly related to the effect of the length of the fin in modifying the streamlines and the thermal boundary layer that is formed adjacent to the right wall. As expected, a longer fin will give rise to the most marked departure for the case with no fin. The presence of a fin on the left wall has more marked influence on the top half than the bottom half of the right wall. A fin placed near the both ends of the left wall ($S_p = 0.125$ and 0.875) can enhance heat transfer on the right wall. Placing a fin at S_p

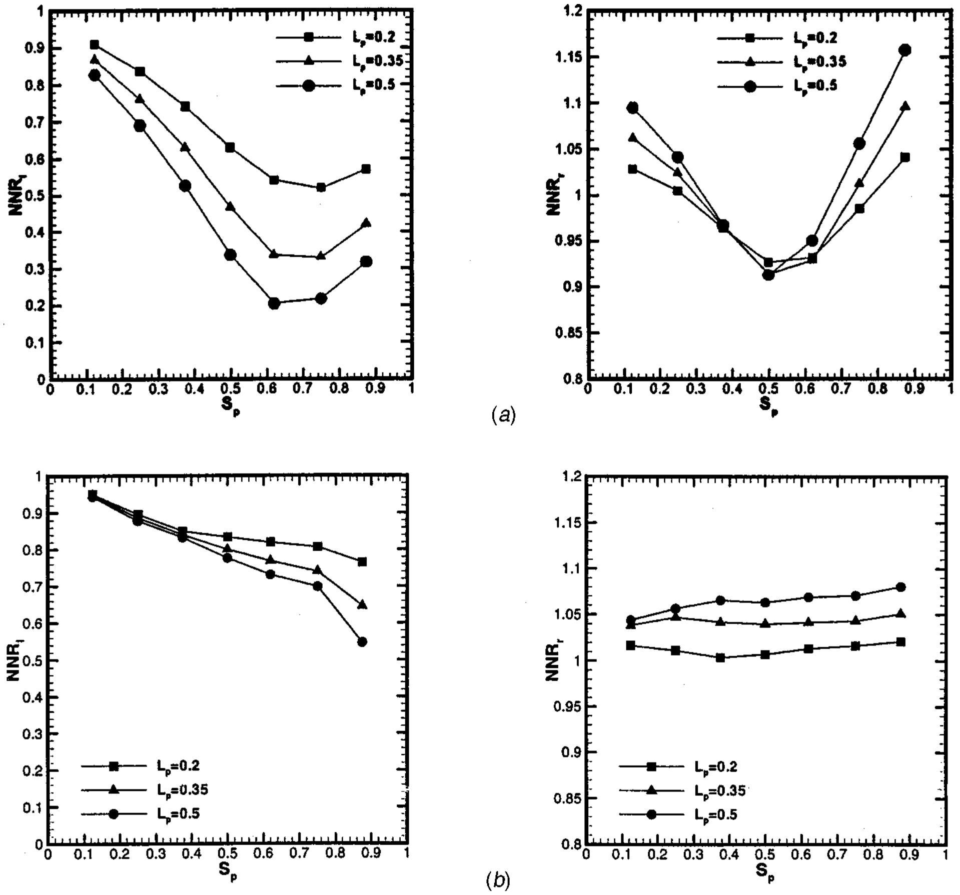

Fig. 9 Variation of the NNR along the left and right walls of the cavity with fins at different positions: (*a*) Ra=10^4 and (*b*) Ra=10^7

=0.375, 0.5 and 0.625 can reduce heat transfer on the right wall. Placing a 0.5 L fin anywhere except at $S_p=0.5$ and 0.625 can enhance heat transfer on the top half of the right wall.

The variation of the local Nusselt number on the hot left and cold right walls for $\mathrm{Ra}=10^7$ is very similar to other cases with low Rayleigh number. However, some details worthy of discussion need explanation. The symmetric variations of the local Nusselt number above and under the fin for a fin placed at the middle of the left wall that was observed in Fig. 8 no longer exists for this case of high Ra number. This is directly related to the non-symmetric streamline patterns of Fig. 5 (second row from top) and the ensuing temperature field of Fig. 7 (second row from top). The asymmetry of the Nusselt number for fins placed near the two insulated walls is similar to those discussed in Fig. 8, however it is more pronounced for this high Ra case.

Variation of the Mean Nusselt Number on the Walls of the Cavity. Another variable utilized to evaluate the heat transfer rate is the mean Nusselt number for every wall. Since the top and bottom walls are insulated, the mean Nusselt numbers on these walls are zero. The mean Nusselt numbers, $\overline{\mathrm{Nu}}$, for the left and right walls were obtained by integrating Eqs. 8 and 9, as given below:

$$\overline{\mathrm{Nu}_l}=\int_0^1 \mathrm{Nu}_l dY, \tag{10}$$

$$\overline{\mathrm{Nu}_r}=\int_0^1 \mathrm{Nu}_r dY. \tag{11}$$

For a cavity without a fin with the top and bottom walls insulated, the mean Nusselt on the left wall equals that on the right wall according to the conservation of energy for the system. With a fin placed on the hot wall, the difference between the two mean Nusselt numbers signifies the enhancing or degrading role of the fin in transferring heat from the hot wall to the cold wall.

In order to study the effect of the fin on the average heat transfer rate for the left and right walls of the cavity, we introduce a variable called the Nusselt Number Ratio (NNR), with its definition given as:

$$\mathrm{NNR}=\frac{\overline{\mathrm{Nu}}|_{\text{with a fin}}}{\overline{\mathrm{Nu}}|_{\text{without a fin}}}. \tag{12}$$

Thus, NNR for every wall (NNR_l and NNR_r) can be obtained according to Eq. 12. Value of NNR greater than 1 indicates that the heat transfer rate is enhanced on that surface, whereas reduction of heat transfer is indicated when NNR is less than 1. Thus, the mean Nusselt number for every wall can be obtained from the product of NNR and mean Nusselt number for that wall in Table 1.

Figures 9(*a–b*) show the variations of NNR for the left and right walls with fin's position for three different lengths of the fin, $L_p=0.2$, 0.35, and 0.5 for $\mathrm{Ra}=10^4$ and 10^7, respectively. Based on these figures, it is observed that placing a fin on the left wall always reduces heat transfer on the left wall, since NNR_l is always less than 1. The deviation of the mean Nusselt numbers on the left wall for different lengths of the fin increases with the increase of S_p. The mean Nusselt number for the left wall becomes smaller with the increase of the fin's length, regardless of the Rayleigh number. This is because the fin can block the flow near the fin and reduce the corresponding convection in that area.

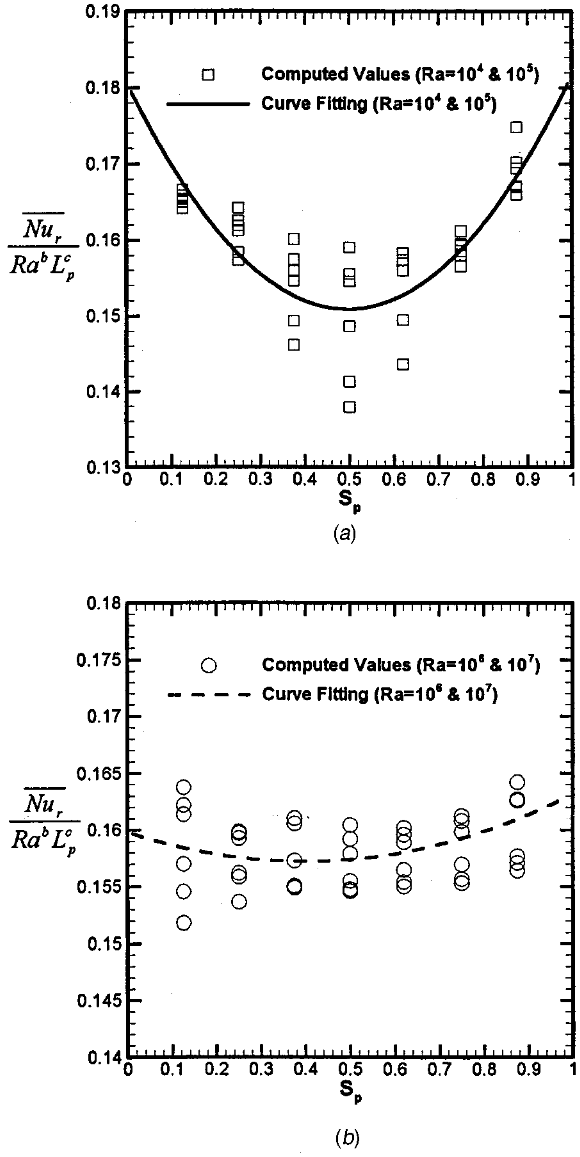

Fig. 10 Curve fitting for the mean Nusselt number: (*a*) Ra $=10^4$ and 10^5, (*b*) Ra$=10^6$ and 10^7

Upon comparing the diagrams on the left column of Fig. 9, one can see that the effect of the fin's length on NNR becomes less remarkable with the rise of the Rayleigh number due to the fact that these three curves come closer. This is because the effect of the hot fin heating the flow and enhancing the primary vortex can compensate the effect of the fin blocking the flow.

Upon comparing the diagrams on the right column of Fig. 9, it is evident that the mean Nusselt number on the right wall was also affected by the position of the fin, length of the fin and the Rayleigh number. For the cases with Ra$=10^4$, the mean Nusselt number of the right wall exhibits insensitivity to the length of the fin if the fin is placed near the middle of the left wall. Also notice that placing a fin at the middle of the left wall has more remarkable effect on the mean Nusselt number on the right wall compared to placing it on the two ends of the left wall. For the cases with Ra$=10^5$ and 10^6, a 0.35 L and 0.5 L fin placed at most positions on the left wall can enhance heat transfer on the right wall. For the case with Ra$=10^7$, placing three different lengths of the fin at any position on the left wall enhances heat transfer on the right wall. The NNR$_r$ becomes more insensitive to the position of the fin on the left wall with the rise of the Rayleigh number.

One should note that for low Rayleigh numbers when convection is not dominant, the isothermal fin is the main source of energy that is brought into the cavity. For instance, for Ra$=10^4$, a 0.5 L fin placed at the middle of the left wall is responsible for bringing in about 58 percent of the energy into the cavity. The same fin is responsible for about 30 percent of the energy for Ra$=10^7$. In general, significant energy can be routed through the fin if the fin is located on the lower half of the left hot wall.

Correlation of the Mean Nusselt Number on the Right Wall. Since the top and bottom walls of the cavity are insulated, the mean Nusselt number on the right wall ($\overline{\mathrm{Nu}}_r$) indicates the heat transfer capability of the system. A correlation in the form of $\overline{\mathrm{Nu}}_r$ as a function of the Rayleigh number, the length of the fin and the position of the fin was obtained. Based on the trends exhibited in Fig. 10, the general form of the correlation was assumed to be:

$$\overline{\mathrm{Nu}}_r=(a_1S_p^2+a_2S_p+a_3)\mathrm{Ra}^bL_p^c. \tag{13}$$

For a square cavity with a fin placed on the left wall when Ra $=10^4\sim10^5$, the recommended correlation is of the form:

$$\overline{\mathrm{Nu}}_r=(0.1213S_p^2-0.1202S_p+0.1807)\mathrm{Ra}^{0.2979}L_p^{0.0656} \tag{14}$$

For Ra$=10^6\sim10^7$, the recommended correlation is of the form:

$$\overline{\mathrm{Nu}}_r=(0.0163S_p^2-0.0129S_p+0.1598)\mathrm{Ra}^{0.2979}L_p^{0.0656}. \tag{15}$$

The values of the coefficients *a*'s, *b*, and *c* are summarized in Table 2. The general trends of the correlation is shown in Fig. 10 where the computed mean Nusselt number for the right wall and the curve fitting correlations are presented.

Conclusions

1. Placing an isothermal horizontal fin on the left hot wall of a differentially heated cavity generally modifies the clockwise rotating primary vortex that is established due to natural convection. Depending on the Rayleigh number, length of the fin and its position, a number of recirculation regions can be formed above and under the fin.
2. Two competing mechanisms that are responsible for flow and thermal modifications are observed. One is the hydrodynamic blockage effect of the fin that directly depends on the length of the fin, whereas the other is due to the extra heating of the fluid that is offered by the fin. The extra heating effect is promoted as the Rayleigh number increases.
3. Viewing the minimum value of the stream function as a measure of the strength of flow modification, it is shown that for high Rayleigh numbers the flow field is enhanced regard-

Table 2 Correlation coefficients a_1, a_2, a_3, b, and c

		a's				
		a_1	a_2	a_3	b	c
Ra$=10^4\sim10^5$	AV*	0.1213	−0.1202	0.1807	0.2979	0.0656
	SD**	0.0585	0.0552	0.0063	0.0173	0.0341
Ra$=10^6\sim10^7$	AV	0.0163	−0.0129	0.1598	0.2979	0.0656
	SD	0.0129	0.016	0.006	0.0173	0.0341

*AV: Average
**SD: Standard Deviation

less of the fin's length and position. This suggests that the extra heating mechanism offsets the hydrodynamic blockage effect and even contributes to the strengthening of the flow field as the Ra number increases.

4. The symmetric and asymmetric variations of the Nusselt numbers on the hot wall were directly linked to the streamline patterns, presence of the recirculations zone(s) and development of the thermal boundary layers above and below the fin. As for the variations of the Nusselt numbers on the cold wall, less marked yet distinguishable modifications were observed.
5. Heat transfer capacity on the anchoring hot wall was always degraded, however heat transfer on the cold wall without the fin can be promoted for high Rayleigh numbers and with the fins placed in the vicinity of the insulated walls. It was noted that significant energy can be routed through the fin if the fin is placed on the lower half of the left wall.

Nomenclature

l_p = length of the fin, m
L = length of the cavity, m
L_p = dimensionless length of the fin, i.e., l_p/L
NNR = Nusselt number ratio, defined by Eq. 17
Nu = local Nusselt number, defined by Eqs. 13 and 14
$\overline{\text{Nu}}$ = average or mean Nusselt number, defined by Eqs. 15 and 16
s = coordinate adopted for distance along the walls, m
S = dimensionless coordinate, i.e., $S=s/L$
T_c = temperature of the right (cold) wall, K
T_h = temperature of the left (hot) wall, K

Greek Symbols

θ = dimensionless temperature, i.e., $(T-T_c)/(T_h-T_c)$

Subscripts

l, r = related to the left and right walls
p = related to the fin (partition)

References

[1] Ostrach, S., 1988, ''Natural Convection in Enclosures,'' ASME J. Heat Transfer, **110**, pp. 1175–1190.
[2] Gebhart, B., Jaluria, Y., Mahajan, R. L., and Sammakia, B., 1988, *Buoyancy-Induced Flows and Transport*, Hemisphere Pub. Co., New York, NY.
[3] Shakerin, S., Bohn, M., and Loehrke, R. I., 1988, ''Natural Convection in an Enclosure with Discrete Roughness Elements on a Vertical Heated Wall,'' Int. J. Heat Mass Transf., **31**(7), pp. 1423–1430.
[4] Frederick, R. L., 1989, ''Natural Convection in an Inclined Square Enclosure with a Partition Attached to its Cold Wall,'' Int. J. Heat Mass Transf., **32**(1), pp. 87–94.
[5] Frederick, R. L., and Valencia, A., 1989, ''Heat Transfer in a Square Cavity with a Conducting Partition on its Hot Wall,'' Int. Commun. Heat Mass Transfer, **16**, pp. 347–354.
[6] Scozia, R., and Frederick, R. L., 1991, ''Natural Convection in Slender Cavities with Multiple Fins Attached on an Active Wall,'' Numer. Heat Transfer, Part A, **20**, pp. 127–158.
[7] Facas, G. N., 1993, ''Natural Convection in a Cavity with Fins Attached to Both Vertical Walls,'' J. Thermophys. Heat Transfer, **7**(4), pp. 555–560.
[8] Nag, A., Sarkar, A., and Sastri, V. M. K., 1993, ''Natural Convection in a Differentially Heated Square Cavity with a Horizontal Partition Plate on the Hot Wall,'' Comput. Methods Appl. Mech. Eng., **110**, pp. 143–156.
[9] Lakhal, E. K., Hasnaoui, M., Bilgen, E., and Vasseur, P., 1997, ''Natural Convection in Inclined Rectangular Enclosures with Perfectly Conducting Fins Attached on the Heated Wall,'' Heat Mass Transfer, **32**, pp. 365–373.
[10] Bilgen, E., 2002, ''Natural Convection in Enclosures with Partial Partitions,'' Renewable Energy, **26**, pp. 257–270.
[11] Shi, X., and Khodadadi, J. M., 2002, ''Laminar Fluid Flow and Heat Transfer in a Lid-Driven Cavity Due to a Thin Fin,'' ASME J. Heat Transfer, **124**(6), pp. 1056–1063.
[12] Patankar, S. V., 1980, *Numerical Heat Transfer and Fluid Flow*, Hemisphere Pub. Co., Washington, DC.
[13] Hayase, T., Humphrey, J. A. C., and Grief, R., 1992, ''A Consistently Formulated QUICK Scheme for Fast and Stable Convergence Using Finite-Volume Iterative Calculation Procedures,'' J. Comput. Phys., **98**, pp. 108–118.
[14] De Vahl Davis, G., and Jones, L. P., 1983, ''Natural Convection in a Square Cavity: A Comparison Exercise,'' Int. J. Numer. Methods Fluids, **3**, pp. 227–248.
[15] De Vahl Davis, G., 1983, ''Natural Convection of Air in a Square Cavity: A Bench Mark Numerical Solution,'' Int. J. Numer. Methods Fluids, **3**, pp. 249–264.
[16] Shi, X., 2003, ''Forced and Natural Convection Heat Transfer within Enclosures with Fixed and Moving Fins and Partitions,'' Ph.D. thesis, Department of Mechanical Engineering, Auburn University.

Effects of Radiative Transfer Modeling on Transient Temperature Distribution in Semitransparent Glass Rod

Zhiyong Wei
e-mail: gte384w@prism.gatech.edu

Kok-Meng Lee
e-mail: kokmeng.lee@me.gatech.edu

Serge W. Tchikanda

The George W. Woodruff School of Mechanical Engineering,
Georgia Institute of Technology,
Atlanta, GA 30332-0405

Zhi Zhou
e-mail: zhizhou@ofsoptics.com

Siu-Ping Hong
e-mail: shong@ofsoptics.com

OFS,
Norcross, GA 30071

This paper presents a method of modeling the radiative energy transfer that takes place during the transient of joining two concentric, semitransparent glass cylinders. Specifically, we predict the two-dimensional transient temperature and heat flux distributions to a ramp input which advances the cylinders into a furnace at high temperature. In this paper, we discretize the fully conservative form of two-dimensional Radiative Transfer Equation (RTE) in both curvilinear and cylindrical coordinate systems so that it can be used for arbitrary axisymmetric cylindrical geometry. We compute the transient temperature field using both the Discrete Ordinate Method (DOM) and the widely used Rosseland's approximation. The comparison shows that Rosseland's approximation fails badly near the gap inside the glass media and when the radiative heat flux is dominant at short wavelengths where the spectral absorption coefficient is relatively small. Most prior studies of optical fiber drawing processes at the melting point (generally used Myers' two-step band model at room temperature) neglect the effects of the spectral absorption coefficient at short wavelengths ($\lambda < 3\ \mu$m)*. In this study, we suggest a modified band model that includes the glass absorption coefficient in the short-wavelength band. Our results show that although the spectral absorption coefficient at short wavelengths is relatively small, its effects on the temperature and heat flux are considerable.* [DOI: 10.1115/1.1565081]

Keywords: *Computational, Cylinder, Heat Transfer, Radiation, Transient*

1 Introduction

The manufacture of optical fibers often requires joining two concentric glass cylinders, in which the partially joined cylinders initially at room temperature are moved into the furnace at a temperature typically in the neighborhood of the glass melting temperature (between 1500 K to 2500 K). Since the glass conductivity is very small, radiation is the dominant mode of heat transfer. During the transient, sufficiently large temperature gradient could result in cracking at the interface. As direct measurement of the temperature field is often impossible, the design and control of the joining process has been accomplished by extensive trial-and-error methods. The ability to predict the thermally induced stresses caused by the transient heating offers a means to optimize the design and improve process speed, which requires a good understanding of the transient temperature distribution. In this paper, numerical methods are developed to predict the transient temperature field and its gradient within the semitransparent glass.

An accurate prediction of the temperature distribution depends on the solution method, and the approximation of the models describing the radiative properties of the medium for a given set of boundary conditions. Over the past two decades, a number of researchers have investigated methods to predict energy transport in glass processing, most notably in applications of optical fiber drawing. Because glass is semitransparent to radiation, emission and absorption exist throughout the medium. The simplest approach, perhaps, has been to assume the participating medium is optically thick (or commonly known as the Rosseland's approximation) such that the radiative energy contributions from the boundary and the far away portions of the medium can be neglected. Rosseland's optically thick approximation reduces the total radiative flux to a simple temperature diffusion term; an effective radiative conductivity can then be used. This approach has been used by a number of researchers (Paek and Runk [1]; Homsy and Walker [2]; Myers [3]; Choudhury et al. [4]) to reduce the overall problem to a more tractable form in modeling multi-dimensional radiative heat transfer in glass. Homsy and Walker [2] pointed out that the Rosseland's assumption would break down at the surface, but no method was suggested to correct for the errors. An alternative approach is to solve the radiative transfer and the energy equations simultaneously using numerical methods. Lee and Viskanta [5] investigated combined conduction and radiation in a one-dimensional glass layer. By comparing the discrete ordinate method and the Rosseland approximation method, Lee and Viskanta [5] concluded that the diffusion approximation greatly underpredicts the temperature and heat flux when the thickness or the opacity of the layer is small. In a different study, Yin and Jaluria [6] employed a zonal method to investigate the radiative exchange within the neck-down profile of a glass perform for an assumed radial temperature profile. Their simulation results suggested that Rosseland's approximation underestimates the heat flux only when the radial temperature variation within the preform is substantial as compared with the zonal method. In these studies, only steady state solutions were considered.

The solution to the radiative transfer equation requires an appropriate model to describe the spectral absorption coefficient of the glass medium. Myers [3] introduced a two-step band model to describe the spectral absorption coefficients of a fused silica glass, which has been commonly used in the prediction of radiative transfer in optical fiber drawing processes. Myers' band model neglects the absorption at short wavelengths ($\lambda < 3.0\ \mu$m), which has a relatively small value about $0.001 \sim 0.3\ \text{cm}^{-1}$ for semitransparent glasses. However, the spectral intensity of a blackbody radiation given by Planck's function (see for example Modest [7])

Contributed by the Heat Transfer Division for publication in the JOURNAL OF HEAT TRANSFER. Manuscript received by the Heat Transfer Division June 3, 2002; revision received January 2, 2003. Associate Editor: J. P. Gore.

suggests that more than 60% of radiative energy concentrates in the band $0.2\ \mu\text{m} \leqslant \lambda < 2.8\ \mu\text{m}$ near the melting temperature range of glass ($1500\ \text{K} \sim 2500\ \text{K}$). The effects of radiation absorption could be considerable in this short-wavelength band, although the absorption coefficient is small. Since the values for the spectral absorption coefficient of fused-silica glass at temperatures near the softening point were not known, Myers' two-step band model has been based on data taken at room temperature. Recent experiments (Endrys [8]; Nijnatten et al. [9,10]) on typical glasses suggested that the absorption coefficient in the $2.8\ \mu\text{m} \leqslant \lambda < 4.8\ \mu\text{m}$ band near the melting temperature is generally 10~25% lower than that at a room temperature of 25°C.

In this paper, we use the discrete ordinate method (DOM) to analyze the radiative transfer during the transient stage as two partially joined, concentric glass cylinders are moved into the furnace. Jamaluddin and Smith [11] used the DOM to predict radiative transfer in gas flame in axi-symmetric cylindrical enclosures. They showed that the results for DOM with S_4 quadrature approximation was in good agreement with the experimental data, and that S_6 approximation did not provide significantly better predictions but required 60% more computer time. More recently, Lee and Viskanta [12] used DOM to predict the spectral radiative transfer in a condensed cylindrical medium and have obtained good agreement with the exact solutions. The main contributions of this paper are summarized as follows:

1. We present the radiation model and the solution method for predicting the two-dimensional transient temperature gradient in joining two concentric glass cylinders as they are advanced into a furnace at a high temperature. The model and solution method serve as a basis for the prediction of the thermally induced stress intensity factors at the tip of the interface.
2. Unlike prior works by others (Jamaluddin and Smith [11], Lee and Viskanta [12]), which used grid face areas in the discretized equation in orthogonal cylindrical coordinates system, we present the fully conservative form of the two-dimensional RTE in both curvilinear and cylindrical coordinates systems so that the numerical scheme can be used for arbitrary axisymmetric cylindrical geometries.
3. We compare the popularly used Rosseland approximation and the numerical DOM in solving RTE for a two-dimensional transient heat transfer problem. Chung et al. [13] compared the accuracy between the Rosseland and P-1 approximations. Since the P-1 approximation drops higher order terms of the Fourier series for intensities, deviation from the exact solution (especially when the dimension of the glass is small) is considerable. Unlike prior comparison by Chung et al. [13] that consider steady-state one-dimensional glass layer for which the exact integration solution is available, this study offers additional insights for the two-dimensional cylindrical glass rod with an interior gap.
4. We show the considerable effect of spectral absorption coefficient at short wavelengths ($0.2\ \mu\text{m} \leqslant \lambda < 2.8\ \mu\text{m}$) in predicting the temperature field, which has been neglected in the previous studies on fiber draw process.

2 Analysis

Consider radiative transfer in a glass rod formed by a pair of concentric fused-silica glass cylinders as shown in Fig. 1. The gap between the two cylinders is very small as compared to the diameter of the cylinders. As the rod (initially at room temperature) is translated axially at a relatively slow, constant speed into a cylindrical furnace at a specified temperature profile, the cylinders become soft and join together at the gap. The interest here is to predict the transient temperature field of the glass rod as it enters the furnace. In addition, it is desired to determine the temperature gradient near the tip of the gap.

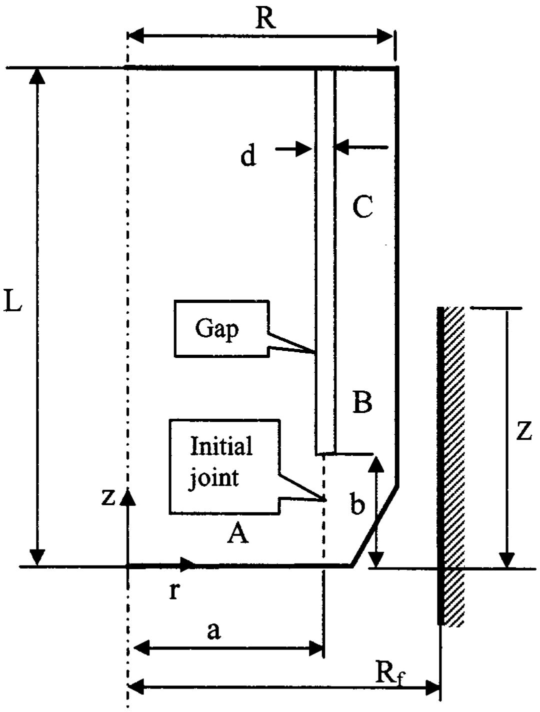

Fig. 1 Schematics illustrating the transient process

Glass is considered a homogeneous material, and scattering of radiation can be neglected in comparison to absorption and emission (Viskanta [14]). It is semitransparent to radiation in the spectral range $0 < \lambda < 5\ \mu\text{m}$ and is almost opaque beyond $5\ \mu\text{m}$. In addition, the following assumptions are made in the following formulation:

1. The system is axisymmetric and two-dimensional.
2. The refractive index of the medium is uniform and does not depend on temperature in the considered range.
3. The furnace walls are gray and diffuse.
4. We consider the case where the inner and outer surfaces at the glass interface and in the gap are diffuse for radiation reflection and transmission since the glass rod (called preform in industry) is not polished.
5. During the transient, the glass has not melted. The effects of the small deformation of the glass rod on the view factors can be neglected.

2.1 Formulation. The radiative transfer in a spectrally absorbing-emitting medium is modeled using the following radiative transfer equation (RTE):

$$\mathbf{s}\cdot\nabla I_\lambda(\mathbf{r},\mathbf{s}) = \kappa_\lambda[n_\lambda^2 I_{b\lambda}(T) - I_\lambda(\mathbf{r},\mathbf{s})] \tag{1}$$

where the spectral radiative intensity $I_\lambda(\mathbf{r},\mathbf{s})$ is a function of the position vector $\mathbf{r}$, orientation vector $\mathbf{s}$, and wavelength λ; $I_{b\lambda}(T)$ is the spectral intensity of a blackbody radiation given by Planck's function; κ_λ is the spectral absorption coefficient; and n_λ is the spectral index of refraction.

The divergence of the spectral radiation heat flux can be obtained by integrating Eq. (1) over the whole solid angle ($\Omega = 4\pi$), which yields

$$\nabla\cdot\mathbf{q}_\lambda = 4\pi\kappa_\lambda n_\lambda^2 I_{b\lambda}(T) - \kappa_\lambda \int_{\Omega=4\pi} I_\lambda(\mathbf{r},\mathbf{s})\, d\Omega \tag{2}$$

By solving the RTE for $I_\lambda(\mathbf{r},\mathbf{s})$, the spectral radiative heat flux can be calculated from Equation (3):

$$\mathbf{q}_\lambda = \int_{\Omega=4\pi} I_\lambda(\mathbf{r},\mathbf{s})\mathbf{n}\cdot\mathbf{s}\, d\Omega \tag{3}$$

where **n** is the normal vector of the surface. The corresponding total radiative heat flux is then given by

$$\mathbf{q}=\int_0^\infty \mathbf{q}_\lambda d\lambda \tag{4}$$

Since there is no glass flow during the transient, the energy equation for control volume fixed with the glass (no advection) only includes conductive and radiative heat transfer as shown in Eq. (5):

$$\rho C\frac{\partial T}{\partial t}=-\nabla\cdot(-k\nabla T+\mathbf{q}) \tag{5}$$

subject to the boundary conditions

$$\partial T/\partial r=0 \quad \text{at } r=0 \tag{5a}$$

$$-k\mathbf{n}\cdot\nabla T=q_{\text{rad,opa}} \quad \text{at the surface} \tag{5b}$$

where ρ, C, and k are the glass density, thermal capacity and conductivity, respectively; **n** is the normal vector of the glass surface, $q_{\text{rad,opa}}$ is the net radiative flux at the opaque band on the glass surface. Natural convection of the air is neglected as compared with the radiative exchange.

The radiation intensity, through emission of the glass medium, depends on the temperature field and, therefore, cannot be decoupled from the overall energy equation. In addition, the solution to Eq. (1) depends on the approximation methods, the boundary conditions and the glass radiation properties. We discuss below two methods to solve for the transient temperature distribution; namely Rosseland approximation and a numerical scheme using the DOM.

2.2 Rosseland Approximation (RA). In the Rosseland's approximation (Modest [7]), the glass is assumed to be optically thick such that the radiative energy contributions from the boundary intensities and the far away portions of the medium are neglected. Thus, the total radiative flux can then be treated as a simple "radiative conduction" as follows:

$$\mathbf{q}\cong-\frac{16n^2\sigma T^3}{3\kappa_R}\nabla T=-k_{\text{rad}}\nabla T \tag{6}$$

where the Rosseland mean absorption coefficient κ_R can be evaluated from the integration of the spectral absorption coefficient with the weighting of $dI_{b\lambda}/dT$:

$$\frac{n^2}{\kappa_R}=\int_0^\infty\left(\frac{n_\lambda^2}{\kappa_\lambda}\right)\frac{dI_{b\lambda}}{dT}d\lambda \Bigg/ \int_0^\infty\frac{dI_{b\lambda}}{dT}d\lambda \tag{7}$$

It can be seen that κ_R depends on temperature.

The radiative conductivity in Eq. (6) can be added to the molecule conductivity in the energy Eq. (5) to account for the radiative heat transfer. Although the RA results in extremely convenient form, it is worth noting that this diffusion approximation is not valid near a boundary and the optically thick assumption should be used with caution.

2.3 Numerical Computation Using DOM. The radiative intensities can be solved numerically from Eq. (1) using the DOM (Modest [7]). Once the intensities have been determined in each time step, the corresponding radiative heat flux inside the glass medium or at a surface can be solved from Eqs. (3) and (4), and the temperature distribution from the energy equation, Eq. (5).

2.3.1 Discrete Ordinate Equation. In the DOM, Eq. (1) is solved for a set of directions $\hat{\mathbf{s}}_i$, $i=1,2,\ldots,N$. For an axisymmetric cylinder, the RTE along each of the N discrete directions can be expressed as

$$\frac{\mu^i}{r}\frac{\partial(rI_\lambda^i)}{\partial r}-\frac{1}{r}\frac{\partial(\eta^i I_\lambda^i)}{\partial\psi}+\xi^i\frac{\partial I_\lambda^i}{\partial z}=\kappa_\lambda[n_\lambda^2 I_{b\lambda}(T)-I_\lambda^i] \tag{8}$$

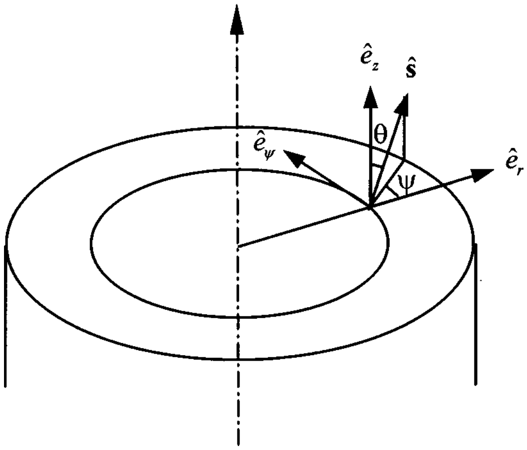

Fig. 2 Coordinates for two-dimensional axisymmetric cylinder

where μ^i, η^i, and ξ^i are the direction cosines of $\hat{\mathbf{s}}_i$ as shown in Fig. 2; and

$$\mu=\sin\theta\cos\psi \tag{9a}$$

$$\eta=\sin\theta\sin\psi \tag{9b}$$

$$\xi=\cos\theta \tag{9c}$$

Then the spectral radiative flux in **r** and **z** directions can be calculated from

$$q_{\lambda,r}=\sum_{i=1}^{N} w_i I_\lambda^i \mu^i \tag{10}$$

$$q_{\lambda,z}=\sum_{i=1}^{N} w_i I_\lambda^i \xi^i \tag{11}$$

and the total radiative fluxes from

$$q_r=\sum_{i=1}^{M} q_{\lambda_i,r} \tag{12}$$

$$q_z=\sum_{i=1}^{M} q_{\lambda_i,z} \tag{13}$$

where w_i is the quadrature weights associated with each direction $\hat{\mathbf{s}}_i$; N is the number of the ordinate directions; and M is the number of the wavelength bands. Based on the study of Jamaluddin and Smith [11], we choose the completely symmetric S_4-approximation quadrature which integrates the zero, first (half and full range), and second-order moments of the intensity distribution.

2.3.2 Transformations and Discretization of RTE. Due to the diameter variation near the bottom of the glass rod, Eq. (8) is cast into the fully conservative form in a general curvilinear coordinate system (α,β)

$$\frac{\partial[rB(\mu^i\alpha_r+\xi^i\alpha_z)I_\lambda^i]}{\partial\alpha}+\frac{\partial[rB(\mu^i\beta_r+\xi^i\beta_z)I_\lambda^i]}{\partial\beta}-B\frac{\partial(\eta^i I_\lambda^i)}{\partial\psi}=\kappa_\lambda rB[n_\lambda^2 I_{b\lambda}(T)-I_\lambda^i] \tag{14}$$

where α_r, α_z, β_r, and β_z are the grid metrics and the Jacobian B is given by

$$B=\frac{\partial(\alpha,\beta)}{\partial(r,z)}=\begin{vmatrix}\alpha_r & \alpha_z\\ \beta_r & \beta_z\end{vmatrix} \tag{15}$$

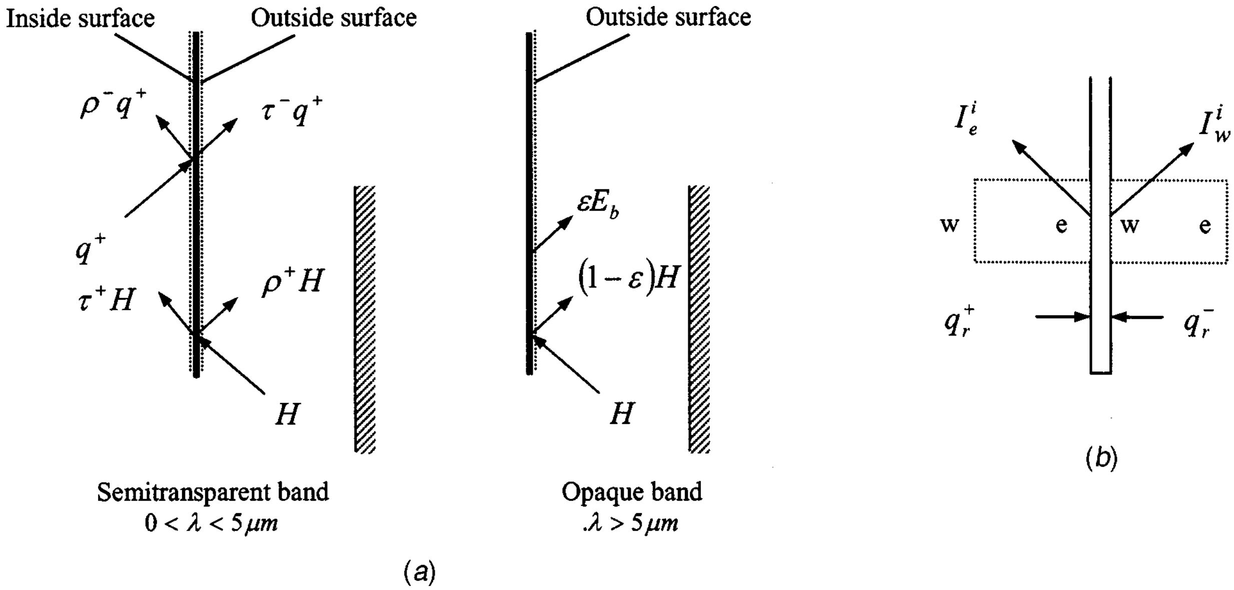

Fig. 3 Schematics illustrating the boundary conditions: (*a*) interface of the glass rod; and (*b*) gap between the two cylinders.

The angular derivative term in Eq. (14) can be discretized by using the direct differencing technique proposed by Carlson and Lathrop [15]:

$$\frac{\partial(\eta^i I_\lambda^i)}{\partial\psi} \cong \frac{\varsigma^{i+1/2} I_\lambda^{i+1/2} - \varsigma^{i-1/2} I_\lambda^{i-1/2}}{w_i} \tag{16}$$

where $i=1,2,\ldots,N_i$ for every fixed ξ. The geometrical coefficient $\varsigma^{i\pm1/2}$ depends only on the differencing scheme, which is independent of radiative intensity and has the following recursive formula:

$$\varsigma^{i+1/2} = \varsigma^{i-1/2} + \mu^i w_i \tag{17}$$

where $\varsigma^{1/2}=0$ when $\psi^{1/2}=0$.

Using finite volume method to discretize the transfer Eq. (14), we have

$$\begin{aligned}
&[rB(\mu^i\alpha_r + \xi^i\alpha_z)I_\lambda^i]_e - [rB(\mu^i\alpha_r + \xi^i\alpha_z)I_\lambda^i]_w \\
&\quad + [rB(\mu^i\beta_r + \xi^i\beta_z)I_\lambda^i]_n - [rB(\mu^i\beta_r + \xi^i\beta_z)I_\lambda^i]_s \\
&\quad - B\frac{(\varsigma^{i+1/2} I_\lambda^{i+1/2} - \varsigma^{i-1/2} I_\lambda^{i-1/2})}{w_i} \\
&= rB\kappa_\lambda(n_\lambda^2 I_{b\lambda} - I_\lambda^i)
\end{aligned} \tag{18}$$

where the subscripts *e*, *w*, *n*, and *s* indicate the values in the brackets are evaluated at the eastern, western, northern and southern grid faces, respectively. In order to reduce the number of unknowns, step scheme is used to relate the intensities on the grid faces with the nodal values. This spatial differencing scheme can guarantee the intensities positive.

2.3.3 Boundary Conditions. The boundary conditions for the DOM are given below.

Symmetry of the Cylinder. The i^{th} direction along the axis of the cylinder is given by

$$r=0: \qquad I_\lambda^i = I_\lambda^{i'}, \quad \mu^i = \mu^{i'} \tag{19}$$

where μ^i is the cosine of the angle between the i^{th} and the r directions.

Interface of the Glass Rod. Figures 3(*a*) and 3(*b*) illustrate the transmission and reflection at the interface of the glass rod, and at the gap between the cylinders respectively. The assumption that the interfaces of the preform are diffuse for both transmission and reflection implies the following:

$$r=R^-: \quad I_\lambda^i = \frac{J_\lambda^-}{\pi} = \frac{\tau_\lambda^+ H_\lambda + \rho_\lambda^- q_{\lambda,r}^+}{\pi} \qquad \mu^i<0 \tag{20a}$$

$$z=0^+: \quad I_\lambda^i = \frac{J_\lambda^-}{\pi} = \frac{\tau_\lambda^+ H_\lambda + \rho_\lambda^- q_{\lambda,z}^-}{\pi} \qquad \xi^i>0 \tag{20b}$$

$$z=L^-: \quad I_\lambda^i = \frac{J_\lambda^-}{\pi} = \frac{\tau_\lambda^+ H_\lambda + \rho_\lambda^- q_{\lambda,z}^+}{\pi} \qquad \xi^i<0 \tag{20c}$$

where ξ^i is the cosine of the angle between the i^{th} direction and the z direction; the superscripts "+" and "−" refer to the quantities at the outer and inner surfaces of the cylinder respectively; τ_λ, ρ_λ, and J_λ are the diffuse transmissivity, reflectivity and radiosity respectively; $q_{\lambda,r}^\pm$, $q_{\lambda,z}^\pm$ are the one-way spectral fluxes in the glass in the r and z directions respectively; and H_λ is the irradiation on the outer surface. Similarly, the radiosities at the surfaces just outside the cylinder

$$r=R^+: \quad J_\lambda^+ = \tau_\lambda^- q_{\lambda,r}^+ + \rho_\lambda^+ H_\lambda \tag{21a}$$

$$z=0^-: \quad J_\lambda^+ = \tau_\lambda^- q_{\lambda,z}^- + \rho_\lambda^+ H_\lambda \tag{21b}$$

$$z=L^+: \quad J_\lambda^+ = \tau_\lambda^- q_{\lambda,z}^+ + \rho_\lambda^+ H_\lambda \tag{21c}$$

The one-way spectral fluxes are calculated as follows:

$$q_{\lambda,r}^+ = \sum_{i=1}^{N/2} w_i I_\lambda^i \mu^i \qquad \mu^i>0 \tag{22a}$$

$$q_{\lambda,z}^- = \sum_{i=1}^{N/2} w_i I_\lambda^i |\xi^i| \qquad \xi^i<0 \tag{22b}$$

$$q_{\lambda,z}^+ = \sum_{i=1}^{N/2} w_i I_\lambda^i \xi^i \qquad \xi^i>0 \tag{22c}$$

The irradiation H_λ is the sum of the energy contribution from all the other surfaces that include the furnace, the cylinder outer surface, and the top and bottom disk openings.

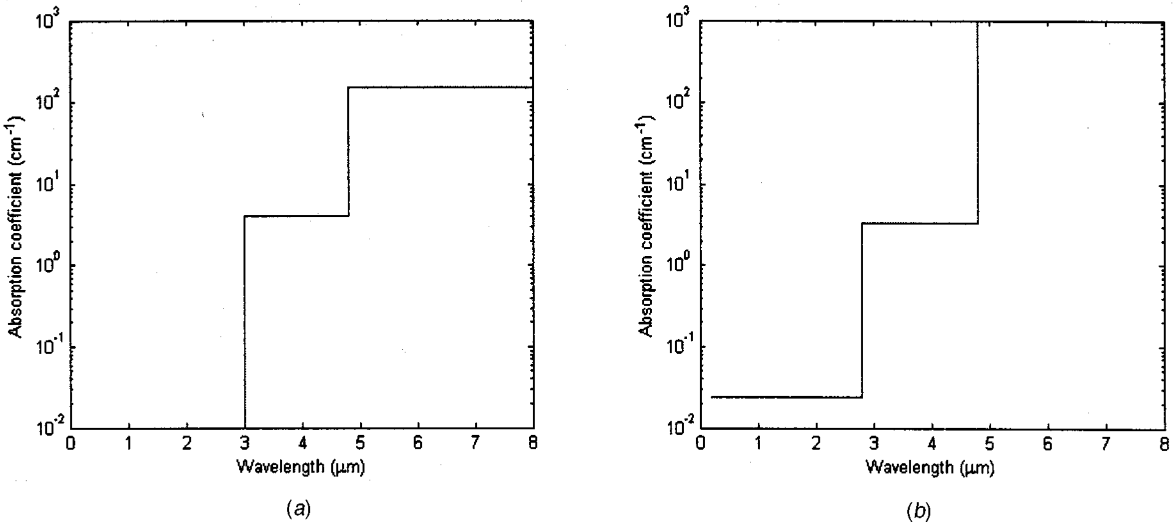

Fig. 4 Band model for absorption coefficient: (*a*) Myers' band model; and (*b*) band model used in this study.

$$H_{\lambda,i}=\sum_{j=1}^{K} J_{\lambda,j}F_{i-j} \tag{23}$$

where F_{i-j} is the diffuse view factor from surface element i to j. K is the total number of the surface elements. Equations (20) and (21) are for the semitransparent band. When $\lambda>5\ \mu\text{m}$ where the glass is considered to be opaque, the radiosities on the outer surface of the glass rod must be calculated from

$$J_{\lambda,i}=\varepsilon E_{b\lambda,i}+(1-\varepsilon)H_{\lambda,i} \tag{24}$$

where ε is the emissivity of the surface; and $E_{b\lambda,i}$ is the blackbody emissive power in the i^{th} surface element. Since the furnace is opaque, its radiosities are also calculated from Eq. (24) in all the spectral range.

Gap Between the Two Cylinders. The transmission and reflection on the gap interfaces between the two cylinders should be considered:

$$I^{i}_{\lambda,e}=\frac{q_r^{-}\tau^{-}\tau^{+}(\rho^{-}+\tau^{-}\rho^{+}\tau^{+})q_r^{+}}{\pi},\quad \mu^{i}<0 \tag{25a}$$

$$I^{i}_{\lambda,w}=\frac{q_r^{+}\tau^{-}\tau^{+}+(\rho^{-}+\tau^{-}\rho^{+}\tau^{+})q_r^{-}}{\pi},\quad \mu^{i}>0 \tag{25b}$$

Since the gap is very thin, it disappears when the glass melts.

2.3.4 Method of Solution. The computation of the intensity begins at the grids adjacent to the boundary surfaces along each specified direction with estimated boundary intensities and proceeds into the medium. Once the intensities in all the directions are obtained, the one-way fluxes at the boundaries are calculated and substituted into Eqs. (21*a*) to (21*c*), and the linear equations for the radiosities on the K surface elements of the outside enclosure are solved. Irradiations on the outer surface of the glass can now be calculated in Eq. (23) and are substituted into Eq. (20*a*) to (20c) to update the estimated inner surface radiosities. The one-way fluxes at the gap are also updated in the process. Iteration is needed for these updating processes.

The energy equation (Eq. (5)) was solved using the finite volume method with a fully implicit time marching scheme. Since the divergence of the radiative flux is strongly dependent on the temperature, an inner iteration for the temperature is carried out at each time step. The time derivative term is discretized by second-order one-sided difference scheme.

A common spatial grid is used in solving both the energy equation and the RTE. The grid is fixed on the glass rod and moves with the rod. The new position of the grid and the view factors of the glass surface are updated at each time step. In this way, there is no convection due to zone traverse since the glass does not move relative to the grid.

In this study, a uniform initial temperature of 300K was used. A sensitivity study showed that a time step of 1 second is enough for the transient problem. The grid spacing is more condensed near the bounding interfaces and the gap to account for the steep spatial change in the physical variables expected in these regions. A grid-refinement study showed that 155×37 (in z and r directions, respectively) grids is enough for the simulation.

2.4 Models of Radiative Properties. The accuracy of the solution to the RTE, or Eq. (1), depends significantly on the knowledge of the radiative properties. Specifically, care must be exercised to appropriately quantify the absorption coefficient of the glass and the reflectivity at the glass surfaces at the operating temperature.

Myers' Band Model for Spectral Absorption Coefficient. Figure 4(*a*) displays the Myers' bands [3] for the spectral absorption coefficient of fused silica glass. The bands commonly used in the prediction of radiative transfer in fiber drawing process are given below:

$$\kappa_\lambda=0,\quad \lambda\leqslant 3\ \ \mu\text{m};$$

$$\kappa_\lambda=4\ \ \text{cm}^{-1},\quad 3\ \ \mu\text{m}<\lambda\leqslant 4.8\ \ \mu\text{m};$$

$$\kappa_\lambda=150\ \ \text{cm}^{-1},\quad 4.8\ \ \mu\text{m}<\lambda\leqslant 8\ \ \mu\text{m};$$

Myers approximates the absorption coefficient at a small wavelength ($\lambda<3.0\ \mu\text{m}$) as zero, and consequently the radiative transfer at that band is not considered. Although the absorption coefficient is small (in the order of 0.001 to 0.3 cm^{-1}) for semitransparent glasses at this band, more than 60% of the emissive power concentrates in these shorter wavelengths for the glass at the (melting) temperature between 1000K and 2500K (see for example, blackbody emissive power spectrum in Modest [7]). Consequently, the effect of the absorption coefficient in this band on radiative transfer is considerable and cannot be neglected as will be shown in our results. It is worth noting that in Myers' band model, the absorption coefficient at the middle band ($3.0\ \mu\text{m}<\lambda<4.8\ \mu\text{m}$) was based on room temperature.

Modified Absorption Band Model Used in This Study. The spectral radiative energy is negligible for short wavelengths $\lambda < 0.2\ \mu$m in the operating temperature range. In the range of $0.2\ \mu\text{m} \leq \lambda < 2.8\ \mu$m, taking the multiple reflections into account, the average internal transmitivity τ_i of a silica glass slab can be calculated from the tabulated data of the apparent slab reflectivity and transmissivity in (Touloukian et al. [16]). With the approximation of

$$\tau_{i,\lambda} = e^{-\kappa_\lambda d} \tag{26}$$

where d is the thickness of the slab, the average absorption coefficient for $0.2\ \mu\text{m} \leq \lambda < 2.8\ \mu$m is determined to be 0.0243 cm^{-1}.

The absorption coefficients of typical glasses near the melting temperature were measured experimentally by Endrys [8] and Nijnatten et al. [9,10]; both published data suggest that the absorption coefficient in the $2.8\ \mu\text{m} \leq \lambda < 4.8\ \mu$m band near melting temperature is generally 10∼25% lower than that at a room temperature of 25°C. In this study, we estimate the absorption coefficient in the $2.8\ \mu\text{m} \leq \lambda < 4.8\ \mu$m band to be 3.4 cm^{-1}.

For $\lambda > 4.8\ \mu$m, the absorption coefficient is large and the spectral radiative flux is relatively small. Thus, the glass is considered opaque for that band. The modified band model is shown in Fig. 4(*b*). The optical thicknesses δ_λ for each band based on a rod radius of 4.5 cm are given as

$$\delta_\lambda = 0.1094, \quad 0.2\ \mu\text{m} < \lambda \leq 2.8\ \mu\text{m};$$

$$\delta_\lambda = 15.3, \quad 2.8\ \mu\text{m} < \lambda \leq 4.8\ \mu\text{m};$$

$$\delta_\lambda \rightarrow \infty, \quad 4.8\ \mu\text{m} < \lambda;$$

Surface Reflectivity. The external surface reflectivity can be calculated from the experimentally tabulated data for the air-to-media interface by the following curve fit (Egan and Hilgeman [17]):

$$\rho^+ = -0.4399 + 0.7099 \times n_m - 0.3319 \times n_m^2 + 0.0636 \times n_m^3 \tag{27}$$

The corresponding internal surface reflectivity for any diffuse media-to-air interface is given by

$$\rho^- = 1 - \frac{(1-\rho^+)}{n_m^2} \tag{28}$$

where n_m is the index of refraction of the medium. In this study, an average refractive index over the whole spectrum is used ($n_m = 1.42$). The consequent reflectivity and transmitivity of the external surface are 0.08 and 0.92, respectively. Those for the internal surface are 0.54 and 0.46.

3 Results and Discussions

In order to investigate the effects of the approximation methods and the models describing the glass radiative properties on the transient temperature distribution, a MATLAB program with C++ subroutines has been written to simulate the process shown in Fig. 1.

3.1 Validation. Exact integral solution of RTE is available for the one-dimensional semitransparent cylinder whose temperature and heat flux only varies in the radial direction (Kesten [18]). In order to validate our two-dimensional solution with this integral solution, the boundary conditions are modified in the codes to obtain an equivalent one-dimensional solution as follows: the diameter of the cylinder is constant; both the top and the bottom interfaces of the cylinder are assumed to be optically smooth with unity reflectivities; the temperatures in the glass and the furnace wall are assumed to be uniform so that the radiation intensity does not vary in the axial direction. Figure 5 shows comparisons of the S-4 DOM solutions and the integral solutions under different glass temperatures and cylinder diameters. The radial flux is normalized by the furnace blackbody emissive power. As shown in Fig. 5, the computed results agree with the exact solutions.

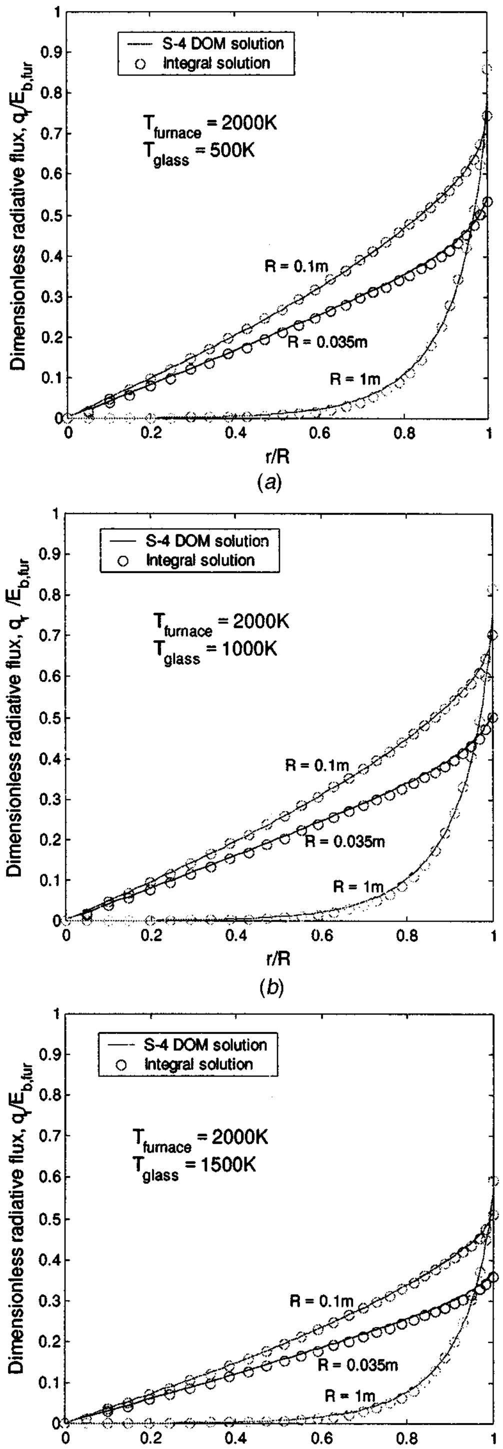

(*a*)

(*b*)

(*c*)

Fig. 5 Comparison of the DOM and the integral solutions (different cylinder diameters, T_f=2000 K): (*a*) T_g=500 K; (*b*) T_g=1000 K; and (*c*) T_g=1500 K.

3.2 Simulation and Discussion. In this study, we compare the following simulations:

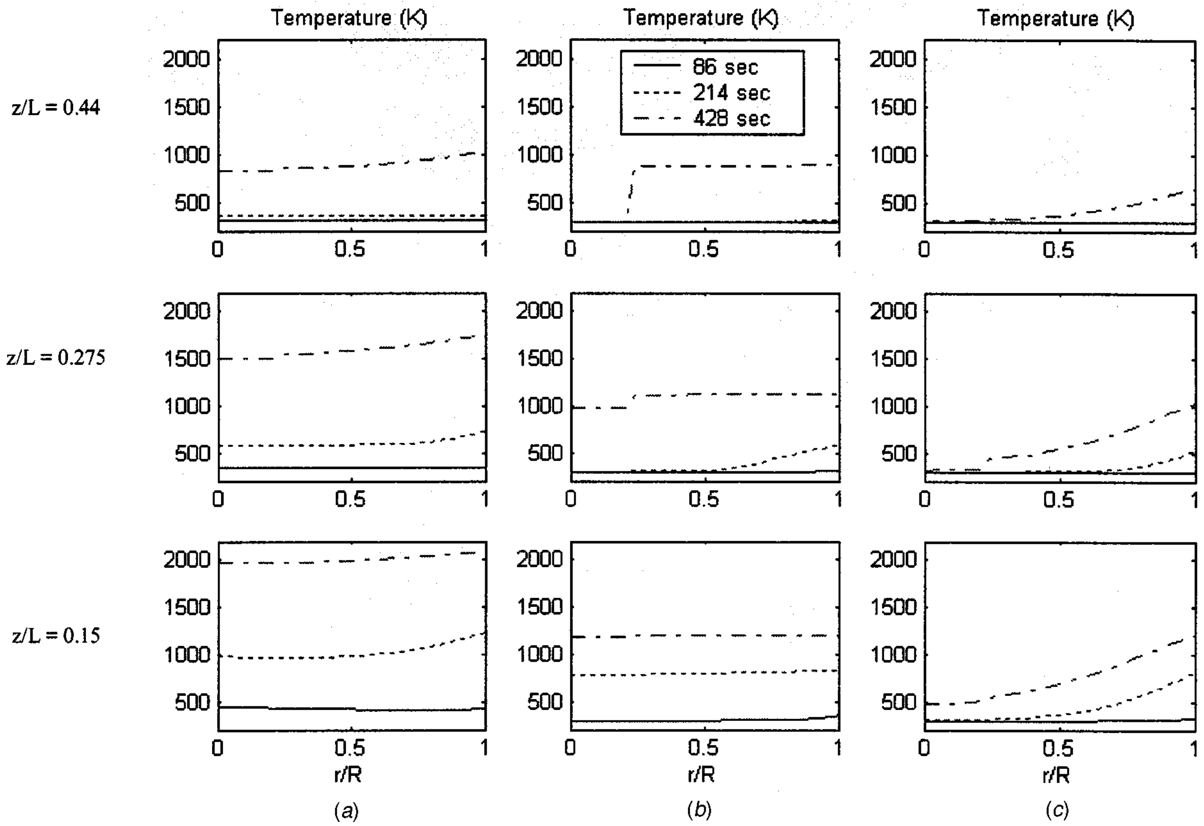

Fig. 6 Temperature distributions: (*a*) DOM, new band model; (*b*) Rosseland; and (*c*) DOM, Myers' band model.

1. DOM with a modified absorption band model given in Fig. 4(*b*)
2. RA method with the modified absorption band model
3. DOM with the Myers' band model given in Fig. 4(*a*).

Simulations 1 and 2 compare the effects of the optically thick assumption on the radiative transfer. Simulations 1 and 3 investigate the effects of absorption band models. Of particular interest is to compare the following:

1. The temperature distributions of the glass cylinders as displayed in Fig. 6,
2. The heat fluxes in both axial and radial directions at the tip of the gap in Fig. 7.
3. The transient temperature gradient at the tip of the gap in Fig. 8.

The values of the parameters used in the simulation are given in Table 1. The temperature distribution of the furnace is parabolic along its wall, and has a maximum value of 2400 K at the middle and a minimum value of 1500 K at both ends. The glass rod of length 0.5 m is fed with a constant speed of 0.75 mm/second into the furnace from $Z=0$ to $Z=0.5L$.

Figure 6 compares the temperature distributions at different locations and time. The total heat fluxes, which are defined in Eqs. (11–14), are compared in Fig. 7, where a positive axial flux indicates heat flowing in the positive *z* direction, but a positive radial flux indicates heat flowing toward the center of the rod (or negative *r* direction).

Effects of the Optically Thick Assumption. As shown in Fig. 6, the RA method highly underestimates the temperature due to the assumption that the glass medium is optically thick. Recall that the optical thickness is a function of both the characteristic dimension and the absorption coefficient. The followings are two causes of the error:

1. The characteristic dimension is relatively small, particularly inside the gap. These results are consistent with those in (Lee and Viskanta [5]) that was computed for glass slab; the RA underpredicts the radiative heat flux even when the thickness of the layer is larger than 1 m.
2. Although the absorption coefficient is relatively large in the middle band ($3.0\ \mu\text{m} < \lambda < 4.8\ \mu\text{m}$), most radiative energy concentrates in the low wavelength band that is characterized by a very small absorption coefficient of 0.0243 cm^{-1}.

Another obvious difference occurs at the gap between the cylinders. Based on several observations made in Figs. 7(*a*) and 7(*b*), the RA incorrectly predicts the heat flux as explained below:

1. When $t=86$ seconds (or $Z=0.13L$), the major portion of the glass rod is outside the furnace and thus the rod is heated mainly by the axial radiative flux from the bottom (indicated as "A" in Fig. 1). As shown in Fig. 7(*a*), the radial flux is negative (or flowing outward) since heat dissipates to the environment from the somewhat heated rod as expected. As a result, the radial temperature gradient at the tip of the gap is negative as reasonably predicted by the DOM with the modified band model in Fig. 8. Note that the RA underestimates the temperature and fails to predict this negative radial heat flux. Furthermore, it predicts an incorrect temperature gradient in the radial direction as shown in Fig. 8.
2. As the glass rod translates further into the furnace, the radial flux becomes positive (or flowing toward the center) and increases with *r*, as simulated by DOM with the modified band model, as expected. The axial flux, however, decreases with *r* because the view factor is larger at the center of the bottom than that at a larger radial distance. Note that since the axial flux is significantly larger than the radial flux at the tip of the gap, the temperature gradient in the radial direction

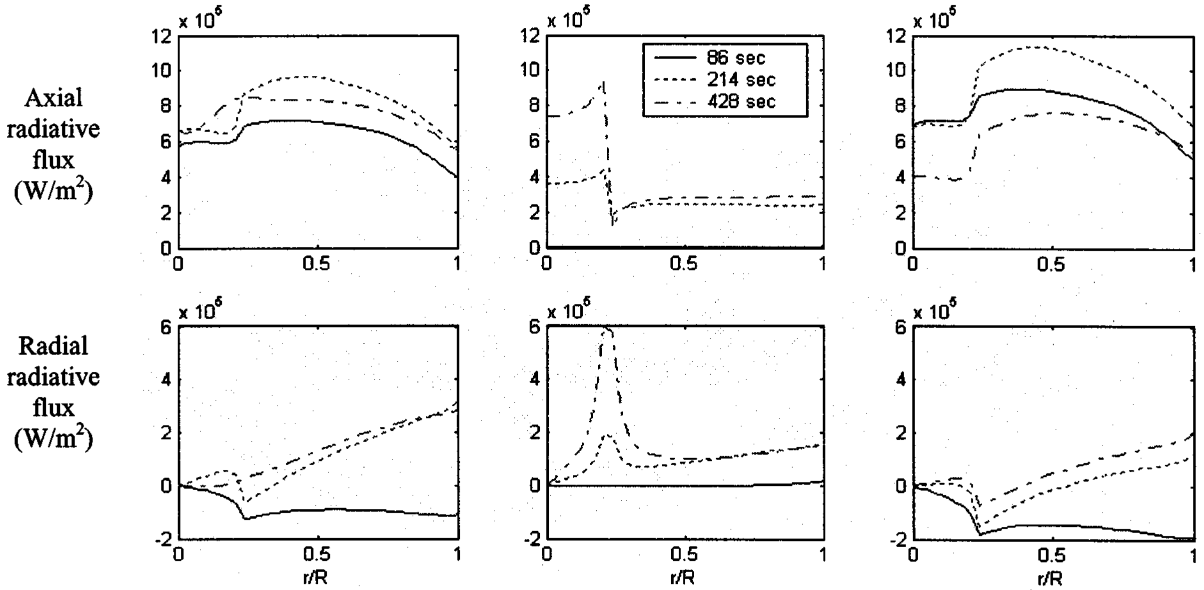

(*a*) (*b*) (*c*)

Fig. 7 Radiative flux distributions at $z/L=0.15$: (*a*) DOM, new band model; (*b*) Rosseland; and (*c*) DOM, Myers' band model.

is positive but small. In RA, the temperature inside the inner cylinder is underestimated. As a result, the corresponding axial temperature gradient and thus the axial heat flux is larger than that in the outer cylinder as shown in Fig. 7(*b*). Figure 8 shows that the temperature discontinuity in the gap results in a large positive temperature gradient at the tip of the gap. Consequently, there is a peak of radial radiative flux near the tip. The sharp drop of the temperature gradient after the temperature is elevated is due to the combination of two factors: radiative conductivity is proportional to T^3; the Rosseland mean absorption coefficient decreases shapely when the temperature is increased.

3. It is interesting to note that the axial flux at $t=428$ is smaller than that at $t=214$ in Fig. 7(*a*). This is because as the glass is heated near the temperature of the furnace, the emitted flux by the glass medium is comparable to the flux from the furnace. Thus, the net radiative flux inside the glass as the process approaches steady state is smaller than that at the initial transient.

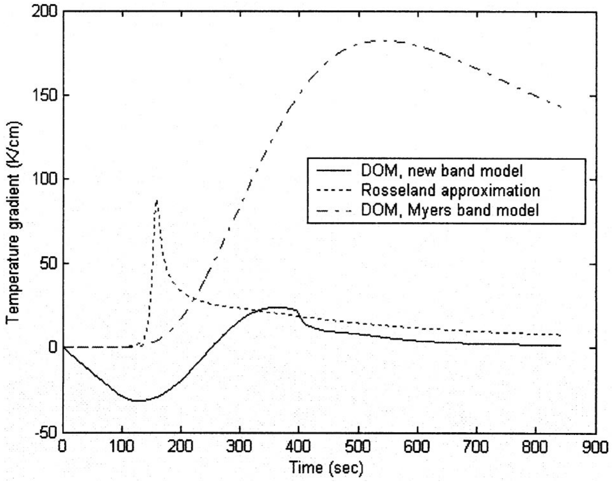

Fig. 8 Transient radial temperature gradient at the tip of the gap ($a/R=0.22$; and $d/L=0.15$).

Effects of Band Models of Absorption Coefficient. Several observations can be made in Figs. 6(*c*), 7(*c*), and 8:

1. In Myers' two-step band model, the glass absorption coefficient at short wavelengths ($0.2\ \mu\text{m} \leq \lambda < 2.8\ \mu\text{m}$) has been neglected. As a result, the heat flux at that band is not absorbed (or attenuated) by the glass medium and thus the temperature is underestimated during the initial transient response as shown in Fig. 6(*c*).
2. In addition, as only the radiative energy at the middle band ($3.0\ \mu\text{m} < \lambda < 4.8\ \mu\text{m}$) is absorbed by the glass in Myers' model that has a κ_λ more than 100 times larger than that at the short-wavelength band, the radiative flux at the middle band from the furnace is greatly attenuated along the path into the glass medium. Consequently, a very large temperature gradient is formed in the radial direction as shown in Figs. 6(*c*) and 8.
3. The total flux in the solution using Myers' band model is somewhat larger than that using the new band model since the flux at the short wavelength band is not attenuated (absorbed) by the glass media in Myers' model.

As mentioned earlier, sufficiently large temperature gradient due to the transient heating could result in cracking at the interface and predictions of thermally induced stresses requires a good understanding of the transient temperature field and its gradient at the interface. Both Rosseland approximation and the neglect of the absorption coefficient in the $0.2\ \mu\text{m} \leq \lambda < 2.8\ \mu\text{m}$ band have led to erroneous prediction of temperature gradient. Most impor-

Table 1 Parameters used in the simulation

a/R	0.22	b/L	0.15	$T_{f,\max}$	2400 K
R/R_f	0.75	R/L	0.09	L/L_f	1

tantly, they fail to predict the negative temperature gradient at the earlier stage of the transient, where cracks at the join interface are most likely.

4 Conclusions

The transient temperature and heat flux distributions in the process of heating two concentric, semitransparent glass cylinders have been presented. Specifically, we have compared two different methods in modeling the radiative transfer; namely, the discrete ordinate method and Rosseland's approximation. In addition, we have investigated the effects of the absorption coefficient at short wavelengths ($0.2\ \mu\text{m} \leqslant \lambda < 2.8\ \mu\text{m}$) on the radiative transfer, which has been neglected in the commonly used Myers' two-step band model.

Our results show that although the spectral absorption coefficient at short wavelengths is relatively small, its effects on the temperature are considerable since most of the radiative power is at this short-wavelength band under the elevated temperatures. The temperature is highly underestimated during this initial transient and its radial variation is overestimated with the Myers' band model.

The comparison between the predictions using DOM and the widely used Rosseland approximation shows that Rosseland's approximation fails miserably when the characteristic dimension is small, particularly at the gap between the cylinders even when the temperature variation is small. In addition, the assumption of optically thick must take into account the glass absorption coefficient at short wavelengths where the radiative transfer is dominant.

The solutions of the temperature field can be further used in the prediction of the thermal stress intensity near the tip of the interface which is important for the design and control of the manufacturing process.

Acknowledgments

This research has been funded by Lucent/OFS. The authors are deeply indebted to Steve Jacobs, Rob Moore, and Mahmood Tabaddor for their contribution to this manuscript.

Nomenclature

Symbols

B = Jacobian of the curvilinear coordinates transformation
$E_{b,\lambda}$ = blackbody emissive power
G_λ = spectral incident radiation
H_λ = spectral irradiation in W/(m^2 μm)
I_λ = spectral radiative intensity in W/(m^2 μm sr)
$I_{b\lambda}$ = spectral blackbody intensity in W/(m^2 μm sr)
J_λ = spectral radiosity in W/(m^2 μm)
T = temperature in K
k_{rad} = radiative thermal conductivity in W/(m μm)
n_λ = spectral index of refraction
q = total radiative heat flux in W/(m^2)
q_λ = spectral radiative heat flux in W/(m^2 μm)
w = quadrature weight

Subscripts and Superscripts

e = east side of the control volume
f = furnace
g = glass
n = north side of the control volume
r = radial coordinate direction
s = south side of the control volume
$\mathbf{n}$ = normal unit vector of the surface
$\mathbf{r}$ = location vector
$\mathbf{s}$ = unit direction vector
Ω = solid angle in sr
τ_λ = spectral diffuse transmissivity
ρ_λ = spectral diffuse reflectivity
κ_λ = spectral absorption coefficient in m^{-1}
ε = emissivity
μ^i = cosine of the angle between the ith direction and the r direction
ξ^i = cosine of the angle between the ith direction and the z direction
δ_λ = optical thickness
(α,β) = general curvilinear coordinates
w = west side of the control volume
z = axial coordinate direction
max = maximum value
$+$ = positive coordinate direction for flux; outer surface at the interface
$-$ = negative coordinate direction for flux; inner surface at the interface

References

[1] Paek, U. C., and Runk, R. B., 1978, "Physical Behavior of the Neck-Down Region During Furnace Drawing of Silica Fibers," J. Appl. Phys., **49**, pp. 4417–4422.
[2] Homsy, G. M., and Walker, K., 1979, "Heat Transfer in Laser Drawing of Optical Fibers," Glass Technol., **20**(1), pp. 20–26.
[3] Myers, M. R., 1989, "A Model for Unsteady Analysis of Preform Drawing," AIChE J., **35**(4), pp. 592–602.
[4] Choudhury, S. R., Jaluria, Y., Lee, S. H.-K., 1999, "A Computational Method for Generating the Free-surface Neck-down Profile for Glass Flow in Optical Fiber Drawing," Numer. Heat Transfer, Part A, **35**, pp. 1–24.
[5] Lee, K. H., and Viskanta, R., 1999, "Comparison of the Diffusion Approximation and the Discrete Ordinates Method for the Investigation of Heat Transfer in Glass," Glass Sci. Technol. (Frankfurt/Main), **72**(8), pp. 254–265.
[6] Yin, Z., and Jaluria, Y., 1997, "Zonal Method to Model Radiative Transport in an Optical Fiber Drawing Furnace," ASME J. Heat Transfer, **119**, pp. 597–603.
[7] Modest, M. F., 1993, *Radiative Heat Transfer*, McGraw-Hill, NY.
[8] Endrys, Jiri, 1999, "Measurement of Radiative and Effective Thermal Conductivity of Glass," Proc. of the 5th ESG Conf., A5 10–17.
[9] Nijnatten, P. A., and Broekhuijse, J. T., 1999, "A High-Temperature Optical Test Facility for Determining the Absorption of Glass at Melting Temperatures," Proc. of the 5th ESG Conf., A5 51–58.
[10] Nijnatten, P. A., Broekhuijse, J. T., and Faber, A. J., 1999, "Spectral Photon Conductivity of Glass at Forming and Melting Temperatures," Proceedings of the 5th ESG Conference, A5 2–9.
[11] Jamaluddin, A. S., and Smith, P. J., 1988, "Predicting Radiative Transfer in Axisymmetric Cylindrical Enclosures Using the Discrete Ordinates Method," Combust. Sci. Technol., **62**, pp. 173–186.
[12] Lee, K. H., and Viskanta, R., 1997, "Prediction of Spectral Radiative Transfer in A Condensed Cylindrical Medium Using Discrete Ordinates Method," J. Quant. Spectrosc. Radiat. Transf., **58**, pp. 329–345.
[13] Chung, K. B., Moon, K. M., and Song, T. H., 1999, "Treatment of Radiative Transfer in Glass Melts: Validity of Rosseland and P-1 Approximations," Phys. Chem. Glasses, **40**, pp. 26–33.
[14] Viskanta, R., and Anderson, E. E., 1975, "Heat Transfer in Semitransparent Solids," Adv. Heat Transfer, **11**, pp. 317–441.
[15] Carlson, B. G., and Lathrop, K. D., 1968, "Transport Theory—The Method of Discrete Ordinates," *Computing Methods in Reactor Physics*, H. Greenspan, C. N. Kelber, and D. Okrent, eds., Gordon & Breach, New York, pp. 165–266.
[16] Touloukian, Y. S., DeWitt, D. P., and Hernicz, R. S., eds., 1973, *Thermal Radiative Properties: Nonmetallic Solids*, **8** of Thermophysical Properties of Matter, Plenum Press, New York, pp. 1569–1576.
[17] Egan, W. G., and Hilgeman, T. W., 1979, *Optical Properties of Inhomogeneous Materials: Applications to Geology, Astronomy, Chemistry and Engineering*, Academic Press, New York.
[18] Kesten, Arthur S., 1968, "Radiant Heat Flux Distribution in a Cylindrically-Symmetric Nonisothermal Gas With Temperature-Dependent Absorption Coefficient," J. Quant. Spectrosc. Radiat. Transf., **8**, pp. 419–434.

Evaporation Heat Transfer in Sintered Porous Media

M. A. Hanlon
e-mail: mhanlon@aperionenergy.com
Aperion Energy Systems, Inc.,
398 Dix Road, Suite 102,
Jefferson City, MO 65109

H. B. Ma
e-mail: mah@missouri.edu
Department of Mechanical
and Aerospace Engineering,
University of Missouri—Columbia,
Columbia, MO 65211

A two-dimensional model is presented to predict the overall heat transfer capability for a sintered wick structure. The model considers the absence of bulk fluid at the top surface of the wick, heat conduction resistance through the wick, capillary limitation, and the onset of nucleate boiling. The numerical results show that thin film evaporation occurring only at the top surface of a wick plays an important role in the enhancement of evaporating heat transfer and depends on the thin film evaporation, the particle size, the porosity, and the wick structure thickness. By decreasing the average particle radius, the evaporation heat transfer coefficient can be enhanced. Additionally, there exists an optimum characteristic thickness for maximum heat removal. The maximum superheat allowable for thin film evaporation at the top surface of a wick is presented to be a function of the particle radius, wick porosity, wick structure thickness, and effective thermal conductivity. In order to verify the theoretical analysis, an experimental system was established, and a comparison with the theoretical prediction conducted. Results of the investigation will assist in optimizing the heat transfer performance of sintered porous media in heat pipes and better understanding of thin film evaporation. [DOI: 10.1115/1.1560145]

Keywords: *Boiling, Heat Transfer, Heat Pipes, Phase Change, Thin Films*

Introduction

The ability to manage the thermal behavior of various electrical components is of paramount importance in many modern electronic systems. Traditionally, the method of choice for dissipating heat from an electronic system such as a computer chip has been the use of a finned heat sink in conjunction with a fan or other means of convection cooling. These components operate primarily on the basis of conduction and convection. The metallic finned unit in effect draws heat from the input heat flux zone and distributes the thermal energy such that it may be removed via the flowing air or other fluid of choice. With the unyielding drive to produce personal computers with more rapid processing speeds, for example, comes the responsibility to effectively remove the additional heat generated by these more powerful chips. The current finned heat sinks function adequately from a thermal management perspective over a wide range of chip operating speeds, but there exists a definite threshold for forced air convection heat transfer involving finned heat sinks. As the chip manufacturers encroach upon the thermal operating limit set by the standby fin-fan heat sinks, thermal engineers must devise new means for managing the thermal behaviors of these electronic components. One such alternative to the well-known finned heat sink is to embed a heat pipe.

While the heat pipe presents a promising approach to a higher level of heat flux and temperature uniformity, the heat pipe cannot remove extremely high levels of heat flux due to limitations such as the capillary force and nucleate boiling. The motivation behind the current work was to determine what effects the thin film evaporation has on the heat transport behavior of the wick structure, whether an optimum wick structure exists, and how the value for maximum heat removal for a wick structure is determined.

Theoretical Analysis

When heat is applied to the evaporating region of a heat pipe, the heat will travel through the wall of the solid container to reach the working fluid. Provided that the fluid level is not above the top surface of the wick, the heat that reaches the top surface of the working fluid in the wick, as shown in Fig. 1, will pass through a thin-film region consisting of three regions: the nonevaporating thin film region, the evaporating thin film region, and the meniscus thin film region. In the presence of a thin film, a majority of the heat will be transferred through a very small region [1–6]. When thin film evaporation is compared to boiling heat transfer [7–11], it is found that thin film evaporation can provide significantly higher overall heat transfer coefficients. When evaporation occurs in a pool boiling system, the heat transfer limit at the evaporating surface depends on the mechanisms of liquid supply to and vapor escape from the phase-change interface. In order to reduce the effects of liquid and vapor flow resistances in the pool boiling system, extensive investigations on enhanced surfaces such as the machined or etched cavities [7], structured surfaces [8], low-permeability evaporating surfaces [10], and coated surfaces [8,9] including modulated porous-layers [11] have been conducted resulting in a better understanding of heat transfer mechanisms. As a result, the heat transfer limit occurring in the pool boiling systems has been continuously pushed. Due to the presence of liquid, however, the resistance to vapor flow still exists and directly limits the further enhancement of boiling heat transfer in the pool boiling systems. In the current study evaporation occurring only at the liquid-vapor interface in thin film region shown in Fig. 1, for which the resistance to vapor flow is negligible, is investigated to determine whether such an evaporating surface exists and how thin film evaporation occurring only at the top surface of wicks is promoted.

Ma and Peterson [12] recently developed a new type of evaporative surface in which variable microgrooves were used to increase the size, the shape, and the number of interline regions, thereby increasing the evaporating heat transfer coefficient. Preliminary investigations of this surface indicated that when the groove width was decreased from 0.6 mm to 0.3 mm, the temperature difference required to remove a heat flux of 10 W/cm^2 would decrease from 16.0 to 8.3°C. Alternatively speaking, the evaporating heat transfer coefficient was almost doubled. Using this information, a new heat pipe was designed for cooling the next generation of computer chips [13]. By using this device and its enhanced evaporation surface, it was demonstrated that the evaporating heat transfer coefficient in the evaporator of a heat pipe, could be significantly increased.

While grooves have been proven to enhance the evaporative heat transfer coefficient, there are some limitations to the level of

---

Contributed by the Heat Transfer Division for publication in the JOURNAL OF HEAT TRANSFER. Manuscript received by the Heat Transfer Division March 11, 2002; revision received November 1, 2002. Associate Editor: H. Bau.

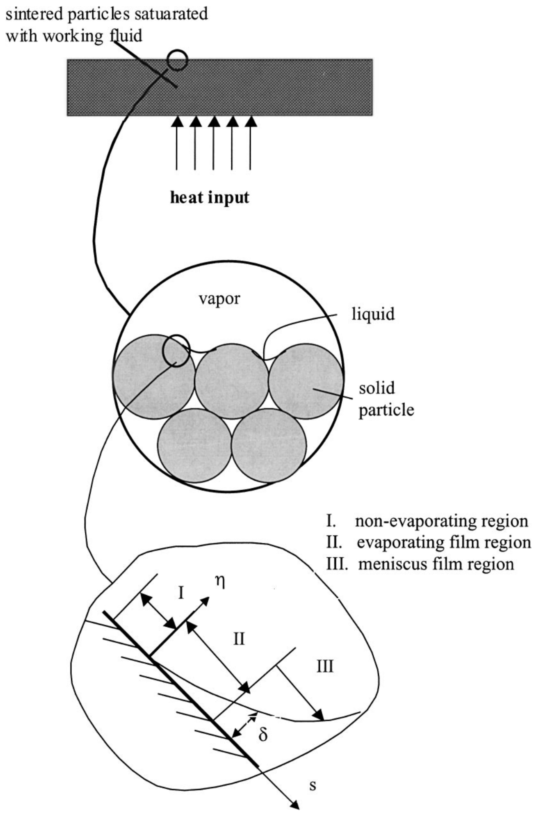

Fig. 1 Thin film evaporation in sintered particles

improvement possible. The work of Ma and Peterson [5] showed that most of the evaporating heat transfer passes through a small region, less than 1 μm. Unfortunately, current fabrication processes preclude the further increase of the groove density and the large-scale manufacture of these types of grooved surfaces. As a result, it is necessary to develop new kinds of evaporative surfaces, with heat transport capabilities comparable to the thin film evaporating heat transfer coefficient required. After examining traditional evaporative surfaces/wick structures used in the design of heat pipes, it was found that sintered metal powders and/or particles could provide a higher thermal conductivity while still facilitating the thin film evaporating heat transfer.

If heat is added to the sintered porous medium fabricated from the round particles, as shown in Fig. 1, the heat is transferred through the sintered particles filled with the working fluid, reaching the top surface where the liquid-vapor-solid interface exists. There, by utilizing the thin film evaporation, the heat is removed. If the radius of a single particle is known, the evaporating heat transfer for that particle may be approximated as

$$Q_p = 2\pi r_p k_l (T_s - T_v) \int_0^{10^{-6}} \frac{1}{\delta} ds \tag{1}$$

where all of the evaporating heat transfer is assumed to pass through the micro-region, i.e., the region less than 1 μm [5]. The film thickness profile can be described by

$$\sigma \frac{d\xi}{ds} - \frac{dp_d}{ds} = -\frac{f_l^+ \cdot \mathrm{Re}_\delta \, \mu_l \int_0^s \frac{q(s)}{h_{fg}} ds}{2\delta^3(s)\rho_l} \tag{2}$$

for the steady-state evaporating process of a thin film, where the meniscus curvature, ξ, and the disjoining pressure, p_d, can be found by

$$\xi = \frac{\dfrac{d^2\delta}{ds^2}}{\left[1 + \left(\dfrac{d\delta}{ds}\right)^2\right]^{3/2}} \tag{3}$$

$$p_d = \rho_l R T_{lv} \ln[a\delta^b] \tag{4}$$

respectively. The boundary conditions corresponding to Eq. (2) are

$$\delta = \delta_0; \quad \xi = 0; \quad \frac{d\delta}{ds} = 0; \quad \text{at } s = 0 \tag{5}$$

where the nonevaporating film thickness is determined by [5]

$$\delta_0 = e\left[\frac{\left(\dfrac{T_w}{T_v} - 1\right)\dfrac{h_{fg}}{RT_w} - \ln a}{b}\right] \tag{6}$$

As the evaporating thin film profile is obtained, the temperature drop across the evaporating thin film can be determined.

If the total number of particles at the top surface of wick is N_b, the total evaporating heat transfer may be determined by

$$Q = \sum_1^{N_p} Q_p \tag{7}$$

where the total number of particles is approximately found by

$$N_p = \frac{A_{sp}}{4\pi r_p^2} \tag{8}$$

and A_{tb} is the total area of top surface of sintered porous medium.

From Eqs. (1) through (8), it may be seen that a decrease in particle size results in an increase in the evaporating heat transfer. Alternatively, the smaller the particle size, the better the evaporating heat transfer performance. However, when the particle size is less than the characteristic length of the evaporating thin film region, continued decreases would effectively reduce the evaporating heat transfer capacity. Therefore, there exists an ideal particle size and packing factor that provides the maximum evaporating heat transfer coefficient.

While for most applications the evaporating thin film region can be used to significantly increase the evaporating heat transfer, it is desirable to also reduce the overall thermal resistance, since the total heat transport capability in a sintered porous medium depends not only on the evaporating heat transfer, but also on the thermal conductivity of the sintered porous medium and the capillary flow. Neglecting the effects of convection heat transfer within the medium, the temperature drop occurring in a sintered porous layer can be approximated by $T_w - T_s = QH/k_{\mathrm{eff}}$, where H is the thickness of the sintered porous medium, and k_{eff} is the effective thermal conductivity. It is clear that for a given heat flux, an increase in the thermal conductivity would reduce the temperature drop across the sintered porous medium. The effective thermal conductivity of the porous medium of metallic spheres is a function of the solid conductivity, k_s, the working fluid conductivity, k_f, and the porosity, and it varies drastically between the limiting cases, i.e., $\lim_{\varepsilon \to 0} k_{\mathrm{eff}} = k_s$ and $\lim_{\varepsilon \to 1} k_{\mathrm{eff}} = k_f$, depending upon the type of arrangement of the metallic particles. For the sintered particles investigated herein, the effective thermal conductivity can be determined by [14]

$$k_{\mathrm{eff}} = \frac{k_s[2k_s + k_l - 2\varepsilon(k_s - k_l)]}{2k_s + k_l + \varepsilon(k_s - k_l)} \tag{9}$$

In order to sustain continuous capillary flow in the wick shown in Fig. 1, the capillary pumping pressure must meet or exceed the sum of all other pressure drops. The maximum capillary pumping pressure may typically be expressed as

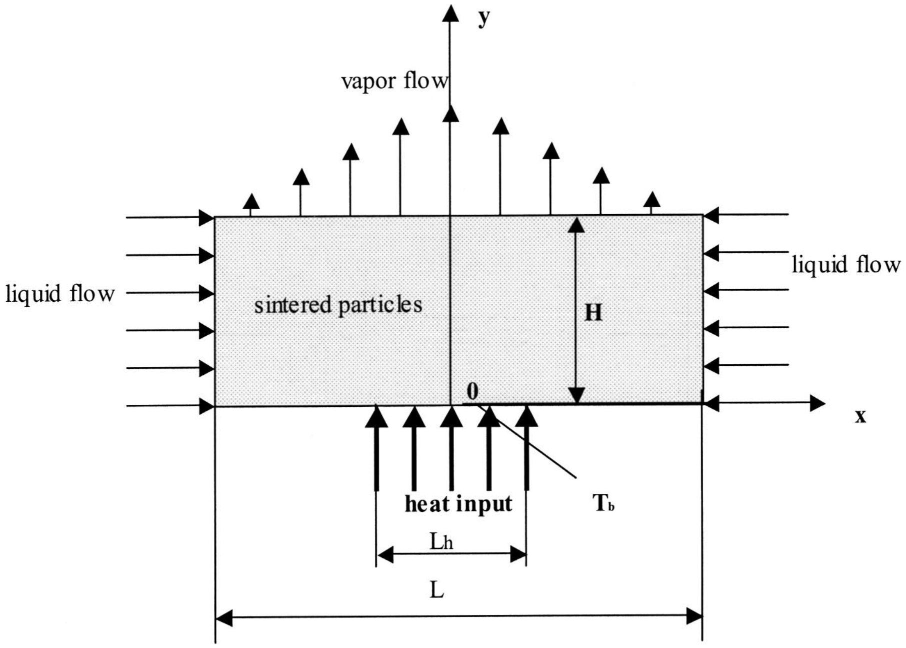

Fig. 2 Schematic of two-dimensional fluid flow and evaporation in a sintered wick structure

$$\Delta p_c = p_v - p_l = \frac{2\sigma}{r_c} \tag{10}$$

where r_c is the meniscus radius at the evaporating surface. The effective capillary radius for a sintered evaporative surface is dependent upon the size of the sintered particles, the mode of packing, and sintering process. When the radius of the particles decreases, the capillary pumping increases, and it is expected that the size of the individual particles should be as small as possible. However, as the particle size becomes smaller, the permeability [15],

$$K = \frac{r_p^2 \varepsilon^3}{37.5(1-\varepsilon)^2} \tag{11}$$

which here represents the ability of a porous materials to transmit liquid, will decrease.

When the fluid temperature reaches some pressure-dependant value above the saturation temperature, boiling occurs near the bottom of the evaporator resulting in two devastating consequences. First, thin film evaporation at the solid-liquid-vapor interface dramatically decreases as the boiling condition dominates the phase change behavior of the system. Secondly, the vapor generating at the base of the porous medium forms a blanket of vapor near the base of the medium, increasing the thermal resistance and preventing re-entry of the wetting fluid. Boiling heat transfer at the base of the wick should thus be avoided, as this condition could lead to an increased temperature drop across the wick structure and result in early wick dryout.

If the wick is constructed such that the temperature difference between the base temperature of the sintered porous medium and the saturation temperature, $T_b - T_{\text{sat}}$, remains less than the superheat for the nucleation, bubble formation will not occur in the wick. Once the pressure distribution is determined, then by utilizing the Clausius-Clapeyron relation and considering the surface tension, the minimum superheat for the onset of bubble formation can be determined by

$$T_l - T_{\text{sat}}(p_l) = \frac{2\sigma T_{\text{sat}}(p_l)}{h_{fg} r_{b,p}} \left(\frac{1}{\rho_v} - \frac{1}{\rho_l} \right) \tag{12}$$

Based on geometrical simplifications of the sintered perfect sphere particles, the maximum meniscus radius of the embryo bubble formed within the sintered sphere particles, i.e., the maximum cavity, may be approximated in terms of the particle radius as

$$r_{b,p} = \frac{r_p}{4} \tag{13}$$

Considering Eq. (13), Eq. (12) may then be expressed as

$$T_l - T_{\text{sat}}(p_l) = \frac{8\sigma T_{\text{sat}}(p_l)}{h_{fg} r_p} \left(\frac{1}{\rho_v} - \frac{1}{\rho_l} \right) \tag{14}$$

An embryo bubble will grow and a cavity will become an active nucleation site if the equilibrium superheat becomes equaled or exceeded one around the perimeter of the embryo. In order to avoid the bubble formation near the base of the porous medium, the temperature difference between the wall and the saturation temperature, $T_b - T_{\text{sat}}$, must be less than the superheat indicated by Eq. (14).

Thin film evaporation can provide significantly higher overall heat transfer coefficients, but it is limited by the capillary force and by the onset of bubble nucleation. Clearly, there must exist a set of properties that will optimize the overall heat transfer capabilities in wick structures investigated here. In order to find the capillary limitation and the boiling limitation, the detailed distributions of temperature and pressure in wicks have to be first determined. Analogous to the actual heat pipe wick, fluid enters the wick from the side, and is pumped toward the mid-plane of the wick due to the capillary pumping force, as shown in Fig. 2. One of objectives in designing a wick structure for the evaporating region of a high heat flux heat pipe is to determine a set of geometric parameters that encourages thin film evaporation at the top surface of the wick. In defining the top surface boundary condition, it is thus assumed that phase-change heat transfer occurs only at the top surface of the sintered porous medium. It is then to determine what set of parameters could lead to such a condition for the largest anticipated heat flux input. Owing to the small size of the wicks investigated here and to the relatively small flow rates of the working fluids through the wick, the Darcy Modified

Rayleigh number, $\mathrm{Ra}=Kg\beta H\Delta T/\alpha_f\nu_f$ is less than 40 for the range of configurations considered herein. Since the Nusselt number due to the convection is less than 1 for these small Rayleigh values, it is reasonable to assume that the contribution of convection to the overall thermal transport may be neglected [16]. Because, by assumption, evaporation occurs only at the liquid-vapor-solid interface on the top surface, the flow in the wick is all single-phase liquid, and use of the area-averaged velocity, i.e.,

$$u=\frac{1}{\Delta y\Delta z}\int_0^{\Delta Z}\int_0^{\Delta Y}u_P\,dy\,dz \qquad (15)$$

in lieu of the actual local velocity of the fluid is appropriate. Using the area-averaged velocity technique, invoking Darcy's Law, and introducing a buoyancy effect term to account for thermally induced flow in the vertical direction, the momentum equations for the system are

$$u=-\frac{K_p}{\mu}\frac{\partial P}{\partial x} \qquad (16)$$

$$v=-\frac{K_p}{\mu}\left[\frac{\partial P}{\partial y}-\rho_f g\beta(T-T_{\mathrm{sat}})\right] \qquad (17)$$

Additional assumptions include constant property values except the wick effective conductivity, since it depends on the porosity. With these assumptions and the continuity relation within the wick, the governing equations describing the temperature distribution and pressure profile in wicks can be written as

$$\nabla^2 T=0 \qquad (18)$$

$$\frac{\partial}{\partial x}\left(\rho\frac{\partial P}{\partial x}\right)+\frac{\partial}{\partial y}\left(\rho\frac{\partial P}{\partial y}\right)=\rho_f g\beta\frac{\partial}{\partial y}(\rho(T-T_{\mathrm{sat}})) \qquad (19)$$

It should be noted that in the development of the Darcy flow model, it is assumed that viscous effects are negligible and a slip condition must accordingly exist between each solid particles and the fluid. For high velocities, the slip condition no longer holds true. In these cases an additional friction term can be added as an extension to Darcy's law, i.e.,

$$\rho_l[(\mathbf{V}\cdot\nabla)\mathbf{V}]=-\nabla P-\frac{\mu}{K}\mathbf{V} \qquad (20)$$

With the appropriate boundary conditions, Eqs. (18) and (19) can be readily solved for the temperature distribution and pressure distribution.

Experimental System and Procedure

In order to determine if a set of wick parameters exists for which the thin film evaporation condition may be established at the top surface, thus providing a maximum evaporating heat transfer coefficient as the forgoing discussion, the experimental system shown in Fig. 3(*a*) was established. The setup consisted of a machined copper housing, to which a sintered porous wick sample was attached shown in Fig. 3(*b*), a reservoir for the liquid supply, a data acquisition system for the temperature measurement, and a personal computer. Attached to the copper housing were barbed hose fittings that enabled plastic tubing to be used to connect the housing with a spigot on a large rectangular tank, which served as the reservoir for the working fluid. By adjusting the height of the tank, the surface height of the working fluid could be manipulated to cause the working fluid to flood the copper housing to the point where the fluid surface was leveled with the top surface of the wick sample. The liquid level maintained during the experiment because the liquid-vapor surface area of the tank was many times greater than the liquid-vapor surface area of the wicks tested.

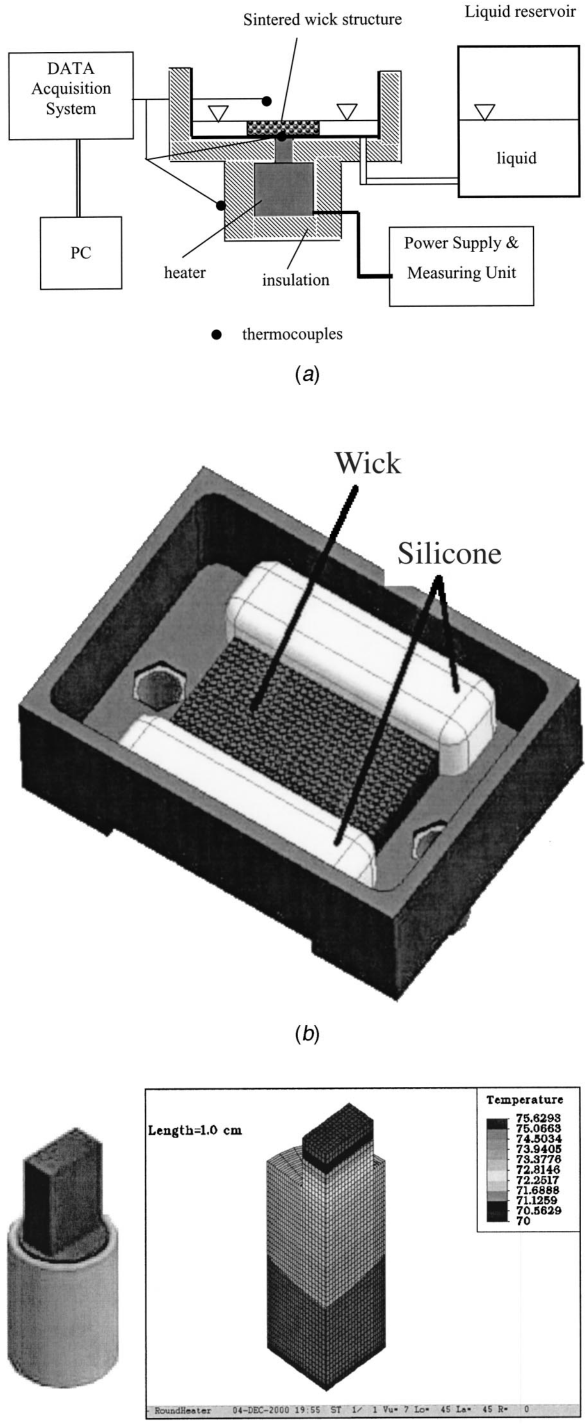

(*a*)

(*b*)

(*c*)

Fig. 3 (a) Schematic of the experimental system; (b) test section; and (c) solid model of the heater fabricated for experimentation (cylinder diameter is 2.54 cm, top surface is 1×2 cm^2, and length of rectangular neck is 2 cm)

A special mounting stand was manufactured from Lexan polycarbonate sheet to enable the heater to be firmly applied to the base of the copper housing. A thermally conductive paste was used at the interface between the copper heater and the copper housing to reduce the effects of contact resistance between the two components. Thermocouples were implemented to monitor the temperatures of the top and bottom surfaces of the sintered wick structure as well as the ambient temperature and outer heater surface temperatures, which were connected in differential mode to a cold junction compensated IO/Tech Personal DAQ56. In order to measure the interfacial temperature, a small groove was machined in the base of the sintered porous medium, where the thermocouple tip was mounted using Omegabond® 100 epoxy.

The sintered porous wick sample was fabricated from 100 Mesh, 99.99% pure copper particles prepared based on the recommended sintering temperature and time ranges of 840–900°C and 12–45 minutes [17]. Since the thermal and fluid transport properties of a sintered porous medium can vary significantly between identically prepared samples, it was difficult to isolate the thickness effect using multiple samples. Thus, an alternative method was proposed wherein a single, somewhat thick sample, was prepared for the testing process. Once testing had been completed on the initial sample, the thickness was decreased by removing layers of the sintered copper particles to allow for subsequent testing and the isolation of the thickness effect.

In order to achieve a heat flux as high as 1.0 MW/m^2, a special pure copper block wrapped by a Minco BB010047 bar heater was designed and fabricated. The heater was well insulated to reduce the effects of heat loss from the heating elements. To obtain a uniform heat flux added on the wick structure, the copper block was analyzed by means of the ALGOR heat transfer analysis software. In establishing the desired level of uniformity of the heat flux at the contacting surface, the copper block with a top contact surface of 1×2 cm^2 and a rectangular neck length of 2 cm, as shown in Fig. 3(*c*), was fabricated.

A voltage transformer was used to alter the electrical power into the resistive heating element. The voltage and current into the heater was monitored using a digital multi-meter. The temperatures of the base and top surface were monitored using the strip chart and digital display features in the DAQView software. When the steady-state temperature was reached for a given power level, the temperature readings of all thermocouples were recorded. The steady-state temperature was defined as the temperature for which less than one degree of change was observed for 5 minutes of continuously applied heat. Once the steady state temperature readings for a given heat rate were recorded, the power was increased in steps of 5 to 10 W and the process was repeated.

Multiple tests were run for each thickness value tested. After the range of heat input values of interest had been tested multiple times, several layers of copper particles were scraped from the top surface of the wick. Once the particles were removed from the test container, the new thickness of the wick was measured and recorded, and the steady state test process was repeated. While the test housing and heater were well insulated, some heat losses due to the combined effects of radiation and natural convection were inevitable. Calculations for the amount of nonevaporative heat loss based on outer insulation temperatures indicated that the loss was equal to 2–5% of the total heat added on the heater.

Numerical Calculation Procedure

Based the experimental investigation specially designed for the two-dimensional physical model shown in Fig. 1, the two-dimensional model, shown in Fig. 2, was employed. Owing to the symmetry, only half of the model was used to calculate the pressure and temperature distributions. The boundary conditions except for the top surface were expressed as follows

$$q''=0 \quad \text{and} \quad \frac{\partial P}{\partial x}=0 \quad \text{at } x=0 \quad \text{and} \quad y\in[0,H] \tag{21}$$

$$q''=0 \quad \text{and} \quad P=P_v \quad \text{at } x=L/2 \quad \text{and} \quad y\in[0,H] \tag{22}$$

$$\left.\begin{aligned} &q''=0,\quad \frac{\partial P}{\partial y}=0 \quad \text{at } y=0 \quad \text{and} \\ &\qquad x\in[L_h/2,L/2] \\ &q''=q''_{\text{in}}=-k\left.\frac{\partial T}{\partial y}\right|_{y=0},\quad \frac{\partial P}{\partial y}=0 \quad \text{at } y=0 \quad \text{and} \\ &\qquad x\in[0,L_h/2] \end{aligned}\right\} \tag{23}$$

At the top surface, thin film evaporation occurs and vapor departs from the wick. Considering Eq. (1) due to the thermal resistance across the thin liquid film, the temperature on the top surface can be determined as

$$T|_{y=H}=T_{\text{sat}}(P_v)+\frac{Q_p}{2\pi r_p k_l \int_0^{10^{-6}}\frac{1}{\delta}\,ds} \tag{24}$$

Once the temperature distribution in the wick is obtained, one can determine the heat flux into the top surface boundary. For steady-state heat transfer, the heat entering the boundary elements through heat conduction must be rejected via phase-change heat transfer at the top surface, i.e.,

$$-k_{\text{eff}}\frac{\partial T}{\partial y}(1\cdot dx)=\dot{m}_l h_{fg} \quad \text{at } y=H \quad \text{and} \quad x\in[0,L/2] \tag{25}$$

where a segment of the top surface of unit depth and width, dx, is considered. With a mass balance relation for the segment, $\dot{m}_l=\rho_L v_l(dx\cdot 1)$, and the Darcy flow equation, $v=-K/\mu\partial P/\partial y$, the top surface boundary condition for Eq. (19) can be found as

$$\frac{\partial P}{\partial y}=\frac{\mu}{K}\left(\frac{k_{\text{eff}}}{\rho_l h_{fg}}\frac{\partial T}{\partial y}\right) \quad \text{at } y=H \quad \text{and} \quad x\in[0,L/2] \tag{26}$$

Once the energy equation with the required boundary conditions was solved, the temperature distribution was used to determine the temperature gradient and the heat flux across the liquid-vapor interface at the top surface of the wick. With the top surface boundary condition specified, the pressure distribution was then calculated. The top surface pressure on the vapor side of the meniscus was then determined using the Laplace-Young relation. The saturation temperature being a function of pressure was next found for the vapor side of the meniscus for each grid point in the wick. Using Eq. (14) and starting with an artificially large heat input value, the critical superheat was calculated for each grid point and compared to the local superheat for the onset of bubble nucleation. If the superheat at any point in the wick exceeded the critical superheat, the heat flux was reduced and the process re-started. After several repetitions, the applied heat flux was finally reduced to the one that every point in the grid remained below the local superheat for bubble nucleation. At that point, the maximum allowable heat flux without bubble nucleation was bounded. Once the heat flux for the nucleate boiling limit was determined for a given wick parameter set, one parameter value, the wick thickness for example, was increased or decreased and the entire process was repeated.

As the thickness, for example, is reduced, the cross-sectional area for fluid flow is subsequently reduced. For a given heat flux input value, assuming all other properties held constant, a decrease in the wick thickness results in an increase in both the liquid flow velocity and the pressure drop through the wick. The capillary pumping pressure must be large enough to compensate for the liquid pressure drop in the wick as well as those occurring along the rest of the working fluid flow path. If the total liquid pressure drop exceeded the capillary limit defined by Eq. (10), the heat flux was reduced and the process re-started. Once the capillary limit was obtained for a given condition, the entire process was repeated. Once both the nucleate boiling and capillary pumping heat transport limits had been obtained for a given thickness, the lesser of the two calculated heat transfer was accepted as the active dryout threshold.

Results and Discussion

Unless stated otherwise, the parameter values for each of the studies below were as follows: working fluid—water; $r_p=0.635$ mm; $L=50.8$ mm; $L_H=10$ mm; $\varepsilon=43\%$. Because of the difficulty in determining the onset of nucleate boiling in the wick and thin film evaporation on the top surface of the wick, the

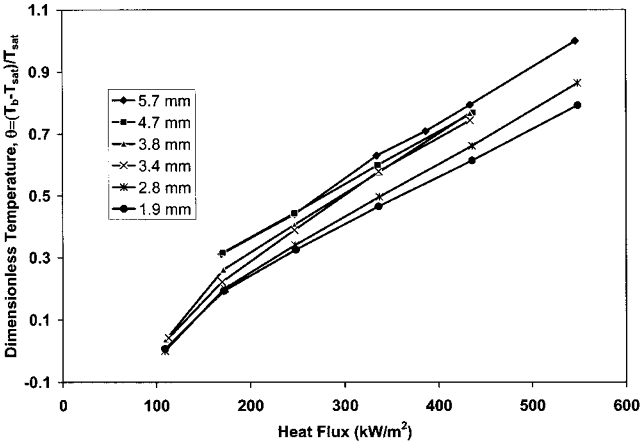

Fig. 4 Wick thickness effect on the temperature drop (r_b =0.635 mm; ε=43 percent; L_H=0.01 m; working fluid=water)

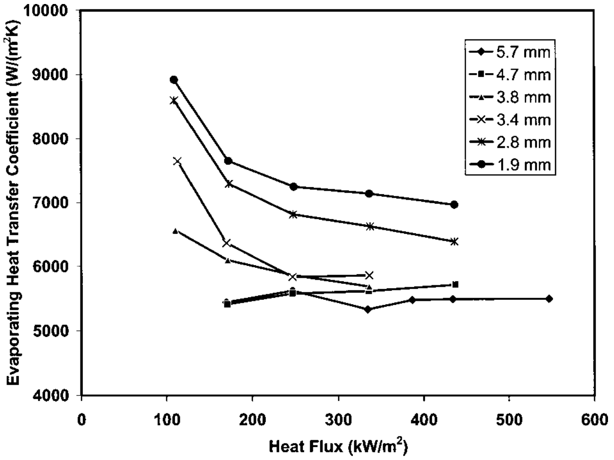

Fig. 6 Wick thickness effect on the evaporating heat transfer coefficients (r_b=0.635 mm; ε=43 percent; L_H=0.01 m; working fluid=water)

experimental data were obtained by the temperature difference between the base (bottom surface) and the top surface as a function of heat flux for a given wick including a known wick thickness, and continuously from the single-phase flow with the thin film evaporating on the top surface to the two-phase flow with the nucleate boiling in the wick.

Experimental results describing the relationship between wick thickness and temperature drop across the sintered wick are presented in Fig. 4 by plotting the dimensionless temperature defined by $\theta = T_b - T_{\text{sat}}/T_{\text{sat}}$, where T_b is the bottom surface (base) temperature, and T_{sat} is the saturation temperature corresponding to the local atmospheric pressure, equal to 743 mm Hg. As the heat flux increased, as shown in Figs. 4 and 5, the temperature drop across the wick increased. When the heat flux was increased to some value between 50 and 200 kW/m^2 for the range of wick sizes tested, the heat flux necessary for bubble nucleation was reached, which could be visually observed. Due to the bubble formation, the region of the wick directly above the heat application zone became saturated with vapor thus blocking the reentrance of liquid to the center of the wick, and thin film evaporation on the top surface of wick no longer existed. As a result, for the heat flux level higher than approximately 200 kW/m^2, the slope of the dimensionless temperature, θ, versus the applied heat flux, q'', was highly linear resulting in a significant decrease of the evaporating heat transfer coefficient shown in Fig. 6. This phenomenon was particularly pronounced for the thinner wick thickness values. It can be concluded that thin film evaporation plays an important role for the maximum evaporating heat transfer coefficient. The evaporation at the liquid-vapor-solid interface, i.e., at the top surface, of the sintered wicks can optimize the thin film evaporation.

Achieving thin film evaporation on the top surface of wick means the vaporization occurs only on the top surface of wick, and a single-phase flow exists in the wick, which is also the basis for the numerical model developed herein. Clearly, the model presented in the paper cannot predict the results shown in Figs. 4, 5, and 6, where the two-phase flow existed already in wicks when the heat flux level was higher than approximate 200 kW/m^2. Utilizing the highest evaporating heat transfer coefficient obtained for each wick, which occurred when the heat flux was equal to some value between 50 and 200 kW/m^2 for the range of wick sizes tested, the relationship between the maximum evaporating heat transfer coefficient and wick thickness was presented in Fig. 7 and compared with the numerical prediction. While the theoretical prediction was higher than the experimental data, the comparison provides insight regarding the importance of thin film evaporation in maximizing evaporating heat transfer coefficient, and it illustrates how failing to establish a thin film evaporation condition results in a significant decrease in the evaporating heat transport capability.

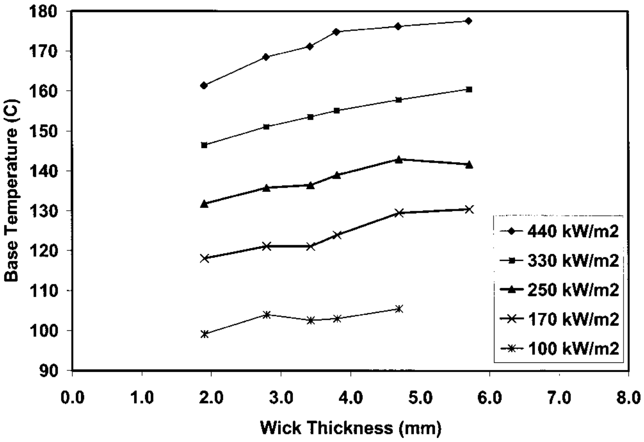

Fig. 5 Heat flux level effect on the temperature drops (r_b =0.635 mm; ε=43 percent; L_H=0.01 m; working fluid=water)

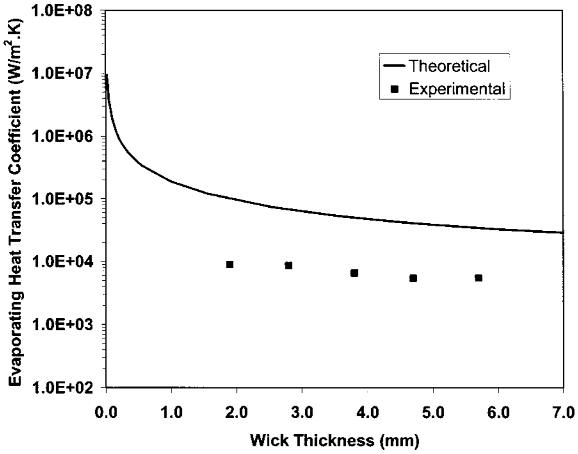

Fig. 7 Comparison of the calculated results with the experimental data (r_b=0.635 mm; ε=43 percent; L_H=0.01 m; working fluid=water)

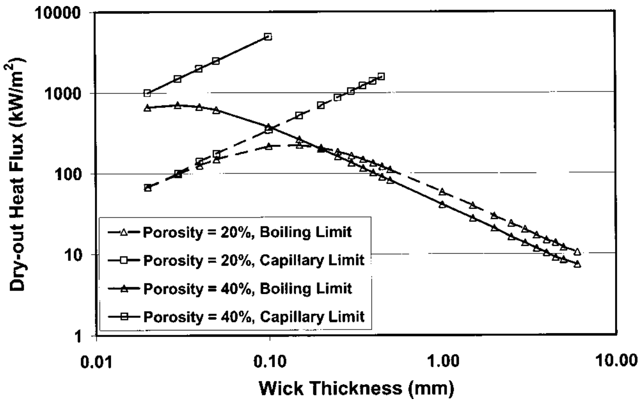

Fig. 8 Wick thickness effect on the capillary and boiling limitations (r_b=0.635 mm; ε=43 percent; L_H=0.01 m; working fluid=water)

As discussed previously, achieving thin film evaporation on the top surface of wicks is limited by the liquid pressure drop and superheat for the onset of bubble nucleation. The numerical simulation results, as shown in Fig. 8, indicate that the boiling limit is always less than the limit determined by the capillary pumping failure criterion for the wick configurations investigated here, which has an agreement with the experimental observation. As the heat flux was increased to some value between 50 and 200 kW/m^2 for the range of wick sizes tested, the bubble nucleation was visually observed. For the range of test wicks, the capillary limit was never reached, even with the maximum heat flux of 1.0 MW/m^2 available from the experimental system. Clearly, the bubble nucleation defined by Eq. (14) is the primary limit affecting the evaporating heat transfer coefficient for the sintered porous media investigated herein.

As shown in Fig. 9, when the wick thickness was decreased from 6 mm to 0.25 mm, the dimensionless temperature difference between the base and the top surface decreased considerably, indicating a dependency on the wick thickness for a given porosity and particle size. Numerical results, shown in Figs. 10, 11, and 12, all indicate that there exists an optimum wick thickness for maximum heat flux, which depends on the particle radius, the porosity, and the entry length, $L-L_h/2$. Results shown in Fig. 10 indicate that when the particle radius decreases, the optimum thickness increases. The effect of porosity on the optimum wick thickness is shown in Fig. 11. Based on the results of Figs. 10 and 11, it is concluded that, if it is possible to decrease the bead radius while maintaining a constant porosity, the bead radius should be as small as possible. The impact of these results is that thicker wicks, which are more readily manufactured and assembled into heat pipes, can provide heat removal capabilities equivalent to the more delicate, thin wicks. For wick thicknesses small enough that the capillary limit becomes dominant, as shown in Fig. 12, the model predicts that shorter entry lengths will yield larger dry-out heat fluxes. Results presented here can effectively direct the new design of high heat flux cooling device. For example, if an evaporating surface for a high heat flux heat pipe is fabricated using the optimum wick thickness shown in Fig. 10, the simple calculation from Figs. 7 and 10 indicates that the temperature drop across the wick is only several degrees for a heat flux of 800 kW/m^2.

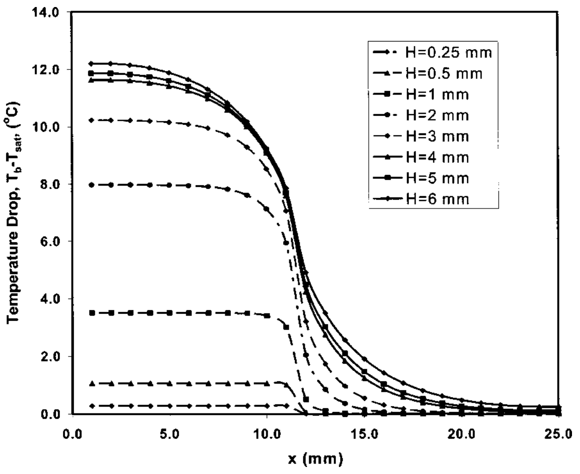

Fig. 9 Wick thickness effect on the temperature distribution (r_b=0.635 mm; ε=43 percent; L_H=0.01 m; working fluid =water)

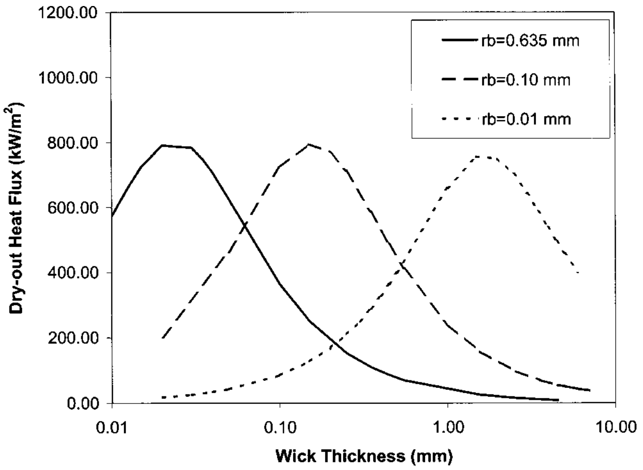

Fig. 10 Particle size effect on the dryout heat flux (L =0.254 mm; ε=43 percent; L_H=0.01 m; working fluid=water)

Conclusions

A theoretical analysis and experimental investigation was conducted to determine that thin film evaporation occurring only at the top surface of a horizontally oriented wick with localized bottom heating plays an important role in the enhancement of evaporating heat transfer and further that there exists a wick that can make this occur. When evaporation occurs only at the top surface of the wick and the effect of bulk liquid on the vapor flow, one of factors limiting the evaporating heat transfer, is removed, the heat conduction resistance, capillary pumping pressure, frictional pressure drop, and the onset of bubble formation become primary

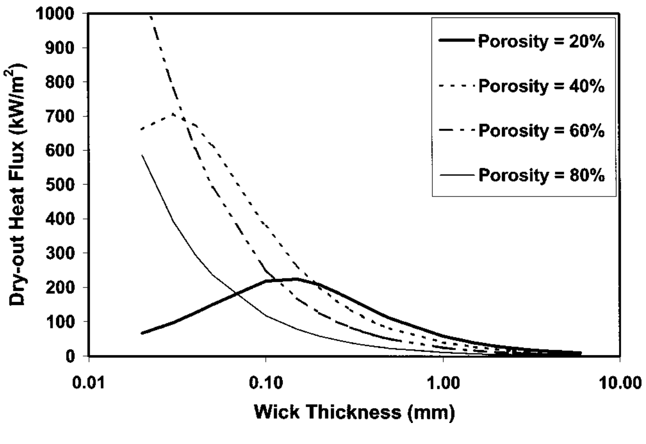

Fig. 11 Porosity effect on the dryout heat flux (r_b =0.635 mm; ε=43 percent; L_H=0.01 m; working fluid=water)

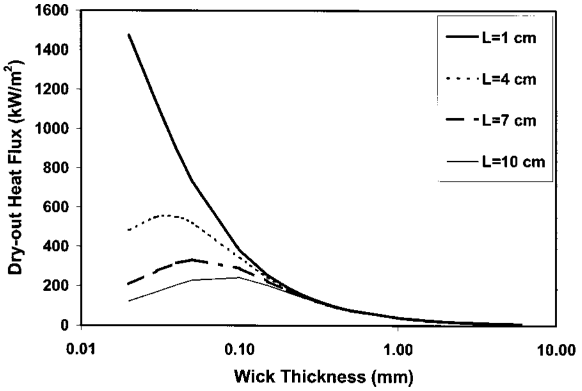

Fig. 12 Entry length effect on the dryout heat flux (r_b = 0.635 mm; T_{sat} = 373.15 K; ε = 43 percent; L_H = 0.01 m; working fluid = water)

factors determining the maximum evaporating heat transfer in the sintered wick structure. A two-dimensional model incorporating the heat conduction, capillary limitation, and the onset of nucleate boiling was developed to predict the overall heat transfer capability in the sintered wick structure. The numerical results show that it is possible to promote thin film evaporation from the top surface of a sintered wick by selecting the appropriate particle size, the porosity, and the thickness. By decreasing the average particle radius, the evaporation heat transfer coefficient can be enhanced. Furthermore, there exists an optimum characteristic thickness for maximum heat removal. In order to verify the theoretical analysis, an experimental investigation was conducted to determine the effect of the thin film evaporation at the top surface on the total evaporation heat transfer in the sintered wick structure. Experimental results show that thin film evaporation plays an important role in the enhancement of evaporating heat transfer, and evaporation occurring at the top surface, where the thin film regions were optimized, could reach the maximum evaporating heat transfer coefficient. Results also indicate that the maximum dry-out heat flux significantly depends on the wick thickness. While the theoretical prediction was higher than the experimental data, the comparison provides insights into how thin film evaporation occurring at the top surface of wicks plays an important role for the maximum evaporating heat transfer coefficient and how failure to establish a thin film evaporation condition results in significant decreases in the evaporating heat transport capability. Results of the investigation will assist in optimizing the heat transfer performance of sintered porous media in heat pipes and better understanding of thin film evaporation.

Acknowledgments

The authors would like to acknowledge the support of the DARPA/MTO HERETIC program under Contract No. F33615-99-C-1443.

Nomenclature

a = constant, 1.5787
A = area, m^2
b = constant, 0.0243
f = friction factor
h_{fg} = latent heat, J/kg
H = thickness, m
k = thermal conductivity, W/m·K
K = permeability, m^2
L = length, m
N = quantity of units
p = pressure, N/m^2
p_d = disjoining pressure, N/m^2
q = heat flux, W/cm^2
Q = Heat transfer, W
r = radius, m
R = gas constant, J/kgK
Ra = Rayleigh number
Re = Reynolds number
s = coordinate, m
T = temperature, K
u = velocity, m/s
v = velocity, m/s
x = coordinate, m
y = coordinate, m

Greeks

α = thermal diffusivity, m/s^2
β = volume thermal expansion coefficient, K^{-1}
δ = film thickness, m
δ_0 = nonevaporating film thickness, m
ε = porosity
η = coordinate, m
μ = dynamic viscosity, Ns/m^2
ν = kinematic viscosity, m/s^2
θ = dimensionless temperature
ρ = density, kg/m^3
σ = surface tension, N/m
ξ = curvature, m^{-1}

Subscripts

c = capillary
eff = effective
f = fluid
H = heated
l = liquid
p = particle
s = solid
sat = saturation
sp = particle surface
v = vapor
w = wall

References

[1] Busse, C. A., and Stephan, P. C., 1993, "Analysis of the Heat Transfer Coefficient of Grooved Heat Pipe Evaporator Walls," Int. J. Heat Mass Transf., **35**(2), pp. 383–391.
[2] Wayner, P. C., 1994, "Thermal and Mechanical Effect in the Spreading of a Liquid Film Due to a Change in the Apparent Finite Contact Angle," ASME J. Heat Transfer, **117**(4), pp. 938–945.
[3] Khrustalev, D., and Faghri, A., 1995, "Heat Transfer During Evaporation on Capillary-Grooved Structures of Heat Pipes," ASME J. Heat Transfer, **117**(3), pp. 938–945.
[4] Kobayashi, Y., Ikeda, S., and Iwasa, M., 1996, "Evaporative Heat Transfer at the Evaporative Section of A Grooved Heat Pipe," J. Thermophys. Heat Transfer, **10**(1), pp. 83–89.
[5] Ma, H. B., and Peterson, G. P., 1997, "Temperature Variation and Heat Transfer in Triangular Grooves with an Evaporating Film," J. Thermophys. Heat Transfer, **11**, pp. 90–97.
[6] Hallinan, K. P., Allen, J. S., and Pratt, D. M., 1999, "Investigation the Relationship between Thin Film Dynamics and Evaporation at a Meniscus in a Capillary," *Proceedings of the 5th ASME/JSME Joint Thermal Engineering Conference*, March 15–19, San Diego, CA.
[7] Thome, J. R., 1990, *Enhanced Boiling Heat Transfer*, Hemisphere Publishing Corporation, New York.
[8] Webb, R. L., 1994, *Principles of Enhanced Heat Transfer*, John Wiley & Sons, Inc, New York.
[9] Kaviany, M., 1995, *Principles of Heat Transfer in Porous Media*, Springer, New York.
[10] Bau, H. H., and Torrance, K. E., 1982, "Boiling in Low-Permeability Porous Materials," Int. J. Heat Mass Transf., **25**(1), pp. 45–55.
[11] Liter, S. G., and Kaviany, M., 2001, "Pool-Boiling CHF Enhancement by Modulated Porous-Layer Coating: Theory and Experiment," Int. J. Heat Mass Transf., **44**, pp. 4287–4311.
[12] Ma, H. B., and Peterson, G. P., 1997, "Experimental Investigation of the Thermal Capillary Limit of a Novel Micro Heat Pipe Design," *Proceedings of the 35th AIAA Aerospace Sciences Meeting*, Reno, NV, Jan. 6–10.

[13] Ma, H. B., 2001, ''Development of Highly Efficient Heat Pipe Cooling Devices,'' *Intel Project Report*, Platform Architecture Lab JF2-54, Intel Corporation, Hillsboro, OR.
[14] Peterson, G. P., 1994, *An Introduction to Heat Pipes*, John Wiley and Sons, Inc., New York.
[15] Luikov, A. K., 1980, *Heat and Mass Transfer*, MIR Publishers, Moscow.
[16] Nield and Bejan, 1992, *Convection in Porous Media*, Springer-Verlag, New York.
[17] Hausner, H., and Mal, M. K., 1982, *Handbook of Powder Metallurgy*, Second Ed., Chemical Publishing Co, Inc., New York.

H. Honda
N. Takata
H. Takamatsu

Institute of Advanced Material Study,
Kyushu University,
Kasuga, Fukuoka 816-8580, Japan

J. S. Kim
K. Usami

Interdisciplinary Graduate School of Engineering Sciences,
Kyushu University,
Kasuga, Fukuoka 816-8580, Japan

Effect of Fin Geometry on Condensation of R407C in a Staggered Bundle of Horizontal Finned Tubes

Experimental results are presented that show the effect of fin geometry on condensation of downward flowing zeotropic refrigerant mixture R407C in a staggered bundle of horizontal finned tubes. Two types of conventional low-fin tubes and three types of three-dimensional-fin tubes were tested. The refrigerant mass velocity ranged from 4 to 23 kg/m^2 s and the condensation temperature difference from 3 to 12 K. The measured condensation heat transfer coefficient was lower than the previous results for R134a, with the difference being more significant for smaller mass velocity. The effect of fin geometry on the condensation heat transfer coefficient was less significant for R407C than for R134a. The effect of condensate inundation was more significant for the three-dimensional-fin tubes than for the low-fin tubes. By using the dimensionless heat transfer correlation for the condensate film that was based on the experimental data for R134a, a superficial vapor-phase heat transfer coefficient was obtained for condensation of R407C. The vapor-phase heat transfer coefficient showed characteristics similar to the vapor-phase mass transfer coefficient that was obtained in the previous study for R123/R134a.
[DOI: 10.1115/1.1560153]

Keywords: *Bundles, Condensation, Enhancement, Finned Surfaces, Refrigeration*

Introduction

In accordance with the international regulation on HCFCs (hydrochlorofluorocarbons), a number of zeotropic mixtures of HFC (hydrofluorocarbons) have been developed as a replacement for R22 that has been widely used as a working fluid of refrigeration and air-conditioning systems. One of the most promising replacement candidates for R22 is zeotropic mixture R407C (R32/R125/R134a=23/25/52 mass%). This mixture shows the temperature glide of about 6 K during the evaporation and condensation processes. While this characteristics can be used to improve the thermodynamic cycle performance of refrigerating machines, it also acts to deteriorate the heat transfer performance of evaporators and condensers.

Horizontal shell-and-tube condensers are commonly used in the centrifugal refrigerating machines. Various types of finned tubes with different fin geometry have been developed to enhance shell-side condensation of pure refrigerants. However, only limited experimental data are currently available regarding the condensation of R407C in a bundle of horizontal finned tubes. Gabrielii and Vamling [1] measured the overall heat transfer coefficient of a shell-and-tube condenser with R22 and its three replacement candidates (i.e, HFC mixtures R404A, R410B, and R407C) as test fluids. All mixtures showed a decrease in the heat transfer performance relative to R22, with the decrease being more significant for lower heat load. The decrease was most significant for R407C with the largest temperature glide.

The objective of the present work is to study the effect of fin geometry on condensation of downward flowing R407C in a staggered bundle of horizontal finned tubes. Two types of conventional low-fin tubes and three types of three-dimensional-fin tubes are tested. The results are compared with previous results for R134a [2] obtained by using the same experimental apparatus and those for R123/R134a [3] condensing in a staggered bundle of four types of low-fin tubes.

Experimental Methods

Apparatus and Procedure. The experimental apparatus, which consisted of a natural circulation loop of refrigerant R407C and forced circulation loops of hot water and cooling water, is schematically shown in Fig. 1. Hot water was supplied to the shell-side of a shell-and-tube evaporator from an electrically heated water tank. R407C liquid returning to the evaporator flowed through the tubes counter-currently and completely evaporated. The test section, shown schematically in Fig. 2, was a 3×15 (columns×rows) staggered bundle of horizontal finned tubes made of copper. The odd rows consisted of three active tubes and the even rows consisted of two active tubes and dummy half tubes on the sidewalls. The horizontal and vertical tube pitches were 26 and 25 mm, respectively. The tube bundle was assembled in a vertical duct with inner dimensions of 78×100 mm^2.

Five types of finned tubes with different fin geometry were tested. The dimensions of the test tubes are listed in Table 1, and the longitudinal cross-section and close-up of these tubes are shown in Fig. 3. Tubes A and B had flat-sided annular fins (low fins), whereas tubes C–E had three-dimensional fins. Tube C had pyramid-shape fins. Tube D had saw-tooth-shape fins. Tube E had a three-dimensional structure at the fin tip that was produced by the secondary machining of the low fins. Experiments were conducted by using two kinds of test sections. One of the test sections consisted of tubes A–E. In this test section, tubes B, C, D, and E were attached at the seventh and tenth rows, ninth and twelfth, eleventh and fourteenth rows, and eighth and thirteenth rows, and the other rows consisted of tube A. The other test section consisted of tube A only.

The vapor pressure at the tube bundle inlet was measured by a precision Bourdon tube gage reading to 3 kPa and a Fortin barometer. The local vapor and condensate temperatures just upstream

---

Contributed by the Heat Transfer Division for publication in the JOURNAL OF HEAT TRANSFER. Manuscript received by the Heat Transfer Division March 19, 2001; revision received November 5, 2002. Associate Editor: V. P. Carey.

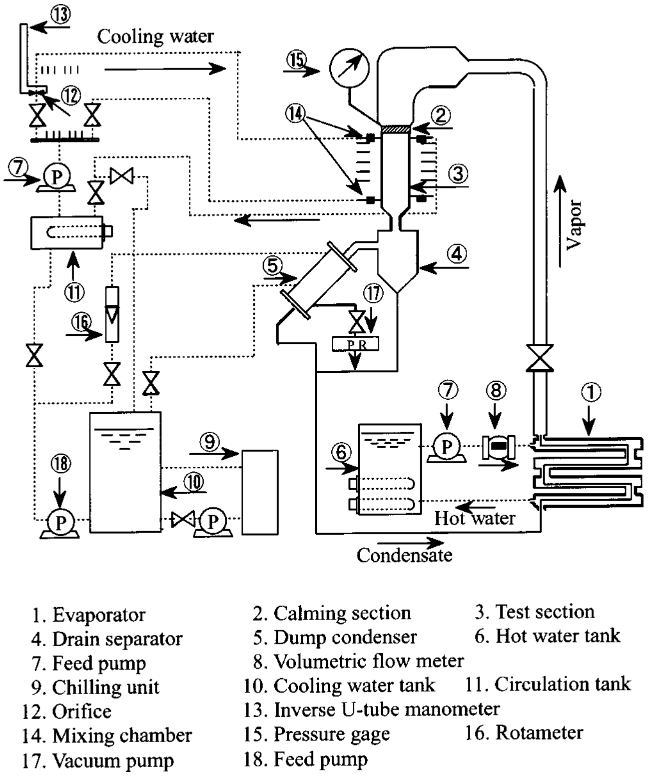

Fig. 1 Experimental apparatus

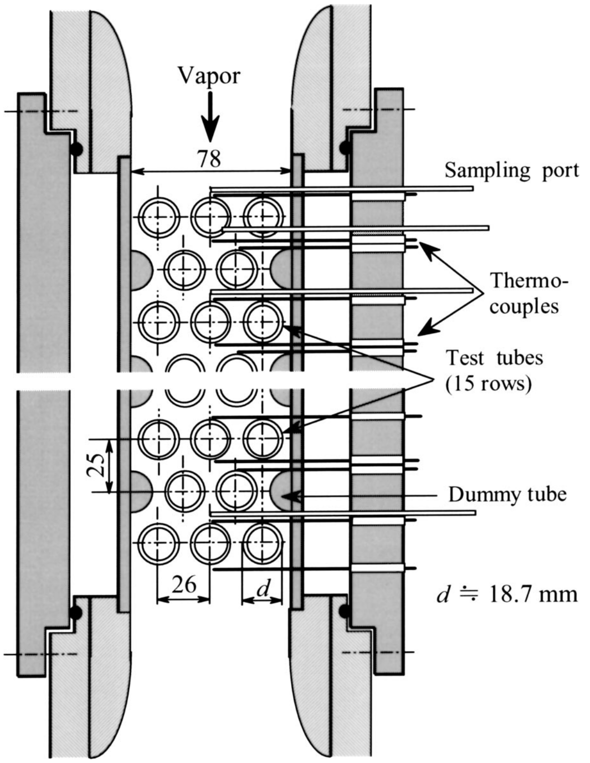

Fig. 2 Cross-sectional view of test section

and/or downstream of each row were measured by T-type thermocouples inserted in the test section. A shield and a gutter were attached just above and below the thermocouples that were used for the measurements of vapor and condensate temperatures, respectively. The hot water temperatures at the inlet and outlet of evaporator were measured by K-type thermocouples inserted in the mixing chambers. The cooling water temperatures at the inlet and outlet of each tube row were measured by two-junction T-type thermopiles inserted in the mixing chambers. The thermocouple and thermopile outputs were read consecutively ten times and recorded by a programmable data logger to 1 μV for the thermocouples and to 0.1 μV for the thermopiles, respectively, and the average values were adopted as the experimental data. The tube wall temperature was measured by a resistance thermometry. All test tubes and a standard resistor of 1 mΩ were connected in series to a 50 A DC current supply to measure the voltage drops. The voltage drops were read consecutively ten times and recorded by the data logger to 0.1 μV. In order to avoid the effect of parasitic voltage, half of the readings were conducted after reversing the DC current and the average values were adopted as the experimental data. The hot water flow rate was measured ten times by a volumetric flow meter with the accuracy of 0.5% RD. Then the mean value was adopted as the experimental data. The cooling water flow rate for each tube row was measured by an orifice and an inverse U-tube manometer reading to 1 mm.

The local composition of refrigerant vapor in the tube bundle was measured by a gas chromatograph. Sampling probes made of a 1.5-mm-o.d. stainless steel tube were inserted just upstream of the odd rows. A shield was attached just above the tip of the probe to avoid sampling of condensate. The probes were connected to buffer tanks of the gas chromatograph via small containers for storing samples. Stop valves were attached to the tubing at the inlet and outlet of each container. The tubing was heated to prevent condensation of vapor. Before sampling the vapor, the valve at the inlet of each container was closed and the tubing was evacuated using a vacuum pump. Then the valve at the outlet of the container was closed and the gas sample was introduced into each container by opening the valve at the inlet. Then the valve at the inlet was closed. The gas samples were introduced to the buffer tanks just before the measurement started. Assuming a linear relation between the sampled mass and the peak area of chromatogram for each component, equations for the relation between the mass fractions of R134a, R125, and R32 ($y_{v,134a}$, $y_{v,125}$, and $y_{v,32}$) and the peak area ratios of the chromatogram were obtained by using the gas sample of R407C.

Preliminary experiments were conducted to obtain calibration curves for the temperature versus e.m.f. relations of thermocouples and thermopiles, the temperature versus resistance relations of test tubes, the heat loss to the environment from the tubing between the inlet and outlet mixing chambers of each tube row Q_l and the sum of heat losses to the environment from the evaporator, vapor supply duct and test section Q_{lt}. The thermocouples and thermopiles were calibrated by using a temperature controlled water bath and a platinum resistance thermometer with an accuracy of 0.03 K. For the measurement of temperature versus resistance relation, the test section was evacuated using a vacuum pump to minimize heat loss from the tube surface. Then water at a prescribed temperature was passed through the test tubes. The water flow rate was kept at a high value so as to minimize the temperature drop of water between the inlet and outlet mixing chambers ($<$0.05 K), and the wall temperature was assumed to be

Table 1 Dimensions of test tubes

	A	B	C	D	E	F*	G*
p (mm)	0.96	1.30	0.71	0.70	0.96	0.96	0.50
h (mm)	1.38	1.29	0.87	0.95	1.11	1.43	1.41
t (mm)	0.45	0.48	⋯	⋯	⋯	0.33	0.17
θ (rad)	0.104	0.065	⋯	⋯	⋯	0.082	0
d (mm)	18.8	18.7	18.7	18.5	18.5	15.6	15.6
d_i (mm)	14.3	14.6	15.4	15.5	14.3	11.2	11.4

*Used in the previous study for R123/R134a

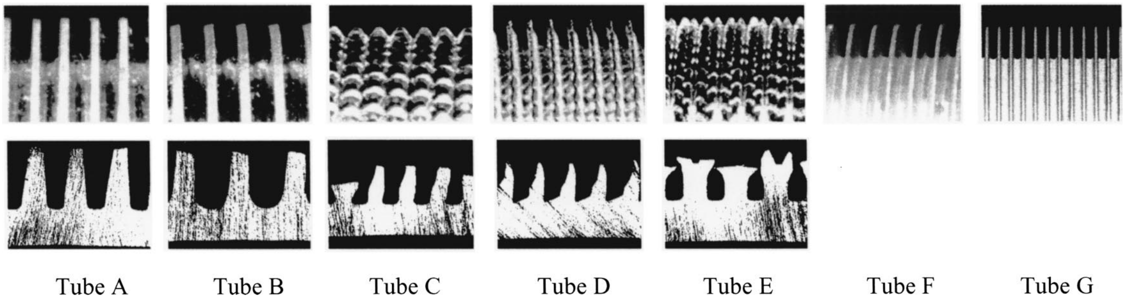

Fig. 3 Close-up and cross-sectional views of test tubes

equal to the average value of the measured water temperatures. For the measurement of Q_l, the water flow rate was kept at a low value so as to obtain a relatively large water temperature variation between the inlet and outlet mixing chambers ($\leqslant 0.2$ K). The value of Q_l, which was obtained from the flow rate and temperature variation of water, was plotted as a function of the temperature difference between the water and the ambient air. The maximum value of Q_l was 12 W at the temperature difference of 20 K. For the measurement of Q_{lt}, the refrigerant loop was shut at the outlet of the test section by using a brass plate. The valve at the inlet of evaporator was also closed. Then hot water was supplied to the shell side of evaporator. After a steady state was reached, the temperatures of vapor in the test section and ambient air were measured. The temperature difference between the vapor and ambient air increased almost linearly with the heat input to the evaporator. It was found that the heat loss was less than 350 W for the experimental conditions described below.

Experiments were conducted at the inlet vapor temperature $T_{v,\mathrm{in}}$ of about 313 K. This corresponded to the inlet vapor pressure P_{in} of about 1.74 MPa. The refrigerant mass velocity G (based on the duct cross-section) was changed in four steps (about 4, 8, 16, and 23 kg/m^2 s) by changing the power input to heaters installed in the hot water tank (about 5, 10, 20, and 30 kW). The condensation temperature difference $\Delta T = T_v - T_w$ was changed in four steps (about 3, 5, 8, and 12 K), where T_v is the local vapor temperature and T_w is the arithmetic mean of wall temperatures at the fin root for two or three active tubes in the same horizontal row. The effect of condensate inundation rate on the heat transfer performance of the test tubes was studied by changing the number of upper tube rows through which the cooling water was passed.

Data Reduction. The average heat flux q and the average heat transfer coefficient α of a horizontal row are respectively defined on the projected area basis as

$$q = (Q + Q_l)/k\pi dl \tag{1}$$

$$\alpha = q/\Delta T \tag{2}$$

where Q is the heat transfer rate for a horizontal row, k is the number of active tubes in a horizontal row ($=2$ or 3) and l ($=100$ mm) is the effective tube length. The value of Q is obtained from the following equation:

$$Q = W_c c_w (T_{c,\mathrm{out}} - T_{c,\mathrm{in}}) \tag{3}$$

where W_c is the flow rate of cooling water, c_w is the specific heat of water, and $T_{c,\mathrm{in}}$ and $T_{c,\mathrm{out}}$ are the cooling water temperatures in the mixing chambers at the inlet and outlet of each horizontal row, respectively.

The value of G is obtained from the following equation:

$$G = (Q_h - Q_{lt})/[h_{lg} + c_{pl}(T_{\mathrm{sat}} - T_{l,\mathrm{in}})]A \tag{4}$$

where Q_h is the heat input to the evaporator, h_{lg} is the specific heat of evaporation, c_{pl} is the specific heat of liquid, T_{sat} is the saturation temperature, $T_{l,\mathrm{in}}$ is the liquid temperature entering the evaporator and A is the cross sectional area of test section without tubes. The value of Q_h is obtained from

$$Q_h = W_h c_w (T_{h,\mathrm{in}} - T_{h,\mathrm{out}}) \tag{5}$$

where W_h is the flow rate of hot water, and $T_{h,\mathrm{in}}$ and $T_{h,\mathrm{out}}$ are the temperatures of hot water in the mixing chambers at the inlet and outlet of evaporator, respectively.

The heat balance for the nth row is written as

$$GA[h_v x + h_l(1-x)]_n = (Q + Q_l)_n + GA[h_v x + h_l(1-x)]_{n+1} \tag{6}$$

where x is the quality, h_l and h_v are the specific enthalpies of falling condensate and bulk vapor, respectively, and subscript n for the refrigerant denotes the condition just upstream of the nth row.

The vapor-liquid interfacial temperature T_i was obtained from the following equation:

$$q = \alpha_s (T_i - T_w) \tag{7}$$

where α_s is the heat transfer coefficient for the condensate film. The value of α_s was estimated by using a dimensionless correlation of the form

$$\alpha_s/\alpha_{\mathrm{Nu}} = f(\mathrm{Re}_v, \mathrm{Re}_f) \tag{8}$$

where α_{Nu} denotes the prediction of the Nusselt [4] equation for a horizontal smooth tube, $\mathrm{Re}_v = \zeta G d/\mu_v$ is the vapor Reynolds number at the tube bundle inlet based on the minimum flow cross-section, Re_f is the film Reynolds number based on the condensate flow rate at the tube bottom for one side of a tube, ζ is the ratio of the maximum and minimum flow cross-sections, and μ_v is the dynamic viscosity of vapor. The value of Re_f was obtained by assuming a gravity drained flow for the falling condensate. The correlation Eq. (8) was determined for each tube row based on the experimental data for R134a [2]. The agreement of measured α_s for R134a with the correlation was within 7%.

In principle, it is possible to estimate the vapor-phase mass transfer coefficient from the measured data if we assume saturated conditions for the bulk vapor and at the vapor-liquid interface. However, uncertainty of the estimated mass transfer coefficient was large, because the row-by-row variation of y_v was small. Thus we will discuss the characteristics of vapor-phase mass transfer by using a superficial heat transfer coefficient for the vapor phase α_v defined by

$$\alpha_v = q/(T_v - T_i) \tag{9}$$

The pressure drop in the tube bundle was obtained from the following equation [3]:

$$P_{n+1} = P_n + [(Gx)^2/\rho_v]_n - [(Gx)^2/\rho_v]_{n+1} - 2c_D\zeta^2[(Gx)^2/\rho_v]_m \tag{10}$$

where c_D is the drag coefficient obtained from the experimental data for R123. The calculated value of the pressure drop was less than 0.02% of the inlet pressure. In the data reduction, the thermophysical properties of R407C were obtained from REFPROP Version 6.0 [5].

Uncertainty Analysis. According to Moffat [6], the uncertainty in the result of a calculation R based on a number of measurements X_i, UR is obtained from

$$UR=\left[\sum_{i=1}^{N}\left(\frac{\partial R}{\partial X_i}BX_i\right)^2+\sum_{i=1}^{N}\left(t_{95}\frac{\partial R}{\partial X_i}SX_i\right)^2\right]^{1/2} \tag{11}$$

where BX_i is the bias limit of X_i, SX_i is the precision index of the mean of X_i, X_i is the ith variable in the measurements, and t_{95} is the Student's multiplier at the 95% confidence level. The SX_i is given by

$$SX_i=\left[\sum_{j=1}^{N}\frac{(X_{ij}-X_{im})^2}{N(N-1)}\right]^{1/2} \tag{12}$$

where N is the number of observations and X_{im} is the mean value of X_i. Since $N=10$ for the present experiment, t_{95} is 2.262.

A sample uncertainty calculations of G, and α and α_v for the first row are presented here for the case of $G=8$ kg/m^2 s and $\Delta T=3$ K. The measured and estimated values relevant to the uncertainty calculation are as follows: $W_h=0.827$ kg/s, $SW_h=1.9\times10^{-3}$ kg/s, $BW_h=4.1\times10^{-3}$ kg/s (0.5% of W_h), $W_c=3.82\times10^{-2}$ kg/s (corresponds to the static head of 160 mm), $SW_c=3.34\times10^{-4}$ kg/s, $BW_c=1.14\times10^{-3}$ kg/s (3% of W_c), $T_{h,\text{in}}-T_{h,\text{out}}=3.28$ K, $ST_{h,\text{in}}=0.002$ K, $ST_{h,\text{out}}=0.004$ K, $BT_{h,\text{in}}=BT_{h,\text{out}}=0.1$ K, $T_{c,\text{out}}-T_{c,\text{in}}=2.62$ K, $ST_{c,\text{in}}=0.003$ K, $ST_{c,\text{out}}=0.004$ K, $BT_{c,\text{in}}=BT_{c,\text{out}}=0.1$ K, $\Delta T=T_v-T_{wm}=3.00$ K, $T_v-T_i=1.78$ K, $T_i-T_w=1.22$ K, $ST_v=0.003$ K, $ST_w=0.081$ K, $BT_v=0.1$ K, $BT_w=0.15$ K, $Q_h=11.33$ kW, $Q_{lh}=301$ W, $Q=422.2$ W and $Q_l=9$ W. Since W_c is measured only once, SW_c is not available. Thus SW_c is assumed to be equivalent to 2 mm of static head reading. Substituting these values into Eq. (11) for G and α yields $UG/G=0.044$ and $U\alpha/\alpha=0.099$, respectively.

Substituting T_i obtained from Eq. (7) into Eq. (9) and rearranging yields

$$\alpha_v=\left[\frac{1}{\alpha}-\frac{1}{\alpha_s}\right]^{-1} \tag{13}$$

Thus the relative uncertainty $U\alpha_v/\alpha_v$ is written as

$$\begin{aligned}\frac{U\alpha_v}{\alpha_v}&=\left[\left(\frac{\alpha_v}{\alpha}\frac{U\alpha}{\alpha}\right)^2+\left(\frac{\alpha_v}{\alpha_s}\frac{U\alpha_s}{\alpha_s}\right)^2\right]^{1/2}\\&=\left[\left(\frac{T_v-T_w}{T_v-T_i}\frac{U\alpha}{\alpha}\right)^2+\left(\frac{T_v-T_w}{T_i-T_w}\frac{U\alpha_s}{\alpha_s}\right)^2\right]^{1/2}\end{aligned} \tag{14}$$

Considering the accuracy of the correlation for α_s described previously, it is assumed that $U\alpha_s/\alpha_s=0.07$. Substituting the measured and estimated values of T_v-T_w, T_v-T_i, T_i-T_w, $U\alpha/\alpha$ and $U\alpha_s/\alpha_s$ into Eq. (14) yields $U\alpha_v/\alpha_v=0.240$. Since $\Delta T\geqslant3$ K for the present experiment, it is supposed that $U\alpha/\alpha\leqslant0.1$ and $U\alpha_v/\alpha_v\leqslant0.24$ for most of the data.

The variation in y_v among five measurements using R407C gas sample was within 0.15%. Thus the uncertainty in y_v is estimated to be less than 0.15%.

Experimental Results and Discussion

Figure 4(a) shows an example of the distributions of the measured values of T_v, T_l, T_w and the calculated values of T_{sat} and T_i in the tube bundle consisting of tube A, where T_l is the temperature of falling condensate and T_{sat} is the saturation temperature corresponding to P and $y_{v,k}$. Due to the temperature glide of R407C, T_v decreases as condensation proceeds. However, T_v does not necessarily agree with T_{sat}. This is probably due to the inaccuracy in the estimated value of T_{sat}. The condensation temperature difference ΔT is almost unchanged along the bundle depth. The T_l decreases with increasing n. However, T_l is always greater than T_i. This is due to the heating of falling condensate by the bulk vapor. Generally, the relation between T_l and T_i depended on the values of n, ΔT and G. When ΔT and G were large, T_l was smaller than T_i for $n\geqslant5$. Figure 4(b) shows the distributions of the measured values of $y_{v,134a}$, $y_{v,125}$, and $y_{v,32}$, and the calculated value of x corresponding to Fig. 4(a). It is seen that the concentration of R134a with a higher boiling point decreases as condensation proceeds, whereas those of R32 and R125 with lower boiling points increase.

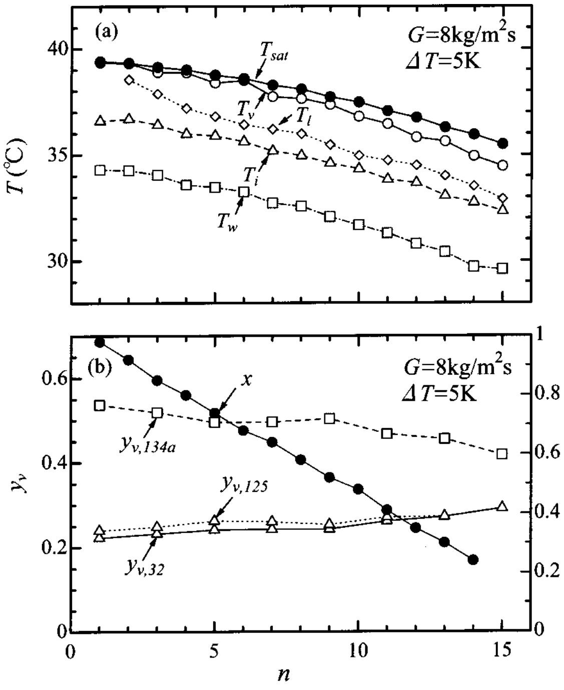

Fig. 4 Distributions of measured and calculated quantities in the tube bundle

Figure 5 shows the temperature drop of bulk vapor, $T_{v,\text{in}}-T_v$, in the tube bundle consisting of tube A plotted as a function of x with G and ΔT as parameters. It is seen that $T_{v,\text{in}}-T_v$ is an almost unique function of x irrespective of G and ΔT. This characteristics may be used to estimate the local vapor temperature in the tube bundle.

Figure 6 shows the ratio of the temperature drop across the condensate film T_i-T_w to the condensation temperature differ-

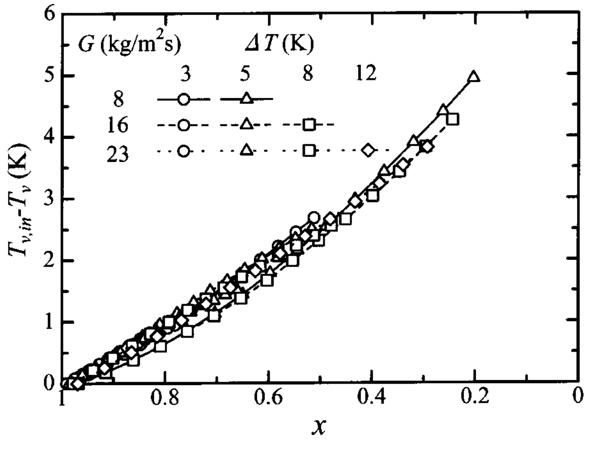

Fig. 5 Variation of $T_{v,\text{in}}-T_v$ with x

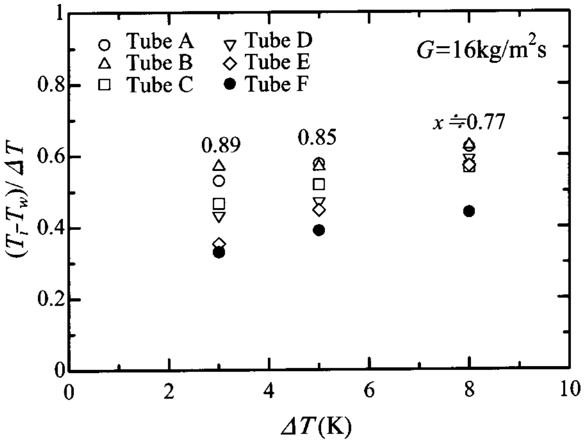

Fig. 6 Variation of $(T_i-T_w)/\Delta T$ with ΔT

ence ΔT, $(T_i-T_w)/\Delta T$, plotted as a function of ΔT. In Fig. 6, the results for tubes A–E at $G=16$ kg/m^2 s are compared. Generally, $(T_i-T_w)/\Delta T$ increases as ΔT increases, whereas the difference among tubes A–E decreases as ΔT increases. This indicates that the ratio of the condensate film resistance to the total resistance increases with ΔT. This is due to the suction effect associated with condensation, which acts to reduce the vapor-phase mass transfer resistance [3]. In Fig. 6, previous results for R123/R134a (≅82/18 mass%) condensing on tube F are also shown for comparison. The fin dimensions and close-up of tube F are also shown in Table 1 and Fig. 3, respectively. This tube had fin dimensions close to those of tube A. The experimental conditions are $T_v=50$°C and $G=19$ kg/m^2 s. Comparison of tubes A and F reveals that the value of $(T_i-T_w)/\Delta T$ for tube F is 62 to 71% of that for tube A. Thus the ratio of condensate film resistance to total resistance is much smaller for R123/R134a with a much larger temperature glide (≅21 K) than for R407C with the temperature glide of ≅6 K.

Figure 7 compares the values of α for all tubes at the first condensing row without condensate inundation from the upper tubes. Figures 7(*a–c*), respectively, show α for $G=4$, 8 and 23 kg/m^2 s plotted as a function of ΔT. Comparison of Figs. 7(*a–c*) reveals that the effect of G is more significant for smaller ΔT. At $\Delta T=3$ K, α increases by 67 to 94% as G increases from 4 kg/m^2 s to 23 kg/m^2 s. This is mainly due to the decrease in the mass transfer resistance in the vapor phase as a result of increased vapor shear. At $\Delta T=12$ K, on the other hand, the increase in α due to the increase in G is only 8 to 16%. This indicates that the decrease in the vapor-phase mass transfer resistance due to the suction effect was much higher than the vapor shear effect. At $G=4$ kg/m^2 s, where the vapor shear effect is smallest, α increases gradually with increasing ΔT for all tubes. At $G=8$ kg/m^2 s, α increases gradually with increasing ΔT for tubes A and C–E, whereas it decreases gradually with increasing ΔT for tube B. At $G=23$ kg/m^2 s, where the vapor shear effect is largest, α decreases gradually with increasing ΔT for all tubes. In Fig. 7, the previous results for R134a [2] and the Nusselt [4] equation are also shown for comparison. Comparison of Figs. 7(*b*) and 7(*c*) reveals that the α value for R134a is not affected so much by G. As expected, α is smaller for R407C than for R134a, with the difference being more significant for smaller G. The heat transfer enhancement as compared to the Nusselt [4] equation increases as G and ΔT increases. At $\Delta T=5$ K, the enhancement ratio for each tube is in the range of 3.1 to 3.7 and 4.1 to 5.6 at $G=4$ and 23 kg/m^2 s, respectively.

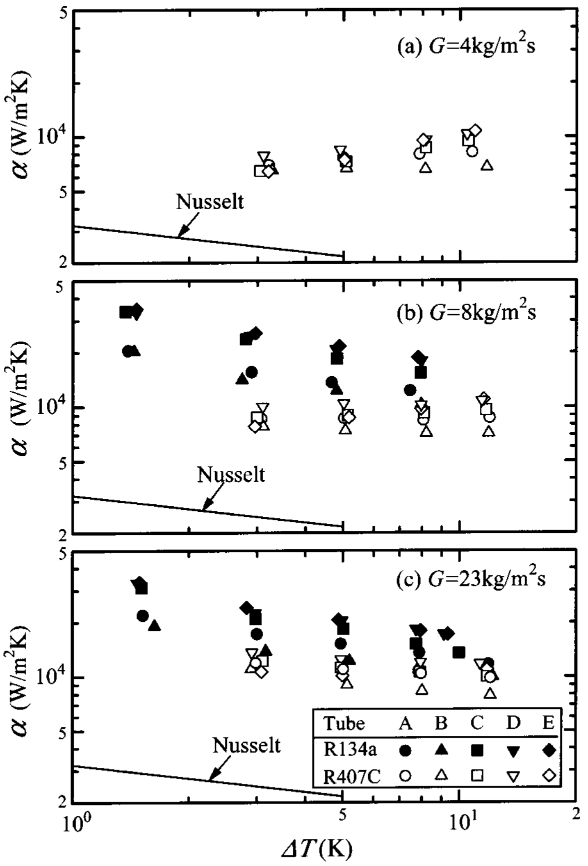

Fig. 7 Variation of α with ΔT; first condensing row

Figures 8(*a–e*), respectively, show Nu* for tubes A–E at $G=23$ kg/m^2 s plotted as a function of Re_f with ΔT as a parameter, where $\mathrm{Nu}^*=\alpha(\upsilon_l^2/g)^{1/3}/\lambda_l$ is the condensation number. Generally, the effect of ΔT is small. For all tubes, Nu* decreases as Re_f increases. The decrease is more significant for the three-dimensional-fin tubes C–E than for the low-fin tubes A and B. The most significant decrease is observed for tube C with the pyramid-shape fins. It is relevant to note here that the actual value of Re_f for each data point is more or less different from that shown in Fig. 8, because the condensate flow pattern in the tube bundle is considerably different from the gravity drained flow model assumed in the calculation of Re_f. Thus the experimented data for each tube show some scatter. In Fig. 8, the previous results for R134a [2] and the Nusselt [4] equation are also shown for comparison. For R134a, Nu* shows a more significant decrease with increasing Re_f than for R407C. As a result, the difference in Nu* between R407C and R134a decreases as Re_f increases. For R407C, the heat transfer enhancement as compared to the Nusselt [4] equation increases as Re_f increases. At $\mathrm{Re}_f=10^3$, the enhancement ratio ranges from 8.2 to 15 depending on the tube.

Figures 9(*a–e*), respectively, show Nu* for tubes A–E at $\Delta T=3$ K plotted as a function of Re_f with G as a parameter. For all tubes, Nu* increases as G increases. The increase is more significant for smaller Re_f. At $G=8$ kg/m^2 s, the effect of Re_f is generally small. It is interesting to note here that for the low-fin tubes A and B and the three-dimensional-fin tube E with secondary machining on the low fins, Nu* increases slightly as Re_f increases. This indicates that the vapor phase resistance is reduced by the mixing of bulk vapor by the falling condensate. At $G=23$ kg/m^2 s with the smallest vapor phase resistance, Nu* decreases with increasing Re_f. Again, the decrease is most significant for tube C. In Fig. 9, the previous results for R134a [2] and the Nusselt equation are also shown for comparison. In the case of R134a, the effect of G is negligible for the low-fin tubes A and B. For the three-dimensional-fin tubes C–E, on the other hand, α increases slightly as G increases. As was the case of Fig. 7 without

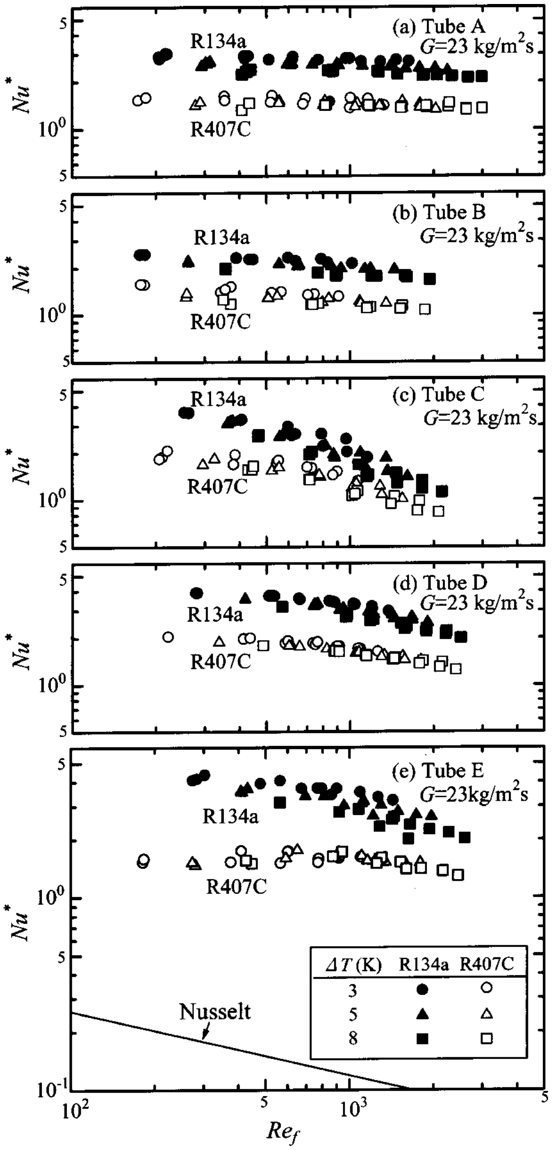

Fig. 8 Variation of Nu* with Re_f; effect of ΔT

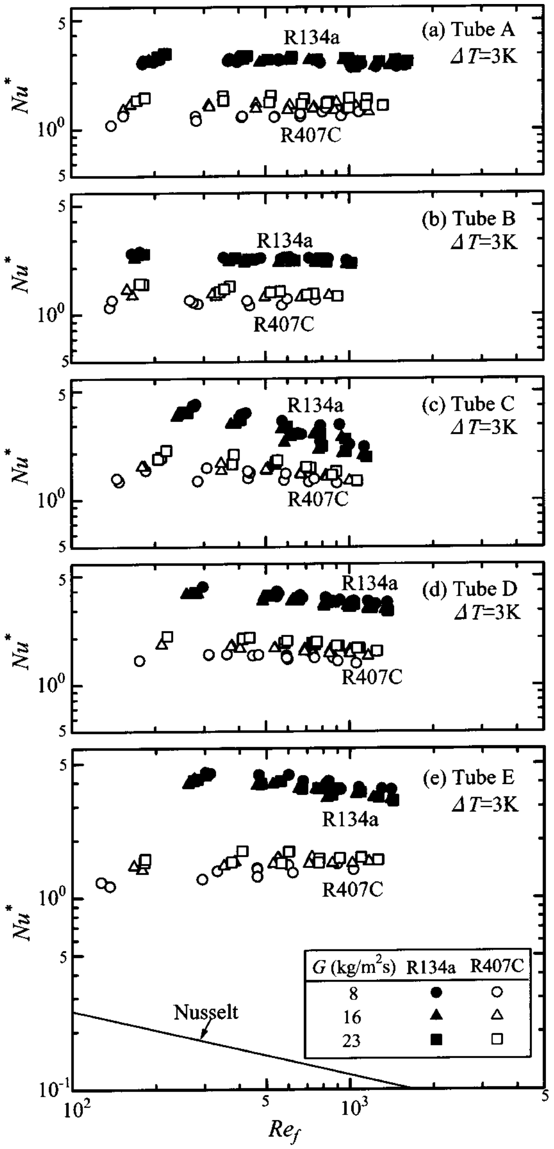

Fig. 9 Variation of Nu* with Re_f; effect of G

condensate inundation from the upper tubes, the difference in α between R407C and R134a is more significant for smaller G.

Figure 10(a) compares Nu* for all tubes at $G=8$ kg/m^2 s and $\Delta T=3$ K. Tubes D and E show almost the same and highest Nu*, whereas tubes A and B show almost the same and lowest Nu* (about 70 to 95% of tubes D and E depending on Re_f). The difference among the tubes is relatively large at small Re_f and decreases with increasing Re_f. In Fig. 10(a), the results for R134a [2] are also shown for comparison. At $Re_f=10^3$, the value of Nu* for R407C ranges from 38 to 58% of that for R134a depending on the tube. The decrease is most significant for tube E that shows the highest Nu* for R134a. It is also seen that for R407C, the difference in the Nu* value among tubes A–E is reduced to about 50% of that for R134a.

Figure 10(b) shows similar comparison at $G=23$ kg/m^2 s and $\Delta T=8$ K. In this case, tubes D and E show almost the same and highest Nu* for $Re_f<2000$, whereas tube A shows the highest Nu* for $Re_f>2000$. The difference among the tubes is more significant than the case of Fig. 10(a). It is also seen that the ratio of Nu* relative to that for R134a (60 to 66% at $Re_f=10^3$ depending on the tube) is larger than the case of Fig. 10(a). This is due to the decrease in the vapor phase resistance as a result of the combined vapor shear and suction effects.

Figure 11 shows the vapor phase heat transfer coefficient α_v for all tubes plotted as a function of Re_v with ΔT as a parameter. Three groups of data with different range of Re_v in Fig. 11 correspond to the cases of $G=8$, 16 and 23 kg/m^2 s, respectively. For each group, the data with the largest Re_v correspond to the first row through which the cooling water was passed and the other data correspond to the lower condensing rows. Condensation proceeds as Re_v decreases. Except for tube B, α_v increases as ΔT increases. This is due to the suction effect associated with condensation. Similar results have been observed for the vapor-phase mass transfer coefficient during condensation of R123/R134a in staggered bundles of horizontal low-fin tubes [3]. For tube B with the largest fin spacing, the effect of ΔT is not clear. This is in accord with the results shown in Fig. 6, where the α value for tube B showed a much smaller dependence on the suction than the other tubes. In Fig. 11, the relation for single-phase heat transfer [7], $\alpha_v \propto Re_v^{0.6}$, is also shown for comparison. It is seen that the α_v value for the first condensing row follows this relation fairly well. However, the experimental data for lower condensing rows do not

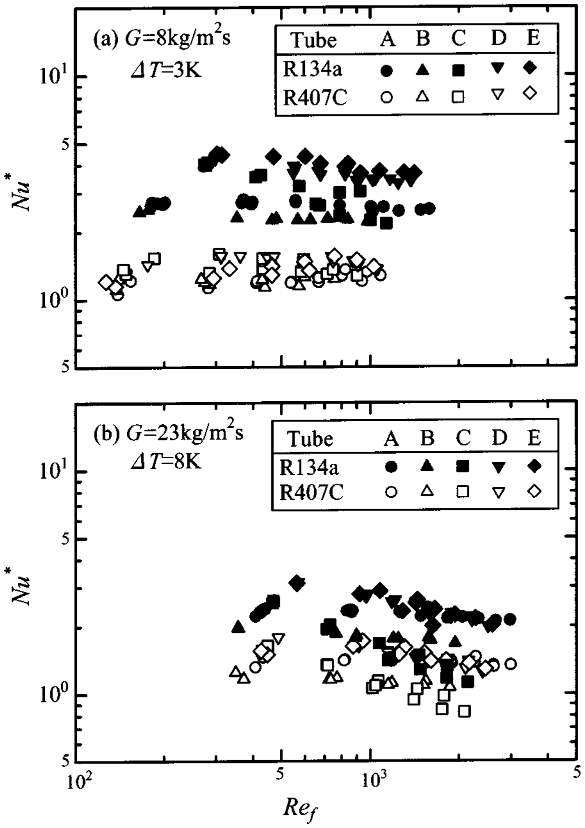

Fig. 10 Variation of Nu* with Re_f; comparison of R407C and R134a

necessarily follow the above relation. It is also seen that, except for the data for tubes B and E at $\Delta T = 3$ K, the α_v value for all tubes agrees fairly well with each other. This characteristics is responsible for the fact that the difference in the Nu* value among the tubes is much smaller for R407C than for R134a (see Fig. 10).

It is relevant to compare the present results with the previous results for R123/R134a [3] condensing in a staggered bundle of four types of low-fin tubes. In this study, the highest α was obtained by tube G which had fin dimensions close to the optimum values obtained by the theoretical analysis of film condensation of R123 in a bundle of horizontal low-fin tubes [8]. This tube showed the α value about 1.37 and 1.25 times as large as that of tube F with fin dimensions close to those of tube A at $G = 9$ and 35 kg/m^2 s, respectively. The dimensions and close-up of tubes F and G are also shown in Table 1 and Fig. 3, respectively. As seen from Fig. 6, the ratio of the condensate film resistance to the total resistance is much greater for R407C than for R123/R134a. Thus, it is probable that the α value at least 30% higher than that for tube A will be obtained for R407C by a low-fin tube with optimized fin dimensions.

Conclusion

Row-by-row heat transfer data were obtained for condensation of R407C in a 3×15 staggered bundle of horizontal finned tubes. Two kinds of low-fin tubes A and B and three kinds of three-dimensional-fin tubes C–E were tested. All tubes were commercially available. Generally, the three-dimensional-fin tubes showed a higher α than the low-fin tubes when the condensate inundation rate was small. However, the three-dimensional-fin tubes were subject to a higher effect of condensate inundation than the low-fin tubes and α decreased with increasing Re_f. The decrease was most significant for tube C with pyramid-shape fins. On the other hand, the low-fin tubes were little affected by the condensate inundation.

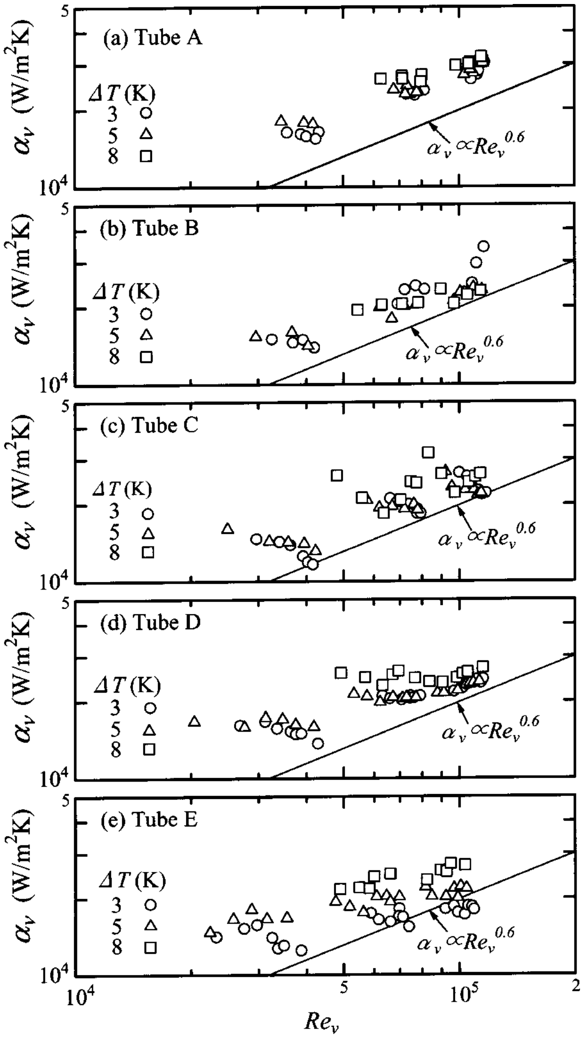

Fig. 11 Variation of α_v with Re_v

The α increased as G increased. The increase was more significant for smaller Re_f. The effect of ΔT was considerably different depending on G. While α increased with increasing ΔT at $G = 4$ kg/m^2 s, it decreased with increasing ΔT at $G = 23$ kg/m^2 s. This was due to the combined effects of vapor shear and vapor suction on the vapor phase mass transfer. For $\mathrm{Re}_f < 2000$, tube D with saw-tooth-shape fins and tube E with secondary machining on the tip of low fins showed almost the same and highest α. For $\mathrm{Re}_f > 2000$, on the other hand, the low-fin tube A showed the highest α. Comparison with previous results for R123/R134a indicated that the α value at least 30% higher than that for tube A is obtained by a low-fin tube with optimized fin geometry.

Comparison with previous results for R134a revealed that α was smaller for R407C, with the difference being more significant for smaller G. This was due to the increase in the mass transfer resistance in the vapor phase. By use of the experimental data for R134a, α_v was obtained for condensation of R407C. The α_v was correlated fairly well as a function of Re_v and ΔT and its value was fairly close to each other among tubes A–E. As a result, the difference in α among tubes A–E was less significant for R407C than for R134a.

Acknowledgment

The authors would like to thank the Daikin Industries Ltd. for providing us with the test tubes and test fluids.

Nomenclature

A = cross-sectional area of duct (m^2)
BX_i = bias limit of X_i
c_w = specific heat of water (kJ/kg K)
d = tube diameter at fin tip (mm)
d_i = tube inside diameter (mm)
G = refrigerant mass velocity based on duct cross-section (kg/m^2 s)
g = gravitational acceleration (m/s^2)
h = fin height (mm)
h_l = specific enthalpy of condensate (kJ/kg)
h_{lg} = specific heat of evaporation (kJ/kg)
h_v = specific enthalpy of vapor (kJ/kg)
l = effective tube length (mm)
N = number of measurements
Nu* = condensation number$=\alpha(v_l^2/g)^{1/3}/\lambda_l$
P = vapor pressure (Pa)
p = fin pitch (mm)
Q = heat transfer rate (W)
Q_l = heat loss from cooling water tubing between inlet and exit mixing chambers (W)
Q_{lt} = sum of heat losses from evaporator, vapor duct and test section (W)
q = average heat flux of a horizontal row (W/m^2)
R = result of a calculation based on a number of measurements
Re$_f$ = film Reynolds number based on gravity drained flow model
Re$_v$ = vapor Reynolds number$=u_v d/v_v$
SX_i = precision index of the mean of X_i
T_c = cooling water temperature (K)
T_h = hot water temperature (K)
T_i = vapor-liquid interfacial temperature (K)
T_l = liquid temperature (K)
T_{sat} = saturation temperature (K)
T_v = vapor temperature (K)
T_w = mean tube wall temperature at fin root for a horizontal row (K)
ΔT = condensation temperature difference$=T_v-T_w$ (K)
t = average fin thickness (mm)
t_{95} = Student's multiplier at 95% confidence level.
u_v = vapor velocity based on minimum flow cross-section (m/s)
W_c = flow rate of cooling water for a horizontal row (kg/s)
W_h = flow rate of hot water (kg/s)
X_i = ith variable
x = quality $(-)$

Greek Symbols

α = average heat transfer coefficient of a horizontal row (W/m^2 K)
α_v = superficial heat transfer coefficient for vapor phase (W/m^2 K)
α_s = heat transfer coefficient for condensate film (W/m^2 K)
ζ = ratio of maximum and minimum flow cross-sections of tube bundle $(-)$
θ = fin half tip angle (rad)
λ_l = thermal conductivity of liquid (W/m K)
μ_v = dynamic viscosity of vapor (Pa s))
v_l = kinematic viscosity of liquid (m^2/s)
ρ_v = density of vapor (kg/m^3)

References

[1] Gabrielii, C., and Vamling, L., 1997, "Replacement of R22 in Tube-and-Shell Condensers: Experiments and Simulations," Int. J. Refrig., **20**, pp. 165–178.
[2] Honda, H., Takata, N., Takamatsu, H., Kim, J. S., and Usami, K., 2002, "Condensation of Downward Flowing HFC134a in a Staggered Bundle of Horizontal Finned Tubes: Effect of Fin Geometry," Int. J. Refrig., **25**, pp. 3–10.
[3] Honda, H., Takamatsu, H., and Takata, N., 1999, "Experimental Measurements for Condensation of Downward-Flowing R123/R134a in a Staggered Bundle of Horizontal Low-Finned Tubes with Four Fin Geometries," Int. J. Refrig., **22**, pp. 615–624.
[4] Nusselt, W., 1916, "Die Oberflächenkondensation des Wasser-dampfles," *Zeit. Ver. Deut. Ing.*, **60**, pp. 541–546, 569–575.
[5] McLinden, M. O., Klein, S. A., Lemmon, E. W., and Peskin, A. P., 1998, NIST Thermodynamic and Transport Properties of Refrigerants and Refrigerant Mixtures—REFPROP, Version 6.0, National Institute of Standards and Technology.
[6] Moffat, R. J., 1989, "Describing Uncertainties in Experimental Results," Exp. Therm. Fluid Sci., **1**, pp. 3–17.
[7] Zukauskas, A., 1972, "Heat Transfer from Tubes in Crossflow," Adv. Heat Transfer, **8**, pp. 93–160.
[8] Honda, H., and Kim, K. H., 1995, "Effect of Fin Geometry on the Condensation Heat Transfer Performance of a Bundle of Horizontal Low-Fin Tubes," J. Enhanced Heat Transfer, **2**, pp. 139–147.

Melting of a Wire Anode Followed by Solidification: A Three-Phase Moving Interface Problem

S. S. Sripada

Ira M. Cohen

P. S. Ayyaswamy

Department of Mechanical Engineering and
Applied Mechanics,
University of Pennsylvania,
Philadelphia, PA 19104-6315

A fine metallic wire electrode is heated from below (by an electric discharge) causing melting and roll-up into a ball by surface tension. After the heating is terminated, a solidification front progresses through the melt until a solid ball is formed and cooled to ambient conditions. In this paper we numerically simulate the heating, melt motion and roll up and subsequent cooling and solidification. This is a three-phase problem (solid, liquid, and the ambient medium—plasma/gas) with two simultaneously moving phase interfaces, the outer one tracked by orthogonal grid generation conformal with the evolving boundary surface at each time interval. A novel observation in this study is that the wire end first drops until the melt radius equals the wire radius and then it begins to roll up into a ball consuming the wire. In other words, the inter-electrode gap first reduces and subsequently increases during an electronic flame off (EFO) discharge heating/phase-change process. [DOI: 10.1115/1.1576811]

Keywords: Heat Transfer, Melting, Multi-Phase, Solidification, Surface Tension

1 Introduction

In the assembly of microelectronic chips, the most reliable means to connect the circuitry in the chip to terminals that connect with an external device is by a process in which a low energy plasma discharge (called an electronic flame off or EFO) is used to heat and melt the end of a very fine (25 μm diameter) wire (anode). The liquid metal surface tension causes the molten metal to roll up into a ball whereupon the discharge is terminated and the melt cools and solidifies. The ball so formed is pressed down on a bond pad of a chip with some heat and ultrasonic power to form a ball bond.

It is important to be able to numerically simulate this process to aid in optimization. The development of the discharge from the high voltage pre-breakdown through the ionization avalanche and current growth to stabilization and steady state aspects of this problem has been treated by Qin et al. [1]. Here we concentrate on the heat transfer to the anode, phase-change, melt motion, and then cooling and solidification. This is a transient three-phase problem and the motion of the phase boundaries is of particular interest because concentricity, sphericity, and solidity of the ball formed are all factors in the quality of the ball bond.

The governing fluid and transport equations are solved numerically in an orthogonally discretized domain. A heat capacity method is used to account for phase-change at the melting and solidifying interfaces. Special procedures are adopted to account for the moving free-surface of the ball. These include regeneration of the grid at each time instant. At all instants a bounding coordinate line coincides with the mobile free-surface. Results include the melt shape evolution in time and the temperature distribution in the anode. A similar methodology is applied to study the solidification of the molten ball once the discharge is terminated. Results presented include the temperature distribution, and the location of the moving phase-change interface.

2 Literature Review

A comprehensive review of early free-surface flow modeling has been provided by Yeung [2]. More recent studies have been presented in [3] and [4]. Numerical methods for moving boundary problems have been described in [5], and modern mathematical modeling of melting, solidification, and freezing processes has been presented in [6] and [7]. The steady state free-surface tracking problem in an orthogonal coordinate system has been analyzed using a finite difference solution of the stream-function-vorticity formulation for the Navier-Stokes equation in [8]. The unsteady version of this method has been presented in [9]. Trygvaason and co-workers [10,11] have described a front-tracking method for multiphase flow and dendritic solidification.

With regard to phase-change problems, both finite difference methods [12,13] and finite element methods [14] have been applied to obtain solutions of phase-change problems with a moving interface. Structured and unstructured meshes with a compatible set of finite volume procedures have also been employed in [7] and [15]. A time variant mesh or a fixed-mesh approach have been used. In the time-variant mesh method of [14], the mesh is regenerated at each time step to account for the moving phase-change interface. In the fixed mesh method of [16], the latent heat of fusion is usually absorbed into the material's specific heat (equivalent specific heat model) or enthalpy (enthalpy model), but this introduces a severe nonlinearity in the material property. The enthalpy method, proposed in [17], treats the enthalpy as an additional variable. The equivalent specific heat model of [12] and [16] superimposes the latent heat effect on the specific heat of the system over a small temperature interval ($2\,\Delta T$) which acts as a range of temperature over which the phase-transition takes place. This introduces a severe nonlinearity in the specific heat and the choice of ΔT becomes crucial for convergence and prevention of oscillatory solutions. An effective algorithm that is insensitive to the choice of ΔT has been presented in [16] which is the method chosen for this study. For the problem of anode melting and motion of the free surface, we have chosen a Lagrangian method since explicit tracking of the moving interface between the arc and melt is desired. On the other hand, an Eulerian method is used to simulate the moving phase-change interface between the melt and the solid regions. This latter choice of an Eulerian method for the melt line was crucial to the success of the numerical algorithm. An attempt at a solution with a Lagrangian approach for the melting was made in the course of the development of this research. Apart from prohibitive cost of the computation in terms of computational time (32 MFLOP increase from 48 MFLOPs in a sample run), the overall algorithm was stable only for a very narrow

---

Contributed by the Heat Transfer Division for publication in the JOURNAL OF HEAT TRANSFER. Manuscript received by the Heat Transfer Division May 22, 2002; revision received February 25, 2003. Associate Editor: V. P. Carey.

choice of convergence parameters in the various iterative procedures and for simple geometries. Here, 1 MFLOP$=$1 million floating point operations. Since the full problem consisted of time-dependent geometry, the Lagrangian approach for melting was abandoned in favor of the Eulerian approach.

References [13] and [18] have described both a simplified model and experiments for the transient heating of a thin wire causing the tip to melt, roll-up of the melt, and subsequent solidification on termination of the arc. The shape of the melt is analytically/numerically determined assuming equilibrium based on minimum energy principles. A constant heat flux from the arc is assumed and is an input parameter for the simulation of the melting process. The fluid in the melt is assumed static and the temperature field in the melt is determined by solving the transient energy equation in a body-fitted coordinate system accounting for phase-change. The domain is remeshed at each time step. Comparisons with scaled-up experimental results are presented. The experimental results included high-speed motion pictures of the melting process for large length-scale and time-scale experiments. (It is very difficult to conduct experiments at the true length scale that also yield transient temperature data.) Results for *equilibrium* shape calculations of the free surface indicate a very small influence of gravity and Marangoni, i.e, surface tension gradient, effects. On this basis, Marangoni effects are assumed to be negligible in this study. A more detailed explanation for the negelect of surface tension gradients in the formulation is included in the next section.

3 Theory

3.1 Anode Melting and Surface Evolution. For applications of interest in microelectronic packaging, the typical wire diameter (the appropriate length scale) is $d=25.4\ \mu$m, and with gold wire in air, the Eötvös number $\mathrm{Eo}=\Delta\rho g d^2/\sigma\approx 9\times 10^{-5}$, where $\Delta\rho$, g, and σ are the density difference between the two media, gravitational acceleration, and surface tension, respectively. This indicates that gravity has a negligible effect on the process compared to surface tension, and it is surface tension which is the prime cause for motion of the molten layer. Although surface tension forces are important, surface tension gradient effects are negligible in this problem. Very briefly, this has to do with the extremely small radii of curvature that arise (wire radius $\sim$13 μm) and very short times for the process (ball formation time $\sim$1 msec) as compared with typical problems in which Marangoni forces play a role. The ratio of surface tension gradient force to surface tension force may be estimated as:

$$\frac{\left(\frac{d\sigma}{dT}\right)\left(\frac{dT}{dr}\right)2\pi r^2}{2\pi r\sigma}=0.01 \quad \text{for gold,} \tag{1}$$

where,

$$\left(\frac{d\sigma}{dT}\right)=0.52\times 10^{-3}\frac{N}{mK}, \quad \sigma=1.14\frac{N}{m}, \quad \text{and} \quad \Delta T\approx 20^\circ, \tag{2}$$

over a distance of the wire radius (twice the computed result). Viscous forces are a factor of 10 smaller and gravitational forces are a factor of 10^3 smaller. In this context, reference may be made to the study of Liu et al. [19] as an example of the importance of thermocapillary forces in driving flows and in phase change. The thermal Marangoni number is defined there by:

$$\mathrm{Ma}=\frac{\frac{d\sigma}{dT}\Delta T\frac{d}{2}}{\hat{\mu}\alpha} \quad \text{and ,} \tag{3}$$

in all cases discussed in Ref. [19], Ma$\sim$1500 or greater. Using the properties of gold wire as above with $\hat{\mu}=5.13\times 10^{-3}$ kg/ms and $\alpha=0.404\times 10^{-4}\ \mathrm{m^2/s}$, for our problem, Ma$=$0.7 or a factor of 10^3 smaller than the exemplar problems cited. It is seen that the inclusion of Marangoni force in our problem would at best introduce a 1% correction to our results. This is the justification for the neglect of the surface tension gradient force in our formulation.

The velocity field is determined purely by the interaction between surface tension (σ) and viscosity ($\hat{\mu}$) of the fluid. The appropriate velocity scale is, then, the ratio $\sigma/\hat{\mu}$. Thus the time scale becomes: $d\hat{\mu}/\sigma$, and the pressure scale is: $\rho\sigma^2/\hat{\mu}^2$. The nondimensional equations governing the motion of the melt become:

$$\nabla\cdot\mathbf{u}=0, \quad \frac{\partial\mathbf{u}}{\partial t}+\mathbf{u}\cdot\nabla\mathbf{u}=-\nabla p+Oh^2\nabla^2\mathbf{u}. \tag{4}$$

Here $\mathbf{u}$ and p are respectively the velocity field and pressure in the melt, respectively. The Ohnesorge number, $Oh=\hat{\mu}/(\rho\sigma d)^{1/2}$, represents the ratio of the viscous forces to those due to surface tension [20]. The flow field in the melt has to satisfy the *dynamic* or stress-free boundary conditions at the free surface:

$$\tau{:}\mathbf{nn}+(p-p_0)+\sigma\left(\frac{1}{R_1}+\frac{1}{R_2}\right)=0, \quad \tau{:}\mathbf{nt}=0. \tag{5}$$

Here, τ, is the viscous stress tensor in the melt, $p-p_0$ is the static pressure in the melt in excess of the ambient pressure, (R_1,R_2) are the principal radii of curvature of the free surface, $\mathbf{n}$ is the local surface normal vector, and $\mathbf{t}$ is the local surface tangent vector. The free surface is also subject to the kinematic boundary condition,

$$\frac{D\mathbf{R}_s}{Dt}=\mathbf{u}|_{\mathbf{R}=\mathbf{R}_s}, \tag{6}$$

where D/Dt is the material derivative, $\mathbf{R}_s$ is the position vector of any point on the free surface. At the interface between the melt and solid regions, the flow is subject to the no-slip boundary condition, $\mathbf{u}\cdot\mathbf{t}=0$ and the normal velocity condition for a melt-solid interface given by Eq. (10) below.

As noted in [21], the fluid dynamics of the melt is inherently coupled to the heat transfer because the fluid volume depends on the heat flux from the arc at the free surface. This volume increases in time as more of the anode becomes molten. As the free surface moves, i.e., the anode deforms, and the gap between the electrodes is modified which affects the arc. Thus the arc problem becomes coupled to the fluid dynamics and transport of the melt. Thus the free surface represents an interface that involves a complex interaction between the arc on one side and the fluid dynamics and heat transfer in the melt side. The heat transfer in the melt is governed by

$$(\rho c)_l\left(\frac{\partial T}{\partial t}+\mathbf{u}\cdot\nabla T\right)=\nabla\cdot(\kappa_l\nabla T), \tag{7}$$

where T is the temperature, and c and κ are the specific heat and thermal conductivity, respectively. The subscript l refers to the liquid phase. The energy equation is subject to a heat flux boundary condition at the free surface:

$$-\kappa_l\nabla T\cdot\mathbf{n}=q_c+q_n-q_L, \tag{8}$$

where, q_c+q_n is the energy flux from the electronic flame off (EFO) as discussed in [21,22], and q_L is the thermal loss by radiation and natural convection from the free surface.

In [23], we present an analysis for the steady state EFO responsible for heating and melting the wire anode. The results in terms of representative charged particle and electron temperature distributions along the wire (symmetry) axis as well as the resultant heat flux to the wire are provided therein.

The heat transfer in the melt is coupled to the energy equation in the solid phase through the conditions at the solid-liquid interface:

$$T_s=T_l=T_m, \quad -\kappa_s\nabla T_s\cdot\mathbf{n}+\kappa_l\nabla T_l\cdot\mathbf{n}=\rho_l\lambda(\mathbf{u}_l-\mathbf{u}_i)\cdot\mathbf{n}, \tag{9}$$

$$\rho_l(\mathbf{u}_l-\mathbf{u}_i)\cdot\mathbf{n}=\rho_s(\mathbf{u}_s-\mathbf{u}_i)\cdot\mathbf{n}, \qquad (10)$$

where subscript s refers to the solid phase, m refers to melting, $\mathbf{n}$ is the local surface normal vector at the phase-change interface, λ is the latent heat of fusion, and $\mathbf{u}_i$ is the velocity of the moving phase-change interface. The energy equations are also governed by the initial and boundary conditions of the phase-change problem. The boundary conditions for the solid region include losses due to radiation and natural convection to the ambient from the lateral surfaces of the anode. The temperature boundary condition $(T=T_\infty)$ applies at the far end of the anode.

3.2 Solidification of the Melt. With the arc extinguished, the anode loses heat by conduction along its axis and by radiation and natural convection from its surfaces.

The velocity field is assumed to be zero in the solid region. In the melt and the solid wire, the temperature field is governed by the equations:

$$(\rho c)_s\frac{\partial T}{\partial t}=\nabla\cdot(\kappa_s\nabla T), \quad (\rho c)_l\left(\frac{\partial T}{\partial t}+\mathbf{u}\cdot\nabla T\right)=\nabla\cdot(\kappa_l\nabla T), \qquad (11)$$

These two equations are coupled through conditions at the solid-liquid interface which were given earlier in Eqs. (9) and (10). The equations are also subject to boundary conditions (in cylindrical coordinates):

Along the end face of the cylinder $(0\leqslant r\leqslant d/2, z=l_w)$:

$$T=T_\infty$$

At the ball surface and curved surface of the cylinder $(\mathbf{R}=\mathbf{R}_s)$:

$$-\kappa\nabla T\cdot\mathbf{n}=h(T-T_\infty)+\varsigma\epsilon(T^4-T_\infty^4)$$

At the axis of symmetry $(r=0, 0\leqslant z\leqslant l_w)$:

$$\nabla T\cdot\mathbf{n}=0.$$

The last condition is just the analyticity boundary condition at the singular point of the axisymmetric coordinate system. All the dimensions are input parameters in the simulation. In the above, T_∞ is the ambient temperature, h is the convective heat transfer coefficient, ϵ is the emissivity of the material surface, and ς is the Stefan-Boltzmann constant. The lateral surfaces are taken to lose heat by radiation and convection, while the end face of the cylinder is considered to be at ambient temperature. In the convective boundary condition, the position vector $\mathbf{R}_s$ is used to denote the anode surface wherein lies the geometric difficulty. The boundary condition cannot be prescribed in a simple fashion in the axisymmetric cylindrical coordinate system. This necessitates the generation of an orthogonal boundary conforming grid system (see [21] for details).

The initial conditions applicable for the above set are those that exist at the instant the arc is extinguished and the anode ceases melting.

The governing equations are nondimensionalized by the wire diameter d as the length scale, T_∞ as the temperature scale, and $d^2/\alpha=d^2(\rho c)_\infty/\kappa_\infty$ as the time scale. The variable properties (ρc) and κ are nondimensionalized by $(\rho c)_\infty$ and κ_∞, respectively.

This is a two region problem and is nonlinear, in general, due to the presence of the unknown location of the moving interface in the interfacial conditions. Except for simple cases, only numerical solutions of the problem exist for most practical applications.

Next, we describe the numerical methodology to solve the free surface, melting and solidification problems using modern computational techniques.

4 Numerical Methodology

4.1 Numerical Methodology for Anode Evolution. The anode tip melts and rolls up due to surface tension as more and more energy is deposited at the anode surface by the plasma.

The orthogonal grid generation method (see [21] for details) is used to discretize the evolving anode domain at each instant of time. An important consideration in the grid generation process is the effect of the sharp corners in a cylindrical anode. A real anode starts with a hooked, jagged edge. In this study, a finite radius of curvature equal to 0.1 wire diameters is assumed at the end face of the cylindrical anode in a plane perpendicular to the curved surface of the cylinder. With this assumption, the problem of generation of an orthogonal grid becomes tractable.

The Navier-Stokes equation and the energy equation are transformed from the axisymmetric physical domain to a rectangular computational domain. A solution of the nonlinear coupled covariant Laplace equations [24,25] with the prescribed domain coordinates as boundary conditions provides the required mapping of the physical domain of our wire-plane problem to a rectangular computational domain:

$$\frac{\partial}{\partial\xi}\left(f\frac{\partial r}{\partial\xi}\right)+\frac{\partial}{\partial\eta}\left(\frac{1}{f}\frac{\partial r}{\partial\eta}\right)=0, \quad \frac{\partial}{\partial\xi}\left(f\frac{\partial z}{\partial\xi}\right)+\frac{\partial}{\partial\eta}\left(\frac{1}{f}\frac{\partial z}{\partial\eta}\right)=0$$

$$\mathbf{R}=\mathbf{R}_b, \quad \text{at } \eta=0,\ \xi\in[0,1], \quad \mathbf{R}=\mathbf{R}_t, \quad \text{at } \eta=1,\ \xi\in[0,1]$$

$$\mathbf{R}=\mathbf{R}_l, \quad \text{at } \eta=0,\ \xi\in[0,1], \quad \mathbf{R}=\mathbf{R}_r, \quad \text{at } \xi=1,\ \eta\in[0,1],$$

where $\mathbf{R}(r,z)$ is the position vector in the (r,z) coordinate system, and the subscripts b, t, l, r denote the bottom, top, left, and right domain boundaries, respectively. f is the "distortion" function of the scaling factors, defined as the ratio h_η/h_ξ, in the (ξ,η) coordinate system. Here,

$$h_\xi=\sqrt{g_{11}}=\sqrt{\left(\frac{\partial r}{\partial\xi}\right)^2+\left(\frac{\partial z}{\partial\xi}\right)^2}, \quad h_\eta=\sqrt{g_{22}}=\sqrt{\left(\frac{\partial r}{\partial\eta}\right)^2+\left(\frac{\partial z}{\partial\eta}\right)^2},$$

where g_{11} and g_{22} are the diagonal components of the covariant metric tensor. As the distortion function f involves derivatives of both the unknown mapping functions $(r(\xi,\eta),z(\xi,\eta))$, the grid generation equations are highly nonlinear and coupled. A finite volume method and a power-law scheme [26] are used to discretize the governing equations. Due to the strong nonlinearities, an iterative algorithm is used for solution. At a given iteration level, a low relative error tolerance of 10^{-6} is used. A robust multigrid solver, MGD9V [27,28] is used to solve the nominally linear equations. The grid error is monitored via the Maximum Deviation from Orthogonality (MDO) defined as

$$\text{MDO}=\max(|90°-\theta_{i,j}|), \quad \text{where}$$

$$\theta=\cos^{-1}\left(\frac{g_{12}}{h_\eta h_\xi}\right), \quad \text{and} \quad g_{12}=\frac{\partial r}{\partial\xi}\frac{\partial r}{\partial\eta}+\frac{\partial z}{\partial\xi}\frac{\partial z}{\partial\eta}.$$

Here, g_{12} is the off-diagonal component of the covariant metric tensor and $\theta_{i,j}$ is the angle between the ξ and η grid line at a grid location $\mathbf{R}(r_i,z_j)$.

The numerical accuracy of the computer programs is tested by grid generation for simple geometries like an annular sector in a polar coordinate system. In all cases the grid obtained gave an $\text{MDO}\leqslant 0.5°$. For example, for a 41×41 grid generated using this method, $\text{MDO}=0.85°$ and this represents an orthogonality error of $\pm 0.94\%$ apart from the standard discretization error resulting from the use of central differences to represent first order derivatives in the partial differential equations. This error is $O(\Delta\xi^2)\approx 10^{-4}$.

The iterative Semi-Implicit Pressure Linked Equation Revised (SIMPLER) algorithm of [26] is used to solve the momentum equation (see also the extension to orthogonal coordinates in [29], to general curvilinear coordinates in [30,31], and to binary systems in [32]). The procedure employs a staggered grid where all the dependent variables except velocities are located at centers of the finite volumes (discretization units). The velocities are located at grid points that lie on the control volume faces. This staggered arrangement prevents pressure oscillations in the numerical solution. The algorithm couples the continuity equation with the momentum equation and iteratively obtains the correct velocity and pressure fields such that mass conservation is strictly satisfied.

For the interface motion, primitive variables are used in the solution of the momentum equation. An explicit implementation of the kinematic boundary condition of Eq. (6) is used to advance the free surface at each time step.

As mentioned earlier, the heat flux boundary condition at the free surface (see equation (8)) couples the plasma model to the model for the energy and flow of the melting anode. To model this coupling and the free surface accurately, strict enforcement of the space conservation law (see [33]) is essential. The space conservation law essentially is a continuity equation for zero fluid velocity in moving volumes. An integral statement of the space conservation law is:

$$\frac{D}{Dt}\int_V dV=\int_A \mathbf{u}_b\cdot d\mathbf{A}. \tag{12}$$

It simply states that a moving material volume is confined by its bounding surfaces moving at velocity $\mathbf{u}_b$ such that they always enclose the same material volume. Although this may seem a belabored point, the inexact nature of computational modeling of the physics of fluid mechanics necessitates an explicit statement of this constraint. For example, in a numerical implementation of integral conservation laws, the integrations are approximated by assuming velocities at discrete points to be prevailing over an entire cell surface of the finite volume. This approximation can lead to errors that propagate and accumulate to significant values in a moving boundary problem although they are acceptable in fixed boundary problems. These errors accumulate as mass sources or sinks and can significantly affect the accuracy, convergence and stability of the numerical algorithm. Here, it is noted that the space conservation law need not be considered for moving control volumes if only one set of coordinate lines is moving (e.g., vaporization of a fuel droplet) or when grid velocities are equal at opposite sides of the control volume.

With regard to the phase-change interface, the equivalent heat capacity method of [16] is used (see below), and this successfully avoids grid instabilities that usually arise while explicitly tracking two interfaces. It may be noted that the explicit tracking of two interfaces (one for the free surface and one for the phase-change as required in the present formulation) is a challenging numerical problem and exhaustive numerical experimentation for the iterative relaxation parameters is required in order to obtain satisfactorily convergent solutions.

4.2 Numerical Modeling of Solidification. Following the procedure described in [16], the two-region solidification is reduced to a one region problem with a jump in the specific heat over a temperature interval 2 ΔT around the melting point for the material.

It has been shown [12] that if the heat capacity per unit volume (ρc) is defined as

$$\rho c=\begin{cases}(\rho c)_s, & \text{if } T<T_m,\\ \rho_s\lambda\,\delta(T-T_m), & \\ (\rho c)_l, & \text{if } T>T_m,\end{cases} \tag{13}$$

and

$$\kappa=\begin{cases}\kappa_s, & \text{if } T<T_m,\\ \kappa_l, & \text{if } T>T_m,\end{cases}$$

then, the Eqs. (11) along with the interfacial coupling conditions in equations (9)–(10) may be reduced to:

$$\rho c\left(\frac{\partial T}{\partial t}+\mathbf{u}\cdot\nabla T\right)=\nabla\cdot(\kappa\nabla T). \tag{14}$$

In Eq. (13), δ is the Dirac delta function. The reduction of the system to one energy equation allows for the use of a fixed grid approach. The velocity field is set to zero in the solid phase. In the numerical solution, the Dirac delta function in Eq. (13) is replaced by a finite delta function with a large specific heat value over a small temperature interval 2 ΔT across the fusion temperature. In the algorithm proposed in [16], nodal temperature values are used to calculate the property at any given location, and an effective specific heat is calculated as an average of the influence of all the neighboring nodal temperatures. This eliminates the dependence of the convergence process on the choice of ΔT. The reduced energy equation is numerically solved in a geometrically irregular domain consisting of a molten ball at the end of a long cylinder of diameter d.

The unsteady heat transfer problem is defined in an axisymmetric domain while the (ξ,η) grid system is two-dimensional. Therefore the equations are first written in the (r,z) coordinate system and *then* transformed to the computational (ξ,η) domain. This preserves the axisymmetric nature of the original problem. A finite volume method and the power law scheme [26] for convection-diffusion equations is employed to discretize the unsteady energy equation. The system of discretized equations at each time step is solved iteratively using the multigrid solver MGD9V. At the end of each iteration, the temperature is used to update the properties. The Neumann boundary conditions are implemented by artificial Dirichlet conditions in the numerical procedure that are updated after each iteration to simulate Neumann conditions. In a converged solution, this results in a correct implementation of the Neumann conditions.

The overall simulations were made on a 800 MHz Pentium 3 processor with 512 MB RAM Dell Optiplex GX300 highend PC and took about 0.25 hours for a typical run. Simulations for a variety of additional cases (not discussed here) were made using the Pittsburgh Supercomputer facility.

5 Results and Discussion

Multigrid based simulations were made for solidification of a molten gold ball pendent at the end of a long slender gold cylinder (wire). Parameters used for the simulation were: wire diameter $d=1$ mil$=25.4$ μm, a wire length $l_w=30d$, and molten ball radius$=0.75d$. The melting temperature of gold is $T_m=1336$ K. The temperature band ΔT in the approximation of the Dirac delta function is taken to be 1 K. Even with the choice of 2 K for ΔT, the results were found to be insensitive to ΔT. All physical prop-

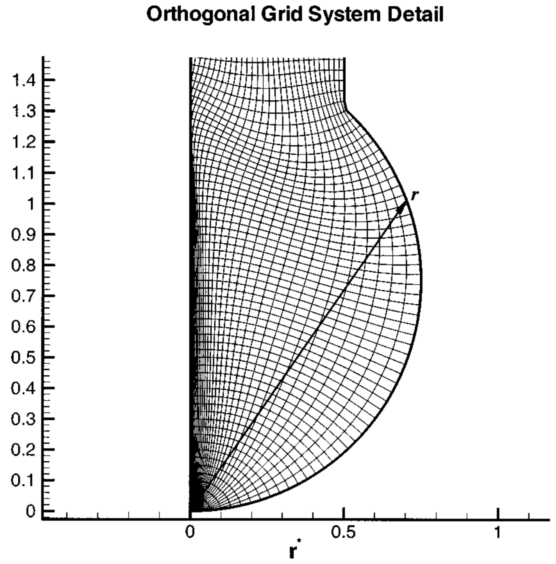

Fig. 1 **(ξ,η) grid system detail: all lengths normalized by wire diameter**

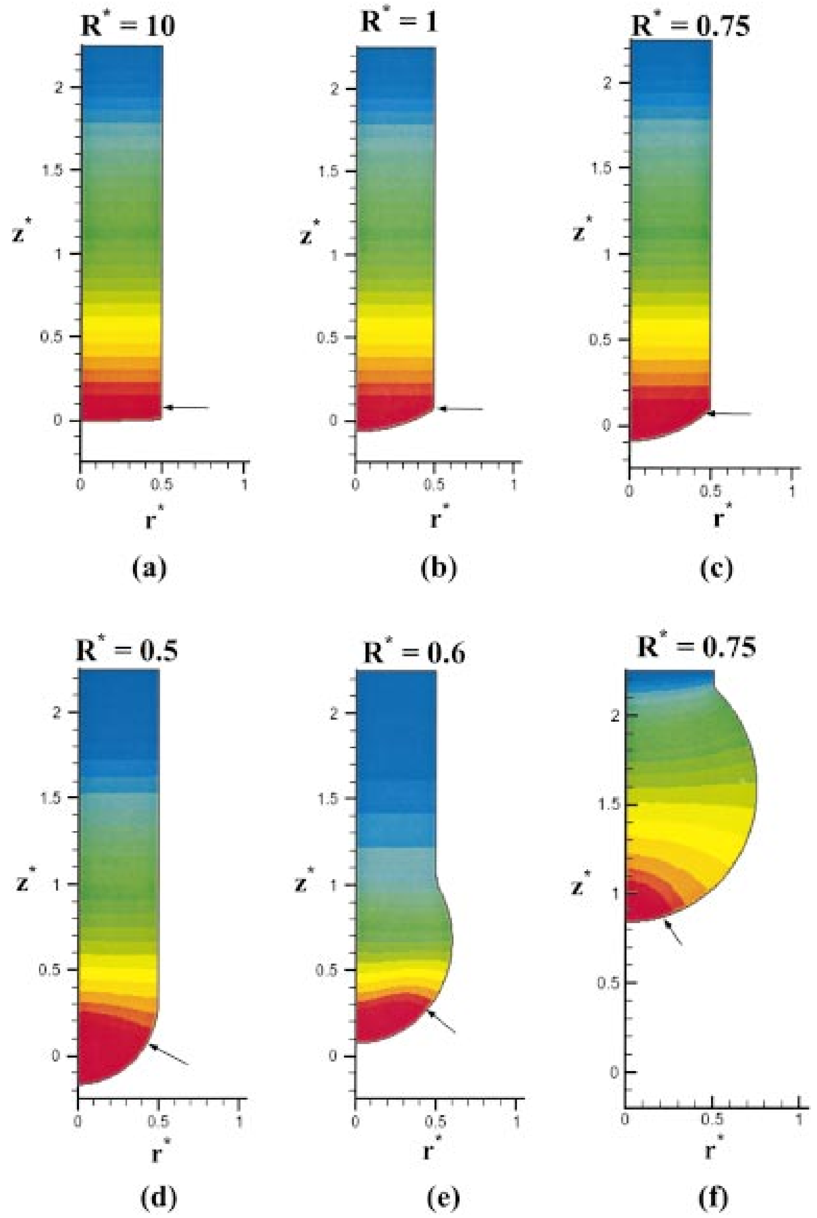

Fig. 2 Evolution of the free surface of the anode during melting: (a) Free surface at $t^*=2.53$, (b) Free surface at $t^*=4.69$, (c) Free surface at $t^*=9.56$, (d) Free surface at $t^*=18.8$, (e) Free surface at $t^*=28.3$, and (f) Free surface at $t^*=45.2$. Arrow denotes location of solid-liquid interface.

erties were from interpolations of handbook data for gold [34–36]. The ambient reference temperature is $T_\infty = 300\,\mathrm{K}$.

Figure 1 illustrates an enlarged view for a 60×60 orthogonal grid in the vicinity of the anode tip at an instant when the wire tip is the segment of a sphere of diameter $1.5d$. For the grid presented, MDO=0.793° which represents an orthogonality error of ±0.88% apart from the standard discretization error resulting from the use of central differences to represent first order derivatives in the partial differential equations after one integration over each control volume. This error is $O(\Delta\xi^2, \Delta\eta^2) \approx 10^{-4}$.

Figure 2 displays a series of figures showing the evolution of the melting anode free surface as the discharge progresses along with the variation in temperature shown by the color maps. Red indicates the hottest region and blue indicates the coldest temperature. The time t has been normalized by 9.16×10^{-6} seconds yielding a nondimensional time t^*. The lengths are all normalized by 1 wire diameter. The ranges of the axes in each plot are identical so the evolution of the free surface can be seen. In Fig. 2(a), the anode tip has just begun melting. The instant is that when the anode tip has a radius of curvature of 10 wire diameters. Due to the sharp corners of the anode, the heat flux in the anode is maximum at those points during the breakdown. The anode begins melting at the periphery of the bottom. The corners are noted to get dulled soon after the initiation of the discharge but only subsequent to the establishment of about 93% of the steady state current. The molten liquid from these corners starts creeping toward the axis as melting progresses inward towards the axis. Thus, the initial melting acts to transfer material from the periphery of the anode tip toward the center. This creates a dip in the anode tip due to the surface tension induced bulge. Thus, the arc gap reduces as the anode starts to melt. This reduction in the arc gap increases the heat flux from the plasma. As melting progresses, more of the anode melts and the radius of curvature of the free surface keeps decreasing in time to support the growing mass of molten liquid. Surface tension acts to support the liquid once the elastic tension, otherwise present in the solid phase, is lost due to phase change.

In Fig. 2(b), the free surface has a radius of curvature equal to 1 wire diameter. As more of the melt material flows towards the center, the tip bulges further down. The rate of reduction of the gap increases significantly for radii of curvature less than 1 wire diameter. In Fig. 2(c), the radius of curvature of the tip is 0.75 wire diameters, and the interelectrode gap is reduced by about 0.1 wire diameters. In Fig. 2(d), the radius of curvature is 0.5 wire diameters, i.e., equal to the wire radius. This is the minimum radius of curvature for the anode tip. This is also the instant of time when the anode tip stops descending into the interelectrode gap. The maximum reduction in the inter-electrode gap equals 0.17 diameters.

We note the surprising feature that the interelectrode gap first reduces and subsequently increases during an EFO discharge.

Any subsequent melting leads to an increase in the gap. This can be explained by mass conservation and geometry. For the large radii of curvature, the volume of molten material is small. The volume of material in the pendent molten region is the spherical cap volume. This volume is the difference between the volume of the segment of a sphere and the cone with its base being the edge of the solid wire and its apex being the center of the imaginary sphere. As the radius of curvature decreases to support the weight of new molten material, the volume enclosed within the spherical segment decreases as the third power of the radius if the solid angle of the spherical segment were to remain constant. In order to accommodate the new material, the solid angle must increase. Moreover, the center of the imaginary sphere moves down along the axis due to the reduction in the radius of curvature. These factors result in the dip into the inter-electrode gap. When the radius of curvature equals the wire radius, the molten region is a hemisphere, i.e., the solid angle is 2π steradians. The center of the imaginary sphere is at the edge of the straight solid cylindrical region. Any molten material added to the pendent region causes an increase in the radius of curvature which implies a cubic increase in the volume of the melt region if the solid angle were to remain 2π steradians. The cone now flips through itself and the solid angle decreases as the center of the imaginary sphere moves from the solid region into the melt region. A much longer portion of the cylindrical solid region melts for each unit increase in the radius of curvature. These factors now contribute toward an ascent of the melt region and the inter-electrode gap begins to increase as shown in Fig. 2(e). Due to the cubic dependence of volume on the radius of curvature, each unit increase in radius of curvature results in a larger ascent of the melt region. This increase in the gap persists until termination of the discharge. In Fig. 2(f), the anode tip is shown at the instant of the termination of discharge when the radius of curvature becomes $R^* = 0.75$ or 1.5 times the wire radius. The time instant is $t^* = 45.2$ which is equivalent to 0.41 ms. Once the radius of curvature reaches the minimum of 0.5 wire diameters, the rate of change in radius of curvature drastically decreases because for a unit change in radius, much more molten material must be melted. Moreover, as the interelectrode gap increases, the magnitude of heat flux from the arc starts decreasing and thus more time is required to melt a unit volume of material. The liquid thermal diffusivity is less than the solid, therefore as the thickness of the liquid layer increases, the thermal resistance in the wire increases. This also contributes in the increase of the time period to melt a unit volume of solid wire.

The interelectrode gap increases by 0.856 diameters by the end of the discharge. In the above discussion, the volume changes are further exaggerated due to volumetric contraction on melting.

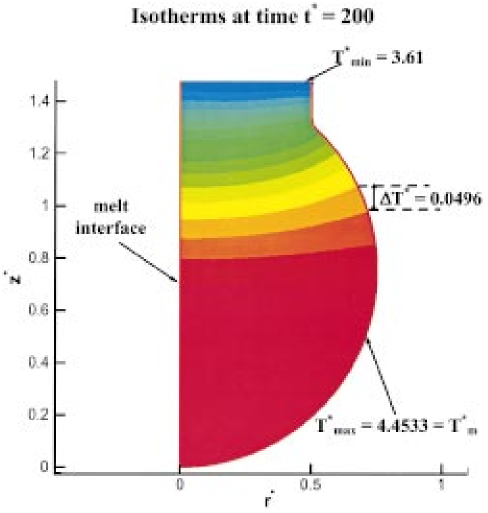

Fig. 3 Isotherms at $t^* = 200$. Nondimensional temperature $T^* = T/T_\infty$.

The isotherms in the vicinity of the anode tip region after 400 nondimensional time steps of $\delta t^* = 0.5$, or $t^* = 200$, subsequent to termination of the discharge are shown in Fig. 3. For the choice of parameters, it takes 13 ms for the domain to attain steady state which numerically corresponds to about within 1% of the ambient temperature. We have also investigated the position of the phase-change interface at different times during this simulation. The solidification progresses from the ''neck'' (joint between the melt to the solid region), downwards and towards the axis of symmetry rather than from the outside inwards. For the fine wire discussed here, conduction through the gold is a far larger effect than cooling by conduction, convection, or radiation from the ball surface. These observations are also supported in our large scale experimental studies [37] for this configuration where heat conduction is found to be the primary mode of heat dissipation from the molten ball. The very large thermal conductivity of gold is an advantage in bonding because if solidification occurred from the outside inwards, then a shrinkage void of about 10% by volume would occur in the center of the ball. Such a void would have a radius of about 47% of the outer radius of the ball and would severely compromise the bond. Thus the calculation of solidification must be done very carefully to assess and mitigate the possibilities for shrinkage void formation. This we have done as described in detail above. With solidification that proceeds from the neck downwards and towards of the axis of symmetry, the void migrates downwards until it is ejected from the bottom of the ball as the last of the melt solidifies and contracts [21].

6 Conclusions

The heat transfer from an EFO discharge to the anode causes it to melt and roll up due to surface tension into a pendent ball at the tip of the anode. The theory for the melting and for the motion of the free surface of the melt has been presented. A discussion of current numerical techniques and the numerical methodology for a simulation of the melting, free surface motion and solidification process (once the EFO discharge is extinguished) has been presented. All of the numerical methodology is based on finite volume discretization of the governing equations and a multigrid iterative solver. Results for simulations of the anode melting and solidification are presented. It has been shown for the first time, that during the EFO discharge, the inter-electrode gap first reduces and then increases. The minimum gap is at the instant when the radius of curvature of the anode tip equals the wire radius.

Thermal characteristics such as those presented above are very important in determining the optimal conditions to generate ''good'' balls for bonding. It is possible to avoid distributed porosity and void formation in the ball by systematically understanding the thermal behavior of the material during this process.

7. Acknowledgments

The authors gratefully acknowledge discussions with Mr. K. Mukundakrishnan. They gratefully acknowledge the support of this work by the U.S. National Science Foundation through NSF grant CTS-94-21598. The support of the Pittsburgh Supercomputer Center through a grant from the U.S. National Science Foundation is also gratefully acknowledged.

Nomenclature

A = area of cross-section, surface area (m^2)
c = specific heat capacity (J/kgK)
d = wire diameter (m)
Eo = *Eötvös* number ($=g\Delta\rho d^2/\sigma$)
f = distortion function of the scaling factors
g = acceleration due to gravity (m/s^2), components of covariant tensor (when subscripted)
h = convective heat transfer coefficient (W/m^{2}K), scaling factors (when subscripted)
l = wire segment length (m)
Ma = Marangoni number
$\mathbf{n}$ = normal vector
Oh = Ohnesorge number ($\hat{\mu}/\sqrt{\rho\sigma d}$)
p = pressure (Pa)
q = heat flux (Watts/m^2)
r = radial coordinate
$\mathbf{R}$ = position vector
R_1, R_2 = principal radii of surface curvature (m)
t = time (s).
$\hat{\mathbf{t}}$ = unit vector tangent to the melt surface
T = temperature (K)
$\mathbf{u}$ = velocity vector
V = volume (m^3)
x, y, z = spatial coordinates

Greek Symbols

α = thermal diffusivity (m^2/s)
δ = Dirac-delta function
ΔT = temperature interval
$\Delta\rho$ = density difference
ϵ = emissivity
η = curvilinear coordinate
θ = polar angle
κ = thermal conductivity (W/mK)
λ = latent heat of melting (J/kg)
$\hat{\mu}$ = dynamic viscosity of fluid (kg/m s)
ξ,η,ϕ = axisymmetric body-fitted coordinates
ρ = density (kg/m^3)
σ = surface tension (N/m)
ς = Stefan-Boltzmann constant
τ = stress tensor

Subscripts

b = bottom
c = conductive
e = electron
i = ion, ionization
ine = inelastic
l = liquid phase, left
m = melting
n = surface normal
r = right
s = at the surface, solid phase
t = top
w = wire
0 = at initial time
∞ = far-field

Superscripts

$\hat{}$ = fluid phase
$*$ = dimensionless

References

[1] Qin, W., Cohen, Ira. M., and Ayyaswamy, P. S., 2000, ‘‘Charged Particle Distributions and Heat Transfer in a Discharge Between Geometrically Dissimilar Electrodes: From Breakdown to Steady State,’’ Phys. Plasmas, **7**(2), pp. 719–728.
[2] Yeung, R. W., 1982, ‘‘Numerical Methods in Free-Surface Flows,’’ Annu. Rev. Fluid Mech., **14**, pp. 395–442.
[3] Tsai, W. T., and Yue, D. K. P., 1996, ‘‘Computation of Nonlinear Free-Surface Flows,’’ Annu. Rev. Fluid Mech., **28**, pp. 249–278.
[4] Shyy, W., Udaykumar, H. S., Rao, M. M., and Smith, R. W., 1996, *Computational Fluid Dynamics With Moving Boundaries*, Taylor & Francis, Washington, DC.
[5] Finlayson, B. A., 1992, *Numerical Methods for Problems With Moving Fronts*, Ravenna Park Publishing, Inc., Seattle, WA.
[6] Alexiades, V., and Solomon, A. D., 1993, *Mathematical Modeling of Melting and Freezing Processes*, Hemisphere, Bristol, PA.
[7] Ryskin, G., and Leal, L. G., 1984, ‘‘Numerical Solution of Free-Boundary Problems in Fluid Mechanics. Part 1. The Finite-Difference Technique,’’ J. Fluid Mech., **148**, pp. 1–17.
[8] Kang, I. S., and Leal, L. G., 1987, ‘‘Numerical Solution of Axisymmetric, Unsteady Free-Boundary Problems at Finite Reynolds Number. I. Finite-Difference Scheme and Its Application to the Deformation of a Bubble in a Uniaxial Straining Flow,’’ Phys. Fluids, **30**, pp. 1929–1940.
[9] Juric, D., and Tryggvason, G., 1996, ‘‘A Front-Tracking Method for Dendritic Solidification,’’ J. Comput. Phys., **123**, pp. 127–148.
[10] Unverdi, S. O., and Tryggvason, G., 1992, ‘‘A Front-Tracking Method for Viscous, Incompressible, Multi-Fluid Flow,’’ J. Comput. Phys., **100**, pp. 25–37.
[11] Bonacina, C., Comini, G., Fasans, A., and Primiceris, M., 1973, ‘‘Numerical Solution of Phase Change Problems,’’ Int. J. Heat Mass Transfer, **16**, pp. 1825–1832.
[12] Huang, L. J., Ayyaswamy, P. S., and Cohen, Ira. M., 1995, ‘‘Melting and Solidification of Thin Wires: A Class of Phase-Change Problems With a Mobile Interface-I. Analysis,’’ Int. J. Heat Mass Transfer, **38**(**9**), pp. 1637–1645.
[13] Yoo, J., and Rubinsky, B., 1983, ‘‘Numerical Computation Using Finite Elements for the Moving Interface in Heat Transfer Problems With Phase Change Transformation,’’ Numer. Heat Transfer, **6**, pp. 209–222.
[14] Bounds, S., Moran, G., Pericleous, K., Cross, M., and Croft, T. N., 2000, ‘‘A Computational Model for Defect Prediction in Shape Castings Based on the Interaction of Free Surface Flow, Heat Transfer, and Solidification Phenomena,’’ Metall. Mater. Trans. B, **31**(3), pp. 515–527.
[15] Hsiao, J. S., 1985, ‘‘An Efficient Algorithm for Finite-Difference Analysis of Heat Transfer With Melting and Solidification,’’ Numer. Heat Transfer, **8**, pp. 653–666.
[16] Shamsundar, N., and Sparrow, E., 1975, ‘‘Analysis of Multidimensional Phase Change via the Enthalpy Model,’’ ASME J. Heat Transfer, **19**, pp. 333–340.
[17] Cohen, Ira. M., Huang, L. J., and Ayyaswamy, P. S., 1995, ‘‘Melting and Solidification of Thin Wires: A Class of Phase-Change Problems With a Mobile Interface-II. Experimental Confirmation,’’ Int. J. Heat Mass Transfer, **38**(9), pp. 1647–1659.
[18] Liu, A., Voth, T. E., and Bergman, T. L., 1993, ‘‘Pure Material Melting and Solidification With Liquid Phase Buoyancy and Surface Tension Force,’’ Int. J. Heat Mass Transfer, **36**, pp. 411–422.
[19] Sadhal, S. S., Ayyaswamy, P. S., and Chung, J. N., 1997, *Transport Phenomena With Bubbles and Drops*, Springer, New York.
[20] Ayyaswamy, P. S., Sripada, S. S., and Cohen, Ira. M., 1999, ‘‘Interfacial Motion of a Molten Layer Subject to Plasma Heating,’’ *Fluid Dynamics at Interfaces*, Wei Shyy and Ranga Narayanan, eds., Cambridge University Press, New York, pp. 320–338.
[21] Sripada, Srinivas. S., 1999, ‘‘Fundamental Studies of Plasma Applications in Microelectronic Manufacturing and Flames: Fluid Mechanics, Phase-Change, and Heat Transfer,’’ Ph.D. thesis, Univ. of Pennsylvania.
[22] Sripada, Srinivas, S., Ayyaswamy, P. S., and Cohen, I. M., 1998, ‘‘Weakly Ionized Plasma Heat Transfer Between Geometrically Dissimilar Electrodes,’’ ASME J. Heat Transfer, **120**(3), pp. 939–942.
[23] Ryskin, G., and Leal, L. G., 1983, ‘‘Orthogonal Mapping,’’ J. Comput. Phys., **50**, pp. 71–100.
[24] Eca, L., 1996, ‘‘2D Orthogonal Grid Generation With Boundary Point Distribution Control,’’ J. Comput. Phys., **125**, pp. 440–453.
[25] Patankar, S. V., 1980, *Numerical Heat Transfer and Fluid Flow*, Hemisphere, Washington, DC.
[26] de Zeeuw, P. M., 1990, ‘‘Matrix-Dependent Prolongations and Restrictions in a Blackbox Multigrid Solver,’’ J. Comput. Appl. Math., **33**, pp. 1–27.
[27] de Zeeuw, P. M., 1997, ‘‘Acceleration of Iterative Methods by Coarse Grid Corrections,’’ Ph.D. thesis, Univ. of Amsterdam.
[28] Raithby, G. D., Galpin, P. F., and Van Doormaal, J. P., 1986, ‘‘Prediction of Heat and Fluid Flow in Complex Geometries Using General Orthogonal Coordinates,’’ Numer. Heat Transfer, **9**, pp. 125–142.

[29] Karki, K. C., and Patankar, S. V., 1988, ''Calculation Procedure for Viscous Incompressible Flows in Complex Geometries,'' Numer. Heat Transfer, **14**, pp. 295–307.

[30] Shyy, W., 1994, *Computational Modeling for Fluid Flow and Interfacial Transport*, Elsevier, Amsterdam.

[31] Bennon, W. D., and Incropera, F. P., 1988, ''Numerical Analysis of Binary Solid-Liquid Phase-Change Using a Continuum Model,'' Numer. Heat Transfer, **13(3)**, pp. 277–296.

[32] Ferziger, J. H., and Peric, M., 1996, *Computational Methods for Fluid Dynamics*, Springer, New York.

[33] Miller, R. R., 1952, *Liquid-Metals Handbook*, 2nd edition, R. N. Lyon et al., eds., Office of Naval Research, Dept. of Navy, Washington, DC, pp. 38–102; Chpt. 2.

[34] Ho, C. Y., Powell, R. W., and Liley, P. E., 1974, ''Thermal Conductivity of the Elements: a Comprehensive Review,'' J. Phys. Chem. Ref. Data, **3**, Suppl. 1.

[35] Beer, S. Z., 1972, *Liquid Metals: Chemistry and Physics*, Marcel Dekker, Inc., New York.

[36] Sripada, S. S., Cohen, I. M., and Ayyaswamy, P. S., ''A Study of the Electronic Flame Off Discharge Process Used for Ball Bonding in Microelectronic Packaging,'' 1996, *Transport Phenomena in Materials Processing and Manufacturing*, Proc. Int. Mech. Eng. Congress & Expo, **HTD-336**, ASME, New York, pp. 129–136.

Heat Transfer Coefficients on the Squealer Tip and Near Squealer Tip Regions of a Gas Turbine Blade

Jae Su Kwak
Postdoctoral Research Assoc.

Je-Chin Han
M. C. Easterling Endowed Chair

Turbine Heat Transfer Laboratory,
Department of Mechanical Engineering,
Texas A&M University,
College Station, TX 77843-3123
e-mail: jchan@mengr.tamu.edu

Detailed heat transfer coefficient distributions on a squealer tip of a gas turbine blade were measured using a hue detection based transient liquid crystals technique. The heat transfer coefficients on the shroud and near tip regions of the pressure and suction sides of a blade were also measured. Tests were performed on a five-bladed linear cascade with a blow-down facility. The blade was a two-dimensional model of a first stage gas turbine rotor blade with a profile of a GE-E^3 aircraft gas turbine engine rotor blade. The Reynolds number based on the cascade exit velocity and axial chord length of a blade was 1.1×10^6 and the total turning angle of the blade was 97.7 deg. The overall pressure ratio was 1.2 and the inlet and exit Mach number were 0.25 and 0.59, respectively. The turbulence intensity level at the cascade inlet was 9.7 percent. The heat transfer measurements were taken at the three different tip gap clearances of 1.0 percent, 1.5 percent, and 2.5 percent of blade span. Results showed that the overall heat transfer coefficients on the squealer tip were higher than that on the shroud surface and the near tip regions of the pressure and suction sides. Results also showed that the heat transfer coefficients on the squealer tip and its shroud were lower than that on the plane tip and shroud. However, the reductions of heat transfer coefficients near the tip regions of the pressure and suction sides were not remarkable. [DOI: 10.1115/1.1571849]

Keywords: *Convection, Cooling, Heat Transfer, Measurement Techniques, Rotating, Turbines*

Introduction

The inlet temperature of gas turbines has been increased in order to increase power output and efficiency. This has resulted in increased heat load on turbine components. The blade tip is one of the most critical regions because of the high heat load caused by hot leakage flow through the tip gap. For the *rotating* blade, there is a gap between the blade tip and shroud, and flow leaks through the gap due to the pressure difference between the blade's pressure side and suction side. This hot leakage flow is the major cause of blade tip failures.

To reduce the leakage flow and heat transfer on the tip, the blades of modern gas turbines are typically grooved chord-wise and are called squealer tip blades. The groove acts as a labyrinth seal to increase flow resistance and thus reduces leakage flow and heat transfer. Detailed turbine heat transfer issues and associated cooling technology are described by Han et al. [1].

In open literature, there is limited information on the flow field and heat transfer of a grooved blade tip. Metzger et al. [2] and Chyu et al. [3] investigated heat transfer in a rectangular grooved tip model. Their work included the effect of the depth to width ratio and the tip gap to width ratio of a cavity with both moving and standing shrouds over the stationary grooved tip model. The result showed that the local heat transfer coefficient upstream end of the grooved cavity was greatly reduced compared to a rectangular plane tip model, while the heat transfer coefficient downstream end of the grooved cavity was enhanced because of the flow reattachment in that region. They concluded that there was an optimum value of depth-to-width ratio for a given pressure difference across the gap. Heyes et al. [4] studied tip leakage flow on plane and squealer tips in a linear cascade and concluded that the use of a squealer tip, especially a suction-side squealer tip, was more beneficial than a flat tip. Yang and Diller [5] studied local heat transfer coefficients on a turbine blade tip model with a recessed cavity (squealer tip) in a stationary linear cascade. Based on the measurement at a single point on the cavity floor, they reported that the convection coefficients were insensitive to the tip gap height. Ameri et al. [6] computed the flow and heat transfer on the squealer tip of a GE-E^3 first stage gas turbine blade. They observed higher heat transfer in the bottom of the cavity, and the heat transfer on the pressure-side rim was comparable to the plane tip case but was higher on the suction-side rim. They concluded that the large heat transfer in the bottom of the cavity was due to flow impingement containing hot gas. Dunn and Haldeman [7] measured time averaged heat flux at a recessed (squealer) blade tip for a full-scale rotating turbine stage at transonic vane exit conditions. They used heat flux gauges and found that the Nusselt number on the suction-side lip and on the floor of the recess near the leading edge of the blade was higher than that of the blade stagnation value. Azad et al. [8,9] studied the flow and heat transfer on the first stage blade tip of an aircraft engine turbine (GE-E^3). They presented the effects of tip gap clearance and free-stream turbulence intensity level on the detailed heat transfer coefficient distributions for both plane and squealer tips under engine representative flow conditions. They used transient liquid crystals technique and found that the overall heat transfer coefficients on the squealer tip were lower than that on the plane tip. Azad et al. [10] also studied the effect of squealer geometry arrangement on gas turbine blade tip heat transfer. They found that a blade tip with a suction-side squealer was more effective in reducing heat transfer than that with a pressure-side squealer.

Contributed by the Heat Transfer Division for publication in the JOURNAL OF HEAT TRANSFER. Manuscript received by the Heat Transfer Division August 26, 2003; revision received February 25, 2003. Associate Editor: J. N. Chung.

Some researchers have studied heat transfer on the plane tip blade. Mayle and Metzger [11] used a two-dimensional rectangular tip model with and without rotating shroud to find the rotating effect on averaged blade tip heat transfer. They noted that the rotating effect could be neglected in order to access the blade tip heat transfer over the entire range of parameters considered in the study. Metzger and Rued [12] presented heat transfer and flow results in the near tip region of the pressure surface using a blade tip simulation and sink flow. Their model simulated a sink flow similar to the sink like characteristics of the blade tip gap on the pressure side. Rued and Metzger [13] presented heat transfer and flow results in the near tip region of the suction surface using a blade tip simulation and a source flow. Their model simulated a blade suction surface with a gap feeding a source flow similar to the flow exiting the tip gap on the suction surface of an airfoil. Metzger et al. [14] measured local heat flux using heat flux sensors in a rotating turbine rig with two different tip gaps. Bunker et al. [15] used a hue detection based liquid crystals technique to investigate the detailed heat transfer coefficient distributions on the blade tip surface. Their results were obtained at three different tip gap sizes and two free-stream turbulence levels with sharp or rounded edges. Bunker and Bailey [16] studied the effect of squealer cavity depth and oxidation on turbine blade tip heat transfer. Teng et al. [17] measured the heat transfer coefficients on the plane tip surface in a large-scale low-speed wind tunnel facility using a transient liquid crystals technique. They concluded that a major leakage flow existed in the mid-chord region, and the unsteady wake augmented the Nusselt number at a large tip gap (3 percent), while the effect of the unsteady wake disappeared with decreasing tip gap clearance.

Some researchers have conducted numerical studies to investigate blade tip heat transfer. Ameri and Steinthorsson [18,19] predicted heat transfer on the tip of the SSME (Space Shuttle Main Engine) rotor blade. Ameri et al. [20] also predicted the effects of tip gap clearance and casing recess on heat transfer and stage efficiency for several squealer blade tip geometries. Ameri and Bunker [21] performed a computational study to investigate the detailed heat transfer distributions on blade tip surfaces for a large power generation turbine and compared the results with the experimental data of Bunker et al. [15]. Ameri and Rigby [22] also calculated heat transfer and film-cooling effectiveness on film cooled turbine blade models. Ameri [23] predicted heat transfer and flow on the blade tip of a gas turbine equipped with a mean-camber line strip.

In addition, Rhee et al. [24] studied the local heat/mass transfer on the stationary shroud with blade tip clearances for *plane* tip geometry. They used the naphthalene sublimation method and concluded that the heat/mass transfer characteristics changed significantly with the gap clearance. Jin and Goldstein [25,26] measured local mass transfer on a simulated high-pressure turbine blade tip and near tip surfaces in a large-scale low-speed wind tunnel facility. They used a naphthalene sublimation technique and investigated the effects of the exit Reynolds number, the tip gap clearance, and the turbulence intensity. Papa et al. [27] measured average and local mass transfer coefficients on a squealer tip and winglet-squealer tip using the naphthalene sublimation technique in the same facility. They also presented the flow visualization on the tip surface using an oil dot technique.

Most of the above referenced studies focused on the heat transfer coefficients on the blade tip surface only for different blade tip profiles under different flow conditions except that reference [24] for the shroud surface measurement and reference [26] for near tip regions of the pressure and suction sides. The present paper is a continuous investigation of the blade tip heat transfer from the same research facility as references [8–10]. In references [8–10], the heat transfer coefficients on the plane tip surface as well as several squealer tip surfaces were reported by using the transient liquid-crystals single-color capturing method in conjunction with the initial temperature measurement with thermocouples. However, the present study reports the heat transfer coefficients on the blade tip surface, the shroud surface, and near tip regions of the pressure and suction sides by using a hue-detection based transient liquid-crystals technique in combination with the wide band-width liquid-crystals for the initial temperature measurement. The measurement technique employed in this paper is considered as an improved step from references [8–10]. The main objective of this paper is to present an integral data set over the entire blade tip region that includes the tip surface, the shroud surface, and the blade pressure and suction surface immediately adjacent to the tip where very limited data is available in the open literature. The present non-rotating blade tip heat transfer data might not be directly applicable to the real engine rotating blade tip design due to the effect of rotation, however, the present data could be valuable in better understanding complex blade tip flows and validating various CFD codes. The results are compared with the plane tip data (Kwak and Han [28]).

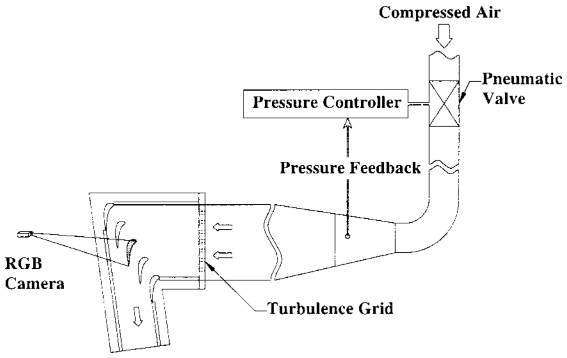

Fig. 1 Schematic of blow-down facility

Experimental Setup

Figure 1 shows the schematic of the test facility. The test section consisted of a stationary blow-down facility with a five-bladed linear cascade. The definition of blade tip and shroud are also shown in the upper part of Fig. 2. The profile of the blade tip is available in the open domain or can be provided by the authors to the interested researchers. Compressed air stored in the tanks entered a high flow pneumatic control valve that was designed to receive feedback from the downstream pressure to maintain a ve-

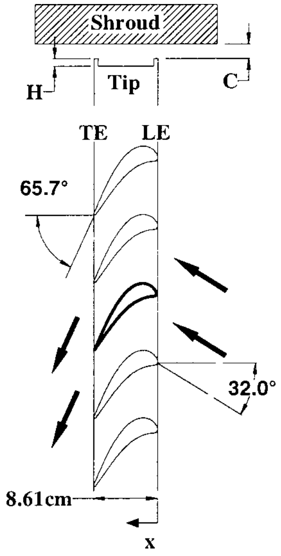

Fig. 2 Definition of blade tip and shroud

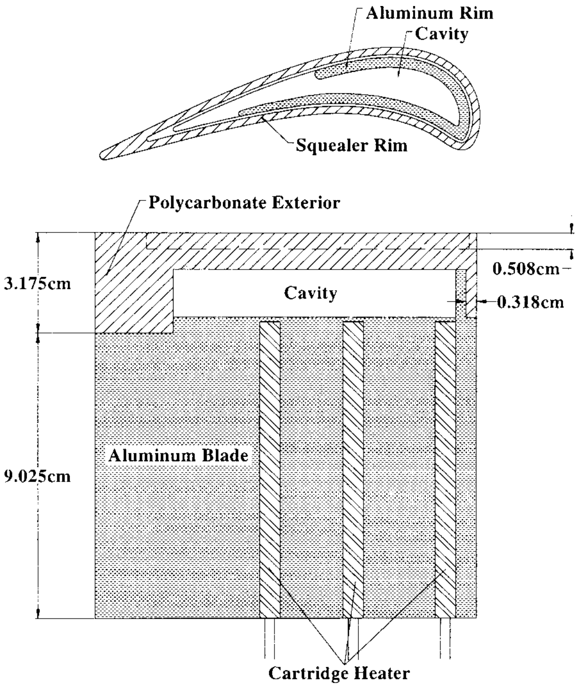

Fig. 3 Heat transfer measurement blade

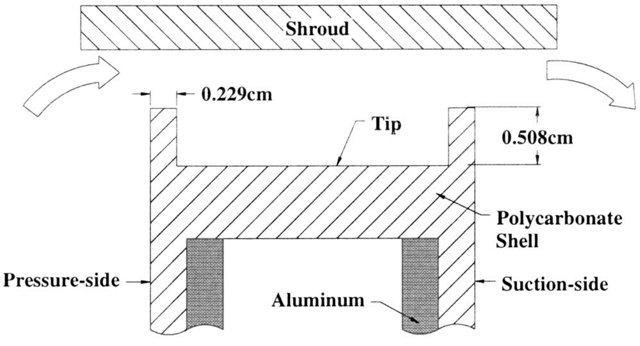

Fig. 4 Detailed view of the blade tip

locity within ±3 percent of the desired value. The inlet of the test section was 31.1 cm wide and 12.2 cm high, and its top, bottom, and sides were made of 1.27 cm thick polycarbonate plates for the pressure measurement test. In the heat transfer test, however, the top plate was replaced with a 1.27 cm thick clear acrylic plate for better optical access to the blade tip. Two adjustable trailing edge tailboards were used to provide identical flow conditions through the two passages adjacent to the center blade. A turbulence-generating grid of 57 percent porosity was placed 26.7 cm upstream of the center blade. The turbulence intensity was measured 6 cm upstream of the center blade with a TSI IFA-100 unit. In this test, the turbulence intensity at that location was 9.7 percent. The turbulence length scale was estimated to be 1.5 cm, which is slightly larger than the grid size. The tip gaps used for this study were 1.31 mm, 1.97 mm, and 3.29 mm, which correspond to about 1.0 percent, 1.5 percent, and 2.5 percent of the blade span (12.2 cm). Hard gaskets of desired thickness were placed on top of the sidewalls, the trailing edge tailboard, and two outer guide blades to create tip gaps of desired height.

During the blow-down test, the cascade inlet air velocity and exit velocity were 85 m/s and 199 m/s, the inlet and exit Mach numbers were 0.25 and 0.59, respectively. The Reynolds number based on axial chord length and exit velocity was 1.1×10^6. The inlet total pressure (P_t) was 126.9 kPa and exit static pressure (P) was 102.7 kPa, which gave an overall pressure ratio (P_t/P) of 1.2. Azad et al. [8,9] described the detailed flow conditions, including the flow periodicity in the cascade.

The blades were made of aluminum and finished with an EDM machine. The blade had a 12.2 cm span and an 8.61 cm axial chord length. These were three times larger than the dimension of a GE-E^3 blade tip profile. Each blade had a constant cross section for the entire span as shown in the lower part of Fig. 2. Figure 3 shows the heat transfer measurement blade. The lower potion of the blade was made of aluminum, and the upper portion consisted of an inner aluminum rim with a cavity and an outer shell made of a polycarbonate with low thermal conductivity. Figure 4 shows a detailed view of the blade tip. The thickness and height (H) of the squealer rim is 0.229 cm and 0.508 cm, respectively. The height of the squealer rim is about 4.16 percent of the blade span. Cartridge heaters were inserted into the blade to heat the aluminum core and consequently to heat the outer polycarbonate shell. For the heat transfer measurement on the shroud, a 300 W plate heater was used to heat the shroud plate and removed before the test.

Pressure Measurement and Results

Figure 5(a) shows the definition of blade coordinate and the location of pressure taps along the blade surface. The pressure taps were located at 50 percent, 80 percent, 90 percent, and 97 percent height of the blade span on both the blade pressure and suction side. Figure 5(b) presents the ratio of the inlet total to the local static pressure (P_t/P) along the blade. The pressure was measured with 1.5 percent of tip gap clearance. The static pressure difference between the pressure side and the suction side is the

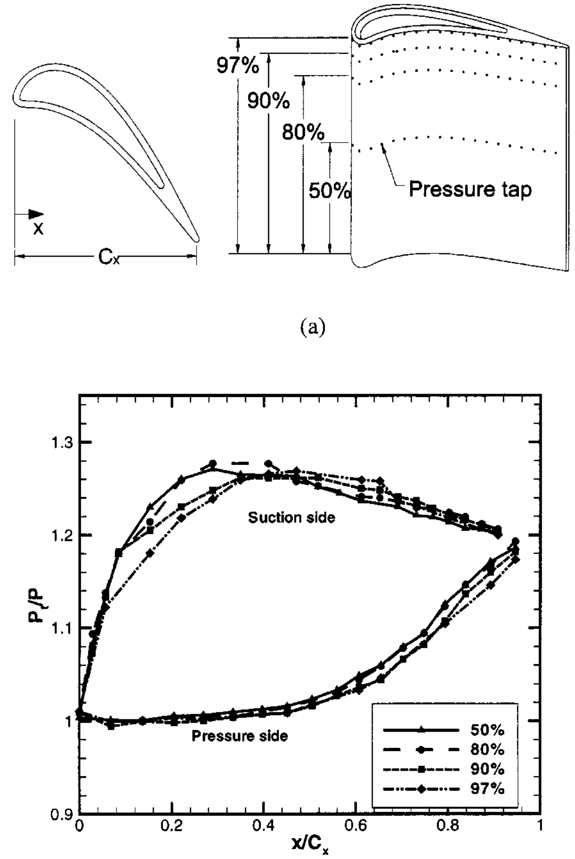

(a)

(b)

Fig. 5 (a) Definition of blade coordinate and location of pressure taps on the blade; and (b) Pressure distributions on the blade pressure and suction side with $C=1.5$ percent.

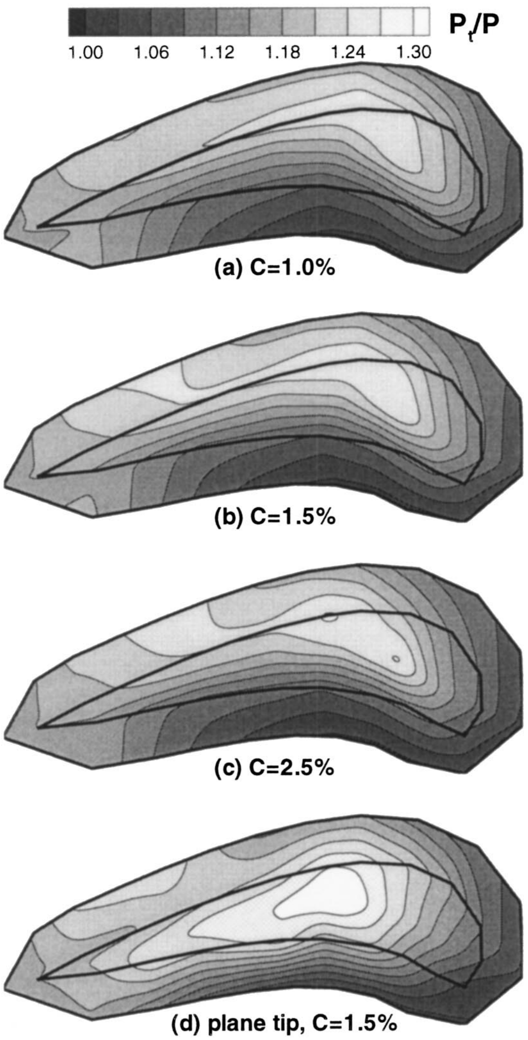

Fig. 6 Pressure distribution on the shroud surface

main driving force of the leakage flow. On the midspan, the maximum static pressure difference occurs near 30 percent of x/C_x. The location of the maximum static pressure difference has shifted toward the trailing edge along 97 percent of the blade span, and the maximum static pressure difference occurs near 50 percent of x/C_x. This shift is due to the leakage flow through the tip gap.

To investigate the pressure distribution on the shroud, 46 pressure taps were instrumented on the shroud surface. Figure 6 shows the inlet total pressure to local static pressure ratio (P_t/P) distributions on the shroud surface for different tip gap clearances. Figures 6(a), (b), and (c) present the pressure distribution on the shroud with a squealer tip, and Fig. 6(d) shows the result with a plane tip. The plane tip case (Fig. 6(d), Kwak and Han [28]) is presented for comparison. A higher value of P_t/P corresponds to a lower static pressure (high velocity), while a lower value corresponds to a higher static pressure (low velocity). The black curves in the contours indicate blade location under the shroud.

Comparing the squealer tip cases (Figs. 6(a)–(c)) with the plane tip case (Fig. 6(d)), the overall P_t/P of the plane tip case is much higher than that of the squealer tip cases. This indicates the leakage flow is significantly reduced by using the squealer tip. Also, high P_t/P regions move toward the leading edge side for the squealer tip cases. For the plane tip case, a high P_t/P region (high velocity region) exists near 35 percent of blade chord, which indicates that the path of main leakage flow is located near this region. For squealer tip cases, however, a high P_t/P region exists near 20 percent of blade chord. Thus, the path of leakage flow is shifted toward the leading edge side. This may be due to the increase of flow resistance near the mid chord region, and result in the shift of the path of leakage flow toward the leading edge.

As the tip gap clearance increases from $C=1.0$ percent (Fig. 6(a)) to $C=2.5$ percent (Fig. 6(c)), the overall value of P_t/P increases, and the P_t/P contour shifts toward the trailing edge side. This indicates that the leakage flow increases and moves toward the trailing edge side as tip gap clearance increases. As the tip gap clearance increases, the flow resistance in the mid chord region may become smaller, and result in the shift of the path of leakage flow toward the trailing edge.

Heat Transfer Measurement Theory

A hue-detection based transient liquid crystals technique was used to measure the heat transfer coefficient on the blade tip. The local heat transfer coefficient over a liquid crystals coated surface can be obtained using a one-dimensional semi-infinite solid assumption for the test surface. The one-dimensional transient conduction equation, the initial condition, and the convective boundary condition are:

$$k\frac{\partial^2 T}{\partial x^2}=\rho c_p\frac{\partial T}{\partial t} \tag{1}$$

$$\text{at } t=0, \quad T=T_i \tag{2}$$

$$\text{at } x=0, \quad -k\frac{\partial T}{\partial X}=h(T_w-T_m); \quad \text{as } x\to\infty, \quad T=T_i \tag{3}$$

The solution of above equations at the convective boundary surface ($x=0$) is the following:

$$\frac{T_w-T_i}{T_m-T_i}=1-\exp\left(\frac{h^2\alpha t}{k^2}\right)\operatorname{erfc}\left(\frac{h\sqrt{\alpha t}}{k}\right) \tag{4}$$

By knowing the initial temperature (T_i) of the test surface, the mainstream temperature (T_m) at the cascade inlet and the color change temperature (T_w) at time t, the local heat transfer coefficient (h) can be calculated from Eq. (4). If the mainstream temperature changes with time, the varying temperature can be represented as a series of step change. Using Duhamel's superposition theorem, Eq. (4) can be written as follows:

$$T_w-T_i=\{T_{m,0}-T_1\}\times F\left(\frac{h\sqrt{\alpha t}}{k}\right)+\sum_{i=1}^{n}\left[F\left(\frac{h\sqrt{\alpha(t-\tau_i)}}{k}\right)\Delta T_{m,i}\right] \tag{5}$$

where, $F(x)=1-\exp(x^2)\operatorname{erfc}(x)$,

ΔT_m is step changes in the mainstream.

The experimental uncertainty was calculated by the methods of Kline and McClintock [29]. Note that the blade tip material (polycarbonate) has a very low thermal conductivity of 0.18 W/mK. The liquid crystals color change transition occurred at the surface which was kept at a uniform initial temperature. Test duration was smaller (10–30 sec) than the time required for the temperature to penetrate the full thickness of the blade tip material. Thus a one-dimensional transient, semi-infinite solid assumption was valid throughout the surface, except near the tip edges. The individual uncertainties in the measurement of the time of color change ($\Delta t=\pm 0.5$ sec), the mainstream temperature ($\Delta T_m=\pm 0.5$°C), the color change temperature ($\Delta T_w=\pm 0.2$°C), the initial temperature ($\Delta T_i=\pm 1$°C), and the blade tip material properties ($\Delta a/k^2=\pm 5$ percent) were included in the calculation of the overall uncertainty of heat transfer coefficient. The uncertainty for the local heat transfer coefficient was estimated to be ±8 percent. However, the uncertainty near the blade tip edge might be much greater up to 15 percent due to the two-dimensional heat conduction effect. The uncertainty in the high heat transfer region also might be higher due to the short color change time.

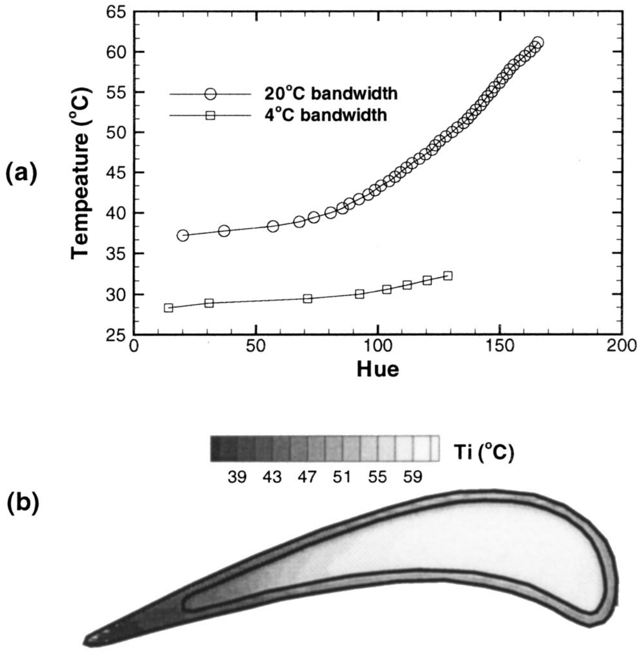

Fig. 7 (**a**) **The relation between hue and temperature; and** (**b**) **initial temperature on the tip for $C = 1.5$ percent.**

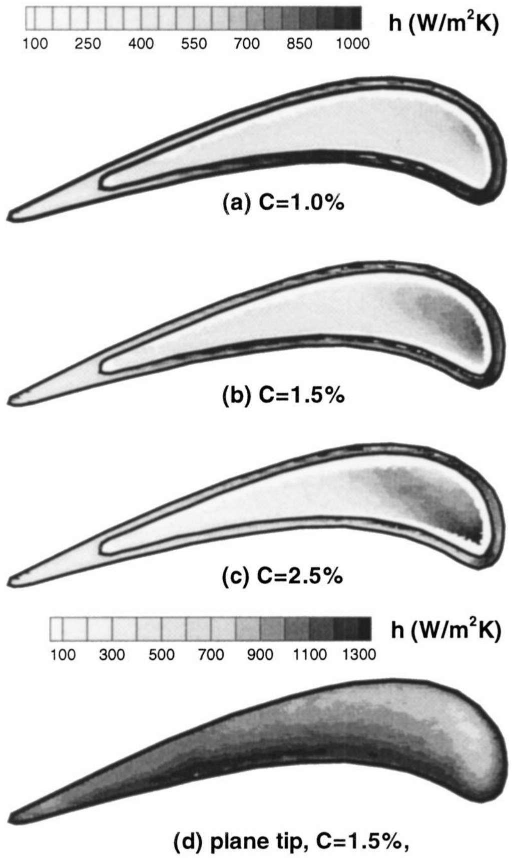

Fig. 8 Heat transfer coefficient on the blade tip

Heat Transfer Measurement and Results

Two different liquid crystals were used in this study. The 20°C bandwidth liquid crystals (R34C20W, Hallcrest) were used to measure the initial temperature of the tip surface, and the 4°C bandwidth liquid crystals (R29C4W, Hallcrest) were used to measure the color changing time. Calibration was performed to find the hue versus temperature relation. A foil heater was placed at the bottom of a 0.635 cm thick copper plate. The black paint (BB-G1, Hallcrest) and liquid crystals were sprayed on the copper plate. Input voltage to the heater was set properly in order to increase the surface temperature by 0.6°C, and enough time was allowed for the temperature to be steady at each temperature step. The surface temperature was then read by a thermocouple that was attached at the surface of the copper plate, and the color of the liquid crystals was recorded by the computer. At each temperature step, the hue was calculated from the stored image, and the relation between hue and temperature was established for both 20°C and 4°C bandwidth liquid crystals. Figure 7(a) shows the results of the calibration for both liquid crystals.

Before the transient test, the black paint and the 20°C bandwidth liquid crystals were sprayed uniformly on the test surface, and the test surface was heated. After the surface temperature reached the desired temperature (about 70°C), the color of the liquid crystals on the test surface was recorded by a RGB color CCD camera with 24-bit color frame grabber board. From every pixel of the stored image, hue was calculated and the initial temperature of the test surface was determined using the pre-calibrated hue versus temperature relation. Figure 7(b) presents the initial temperature on the tip for $C = 1.5$ percent case.

After the initial temperature measurement on the test surface, the 20°C bandwidth liquid crystals were removed. Then the black paint and the 4°C bandwidth liquid crystals were sprayed on. It is noted that the sprayed liquid crystals could result in a rough surface. The measured roughness of the present liquid-crystal-coated blade tip was around 5–10 microns, an averaged value of 7.5 microns by using a surface profilometer. However, this study did not evaluate the roughness effects on the blade tip heat transfer. The test surface was heated until the reference temperatures became the same as those of the initial temperature measurement test. Reference temperatures were measured by thermocouples located inside the cavity and the shroud surface to ensure the same temperature conditions for the initial temperature measurements and the transient tests. After temperatures reached the desired value, the compressed air was allowed to flow by turning on the flow controller. When the mainstream velocity reached the preset value by the end of 4 sec, the color change of the liquid crystals was recorded at the speed of 30 frames per sec. The test duration time was short enough (10–30 sec) to make a semi-infinite solid assumption. From every pixel at each stored image, hue was evaluated and used to calculate the time from the initial condition (about 40–60°C, depending on location) to a given hue value (50), which corresponded to the temperature of 29°C for the tip and shroud test, and 29.6°C for the pressure and suction sides test. Due to the different view angle and lighting condition, the corresponding temperature to hue value of 50 is different on the tip (shroud), and pressure and suction side. Then, the local heat transfer coefficient, *h*, was calculated from Eq. (5).

Heat Transfer Coefficient on the Squealer Tip. Figure 8 shows the heat transfer coefficient distribution on the squealer tip. The plane tip result (Fig. 8(d)) is presented for comparison. Detailed results of the plane tip cases are discussed by Kwak and Han [28]. Due to the shadow of the squealer rim, data near the cavity edge could not be taken. Compared to the plane tip case (Fig. 8(d)), the squealer tip cases (Figs. 8(a)–(c)) show a much lower heat transfer coefficient in the cavity. However, the heat transfer coefficient on the squealer rim is comparable to the high heat transfer coefficients of the plane tip. For the squealer tip cases, the heat transfer coefficients on the squealer rim are generally higher than that on the cavity surface. The heat transfer coefficients near the trailing edge cavity are low because of the recirculation of leakage flow as illustrated in Fig. 9(a). Figure 9

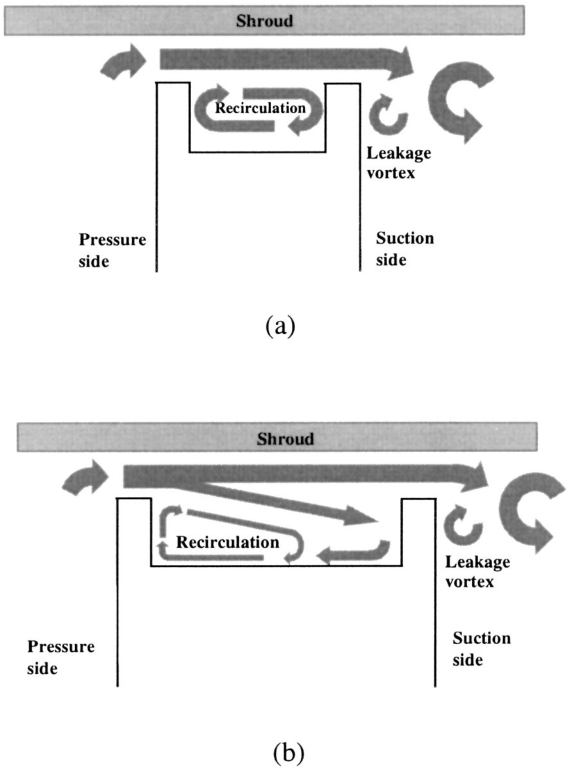

Fig. 9 Conceptual view of flow near squealer tip: (a) the cavity closer to the trailing edge; and (b) the cavity closer to the leading edge

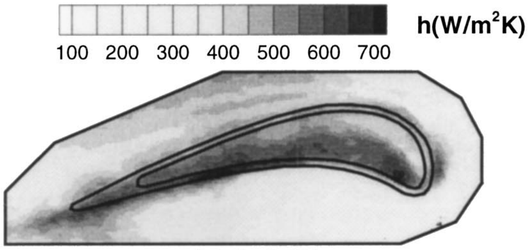

(a) C=1.0%

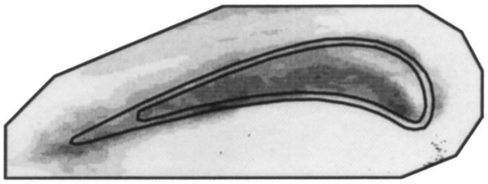

(b) C=1.5%

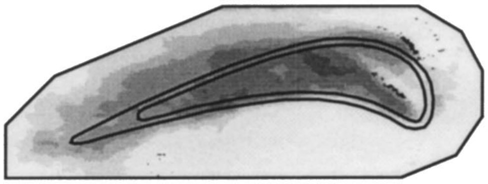

(c) C=2.5%

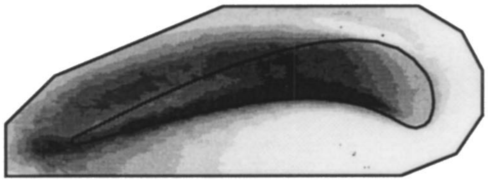

(d) plane tip, C=1.5%

Fig. 10 Heat transfer coefficient on the shroud

presents the conceptual view of the flow near the squealer tip of the blade. The real flow near the blade tip and in the cavity may be fully three-dimensional phenomena. However, Fig. 9 shows the simplified view of the flow in two-dimensional. As the flow tries to leak through the tip gap, a small vortex may appear near the tip of the pressure side. On the suction side, the leakage flow interacts with the passage vortex and may create the leakage vortex near the tip of the suction side. The flow inside the cavity may depend on the width of the cavity. If the width of the cavity is relatively small, the leakage flow may not reattach to the cavity, and recirculation may occur in the cavity as shown in Fig. 9(a). This could explain the low heat transfer coefficient region on the trailing edge side of the cavity in Fig. 8. If the width of the cavity is relatively large, the leakage flow may reattach to the suction side rim or the cavity surface and form a recirculation region near the pressure side of the cavity as shown in Fig. 9(b). This trend happens near the leading edge side of the cavity. The heat transfer coefficients near the leading edge cavity are relatively high because of the reattachment of the leakage flow. Due to the recirculation in the cavity (see Fig. 9), heat transfer coefficients near the pressure side of the cavity are lower than that near the suction side of the cavity. As the tip gap clearance increases from $C=1.0$ percent to 2.5 percent, the overall heat transfer coefficient increases.

Heat Transfer Coefficient on the Shroud Surface. Figure 10 presents the heat transfer coefficient distribution on the shroud surface. The plane tip case (Fig. 10(d), Kwak and Han [28]) is presented for comparison. Compared to the plane tip case, the squealer tip cases (Figs. 10(a)–(c)) show a lower heat transfer coefficient. The distribution of the shroud heat transfer coefficient is similar to the distribution of the pressure on the shroud as shown in Fig. 6.

For the squealer tip cases (Figs. 10(a)–(c)), a low heat transfer region exists on the pressure side of the shroud surface. As flow leaks through the tip gap, the heat transfer coefficient increases on the shroud above the blade tip and on the suction side. The high heat transfer region on the shroud may exist along the path of the main leakage flow. Results show that the main leakage flow may enter the tip gap near 10 percent of the blade chord and exit at 40–60 percent of the blade chord depending on the tip gap size.

For the squealer tip cases, there are relatively high heat transfer regions on the shroud above the suction side squealer rim near 10 percent of the blade chord. The high heat transfer coefficient in this region is about 700 W/m^2K and is about 70 percent of the high heat transfer coefficient on the cavity surface. The high heat transfer coefficient in this region may be caused by the shifting of the path of leakage flow. Compared to the plane tip case, the path of leakage flow for the squealer tip case moves toward the leading edge side as shown in Fig. 6. The interaction between the leakage flow and the suction side mainstream increases the shroud heat transfer on the shroud above the suction side squealer rim near 10 percent of the blade chord region. However, the effect decreases as the tip gap clearance increases.

As the tip gap increases from $C=1.0$ percent to 2.5 percent, the overall heat transfer coefficient on the shroud increases and the high heat transfer region above the blade tip moves toward the trailing edge. This trend corresponds well with the pressure distribution on the shroud shown in Fig. 6, as well as the mass transfer results by Rhee et al. [24].

Heat Transfer Coefficient on the Near Tip Region of the Pressure Side. Figure 11 shows the heat transfer coefficient dis-

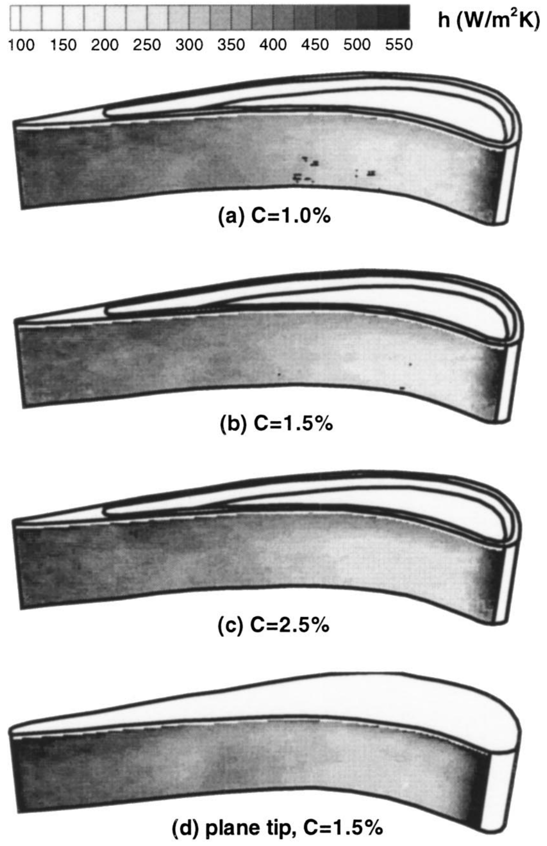

Fig. 11 Heat transfer coefficient on the pressure side

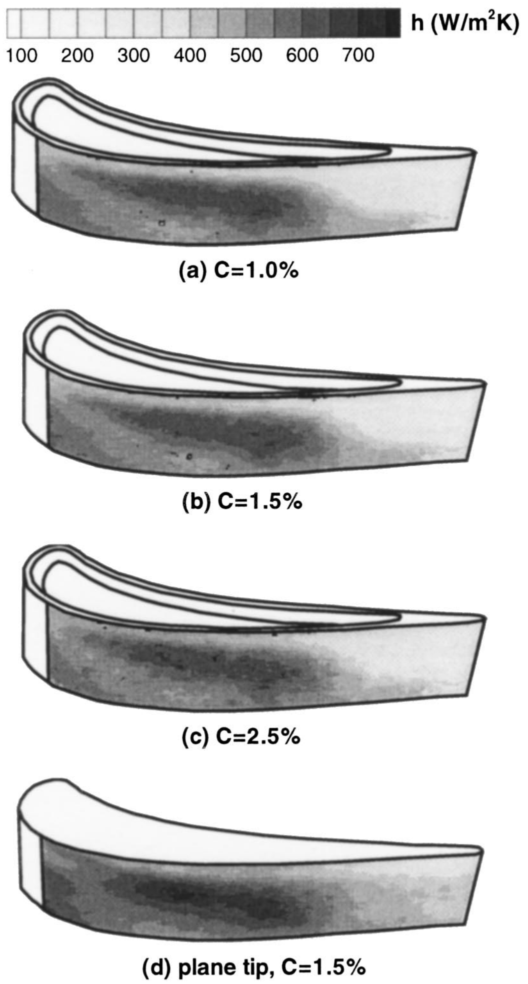

Fig. 12 Heat transfer coefficient on the suction side

tribution on the near tip region of the pressure side. The height of the test area was 2.5 cm from the blade tip, which corresponds to about 20 percent of the blade span. The plane tip result (Fig. 11(d), Kwak and Han [28]) is shown for comparison. Compared to the plane tip case (Fig. 11(d)), the squealer tip case (Figs. 11(a)–(c)) shows similar trend and magnitude of heat transfer coefficient. Results show a high heat transfer coefficient near the leading edge and the trailing edge. The heat transfer coefficients near 10–30 percent of the blade chord are lowest and gradually increase toward the trailing edge due to the boundary layer transition. The distribution of the heat transfer coefficient on the pressure side is laterally uniform except very near the tip edge. This may be caused by the leakage flow entrance effect as shown in Fig. 9.

The high heat transfer coefficient (550 $\mathrm{W/m^2K}$) is seen near the trailing edge and is about 55 percent of the maximum heat transfer coefficient on the cavity surface. Generally, the heat transfer coefficient on the near tip of the pressure side is lower than that on the shroud and the cavity surface.

Heat Transfer Coefficient on the Near Tip Region of the Suction Side. Figure 12 shows the heat transfer coefficient distribution on the near tip region of the suction side. The height of the test area was 2.5 cm from the blade tip, which corresponds to about 20 percent of the blade span. Due to the large view angle between the camera and the test surface, data could not be taken from near the leading edge region. The plane tip result (Fig. 12(d), Kwak and Han [28]) is shown for comparison. All cases show a high heat transfer coefficient region along the suction side of the blade tip. This high heat transfer coefficient region may be caused by the leakage vortex. As the leakage flow exits from the tip gap, the leakage flow separates from the tip surface or the squealer rim and forms a leakage vortex due to the interaction with the mainstream flow. Compared to the plane tip case, the squealer tip case shows slightly lower heat transfer coefficient, but similar trend.

For the squealer tip, a high heat transfer region exists along the suction side tip. This high heat transfer region starts near 20–30 percent of the blade chord and corresponds to the leakage flow path on the shroud as shown in Fig. 6. The high heat transfer coefficient on this region slightly increases as the tip gap clearance increases. Between this high heat transfer region and the blade tip, there is a low heat transfer region. This corner region with a low heat transfer coefficient is caused by the separation of the leakage flow as shown in Fig. 9.

Generally, the heat transfer coefficient on the near tip of the suction side is higher than that on the pressure side and comparable with that on the shroud.

Averaged Heat Transfer Coefficient. Figure 13 shows the averaged heat transfer coefficient on the blade tip. The local heat transfer coefficients on the pressure side rim, suction side rim, and cavity are averaged at a given x/C_x location. Results show that the heat transfer coefficient on the squealer rim is generally higher than that on the cavity. Figures 14, 15, and 16 present the averaged heat transfer coefficient on the shroud, the near tip region of the pressure side, and the near tip region of the suction side, respectively. For the shroud surface, the average was taken from the region above the tip only. Results show that, in general, the heat transfer coefficient on the shroud surface increases slightly as the tip gap clearance increases for $x/Cx > 0.2$. However, the heat

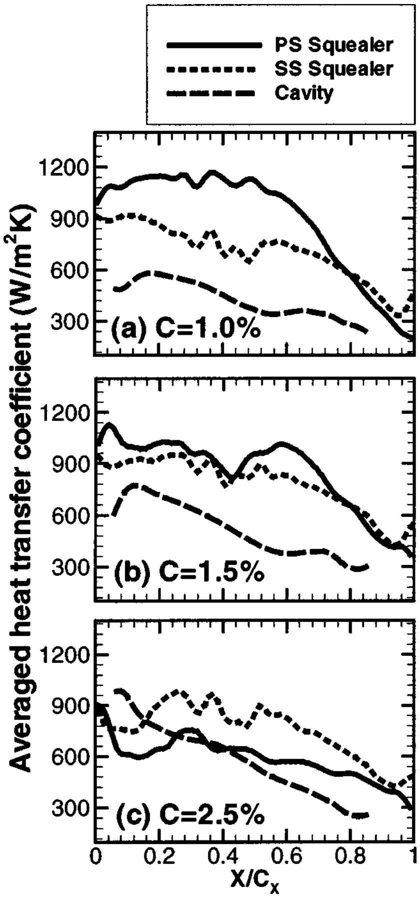

Fig. 13 Averaged heat transfer coefficient on the tip

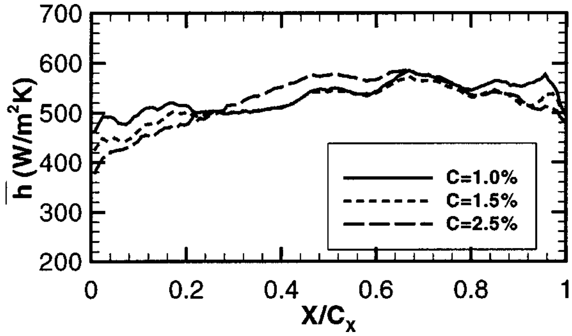

Fig. 14 Averaged heat transfer coefficient on the shroud

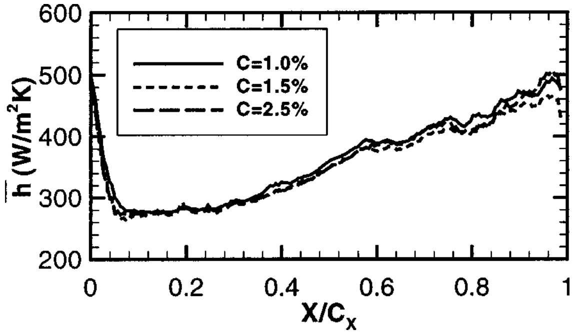

Fig. 15 Averaged heat transfer coefficient on the pressure side

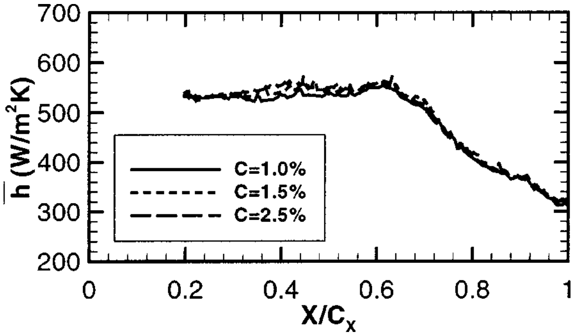

Fig. 16 Averaged heat transfer coefficient on the suction side

transfer coefficients near the tip regions of the blade pressure side and the suction side are insensitive to the tip gap clearance.

Conclusions

The detailed heat transfer coefficients on the squealer tip, the shroud surface, and the near tip regions of the blade pressure and suction sides were measured using a hue-detection based transient liquid crystals technique. The major findings based on the experimental results are as follows:

1. From pressure and heat-transfer coefficient measurements, results showed that leakage flow through the tip gap clearance and heat transfer coefficient on the tip surface were reduced by using a squealer tip design.
2. The cavity heat transfer coefficient near the leading edge was higher than that near the trailing edge. However, the cavity heat transfer coefficient was generally lower than that on the squealer rim.
3. Generally, the heat transfer coefficient on the shroud followed the tip leakage flow path. The shroud heat transfer coefficient above the tip and the blade suction side was much higher than that above the blade pressure side.
4. The heat transfer coefficient on the near tip region of the pressure side was laterally uniform except a higher value near the tip edge due to the leakage entrance effect.
5. The heat transfer coefficient along the suction side near the tip region showed a high value due to the leakage vortex interacting with the mainstream.
6. The overall blade tip heat transfer coefficient slightly increased as the tip gap clearance increased.
7. The overall heat transfer coefficient on the blade tip showed a higher value than that on the shroud and the near tip regions of the blade pressure and suction sides.
8. By using a squealer tip blade, the heat transfer coefficients on the tip and the shroud were reduced. However, the reduction of heat transfer coefficients on the pressure and suction sides were not remarkable.

The observation and conclusions from this study are limited for the stationary blades. Cautions need to be taken in extending the results to the rotating blades. In addition, the overall pressure ratio in this non-rotating blade cascade was lower than the real engine rotating blade conditions.

Acknowledgments

This work was prepared with the support of the NASA Glenn Research Center under grant number NAG3-2002. The NASA technical team is Mr. Robert Boyle and Dr. Raymond Gaugler. Their support is greatly appreciated. Technical discussions with Dr. C. Pang Lee of GE Aircraft Engines, Dr. Ron Bunker of GE R&D Center, and Dr. GM S. Azad of Siemens-Westinghouse were helpful and are acknowledged.

Nomenclature

C = tip clearance gap (percent of the blade span, or mm)
C_x = axial chord length of the blade (8.61 cm)
h = local convective heat transfer coefficient (W/m^{2}K)
$\overline{h}$ = averaged heat transfer coefficient at a given x/C_x (W/m^{2}K)
H = cavity depth (recess) (0.508 cm)
k = thermal conductivity of blade tip material (0.18 W/m K)
LE = leading edge of the blade
P = local static pressure (kPa)
P_t = total pressure at the cascade inlet (kPa)
PS = blade pressure side
t = transition time for liquid crystals color change (second)
TE = trailing edge of the blade
T_i = initial temperature of the blade tip surface (°C)
T_m = temperature of the mainstream at the cascade inlet (recovery temperature) (°C)
T_w = color change temperature of the liquid crystals (°C)
Tu = turbulence intensity level at the cascade inlet (percent)
SS = blade suction side
x = axial distance (cm)
α = thermal diffusivity of blade tip material (1.25×10^{-7} m^2/s)

References

[1] Han, J. C., Dutta, S., and Ekkad, S. V., 2000, *Gas Turbine Heat Transfer and Cooling Technology*, Taylor & Francis, New York
[2] Metzger, D. E., Bunker, R. S., and Chyu, M. K., 1989, ''Cavity Heat Transfer on a Transverse Grooved Wall in a Narrow Flow Channel,'' ASME J. Heat Transfer, **111**, pp. 73–79.
[3] Chyu, M. K., Moon, H. K., and Metzger, D. E., 1989, ''Heat Transfer in the Tip Region of Grooved Turbine Blades,'' ASME J. Turbomach., **111**, pp. 131–138.
[4] Heyes, F. J. G., Hodson, H. P., and Dailey, G. M., 1991, ''The Effect of Blade Tip Geometry on the Tip Leakage Flow in Axial Turbine Cascades,'' ASME Paper No. 91-GT-135.
[5] Yang, T. T., and Diller, T. E., 1995, ''Heat Transfer and Flow for a Grooved Turbine Blade Tip in a Transonic Cascade,'' ASME-95-WA/HT-29.
[6] Ameri, A. A., Steinthorsson, E., and Rigby, L. David, 1997, ''Effect of Squealer Tip on Rotor Heat Transfer and Efficiency,'' ASME Paper No. 97-GT-128.
[7] Dunn, M. G., and Haldeman, C. W., 2000, ''Time-Averaged Heat Flux for a Recessed Tip, Lip, and Platform of a Transonic Turbine Blade,'' ASME J. Turbomach., **122**, pp. 692–697.
[8] Azad, G. M. S., Han, J. C., Teng, S., and Boyle, R., 2000, ''Heat Transfer and Pressure Distributions on a Gas Turbine Blade Tip,'' ASME J. Turbomach., **122**, pp. 717–724.
[9] Azad, G. M. S., Han, J. C., and Boyle, R., 2000, ''Heat Transfer and Pressure Distributions on the Squealer Tip of a Gas Turbine Blade,'' ASME J. Turbomach., **122**, pp. 725–732.
[10] Azad, G. M. S., Han, J. C., Bunker, R. S., and Lee, C. P., 2002, ''Effect of Squealer Geometry Arrangement on a Gas Turbine Blade Tip Heat Transfer,'' ASME J. Heat Transfer, **124**, pp. 452–459.
[11] Mayle, R. E., and Metzger, D. E., 1982, ''Heat Transfer at the Tip of an Unshrouded Turbine Blade,'' *Proc. Seventh Int. Heat Transfer Conf.*, Hemisphere Pub., pp. 87–92.
[12] Metzger, D. E., and Rued, K., 1989, ''The Influence of Turbine Clearance Gap Leakage on Passage Velocity and Heat Transfer Near Blade Tips. Part I: Sink Flow Effects on Blade Pressure Side,'' ASME J. Turbomach., **111**, pp. 284–292.
[13] Rued, K., and Metzger, D. E., 1989, ''The Influence of Turbine Clearance Gap Leakage on Passage Velocity and Heat Transfer Near Blade Tips. Part II: Source Flow Effects on Blade Pressure Side,'' ASME J. Turbomach., **111**, pp. 293–300.
[14] Metzger, D. E., Dunn, M. G., and Hah, C., 1991, ''Turbine Tip and Shroud Heat Transfer,'' ASME J. Turbomach., **113**, pp. 502–507.
[15] Bunker, R. S., Baily, J. C., and Ameri, A. A., 2000, ''Heat Transfer and Flow on the First Stage Blade Tip of a Power Generation Gas Turbine: Part 1: Experimental Results,'' ASME J. Turbomach., **122**, pp. 272–277.
[16] Bunker, R. S., and Baily, J. C., 2001, ''Effect of Squealer Cavity Depth and Oxidation on Turbine Blade Tip Heat Transfer,'' ASME Paper No. 2001-GT-0155.
[17] Teng, S., Han, J. C., and Azad, G. M. S., 2001, ''Derailed Heat Transfer Coefficient Distributions on a Large-Scale Gas Turbine Blade Tip,'' ASME J. Heat Transfer, **123**, pp. 803–809.
[18] Ameri, A. A., and Steinthorsson, E., 1995, ''Prediction of Unshrouded Rotor Blade Tip Heat Transfer,'' ASME Paper No. 95-GT-142.
[19] Ameri, A. A., and Steinthorsson, E., 1996, ''Analysis of Gas Turbine Rotor Blade Tip and Shroud Heat Transfer,'' ASME Paper No. 96-GT-189.
[20] Ameri, A. A., Steinthorsson, E., and Rigby, L. David, 1999, ''Effects of Tip Clearance and Casing Recess on Heat Transfer and Stage Efficiency in Axial Turbines,'' ASME J. Turbomach., **121**, pp. 683–693.
[21] Ameri, A. A., and Bunker, R. S., 2000, ''Heat Transfer and Flow on the First Stage Blade Tip of a Power Generation Gas Turbine: Part 2: Simulation Results,'' ASME J. Turbomach., **122**, pp. 272–277.
[22] Ameri, A. A., and Rigby, D. L., 1999, ''A Numerical Analysis of Heat Transfer and Effectiveness on Film Cooled Turbine Blade Tip Models,'' NASA/CR 1999-209165.
[23] Ameri, A. A., 2001, ''Heat Transfer and Flow on the Blade Tip of a Gas Turbine Equipped With a Mean-Camberline Strip,'' ASME J. Turbomach., **123**, pp. 704–708.
[24] Rhee, D. H., Choi, J. H., and Cho, H. H., 2001, ''Effect of Blade Tip Clearance on Turbine Shroud Heat/Mass Transfer,'' ASME Paper No. 2001-GT-0158.
[25] Jin, P., and Goldstein, R. J., 2002, ''Local Mass/Heat Transfer on a Turbine Blade Tip,'' The 9th International Symposium on Transport Phenomena and Dynamics of Rotating Machinery, Honolulu, February 10–14, HT-ABS-012, pp. 1–11.
[26] Jin, P., and Goldstein, R. J., 2002, ''Local Mass/Heat Transfer on Turbine Blade Near-Tip Surfaces,'' ASME Paper No. GT-2002-30556.
[27] Papa, M., Goldstein, R. J., and Gori, F., 2002, ''Effects of Tip Geometry and Tip Clearance on the Mass/Heat Transfer From a Large-Scale Gas Turbine Blade,'' ASME Paper No. GT-2002-30192.
[28] Kwak, J. S., and Han, J. C., 2003, ''Heat Transfer Coefficient on a Gas Turbine Blade Tip and Near Tip Regions,'' presented at the 8th AIAA/ASME Joint Thermophysics and Heat Transfer Conference, St. Louis, June, Paper No. AIAA-2002-3012; Also, AIAA J. Thermophysics and Heat Transfer, **17**(3).
[29] Kline, S. J., and McClintock, F. A., 1953, ''Describing Uncertainties in Single Sample Experiments,'' Mech. Eng. (Am. Soc. Mech. Eng.), **75**, pp. 3–8.

Yuan Zheng
Maurice. J. Zucrow Laboratories,
School of Mechanical Engineering,
Purdue University,
W. Lafayette, IN 47907-2014

R. S. Barlow
Combustion Research Facility,
Sandia National Laboratories,
Livermore, CA 94551-0969

Jay P. Gore
Maurice. J. Zucrow Laboratories,
School of Mechanical Engineering,
Purdue University,
W. Lafayette, IN 47907-2014

Measurements and Calculations of Spectral Radiation Intensities for Turbulent Non-Premixed and Partially Premixed Flames

Spectral radiation intensities leaving diametric and chord-like paths for six non-sooting flames were measured using an infrared array spectrometer. The spectral radiation intensities were also computed using the mean property approach and a time and space series simulation approach. Turbulence/radiation interactions (TRI) in these flames were investigated by comparing the two sets of computations to the experimental data. The effects of TRI are significant for regions away from the flame axis. The new data and findings are of value in the evaluation of radiation models, which are increasingly used in turbulent combustion calculations. [DOI: 10.1115/1.1589502]

Keywords: *Combustion, Heat Transfer, Modeling, Radiation, Turbulence*

Introduction

Accurate computation of radiation heat loss is very important in determining the nitric oxide (NO) formation in some nonluminous turbulent flames [1–3]. For a small control volume in the flame, the time averaged net radiation heat loss ($\overline{Q_r}$) consists of energy emitted ($\overline{Q_e}$) by the participating media in that volume to the surroundings minus the energy absorbed ($\overline{Q_a}$) by that media from the incident radiation field [4]. The incident radiation is a summation of spectral radiation intensities (I_λ) from all directions. Since the radiation quantities are determined by the scalar (temperature and species concentrations) fields through highly nonlinear relations, $\overline{Q_e}$ and $\overline{Q_a}$ may differ a lot from the calculations based on the mean scalar properties [5]. These effects of fluctuations in the scalar fields on the mean radiation quantities are referred as turbulence/radiation interactions (TRI) [6,7]. The determination of $\overline{Q_e}$ only requires single-point statistics of the turbulent scalar field, while the determination of $\overline{Q_a}$ requires more complicated multipoint statistics.

During the last two decades, the effects of TRI in non-sooting jet flames have been investigated using measurements and computations of I_λ leaving horizontal diametric radiation paths through the flames. The computations of mean I_λ including the effects of TRI have relied on stochastic simulation approaches. The effects of TRI in various flames have been evaluated by comparing the differences between the mean I_λ calculated by using the mean scalar properties and those calculated using the stochastically simulated scalar properties. Both sets of calculations have been compared with experimental data. Significant effects of TRI were observed in hydrogen flames [7,8], with stochastically predicted mean I_λ being as much as twice those based on the mean property (MP) calculations. The measured I_λ were closer to the results of the stochastic calculations. In contrast, the measured and stochastically computed mean I_λ for most diametric paths in carbon monoxide flames [9,10] were only 10~30% higher than those computed using the MP method. TRI enhancements approaching 100% were observed only for the diametric path near the flame tip. Moderate levels (10~30%) of TRI enhancements in mean I_λ were also reported for CH_4 flames by Jeng et al. [11] and for a CH_4/H_2 flame by Hall and Vranos [12].

Frank et al. [2] calculated I_λ for a methane/air partially premixed flame (flame D defined in Ref. [2] and later in this paper) using the mean property method with the emission only and the emission/absorption approximations for a diametric path at $x/D=45$. The emission only approximation led to a factor of two increase in the computed intensities. However, experimental data for an evaluation of their predictions were not available.

Kounalakis et al. [13] developed a stochastic time and space series (TASS) simulation method to account for TRI in turbulent CO/H_2 flames. By using measured mixture fraction statistics, they achieved excellent calculations of mean I_λ within 10% of the experimental data. More recently, Zheng et al. studied I_λ for a turbulent $CH_4/H_2/N_2$ jet flame by adapting a tomography-like TASS simulation [14]. This study indicated the importance of investigating TRI for I_λ leaving horizontal chord-like paths in addition to those leaving the diametric paths. The flame considered in Ref. [14] is one of the Sandia workshop [15] flames. Well-documented experimental data for velocity and scalar fields of that and other workshop flames are already available in the literature [15–18]. The data for I_λ of additional workshop flames, which are very useful for the evaluation of the radiation submodels incorporated in the current and future computational tools, are necessary.

Motivated by this, the present work consisted of the following:

1. Instantaneous I_λ leaving diametric and various chord-like paths at three heights from six workshop flames were measured by using a fast infrared (IR) array spectrometer (FIAS) [19]. The turbulent jet flames to be studied here consist of one H_2/N_2 flame [16], two $CH_4/H_2/N_2$ flames [17] and three piloted CH_4/air flames [18].
2. Based on the TASS simulated instantaneous scalar fields, the instantaneous I_λ were calculated by integration of the radiation transfer equation (RTE) for non-homogenous paths over a range of optical thickness.
3. The mean I_λ were also calculated by integration of the RTE using the mean scalar properties. The effects of TRI in these flames were studied by comparing the mean I_λ from the MP calculations to those extracted from the measurements and the TASS calculations.

In the I_λ calculations, the measured mean properties and other

---

Contributed by the Heat Transfer Division for publication in the JOURNAL OF HEAT TRANSFER. Manuscript received by the Heat Transfer Division September 16, 2002; revision received March 20, 2003. Associate Editor: S. T. Thynell.

Table 1 Flame conditions [2]

Flame	Fuel mixture (by volume)	D (burner diameter), mm	Re	Normalized Stoichiometric Flame Height $L_{\mathrm{stoich}/D}$
DLR_A	22% CH_4, 33% H_2, 45% N_2	8	15200	64
DLR_B	22% CH_4, 33% H_2, 45% N_2	8	22800	68
C	25% CH_4, 75% air	7.2	13400	47
D	25% CH_4, 75% air	7.2	22400	47
E	25% CH_4, 75% air	7.2	33600	47
H3	50% H_2, 50% N_2	8	10000	36 [15]

statistics for the scalar fields [15–18] were adopted to isolate the uncertainties of specific computational fluid dynamics (CFD) and combustion models.

Experimental Method

The radiation measurements were conducted at the Turbulent Diffusion Flame (TDF) Laboratory and the Turbulent Combustion Laboratory (TCL) at Sandia National Laboratories. The operating conditions for the flames under investigation are listed in Table 1, where L_{stoich} is the height above the burner at which the measured Favre averaged mixture fraction reaches the stoichiometric value [2]. The flow facilities for the simple jet flames (DLR_A and B, H3) and the piloted flames (C,D,E) have been discussed elsewhere [1,17,18], and [20] and will only be briefly described here.

The simple jet burner, on which flames H3, DLR_A and B are stabilized, is a long tube with an inner diameter of 8 mm tapered to a thin edge. The piloted burner, on which flames C, D, and E are stabilized, has a main jet diameter of 7.2 mm and a pilot diameter of 18.2 mm. The main CH_4/air jet is partially premixed with an equivalence ratio of 3.17 (25% CH_4 by volume). The lean premixed pilot flame burns a mixture of C_2H_2, H_2, CO_2, N_2, and air, having the same enthalpy and equilibrium composition as a CH_4/air flame with an equivalence ratio of 0.77. Both burners can be moved in three dimensions for positioning. Air co-flows were fed for all six flames through a wind tunnel, with velocities of 0.3 m/s for the simple jet flames and 0.9 m/s for the piloted flames.

For each flame, the instantaneous I_λ for the diametric and many chord-like paths at three heights were measured using FIAS [19]. Figure 1 illustrates the geometry for the spectral radiation intensity measurements and calculations. The spectral range of the FIAS is from 1.4 to 4.8 μm covering the important molecular radiation bands of H_2O and CO_2. The mean spectral resolution is 42 nm with a maximum of 70 nm at $\lambda=1.5$ μm and a minimum of 33 nm at $\lambda=4.5$ μm. The spatial resolution of the present measurements is 2 mm based on the FIAS optics. The sampling rate for the individual wavelengths is 6250 Hz. For each radiation path, 6000 samples were collected. The wavelength readings corresponding to the pixels were calibrated by using 6 different narrow band IR filters in conjunction with a black body source. The intensity responses of each pixel were then calibrated using the black body source operated at 6 different temperatures. The background noise signals were subtracted during the measurements.

Experimental uncertainties were estimated following the guidelines in Ref. [21]. The bias in the data is due to the uncertainties in the calibration process. The uncertainty in the output voltage during calibrations was experimentally found to be less than 2% (95% confidence). The uncertainties in the wavelength reading and the black body temperature also affect the accuracy of intensity response calibration. In the present study, since the uncertainty in wavelength reading was 10 nm and the uncertainty in the black body temperature was 1 K, the uncertainty in mean I_λ measurements caused by these two factors was only 0.5%. Therefore, the combined bias limit is of the order of 2%. The precision limit (95% confidence) due to finite sampling time available in the continuous scanning process was experimentally found to be less than 10%. The measurements were repeatable within this range. Therefore, the combination of the bias limit and the precision limit gave an overall system uncertainty (95% confidence) in the order of 10%. The overall uncertainty was dominated by the precision limit.

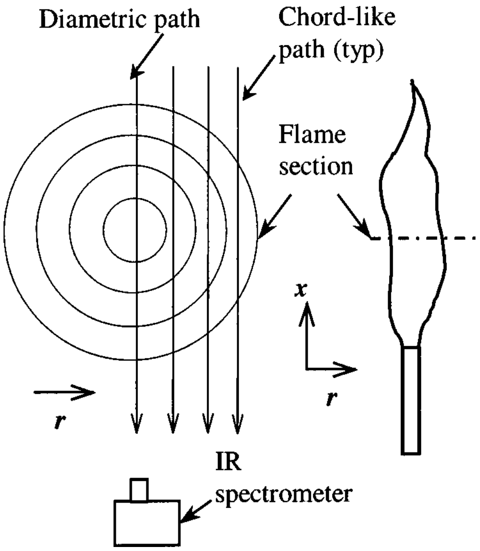

Fig. 1 Geometry for measurement and calculation on spectral radiation intensities

Computational Method

For all six flames, the mean spectral radiation intensities were first computed by adopting the mean property distributions along the radiation paths ignoring TRI. The RTE was solved for various non-homogeneous paths through the flames using the RADCAL program with a narrow band radiation model [22,23]. The properties needed for the computations were taken from the experimental data available in the literature [15–18] discussed briefly in the next section.

Time and space series analyses that account for TRI were also considered in present work. The instantaneous multipoint realizations of the scalar properties along the non-homogenous radiation paths were simulated first by using the single point experimental data and TASS analysis. Then, the instantaneous I_λ for that path were calculated by using RADCAL. Finally the mean I_λ were obtained from the 6000 simulated realizations for each radiation path.

The TASS based computation, involving a tomography-like procedure to determine the integral length scales (l_{I}) along the radiation paths, has been discussed in detail elsewhere [14] and will only be briefly described here. In order to simulate instantaneous scalar realizations, the fluctuating value of a time varying scalar at a specific spatial location is modeled as a linear combination of its nearby spatial values, its previous temporal value and a random shock. The model parameters can be determined by the two-time/two-point scalar correlations, which are assumed to be exponent decaying. The measured single-point PDFs of scalar properties in conjunction with prescriptions of the integral length and time scales for scalar fluctuations are required as the model inputs.

The integral time scales (τ_{I}) are determined using the Taylor's hypothesis as long as velocity data are available. For some cases, however, the velocity data are not available. Therefore τ_{I} and l_{I} are determined separately. A least mean square (LMS) scheme was developed in the present work to determine the best-fit integral scales. Spectral radiation intensities at two wavelengths were considered in order to minimize the computational time. The procedure involved calculations of RMS values and power spectral densities (PSD) for the spectral radiation intensities and is briefly described as follows,

Step 1: Guess l_I and τ_I so that a time series of instantaneous I_λ can be simulated.

Step 2: Obtain RMS and PSD from the simulated instantaneous values.

Step 3.1: Calculate the error square in RMS for selected λ_1 and λ_2.

Step 3.2: Calculate the error square in PSD for λ_1 and λ_2.

Step 3.3: Calculate the weighted mean square error (e).

Step 4: Check the least error criteria to iterate on l_I and τ_I. i.e.,

$$\frac{\partial e}{\partial l_I}=0 \quad \text{and} \quad \frac{\partial e}{\partial \tau_I}=0 \Rightarrow l_I, \tau_I \tag{1}$$

When applying this scheme, l_I and τ_I were determined successively and several iterations were required to reach the least mean square error. This scheme can be extended if considering more than two wavelengths.

The accuracy of the calculated spectral radiation intensities is affected by the accuracy of the adopted scalar data. The uncertainties in temperature and species (H_2O,CO_2) concentration measurements are 3% and 4% respectively [17,18]. The computational uncertainty resulting from this depends on wavelength and the optical depth. As an example for a homogeneous segment of 10 mm within a diametric radiation path in flame DLR_A at $x/D=60$, the computational uncertainty in the emitted intensity was estimated and described in the following. The mean scalar properties for this segment are temperature equal to 1838 K, mean H_2O mole fraction equal to 0.191 and mean CO_2 mole fraction equal to of 0.042. The resulting computational uncertainties in the spectral radiation intensities at $\lambda=1.81$, 2.51, 2.72, 2.91, 4.31, and 4.54 μm are estimated to be 11%, 6%, 5%, 7%, 5%, and 10% respectively.

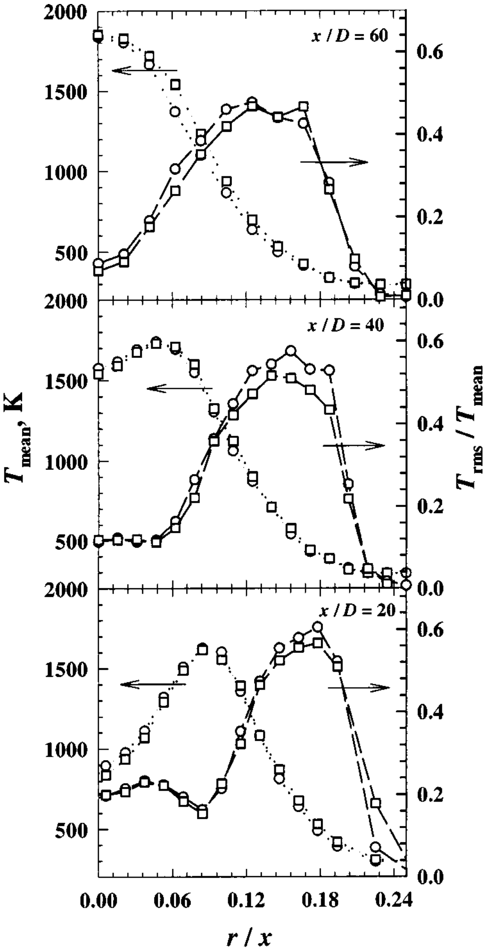

Fig. 2 Temperature distributions in flames DLR_A (circle) and B (square)

Input Scalar Experimental Data

Figure 2 illustrates the temperature distributions in flames DLR_A and B. The mean temperatures are within 50 to 100 K of each other for the two flames. At $x/D=20$, the mean temperature in these flames reaches a peak at a radial location around $r/x=0.08$, which defines the mean radial location of the flame sheet. The mean temperature peak moves closer to the flame axis at $x/D=45$ and reaches the axis at $x/D=60$ defining the flame tip. The normalized temperature fluctuations ($T_{\mathrm{rms}}/T_{\mathrm{mean}}$), which define the levels of turbulence in temperature and are the basis for the TRI, are similar in flames DLR_A and B. The fluctuations in the mean flame region are stronger than those near the flame axis by up to a factor of 4.

Mean temperature distributions of flames C, D, and E are presented in Fig. 3. At the axial locations of $x/D=30$ and 45, the mean temperature distributions are in a small range for the three flames, even though the fuel flow rate increases significantly from flame C to D and D to E. At the downstream location of $x/D=60$, however, significantly higher temperatures can be observed for the flames with the higher Reynolds number. For all the piloted flames, the normalized temperature fluctuations reach their peak values at a radial location away from the flame axis.

The temperature distributions of flame H3 are illustrated in Fig. 4. At $x/D=20$, the mean temperature profile has a peak around $r/x=0.06$. The mean temperature peak is near or at the flame axis for the two downstream locations. At all three axial locations, the normalized temperature fluctuations in the region away from the axis are stronger than those near the axis by factors of 2 to 4.

Results and Discussion

At each of the three axial locations in the 6 flames, spectral radiation intensities were measured and calculated for many chord-like paths. The mean spectral radiation intensities for the diametric path ($r/x=0$) and for one of the chord-like paths are selected here for further discussion. At a fixed axial location, the mean I_λ for the diametric radiation path are higher than those for most of the chord-like paths, which are shorter. The mean intensities for some chord-like paths that are near the flame sheet location are higher than those for the diametric path. However, the chord-like paths selected here are always farther out on the lean side of the flame sheet therefore have lower mean intensities but much higher relative RMS intensities compared to those for the diametric path.

Measurements and calculations of spectral radiation intensities for $x/D=20$, 30, and 40 in flame H3 (H_2/N_2) are illustrated in Figs. 5–7. The results of the TASS based computations are presented together with the mean property calculations and experimental data. The spectral radiation intensities for this dilute hydrogen flame, with 50% nitrogen by volume, are relatively low. The 1.87 and 2.7 μm bands of water vapor dominate the spectra. In this flame, the combustion process is complete at approximately $L_{\mathrm{stoich}}/D=36$. Therefore, the measured mean I_λ at $x/D=30$ and 40 are almost identical and are 50% stronger than those at $x/D=20$. The I_λ calculations ignoring TRI agree with the measurements quite well for diametric paths therefore the effects of TRI are not significant for I_λ leaving these paths. The MP approach seriously under-estimated the mean I_λ for the radiation path leaving $r/x=0.09$ at $x/D=20$. The TRI enhanced the spectral radiation intensities by about 80%. The TASS calculations, however, successfully captured the TRI enhancements. The TRI

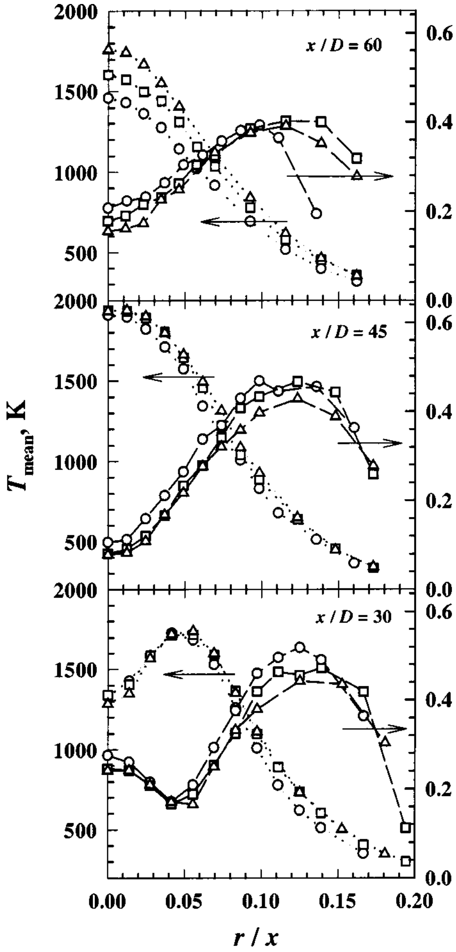

Fig. 3 Temperature distributions in flames C (circle), D (square), and E (triangular)

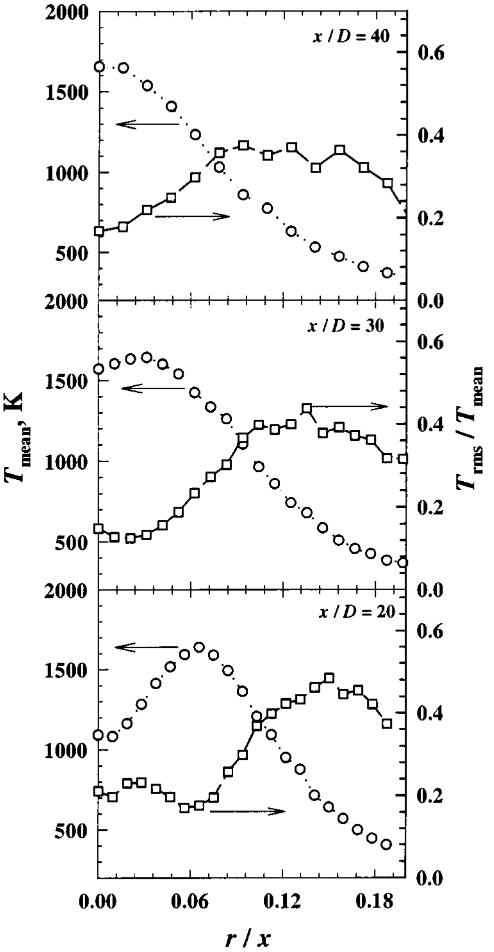

Fig. 4 Temperature distributions in flame H3

enhancements for the radiation path leaving $r/x = 0.06$ at $x/D = 30$ and $r/x = 0.05$ at $x/D = 40$ were around 25%.

Measurements and calculations of spectral radiation intensities for downstream locations at $x/D = 20$, 40 and 60 in the DLR_A flame ($CH_4/H_2/N_2$) are illustrated in Figs. 8–10. In this flame, the spectra are dominated by radiation from water vapor and CO_2. The measured mean I_λ at $x/D = 40$ are much higher than those at $x/D = 20$. The I_λ at $x/D = 60$, which is near the stoichiometric flame height ($L_{stoich}/D = 64$), are slightly higher than those at $x/D = 40$. For the diametric paths at three axial locations, both the mean property and the TASS based calculations agree with the data. Thus, the effects of TRI are weak for the diametric paths. For chord-like paths, where the mean I_λ are one third to half of those for the diametric paths, the mean property method significantly under-predicts the spectral radiation intensities for the 2.7 μm H_2O/CO_2 band and the long wavelength wings of the 4.3 μm CO_2 band. Around the peak of the 4.3 μm band, the experimental data lie mostly between the TASS and MP results for the selected chord-like paths. The reasons for the differences in the experimental data, the mean property and TASS based computations for the diametric paths near the band center of the 4.3 μm CO_2 band deserve further study. As illustrated in these figures, TRI are significant for regions away from the axis for this flame, where the turbulent intensities (T_{rms}/T_{mean}) are higher.

Figures 11–13 demonstrate the mean spectral radiation intensities for the flame DLR_B, which has a 50% higher Reynolds number than the DLR_A flame. The stoichiometric flame height does not change significantly ($L_{stoich}/D = 68$) due to the momentum-controlled nature of these flames. In addition, the measured radiation intensities remain almost constant in spite of the 50% increase in the fuel input. This is a result of similar flame structure. For the diametric paths, the calculated mean I_λ ignoring TRI agree with the measurements quite well. For the paths away from the flame axis, however, more than 50% under-prediction can be observed indicating very strong TRI. Especially, the MP calculated mean I_λ from the 2.7 μm H_2O/CO_2 band almost disappears for the path at $r/x = 0.12$ mm at $x/D = 60$.

Measurements and calculations of spectral radiation intensities for $x/D = 30$, 45 and 60 in the flame D (piloted CH_4/air) are illustrated in Figs. 14–16. These spectra are also dominated by radiation from water vapor and CO_2. Being close to the stoichiometric flame height ($L_{stoich}/D = 47$), the measured I_λ are the highest at $x/D = 45$ and decrease on the upstream ($x/D = 30$) and the downstream ($x/D = 60$) sides. For the diametric paths, the calculations based on mean properties under-predict the radiation intensities by 5 to 20%. The present MP calculations for the diametric path at $x/D = 45$ are in agreement with the results of Frank et al. [2]. Up to 50% under-prediction is observed for paths away from the flame center at all three heights. The calculations considering TRI (TASS), however, match the experimental data very well for all radiation paths. Thus, the effect of TRI is significant in this flame.

Figures 17–19 and 20–22 present the spectral radiation intensities for two additional piloted CH_4/air flames with lower and higher Reynolds numbers. There is no significant change in the measured stoichiometric flame height because of the momentum-controlled nature of this quantity. For chord-like paths at identical radial locations and height above the burner, the measured radiation intensities are greater for flame E than those for flame D,

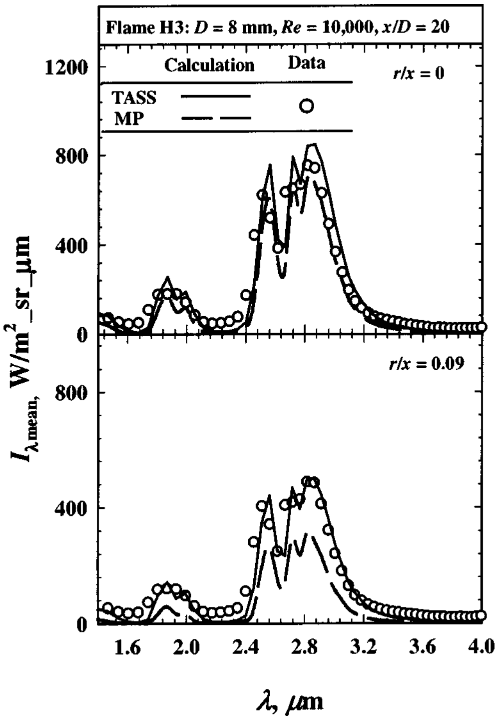

Fig. 5 Spectral radiation intensities in flame H3 (x/D=20)

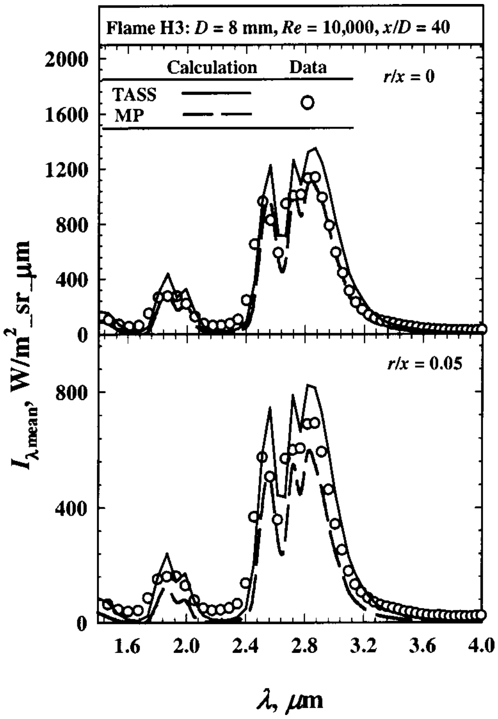

Fig. 7 Spectral radiation intensities in flame H3 (x/D=40)

which are greater than those for flame C. This is a result of the increasing radial extent of the hot gas region with increasing Re number as indicated by Fig. 3. The changes for diametric paths, however, are small compared to the significant increases in the fuel flow rate especially for the flames D and E. This is a result of self-absorption of radiation over a longer path and effects of increases in volumetric combustion rates by turbulence without an increase in temperature. Similarly, the spectral radiation intensities for the diametric paths were slightly under-predicted by the mean property method. Significant under-predictions (50%) occurred for paths away from the flame axis in both flames using the mean property method. In contrast, the TASS provided significantly improved estimates of TRI for all conditions.

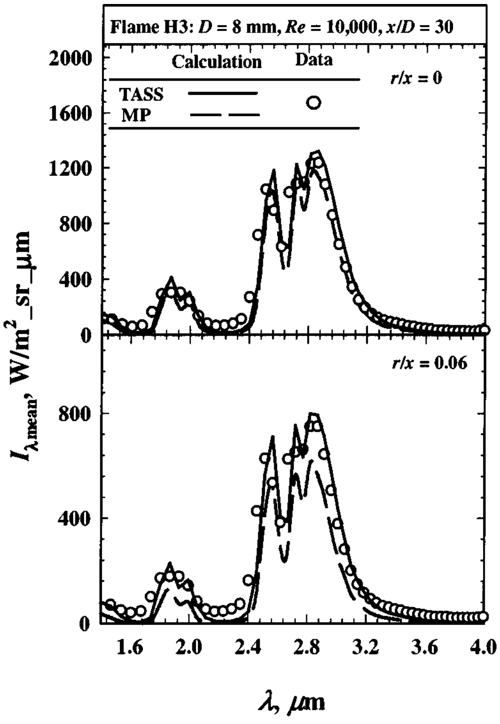

Fig. 6 Spectral radiation intensities in flame H3 (x/D=30)

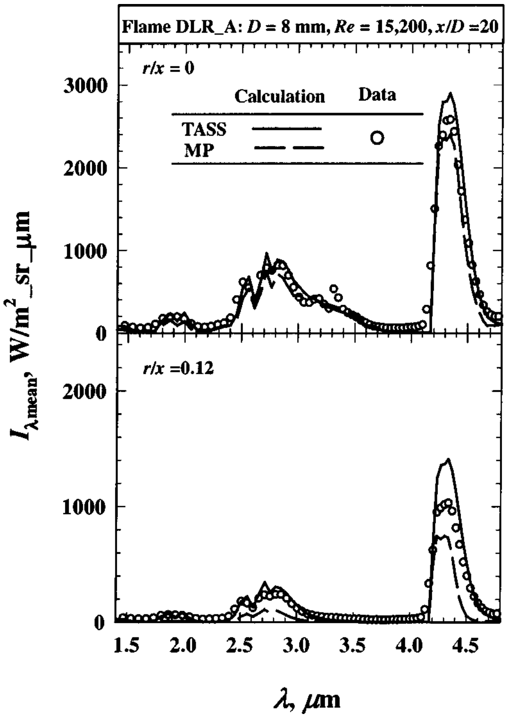

Fig. 8 Spectral radiation intensities in flame DLR_A (x/D =20)

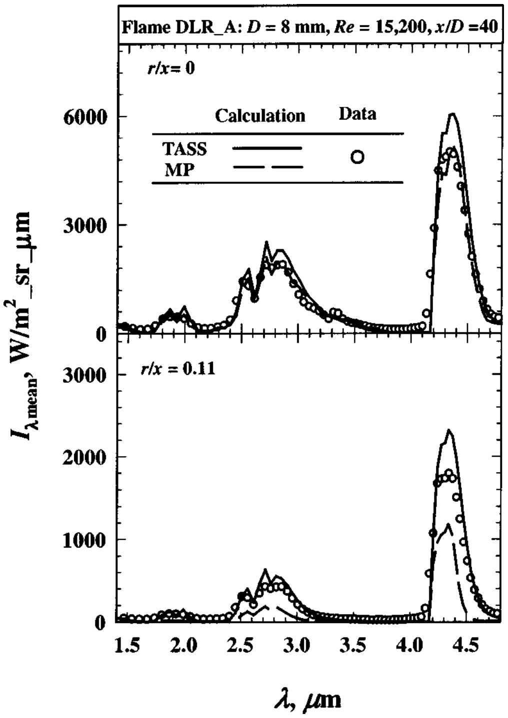

Fig. 9 Spectral radiation intensities in flame DLR_A ($x/D = 40$)

Conclusions

In order to evaluate the effects of turbulence/radiation interactions (TRI) in non-sooting flames, spectral radiation intensities for six well-documented flames burning various fuels and with different Reynolds numbers were investigated experimentally and computationally. The specific conclusions are as follows,

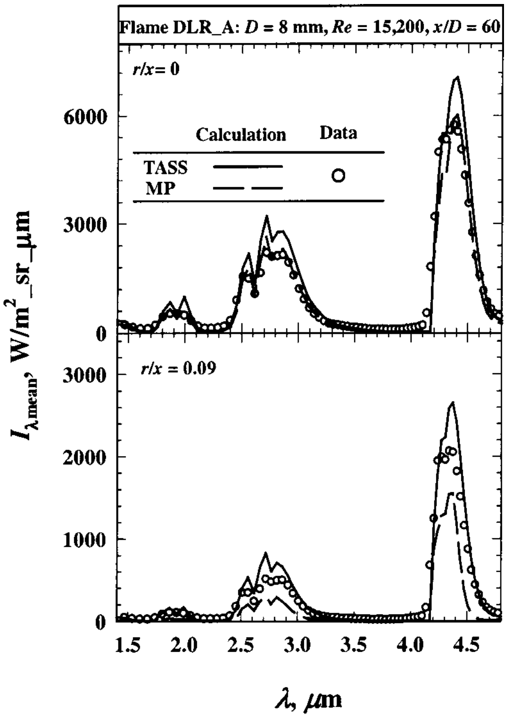

Fig. 10 Spectral radiation intensities in flame DLR_A ($x/D = 60$)

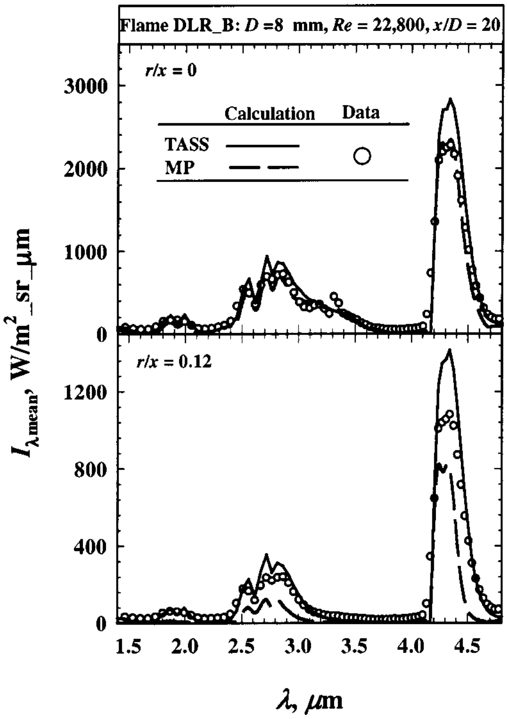

Fig. 11 Spectral radiation intensities in flame DLR_B ($x/D = 20$)

1) For all the flames studied, the mean spectral radiation intensities for the diametric paths reach maximum near the axial location corresponding to the stoichiometric flame height.

2) In the range of this study, the effect of Reynolds number on the mean radiation intensities is not strong. This observation is inconsistent with the scalar measurements.

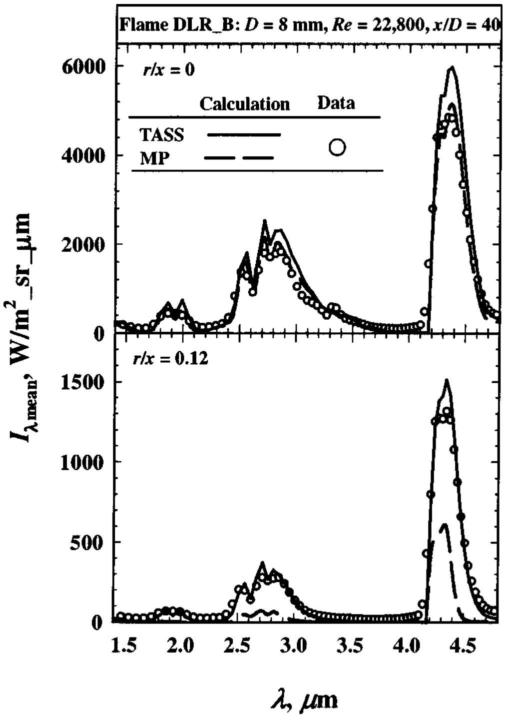

Fig. 12 Spectral radiation intensities in flame DLR_B ($x/D = 40$)

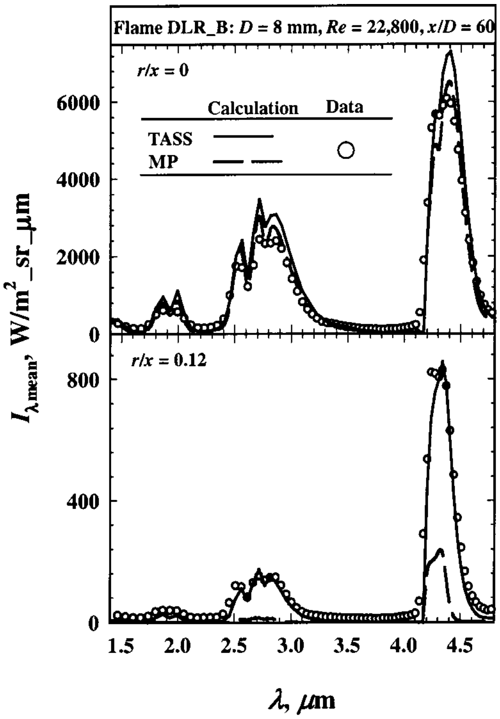

Fig. 13 Spectral radiation intensities in flame DLR_B ($x/D=60$)

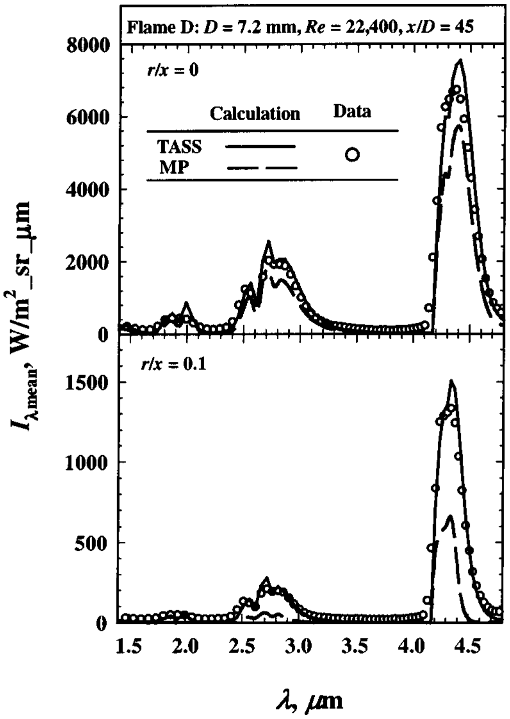

Fig. 15 Spectral radiation intensities in flame D ($x/D=45$)

3) In these six flames, the effects of TRI are not significant for regions near the flame axis. Therefore mean property approach for radiation heat loss calculations is adequate for these paths.

4) In these six flames, the effects of TRI are significant for regions away from the flame axis where the turbulent intensities are higher. The stochastic time and space series simulation method adapted in the present study successfully captured the effects of TRI on mean I_λ for all the paths.

Acknowledgment

The Indiana 21st Century Research and Technology Fund supported this work with a grant to the Mid Infrared Sensing Diag-

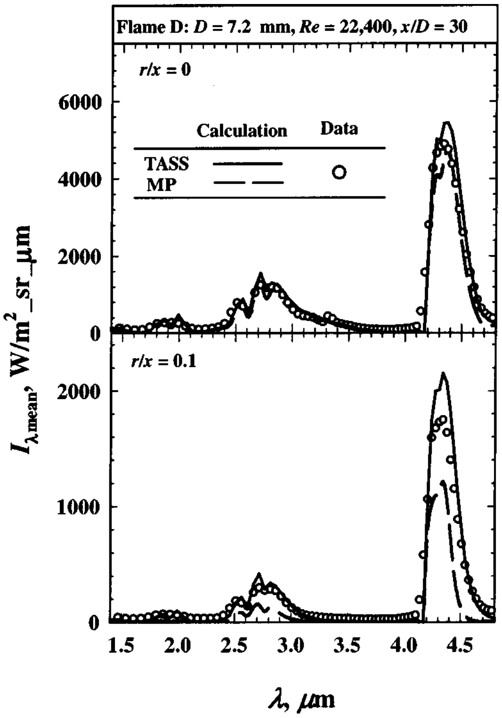

Fig. 14 Spectral radiation intensities in flame D ($x/D=30$)

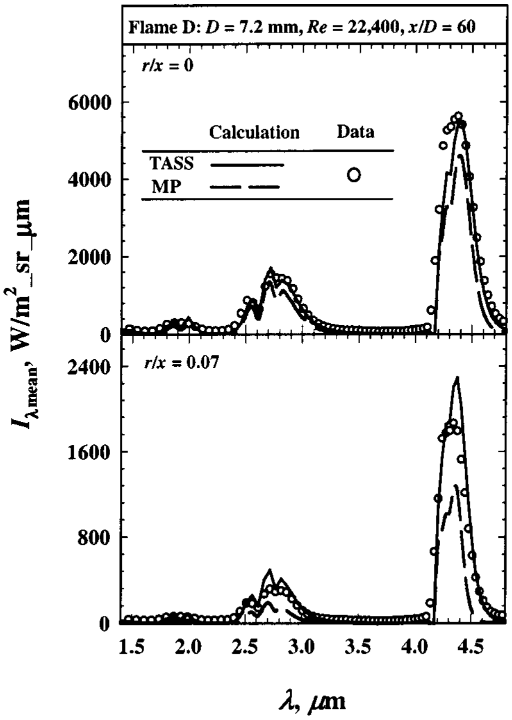

Fig. 16 Spectral radiation intensities in flame D ($x/D=60$)

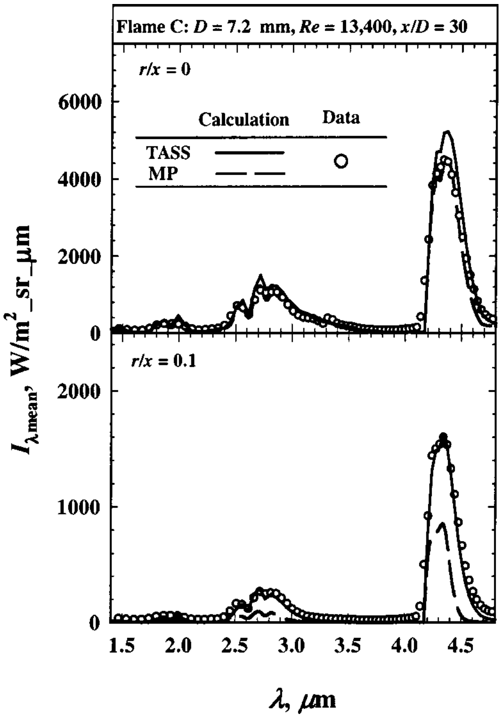

Fig. 17 Spectral radiation intensities in flame C (x/D=30)

nostics and Control Consortium with additional support provided by the Air Force Office of Scientific Research. Experiments at Sandia were supported by the Department of Energy, office of Basic Energy Sciences. Dr. Andreas Dreizler, from TU Darmstadt, Germany, provided the velocity data used in this work. His kind help is highly appreciated.

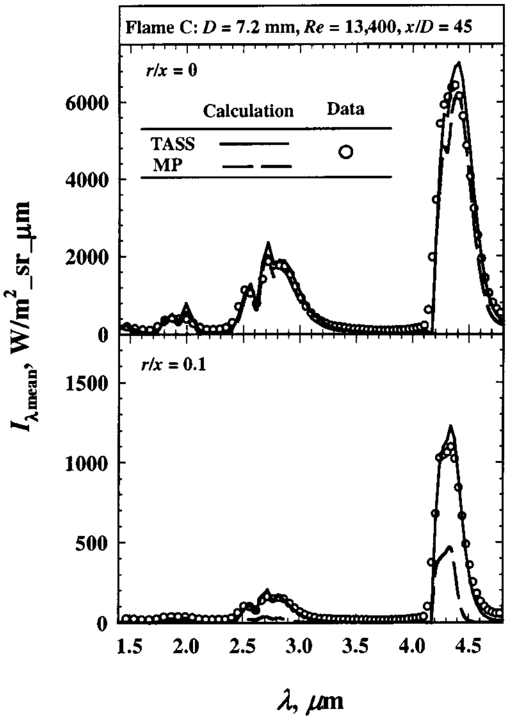

Fig. 18 Spectral radiation intensities in flame C (x/D=45)

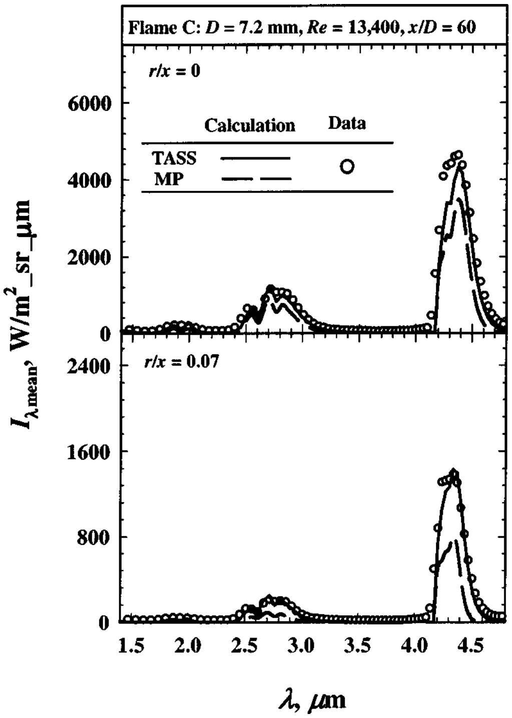

Fig. 19 Spectral radiation intensities in flame C (x/D=60)

Nomenclature

D = burner diameter
I_λ = spectral radiation intensities
Q = time averaged heat loss/gain
r = radial distance
x = height above burner exit
λ = wavelength

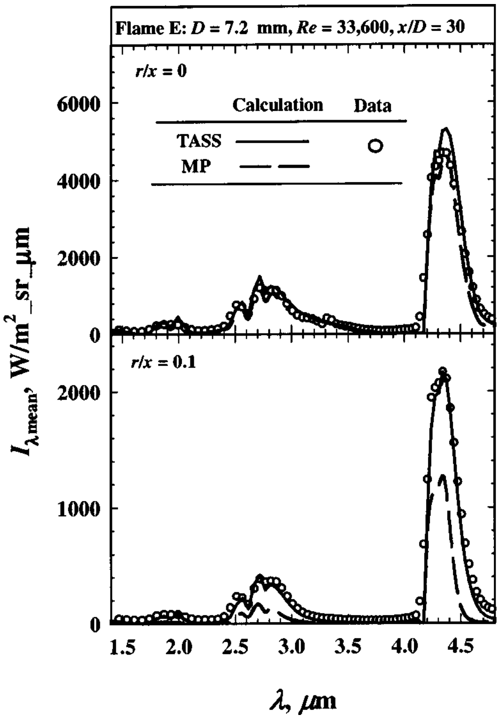

Fig. 20 Spectral radiation intensities in flame E (x/D=30)

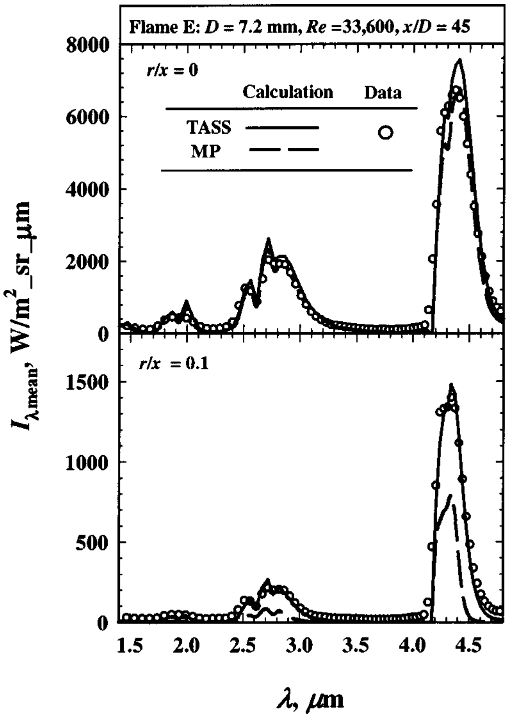

Fig. 21 Spectral radiation intensities in flame E ($x/D=45$)

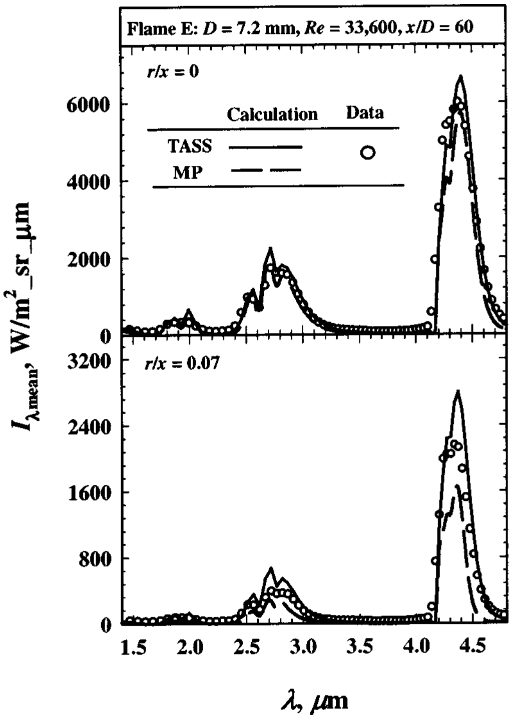

Fig. 22 Spectral radiation intensities in flame E ($x/D=60$)

Subscripts

a = absorption
e = emission
r = radiation

References

[1] Barlow, R. S., Smith, N. S. A., Chen, J.-Y., and Bilger, R. W., 1999, "Nitric Oxide Formation in Dilute Hydrogen Jet Flames: Isolation of the Effects of Radiation and Turbulence-Chemistry Submodels," Combust. Flame, **117**, pp. 4–31.

[2] Frank, J. H., Barlow, R. S., and Lundquist, C., 2000, "Radiation and Nitric Oxide Formation in Turbulent Non-Premixed Jet Flames," Proc. of the Combustion Institute, A. R. Burgess and J. P. Gore, eds., The Combustion Institute, Pittsburgh, PA, **28**, pp. 447–454.

[3] Hartick, J. W., Tacke, M., Fruchtel, G., Hassel, E. P., and Janicka, J., 1996, "Interaction of Turbulence and Radiation in Confined Diffusion Flames," Proc. of the Combustion Institute, A. R. Burgess and F. L. Dryer, eds., The Combustion Institute, Pittsburgh, PA, **26**, pp. 75–82.

[4] Gore, J. P., Ip, U.-S., and Sivathanu, Y. R., 1992, "Coupled Structure and Radiation Analysis of Acetylene/Air Flames," ASME J. Heat Transfer, **114**, pp. 487–493.

[5] Li, G., and Modest, M. F., 2002, "Application of Composition PDF Methods in the Investigation of Turbulence-Radiation Interactions," J. Quant. Spectrosc. Radiat. Transf., **72**, pp. 461–472.

[6] Song, T. H., and Viskanta, R., 1987, "Interaction of Radiation With Turbulence: Application to a Combustion System," AIAA J. Thermophysics, **1**, pp. 56–62.

[7] Gore, J. P., Jeng, S.-M., and Faeth, G. M., 1987, "Spectral and Total Radiation Properties of Turbulent Hydrogen/Air Diffusion Flames," ASME J. Heat Transfer, **109**, pp. 165–171.

[8] Kounalakis, M. E., Gore, J. P., and Faeth, G. M., 1988, "Turbulence/Radiation Interactions in Nonpremixed Hydrogen/Air Flames," Proc. of the Combustion Institute, The Combustion Institute, Pittsburgh, PA, **22**, pp. 1281–1290.

[9] Gore, J. P., Jeng, S.-M., and Faeth, G. M., 1987, "Spectral and Total Radiation Properties of Turbulent Carbon Monoxide/Air Diffusion Flames," AIAA J., **25**, pp. 339–345.

[10] Kounalakis, M. E., Gore, J. P., and Faeth, G. M., 1989, "Mean and Fluctuating Radiation Properties of Nonpremixed Turbulent Carbon Monoxide/Air Flames," ASME J. Heat Transfer, **111**, pp. 1021–1030.

[11] Jeng, S.-M., Lai, M.-C., and Faeth, G. M., 1984, "Nonluminous Radiation in Turbulent Buoyant Axisymmetric Flames," Combust. Sci. Technol., **40**, pp. 41–53.

[12] Hall, R. J., and Vranos, A., 1994, "Efficient Calculation of Gas Radiation From Turbulent Flames," Int. J. Heat Mass Transfer, **37**, pp. 2745–2750.

[13] Kounalakis, M. E., Sivathanu, Y. R., and Faeth, G. M., 1991, "Infrared Radiation Statistics of Nonluminous Turbulent Diffusion Flames," ASME J. Heat Transfer, **113**, pp. 437–445.

[14] Zheng, Y., Sivathanu, Y. R., and Gore, J. P., 2002, "Measurements and Stochastic Time and Space Series Simulations of Spectral Radiation in a Turbulent Non-Premixed Flame," Proc. of the Combustion Institute, J. H. Chen and M. D. Colket, eds., The Combustion Institute, Pittsburgh, PA, **29**, pp. 1957–1963.

[15] International Workshop on Measurement and Computation of Turbulent Nonpremixed Flames, 2003, www.ca.sandia.gov/TNF, Sandia National Laboratories.

[16] Meier, W., Prucker, S., Cao, M.-H., and Stricker, W., 1996, "Characterization of Turbulent H_2/N_2/Air Jet Diffusion Flames by Single-Pulse Spontaneous Raman Scattering," Combust. Sci. Technol., **118**, pp. 293–321.

[17] Meier, W., Barlow, R. S., Chen, Y.-L., and Chen, J.-Y., 2000, "Raman/Rayleigh/LIF Measurements in a Turbulent $CH_4/H_2/N_2$ Jet Diffusion Flame: Experimental Techniques and Turbulence-Chemistry Interaction," Combust. Flame, **123**, pp. 326–343.

[18] Barlow, R. S., and Frank, J. H., 1998, "Effects of Turbulence on Species Mass Fractions in Methane/Air Jet Flames," Proc. of the Combustion Institute, A. R. Burgess and F. L. Dryer, eds., The Combustion Institute, Pittsburgh, PA, **27**, pp. 1087–1095.

[19] Ji, J., Gore, J. P., Sivathanu, Y. R., and Lim, J., 2000, "Fast Infrared Array Spectrometer Used for Radiation Measurements of Lean Premixed Flames," *Proc. of the 34th National Heat Transfer Conference*, S. C. Yao and A. Jones, eds., ASME, New York, **2**, pp. 73–78.

[20] Masri, A. R., Dibble, R. W., and Barlow, R. S., 1996, "The Structure of Turbulent Nonpremixed Flames Revealed by Raman-Rayleigh-LIF Measurements," Prog. Energy Combust. Sci., **22**, pp. 307–362.

[21] Kim, J. H., Simon, T. W., and Viskanta, R., 1993, "Journal of Heat Transfer Policy on Reporting Uncertainties in Experimental Measurements and Results," ASME J. Heat Transfer, **115**, pp. 5–6.

[22] Grosshandler, W. L., 1993, "RADCAL: A Narrow-Band Model for Radiation Calculations in a Combustion Environment," NIST Technical Note 1402, U.S. Government Printing Office, Washington.

[23] Grosshandler, W. L., 1980, "Radiation Heat Transfer in Nonhomogenous Gases: A Simplified Approach," Int. J. Heat Mass Transfer, **23**, pp. 1447–1459.

Jung-Yeop Lee
Hong-Chul Park
Jung-Yeul Jung
Ho-Young Kwak
e-mail: kwakhy@cau.ac.kr

Mechanical Engineering Department,
Chung-Ang University, Seoul 156-756,
Korea

Bubble Nucleation on Micro Line Heaters

Nucleation temperatures on micro line heaters were measured precisely by obtaining the I-R (current-resistance) characteristic curves of the heaters. The bubble nucleation temperature on the heater with 3 μm width is higher than the superheat limit, while the temperature on the heater with broader width of 5 μm is considerably less than the superheat limit. The nucleation temperatures were also estimated by using the molecular cluster model for bubble nucleation on the cavity free surface with effect of contact angle. The bubble nucleation process was observed by microscope/35 mm camera unit with a flash light of μs duration. [DOI: 10.1115/1.1571844]

Keywords: *Bubble Growth, Heat Transfer, Microscale, Phase Change*

Introduction

Device miniaturization evolved from IC-based microfabrication technology has brought forth rapidly increasing importance of understanding fluid flow in micro channel and phase change in micro geometry. Especially bubble nucleation on micro heaters, which has been successfully utilized for bubble jet printers [1], has many potential applications of bubble powered micro thermal machines [2]. Considerable studies on boiling process have been performed so far with various metal surfaces for enhancing heat transfer [3], with small diameter of metal cylinder [4] related to enhancing the critical heat flux, and with a small patch [5] for cooling electronic chip. However extensive study of the boiling process on smooth surface in atomic scale is rare at present. Therefore, for clear understanding of the mechanism of bubble nucleation on micro heaters, more study is required for future applications.

In this study, bubble nucleation and growth on micro line heaters were investigated experimentally and theoretically. Two types of micro heaters with different width of 3 μm and 5 μm but with same length of 50 μm and thickness of 0.523 μm were utilized. Dielectric liquids such as FC-72, FC-77, and FC-40 were employed as working fluids. DC voltage to the heaters was increased in 0.01 V∼0.1 V increment to obtain I-R (current-resistance) characteristic curves for the heaters, from which the temperature for bubble nucleation can be deduced. Bubble nucleation process was also observed by using microscope/35 mm camera unit with μs duration flash light. Also the temperatures for the incipient bubble nucleation were estimated by using the molecular cluster model [6,7] for bubble formation.

A Vapor Bubble Formation Model Based on Molecular Interactions

The essential element of the molecular cluster model for vapor bubble formation is that the surface energy for the formation of the critical cluster grounded at the molecular level is utilized while keeping the kinetic formalism of the classical theory of nucleation. In this model, it is also assumed that the driving force for the clustering process is just the chemical potential difference of liquid molecules between the saturated state and the metastable one.

Employing the assumptions mentioned above, Kwak and Panton [6] obtained a stability condition of the critical cluster and the corresponding free energy for the bubble formation. These are

$$-(P_\infty - P_v)n_c^{1/3} = \frac{Z\varepsilon_m}{3} \bigg/ V_m \tag{1}$$

$$F_{nc} = \frac{Z\varepsilon_m}{6} n_c^{2/3} \tag{2}$$

The energy to separate a pair of molecules ε_m given in Eqs. (1) and (2) can be obtained when molecular properties such as ionization potential, polarizability, and van der Waals' diameter of molecule are provided. If any cluster, an aggregate of the liquid molecules in the metastable state meets the stability condition, the molecules in the cluster vaporize spontaneously by breaking the interaction between molecules.

Using the kinetic theory argument analogous to the condensation case, they also obtained the steady state nucleation per unit volume. With the minimum free energy for the formation of the critical cluster, Eq. (2), the nucleation rate of the critical cluster, $J_{nc}(\text{nuclei/cm}^3\ \text{s})$, is given by

$$J_{nc} = \beta N \left(\frac{k_B T}{2\pi m}\right)^{1/2} \left[\frac{Z}{18\pi}\left(\frac{\varepsilon_m}{k_B T}\right)\right]^{1/2} 4\pi \left(\frac{3V_m}{4\pi}\right)^{2/3} \cdot \exp\left[-\frac{\Delta H_{\text{vap}}}{RT} - \frac{\Delta H_f}{RT_f}\right] \cdot N \cdot \exp\left[-\frac{Z}{6}\left(\frac{\varepsilon_m}{k_B T}\right) n_c^{2/3}\right] \tag{3}$$

If we choose a level for the nucleation rate of the critical cluster, J_{nc}, the Eq. (3) becomes a relation for determining n_c. With n_c and the molecular properties known, the vapor pressure, P_v and the corresponding superheat limit is found from Eq. (1).

For the case that liquid is in contact with a solid surface on which no cavity exists, the nucleation temperature with considering the effect of contact angle may be obtained by the following equation [8].

$$T = \frac{F_{nc}\Phi}{k} \bigg/ \left[\ln \frac{CN^{-1/3}(\xi/\Phi^{1/2})}{J_s}\right] \tag{4}$$

where C is the pre-exponential factor in Eq. (3), and the factors Φ and ξ account for the volume and surface area truncation, respectively of the bubble due to the contact angle, which are given in Avedisian et al. [8].

The surface nucleation rate may be obtained by using the following equation [9].

$$J_s = \frac{1}{A_s}\left|\frac{d(F_n/k_B T)}{dT}\right| \dot{T} \tag{5}$$

Contributed by the Heat Transfer Division for publication in the JOURNAL OF HEAT TRANSFER. Manuscript received by the Heat Transfer Division April 30, 2001; revision received February 20, 2003. Associate Editor: V. P. Carey.

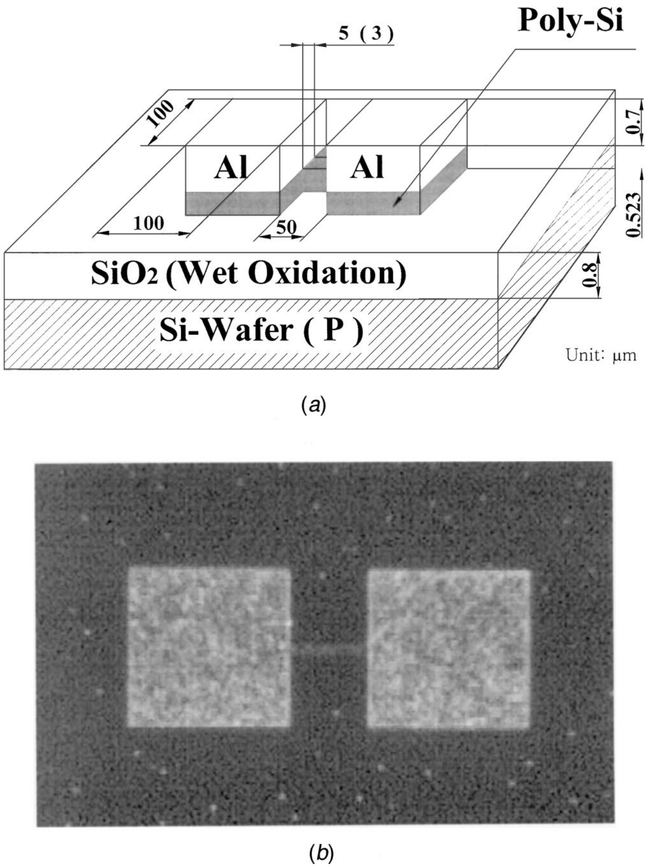

(*a*)

(*b*)

Fig. 1 Schematic (a) and enlarged (b) view of micro line heater

where $\dot{T}$ is the measured heating rate, which is about 5 $\times 10^7$°C/s for the micro line heater used in this study so that the nucleation rate for the micro line heater employed is about 10^{13}/cm^{2}s.

Micro Line Heater

(a) Experimental Apparatus and Procedures. Two types of micro line heater have been designed and fabricated by using the standard IC process [10]. The polysilicon heaters fabricated on the 0.8 μm silicon dioxide layer with P-type prime wafer have same length of 50±0.1 μm and thickness of 0.523±0.004 μm and two different width of 3±0.1 μm and 5±0.1 μm. No cavity was found on the micro line heaters fabricated when we inspected those with microscope and CCD camera. Two driving pads, which connect with the line heater electrically, have dimension of 100 $\times 100$ μm^2. The pads were made by deposition of aluminum film with thickness of 0.7 μm on the polysilicon pads. Schematic and enlarged views of the micro line heater on the silicon wafer are shown in Fig. 1.

A pressure tight test chamber as shown in Fig. 2(a) was made acryl. Inner dimension of the chamber to hold working fluid is $30\times30\times10$ mm^3. Two 4 mm OD copper tubes that provide current to the heater as well as working fluid to the chamber were connected to the probe tips in the chamber through the two sides of the wall. Two tungsten probe tips which have 25 μm diameter end were contact with the aluminum film pads. The other ends whose diameter is 0.5 mm were forced to contact with the copper tube inside the chamber as shown in Fig. 2(b).

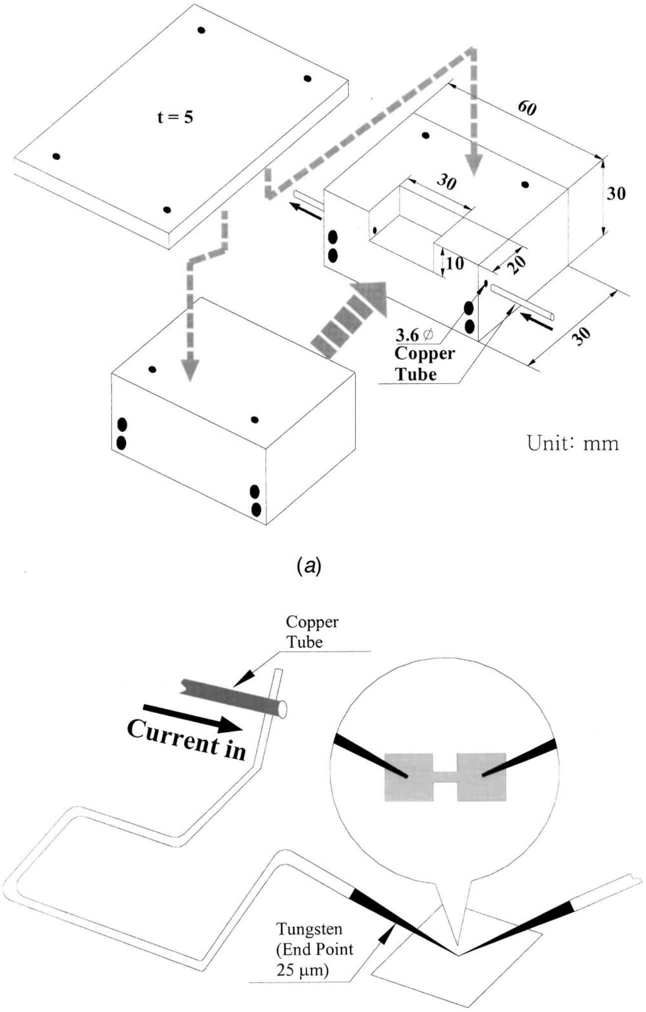

(*a*)

(*b*)

Fig. 2 Schematic of acryl chamber and tungsten probe tip contacting on driving pads

Fluorinert liquids such as FC-72, FC-77, and FC-40 were employed as working fluids. However methanol and ethanol turned out to be not appropriate for working fluid to the polysilicon heater. In fact, once the heater was wetted by methanol or ethanol, the heater was damaged permanently or resistance of the heater became infinity.

DC-voltage current standard (Yokogawa 2553) was used to supply current to the heater. The current and voltage to the heater were monitored simultaneously. Calculated heater resistances obtained by this measurement were also compared to the values by direct measurement. DC voltage to the heater was increased by 0.1 V increment to obtain current resistance (I-R) characteristic curve for each heater-liquid combination, from which the temperature for bubble nucleation on the heater-liquid system can be deduced. More fine increment of 0.01 V was employed near the nucleation point to measure the bubble nucleation temperature accurately. Experiments were carried out under room temperature condition of working fluids. At each interval of experiment, which was approximately 5 min, wait for 10 s or so to see whether bubble formation occurs. Such interval of 5 min is enough to maintain the liquid temperature at room condition.

Bubble nucleation process was also observed by using microscope-CCD camera or microscope-35 mm camera unit with a flash (Palflash 501) of μs duration.

(b) A Model for Micro Line Heaters. The heater works when a current is applied through the two driving pads that have much larger volume than that of the heater. The silicon substrate beneath the silicon dioxide layer acts as heat sinks. Applying the energy conservation to the differential element in the heater, one may obtain the following heat diffusion equation for the heater [10].

$$\frac{\partial^2 T}{\partial x^2} = \frac{1}{\alpha_p}\frac{\partial T}{\partial t} + \varepsilon(T - T_r) \tag{6}$$

where,

$$\alpha_p = \frac{k_p}{C_p \rho_p} \tag{7-1}$$

$$\varepsilon = \frac{k_s}{k_p}\frac{1}{z_h s} + \frac{h}{k_p}\left(\frac{1}{z_h} + \frac{2}{w}\right) - \frac{J_i^2 \rho_0 \xi}{k_p} \tag{7-2}$$

and

$$T_r = T_\infty + \frac{J_i^2 \rho_0}{k_p \xi} \tag{7-3}$$

The steady state solution of Eq. (6) can be obtained with appropriate initial and boundary conditions [10]. The temperature distribution along the line heater at the steady state by solving Eq. (6) is given by [10]

$$T(x) = T_r - \frac{J_i^2 \rho_0}{k_p \varepsilon}\frac{\cosh[\sqrt{\varepsilon}(x - L/2)]}{\cosh[\sqrt{\varepsilon}(L/2)]} \tag{8}$$

The resistance of the heater can be obtained by considering the power dissipation in the heater. That is

$$R_p = \int_0^L dR_p(T) = \frac{\rho_0 L}{w z_h}[1 + \xi(\overline{T} - T_\infty)] \tag{9}$$

where $\overline{T}$ is the average temperature of the line heater and is given by

$$\overline{T} = \frac{1}{L}\int_0^L T dx = T_r - (T_r - T_\infty)\tanh\left(\frac{\sqrt{\varepsilon}}{2}L\right) \bigg/ \frac{\sqrt{\varepsilon}}{2}L \tag{10}$$

Of course, the theoretical solution of the heat diffusion equation for the micro line heater and consequently the resistance heater at steady state given in Eq. (8) and (9), respectively, were obtained with assumption that both ends of the line heater remain at an ambient temperature during heating process. This assumption was confirmed to be reasonable by a finite element analysis [11]. However large heat flows from heater to the pads because there exists large temperature gradient at the boundary [12]. Therefore, the nucleation temperature was determined by fitting the theoretical I-R curve to the measured I-R curve with adjusting the property values of polysilicon heater such as ρ_0 and ζ. This procedure, which is a key element in this study, is crucial to measure the correct temperature for bubble nucleation on the heater.

Results and Discussions

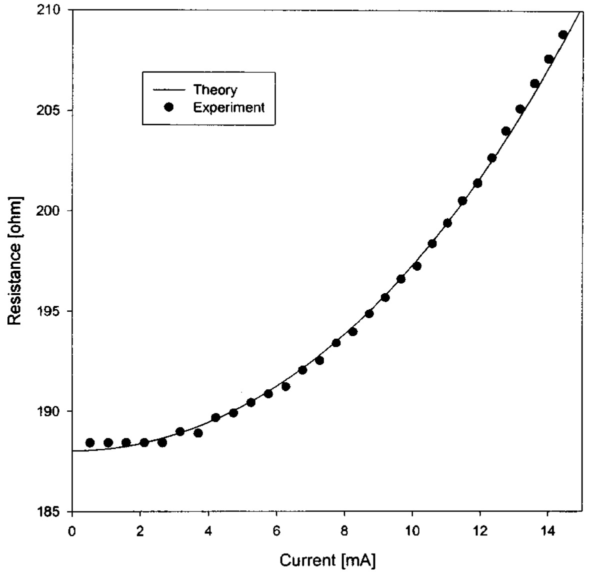

Fig. 3 Calculated (——) and experimental (●) I-R characteristics for the polysilicon heater of 50×3×0.523 μm^3 in FC-72. The theoretical characteristics was obtained with $\rho_0 = 5.90 \times 10^{-4}$ Ω-cm and $\xi = 0.75 \times 10^{-3}$/°C.

Measured I-R characteristic curve up to the bubble nucleation point for the 3 μm-width heater in FC-72 is shown in Fig. 3. The corresponding theoretical I-R curve which is fitted closely to the measured one by adjusting the variables such as polysilicon resistivity ($\rho_0 = 5.9 \times 10^{-4}$ Ω-cm) and its temperature coefficient ($\xi = 0.75 \times 10^{-3}$/°C) is also shown in Fig. 3. Hardly one can obtain such closely fitted curves by adjusting the variables related to the heat transfer mechanism [11]. With these adjust values of ρ_0 and ξ, one can obtain the accurate nucleation temperature, which is shown in Fig. 4. For the heater with 5 μm-width, the measured and theoretical I-R curves are shown in Fig. 5. The temperature distribution along the line heater at the bubble nucleation point is also shown in Fig. 6. Drastically different nucleation temperatures for the different width heaters were obtained. For the 3 μm-width heater, the bubble nucleation temperature 430.4 K is certainly greater than the superheat limit of FC-72, 421.0 K by 9.4°C. On the other hand, for the 5 μm-width heater, the nucleation temperature 389.7 K is less than the superheat limit by as much as 31.3°C where heterogeneous nucleation might take place. The measured nucleation temperatures on the micro line heater in FC-72 are certainly lower than that of 451.2, (the critical temperature of FC-72) obtained by Lin et al. [11]. The measured temperature by us may be the minimum temperature for bubble nucleation at given conditions. In fact, it has been found that the bubble nucleation temperature on the Ta/Al micro heater immersed in water depends crucially on the applied heating rate [9].

Same experiment was done with another fluorinerts such as FC-77 and FC-40 and similar results were obtained. The measured nucleation temperatures along with the superheat limit calculated by the molecular cluster model [6] and the thermodynamic limit estimated by the Berthelot equation of state [13] are given in Table 1. The adjusted values of resistivity and its temperature coefficient for liquid-heater combinations to obtain the nucleation temperature are also given in this table. Only slight change in the

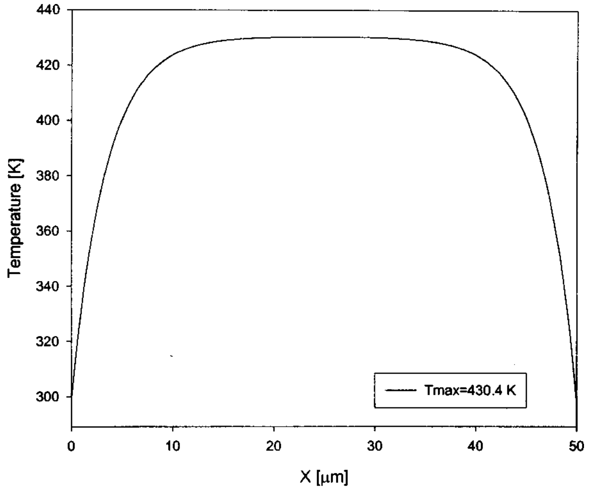

Fig. 4 Steady state temperature distribution along the 3 μm-width line heater at the current of 13.45 mA

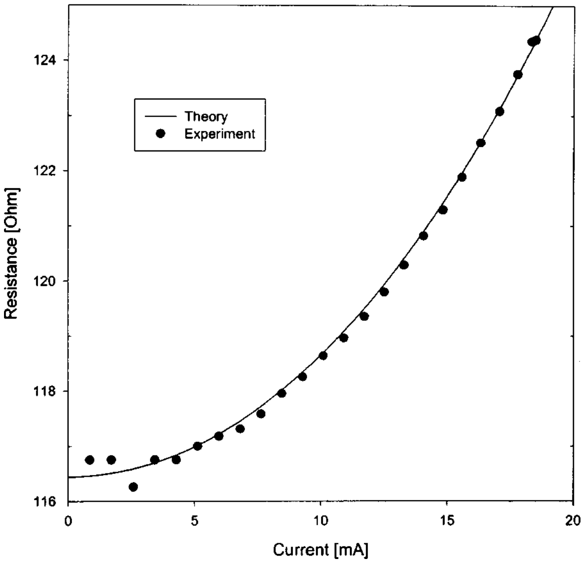

Fig. 5 Calculated (——) and experimental (●) I-R characteristics for the polysilicon heater of $50\times5\times0.523\ \mu\text{m}^3$ in FC-72. The theoretical characteristics was obtained with $\rho_0=6.09\times10^{-4}\ \Omega$-cm and $\xi=0.80\times10^{-3}$/°C.

resistivity and its temperature coefficient values depending on the liquid-heater combinations employed can be seen. It should be noted that the uncertainty in the width of heater, ±0.1 μm gives substantial error of ±20°C for the 1 μm-width and of ±10.0°C for the 3 μm-width heater but error of ±2.0°C for the 5 μm-width heater in the measurement of the nucleation temperature. Also the heater temperature is very sensitive to the input current for such narrow width heater, for example, 0.5 mA increase in the current yield 30.0°C increase in heater temperature for 1 μm-width heater. This is a reason why we did not use 1 μm-width heater in this experiment. The uncertainty in the thickness of heater, ±0.004 μm and the uncertainty in the current to the heater, ±0.05 mA give error of ±1.0°C respectively so that the total uncertainly in the measurement of the nucleation temperature for the 3 μm-width heater is about ±12°C. The total uncertainty in the measurement of the nucleation temperature for the 5 μm-width heater is only ±3°C under the same uncertainty in the variables concerned. However, the comparison of electrical resistance between measurement and the calculation values by the relation $R=\rho_0 L/(w z_h)$ at the ambient temperature provides us the dimension of heater, 50 μm×3.1 μm×0.527 μm for 3 μm-width heater and 49.9 μm×5.1 μm×0.527 μm for 5 μm-width heater. The estimated nucleation temperatures with these dimensions of heater, which are listed in Table 1, certainly reduce error in the measurement of heater temperature considerably.

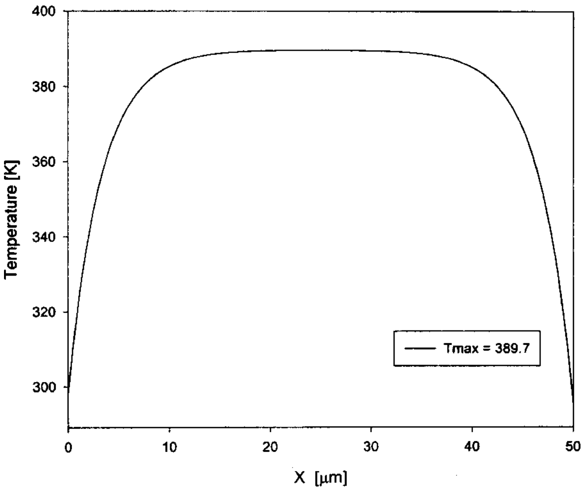

Fig. 6 Steady state temperature distribution along the 5 μm-width line heater at the current of 18.34 mA

Even with taking account of the error in the nucleation temperature measurement, bubble nucleation on the 3 μm-width heater was found to occur above the superheat limit of liquid. This observation indicates that enough liquid volume evaporated is needed for bubble formation so that thinner width heater needs higher nucleation temperature and consequently sufficient evaporated volume for nucleation [14]. For 2 μm-width heater Lin et al. [11] have observed that bubble nucleates at near the critical temperature of liquid.

Apparently heterogeneous nucleation even on a cavity free surface takes place on the 5 μm-width heater. With the nucleation rate of $10^{11}-10^{13}/\text{cm}^2\,\text{s}$, the nucleation temperatures depending on contact angle, which are obtained by Eq. (4) are shown in Fig. 7. With a contact angle of 110 deg, which supposed to be reasonable for such well wetted liquids, the nucleation temperature turns out to be good agreement with the measured values as shown in Table 1. Note that the minimum surface temperature required for bubble formation in water on a 65 μm×65 μm heater element used in commercial thermal ink-jet printers is about 178.9°C [9], which is also certainly far below the superheat limit of water while the highest nucleation temperature measured was 560 K at the heating rate of 0.25×10^9 °C/s. One may obtain the homogeneous superheat limit at the contact angle of 0 deg, as shown in Table 1. For the cases shown in Fig. 7, appropriate nucleation rate values were employed to obtain smooth nucleation temperature curve up to the boiling point. The nucleation rate values are $10^{13}/\text{cm}^2\,\text{s}$ for FC-72, $10^{12}/\text{cm}^2\,\text{s}$ for FC-77 and $10^{11}/\text{cm}^2\,\text{s}$ for FC-40. Note that the ionization potential for the fluorinerts, which are not available at present, were estimated so that the nucleation temperature at the contact angle of 180 deg becomes the boiling point of liquid as shown in Fig. 7, which was suggested by Avedisian [9]. The polarizability of working fluids was obtained by

Table 1 Measured nucleation temperature depending on heater width in various fluorinerts and the liquid superheat limits estimated by theoretically.

Liquids	Heater width (μm)	Measured Nucleation Temperature (K)	Superheat Limit, T_S (K)	Adjusted resistivity**, ρ_0 (Ω-cm)/ and temperature coefficient, ξ(/°C)
FC-72	3	430.4	421.0	$5.90\times10^{-4}/0.75\times10^{-3}$
	5	389.7	(414.6*)	$6.09\times10^{-4}/0.80\times10^{-3}$
FC-77	3	467.8	473.2	$5.90\times10^{-4}/0.78\times10^{-3}$
	5	424.5	(458.7*)	$6.11\times10^{-4}/0.79\times10^{-3}$
FC-40	3	515.7	515.8	$5.91\times10^{-4}/0.80\times10^{-3}$
	5	464.2	(499.2*)	$6.09\times10^{-4}/0.84\times10^{-3}$

*Calculated from the Berthelot equation of state.

**Listed values of resistivity and temperature coefficient for polysilicon are 7.5×10^{-4} Ω-cm and 1.2×10^{-3}/°C respectively [Lin and Pisano, 1991].

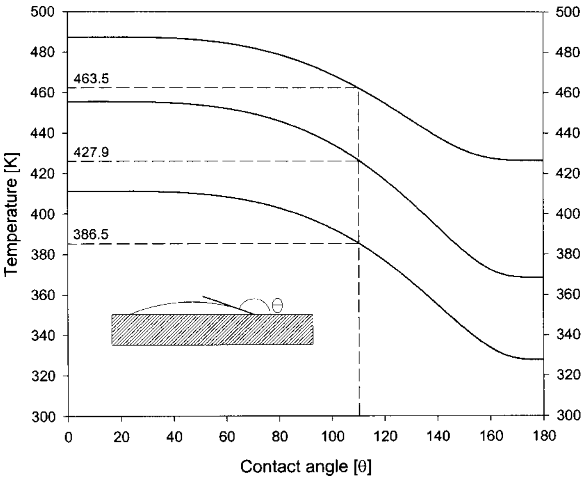

Fig. 7 Predicted nucleation temperature with contact angle for FC-72, FC-77, and FC-40 with the nucleation rate values of 10^{13}, 10^{12} and 10^{11}/cm^2 s respectively

Lorentz-Lorenz formula [15]. The temperature dependence of the saturated liquid density and the effective diameter of the molecules were estimated by the Gunn-Yamada [16] method. To estimate the vapor pressure dependence on pressure, a corresponding-states formula by Dong and Linhard [17] was employed.

As has been observed in the previous study by Lin et al. [11], the liquid around the heater turns out to be white before the bubble nucleation occurs. This may be due to the evaporation of liquid adjacent to the heater. A series of bubble nucleation, growth and subsequent collapse processes were visualized when the voltage of 3 V was applied to the 5 μm-width heater in FC-72. A delay generator (SRS DG535) with zitter of 50 ps only supplied the current to the heater and voltage signal to the flash (Palflash 501, pulse duration, 0.5 μs) with an appropriate delay. The duration of current applied to the heater was about 200 μs and the exposure time of 35 mm camera was 50~100 s. As shown in Fig. 8(a) the bubble continues to grow until heat supply to the heater stops. After the heat discontinues, the bubble turns to decrease and finally collapses. The period of growth is almost same as that of collapse. As clearly seen in first two frames of Fig. 8(a), when a spherical bubble formed from the spheroidal shape of superheated liquid layer above the heater, the bubble dimension shrank because the evaporated liquid which covers the heater broadly accumulates to become a bubble. This finding suggests that a bubble can form on the micro line heater if enough evaporated volume above the heater is created [14]. Also the measured bubble nucleation time of 30 μs is good agreement with the predicted value by Oh et al. [16]. Note that the average temperature achieved at steady state, which was measured by a bridge circuit and a dynamic amplifier is about 433.0 K [18]. This measured value is much higher than the minimum temperature for bubble nucleation as shown in Fig. 6. In Fig. 8(b) side view of the bubble growth for the case of applying longer duration of current of 13.56 mA (3 V) to the 3 μm width heater is shown. The bubble nucleation temperature in this case is about 430.4 K as shown in Fig. 4. Microscope/CCD camera unit was employed to take these pictures. About 30 ms was taken until the bubble grows to become the length of the heater.

At the time of nucleation, 30 μs, the bubble radius estimated by this correlation is about 4.5 μm. The number of molecules inside the very first bubble, 10^{10} molecules estimated by the ideal gas law suggests that the bubble may be formed from the evaporated volume of $z_c w^2$, which is about $2\times10^{-18}\,\mu\mathrm{m}^3$ for 3 μm-width heater. Assuming that the bubble can nucleate with this minimal amount of evaporated volume, smaller width heater needs more larger evaporated layer thickness for bubble formation.

Conclusion

The bubble nucleation temperatures on the micro line heater were measured precisely by obtaining the I-R characteristic curves

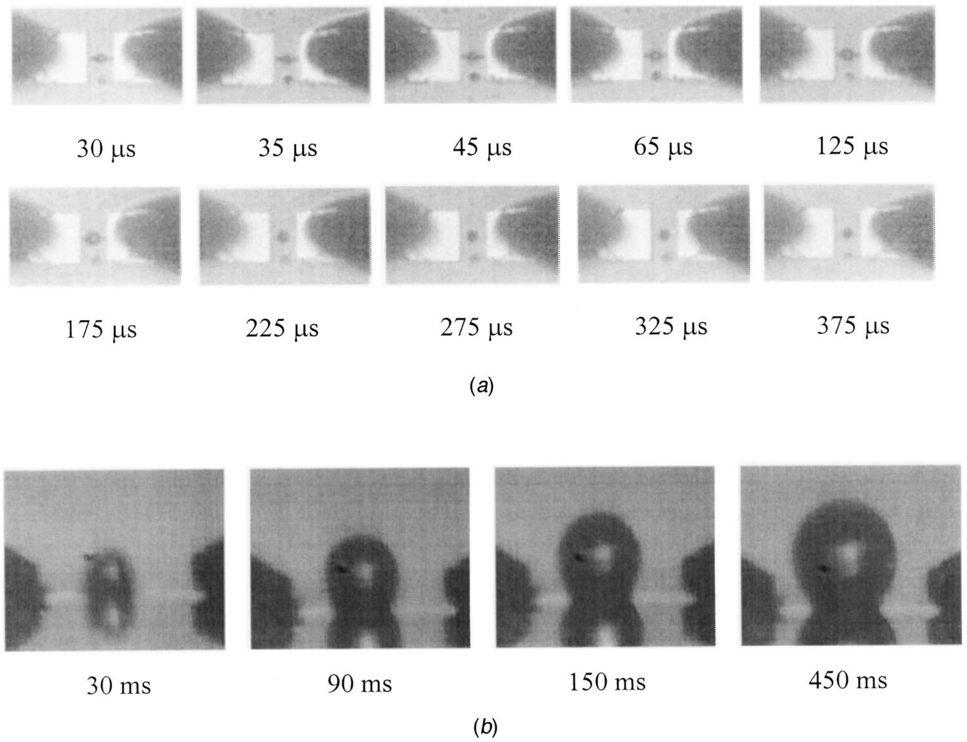

Fig. 8 Bubble nucleation and growth when a finite current pulse of 200 μs is applied (a) and bubble nucleation and growth when longer duration of current is applied to the heater (b)

of the heater. The nucleation temperature on the 3 μm-width heater is higher than the superheat limit estimated by molecular cluster model for bubble nucleation by 6∼10°C, which could be also predicted by analytically. On the other hand, the activation temperature for nucleation on the 5 μm-width heater is considerably less than the superheat limit of liquid, where heterogeneous nucleation may occur. The measured temperature for the heterogeneous bubble nucleation are in close agreement with the values estimated by using the molecular cluster model as applied to a surface with appropriate value of contact angle. In addition, the bubble nucleation time of 30 μs, predicted by the previous analysis for the micro line heater has been confirmed by the visual observation of microscope/35 mm camera unit with a flash of μs duration, so that one can predict the bubble nucleation process on the heater reasonably with the molecular cluster model for bubble formation.

Nomenclature

A_s = heater area
C_p = heat capacity of polysilicon heater (700 J/kg·°C)
F_n = free energy needed to form n-mer cluster
h = convection heat transfer coefficient (284 W/m^2/°C)
J_i = current density
J_n = nucleation rate of n-mer cluster per unit volume
J_s = nucleation rate per unit area
k_B = Boltzmann constant
k_p = conductivity of polysilicon heater (34 W/m/°C)
k_s = conductivity of silicon dioxide layer (1.4 W/m/°C)
L = heater length
m = mass of molecule
n = number of molecules in a cluster
N = number density
p_v = vapor pressure
p_∞ = ambient pressure
R = gas constant
R_p = resistance of heater
s = thickness of silicon dioxide layer
T = temperature of liquid
T_f = melting temperature of liquid
T_s = superheat limit of liquid
V_m = effective molecular volume of liquid
w = heater width
z_h = heater thickness
Z = coordination number

Greek Letters

β = accommodation coefficient
ΔH_{vap} = enthalpy of evaporation
ΔH_f = enthalpy of fusion
ε_m = energy needed to separate a pair of molecules
ξ = temperature coefficient of resistivity (0.0012°C)
ρ_0 = resistivity of polysilicon heater (7.42×10^{-6} ohm-m)
ρ_p = density of polysilicon heater (2.32×10^3 kg/m^3)

Subscript

c = critical cluster or critical size bubble

Acknowledgment

This work has been supported by grants from the Korea Science and Engineering Foundation under Contract No. 1999-1-304-002-5.

References

[1] Nielson, N. J., 1985, ‘‘History of Thinkjet Printerhead Development,’’ HP Journal, **36**(5), pp. 4–10.
[2] Lin, L., and Pisano, A. P., 1994, ‘‘Thermal Bubble Powered Microactuators,’’ Microsystem Technology, **1**, pp. 51–58.
[3] Marto, P. J., and Rohsenow, W. M., 1966, ‘‘Effects of Surface Conditions on Nucleate Pool Boiling of Sodium,’’ ASME J. Heat Transfer, **88**, pp. 196–204.
[4] Sun, K., and Lienhard, J. H., 1970, ‘‘The Peak Pool Boiling Heat Flux on Horizontal Cylinders,’’ Int. J. Heat Mass Transf., **13**, pp. 1425–1439.
[5] Baker, E, 1973, ‘‘Liquid Immersion Cooling of Small Electronic Devices,’’ Microelectron. Reliab., **12**, pp. 163–763.
[6] Kwak, H., and Panton, R. L., 1985, ‘‘Tensile Strength of Simple Liquids Predicted by a Molecular Interaction Model,’’ J. Phys. D, **18**, pp. 647–659.
[7] Kwak, H., and Lee, S., 1991, ‘‘Homogeneous Bubble Nucleation Predicted by a Molecular Interaction Model,’’ ASME J. Heat Transfer, **113**, pp. 714–721.
[8] Avedisian, C. T., 1998, ‘‘Modeling Homogeneous Bubble Nucleation in Liquids,’’ in *Modeling of Engineering Heat Transfer Phenomena*, Computational Mechanics Publications, London, Chap. 11.
[9] Avedisian, C. T., Osborne, W. S., McLeod, F. E., and Curley, C. M., 1999, ‘‘Measuring Bubble Nucleation Temperature on the Surface of a Rapidly Heated Thermal Inkjet Heater Immersed in a Pool of Water,’’ Proc. R. Soc. London, Ser. A, **455**, pp. 3875–3899.
[10] Lin, Li., and Pisano, A. P., 1991, ‘‘Bubble Forming on Micro Line Heater,’’ in *Micromechanical Sensors, Actuators, and Systems*, DSC-Vol. 32, pp. 147–163.
[11] Lin, L., Pisano, A. P., and Carey, V. P., 1998, ‘‘Thermal Bubble Formation on Polysilicon Micro Resistors,’’ ASME J. Heat Transfer, **20**, pp. 735–742.
[12] Oh, S., Seung, S., and Kwak, H., 1992, ‘‘A Model of Bubble Nucleation on a Micro Line Heater,’’ *Micromechanical Systems*, DSC-Vol. 40, pp. 313–328.
[13] Eberhart, J. G., and Schnyders, H. C., 1973, ‘‘Application of the Mechanical Stability Condition to the Prediction of the Limit of Superheat for Normal Alkanes, Ether, and Water,’’ J. Phys. Chem., **77**, pp. 2730–2736.
[14] Oh, S., Seung, S., and Kwak, H., 1999, ‘‘A Model of Bubble Nucleation on a Micro Line Heater,’’ ASME J. Heat Transfer, **121**, pp. 220–225.
[15] Born, M., and Wolf, E., 1975, *Principles of Optics*, Pergamon, Oxford.
[16] Gunn, R. D., and Yamada, T., 1971, ‘‘A Corresponding States Correlation of Saturated Liquid Volumes,’’ AIChE J., **17**, pp. 1341–1345.
[17] Dong, W-G., and Lienhard, J. H., 1986, ‘‘Corresponding States Correlation of Saturated and Metastable Properties,’’ Can. J. Chem. Eng., **64**, pp. 158–161.
[18] Jung, J., Park, H., and Kwak, H., 2002, ‘‘Bubble Nucleation and Growth on Surface of Rapidly Heated Micro Heaters,’’ presented at the 2002 International Mechanical Engineering Congress and Exposition, New Orleans, LA, USA, Paper No. IMECE 2002-32777.

G. Buonanno
e-mail: buonanno@unicas.it

A. Carotenuto
Prof. Mem. ASME

G. Giovinco

N. Massarotti

Dipartimento di Meccanica Strutture Ambiente e
Territorio (Di.M.S.A.T.),
Università di Cassino, Via Di Biasio 43,
03043 Cassino,
Italia

Experimental and Theoretical Modeling of the Effective Thermal Conductivity of Rough Steel Spheroid Packed Beds

The upper and lower bounds of the effective thermal conductivity of packed beds of rough spheres are evaluated using the theoretical approach of the elementary cell for two-phase systems. The solid mechanics and thermal problems are solved and the effects of roughness and packed bed structures are also examined. The numerical solution of the thermal conduction problem through the periodic regular arrangement of steel spheroids in air is determined using the Finite Element Method. The numerical results are compared with those obtained from an experimental apparatus designed and built for this purpose.
[DOI: 10.1115/1.1578504]

Keywords: *Contact Resistance, Heat Transfer, Packed Beds, Porous Media, Spheres*

1 Introduction

The effective thermal conductivity, k_e, rigorously defined on the basis of the local volume averaging method [1], is an important parameter in porous media. Its proper evaluation has been of interest for a wide range of engineering problems such as packed bed catalytic reactors [2–4], drying processes [5,6], processes involving transpiration cooling [7], in a nonisothermal catalyst pellet, in the thermal process of oil recovery and in a variety of other technologies [8–12]. The problem of determining the effective thermal conductivity of a saturated porous medium has been investigated in literature by various authors and many theoretical and numerical solutions have been proposed [13–18]. The results available demonstrate that the k_e value is influenced by several parameters such as: (i) the thermal and mechanical properties of the multiphase porous medium, (ii) the phase volumetric fractions, and (iii) the geometrical shape and the spatial distribution of the solid matrix and, in particular, the contact area between the solid particles.

Due to the great number of the parameters involved in the k_e evaluation and their wide variability, it is extremely difficult to formulate a model that completely defines the effective thermal conductivity. Recent research tends to simplify the porous media structure and provide some useful applicative results. In fact, as reported in [19,20], the effective thermal conductivity of random arrangement of solid particles fully saturated by a single phase fluid presents two limits, the thermal conductivities of the solid and liquid phase and the applied pressure being the same. The upper bound can be obtained considering face-centred cubic packed beds of monosize spheroids (FCC), whereas the lower bound can be represented by simple cubic packed beds (SC) using the same spheroids. Even if the applications of these packed bed configurations are restricted, their analysis allow to point out all the variables involved in the problem description and to develop theories that could be extended to study more complex packed beds such as the random ones.

In [15] a theoretical model is presented to predict the effective thermal conductivity of simple cubic (SC) and body-centered cubic (BCC) packed beds made up of stainless steel spheroids saturated with a single phase fluid as a function simultaneously of (i) the thermal conductivity of each phase, (ii) the structure of the solid phase, (iii) the contact resistance between the unconsolidated particles (as a function of the superficial roughness of the spheroids) and (iv) the mean applied pressure on the packed bed.

Unfortunately, experimental data of the effective thermal conductivity of stainless steel spheroids packed beds as a function of all the above-mentioned influence parameters are not available in literature. Consequently, in [15] only a qualitative comparison of the numerical results with the experimental data available in literature was carried out.

For this reason, in the present work, the authors have designed and built an experimental apparatus able to measure the effective thermal conductivity of porous media as a function of the most important influence parameters accurately measured.

Furthermore, because of the calculative difficulty of the three-dimensional model reported in [15], the authors propose a new numerical two-dimensional simplified model comparing the numerical results with the experimental data.

2 Experimental Apparatus

The experimental apparatus, reported in Fig. 1, is a hybrid arrangement of two typical measurement configurations of the thermal conductivity that are: (i) the heat flowmeter and (ii) the guarded hot plate instrument. The apparatus measures the effective thermal conductivity on the base of one-dimensional steady state comparative method. Energy is supplied at the top of the apparatus by means of electrical resistance and it is withdrawn using a water cooling system at the bottom (Fig. 1(a)).

The packed bed is bounded, both above and below, by two structures made up of reference material (Foamglas®) between two copper parallel plates (Fig. 1(b)). The dimensions of the measurement chamber are large enough to allow the arrangement of a great number of spheroids, assuring a valid effective thermal conductivity measurement from a statistical point of view and in accordance to the Representative Elementary Volume (REV) definition [5,21]. The choice of a parallelepiped as measurement chamber (with a base of 19.5×19.5 cm^2 and a height of 15 cm) allowed the authors to test theoretically different cubic interconnected pack arrangements such as simple and face-centered cubic ones.

Under the above mentioned hypotheses and neglecting the cross-sectional area variation, the effective thermal conductivity, k_e can be evaluated as:

Contributed by the Heat Transfer Division for publication in the JOURNAL OF HEAT TRANSFER. Manuscript received by the Heat Transfer Division August 5, 2002; revision received March 14, 2003. Associate Editor: V. Prasad.

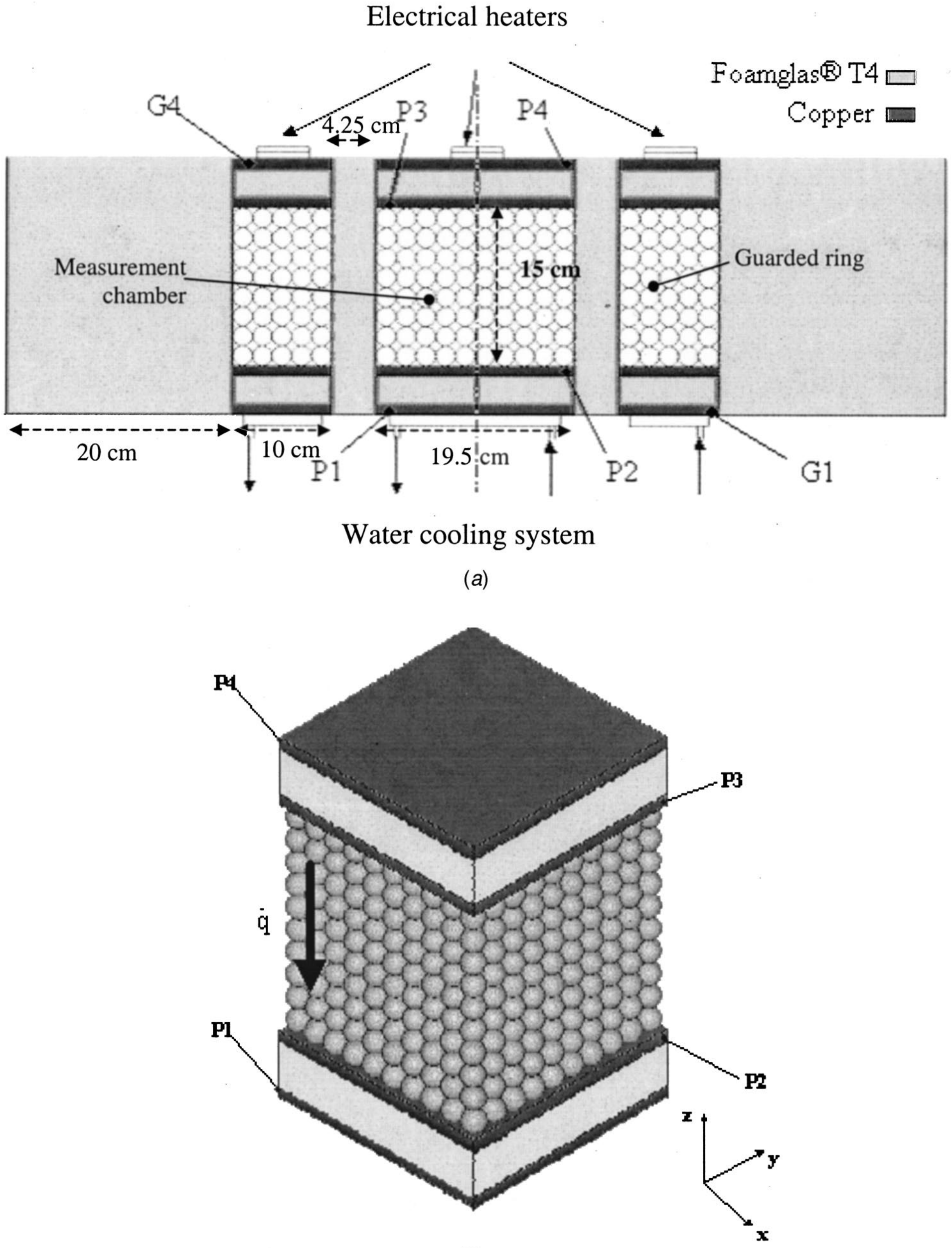

(*a*)

(*b*)

Fig. 1 (a) The experimental apparatus; and (b) Measurement chamber

$$k_e = \tfrac{1}{2} \cdot (k_e|_s + k_e|_i) \tag{1}$$

with

$$k_e|_s = k_F|_s \cdot \frac{T_{P4} - T_{P3}}{T_{P3} - T_{P2}} \cdot \frac{L_m}{L|_s} \tag{2}$$

$$k_e|_i = k_F|_i \cdot \frac{T_{P2} - T_{P1}}{T_{P3} - T_{P2}} \cdot \frac{L_m}{L|_i} \tag{3}$$

where $k_F|_s$ and $k_F|_i$ are the Foamglas® thermal conductivity of the upper and lower structure respectively evaluated at their mean temperature, L_m is the packed bed height, $L|_s$ and $L|_i$ are the thickness of the upper and lower comparative material respectively, and T_{Pj} is the temperature of the ${P_j}^{\text{th}}$ copper plate (Fig. 1).

As stated by Eq. (1), the thermal conductivity k_e in the packed bed is evaluated as the arithmetic average of the k_e obtained by equating the heat fluxes measured at the top, middle and at the bottom of the sample. In order to assure both one dimensional heat transfer and heat flux differences smaller than 3 percent, a thermal guard system was built around the measurement chamber (Fig. 1(a)).

The copper plate temperatures are measured by means of miniaturised Pt100 resistance thermometers inserted in 2 mm holes at the center of each 1 cm thick plate. These resistance temperature detectors were calibrated using a thermostatic bath at the Laboratory for Industrial Measurements (LAMI) at the University of Cassino. The bath is characterized by a stability of 0.005°C and an uniformity of 0.02°C and a Pt25 transfer standard (with an uncertainty equal to 0.014°C) directly traceable to the National primary standards. The calibration curves were obtained on the basis of 7 calibration points in the range 0 to 80°C using the generalized least squares technique [22,23]. The combined standard uncertainty was equal to 0.08°C in the above mentioned temperature

Table 1 Thermo physical and mechanical properties of the materials constituting the apparatus

Material	Thermal conductivity $k/(W\cdot m^{-1}\cdot K^{-1})$	Young modulus E/(MPa)	Poisson ratio ν
Foamglas®	$1.5\cdot 10^{-4}\cdot T/°C+4\cdot 10^{-2}$	⋯	⋯
Copper	398	⋯	⋯
100Cr6 Steel (spheroids)	60	200000	0.30

range. The acquisition data system, interfaced by means of a RS-232C connector to a personal computer, allows a scan interval equal to 1 minute.

Concerning the porous medium, the experimental tests were carried out on two different packed bed structures (SC and FCC) of steel spheroids. The spheroid diameter was chosen considering that in traditional studies of heat conduction in porous media [24] relatively small particles are used in order to neglect the effects of radiation, and the sample dimensions are chosen so that one-dimensional heat flux is achieved. On the other hand, if the dimensions of the spheroids are too small, it would be difficult to set up a particular interconnected pack arrangement. For this reason, the diameter of the spheroids was chosen equal to 19.05 mm in order to overcome the above mentioned difficulties and, to allow a manual positioning of the spheres in the packed bed. The radiative contribution to the heat transferred can be estimated by applying a parallel plate gray body model of conductive and radiative heat transfer. The ratio of radiative transfer to conductive transfer can then be evaluated as [21]:

$$\frac{\text{radiation}}{\text{conduction}} \approx \frac{4\varpi \varepsilon T_m^3 D}{k_e} \tag{4}$$

where ϖ is the Stefan-Boltzmann constant; ε is the spheroid emissivity (assumed equal to 0.1), T_m is the packed bed mean temperature (assumed equal to 310 K), k_e represents the measured effective thermal conductivity (whose order of magnitude is assumed equal to 1.0 $W\,m^{-1}\,K^{-1}$) and D is the spheroid diameter. Consequently, the ratio of radiative transfer to conductive transfer is less than 2 percent. The thermo-physical properties of the materials used in the apparatus are reported in Table 1.

Regarding the steel 100Cr6 constituting the spheroids, four sample sets with different superficial characteristics were used. In order to have a wide experimental range, the peak height standard deviation surface roughness, σ, varies from the value after a lapping machining (σ=0.02 μm) and the one referred to a grinding surface machining (σ=1.2 μm) (Fig. 2). The superficial roughness of the spheroids has been measured using a Talysurf profilometer with a vertical resolution of 0.8 nm, and a data sampling interval in a horizontal direction of 0.25 μm. Typically, three traces randomly distributed on the spheroid surface were determined for three different spheroids obtained through the same machining

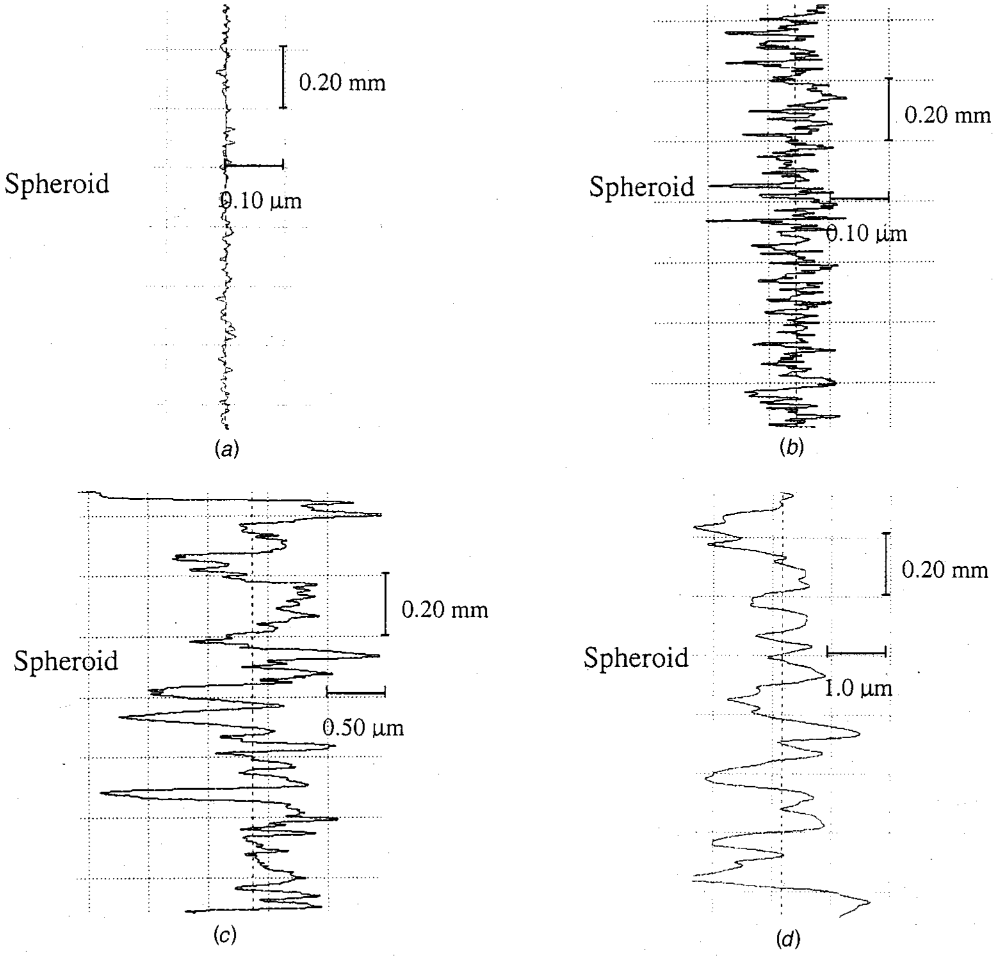

Fig. 2 Surface roughness and mean absolute slope of the spheroids used in the analysis: (a) lapped spheroids (σ=0.02 μm and m=0.0017), (b) prelapped spheroids (σ=0.11 μm and m=0.0054), (c) hard grinded spheroids (σ=0.96 μm and m=0.0231), and (d) soft grinded spheroids (σ=1.20 μm and m=0.0270)

Table 2 Uncertainty analysis of the effective thermal conductivity experimentally evaluated in the case of face-centered cubic packed beds of lapped spheroids

Quantity	Standard uncertainty	Contribution to the combined standard uncertainty	
x_i	$u(x_i)$	$u_i(k_e)$/W m^{-1} K^{-1}	$u_i(k_e)/k_e\ 10^2$
$k_F\|_s = 0.048$ W m^{-1} K^{-1}	1.2 10^{-3} W m^{-1} K^{-1}	0.018	2.68
$k_F\|_i = 0.044$ W m^{-1} K^{-1}	1.1 10^{-3} W m^{-1} K^{-1}	0.016	2.32
$\Delta T_s = 24.00$°C	0.1°C	0.0023	0.34
$\Delta T_i = 22.64$°C	0.1°C	0.0021	0.31
$\Delta T_m = 1.82$°C	0.06°C	0.028	4.2
$L_s = 4.05\ 10^{-2}$ m	3.0 10^{-4} m	0.0053	0.79
$L_i = 4.06\ 10^{-2}$ m	3.0 10^{-4} m	0.0046	0.68
$L_m = 4.6\ 10^{-2}$ m	1.0 10^{-3} m	0.014	2.17

process. Furthermore, a three-dimensional Finite Element Method (FEM) code [25] was used both in the design and in the characterization of the experimental apparatus and to verify the heat flow to be one-dimensional and constant [26]. In particular, an order of magnitude of the characteristic response time was found to be circa 60–70 hours.

2.1 Experimental Uncertainties of the Apparatus. The estimation of the measured effective thermal conductivity depends on different parameters as reported in Eqs. (1–3). The corresponding standard uncertainty, $u(k_e)$, is evaluated by considering the standard uncertainties of the input quantities, $(\partial k_e/\partial x_i)\cdot u(x_i)$, where $(\partial k_e/\partial x_i)$ are the sensitivity coefficients of each parameter or physical quantity x_i $(k_F|_\beta, \Delta T_\beta, \Delta T_m, L_m, L|_\beta)$ [27]. Applying the above mentioned procedure in the hypothesis of uncorrelated variables, the combined standard uncertainty can be evaluated as:

$$u^2(k_e|_\beta)=\left(\frac{\partial k_e|_\beta}{\partial k_F|_\beta}\right)^2\cdot u^2(k_F|_\beta)+\left(\frac{\partial k_e|_\beta}{\partial \Delta T_\beta}\right)^2\cdot u^2(\Delta T_\beta)+\left(\frac{\partial k_e|_\beta}{\partial \Delta T_m}\right)^2 \cdot u^2(\Delta T_m)+\left(\frac{\partial k_e|_\beta}{\partial L_m}\right)^2\cdot u^2(L_m)+\left(\frac{\partial k_e|_\beta}{\partial L|_\beta}\right)^2\cdot u^2(L|_\beta) \tag{5}$$

where β is equal to s or i as the upper or lower structure is considered, ΔT_m is the temperature drop across the measurement chamber $(T_{P3}-T_{P2})$, ΔT_β is the temperature drop across the β structure.

As regards the standard uncertainties of the temperature and the temperature differences, it must be pointed out that:

- the temperature uncertainty is evaluated on the basis of four different contributions such as (i) calibration uncertainty (0.08°C), (ii) copper plate temperature uniformity (0.01/(2√3)°C, obtained from the numerical simulations carried out for the characterization of the experimental apparatus), (iii) copper plate temperature stability (0.2/(2√3)°C, evaluated considering the maximum oscillation amplitude experimentally observed at operating conditions in the middle point of each copper plate), and (iv) the data acquisition system uncertainty for the Pt100 electrical resistance (0.02 Ω).
- only in the evaluation of the temperature difference uncertainty, the presence of correlation must be considered. In fact, (i) the temperature sensors were made by the same manufacturer and they belong to the same production lot, (ii) the temperature sensors were calibrated at the same time using the same primary standard, (iii) the stability and uniformity uncertainties of the temperature sensors have the same order of magnitude, and (iv) the time drift of the acquisition data system is the same for all the temperature sensors. For these reasons, considering that the correlation factor increases as the temperature drop diminishes and that the observed temperature differences are lower than 20°C, the authors assume a correlation factor equal to 0.7.

In order to minimize the uncertainty in the evaluation of the thickness of the reference material, since it is a porous medium, the thickness of the copper plates is determined in several points (15 points), using a three-dimensional coordinate measuring machine (CMM) with an uncertainty equal to $3.0\cdot(1+L/\mathrm{m})$ μm where L is the measured thickness. Subsequently, under the same load conditions, the thickness of the sandwich structure is measured. From the difference of the measurements obtained, on the basis of [27], it was possible to determine the reference thickness and the corresponding uncertainty. Using the same CMM, it was possible to verify the hypothesis of the constant area assumed for the four copper plates. For example, in Table 2 the standard uncertainties of the input variables are reported for the case of face-centered cubic packed beds of lapped spheroids.

This table shows that the most important contribution to the k_e uncertainty is related to the temperature drop across the measurement chamber. In order to reduce such contribution the authors intend to improve the experimental apparatus using Pyrex as reference material. In this way it is possible to reduce the uncertainty in the evaluation of ΔT_m because this parameter increases.

By using the procedure reported in [27], in order to estimate the uncertainty budget for Eq. (1), it is possible to obtain a maximum uncertainty in the evaluation of the measured effective thermal conductivity. This uncertainty is equal to 0.025 W m^{-1} K^{-1} (corresponding to a relative uncertainty of 4.7 percent) for the FCC packed beds and to 0.016 W m^{-1} K^{-1} (corresponding to a relative uncertainty of 4.4 percent) for the SC packed beds in the whole experimental range.

3 Numerical Model

The effective thermal conductivity was defined in [1] on the basis of the local volume averaging method. This methodology allows one to analyze the temperature distribution only in an elementary cell (Fig. 3). A three-dimensional model was used in [15] to evaluate the effective thermal conductivity of simple cubic and body-centred cubic packed bed of stainless steel spheroids as a function of the thermal conductivity of each phase, the structure of the solid phase, the contact resistance between the nonconsolidated particle and the applied pressure. It is important to point out that the combined thermal and mechanical three-dimensional model is very expensive from a calculative point of view. Consequently, the authors propose a new two-dimensional-axisymmetric model that takes into account a detailed description both of the mechanical contact of the curved rough surfaces of the spheroids and of the heat transfer in an equivalent unit cell.

The new model proposed in this paper is based on the simplified hypothesis that for regular sphere arrangement and for $k_s \gg k_a$, where k_s and k_a are the thermal conductivities of the steel spheroids and air respectively, the influence of the spheroids spatial distribution on the three-dimensional thermal field, and consequently on the effective thermal conductivity, can be neglected, once the mechanical contact has been correctly simulated as a

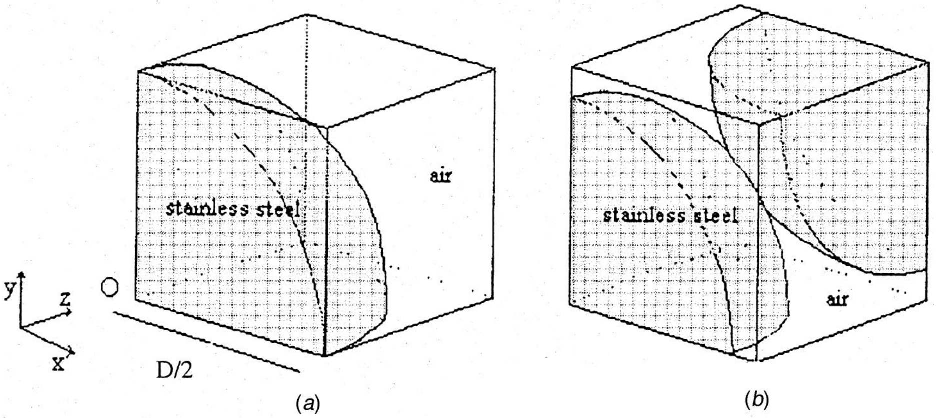

(*a*) (*b*)

Fig. 3 Elementary cell in *a)* SC and *b)* BCC packed beds

function of the load and of the solid matrix structure. Under the above mentioned hypotheses an equivalent two-dimensional cell can be defined as shown in Fig. 4. The first dimension, *D*, is determined in accordance with the spheroid diameters, and the second dimension, *B*, on the basis of the three-dimensional cell porosity. In fact, the two-dimensional modified elementary cell presents the same porosity value of the corresponding three-dimensional elementary cell. For this reason, the dimension *B* in the *SC* packed bed is greater, $B/D \cong 0.56$, than the corresponding one in the FCC configuration, $B/D \cong 0.46$, (Fig. 4).

As regards to the contact mechanics, the contact pressure distribution $p(r)$ and the contact radius *a*, (Fig. 4), have been evaluated by means of an iterative methodology, similar to those reported in [28,29]. The main difference between these and the present procedure is that an elasto-plastic model is here introduced to describe the asperity deformation for spherical surfaces, while in [28,29] only an elastic deformation is considered. The use of the elasto-plastic model is necessary in accordance to the evaluation of the plasticity index Ψ [30] for the four profiles (Table 3). In fact, on the basis of the applied load, the elasto-plastic contribution to the total contact area varies from 54 percent (lapped spheroids) to 99 percent (soft grinded spheroids).

The present model is based on an equivalent contact between a smooth deformable sphere and a rigid rough plane [28]. The equivalent smooth sphere radius *R* can be evaluated as [28]:

$$\frac{1}{\mathrm{R}}=\frac{1}{\mathrm{R}_1}+\frac{1}{\mathrm{R}_2} \tag{6}$$

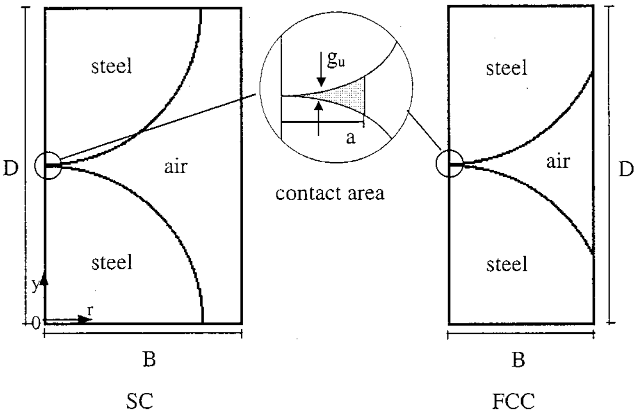

Fig. 4 Modified elementary cells adopted in the numerical model

where R_1 and R_2 are the radii of the two spheroids in contact. During the contact, each asperity of height *z*, modeled with a spherical summit of constant radius, measured from the peak height mean line, is flattened by an amount $w(r,z)$ (Fig. 5):

$$w=w(r,z)=\begin{cases} z-g(r) & \text{for } z>g(r) \\ 0 & \text{for } z\leqslant g(r) \end{cases} \tag{7}$$

where $g(r)$ is the separation between the rough surface peak height mean line and the smooth equivalent sphere, and can be written as [29]:

$$g(r)=g_0+\frac{r^2}{2R}+S(r) \tag{8}$$

where $S(r)$ is the axial deformation of the equivalent sphere of radius *R*, *r* is the contact radial coordinate, and g_0 is the distance between the undeformed sphere and the peak height mean line at the contact center (Fig. 5).

As mentioned before, three different deformation regimes of the asperities in contact (elastic, elasto-plastic and plastic) can be observed in the problem examined. Transition from the elastic to the elasto-plastic regime is obtained for a value of the deformation *w* equal to [31]:

$$w_{t1}=\left(\frac{3\pi\lambda H}{4E^*}\right)^2\rho \tag{9}$$

where $\lambda \approx 0.4$ for metallic materials [31], ρ is the equivalent peak summit curvature radius equal to:

$$\frac{1}{\rho}=\frac{1}{\rho_1}+\frac{1}{\rho_2} \tag{10}$$

where ρ_1 and ρ_2 are the peak curvature radii of the two spheroids in contact, *H* is the Brinell microhardness of the softer material, and [28]:

$$\frac{1}{E^*}=\left(\frac{1-\nu_1^2}{E_1}+\frac{1-\nu_2^2}{E_2}\right) \tag{11}$$

Table 3 Micro-geometrical properties of the spheroids

	σ^*/μm	m*	Ψ
Lapped spheroids	0.03	$2.4\ 10^{-3}$	1.08
Pre-lapped spheroids	0.16	$7.6\ 10^{-3}$	1.99
Hard-grinded spheroids	1.36	$3.3\ 10^{-2}$	4.32
Soft-grinded spheroids	1.70	$3.8\ 10^{-2}$	4.69

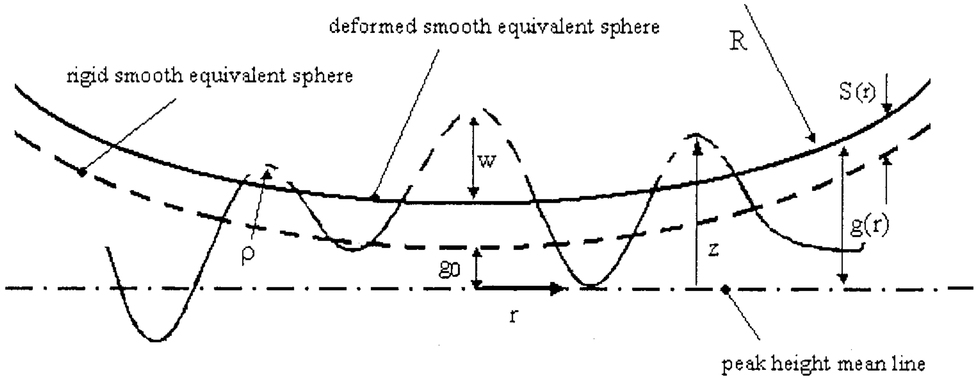

Fig. 5 Mechanical model of the surfaces in contact

Transition from the elasto-plastic to the fully plastic regime is reached at the value [31]:

$$w_{t2}=K\cdot w_{t1} \tag{12}$$

where K is a factor that can be experimentally determined [28]. In the present paper, the authors report the relationship proposed in [32] to estimate its value, which relates K to all the variables that influence the mechanical behavior of the surface:

$$K=\frac{E^*}{H}\left(\frac{\rho}{\sigma^*}\right)^{0.5} \tag{13}$$

where σ^* is the square root of the sum of σ^2 for each profile in contact.

Introducing a statistical Gaussian distribution for the peak height $\Phi(z)$:

$$\Phi(z)=N_A\frac{1}{\sigma^*\sqrt{2\pi}}\exp\left[-\frac{1}{2}\left(\frac{z}{\sigma^*}\right)^2\right] \tag{14}$$

where

$$N_A=\frac{1}{2\pi\int_{z=0}^{+\infty}\frac{1}{\sigma^*\sqrt{2\pi}}\exp\left[-\frac{1}{2}\left(\frac{z}{\sigma^*}\right)^2\right]\cdot(2\rho z-z^2)dz} \tag{15}$$

is the number of peaks per unit area [32,33], the contact pressure $p(r)$, is equal to

$$p(r)=\int_{z=g(r)}^{+\infty}F(r,z)\Phi(z)dz \tag{16}$$

where the force acting on the single peak of height z, $F(r,z)$, is equal to (i) $4/3E^*\cdot\sqrt{\rho}\cdot w^{3/2}$ in the elastic regime ($w<w_{t1}$) [28,31], (ii) $2\pi\rho H\cdot w$ in the plastic regime ($w>w_{t2}$) [28,31], and (iii) $F_{ep}(r,z)$ in the elastoplastic regime ($w_{t1}\leqslant w\leqslant w_{t2}$):

$$F_{ep}(r,z)=P_{ep}\cdot A_{ep} \tag{17}$$

where P_{ep} and A_{ep} are the elastoplastic contact pressure and area respectively.

The material is assumed to be homogeneous and isotropic and these characteristics are preserved during the deformation, therefore the derivatives of the mechanical properties should be continuous in the hypotheses of absence of phase changes or material inclusions. By assuming for the elastoplastic pressure an elliptical functional relationship [32,33]

$$P_{ep}=[\delta_1+\sqrt{\delta_2^2-\delta_3^2(w-w_{t2})^2}] \tag{18}$$

where

$$\delta_1=\frac{H}{2}\,\frac{3\cdot\pi\cdot\rho\cdot H\cdot\sqrt{\frac{w_{t1}}{\rho}}(\lambda^2-1)+2\lambda E^*(w_{t2}-w_{t1})}{3\cdot\pi\cdot\rho\cdot H\cdot\sqrt{\frac{w_{t1}}{\rho}}(\lambda-1)+E^*(w_{t2}-w_{t1})}$$

$$\delta_2=\mathrm{H}-\delta_1 \tag{19}$$

$$\delta_3=\sqrt{\frac{2}{3}\,\frac{E^*(\lambda H-\delta_1)}{\pi\sqrt{\rho w_{t1}}\cdot(w_{t2}-w_{t1})}}$$

and for the elastoplastic area a polynomial functional relationship [31]:

$$A_{ep}=\pi\cdot\rho\cdot w\cdot\left[1+3\cdot\left(\frac{w-w_{t1}}{w_{t2}-w_{t1}}\right)^2-2\cdot\left(\frac{w-w_{t1}}{w_{t2}-w_{t1}}\right)^3\right] \tag{20}$$

the continuity of the function and its derivative at the limits w_{t1} and w_{t2} are preserved for both the pressure and the area.

The proposed Eqs. (18),(19) represent an improvement respect to the elasto-plastic pressure law assumed in [31], that can not assure the continuity of the pressure derivatives being a logarithmic one.

However, Eq. (16) can be used to calculate iteratively $p(r)$ only if g_0 is determined at the starting integration point $g(r)$ (see Eq. (8)). This value can be obtained from the balance between the contact pressure distribution and the applied load, which is stated by the following equation:

$$F_c=2\cdot\pi\cdot\int_0^a r\cdot p(r)\cdot dr \tag{21}$$

where F_c is the component of the applied load normal to the contact surface between the two spheres.

At the beginning of the iterative procedure a Hertzian pressure distribution [28] is assumed for $p(r)$. Then, the deformation $S(r)$ of the equivalent sphere, introduced in Eq. (8), is obtained through the solution of the elastic problem for the equivalent sphere [28]. The distance g_0 is iteratively evaluated by coupling Eq. (16) with Eq. (21). The new pressure distribution can be now evaluated through Eq. (16) and used to restart the iterative procedure to evaluate the contact radius. Since the contact effective pressure goes asymptotically to zero far from the contact center, the contact radius can not be precisely defined, and its value has to be arbitrarily determined [28]. In the present model the contact radius, a, is obtained for a value of $g(r)$ equal to $4\sigma^*$. This value assures an error less than 0.02 percent on the total number of the contact asperities.

The convergence of the iterative procedure is reached when the difference between the new contact radius and the previous one is less than 0.2 percent. A detailed comparison between the present

Table 4 Coefficients of Eq. (25) [32]

Coefficient	Value
c_1	$-1.120\cdot 10^{-1}$
c_2	$-5.258\cdot 10^{-1}$
c_3	$8.577\cdot 10^{-1}$
c_4	$-8.794\cdot 10^{-3}$
c_5	$2.075\cdot 10^{2}$
c_6	$1.355\cdot 10^{2}$
c_7	1.018

contact model and experimental and numerical data of different researchers for flat surfaces, is reported in [32], showing a good agreement. From the contact pressure distribution, obtained using the above mentioned iterative procedure, the mean contact pressure, $\overline{p}$, can be evaluated as

$$\overline{p}=\frac{2\cdot\pi\cdot\int_0^a p(r)\cdot r\cdot dr}{\pi\cdot a^2}. \tag{22}$$

The average thermal contact conductance, $\overline{h}_c$, can be evaluated as a function of the mean contact pressure using a functional relationship similar to those reported in [34,35]:

$$\overline{h}_c=\alpha\cdot\frac{k_s\cdot m^*}{\sigma^*}\cdot\left(\frac{\overline{p}}{H}\right)^{\gamma} \tag{23}$$

where m^* is the mean absolute slope of the equivalent profile in contact, α and γ are two coefficients depending only on the plasticity index, Ψ, defined as

$$\Psi=\frac{E^*}{H}\cdot\left(\frac{\sigma^*}{R}\right)^{1/2} \tag{24}$$

In particular,

$$\begin{gathered}\alpha=\left[1+\frac{E^*\cdot m^*}{H}\left(c_1+\frac{1}{c_2+c_3\cdot\Psi}\right)\right].\sqrt{\pi}\\ \gamma=\frac{E^*\cdot m^*}{H}\left(c_4+\frac{c_5}{(1+c_6\cdot\Psi)^{1/c_7}}\right)\end{gathered} \tag{25}$$

valid for $\overline{p}/H\leqslant 0.05$ and $1\leqslant\Psi\leqslant 10$ and where the coefficients c_i, reported in Table 4, were obtained by means of a least squares regression [32], for materials with a λ value equal to circa 0.4.

The dimensionless contact radius and mean thermal conductance trends against the equivalent peak height standard deviation are reported in Fig. 6(a) and 6(b) respectively. For the same applied load, the contact radius increases as the surface roughness increases, in accordance to the assumption that the contact radius corresponds to a gap of $4\sigma^*$. The results obtained are in agreement with those reported in [28,29]. Furthermore, if the contact radius increases, according to Eqs. (19),(20) the mean contact pressure decreases and, consequently, the mean contact conductance decreases in accordance to Eq. (21).

When small contact pressures occur, the gas could give not negligible contributions to the heat transfer in the contact region [36,37]. The authors have evaluated the air contribution through the additional thermal conductance of the air, h_a, in accordance to the model reported in [37].

Hence, the thermal conductivity of the contact spot, k_c, is determined as

$$k_c=(\overline{h}_c+h_a)\cdot\overline{g}_u \tag{26}$$

where $\overline{h}_c$ is the average thermal contact conductance, and $\overline{g}_u$ is the average undistorted gap between the two spheroids in the contact spot (Fig. 4).

The effective thermal conductivity for the two-dimensional axisymmetric elementary cell is obtained in accordance to [1] as

$$k_e=-\frac{\langle q\rangle}{\Delta\langle T\rangle}=-\frac{D}{V}\frac{\int_V q dV}{\Delta T} \tag{27}$$

where q is the thermal flux, $\langle\ \rangle$ is the volumetric mean, D and V are the cell height and volume respectively, and ΔT is the temperature drop across the elementary cell.

The temperature field in the modified elementary cell is obtained using the FEM with the following boundary conditions

$$T(0\leqslant r\leqslant B,z=0)=0 \tag{28}$$

$$T(0\leqslant r\leqslant B,z=D)=T^* \tag{29}$$

$$\frac{\partial T(r=0\quad\text{and}\quad r=B,0\leqslant z\leqslant D)}{\partial r}=0 \tag{30}$$

where B is the radius of the elementary cell and T^* is an imposed temperature.

The discretization of the domain was obtained using triangular linear elements. The mesh sensitivity analysis showed that a mesh of 11,000 element can be considered satisfactory from a calculative point of view.

Concerning the uncertainty in the numerical evaluation of k_e, as previously shown, the functional relationship is

$$k_e=k_e(k_s,k_a,E_s,\nu_s,H_s,\sigma^*,m^*,F_c,R_s,\phi,\rho) \tag{31}$$

where E_s, ν_s, H_s, and R_s are the Young modulus, the Poisson ratio, the Brinell microhardness and the radius of the steel spheroids, ϕ is the porosity, and k_a is the thermal conductivity of the air in the elementary cell (Fig. 4). The combined standard uncertainty, $u(k_e)$, of the effective thermal conductivity numerically evaluated is determined by considering the standard uncertainties of the input quantities. The complexity of the functional relation-

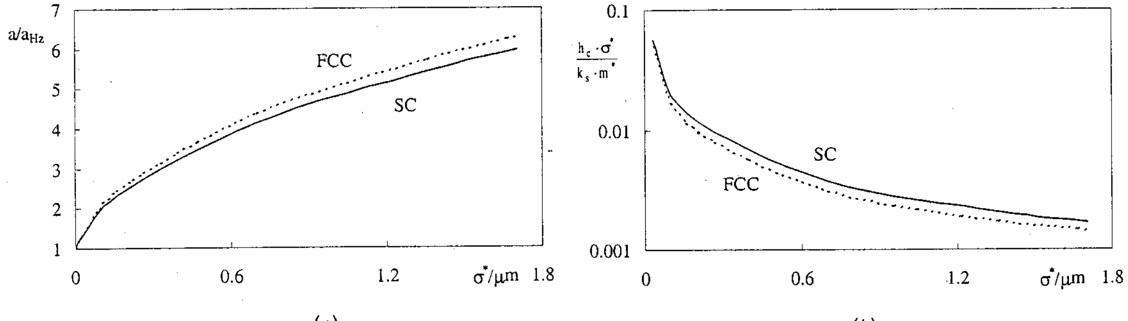

(a) (b)

Fig. 6 (a) Dimensionless contact radius; and (b) mean thermal conductance trends versus the equivalent peak height standard deviation

Table 5 Uncertainty analysis of the effective thermal conductivity numerically evaluated in the case of simple cubic packed beds of hard grinded spheroids

Quantity	Standard uncertainty	Contribution to the combined standard uncertainty	
x_i	$u(x_i)$	$u_i(k_e)/\mathrm{W\,m^{-1}\,K^{-1}}$	$u_i(k_e)/k_e\ 10^2$
$k_s = 60\ \mathrm{W\,m^{-1}\,K^{-1}}$	$3.0\ \mathrm{W\,m^{-1}\,K^{-1}}$	0.004	1.03
$k_a = 2.70\ 10^{-2}\ \mathrm{W\,m^{-1}\,K^{-1}}$	$1.4\ 10^{-3}\ \mathrm{W\,m^{-1}\,K^{-1}}$	0.017	4.36
$E_s = 200$ GPa	4.0 GPa	$5.8\ 10^{-3}$	1.49
$\nu_s = 0.30$	0.02	$4.0\ 10^{-3}$	1.03
$H_s = 8316$ MPa	249 MPa	$8.7\ 10^{-3}$	2.24
$\sigma = 1.05\ 10^{-6}$ m	$1.05\ 10^{-7}$ m	0.015	3.74
$m^* = 0.033$	0.0020	0.002	0.51
$F_c = 0.983$ N	0.01 N	negligible	···
$\phi = 0.476$	0.019	0.012	3.08
$R_s = 9.525\ 10^{-3}$ m	$3.0\ 10^{-5}$ m	negligible	···
$\rho = 1.3\ 10^{-5}$ m	$6.6\ 10^{-7}$ m	$7.4\ 10^{-3}$	1.90

ship does not allow one to obtain a mathematical formulation to evaluate these coefficients analytically. Therefore, the most suitable approach to determine the sensitivity coefficients seems to be the numerical approach based on the differences [27]. In Table 5 the standard uncertainties of the input variables are reported in the case of the evaluation of the effective thermal conductivity numerically evaluated for simple cubic packed beds of hard grinded spheroids (Fig. 2(c)).

By applying the procedure reported in [27] to estimate the uncertainty budget in the case of uncorrelated variables, one can obtain a maximum uncertainty in the evaluation of the numerical effective thermal conductivity equal to 0.033 $\mathrm{W\,m^{-1}\,K^{-1}}$ (corresponding to a relative uncertainty of 5.9 percent) for the FCC packed beds and to 0.029 $\mathrm{W\,m^{-1}\,K^{-1}}$ (corresponding to a relative uncertainty of 6.9 percent) for the SC packed beds in the whole experimental range.

4 Comparison and Discussion of the Results

For one of the experiments performed, the temperature of the four copper plates is reported in Fig. 7(a) as the time varies. From this figure, it can be seen that the characteristic time for the experimental system is about 60 hours, in accordance with the value obtained from numerical simulations carried out using a three-dimensional Finite Element Method.

Even if the characteristic time is so long, in order to assure the one-dimensionality and the conservation of the heat flux, the authors verified that only 7 to 8 hours are necessary to have variations of the effective thermal conductivity of 0.01 $\mathrm{W\,m^{-1}\,K^{-1}}$ respect to the value obtained in the stationary regime (see for example Fig. 7(b)).

In Fig. 8, the effective thermal conductivity of FCC and SC packed beds as the surface roughness of the spheroids in contact, σ^*, varies for a contact force of 0.98 and 0.79 for the SC and FCC elementary cell respectively. It should be pointed out that the load acting on the packed bed is applied gravimetrically and friction contribution between the upper Foamglas® structure and the walls can be neglected because of the presence of a small gap (with a dimension lower than 1.0 mm). The dots correspond to the experimental data with the corresponding measurement uncertainty, whereas the continuous line represents the values obtained from the numerical model with the corresponding uncertainty range (dashed lines). The experimental results confirm the existence of an upper (FCC) and lower (SC) bound and a wide range for the effective thermal conductivity of random packed bed of spheroids. Concerning the surface roughness, these results point out the great influence of this parameter on k_e. In particular, Fig. 8 shows a significant increase in the effective thermal conductivity as the surface roughness, and consequently the thermal contact resistance between the spheroids, diminishes. In the roughness range examined, a maximum variation of the measured effective thermal conductivity between the lapped and soft grinded spheroids is observed equal to 24 percent and 27 percent for FCC and SC packed beds respectively.

The present numerical model is in excellent agreement with the experimental values in all the ranges analyzed. In particular, the maximum percentage difference between numerical and experimental results is less than 6 percent assuring the compatibility of the data.

5 Conclusions

A two-dimensional-numerical model, based on the equivalent elementary cell and finite element analysis, to calculate the effective thermal conductivity of compressed packed beds of steel spheroids saturated with a static gas (air) is reported. The numeri-

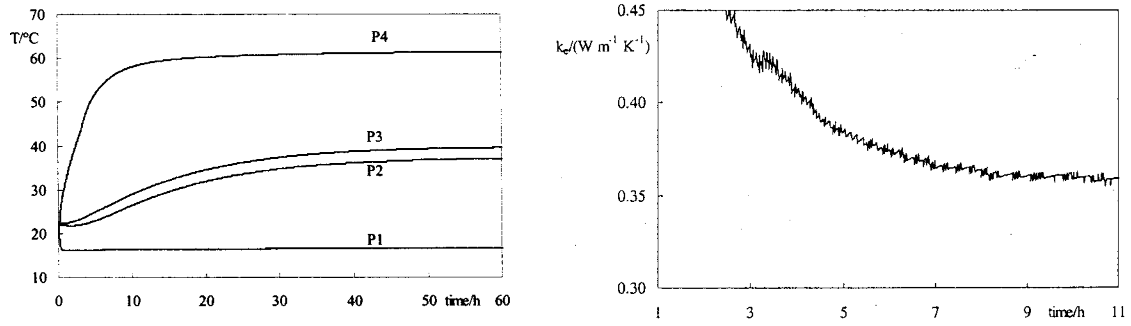

(*a*) (*b*)

Fig. 7 (a) Typical temperature; and (b) effective thermal conductivity trends measured

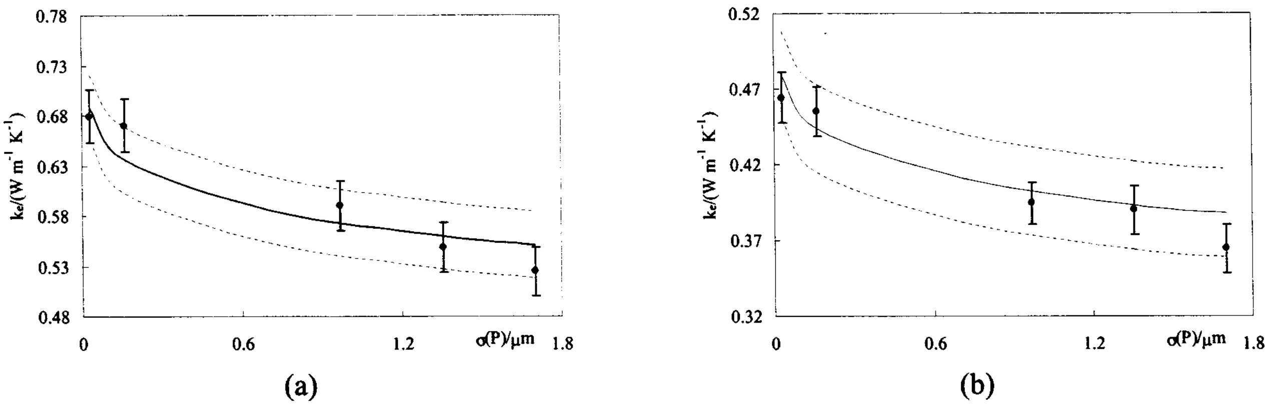

Fig. 8 Effective thermal conductivity as the peak height standard deviation varies for (a) face centered cubic, and (b) simple cubic packed bed (dots are experimental data with the corresponding measurement uncertainty, continuous line is the present numerical model with the corresponding uncertainty represented by dashed lines)

cal results are compared with the experimental data obtained from an apparatus constructed for this purpose. The main innovation of the current theory is that the model explicitly takes into account the particle roughness. In fact, it clearly shows the effects of the surface roughness on the effective thermal conductivity of the bed: conduction is significantly higher for the smoother than the rough steel spheroids. Unfortunately, the lack of published results of the effective thermal conductivity of spheroid packed beds, that include an accurate measurement of particle roughness, does not allow the authors to compare the present theory with other published experimental data. The model is proved to be in very good agreement with the experimental data provided, without the need to assume unrealistic adjustable parameters. The authors plan to extend their analysis to the effective thermal conductivity of packed beds of spheroids considering the variations of other parameters such as the spheroid material, the static gas and its pressure, the applied load and the packed bed structures including random or disordered ones. However, this analysis should serve as a useful starting point for developing models for such beds [38].

Nomenclature

a = contact radius, m
A = area, $\mathrm{m^2}$
a_{Hz} = Hertzian contact radius $\sqrt[3]{(0.75 \cdot F_c \cdot \rho)/E}$, m
B = equivalent two-dimensional cell radius, m
c_i = coefficients in Eq. (25) ($i=1,\ldots,7$)
D = equivalent two-dimensional cell height and sphere diameter, m
E = Young modulus, Pa
E^* = equivalent Young modulus, Pa
F = force, N
$F(z)$ = force acting on the single peak of height z, N
$g(r)$ = surface separation, m
$\underline{g}_u$ = average undistorted gap, m
g_0 = distance between the undeformed sphere and the peak height mean line at the contact center, m
h = thermal contact conductance, $\mathrm{W\,m^{-2}\,K^{-1}}$
H = Brinell hardness, Pa
k = thermal conductivity, $\mathrm{W\,m^{-1}\,K^{-1}}$
K = constant in Eq. (12)
L = thickness, m
m = roughness mean absolute slope
m^* = combined mean absolute slope of the two contacting profiles
N_A = peak number for a unit area, $\mathrm{m^{-2}}$
$p(r)$ = contact pressure distribution, Pa
$\overline{p}$ = mean contact pressure, Pa
q = thermal flux, $\mathrm{W\,m^{-2}}$
r = radial coordinate, m
R = radius, m
$S(r)$ = sphere deformation, m
T = temperature, K
T^* = imposed temperature, K
u = standard uncertainty
V = two-dimensional equivalent cell volume, $\mathrm{m^3}$
x_i = physical quantity
y = axial coordinate, m
w = contact interference, m
z = peak height evaluated from the profile mean line, m
α = coefficient in Eq. (25)
γ = coefficient in Eq. (25)
$\delta_1,\ \delta_2,\ \delta_3$ = coefficients in Eq. (19)
ΔT = temperature drop, K
ε = emissivity
ϕ = porosity
$\Phi(z)$ = peak height distribution, $\mathrm{m^{-3}}$
λ = constant in Eq. (9)
ν = Poisson ratio
ρ = peak summit curvature radius, m
σ = peak height standard deviation, m
σ^* = combined peak height standard deviation of the two contacting profiles, m
ϖ = Stefan-Boltzmann constant, $\mathrm{W\,m^{-2}\,K^{-4}}$
Ψ = plasticity index
$\langle\ \rangle$ = volumetric mean
$\overline{}$ = mean value
$|_{\mathrm{i}}$ = lower
$|_{\mathrm{s}}$ = upper

Subscripts

a = air
c = contact
e = effective
ep = elasto-plastic
F = Foamglas®
m = measured
Pj = jth copper plate ($j=1,\ldots,4$)
s = spheroid
$t1$ = transition from elastic to elasto-plastic regime
$t2$ = transition from elasto-plastic to plastic regime
1,2 = surface 1,2

References

[1] Whitaker, S., 1999, *The Method of Volume Averaging*, Kluwer Academic Publishers, Dordrecht, The Netherlands.

[2] Fogler, S., 1992, *Elements of Chemical Reaction Engineering*, Prentice Hall, Englewood Cliffs, New Jersey.

[3] McGreavy, C., Foumeny, E. A., and Javed, K. H., 1986, ''Characterization of Transport Properties for Fixed Bed in Terms of Local Bed Structure and Flow Distribution,'' Chem. Eng. Sci., **41**, pp. 787–797.

[4] Demirel, Y., Sharma, R. N., and Al-Ali, H. H., 2000, ''On the Effective Heat Transfer Parameters in a Packed Bed,'' Int. J. Heat Mass Transfer, **43**, pp. 327–332.

[5] Whitaker, S., 1980, *Heat and Mass Transfer in Granular Porous Media, in Advances in Drying*, Hemisphere Publishing Corporation, New York, pp. 23–61, Chap. 1.

[6] Ringer, D. U., 1986, *Heat Transfer Across Small Gaps, Drying of Solids*, S. Mujumdar, ed., Wiley (Halstead Press), New York, pp. 84–90.

[7] Cho, H. H., and Eckert, E. R. G., 1994, ''Transition From Transpiration to Film Cooling,'' Int. J. Heat Mass Transfer, **37**, pp. 3–8.

[8] Alazmi, B., and Vafai, K., 2000, ''Analysis of Variance Within the Porous Media Transport Models,'' ASME J. Heat Transfer, **122**, pp. 303–326.

[9] Cheng, P., Hsu, C. T., and Chowdhury, A., 1988, ''Forced Convection in the Entrance Region of a Packed Channel With Asymmetric Heating,'' ASME J. Heat Transfer, **110**, pp. 946–954.

[10] Londry, F. A., and Slavin, A. J., 1991, ''Thermal Conductivity of a Packed Bed of Hollow Zirconia Microspheres, Under Vacuum and Under 100 kPa of Argon,'' J. Am. Ceram. Soc., **74**, pp. 3118–3125.

[11] Nield, D. A., and Bejan, A., 1998, *Convection in Porous Media*, 2nd ed., Springer, New York.

[12] Freiwald, M. G., and Paterson, W. R., 1992, ''Accuracy of Model Predictions and Reliability of Experimental Data for Heat Transfer in Packed Beds,'' J. Am. Chem. Soc., **47**, pp. 1545–1560.

[13] Argento, C., and Bouvard, D., 1996, ''Modelling the Effective Thermal Conductivity of Random Packing of Spheres Through Densification,'' Int. J. Heat Mass Transfer, **39**, pp. 1343–1350.

[14] Cheng, G. J., Yu, A. B., and Zulli, P., 1999, ''Evaluation of Effective Thermal Conductivity From the Structure of a Packed Bed,'' Chem. Eng. Sci. **54**, pp. 4199–4209.

[15] Buonanno, G., and Carotenuto, A., 2000, ''The Effective Thermal Conductivity of Packed Beds of Spheres for a Finite Contact Area,'' Numer. Heat Transfer, **37**, pp. 343–357.

[16] Slavin, A. J., Londry, F. A., and Harrison, J., 2000, ''A New Model for the Effective Thermal Conductivity of Packed Beds of Solid Spheroids: Alumina in Helium Between 100 and 500°C,'' Int. J. Heat Mass Transfer, **43**, pp. 2059–2073.

[17] Duncan, A. B., Peterson, G. P., and Fletcher, L. S., 1989, ''Effective Thermal Conductivity Within Packed Beds of Spherical Particles,'' ASME J. Heat Transfer, **111**, pp. 830–836.

[18] Kikuchi, S., 2001, ''Numerical Analysis Model of Thermal Conductivities of Packed Beds With High Solid-to-Gas Conductivity Ratio,'' Int. J. Heat Mass Transfer, **44**, pp. 1213–1221.

[19] Tien, C. L., and Vafai, K., 1979, ''Statistical Bounds for the Effective Thermal Conductivity of Microsphere and Fibrous Insulation,'' AIAA Progress Series, **65**, pp. 135–148.

[20] Rohsenow, W. M., Hartnett, J. P., and Ganic, E. N., 1985, *Handbook of Heat Transfer Applications*, McGraw-Hill Publishing Company, New York.

[21] Shonnard, D. R., and Whitaker, S., 1989, ''The Effective Thermal Conductivity for a Point Contact Porous Medium,'' Int. J. Heat Mass Transfer, **32**, pp. 503–512.

[22] Deming, W., 1943, *Statistical Adjustment of Data*, John Wiley & Sons, New York.

[23] Forbes, A. B., 1993, ''Generalized Regression Problems in Metrology,'' Numer. Algorithms, **5**, pp. 523–533.

[24] Hadley, G. R., 1986, ''Thermal Conductivity of Packed Metal Powders,'' Int. J. Heat Mass Transfer, **29**, pp. 909–920.

[25] Zienkiewicz, O. C., and Taylor, R. L., 2000, *The Finite Element Method*, 5th ed. Butterworth-Heinemann, Oxford.

[26] Buonanno, G., Carotenuto, A., Giovinco, G., and Massarotti, N., 2002, ''Conducibilità termica effettiva di impaccamenti di sfere: analisi numerica e sperimentale preliminare per sferoidi in acciaid,'' Proc. 57th ATI Congress, 17–20 Sept., Pisa, Italy.

[27] *Guide to the Expression of Uncertainty in Measurement*, 1993, ISO, Geneve.

[28] Johnson, K. L., 1992, *Contact Mechanics*, Cambridge University Press, Cambridge, Chap. 4 and 9.

[29] Lambert, M. A., and Fletcher, L. S., 1997, ''Thermal Contact Conductance of Spherical Rough Metals,'' ASME J. Heat Transfer, **119**, pp. 684–690.

[30] Greenwood, J. A., and Williamson, J. B. P., 1966, ''Contact of Nominally Flat Surfaces,'' Proc. R. Soc. London, Ser. A, **A**, pp. 295–300.

[31] Zhao, Y., Maietta, D. M., and Chang, L., 2000, ''An Asperity Microcontact Model Incorporating the Transition From Elastic Deformation to Fully Plastic Flow,'' ASME J. Tribol., **122**, pp. 86–93.

[32] Buonanno, G., Carotenuto, A., Giovinco, G., and Vanoli, L., 2003, ''Influence of Contact Mechanics on the Prediction of the Effective Thermal Conductivity of Spheroids Packed Beds,'' accepted for Summer ASME Heat Transfer Conference, Las Vegas, Nevada, USA, July 21–23, 2003.

[33] Giovinco, G., 2002, ''Effective Thermal Conductivity of Packed Beds of Spheroids: Numerical and Experimental Analysis,'' Ph.D. Thesis, University of Cassino.

[34] Cooper, M. G., Mikic, B. B., and Yovanovich, M. M., 1969, ''Thermal Contact Conductance,'' Int. J. Heat Mass Transfer, **12**, pp. 279–300.

[35] Leung, M., Hsieh, C. K., and Goswami, D. Y., 1998, ''Prediction of Thermal Contact Conductance in Vacuum by Statistical Mechanics,'' ASME J. Heat Transfer, **120**, pp. 51–57.

[36] Song, S., Yovanovich, M. M., and Goodman, F. O., 1993, ''Thermal Gap Conductance of Conforming Surfaces in Contact,'' ASME J. Heat Transfer, **115**, pp. 533–540.

[37] Turyk, P. J., and Yovanovich, M. M., 1985, ''Modified Effective Conductivity Models for Basic Cells of Simple Cubic Packed Beds,'' Proc. 23rd National Heat Transfer Conference, Aug. 4–7, Denver, Colorado, HTD, **46**, p. 9

[38] Slavin, A. J., Arcas, V., Greenhalgh, C. A., Irvine, E. R., and Marshall, D. B., 2002, ''Theoretical Model for the Thermal Conductivity of a Packed Bed of Solid Spheroids in the Presence of a Static Gas, With No Adjustable Parameters Except at Low Pressure and Temperature,'' Int. J. Heat Mass Transfer, **45**(20), pp. 4151–4161.

Thermosolutal Convection in a Partly Porous Vertical Annular Cavity

M. Benzeghiba

S. Chikh

Département de Génie Mécanique, USTHB,
B.P. 32, El Alia, Bab Ezzouar 16111, Alger,
Algeria

A. Campo

Department of Mechanical Engineering,
The University of Vermont,
Burlington, VT 05405, USA

Numerical solutions for thermosolutal convection in a vertical concentric cavity partly filled with a porous medium are presented in this paper. The cavity is subject to preselected horizontal temperature and concentration gradients. The general Brinkman-Forchheimer-extended Darcy model is adopted to formulate the fluid flow through the porous matrix in the cavity. The effects of the controlling parameters on the flow patterns and heat and mass transfer behavior are thoroughly documented. Different flow structures are produced in the course of the computations, which respond to the geometric parameters, fluid nature, thermofluid dynamic parameters and porous matrix characteristics. The collection of numerical results elucidates that the double diffusion zone varies and, besides it is strongly dependent on the coupling between the Prandtl and Lewis numbers. Moreover, the variations of the Sherwood number show the presence of an extended range of double diffusion phenomena within the conditions pertinent to Darcian flow at $Da = 10^{-5}$. *It has been discovered that a partly porous annular cavity is more efficient than a fully porous annular cavity. This aspect may have a beneficial impact on engineering applications in the areas of filtration and thermal insulation.* [DOI: 10.1115/1.1589501]

Keywords: *Double Diffusion, Heat Transfer, Laminar, Mass Transfer, Porous Media*

1 Introduction

During the last three decades, innumerable theoretical, numerical and experimental studies have dealt with natural convection confined to vertical enclosures completely filled by a fluid, completely filled with a porous medium or partly filled with a porous medium. In the area of fluid-filled cavities, the numerical studies of Thomas and De Vahl Davis [1], Kumar and Kalam [2] and Khellaf and Lauriat [3] are representative of the effort. Directing the attention to porous cavities, Lauriat and Prasad [4] carried out an exhaustive literature review and showed the importance of channeling on the heat transfer across the cavities. At the same period, Campos et al. [5] reported that a partly porous annular cavity presents better thermal insulation than a completely porous cavity.

Most recently, the trend in the research community has shifted to the examination of simultaneous heat and mass transfer or double diffusion convection in enclosures. As expected, this situation is generally more complex than those when each phenomenon acts alone. Double diffusive convection is encountered in many practical engineering applications, such as crystal growth applied to semiconductors, melting and solidification processes in binary mixtures, storage of liquefied gases, underground infiltration of pollutants and many others. An in-depth literature survey revealed that most of the works in the area of annular cavities was restricted to the analysis of thermal convection. The majority of the studies dealing with double diffusive natural convection have been restricted to rectangular enclosures subject to horizontal thermal and concentration gradients. Most of the research was focused on one of two options for convection with dominating thermal or solutal buoyant forces. In this context, Beghein et al. [6] established numerical correlations to quantify the transport of pollutants suspended in air at low Lewis numbers. For tall rectangular cavities, Han and Kuehn [7,8] predicted numerically and also visualized experimentally by way of the electrochemical technique the multicellular flow structure that occurs at high values of Lewis number. Shipp et al. [9,10] performed a study on double diffusion in vertical annular enclosures and analyzed the effect of wall curvature on the mechanism of transition from a flow driven by opposing buoyant forces to a flow induced by aiding thermal and solutal forces. This peculiar transition is accompanied by a multiplicity of flow structures, which are susceptible to the nature of the initial conditions.

Porous enclosures have also been the subject of a vast number of studies. Trevisan and Bejan [11] used a Darcy model to solve numerically and by scale analysis a thermosolutal convection problem in a rectangular porous cavity. These authors reported variations of the Nusselt and Sherwood numbers as a function of the Lewis number in reference to the superposition model of thermal and solutal buoyant forces (i.e., opposing or cooperating). The same authors carried out a parallel study with imposed thermal and concentration gradients at the vertical active walls of the enclosure and explored the significance of the aspect ratio on the multicellular flow regime. Mamou et al. [12] considered the same problem treated in [11] and analyzed it analytically and numerically. The outcome of this investigation showed the presence of a multiplicity of stationary solutions; this peculiarity was more pronounced for opposing buoyant forces. Later, Goyeau et al. [13] simulated a solidification process by considering a Darcy-Brinkman model in a porous cavity saturated by a binary fluid subject to horizontal thermal and concentration gradients. Their results reported a significant effect of the permeability on heat transfer, which is more complex than in thermal convection. At the same time, Nithiarasu et al. [14] relied on a generalized non-Darcy approach to numerically predict the double diffusive natural convection in a rectangular enclosure. A strong influence of the buoyancy ratio, both on flow pattern and heat and mass transfer, was found in this publication. Recently, other authors considered double diffusion in annular vertical porous cavity. Marcoux et al. [15] reported on the good agreement between analytical and numerical results with a Darcy model whereas Benacer et al. [16] showed in their study the significant effect of both the Darcy number and the radius ratio on heat and mass transfer with a Brinkman model.

Thermosolutal convection in partly porous cavities has received

---

Contributed by the Heat Transfer Division for publication in the JOURNAL OF HEAT TRANSFER. Manuscript received by the Heat Transfer Division May 3, 2002; revision received March 21, 2003. Associate Editor: H. Bau.

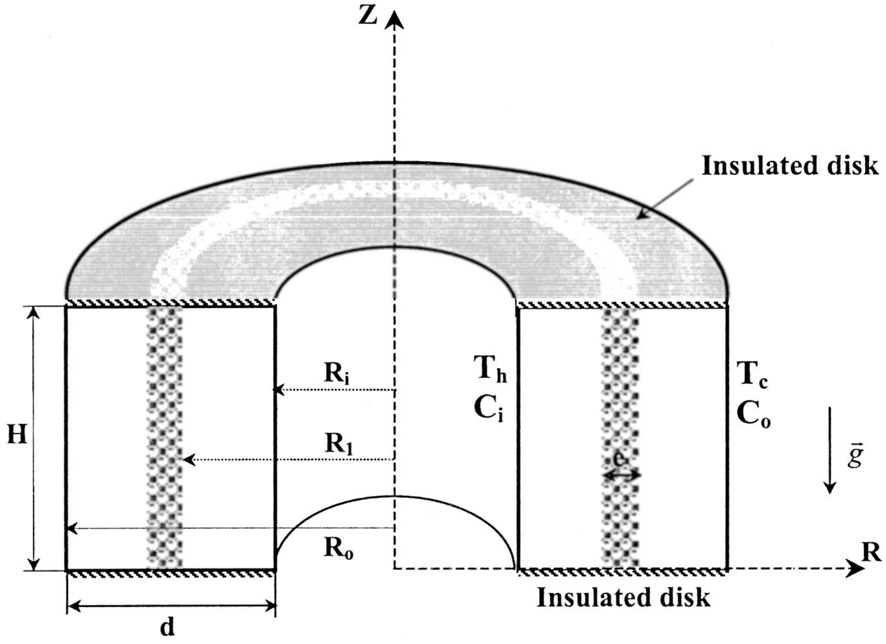

Fig. 1 Schematic of physical domain

less attention in the literature until the appearance of a recent study by Gobin et al. [17] and Merrikh and Mohamad [18]. For the first group the aim was to analyze the displacement of the solidification front in a tall rectangular enclosure; these authors modeled the mushy zone during the phase change process using a saturated porous medium. The results demonstrated in a convincing manner a decrease in heat and mass transfer at the wall for a low permeability of the porous layer. The second group worked out their problem with a general model; it was found that there was significant difference between Darcy model and the general model predictions. Their results showed that for $K_r > 1$, increasing permeability ratio decreases flow penetration from one layer to another while the opposite effect was observed for $K_r < 1$. Benzeghiba and Chikh [19] carried out a preliminary investigation employing a partly porous annular cavity. Focusing on a non-Darcy flow model, they predicted a decrease in heat transfer at low permeability even if the porous layer has a good effective thermal conductivity. Besides, it was noticeable that the opposite effect occurs for a Darcian flow.

The present study is devoted to the analysis of simultaneous heat and mass transfer caused by natural convection in a partly filled or a completely filled porous vertical annular enclosure. Such a geometry may be encountered in energy batteries, in thermal insulation and in storage of liquified gas in cryogenic systems. The formulation rests on the general Darcy-Brinkman-Forchheimer model for the fluid motion in the porous region. This work copes with the effect of the relative magnitude of the thermal and the solutal buoyant forces through the buoyancy ratio (N),

Table 1 Comparison of the average Nusselt and Sherwood numbers in annular cavity for Ra $=10^4$, $N=1$, $A=1$, $K_r=5$, Pr=0.71, and Le=0.86

	Fluid case				Partly porous case E=0.3, Da=10^{-3}, $\varepsilon=0.7$			
Mesh	Nu	Relative difference (%)	Sh	Relative difference (%)	Nu	Relative difference (%)	Sh	Relative difference (%)
11×11	2.298	⋯	2.154	⋯	1.813	⋯	1.683	⋯
21×21	2.302	0.191	2.149	0.261	1.847	1.895	1.713	1.775
31×31	2.244	2.510	2.100	2.259	1.816	1.712	1.688	1.471
41×41	2.230	0.653	2.088	0.592	1.807	0.496	1.681	0.438
51×51	2.222	0.339	2.081	0.307	1.803	0.191	1.678	0.155
61×61	2.219	0.151	2.079	0.138	1.801	0.096	1.677	0.081
71×71	2.217	0.090	2.077	0.090	1.801	0.038	1.676	0.026

Table 2 Comparison of the average Nusselt number in the fluid filled annular cavity for $A=10$, $K_r=2$, and Pr=1

Ra	Present study	Ref. [1]	Relative difference (%)	Ref. [2]	Relative difference (%)	Ref. [3]	Relative difference (%)
10^4	2.399	2.333	2.83	2.355	1.87	2.394	0.18
$5\cdot10^4$	3.768	3.758	0.27	3.718	1.34	3.759	0.23
10^5	4.495	4.568	1.60	4.558	1.38	4.588	0.16

Table 3 Comparison of the average Nusselt and Sherwood numbers in a porous filled rectangular cavity using the Darcy model for $A=1$, $K_r=1$, $E=1$, Pr=1, Le=1, $N=0$, and $R_k=1$

Ra×Da	Present study	Ref. [23]	Relative difference (%)	Ref. [13]	Relative difference (%)	Ref. [24]	Relative difference (%)
50	2.023	2.02	0.148	1.98	2.17	1.97	2.69
10^2	3.144	3.27	3.85	3.11	1.1	3.07	2.41
$4\cdot 10^2$	7.766	9.69	19.85	7.77	0.05	7.58	2.54

Table 4 Comparison of the average Nusselt number in a porous filled rectangular cavity with the Darcy-Brinkman-Forchheimer model for $A=1$, $K_r=1$, $E=1$, $P_r=1$, $N=0$, $R_k=1$, and $\varepsilon=0.4$

Ra_T	Da	Present study	Ref. [25]	Relative difference (%)	Ref. [4]	Relative difference (%)	Ref. [14]	Relative difference (%)
	10^{-1}	4.66	4.39	6.15	4.36	6.88	4.49	3.78
10^4	10^{-4}	21.268	20.59	3.29	18.4	15.58	21.99	3.28

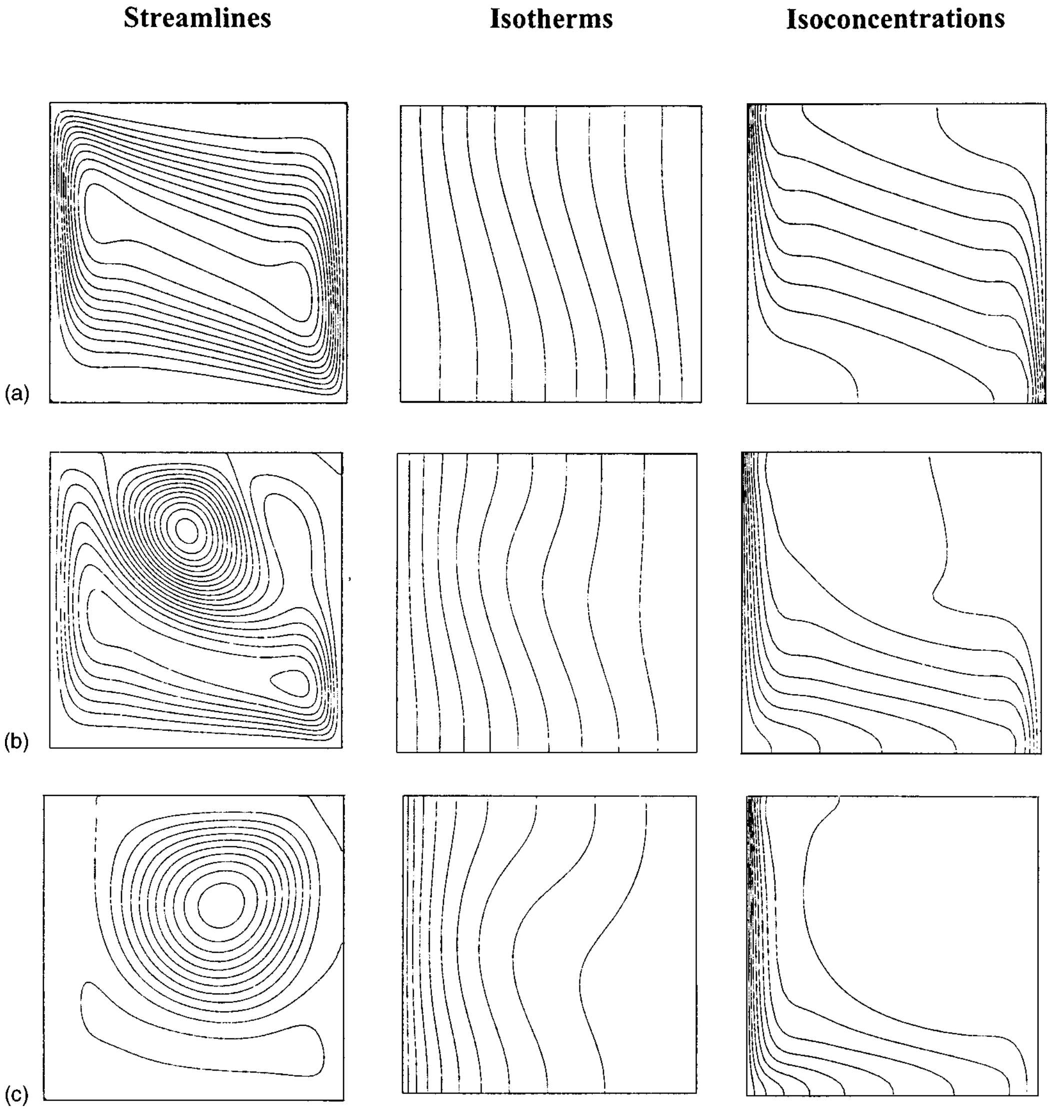

Fig. 2 Flow, isothermal, and isoconcentrations patterns in fluid case for different radii ratios, Ra $=10^4$, $N=-3$, Pr=7, Le=21.71, and $A=1$: (a) $K_r=1$, $\Psi_{min}=-6$, $\Delta\Psi=0.5$, $\Psi_{max}=0$; (b) $K_r=4$, $\Psi_{min}=-0.45$, $\Delta\Psi=0.5$, $\Psi_{max}=0.6$; and (c) $K_r=20$, $\Psi_{min}=-0.2$, $\Delta\Psi=0.1$, $\Psi_{max}=1.1$.

as well as the physical properties of the solvent and solute represented by the Prandtl and Lewis numbers. These combined effects are analyzed in detail and documented extensively in terms of two key parameters: the porous layer permeability (Da) and the porous layer thickness (E).

2 Mathematical Formulation

We consider a vertical annular enclosure of height H, closed at the bottom and at the top by two insulated disks being impermeable to mass transfer. The inner cylinder is maintained at a constant high temperature and high concentration, while the outer cylinder is kept at a constant low temperature and low concentration. A homogeneous and isotropic porous layer of thickness e (which may play the role of a filter or a layer of insulation) is inserted in the annular gap and placed at a distance R_1 from the hot inner cylinder as shown in Fig. 1.

An incompressible Newtonian fluid, constituted by a solvent and a solute, fills the annular cavity and saturates the porous medium completely. The porous-fluid assembly is subject to the action of horizontal thermal and concentration gradients. We assume that all thermophysical properties of the fluid are constant, except the density in the buoyant term. Here, the Boussinesq approximation is represented by the additive relation

$$\rho=\rho_r[1-\beta_T(T-T_r)-\beta_C(C-C_r)] \tag{1}$$

where the subscript r stands for a reference state corresponding to the average conditions between the values of the quantities (temperature and concentration) at the inner and the outer vertical walls.

Under steady state, axisymmetric conditions, and laminar regime, the fluid motion in the open and porous regions of the cavity is described by a general Darcy-Brinkman-Forchheimer model by virtue of the so-called one-domain approach. This approach avoids considering explicitly the conditions at the porous/fluid interface as in Gobin et al. [17]. This problem was addressed by several authors among them Alazmi and Vafai [20] who reported most of the previous works. Besides, viscous dissipation and thermodynamic coupling due to Sorêt and Dufour effects have been neglected. Actually, the fluid is considered as a porous medium having unitary porosity and infinity permeability. Under these circumstances, the governing equations reduce to the Navier-Stokes equations. The abrupt changes at the fluid-porous-fluid interfaces are handled by averaging the thermophysical properties via the harmonic mean as suggested by Patankar [21]. Moreover, within the porous layer local thermal equilibrium is invoked.

Accordingly, the double diffusive natural convection phenomenon is governed by the following dimensionless equations of conservation of mass, momentum, energy and species.

$$\nabla\cdot\vec{V}=0 \tag{2}$$

$$\frac{1}{\varepsilon}\vec{V}\cdot\nabla u=-\frac{\partial P}{\partial z}+\frac{R_v}{\varepsilon}\Pr\nabla^2 u+\mathrm{Ra}\ \Pr[\theta+N\cdot S]-\left[\frac{\Pr}{\mathrm{Da}}+\frac{C_f}{\sqrt{\mathrm{Da}}}|\vec{V}|\right]u \tag{3}$$

$$\frac{1}{\varepsilon}\vec{V}\cdot\nabla v=-\frac{\partial P}{\partial r}+\frac{R_v}{\varepsilon}\Pr\left[\nabla^2 v-\frac{v}{r^2}\right]-\left[\frac{\Pr}{\mathrm{Da}}+\frac{C_f}{\sqrt{\mathrm{Da}}}|\vec{V}|\right]v \tag{4}$$

$$\vec{V}\cdot\nabla\theta=R_k\nabla^2\theta \tag{5}$$

$$\frac{1}{\varepsilon}\vec{V}\cdot\nabla S=\frac{1}{\mathrm{Le}}\nabla^2 S \tag{6}$$

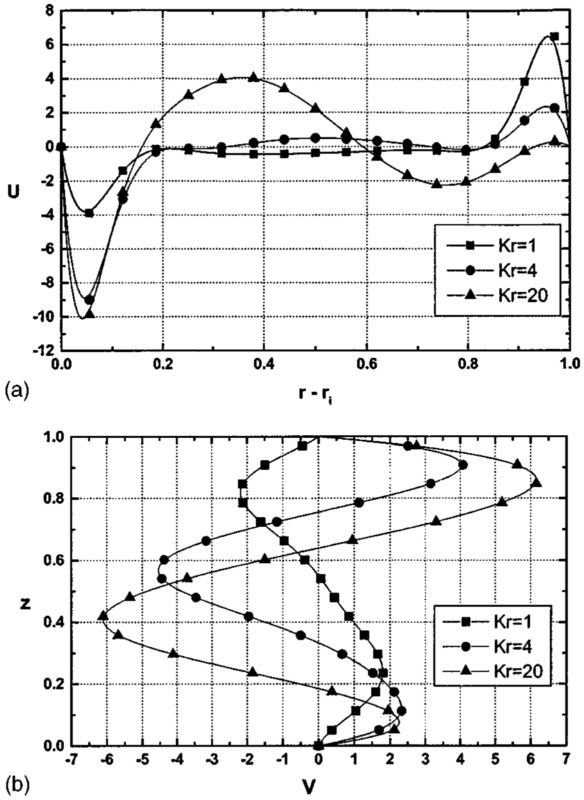

Fig. 3 Velocity distribution in the middle plans in fluid case for different radii ratios, Ra=10^4, N=−3, Pr=7, Le=21.71, and A =1: (a) Axial velocity at z=0.5; and (b) Radial velocity at r =0.5.

In these equations, the length scale is the gap width d, the velocity scale is the reference velocity α/d where α is the fluid thermal diffusivity, the temperature scale is ΔT, and the concentration scale is ΔC.

At this stage, it should be mentioned that the parameter N in Eq. (3) representative of the ratio of solutal to thermal buoyant forces can be either positive or negative because the volumetric expansion coefficient β_c can take both signs positive or negative, depending on the nature of the fluid and the solute.

The boundary conditions pertaining to cooperating ($N>0$) or opposing ($N<0$) thermal and solutal buoyant forces can be considered at unison: That is

$$\text{at } r_i=1/(K_r-1)\quad \vec{V}=\vec{0}\quad \theta=0.5\quad \mathrm{S}=0.5 \tag{7a}$$

$$\text{at } r_o=K_r/(K_r-1)\quad \vec{V}=\vec{0}\quad \theta=-0.5\quad \mathrm{S}=-0.5 \tag{7b}$$

$$\text{at } z=0\quad\text{and}\quad z=A\quad \vec{V}=\vec{0}\quad \frac{\partial\theta}{\partial z}=0\quad \frac{\partial \mathrm{S}}{\partial z}=0 \tag{7c}$$

For the evaluation of the heat and mass transfer rates across the cavity under steady-state conditions, it is evident that the average Nusselt and the average Sherwood numbers are not functions of the dimensionless radial coordinate r. Both numbers are adequately computed at the inner wall of the cavity as recommended in Trevisan and Bejan [11]. The corresponding expressions are:

$$\mathrm{Nu}=\frac{r_i}{A}ln(K_r)\int_0^A\left[-\frac{\partial\theta}{\partial r}+u.\theta\right].dz \tag{8}$$

$$\mathrm{Sh}=\frac{r_i}{A}\,ln(K_r)\int_0^A\left[-\frac{\partial S}{\partial r}+u.S\right].dz \tag{9}$$

3 Numerical Solution

The set of governing Eqs. (2)–(6) subject to the imposed boundary conditions in Eq. (7) is solved numerically by the finite-difference based control volume method. The power law differencing scheme is utilized and the SIMPLER algorithm is implemented to handle the velocity-pressure coupling as in Patankar [21]. Thereafter, a line-by-line technique is applied to solve the resulting system of algebraic equations.

In the closed partly porous cavity, steep velocity, temperature and concentration gradients are present in several zones such as the boundary layers along the walls, at the fluid-porous-fluid interfaces, and between the cells in the multicellular regime. Consequently, very fine grids become necessary in these particular regions to capture the high gradients. In this regard, several authors have adopted irregular grids with exponential variation (Khellaf and Lauriat [3]) or geometric progression (Bénard et al. [22]).

In the present work, an irregular exponential distribution of nodes in the radial direction in conjunction with a uniform distribution of nodes in z direction was employed. A 41×41 grid turned out to be reasonable enough to handle the details of the flow structure. Additionally, it is worth commenting that a lower number of nodes did not allow to retrieve the final flow pattern and a finer grid did not affect the flow structure and yielded variations in average Nusselt and Sherwood numbers less than 0.6%. Table 1 gives a quantitative sample of mesh convergence study for the average heat and mass transfer coefficients.

The convergence criterion was set at a maximum relative error for all dependent variables (u,v,θ,S) to be less than 10^{-4}. In ratio form, this statement corresponds to the relation

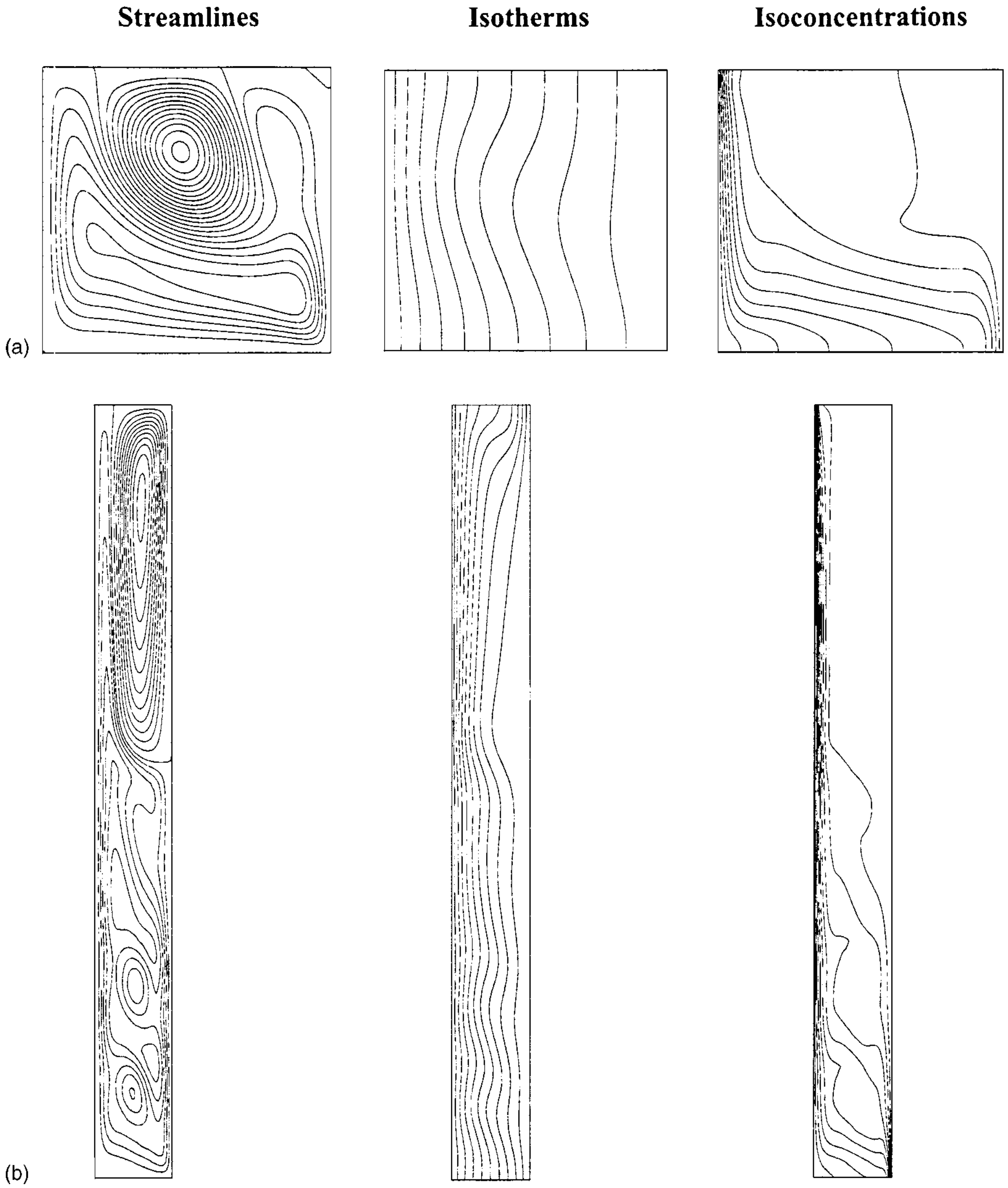

Fig. 4 Effect of A on flow, isothermal, and isoconcentrations patterns in fluid case for $\mathrm{Ra}=10^4$, $N=-3$, $\mathrm{Pr}=7$, $\mathrm{Le}=21.71$, and $\mathrm{Kr}=5$: (a) $A=1$, $\Psi_{\min}=-0.35$, $\Delta\Psi=0.05$, $\Psi_{\max}=0.7$; and (b) $A=10$, $\Psi_{\min}=-2$, $\Delta\Psi=0.5$, $\Psi_{\max}=6$.

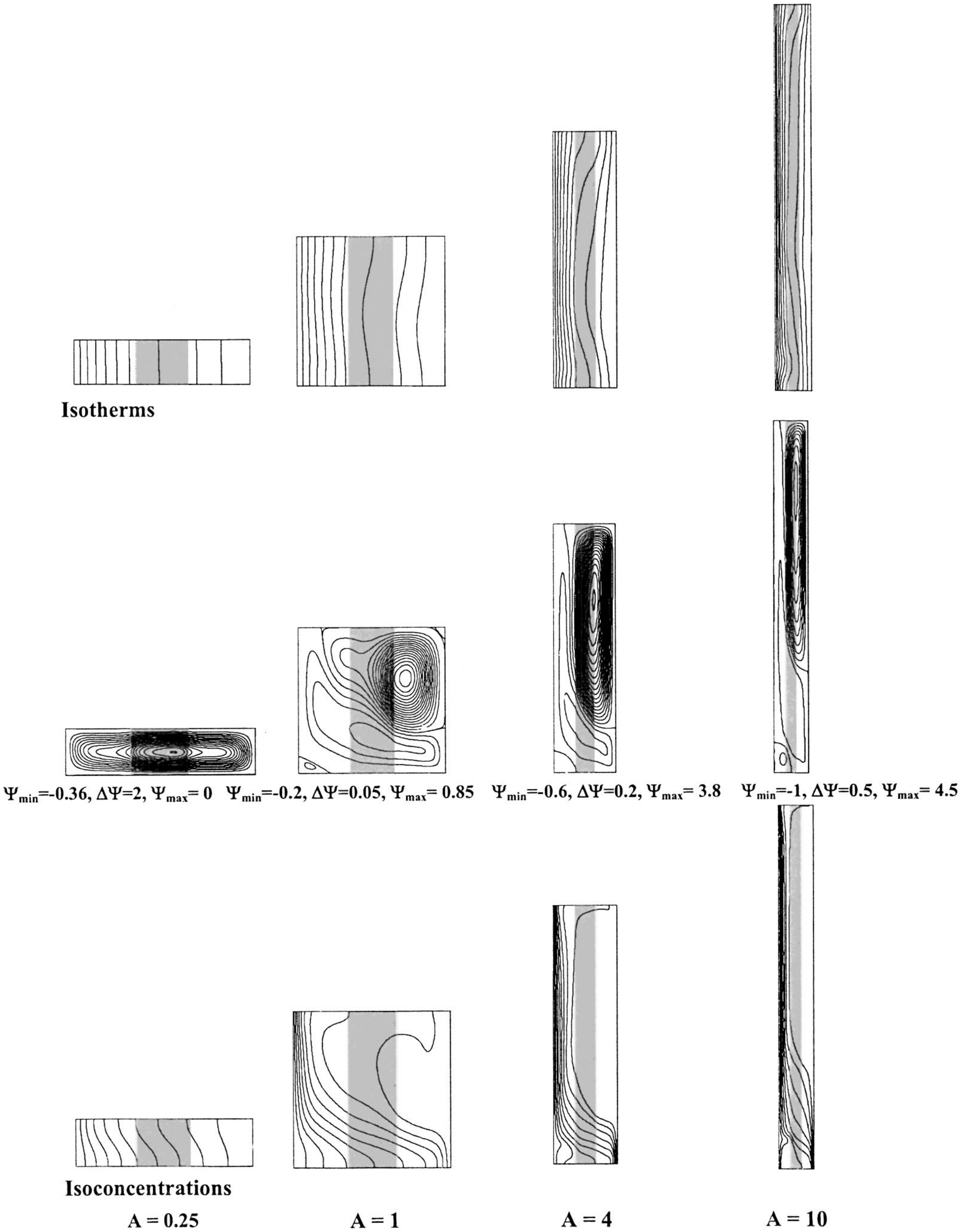

Fig. 5 Effect of A in partly porous cavity for $Ra=10^4$, $N=-1.5$, $Pr=7$, $Le=21.71$, $Kr=5$, $E=0.3$, $r_1=0.35$, and $Da=10^{-3}$

$$\mathrm{Max}\left|\frac{\phi^{n+1}-\phi^{n}}{\phi^{n}}\right| \leqslant 10^{-4} \tag{10}$$

Furthermore, other authors have added another stringent criterion, which relates to the average Nusselt and Sherwood numbers on the vertical active walls. For instance, Trevisan and Bejan [11,23] suggested that this error should be smaller than 1%. In a similar manner, we echoed this proposal and have coupled the latter criterion to the former one in order to establish an error E (on Nu and Sh)

$$E=\frac{\mathrm{Nu}_i-\mathrm{Nu}_o}{\mathrm{Nu}_i+\mathrm{Nu}_o} \tag{11}$$

to be less than 0.5%. To validate the computer code, we first compared our numerical results with published ones for a fully fluid cavity by setting the porosity of the porous matrix ε equal to unity and the Darcy number Da equal to infinity. Several comparisons have been made against the semi-empirical relationships presented by Thomas and de Vahl Davis [1] and Kumar and Kalam [2], as well as the numerical findings of Khellaf and Lauriat [3]. Within the boundaries of these three references, the numbers listed in Table 2 showed excellent agreement, e.g., the difference in the computed average Nusselt number does not exceed 3%. Next, switching to porous cavities, the numerical results were compared with those available in the literature under the premises of a Darcy regime. Table 3 illustrates these comparisons for the average heat and mass transfer coefficients at a Lewis number of unity which yields an equal value for Nu and Sh; the comparisons are of satisfactory quality. The detected maximum difference with the results of Goyeau et al. [13] and Getachew et al. [24] is less than 2.7%. The discrepancy with results of Trevisan and Bejan [23] is equal to the one found by the authors of the two other papers with this reference. This is due to the size of the mesh used by Trevisan and Bejan [23]. The accuracy is quite good in comparison with references [13] and [25] in which non uniform grids were used with finer step size in order to detect the solutal boundary layers.

Other authors have utilized the general Darcy-Brinkman-Forchheimer model including inertia terms. The proper comparison with these references is reported in Table 4. For instance, the difference with the results of Nithiarasu et al. [14] is smaller than 4%. The slight discrepancy with the results of Beckermann et al. [25] and Lauriat and Prasad [4] may be due to a possible difference in the porosity considered by these authors, which was not indicated explicitly in their papers. Moreover, the discrepancy with the results of Lauriat and Prasad [4] at $\mathrm{Da}=10^{-4}$ may be explained by the fact that the authors used a finite difference method with regular grid while non uniform grid with a finer mesh at the walls is used in the present study. It is worth mentioning that Nithiarasu et al. [14] have also reported a discrepancy between their results and the ones of Lauriat and Prasad [4]. Overall, the comparisons serve to confirm and validate our numerical code.

4 Results and Discussion

Results of the numerical simulations are presented in this subsection with the objective to better understand the coupling between thermal and solutal buoyancy driven flows in vertical annular cavities and also to evaluate the rates of heat and mass transfer in these cavities. Despite of the superabundance of parameters, for the sake of brevity, only a selected number of them are analyzed in depth while others are maintained fixed.

In order to investigate the effect of geometry, the curvature and the aspect ratio of the vertical annular cavity are examined for vast ranges of the radii ratio $1 \leqslant K_r \leqslant 20$ and the aspect ratio $0.25 \leqslant A \leqslant 10$. For simplicity, r_i is kept constant whereas r_o is allowed to vary. Two types of fluids are considered which encompass numerous applications of air and aqueous solutions. In view of this, we opted to test air ($\mathrm{Pr}=0.7$ and $0.01 \leqslant \mathrm{Le} \leqslant 10$) and water ($\mathrm{Pr}=7$ and $0.01 \leqslant \mathrm{Le} \leqslant 100$) as the two fluids filling the cavity. The dynamic parameters representing the driving forces are analyzed through an ample buoyancy ratio $-5 \leqslant N \leqslant 5$, covering both ranges of aiding and opposing thermal and solutal buoyancy effects. The influence of the porous matrix is investigated through its thickness ($0 \leqslant E \leqslant 1$), its permeability ($\mathrm{Da}=10^{-3}$ or 10^{-5}) and its thermal conductivity ($1 \leqslant R_k \leqslant 100$) while maintaining the porosity constant at a value of $\varepsilon=0.4$. It should be mentioned that the case related to a cavity absent of porous matrix, referred here as the fluid case, is obtained by setting the permeability at infinity ($\mathrm{Da} \rightarrow \infty$) and assigning a unitary value to the porosity ($\varepsilon=1$). Unless otherwise specified, the temperature and concentration fields are represented in all the plots with $\theta_{\min}=-0.5$, $\Delta\theta=0.1$, $\theta_{\max}=0.5$ and $S_{\min}=-0.5$, $\Delta S=0.1$, $S_{\max}=0.5$. The partly porous case indicates a centered porous layer occupying 30% of the gap width with $R_k=R_v=1$. In the companion set of figures, the left and right vertical sides correspond to the inner and outer cylinders, respectively.

4.1 Effect of Cavity Geometry. The influence of the curvature of the vertical annular cavity in the fluid case is analyzed first. The streamlines, isotherms and isoconcentrations are illustrated in Fig. 2 for three values of the radii ratio, namely $K_r=1$, 4 and 20. In theory, the case of infinite curvature characterized by $K_r=1$ represents a rectangular cavity in Fig. 2(a). In practice, this limiting configuration is generated numerically by setting $K_r=1.001$. The flow patterns are displayed for a situation of opposing buoyancy forces, which seems to be of greater interest. Unlike the rectangular cavity, it is evident that in Fig. 2(b) for an annular cavity ($K_r=4$) and in Fig. 2(c) for a nearly cylindrical cavity ($K_r=20$), the thermal gradients induce a second cell. This cell occupies the upper zone of the cavity and, as $\mathrm{K_r}$ increases, takes over the solutal cell, which had been established in the lower part. The absence of symmetry is also exhibited in the thermal and concentration fields. At $K_r=1$, the isotherms show a conductive regime, which manifests a domination of thermal diffusion over solutal diffusion. When the radii ratio K_r increases, the cylinders are further and further far away from each other and the surface area of the outer cylinder becomes increasingly higher than the inner one. Consequently, the gradients are perceptibly smaller at the outer wall as it is clearly illustrated through the concentration field which now is stratified at the bottom of the cavity, particularly at $K_r=20$. The effect of enlarging the outer surface area relative to the inner one is also depicted through the velocity profiles in midplanes of the cavity in Fig. 3. This figure confirms the loss of symmetry at $K_r>1$ and the decrease of the fluid circulation near the outer cylinder, as well as solutal stratification at the bottom of the cavity. In fact, in Fig. 3(b) for $K_r>1$ the magnitude of the radial velocity in the zone where the fluid motion is mainly due to solutal forces is smaller than its counterpart in the upper region where the flow is thermally driven. For the remainder part of the study, we used a moderate value of $K_r=5$, which is representative of an annular cavity of intermediate size.

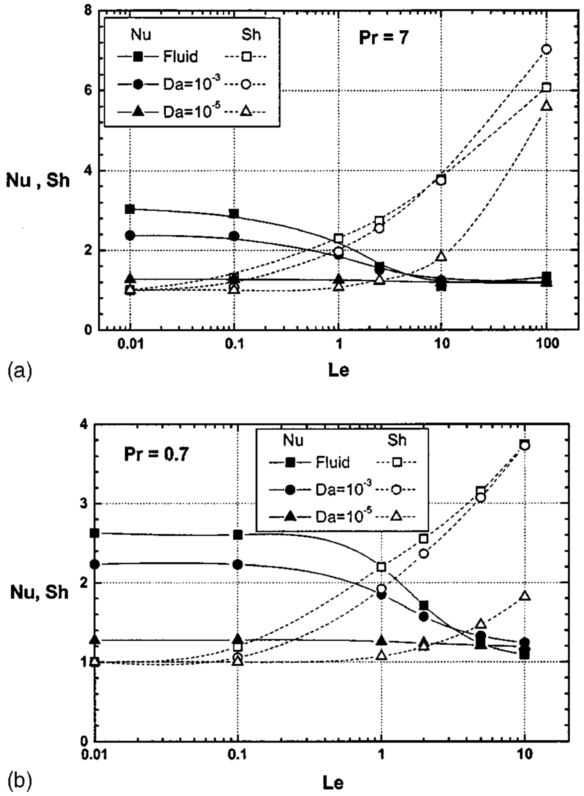

Fig. 6 Variations of Nusselt and Sherwood numbers with Lewis number for $\mathrm{Ra}=10^4$, $N=-3$, $A=1$, and $K_r=5$

The effect of aspect ratio is further reported in Figs. 4 and 5. The fluid case is first considered in Fig. 4(a) for $A=1$. Here, we observe that the fluid is mainly driven by the thermal buoyancy delivering the largest cell occupying the core of the cavity in a zone of constant concentration. The solutal gradient gives rise to two minor cells in the lower left and upper right corners where concentration stratification occurs and near the inner cylinder.

For taller cavities $A=10$ in Fig. 4(b), several thermal cells appear in the cavity. Indeed, the presence of a multicellular structure is due to the fact that the solutal stratification cannot go above a

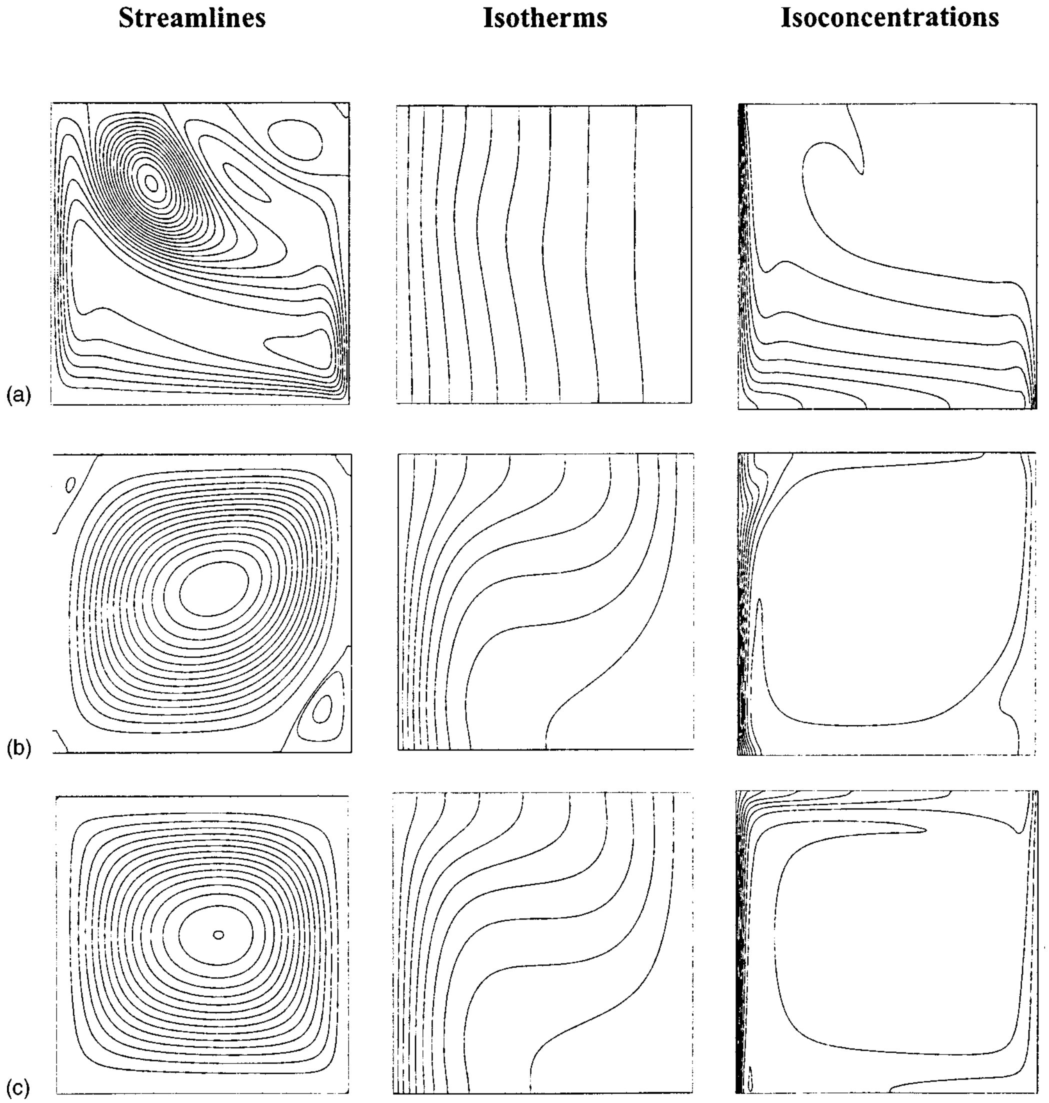

Fig. 7 Effect of N on flow, isothermal, and isoconcentrations patterns in fluid case for $\mathrm{Ra}=10^4$, $\mathrm{Pr}=7$, $\mathrm{Le}=21.71$, $A=1$, and $K_r=5$: (a) $N=-5$, $\Psi_{\min}=-0.16$, $\Delta\Psi=0.02$, $\Psi_{\max}=0.28$; (b) $N=-1.5$, $\Psi_{\min}=-0.05$, $\Delta\Psi=0.2$, $\Psi_{\max}=3.18$ and -0.15; and (c) $N=5$, $\Psi_{\min}=0$, $\Delta\Psi=0.2$, $\Psi_{\max}=3$.

certain height without being destabilized by the thermal gradient. The flow driven by thermal buoyancy forces imposes itself within the stratification zone yielding the thermal cells that are more dominating as the flow progresses upward. Each thermal cell may be seen as corresponding to a small cavity. The interfaces between the cells (thermal cell to solutal cell and solutal cell to thermal cell) constitute regions of high shear and local thermal and solutal gradients as it is revealed in the temperature and concentration fields. It is worth mentioning that similar structures, but for rectangular cavities have been reported by Lee and Hyun [26].

Figure 5 represents the flow patterns, isotherms and isoconcentrations for the partly porous case with a buoyancy ratio of $N=-1.5$; this characterizes a transition regime between the opposing and aiding buoyancy forces. For shallow cavities of aspect ratio $A=0.25$, the active walls are restricted areas, and the sole mode of heat transfer is conduction, while mass transfer occurs by convection because of the small mass diffusivity ($\mathrm{Le}=21.71$) in the thin boundary layers along the vertical walls. It should be mentioned that the thermal and concentration fields are different in the porous region because both the solid matrix and fluid constitute transport media for heat effectively, whereas mass transfer has only the fluid as a vehicle.

With higher aspect ratios ($A\geqslant 1$), the effect of the active walls is amplified and two thermal cells appear. An important cell shows up in the upper right zone because of lighter fluid and another of lesser magnitude shows up in the opposite corner. In the space between the two cells, a fluid motion of solutal origin possesses weak circulation. As opposed to the fluid case, the partly porous case retains this flow structure even with very tall cavities ($A=10$). Hence, the role of the porous matrix is to stabilize the flow avoiding the formation of a multicellular pattern.

4.2 Effect of Fluid Nature. In this subsection, we consider two types of fluids which are frequently encountered in a multitude of practical engineering applications, namely aqueous solutions with $\mathrm{Pr}=7$ and air with $\mathrm{Pr}=0.7$. The types of solute cover a wide spectrum of Lewis number ranging from 0.01 to 10 with air as a solvent, and from 0.01 to 100 when water is used as a solvent. The Lewis number, which embraces the relative importance of thermal to mass diffusion, has a direct bearing on the heat and mass transfer coefficients as exemplified in Fig. 6. At first, we notice the equality between the heat and mass transfer coefficients at $\mathrm{Le}=1$ for both the fluid case as well as the partly porous case in the non-Darcian flow. Then, for a simple Darcy flow in a weakly

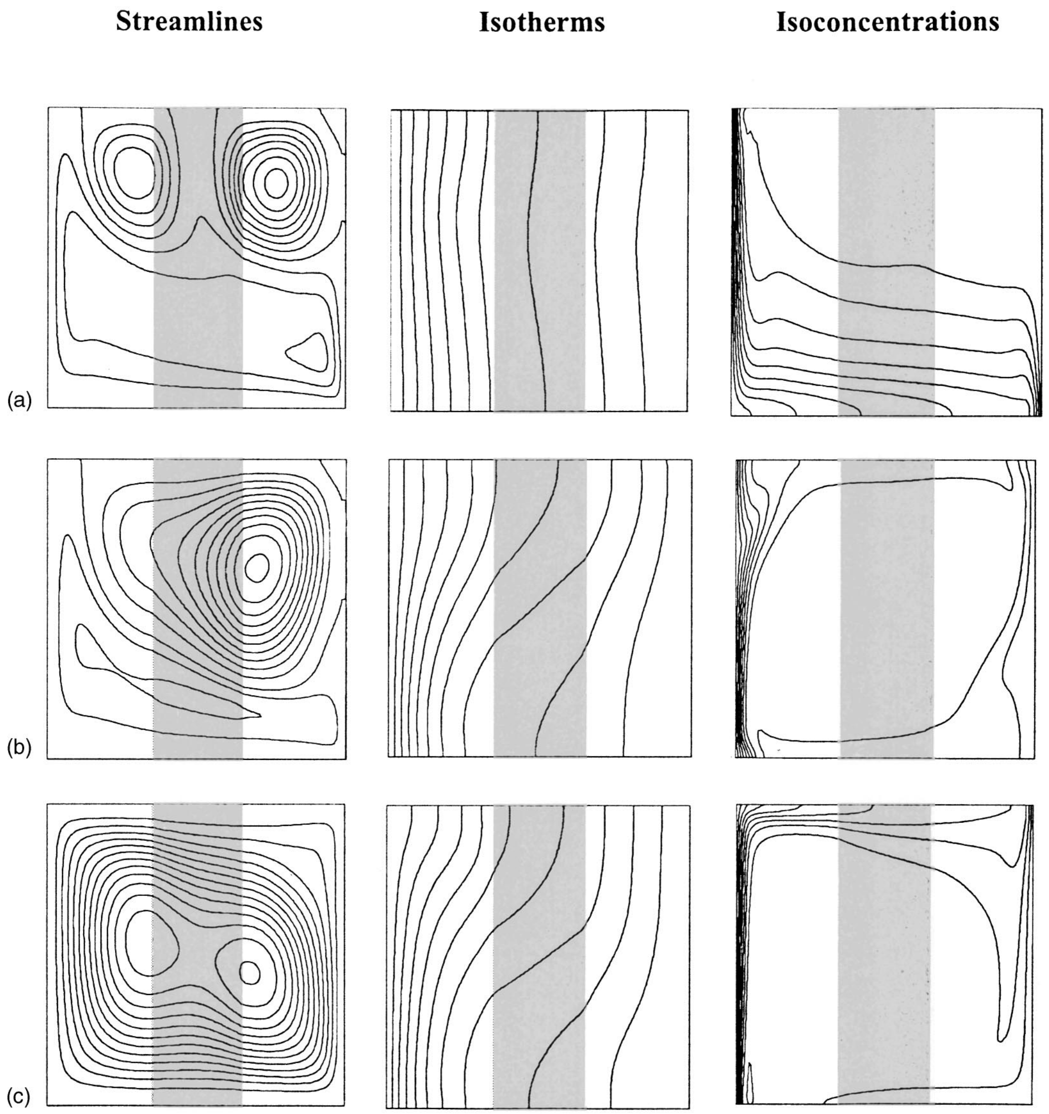

Fig. 8 Effect of N in partially porous case for $\mathrm{Ra}=10^4$, $\mathrm{Pr}=7$, $\mathrm{Le}=21.71$, $A=1$, $K_r=5$, and $\mathrm{Da}=10^{-3}$: (a) $N=-5$, $\Psi_{\min}=-0.15$, $\Delta\Psi=0.05$, $\Psi_{\max}=0.4$; (b) $N=-1.5$, $\Psi_{\min}=-0.1$, $\Delta\Psi=0.1$, $\Psi_{\max}=1.5$ and -0.05; and (c) $N=5$, $\Psi_{\min}=0$, $\Delta\Psi=0.1$, $\Psi_{\max}=1.3$.

permeable porous matrix ($\mathrm{Da}=10^{-5}$), the equality is reached at a value of Lewis number between 2 and 3. This is explained by the fact that the porous layer with a small permeability reduces mass diffusion for both solvents ($\mathrm{Pr}=0.7$ and 7). The role played by the permeability of the porous medium on the average Nusselt and Sherwood numbers is also illustrated in Fig. 6; this issue is of singular importance on both transfer coefficients in the range of $0.1\leqslant\mathrm{Le}\leqslant 3$. Whenever $\mathrm{Le}<0.1$, the presence of thermal convection and mass diffusion is accentuated. So, with or without the porous layer, the flow is driven by the action of a thermal buoyant force exclusively. Thus, there is no influence of Da on the Sherwood number. For $\mathrm{Le}>3$, mass transfer occurs by convection whereas heat is transferred by diffusion. Under these circumstances, the driving force is produced by solutal buoyancy. Hence, there is no effect of Da on the Nusselt number. Moreover, in the non-Darcian flow regime, the porous matrix placed equidistant in the cavity has a greater influence on the thermal cell, which occupies the core of the cavity. For instance, the fluid motion of thermal origin is reduced, while the fluid driven by solutal force, which is of higher magnitude near the vertical walls, is marginally affected. Furthermore, in the range $3<\mathrm{Le}<10$ in conjunction with a non-Darcian regime ($\mathrm{Da}>10^{-4}$), the following correlations can be proposed for purposes of evaluating the mass transfer coefficient.

$$\mathrm{Sh}=1.115\ \mathrm{Le}^{0.289} \quad \text{for } N=-1.5$$

$$\mathrm{Sh}=2.351\ \mathrm{Le}^{0.342} \quad \text{for } N=2$$

Note that these correlations are independent of the Prandtl number. This peculiarity was confirmed in the work of Thomas and De Vahl Davis [1] when treating pure thermal convection. In addition, our correlations are close to the ones of Trevisan and Bejan [11] who proposed a proportionality between Sh and $\mathrm{Le}^{1/3}$ for $\mathrm{Pr}>0$ and $\mathrm{Le}>0$ in the case of a vertical plate.

4.3 Effect of Buoyancy Forces. The relative importance of buoyancy driving forces is expressed by the buoyancy ratio N and its impact on flow patterns, isotherms and isoconcentrations is illustrated in Figs. 7, 8, and 9 for an aqueous solution with $\mathrm{Pr}=7$. Negative values of N corresponding to opposing forces are caused by negative coefficient of concentration expansion. In order to accomodate the transition zone in our analysis, we decided to cover the range $-5\leqslant N\leqslant 5$. It is important to recognize that solutions based on scale analysis are not valid for the ratio N^2/Le approximately near unity and, on the other hand similarity solutions are impossible to obtain, Li and Lai [27]. Three values of N (-5, -1.5 and 5) are considered sufficient to represent the flow

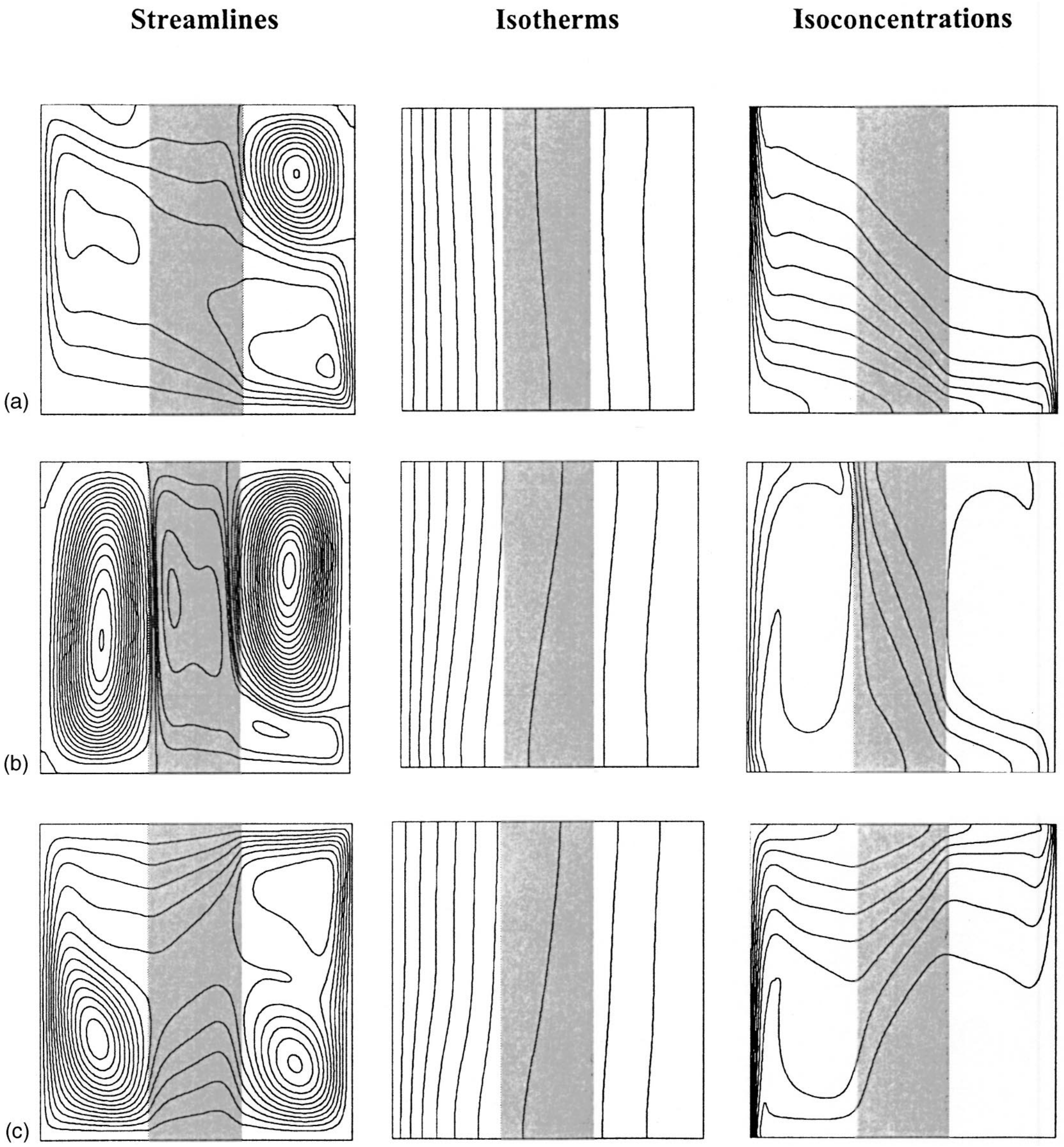

Fig. 9 Effect of N in partly porous case for $\mathrm{Ra}=10^4$, $\mathrm{Pr}=7$, $\mathrm{Le}=21.71$, $A=1$, $K_r=5$, and $\mathrm{Da}=10^{-5}$: (a) $N=-5$, $\Psi_{\min}=-0.14$, $\Delta\Psi=0.05$, $\Psi_{\max}=0.22$; (b) $N=-1.5$, $\Psi_{\min}=-0.06$, $\Delta\Psi=0.02$, $\Psi_{\max}=0.4$ and -0.05, -0.01; and (c) $N=5$, $\Psi_{\min}=0$, $\Delta\Psi=0.02$, $\Psi_{\max}=0.3$.

structures for different situations of thermal or solutal force domination. Figure 7 is associated with the fluid case. For $N=-5$, we observe the opposition of two cells: the one driven by thermal force occupying the central upper zone with a clockwise fluid motion, and the cell driven by solutal force in the bottom part of the cavity where the fluid is denser and near the vertical walls and with a counter clockwise motion. The plots of isotherms and isoconcentrations manifest a nearly conductive mode of heat transfer with very a small fluid circulation, and the development of concentration boundary layer on the active walls generating the fluid circulation of solutal origin.

For $N=-1.5$ in Fig. 7(b), the flow changes its structure and the thermal cell, which becomes the main cell, settles almost in the entire cavity. The cells of solutal origin are confined in the corners. In fact, at this value of N the driving forces are still opposed to each other, but the thermal buoyant force takes over the solutal force. This transition zone is characterized by the development of a thermal boundary layer on the inner cylinder, and a hesitation between the top and bottom of the vertical walls for the starting of concentration boundary layers. The cooperating case ($N=5$) is reported in Fig. 7(c) indicating that a monocellular flow is obtained; a situation similar to thermal convection but with thermal and concentration boundary layers developing in the same direction. The insertion of the porous layer strongly affects the flow structure as reported in Figs. 8 and 9. For a highly permeable ($\mathrm{Da}=10^{-3}$) porous matrix, Fig. 8(a), the flow driven by solutal force settles mostly in the first compartment near the inner cylinder while in the outer part of the cavity the flow driven by thermal force takes over. The thermal cell dominates in that part as shown in Fig. 8(b). As N increases, Fig. 8(c), the thermal cell pushes down the solutal one, starting from the outer compartment near the outer cylinder to end up occupying the whole cavity for the case of aiding thermal and solutal forces. In fact, the porous matrix moderately alters heat convection but it does not affect heat conduction, since the effective thermal conductivity of the porous medium is taken equal to the fluid one. However, mass transfer is substantially affected because of the considerable reduction of mass diffusion. Indeed, within the porous layer the fluid is the only medium allowing mass transfer and the solid matrix acts as a

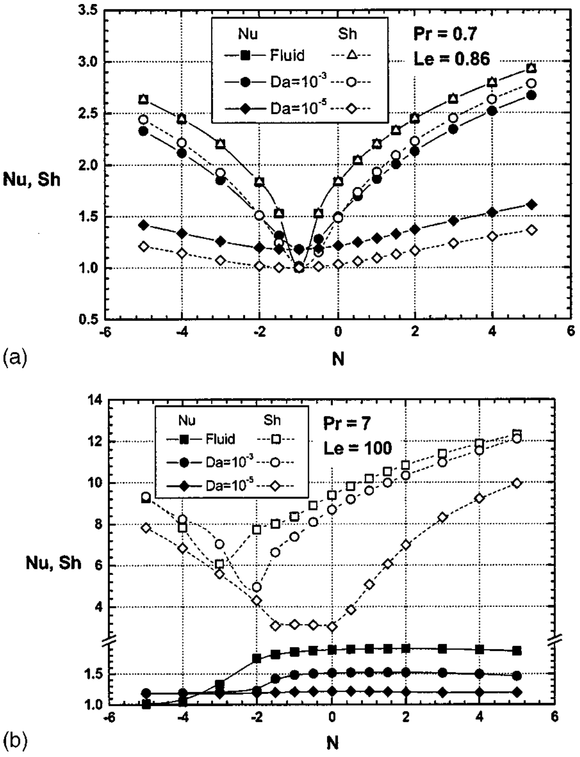

Fig. 10 Variations of Nusselt and Sherwood numbers with buoyancy ratio for Ra=10^4, A=1, and Kr=5

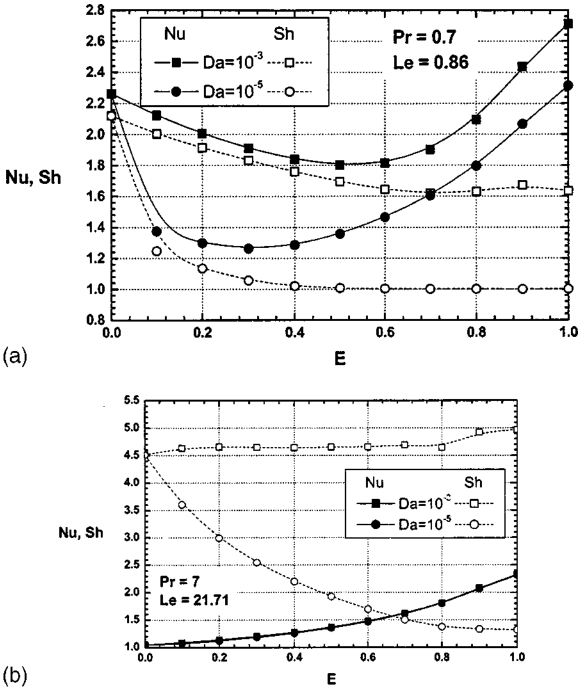

Fig. 11 Variations of Nusselt and Sherwood numbers with thickness of porous layer for Ra=10^4, N=−3, A=1, and Kr=5

brake. With a less permeable porous layer (Da$=10^{-5}$), Fig. 9, it is almost like a divided cavity with two compartments separated by the porous wall. Figure 9 shows the flow structure with nearly independent fluid motions in each part of the cavity. A solutal monocellular pattern is obtained in the inner compartment (Figs. 9(a) and 9(b)). In the outer part of the cavity, the thermal cell occupies most of the space because of the curvature (Kr=5) which reduces considerably the flow driven by solutal buoyancy although the Lewis number is greater than 1. In the case of aiding forces (N=5), Fig. 9(c), the fluid is convected near the vertical walls and is quasi stagnant in the center of the cavity as it is shown through temperature and concentration fields. Though, it should be mentioned that in the transition zone ($N=-1.5$) we may switch from a thermal regime to a solutal regime just by varying the permeability of the porous medium Figs. 7(b), 8(b), and 9(b). Reducing Da renders the porous layer as an obstacle to mass transfer and consequently the solutal cell is pushed away from the outer compartment. In terms of heat and mass transfer coefficients, Fig. 10 illustrates the variations of Nu and Sh for 2 types of fluids, Pr=0.7, Le=0.86, and Pr=7, Le=100. For the case of moist air (Fig. 10(a)), the double diffusion is obtained at $N=-1$ independently of the Rayleigh number or the permeability of the porous matrix. In fact, for a Lewis number close to unity the opposition of the thermal and solutal driving forces of equal magnitude occurs at $N=-1$, as previously reported by Trevisan and Bejan [11]. Moreover, it should be pointed out that the presence of the porous layer eliminates the equality of Nu and Sh at $N=-1$. A slight decrease, about 15%, is observed in Sh as was previously shown by Benzeghiba and Chikh [19]. For the case of brine (Fig. 10(b)), the double diffusion regime takes place at $N=-3$. This is due to the fact that thermal and solutal buoyancy forces do not cancel each other at $N=-1$ because of the difference in thermal and mass diffusivities at Le=100. Multicellular flow, which is particularly unstable, is observed near $N=-1$ at Pr=0.7 and $N=-3$ at Pr=7. The insertion of the porous matrix reduces the transport by convection and yields a double diffusion regime at higher values of N, at $N=-2$ for Da$=10^{-3}$ and in a whole range $-1.5\leq N\leq 0$ for Da$=10^{-5}$. Indeed, within this range, mass convection is substantially weakened, but still exists near the vertical cylinders, while heat transfer occurs only by conduction. This allows an optimum filtration in this transition zone over a larger range of N. In addition, we notice that the symmetry is lost in these plots for Pr=7 and Le=100.

4.4 Effect of Porous Matrix. The impact exerted by the porous layer centered midway between the two cylinders is analyzed through its thickness and the ratio of the effective thermal conductivity to the fluid conductivity R_k. As expected, the porous matrix offers a resistance to mass transfer. Thus, increasing the porous layer thickness reduces the mass transfer coefficient as evidenced in Fig. 11. With respect to heat transfer, the insertion of the porous layer reduces the Nusselt number attaining a minimum value at a critical thickness depending on the permeability as reported for the case of air in Fig. 11(a). This is indeed a remarkable result from the standpoint of thermal insulation. However, particular attention should be brought to the limiting case of a completely porous cavity, which is connected to a better heat transfer coefficient. This result is in agreement with the one reported by Chikh et al. [28] and may be explained by the fact that the porous matrix acts as a resistance to the flow from the hydrodynamics point of view. Within the porous matrix of small effective thermal conductivity corresponding to $R_k=1$, the magnitude of heat transfer by conduction is of the same order as convected heat by the fluid. Hence, the convected heat is reduced implying a decrease in the Nusselt number. Figure 11(b) displays the variation of Nu and Sh for water (Pr=7). With the same features (Da, R_k) of the porous matrix, paradoxically heat transfer is augmented by the presence of the porous layer and resulting improvement is independent of Da. Essentially, it is similar to the first case (Fig. 11(a)), but exhibiting a critical thickness equal to zero. The augmentation of the Nusselt number above the critical point may be due to the fact that for air a thick layer is necessary ($E>E_{\text{critical}}$) to reduce the fluid circulation. This phenomenon is responsible for better heating in the fluid, while a thin layer produces a reduction of fluid circulation in the case of water. The influence of R_k on the heat transfer

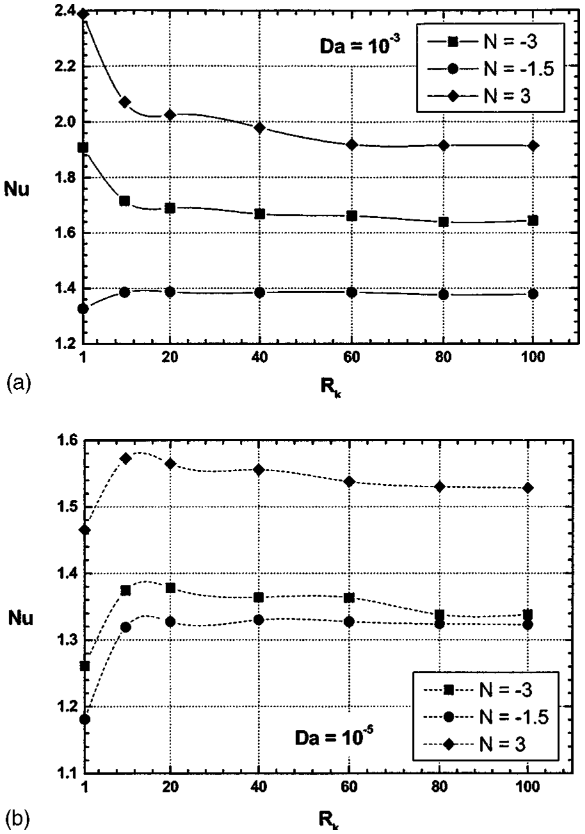

Fig. 12 Variation of Nusselt number with conductivity ratio in porous layer for Ra=10^4, $N=-3$, Pr=0.7, Le=0.86, $A=1$, and Kr=5

coefficient is reported in Fig. 12. It is observable that R_k has practically no effect on mass transfer since the fluid is the only material that sustains the transport of concentration within the porous medium. So, Sherwood number is not included in this figure. The evolution of Nu with respect to R_k seems to strongly depend on the permeability of the porous medium as shown in Figs. 12(a) and 12(b). Indeed, with a highly permeable porous layer ($\mathrm{Da}=10^{-3}$), the fluid circulation is slightly affected. Thereby, the convected heat at the inner wall is not altered significantly. On the contrary, an increase in R_k is beneficial because it improves the heat conduction. For instance, since the Nusselt number may be expressed as the ratio of the convected heat to the conductive one, the end result is that Nu increases with R_k as may be confirmed in Fig. 11(a). It is worth mentioning that an exception is made for the case of $N=-1.5$ in the transition regime of double diffusion which is related to a Nu that is nearly constant. For a weakly permeable porous matrix ($\mathrm{Da}=10^{-5}$), the cavity is divided in two compartments and the porous layer constitutes a barrier to the fluid motion outwards. The fluid confined in the inner compartment is then heated more vigorously, yielding a higher Nusselt number at the inner wall. Both rates of heat conduction and heat convection tend to be amplified, but such that the ratio (Nu) is also increased.

5 Conclusions

Simultaneous heat and mass transfer by natural convection is investigated for a vertical annular cavity partly filled with a porous medium. Temperature and concentration gradients are applied in the horizontal direction on this cavity. The interaction between the thermal and solutal buoyancy forces driving the flow may be either aiding or opposing to each other. Numerical results are presented for several situations involving the cavity geometry, the fluid type, the magnitude of driving forces as well as the characteristics of the porous matrix. It is demonstrated that the flow structures are quite complex when buoyancy effects are articulated with the porous matrices. This unique combination adds complexity and substantially alters the flow patterns and the heat and mass transfer regimes. Thus, it was concluded that double diffusion occurs in a wider range of N for Darcian flow conditions. Moreover, the numerical results indicate that partly porous cavities ensure better filtration performance and superior thermal insulation behavior when compared to a fully porous cavity.

Nomenclature

A = aspect ratio (H/d)
C = solute mass fraction
C_f = microscopic inertial coefficient ($=0.35$)
C_r = reference concentration $(C_i+C_o)/2$
D = mass diffusivity of the solute in the fluid, m^2/s
Da = Darcy number (K/d^2)
d = gap width (R_o-R_i), m
e = porous matrix thickness, m
E = dimensionless thickness of the porous matrix (e/d)
$\vec{g}$ = acceleration of gravity, m/s^2
H = height, m
k = thermal conductivity, W/m.K
K = permeability of the porous medium, m^2
K_r = radius ratio (r_o/r_i)
Le = Lewis number (α/D).
N = ratio of buoyancy forces $(\beta_c\cdot\Delta C/\beta_T\cdot\Delta T)$
Nu = Nusselt number, Eq. (8)
P = dimensionless pressure $(p/\rho(\alpha/d)^2)$
Pr = Prandtl number (ν_F/α_F)
R = radial coordinate, m
r = dimensionless radial coordinate (R/d)
R_1 = radial position of the porous matrix, m
r_1 = dimensionless radial position of the porous matrix
R_v = viscosity ratio $(\mu_{\mathrm{eff}}/\mu_F)$
R_k = thermal conductivity ratio (k_{eff}/k_F)
Ra$_T$ = thermal Rayleigh number $(\mathrm{g}\cdot\beta_T\cdot\Delta T\cdot d^3/\alpha\nu)$
Ra$_c$ = solutal Rayleigh number $(\mathrm{N}\cdot\mathrm{Ra}_T)$
S = dimensionless solute mass fraction $(C-C_r)/\Delta C$
Sh = Sherwood number, Eq. (8)
Sc = Schmidt number (ν_F/D_F)
T = temperature, K
T_r = reference temperature $(T_h+T_c)/2$, K
u = axial velocity, m/s
$\vec{V}$ = velocity vector
v = radial velocity, m/s
Z = axial coordinate, m
z = dimensionless axial coordinate (Z/d)

Greek Symbols

α = thermal diffusivity, m^2/s
β_C = coefficient of concentration expansion $(\beta_c=-1/\rho[\partial\rho/\partial C]_T)$
β_T = coefficient of thermal expansion $(\beta_T=-1/\rho[\partial\rho/\partial T]_C)$, 1/K
ΔC = concentration difference (C_i-C_o)
ΔT = temperature difference (T_h-T_c), K
ε = porosity of porous matrix
μ = dynamic viscosity, kg/m·s
ν = kinematic viscosity (μ/ρ), m^2/s
ρ = density, kg/m^3
θ = dimensionless temperature $(T-T_r)/\Delta T$
Ψ = stream function, m^2/s

Subscripts

c = cold
eff = effective property of porous medium

F = fluid
h = hot
i = inner cylinder
o = outer cylinder
p = porous medium

References

[1] Thomas, R. W., and De Vahl Davis, G., 1970, ''Natural Convection in Annular and Rectangular Cavities: A Numerical Study,'' Heat Transfer, Paper NC.2.4.

[2] Kumar, R., and Kalam, M. A., 1991, ''Laminar Thermal Convection Between Vertical Coaxial Isothermal Cylinder,'' Int. J. Heat Mass Transfer, **34**, pp. 513–524.

[3] Khellaf, K., and Lauriat, G., 1995, ''Transfert De Chaleur Dans Des Espaces Annulaires Cylindriques Verticaux Mis En Rotation: Étude Numérique,'' Revue Générale de Thermique 398, pp. 104–116.

[4] Lauriat, G., and Prasad, V., 1991, ''Natural Convection in a Vertical Porous Annulus,'' *Convective Heat Transfer in Porous Media*, S. Kacac, B. Kilkis, F. A. Kulacki, and F. Arinc, eds., Kluwer Academic, Dordrecht, pp. 143–177.

[5] Campos, H., Morales, J. C., Lacoa, U., and Campo, A., 1990, ''Thermal Aspects of a Vertical Annular Enclosure Divided Into a Fluid Region and a Porous Region,'' Int. Comm. Heat Mass Transfer, **17**, pp. 343–354.

[6] Béghein, C., Haghighat, F., and Allard, F., 1992, ''Numerical Study on Double Diffusive Natural Convection in a Square Cavity,'' Int. J. Heat Mass Transfer, **35**, pp. 833–846.

[7] Han, H., and Kuehn, T. H., 1991, ''Double Diffusive Natural Convection in a Vertical Rectangular Enclosure. I. Experimental Study,'' Int. J. Heat Mass Transfer, **34**, pp. 449–459.

[8] Han, H., and Kuehn, T. H., 1991, ''Double Diffusive Natural Convection in a Vertical Rectangular Enclosure. II. Numerical Study,'' Int. J. Heat Mass Transfer, **34**, pp. 461–471.

[9] Shipp, P. W., Shoukri, M., and Carver, M. B., 1993, ''Double Diffusive Natural Convection in a Closed Annulus,'' Numer. Heat Transfer, Part A, **24**, pp. 339–356.

[10] Shipp, P. W., Shoukri, M., and Carver, M. B., 1993, ''Effect of Thermal Rayleigh and Lewis Numbers on Double Diffusive Natural Convection in Closed Annulus,'' Numer. Heat Transfer, Part A, **24**, pp. 451–465.

[11] Trevisan, O. V., and Bejan, A., 1985, ''Natural Convection With Combined Heat and Mass Transfer Buoyancy Effects in a Porous Medium,'' Int. J. Heat Mass Transfer, **28**, pp. 1597–1611.

[12] Mamou, M., Vasseur, P., and Bilgen, E., 1995, ''Multiple Solutions for Double Diffusive Convection in a Vertical Porous Enclosure,'' Int. J. Heat Mass Transfer, **38**, pp. 1787–1798.

[13] Goyeau, B., Songbe, J. P., and Gobin, D., 1996, ''Numerical Study of Double Diffusive Natural Convection in a Porous Cavity Using the Darcy-Brinkman Formulation,'' Int. J. Heat Mass Transfer, **39**, pp. 1363–1378.

[14] Nithiarasu, P., Seetharamu, K. N., and Sundararajan, T., 1996, ''Double Diffusive Natural Convection in an Enclosure Filled With Fluid Saturated Porous Medium: A Generalised Non-Darcy Approach,'' Numer. Heat Transfer, Part A, **30**, pp. 413–426.

[15] Marcoux, M., Charrier Mojtabi, M.-C., and Azaiez, M., 1999, ''Double Diffusive Convection in Annular Vertical Porous Layer,'' Int. J. Heat Mass Transfer, **42**, pp. 2313–2325.

[16] Benacer, R., Beji, H., and Duval, R., 2000, ''The Brinkman Model for Thermosolutal Convection in a Vertical Annular Porous Layer,'' Int. Commun. Heat Mass Transfer, **27**, pp. 69–80.

[17] Gobin, D., Goyeau, B., and Songbe, J. P., 1998, ''Double Diffusive Natural Convection in a Composite Fluid-Porous Layer,'' ASME J. Heat Transfer, **120**, pp. 234–242.

[18] Merrikh, A. A., and Mohamad, A. A., 2002, ''Non Darcy in buoyancy Driven Flows in an Enclosure Filled With Vertically Layered Porous Media,'' Int. J. Heat Mass Transfer, **45**, pp. 4305–4313.

[19] Benzeghiba, M., and Chikh, S., 1999, ''Natural Heat and Mass Convection in Partially Porous Vertical Annulus,'' ImechE Transactions, 6th UK National Conference on Heat Transfer, Edinburgh, UK, pp. 475–480.

[20] Alazmi, B., and Vafai, K., 2001, ''Analysis of Fluid Flow and Heat Transfer Interfacial Conditions Between a Porous Medium and a Fluid Layer,'' Int. J. Heat Mass Transfer, **44**, pp. 1735–1749.

[21] Patankar, S. V., 1980, *Numerical Heat Transfer and Fluid Flow*, McGraw Hill, New York.

[22] Benard, C., Gobin, D., and Trevisan, J., 1989, ''Thermosolutal Natural Convection in a Rectangular Enclosure: Numerical Results,'' *Heat Transfer in Convective Flows*, ASME HTD-107, pp. 249–254.

[23] Trevisan, O. V., and Bejan, A., 1986, ''Mass and Heat Transfer by Natural Convection in a Vertical Slot Filled With a Porous Medium,'' Int. J. Heat Mass Transfer, **29**, pp. 403–415.

[24] Getachew, D., Poulikakos, D., and Minkowycz, W. J., 1998, ''Double Diffusion in Porous Cavity Saturated With Non-Newtonian Fluid,'' J. Thermophys. Heat Transfer, **12**, pp. 437–446.

[25] Beckermann, C., Viskanta, R., and Ramadhyani, S., 1986, ''A Numerical Study of Non-Darcian Natural Convection in Vertical Enclosure Filled With Porous Medium,'' Numer. Heat Transfer, **10**, pp. 557–570.

[26] Lee, W., and Hyun, I. M., 1991, ''Double-Diffusive Convection in a Rectangle With Opposing Horizontal Temperature and Concentration Gradients,'' Int. J. Heat Mass Transfer, **33**, pp. 1619–1637.

[27] Li, C. T., and Lai, F. C., 1998, ''Re-Examination of Double-Diffusive Natural Convection From Horizontal Surfaces in Porous Media,'' J. Thermophysics, **12**(3), pp. 449–452.

[28] Chikh, S., Boumedien, A., Bouhadef, K., and Lauriat, G., 1995, ''Analytical Solution of Non-Darcian Forced Convection in an Annular Duct Partially Filled With a Porous Medium,'' Int. J. Heat Mass Transfer, **38**, pp. 1543–1551.

Time Scales for Unsteady Mass Transfer From a Sphere at Low-Finite Reynolds Numbers

Stanley J. Kleis
e-mail: kleis@uh.edu

Ivan Rivera-Solorio

Department of Mechanical Engineering,
University of Houston,
Houston, TX 77204-4006

The problem of unsteady mass transfer from a sphere that impulsively moves from rest to a finite velocity in a non-uniform concentration distribution is studied. A range of low Reynolds numbers (Re<1) and moderate Peclet numbers (Pe ranges from 5.6 to 300) is investigated (typical of the parameters encountered in anchorage dependent cell cultures in micro gravity). Using time scales, the effects of flow field development, concentration boundary layer development and free stream concentration variation are investigated. For the range of parameters considered, the development of the flow field has a negligible effect on the time variation of the Sherwood number (Sh). The Sh time dependence is dominated by concentration boundary layer development for early times and free stream concentration variations at later times. [DOI: 10.1115/1.1576813]

Keywords: *Forced Convection, Mass Transfer, Microgravity, Spheres, Unsteady*

1 Introduction

The physical problem motivating the present study is the unsteady transport of dissolved oxygen to freely suspended cell aggregates cultured in a bioreactor in the micro gravity environment of space. The anchorage dependent mammalian cells first form a confluent monolayer on the surface of small micro carriers (~170 μm dia.). Then, individual cell covered micro carriers attach to others to form aggregates, which remain nearly spherical for assemblages as large as 3 mm in diameter. The cell-covered micro carriers are suspended in the culture media by slowly stirring the bioreactor vessel. As the cells metabolize, they consume oxygen at a nearly constant rate for a concentration above a critical value, and below this value, the oxygen consumption decreases as a function of the oxygen concentration. This critical value is in general low (~1% air saturation) for animal cells [1]. Thus, a constant oxygen consumption rate is a reasonable model for the present purposes.

The aggregates of cells travel in the bioreactor with a local environment that is continuously changing. That is, the local flow field and concentration distribution vary with the position of the aggregate. These aggregates move with a relative velocity that corresponds to the difference of velocity between the fluid and the cells. In micro gravity, the Reynolds numbers (Re), based on relative velocity, that the aggregate experiences are in general low with values that range from $O(0.01)$ to $O(0.1)$ and with a Peclet number (Pe) that varies from $O(1)$ to $O(100)$.

This mass transport scenario in the bioreactor can be modeled as the transport of scalars to a sphere in a laminar flow field. The values of Re and Pe for the sphere are given by those corresponding to the position of the cell aggregate in the bioreactor. Thus, the problem is unsteady, three-dimensional, and with time dependent boundary conditions.

The problem of unsteady forced convection to a sphere for low Reynolds numbers has been studied for asymptotically large or small Pe. For low Pe, Konopliv and Sparrow [2] analyzed the unsteady heat transfer from a sphere in a steady laminar flow. They considered two types of transient problems started by suddenly exposing the sphere to a flow field of a different temperature: one when the sphere is isothermal but its temperature changes with time and the other when the temperature of the sphere is uniform and independent of time. For a uniform free stream velocity field, solutions for the Nusselt number (Nu) were obtained for small and large times. Feng and Michaelides [3] analyzed the problem of unsteady heat transfer on a sphere in a creeping flow for very low Pe. With a steady, fully developed flow with uniform temperature, a step change in temperature was imposed on the sphere and a singular perturbation technique was used to find the Nu expressions for asymptotically small and large times. For asymptotically large Pe, Konopliv and Sparrow [4] studied a similar problem of unsteady forced convection. The flow imposed on the sphere corresponded to the Stokes solution with a high Pe, which implies a thin thermal boundary layer. Solutions for Nu were obtained for large and small times for high Pe.

For situations where the Pe and the time are not asymptotically large or small, studies of unsteady forced convection are based upon numerical solutions [5–9]. Abramzon and Elata [5] numerically solved the case of unsteady heat transfer on a sphere for an intermediate Pe that ranges from 1 to 10,000. A steady creeping flow was assumed and the temperature of the sphere was allowed to vary with time. It was concluded that the characteristic time of heating or cooling of the sphere is comparable with the time required to stabilize the thermal field near the sphere. Thus, a quasi-steady approach would not be valid for this type of unsteady problem.

Bentwich et al. [6] made use of the Boussinesq transformation modified for time dependency to solve the time dependent diffusion equation in steady incompressible flow over a sphere. The authors were able to extend previous results restricted to high Peclet number to a range of Peclet numbers from 1 to 1000. The flow field was assumed irrotational and steady. The initial fluid temperature distribution was assumed uniform, with a step change in the (uniform) sphere temperature.

Brauer [7] presented a theoretical discussion of the mass transfer through the interface of a spherical fluid particle. Limiting cases of internal and external mass transfer resistance and zero motion systems were investigated. Creeping flow was assumed for the surrounding fluid.

Feng and Michaelides [8] numerically investigated the problem of heat transfer from a sphere with uniform surface temperature at high Reynolds and Peclet numbers. Transient results were computed for a step change in surface temperature with an initially uniform external temperature field.

Juncu [9] numerically solved the problem of heat and/or mass transfer from a sphere with internal circulation assuming creeping

---

Contributed by the Heat Transfer Division for publication in the JOURNAL OF HEAT TRANSFER. Manuscript received by the Heat Transfer Division July 12, 2002; revision received March 10, 2003. Associate Editor: A. F. Emery.

flow. The conjugate problem, where the transfer resistance inside and outside the sphere are comparable, was investigated assuming uniform temperature/concentration inside the sphere. Again, the transient results were computed for a step change in sphere temperature/concentration with an initially uniform external scalar field.

These studies provide some insight, but are different than, the problem of mass transport in the bioreactor. First, a different type of boundary condition is specified on the surface of the sphere. In the bioreactor, a uniform mass influx of oxygen on a spherical surface is used as a model to represent the oxygen consumption of the aggregate of cells [1,10]. Second, the local flow field that surrounds the sphere (aggregate) is unsteady and non-uniform. Third, in the bioreactor, the scalar concentration in the fluid approaching the sphere is varying with time. The evolution of the local flow field, the development of the concentration boundary layer and the motion of the sphere in a non-uniform concentration distribution can all affect the development of the local concentration distribution that surrounds the sphere.

In this study, the unsteady mass transport on a sphere is numerically solved for the range of parameters typically found in the bioreactor operated in space. The purpose is to analyze the different processes that affect the development of the concentration field. A better understanding of the fundamental processes of the unsteady mass transport to a sphere can be very helpful in the solution of the more complicate problem of mass transport in the bioreactor.

2 Mathematical Model

Consider a concentric spherical domain about the sphere that extends to a large, but finite distance. In this domain, the flow is assumed axisymmetric about an axis in the incoming flow direction, incompressible and laminar. The fluid is considered Newtonian with constant viscosity, μ, and density, ρ. The scalar is assumed dilute with a constant mass diffusivity, D_{AB}, that corresponds to a binary mixture. Based on these assumptions, the governing equation for the unsteady mass transport problem is

$$\frac{\partial c}{\partial t^*}+(\vec{v}\cdot\nabla)c=\mathrm{Pe}^{-1}\nabla^2 c, \tag{1}$$

where the dimensionless fluid velocity, $\vec{v}$, and concentration distribution, c, are normalized with the free stream velocity, U_∞, and concentration, C_∞, respectively. The nondimensional time, t^*, results from normalizing the time, t, with the time scale $t_{c1}=d/U_\infty$. The Peclet number is based on the diameter of the sphere and is defined as $\mathrm{Pe}=U_\infty d/D_{AB}$.

The average Sherwood number (Sh) is defined as $\overline{\mathrm{Sh}}=\overline{h}_m d/D_{AB}$, where the mass transfer coefficient is averaged over the surface of the sphere

$$\overline{h}_m=\frac{1}{A}\int_A \frac{q_w}{C_\infty(1-c_w)}\,dA. \tag{2}$$

The mass influx at the surface, q_w, and the free stream concentration, C_∞, are specified by the boundary conditions, while the concentration distribution at the surface of the sphere, c_w, has to be obtained from the solution of the mass transport problem.

3 Numerical Solution Technique

The spherical domain was divided into a finite number of small control volumes or elements and the governing equations were solved using a two-dimensional axisymmetric model. Figure 1 illustrates the meshed domain used in this simulation. The grid was uniformly spaced in the angular direction using 72 nodes. In the radial direction, an overall domain size of 12 sphere diameters in all directions from the center (24 radii) was selected with 22 nodes. The radial direction grid was non-uniform with a finer mesh close to the sphere and a coarser mesh in the outer region. A finer mesh was employed in order that the numerical scheme could resolve the higher gradients of velocity and concentration that exist in the region near the sphere. Tests were conducted in order to ensure that the domain size and the mesh resolution were appropriate (for details, see Rivera [10]).

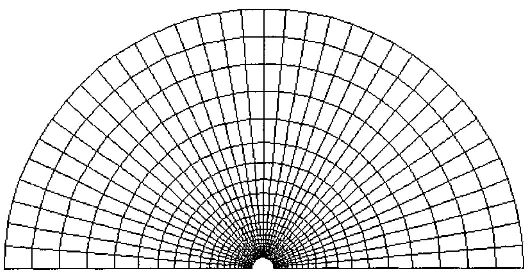

Fig. 1 Mesh of the computational domain

Figure 2 shows the effects of overall domain size on the distribution of surface concentration for the smallest and largest Pe cases. The vertical scale has been expanded to show the small differences between the two domain sizes. The surprisingly small differences result because, even for Pe=5.6, the concentration distribution reaches the free stream value over a much shorter distance than is required for the velocity distribution. The outer portion of the velocity distribution for the smaller domain is significantly distorted by the presence of the outer boundary condition. However, the velocity distribution over the region where the concentration varies is not much different from the larger domain results. Thus, the convective transport for the two cases is nearly the same.

For the constant wall mass flux boundary condition of the present study, the mass transfer results will be accurately determined when the surface concentration distributions are correct. Thus, Fig. 2 shows that either domain size would be adequate for computing mass transport. The larger domain was used for all results.

Figure 3 shows the dimensionless surface concentration distributions computed with two different mesh resolutions at Re=0.59 and Pe=236. Mesh resolution I had 22 radial nodes and 72 azimuthal nodes as described above. Mesh resolution II had 44 radial nodes and 144 azimuthal nodes. Again, the vertical scale has been expanded to show the small differences. The Re and Pe values are the largest of the present investigation, resulting in the steepest gradients of velocity and concentration. The results indicate that

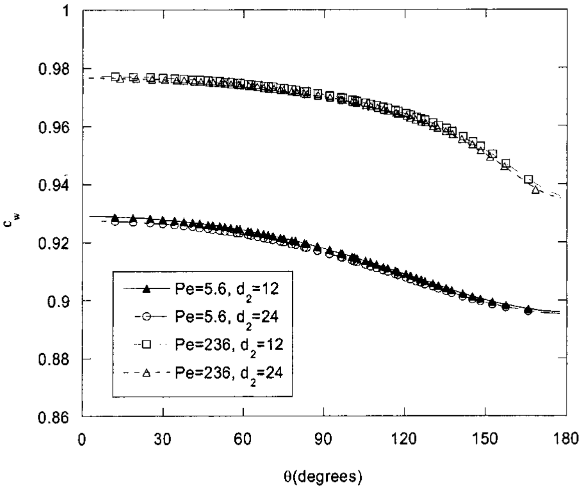

Fig. 2 Domain size effects on wall concentration distributions

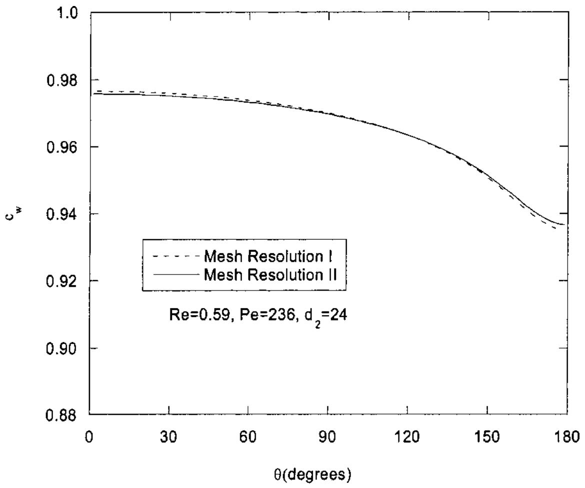

Fig. 3 Mesh resolution effects on wall concentration distribution

the mesh resolution I is sufficiently fine to resolve the velocity and concentration gradients. Mesh resolution I was used for all results.

The high Sc values of interest for the present study (Sc=380) limits the experimental results available in the literature to test the computational scheme. Kramers [11] in 1946 conducted heat transfer measurements on a sphere in a small oil tunnel. The Re range of that study was from ~0.5 to 12. The spherical domain described above was used to compute Sh over a similar Re range as shown in Fig. 4. Also shown is a heat transfer correlation of Whitaker [12], evaluated for Pr=380. The Whitaker correlation is shown only down to Re=3.5, since this is the lower limit of applicability for the correlation. The present results are generally in good agreement with Whitaker and Kramers. The departure of Whitaker is assumed to be indicative of applying the correlation at the lower limit for which it was developed. The agreement with Kramers is very good, with a slight departure at low Re. Rivera [10] was able to show, with a computational domain similar to Kramers' oil tunnel geometry, that the low Re difference is due to increased blockage effects from the tunnel.

The governing equations were solved using the CFD software package FLUENT™ that is based upon a Finite Volume Method. A second-order upwind scheme was used to interpolate the convective terms [13]. This scheme was chosen because it minimizes the false diffusion presented in other interpolation techniques such as the first order upwind. The diffusive term was approximated with a central difference method of second order. A finite difference second order implicit scheme was used to discretize the governing equations in time.

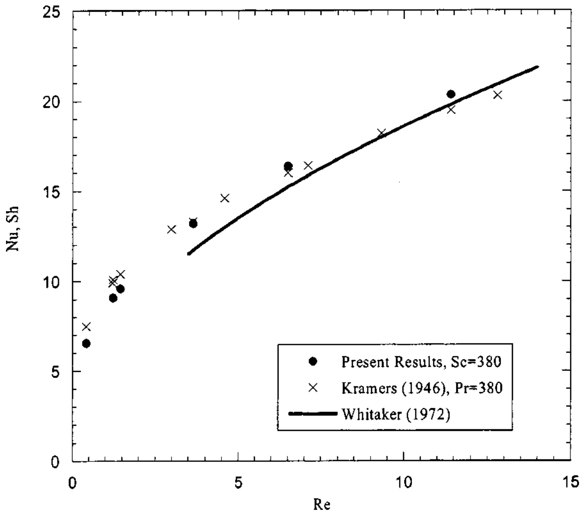

Fig. 4 Comparison of computed results with accepted results

The Navier-Stokes equations were solved on a staggered grid in order to avoid unrealistic results such as oscillation in pressure or fluid velocity. A scheme based upon the coupled pressure-velocity correction method was used to solve the momentum equations [14].

The Navier-Stokes equations and the scalar transport equation were solved in a sequential manner. That is, the flow field was calculated first and then the velocity values were used for the solution of the scalar transport equation. Iterations were performed until the normalized residual for the continuity equation was reduced by more than four orders of magnitude.

4 Results and Discussion

The general unsteady mass transport problem can be thought of as having three different mechanisms that affect the concentration field that surrounds the sphere. The first mechanism is time dependent transport due to the development of an unsteady flow field. The second mechanism is changes of the concentration field resulting from unsteady scalar flux at the sphere surface. The third mechanism is variations of the free stream concentration boundary condition due to the motion of the sphere in a fluid environment with a non-uniform concentration distribution. To determine the importance of each of these mechanisms in the mass transport process for the range of parameters of interest, some special cases were investigated.

In the first case a sphere is located in a fully developed, steady flow field with a uniform initial concentration field. At time $t=0$, a step change in the uniform mass influx boundary condition is specified on the sphere surface. This case is used to study the development of the concentration field, independent of the flow field development (second mechanism).

The second case consists of the unsteady forced convection problem with a step change in the free stream velocity with the scalar flux at the surface held constant. The sphere is impulsively started at $t=0$ from rest to a finite velocity. The initial concentration distribution of this case is given by the solution of the steady mass diffusion problem. The boundary conditions are a constant and uniform mass influx of species on the sphere and a uniform free stream concentration in the far field. In this case, the importance of each of the three mechanisms is studied.

The third case is the same as the second case except that the velocity field undergoes a step change from rest to the steady state velocity field at $t=0$. This case, when compared with the second case, shows the dependence of the solution on the velocity field development.

The second and third cases were chosen to study the problem as the mass transport solution goes from one steady state solution to another. The zero velocity initial state was chosen to give the largest change possible between the initial and final states. A uniform initial concentration distribution was not used for this case because that problem results in a more complicated solution due to simultaneous changes in both velocity and mass influx boundary conditions at $t=0$. Also, other initial spatial distributions (other than that due to steady state diffusion) tend to have significant changes in the far field spatial distribution over the time it takes for the sphere to pass through the domain, thus further complicating the transient response.

Each of these three cases was studied over a typical range of Re and Pe values that the sphere experiences in the bioreactor in micro gravity. The results obtained from the numerical solution of the unsteady mass transport for each case are first presented then the importance of each of the mechanisms mentioned above is analyzed with the use of appropriate time scales.

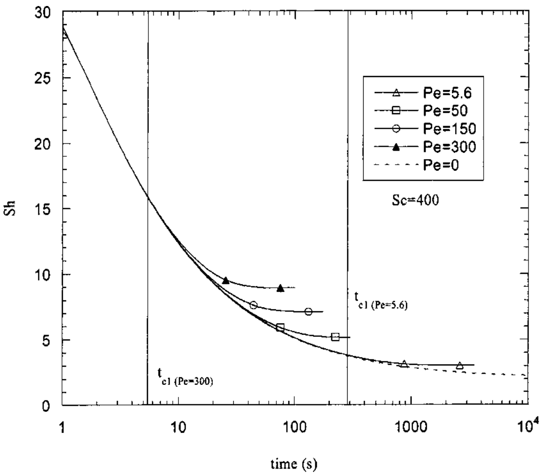

Fig. 5 Mass transport response for a step change in mass influx

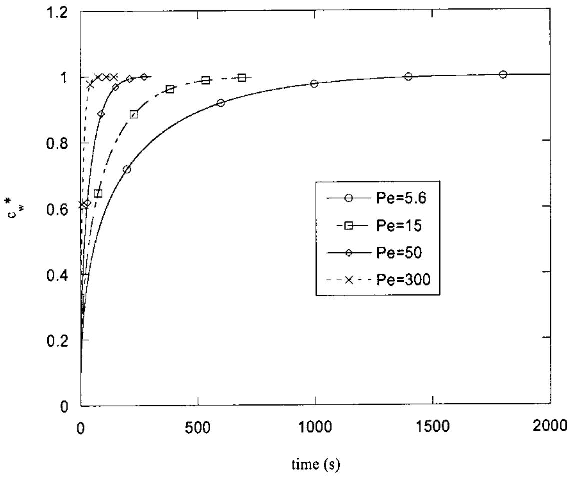

Fig. 6 Time response of the average surface concentration for a step change in the mass influx boundary condition

4.1 Step Change in Mass Influx (Case 1). Since the flow field is steady for this case, the unsteady mass transport problem is modeled with the scalar transport Eq. (1) with constant coefficients (with respect to time). Assuming the axis of symmetry to be the $\theta=0$ axis, the initial and boundary conditions are

$$c(r,\theta,t)=1, \quad t<0, \tag{3}$$

$$\nabla c(0.5,\theta,t)=\frac{dq_w}{C_\infty D_{AB}}\hat{r}, \quad t>0, \tag{4}$$

$$c(r_\infty,\theta,t)=1, \tag{5}$$

$$\frac{\partial c}{\partial \theta}(r,\theta,t)=0 \quad \text{at } \theta=0 \quad \text{and} \quad \theta=\pi. \tag{6}$$

For these equations, the radius, *r*, is scaled with the diameter, *d*, of the sphere. Condition (3) refers to an initial uniform concentration distribution at $t=0$. Condition (4) represents the step change in the surface mass influx of species. Condition (5) indicates a uniform concentration specified on the outer boundary of the domain. Condition (6) is a result of (assumed) symmetry in the problem.

The velocity field in Eq. (1) is obtained by solving the steady Navier-Stokes equations. The boundary conditions are: no-slip and no-penetration of fluid at the surface of the sphere and a normalized uniform velocity of the fluid imposed at the outer boundary of the domain in the $\theta=0$ direction.

4.1.1 Mass Transport Response. This mass transport problem is numerically solved for a Pe that varies from 5.6 to 300. For Sc of 400, the Re ranges from 0.014 to 0.75, respectively. Figure 5 shows the time variation of Sh for these Pe values and for the mass diffusion problem (Pe=0). The locations of one convective time scale $t_{c1}=d/U_\infty$ are indicated on the figure for Pe=5.6 and Pe=300. The Sh starts from a large value and decreases continuously until a steady state solution is approached. The initial large value for the Sh number can be understood by referring to its definition (see Eq. (2)). The Sh is proportional to the surface integral of the scalar flux divided by the difference between the wall and free stream concentrations $(1-c_w)$. After the uniform mass influx is imposed for $t>0$, the value of the concentration difference $(1-c_w)$ is very small resulting in large values for the Sh. As the concentration boundary layer develops, the Sh decreases because the value of $(1-c_w)$ increases.

Notice in Fig. 5 that the Sh curves for Pe=5.6 and Pe=300 collapse with the mass diffusion solution for times smaller than the corresponding convective time scale for each Pe. For times shorter than one convective time scale, diffusion dominates the convection in the overall mass transport process, and the growth of the concentration boundary layer is independent of the flow field. For times larger than the convective time scale, t_{c1}, the convection process starts to be important, and the Sh curves for Pe=5.6 and Pe=300 diverge from the one for Pe=0 approaching their steady-state values. The other Pe values considered also present similar behavior. The Sh converges to steady state faster as the Pe is increased because the concentration boundary layer is thinner for larger Pe and the free stream velocity is larger.

A similar behavior in the response of the Nu values, for the analogous heat transfer problem, was observed in the numerical solution of Abramzon and Elata [5]. However, the asymptotic steady state values for Nu were lower because a Dirichlet boundary condition was specified on the sphere instead of a Neumann boundary condition as in the present study.

4.1.2 Time Scales. For case 1, the sphere moves in a steady flow field with a uniform concentration distribution. That is, after the step change of uniform mass influx is imposed on the sphere, the concentration boundary layer grows with a concentration value at its edge equal to the constant free stream concentration. For this case, only time scales that correspond to the development of the concentration boundary layer need to be considered. Other time scales of the unsteady mass transport process due to the development of the flow field and the free stream variations of the concentration are not relevant for this case.

Two types of time scales for this case are considered. First, the time scales that are traditionally used to normalize the time for the unsteady mass transport problem are presented. Later, a new method to compute time scales that produce better results for larger times is presented.

Figure 6 shows the variation of the computed average wall concentration difference, c^*_w, with respect to the dimensional time, *t*, for different Pe values. The normalized wall concentration difference c^*_w is defined as

$$c^*_w=\frac{(1-c_w)}{(1-c_{w\_st})}, \tag{7}$$

where c_{w_st} correspond to the asymptotic steady state value of the surface concentration.

The results are presented in terms of the surface concentration difference as an alternative indication of the mass transport response. Since the free stream concentration, C_∞, and the mass flux, q_w, are constants, the variation of Sh with time is directly related to the variation of the surface concentration difference, c^*_w. For $t>0$, the c^*_w values increase at different rates until an

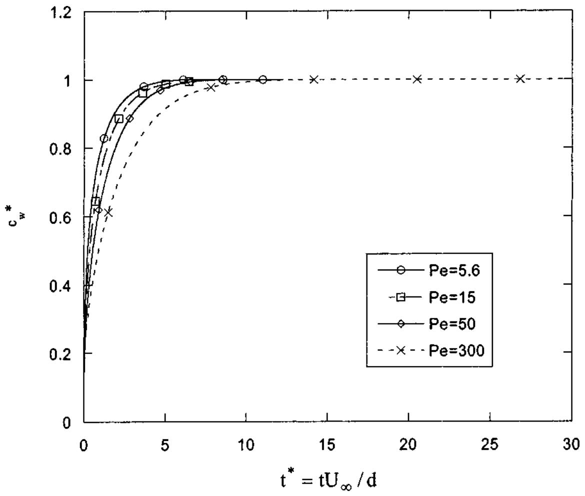

Fig. 7 Time response of the average surface concentration for a step change in the mass influx boundary condition using as a time scale $t_{cl}=dU_\infty$

asymptotic steady state value of 1.0 is reached. The c_w^* curves approach steady state faster as the Pe is increased.

Traditional Time Scales. For Pe>1 a natural choice for the time scale is the convective time scale $t_{c1}=d/U_\infty$. Figure 7 shows the variation of c_w^* as functions of dimensionless time $t^*=t/t_{c1}=tU_\infty/d$ for the same Pe values considered above.

The c_w^* variations with t^* show that $t_{c1}=d/U_\infty$ is not an appropriate time scale because the mass transport responses in t^* still show high dependence on Pe.

Konopliv and Sparrow [4] proposed a modified diffusive time scale to normalize the time for low Re and high Pe as $t_{d1}\propto(d^2/D_{AB})\mathrm{Pe}^{-2/3}$. This time scale is based upon an assumed linear variation of velocity in a thin scalar concentration boundary layer and is obtained by equating the diffusive and convective time scales at a point in the boundary layer development. This can also be written in the form of a convective time scale as $t_{c2}=(d/U_\infty)\mathrm{Pe}^{1/3}$. Figure 8 shows the variations of the wall concentration difference, c_w^*, with the nondimensional time $t^*=t/t_{c2}=(tU_\infty/d)\mathrm{Pe}^{-1/3}$ for the Pe values used above. The c_w^* curves for the different Pe values collapse to a single curve for a time $t^*<0.5$. This collapsing for the small times can be explained as follows: For small times, the development of the concentration boundary layer is again independent of the Pe because the mass transport process is dominated by pure diffusion. That is, the time scale t_{c2} has removed the Pe dependence introduced by the Pe dependent scaling of c_w^*. For larger times, $(t^*>0.5)$, convection start to be important and the development of the concentration boundary layer depends upon the values of Pe. For the low Re situations of the present study, the dimensionless velocity field remains constant and the concentration fields change with Pe. Thus, the time scale t_{c2} cannot predict well this dependence on Pe, resulting in a convergence of c_w^* to steady state at different rates for larger times. This is a manifestation of the nonlinear velocity distribution over the concentration boundary layer thickness, where linearity was assumed in the original model. As the Pe is reduced, the concentration boundary layer thickness increases and nonlinearity of the velocity profile becomes more important.

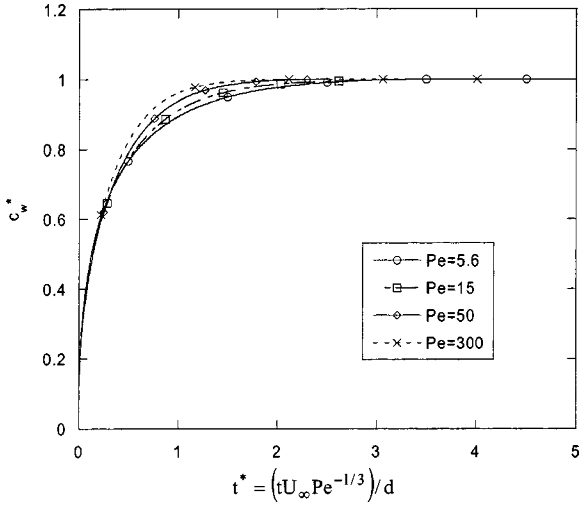

Fig. 8 Time response of the average surface concentration for a step change in the mass influx boundary condition using as a time scale $t_{c2}=(dU_\infty)\mathrm{Pe}^{-1/3}$

Modified Convective Time Scale. In order to find a time scale that is more appropriate for large times and lower Pe, the following approach was taken. Consider the two processes that determine the development of the concentration boundary layer for this transient problem: diffusion that produces an increase in the thickness of the concentration boundary layer and convection that tends to reduce it. Two different time scales exist for these competing processes. A diffusive time scale $t_{d2}=\delta_m^2/D_{AB}$ defined in terms of the thickness of the concentration boundary layer δ_m and the mass diffusivity D_{AB}, and a convective time scale $t_{c3}=d/U_{\delta m}$, where d is the sphere diameter and $U_{\delta m}$ is the velocity at the edge of the mass boundary layer. Equating the time scales t_{d2} and t_{c3} at some position in the boundary layer, an equation in terms of Pe is obtained as

$$\mathrm{Pe}^{-1}=\left(\frac{\delta_m}{d}\right)^2\left(\frac{U_{\delta m}}{U_\infty}\right). \tag{8}$$

For low Reynolds numbers (Re<1), the velocity field can be obtained from the Stokes' solution (see for example Eq. (5) in Abramzon and Elata [5]). The ratio of velocity $U_{\delta m}/U_\infty$ at a location $\theta=\pi/2$ is given as

$$\frac{U_{\delta m}}{U_\infty}=f(z)=\frac{8z^3+9z^2+3z}{8(z+0.5)^3}, \tag{9}$$

where $z=\delta_m/d$. Using Eq. (9), Eq. (8) can be written

$$\mathrm{Pe}^{-1}=\frac{z^2(8z^3+9z^2+3z)}{8(z+0.5)^3}. \tag{10}$$

The following procedure was used to compute the characteristic time scale of this unsteady problem. First, z is computed from Eq. (10) for a given Pe. Second, $U_{\delta m}$ is determined from Eq. (9) for this z. Third, the computed time scale t_{c3} is obtained as

$$t_{c3}=d/U_{\delta m}=d/U_\infty f(z). \tag{11}$$

Figure 9 shows the wall concentration difference, c_w^*, variation with the dimensionless time $t^*=t/t_{c3}$ for each Pe. The surface concentration differences, c_w^*, collapse into a single curve for the different Pe for $t^*>1$. Thus, the computed time scale effectively removes the Pe dependence in c_w^* for large times. For smaller times $(t^*<1)$, diffusion dominates convection and the curves depart from a single curve.

In the proposed method the variation of the fluid velocity within the concentration boundary does not have to be linear. That is, the computed time scale t_{c3} is not restricted to asymptotically high Pe values. Since, the Stokes' solution was used to obtain the velocity $U_{\delta m}$, the method applies for Re<1 (a maximum Re of 0.75 was used in the computation of c_w^*).

For the moderate Pe range of interest, the proposed method improves the collapse at larger times, but worsens the collapse at

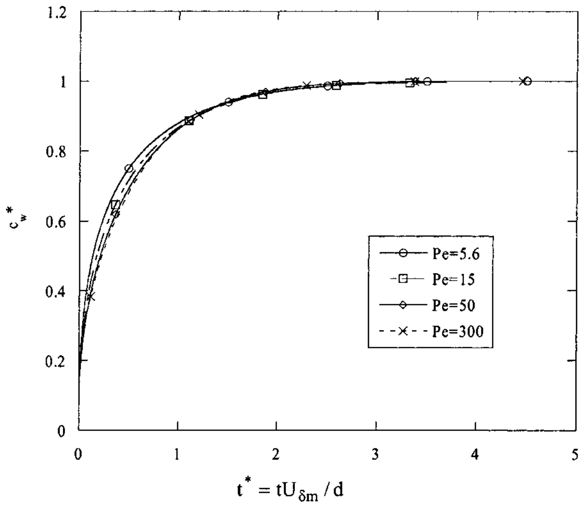

Fig. 9 Time response of the average surface concentration for a step change in the mass influx boundary condition using the computed time scale $t_{c3}=d/U_{\delta m}$

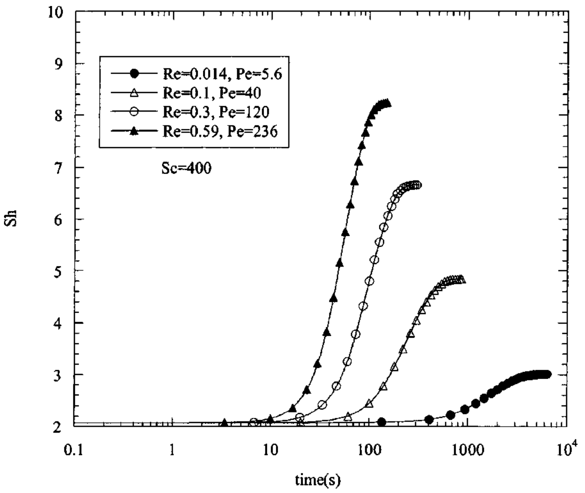

Fig. 10 Mass transport response for a step change in the free stream velocity

shorter times. This is a result of the concentration boundary layer passing through a diffusion dominated growth process for short times, followed by a Pe dependent growth at larger times. For the limited Re and Pe range of interest, no single time scale (itself independent of time) can collapse both the diffusion dominated and the convection dominated processes.

4.2 Step Changes in Velocity (Cases 2 and 3). The problem of unsteady mass transport is solved for a sphere that is impulsively moved from rest. These cases are modeled with the unsteady scalar transport equation, Eq. (1). For case 2, the velocity field is determined from the solution of the Navier-Stokes equation for a step change in the free stream velocity from $U_\infty=0$ at $t=0$ to $U_\infty=\text{constant}$ for $t>0$. For case 3, the step change in the velocity field is from rest to the steady Stokes solution at $t=0$. The concentration field boundary conditions are a uniform mass influx on the sphere and a uniform free stream concentration far from the sphere (on the outer domain boundary). The initial concentration field corresponds to the distribution of the steady mass diffusion problem. A sufficiently large domain was chosen in order to have a solution that is insensitive to the size of the domain.

The concentration field development for case 2 is subject to all three of the mechanisms identified above: flow field development, concentration boundary layer development, and free stream concentration variations (in the sense that a new boundary layer is developing within an existing nonuniform concentration field). Case 3 is a nonphysical situation that, when compared with case 2, is used to isolate the effects of velocity field development.

4.2.1 Mass Transport Response. The response of the Sh to a step change of the free stream velocity (case 2) is shown in Fig. 10 for a series of Pe values that range from Pe=5.6 to Pe=236. The Sh responses start from the diffusion value of 2 for all the Pe considered. After the sphere is impulsively moved, the difference $(1-c_w)$ decreases with time resulting in a continuous increase in the Sh until a steady state value is reached. A more rapid convergence of the Sh to steady state is obtained as the value of the Pe is increased.

4.2.2 Time Scales. By defining appropriate time scales for the different development mechanisms, it is possible to assess the relative importance of each mechanism in the overall Sh time dependence.

Velocity Field Development Time Scale. To characterize the evolution of the flow field (first mechanism), the diffusive time scale, $t_{fd}=\delta_m^2/\nu$, is selected as representative of the growth of the viscous region. This is appropriate because, for these low Re values, the inertia effects are small compared with the viscous and pressure gradient effects. Thus, the velocity field development is dominated by viscous diffusion. Note that δ_m was selected as the characteristic length for t_{fd} because, for the large Sc considered (Sc=400), the thickness δ_m of the concentration boundary layer is small compared with the thickness of the viscous region. Thus, the part of the flow field that affects the development of the local concentration distribution is primarily that near the sphere, within a distance δ_m.

Figure 11 shows the transient response of the Sh computed for cases 2 and 3 for Pe of 40 and 236. For a Sc of 400, these Pe values correspond to Re of 0.1 and 0.59, respectively ($U_\infty=2.95\times10^{-4}$ m/s for Re=0.59 and $U_\infty=5\times10^{-5}$ m/s for Re=0.1). The time has been normalized with a convective time scale $t^*=t/t_{c1}$. The effect of the velocity field development on the mass transport response is very small. This difference is small because the ratio of t_{fd}/t_{c1} is small. For Re=0.59 and 0.1, the ratios of t_{fd}/t_{c1} are 0.009 and 0.006, respectively. Thus, the velocity field

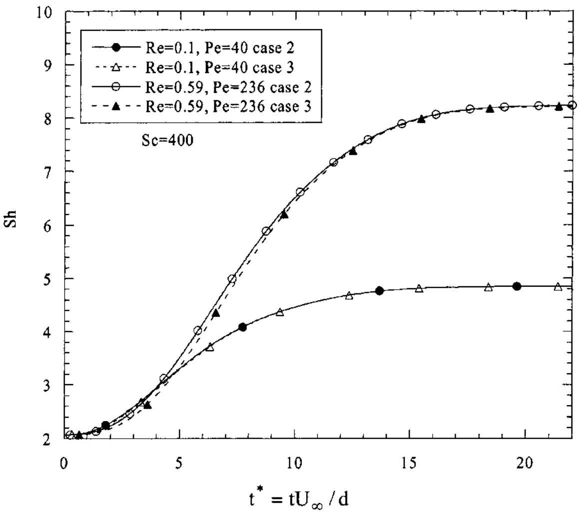

Fig. 11 Effect of the evolution of the flow field on the mass transport response. Case 2: solution for a step change in velocity. Case 3: solution using a steady Stokes flow field for $t>0$. An initial diffusion distribution is specified for both simulations.

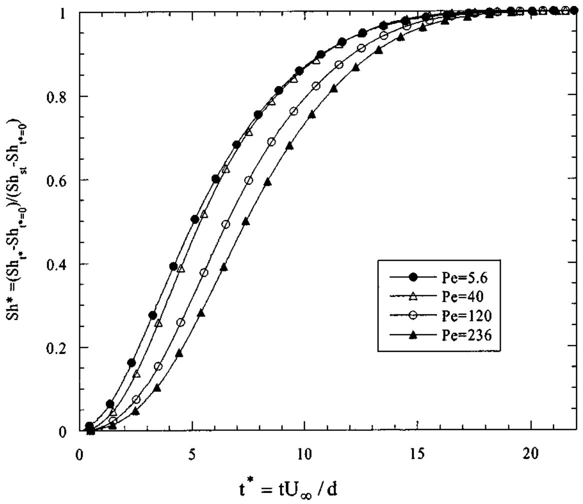

Fig. 12 Response of the normalized Sherwood number using a convective time scale, $t_{cl}=dU_\infty$

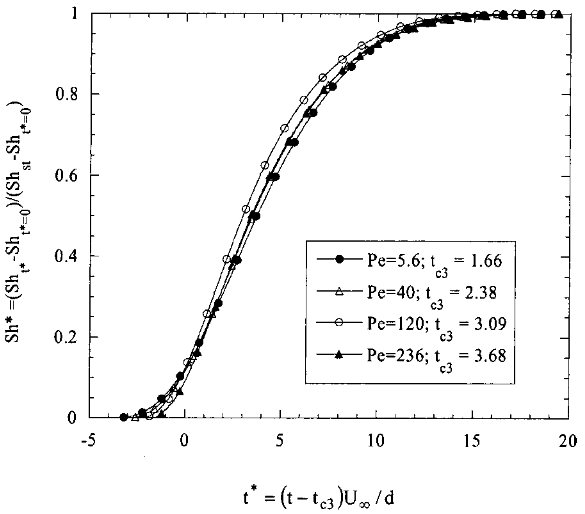

Fig. 13 Response of the normalized Sherwood number using a convective time scale with time delay

development time is much shorter than one convective time scale and differences in the velocity field development cause negligible delays in the concentration field development.

Free Stream Concentration Time Scale. The third mechanism for this case corresponds to variations in the local concentration field due to the motion of the sphere through the initial diffusion concentration distribution. The time scale of this process is just the convective scale t_{c1}. A value of $6.35t_{c1}$ corresponds to the time for the sphere moving at U_∞ to travel a radial distance from the center of the sphere to the position where the initial concentration is 99% of the free stream concentration.

The transient response of the Sh for different Pe values using this convective time scale is shown in Fig. 12. Here, the Sh has been normalized as

$$\mathrm{Sh}^* = \frac{\mathrm{Sh}_{t*} - \mathrm{Sh}_{t*=0}}{\mathrm{Sh}_{st} - \mathrm{Sh}_{t*=0}}, \tag{12}$$

where $t^* = t/t_{c1} = tU_\infty/d$. For $t^* > 0$ the Sh* increase at different rates until they approach a value of Sh*=1 for $t^* > 22$. In this dimensionless time, the Sh* values approach steady state faster as the Pe decreases. Also, for Pe=40 the curve for Sh* is nearly the same as for Pe=5.6 while the curves for higher Pe are distinct.

For low Pe values, the concentration boundary layer is thick and the free stream velocity is a good estimation of the characteristic velocity $U_{\delta m}$. Therefore, the Sh curves tend to collapse with the convective time scale. For higher Pe values, the concentration boundary layer becomes smaller relative to the hydrodynamic boundary layer. Thus, the velocity ratio at the edge of the concentration boundary layer, $U_{\delta m}/U_\infty$ becomes smaller as the Pe increases. In this case, the time scale for the growth of the concentration boundary layer, $t_{c3} = d/U_{\delta m}$, increases relative to the time scale associated with the effect on the local concentration field due to the motion of the sphere in the nonuniform concentration distribution, $t_{c1} = d/U_\infty$. Thus, the higher Pe cases are delayed in time relative to the low Pe cases.

Figure 13 is a plot of Sh* variations as functions of dimensionless time after subtracting the time for boundary layer development, $t^* = (t - t_{c3})/t_{c1}$. The times for concentration boundary layer development, t_{c3}, are shown for each Pe. The near collapse of the Sh* to one curve indicates that the choice of a convective time scale with a Pe dependent delay, for concentration boundary layer development, is a realistic model for this situation. This can also be supported by the collapse of the Sh* plots for times less than t_{c3} when plotted as functions of $t^* = t/t_{c3}$ (not shown).

This type of response to a time varying free stream concentration (at the edge of the concentration boundary layer) can also be viewed as follows. In a time dependent boundary layer problem, it takes some time for concentration variations at the outer edge of the concentration boundary layer to propagate through the layer to the sphere surface. This time is a diffusion time through the boundary layer thickness, $t_{d2} = \delta_m^2/D_{AB}$, which must be equal to the associated convective time scale $t_{c3} = d/U_{\delta m}$. This type of time delay is typical of first order systems with time dependent boundary conditions.

5 Conclusions

The transient mass transport to a sphere starting at one steady state condition and moving to a second steady state condition in response to a step change in velocity has been studied. Special cases have been presented to illustrate the relative importance of the three mechanisms: concentration boundary layer development, velocity field development, and time dependent free stream concentration field. From these cases, the following conclusions can be drawn.

There is more than one time scale associated with the development of the concentration boundary layer. For smaller times, diffusion is the dominant process and the growth of the concentration boundary layer is independent of Pe. For longer times, convection becomes important and the mass transport response depends upon the Pe. A time scale based upon a convection velocity at the edge of the concentration boundary layer is presented that provides good collapse of the time dependent surface concentration curves for different Pe. The computed time scales using this method are valid for a larger range of Pe values than those obtained in previous investigations, because the variation of the fluid velocity within the concentration boundary layer is not assumed linear. Although, the Stokes solution is used in this method, the computed time scales are shown to provide good results for Re up to 0.75.

For the Re and Pe considered in this study (Re varies from $O(0.01)$ to $O(0.1)$ and Pe does from $O(1)$ to $O(100)$), the evolution of the flow field has a negligible effect in the time response of the Sherwood number. That is, the flow field develops much faster than the concentration field.

For this problem and this range of parameters, the unsteady mass transport process is primarily a function of two convective time scales. For short times, the dominant time scale is that associated with the concentration boundary layer development. For longer times, the time scale associated with the free stream concentration variation (the convective time scale) is dominant. By subtracting the time for concentration boundary layer development, the results scale well with a simple convection time.

Acknowledgment

This work was supported in part with funds from Universities Space Research Association subcontract #9920-213-33. The authors would like to express their appreciation to Dr. Steve Gonda, the NASA/JSC Biotechnology group, and the bioreactor development team for their continued support and technical assistance.

Nomenclature

A = Sphere surface area, [m^2]
c = Scalar concentration normalized by C_∞
c_w^* = Normalized surface concentration difference, $c_w^* = (1 - c_w)/(1 - c_{w\_st})$
C_∞ = Free stream concentration, [kg/m^3]
D_{AB} = Mass diffusivity of species A into fluid media B, [m^2/s]
d = Sphere diameter, [m]
d_2 = dimensionless domain outer diameter
$\bar{h}$ = Surface-average heat transfer coefficient, [W/m^2 K]
$\bar{h}_m$ = Surface average mass transfer coefficient, [m/s]
Nu = Nusselt number, $\bar{h}d/\alpha$
Pe = Peclet number, dU_∞/D_{AB}
Pr = Prandtl number, ν/α
q_w = Mass flux of species at the sphere surface, [kg/m^2 s]
Re = Sphere Reynolds number, dU_∞/ν
r = Radial coordinate normalized by d
$\hat{r}$ = unit vector in r direction
Sc = Schmidt number, ν/D_{AB}
Sh = Sherwood number, $\bar{h}_m d/D_{AB}$
Sh* = Normalized Sherwood number, $\text{Sh}^* = (\text{Sh}_{t^*} - \text{Sh}_{t^*=0})/(\text{Sh}_{st} - \text{Sh}_{t^*=0})$
t = Time, [s]
t^* = Time normalized by a time scale
t_{c1} = Convective time scale, d/U_∞
t_{c2} = Convective time scale, $(d/U_\infty)\text{Pe}^{1/3}$
t_{c3} = Convective time scale, $d/U_{\delta m}$
t_{d1} = Diffusive time scale, $(d^2/D_{AB})\text{Pe}^{-2/3}$
t_{d2} = Diffusive time scale, δ_m^2/D_{AB}
t_{fd} = Viscous diffusive time scale, δ_m^2/ν
U_∞ = Free stream fluid velocity, [m/s]
$U_{\delta m}$ = Velocity at the edge of the concentration boundary layer at $\theta = \pi/2$
$\vec{v}$ = Fluid velocity normalized by U_∞
z = δ_m/d

Greek Letters

α = Thermal diffusivity, [m^2/s]
δ_m = Concentration boundary layer thickness, [m]
μ = Fluid dynamic viscosity, [kg/m s]
ν = Fluid kinematic viscosity, [m^2/s]
ρ = Fluid density, [kg/m^3]
θ = Polar coordinate, [rad]

Subscripts

st = Steady state value
w = Surface or wall value
∞ = Free stream value for viscous region
δm = Concentration boundary layer thickness value

References

[1] Miller, W. M., Wilke, C. R., and Blanch, H. W., 1987, ‘‘Effects of Dissolved Oxygen Concentration on Hybridoma Growth and Metabolism in Continuous Culture,’’ J. Cell Physiol., **132**, pp. 524–530.
[2] Konopliv, N., and Sparrow, E. M., 1971, ‘‘Temperature and Heat Transfer History of a Solid Body in Forced Convection Flow,’’ Q. Appl. Math., **29**, pp. 225–235.
[3] Feng, Z.-G., and Michaelides, E. E., 1996, ‘‘Unsteady Heat Transfer From a Sphere at Small Peclet Numbers,’’ ASME J. Fluids Eng., **118**, pp. 96–102.
[4] Konopliv, N., and Sparrow, E. M., 1972, ‘‘Unsteady Heat Transfer and Temperature for Stokesian Flow About a Sphere,’’ ASME J. Heat Transfer, **94**(3), pp. 266–272.
[5] Abramzon, B., and Elata, C., 1984, ‘‘Unsteady Heat Transfer From a Single Sphere in Stokes Flow,’’ Int. J. Heat Mass Transfer, **27**(5), pp. 687–695.
[6] Bentwich, M., Szwarcbaum, G., and Siderman, S., 1965, ‘‘Time-Dependent Temperature Distribution in Flow Past a Sphere,’’ ASME Paper 65-HT 38.
[7] Brauer, H., 1978, ‘‘Unsteady State Mass Transfer Through the Interface of Spherical Particles-II,’’ Int. J. Heat Mass Transfer, **21**, pp. 455–465.
[8] Feng, Z.-G., and Michaelides, E., 2000, ‘‘A Numerical Study on the Transient Heat Transfer From a Sphere at High Reynolds and Peclet Numbers,’’ Int. J. Heat Mass Transfer, **43**, pp. 219–229.
[9] Juncu, Gh., 2001, ‘‘Unsteady Heat and/or Mass Transfer From a Fluid Sphere in Creeping Flow,’’ Int. J. Heat Mass Transfer, **44**, pp. 2239–2246.
[10] Rivera, I. S., 2001, ‘‘Local Mass Transfer for Bioreactors in Micro-Gravity,’’ Ph.D. thesis, University of Houston, Houston, TX.
[11] Kramers, H., 1946, ‘‘Heat Transfer From Spheres to Flowing Media,’’ Physica XII, **2–3**, pp. 61–80.
[12] Whitaker, S., 1972, ‘‘Forced Convection Heat Transfer Correlations for Flow in Pipes, Past Flat Plates, Single Cylinders, Single Spheres, and for Flow in Packed Beds and Tube Bundles,’’ American Institute of Chemical Engineers Journal, **18**(2), pp. 361–371.
[13] Barth, T. J., and Jespersen, D., 1989, ‘‘The Design and Application of Upwind Schemes on Unstructured Meshes,’’ Technical Report AIAA-89-0366.
[14] Ferziger, J. H., and Peric, M., 1999, *Computational Methods for Fluid Dynamics*, second ed., Springer, New York.

Evaluation of Combined Heat and Mass Transfer Effect on the Thermoeconomic Optimization of an Air-Conditioning Rotary Regenerator

Rahim K. Jassim
e-mail: rkjassim@yahoo.com
College of Technology at Jeddah,
P.O. Box 42204, Jeddah 21541,
Kingdom of Saudi Arabia

The purpose of this paper is to demonstrate the importance of the use of the exergy analysis in the optimization of the geometry of a periodic-flow regenerator. The optimum geometry of the regenerator is determined using the unit cost of exergy of the warm air delivered as the objective function. The running cost is determined using different unit costs for the pressure component of exergy $\dot{E}^{\Delta P}$ *and the thermal component of exergy* $\dot{E}^{\Delta T}$*, which are evaluated separately. The ratio of the two unit costs has been calculated for an air-conditioning application in which the regenerator is used. A mathematical model of condensation, evaporation, thermal conductivity and heat transfer is presented for calculating the fluid and matrix temperatures effect on the regenerator performance. The governing differential equations have been formulated in terms of the characteristic dimensionless groups (*Π_t*,* Λ_t*, and* Z_t*).* [DOI: 10.1115/1.1589504]

Keywords: Exergy Analysis, Heat Transfer, Heat Exchangers, Optimization, Regenerators, Thermoeconomic

Introduction

Regenerators are heat exchangers in which the hot and cold fluids flow alternately with as little physical mixing between the two streams as possible. The amount of energy transfer is dependent upon the geometry and thermal properties of the matrix as well as fluid and flow properties of the fluid stream.

Mass transfer plays an important role in many industrial processes such as removal of pollutants from plant discharge streams by absorption, the stripping of gases from waste water, the diffusion of adsorbed substances within the pores of activated carbon, air conditioning, etc.

Condensation can occur in regenerators when the matrix temperature is below the dew-point temperature of inlet exhaust air. The performance of a regenerator in which only sensible heat is transferred has been analyzed by several authors [1–3]. Hausen [2], van Leersum and Ambrose [4] studied the effect of both sensible heat and latent heat.

Hausen [2] has considered the problem of condensation in a regenerator using a graphical step by step process of solution based on the finite difference techniques. His method is approximate, and the only results given apply to extremely low temperature applications of the regenerator. van Leersum and Ambrose [4] have modeled condensation and evaporation processes in a regenerator using a finite temperature scheme. Although they described the mathematical model used, few details of the numerical model of finite difference scheme are given. They have also shown the effect of condensation and evaporation on the regenerator performance. van Leersum and Ambrose [4] have compared their numerical results for their model with experimental results and have shown good agreement. van Leersum [5] described a numerical method which allows accurate simulation of a counter flow thermal regenerator when condensation and evaporation occur.

This paper presents a numerical model of a periodic-flow regenerator with non-hygroscopic material in which condensation and evaporation occur. A finite difference method has been used for calculating the fluid and matrix temperatures and the moisture content distributions, and applied to the steady-state performance under conditions of finite rotational speed, finite heat conduction and finite mass transfer, and evaluated for different parameters. The thermal conductivity parameter Z_t, presented by Jassim [3] is used to determine the influence of thermal conductivity of the material on the regenerator performance and Π and Λ method is used to determine the effectiveness. The regenerator effectiveness has been evaluated over the following range of the dimensionless parameters.

$$k^*=C^*=(hA)^*=(A_s)^*=1.0$$

$$50.0\geqslant\Lambda_t\geqslant 0 \quad [\Lambda_t=(2\Lambda_c\Lambda_h/(\Lambda_c+\Lambda_h)]$$

$$50.0\geqslant\Pi_t\geqslant 0 \quad [\Pi_t=(2\Pi_c\Pi_h/(\Pi_c+\Pi_h)]$$

$$0.016\geqslant Z_t\geqslant 0$$

In this paper, the governing differential equations are formulated in terms of characteristics dimensionless groups Π_t, Λ_t, and Z_t.

The theory which has been developed by Jassim [6] and Kotas and Jassim [7] is applied here to an air-conditioning rotary regenerator to determine the effect of mass transfer on the performance and the cost ratio R_c.

Regenerator Performance

The overall regenerator effectiveness may be defined as,

$$\frac{1}{\mathrm{HEE}}=\frac{1}{2}\left(\frac{1}{\mathrm{HEE}_h}+\frac{1}{\mathrm{HEE}_c}\right) \tag{1}$$

For symmetric and balanced regenerator, the effectiveness for hot side and cold side are

---

Contributed by the Heat Transfer Division for publication in the JOURNAL OF HEAT TRANSFER. Manuscript received by the Heat Transfer Division September 10, 2002; revision received April 1, 2003. Associate Editor: J. N. Chung.

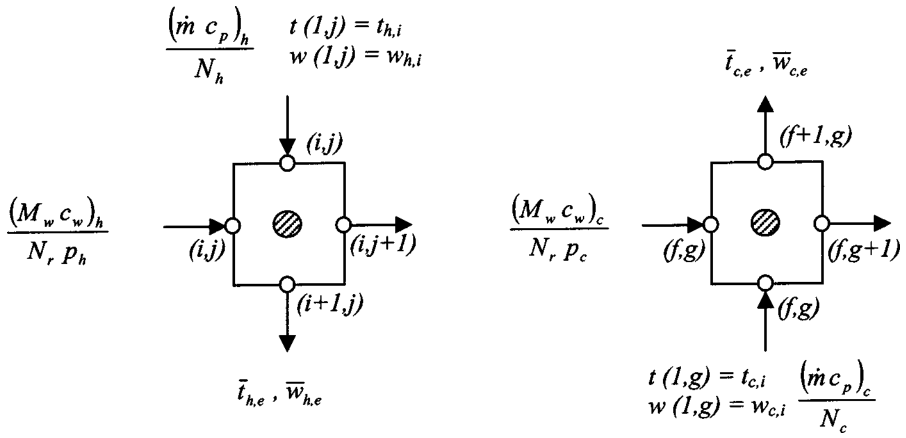

Fig. 1 Schematic representation heat exchange elements of a rotary regenerator

$$\mathrm{HEE}_h=\frac{(t_{h,i}-\overline{t_{h,e}})}{(t_{h,i}-t_{c,i})} \tag{2a}$$

$$\mathrm{HEE}_c=\frac{(\overline{t_{c,e}}-t_{c,i})}{(t_{h,i}-t_{c,i})} \tag{2b}$$

The overall humidity effectiveness is presented as a harmonic mean,

$$\frac{1}{\mathrm{HEE}_{hu}}=\frac{1}{2}\left(\frac{1}{\mathrm{HEE}_{hu,h}}+\frac{1}{\mathrm{HEE}_{hu,c}}\right) \tag{3}$$

For symmetric and balanced regenerator, the humidity effectiveness for hot side and cold side are [8],

$$\mathrm{HEE}_{hu,h}=\frac{w_{h,i}-\overline{w_{h,e}}}{w_{h,i}-w_{c,i}} \tag{4a}$$

$$\mathrm{HEE}_{hu,c}=\frac{\overline{w_{c,e}}-w_{c,i}}{w_{h,i}-w_{c,i}} \tag{4b}$$

where

$$\overline{w_{h,e}}=\frac{1}{N_h}\sum_{j=1}^{N_h} w_{h,e}(L1,j) \tag{5a}$$

$$\overline{w_{c,e}}=\frac{1}{N_c}\sum_{g=1}^{N_c} w_{c,e}(L1,g) \tag{5b}$$

and

$$L1=N_r+1$$

The Mathematical Model

The following assumptions have been used in the derivation of the mathematical model: (1) The convective mass transfer coefficient is constant throughout the regenerator; and (2) The transferred water vapor is condensed and evaporated at the same cross section viewed in the fluid flow direction.

The mass transfer rate equation for hot side can be expressed as [8]

$$\dot m_h=\frac{\partial w_h}{\partial y}=\frac{(\beta A)_h}{L}\Delta w_{av,h} \tag{6}$$

where

$$\beta_h=\frac{h_h}{\mathrm{Le}c_{p,h}}=h_m\rho \tag{7}$$

and Le is the Lewis relation and is equal to 1 [8].

($\Delta w_{av,h}$) represents the mean difference between the absolute humidity in the air and at the matrix surface which is given by

$$\Delta w_{av,h}=(1/2)[w_h(i,j)+w_h(i+1,j)]-(1/2)[w_{sa,h}(i,j)+w_{sa,h}(i,j+1)] \tag{8}$$

Considering the energy balance for an element as shown in Fig. 1, the energy transferred to the element by convection plus the energy accumulated in the element due to conduction, plus energy transferred to the element by mass transfer must equal the energy storage in the element. Thus,

$$t_h(i,j)-t_h(i+1,j)+\frac{k_h(A_s)_hN_r\Lambda_h}{2L(hA)_h}[T_{w,h}(i-1,j)+T_{w,h}(i-1,j+1)-2T_{w,h}(i,j)-2T_{w,h}(i,j+1)+T_{w,h}(i+1,j)+T_{w,h}(i+1,j+1)]+\frac{(h_v\dot m)_h\Lambda_h}{(hA)_h}[w_h(i,j)-w_h(i,j+1)]=\frac{N_h\Lambda_h}{N_r\Pi_h}[T_{w,h}(i,j+1)-T_{w,h}(i,j)] \tag{9}$$

The outlet fluid temperature, humidity and matrix temperature for an element on the side of Λ_h, can be obtained from the following simplified equation [6]

$$t_h(i+1,j)=R1t_h(i,j)+R2[T_{w,h}(i,j)+T_{w,h}(i,j+1)] \tag{10}$$

$$w_h(i+1,j)=R3w_h(i,j)+R4[w_{sa,h}(i,j)+w_{sa,h}(i,j+1)] \tag{11}$$

$$T_{w,h}(i,j+1)=R5t_h(i,j)+R6[w_h(i,j)-w_h(i+1,j)]-R7T_{w,h}(i,j)+R8[T_{w,h}(i-1,j)+T_{w,h}(i-1,j+1)+T_{w,h}(i+1,j)+T_{w,h}(i+1,j+1)] \tag{12}$$

Since the longitudinal heat transfer by conduction to the first row elements and transfer from the last row elements is zero, the matrix temperature at the first and last row can be stated as

$$T_{w,h}(1,j+1)=R9t_h(1,j)-R10T_{w,h}(1,j)+R11[w_h(1,j)-w_h(2,j)]+R12[T_{w,h}(2,j)+T_{w,h}(2,j+1)] \tag{13}$$

$$T_{w,h}(N_r,j+1)=R9t_h(N_r,j)-R10T_{w,h}(N_r,j)+R11[w_h(N_r,j)-w_h(N_r+1,j)]+R12[T_{w,h}(N_r-1,j)+T_{w,h}(N_r-1,j+1)] \tag{14}$$

Similarly, for an element on the side of Λ_c the rate equation is

$$\dot{m}_c=\frac{\partial w_c}{\partial y}=\frac{(\beta A)_c}{L}\Delta w_{av,c} \tag{15}$$

$$\beta_c=\frac{h_c}{\mathrm{Le}c_{p,c}}=h_m\rho \tag{16}$$

and $(\Delta w_{av,c})$ represents the mean difference between the absolute humidity in the air and at the matrix surface, is assumed to be

$$\Delta w_{av,c}=(1/2)[w_{sa,c}(f,g)+w_{sa,c}(f,g+1)]-(1/2)[w_c(f,g)+w_c(f+1,g)] \tag{17}$$

Substituting Eq. (16) into Eq. (15), we have

$$\dot{m}_c=\frac{\partial w_c}{\partial y}=\frac{(hA)_c}{L\mathrm{Le}c_{p.c}}\Delta w_{av,c} \tag{18}$$

The specific heat of cold side air can be expressed as

$$c_{p,c}=c_{p,a}+w_{av,c}c_{p,v} \tag{19}$$

$c_{p,c}$ and $c_{p,v}$, for the element on side of Λ_c are evaluated at $t_{av,c}$ where

$$w_{av,c}=\frac{w_{c,i}+\overline{w}_{c,e}}{2} \tag{20a}$$

$$t_{av,c}=\frac{t_{c,i}+\overline{t}_{c,e}}{2} \tag{20b}$$

Rearranging Eq. (18), we have

$$\frac{\dot{m}_c}{N_c}[w_c(f+1,g)-w_c(f,g)]=\frac{(hA)_c\Lambda_h}{N_cN_r\mathrm{Le}c_{p,c}}\Delta w_{av,c} \tag{21}$$

The energy balance for Λ_c side is

$$t_c(f+1,g)-t_c(f,g)+\frac{k_c(A_s)_cN_r\Lambda_c}{2L(hA)_c}[2T_{w,c}(f,g)+2T_{w,c}(f,g+1)-T_{w,c}(f-1,g)-T_{w,c}(f-1,g+1)-T_{w,c}(f+1,g)-T_{w,c}(f+1,g+1)]+\frac{(h_v\dot{m})_c\Lambda_c}{(hA)_c}\times[w_c(f+1,g)-w_c(f,g)]=\frac{N_c\Lambda_c}{N_r\Pi_c}[T_{w,c}(f,g)-T_{w,c}(f,g+1)] \tag{22}$$

The outlet temperatures and humidity of the elements on the side of Λ_c can be obtained as follows (see Appendix A)

$$t_c(f+1,g)=S1t_c(f,g)+S2[T_{w,c}(f,g)+T_{w,c}(f,g+1)] \tag{23}$$

$$w_c(f+1,g)=S3w_c(f,g)+S4[w_{sa,c}(f,g)+w_{sa,c}(f,g+1)] \tag{24}$$

$$T_{w,c}(f,g+1)=S5t_c(f,g)+S6[w_c(f,g)-w_c(f+1,g)]-S7T_{w,c}(f,g)+S8[T_{w,c}(f-1,g)+T_{w,c}(f-1,g+1)+T_{w,c}(f+1,g)+T_{w,c}(f+1,g+1)] \tag{25}$$

The matrix temperature for the last and first row can be stated as

$$T_{w,c}(1,g+1)=S9t_c(1,g)-S10T_{w,c}(1,g)+S11[w_c(1,g)-w_c(2,g)]+S12[T_{w,c}(2,g)+T_{w,c}(2,g+1)] \tag{26}$$

$$T_{w,c}(N_r,g+1)=S9t_c(N_r,g)-S10T_{w,c}(N_r,g)+S11[w_c(N_r,g)-w_c(N_r+1,g)]+S12[T_{w,c}(N_r-1,g)+T_{w,c}(N_r-1,g+1)] \tag{27}$$

Calculation Procedure

The governing differential equations are solved by finite difference technique following the approach proposed by Holmberg for mass transfer [8]. The solution has three boundary conditions as mentioned by Jassim [6] and the same procedures are used for the special case when $\Pi_h=\Pi_c=0$ and for the evaluation of the matrix temperature [3]. Another condition for absolute humidity is added here

$$w_h(1,j)=w_{h,i} \quad j=1,2\ldots N_h \tag{28}$$

$$w_c(1,g)=w_{c,i} \quad g=1,2\ldots N_c \tag{29}$$

The specific heat capacity of moist air should be evaluated at $t_{av,h}$ and $w_{av,h}$ (similar to Eqs. (20*a*) and (20*b*) except the subscript should be changed to "h". In order to find their values, it is necessary to calculate the average temperature and relative humidity. Therefore an estimate can be made by assuming the $t_{av,h}=t_{h,i}$ and $w_{av,h}=w_{h,i}$.

The absolute humidity of the air at the matrix surface is related to the surface temperature. When this temperature is lower than the dew-point temperature of the exhaust air $(d_{pt,h})$ the condensation will occur, the saturation absolute humidities are obtained from the following equations,

$$w_{sa,h}=0.622\frac{P_{vs,sh}}{P_{atm}-P_{vs,sh}} \tag{30}$$

$$w_{sa,c}=0.622\frac{P_{vs,sc}}{P_{atm}-P_{vs,sc}} \tag{31}$$

where

$P_{vs,s}$=the saturation pressure of water vapor at the matrix surface temperature

P_{atm}=atmospheric pressure (101.325 kPa)

The absolute humidity at the inlet states and the relative humidity can be obtained from

$$w_{h,i}=0.622\frac{P_{v,h}}{P_{\mathrm{atm}}-P_{v,h}} \tag{32}$$

$$\Phi_h=\frac{P_{v,h}}{P_{vs,h}} \tag{33}$$

$$w_{c,i}=0.622\frac{P_{v,c}}{P_{\mathrm{atm}}-P_{v,c}} \tag{34}$$

$$\Phi_c=\frac{P_{v,c}}{P_{vs,c}} \tag{35}$$

where

P_v=partial pressure of water vapor

P_{vs}=saturation pressure of water vapor at air temperature (ASHRAE fundamentals [9]).

The moisture of the exhaust air is transferred on the matrix surface by condensing, when the surface temperature for elements falls below the inlet dew-point temperature of the exhaust air $d_{pt,h}$. The surface temperature for element is expressed by

$$T_{w,hav}(i,j)=\frac{T_{w,h}(i,j)+T_{w,h}(i,j+1)}{2} \tag{36}$$

From this temperature, the saturation absolute humidity $w_{sa,hav}$ for the element would be evaluated, and is expressed by,

$$w_{sa,hav}(i,j)=\frac{w_{sa,h}(i,j)+w_{sa,h}(i,j+1)}{2} \tag{37}$$

If $T_{w,hav}(i,j)$ is less than $d_{pt,h}$, the absolute humidity for the next node $w_h(i+1,j)$ obtained from Eq. (11) after the saturation absolute humidity for both nodes are obtained from Eq. (37).

The gas temperatures for the first row on the side of Λ_h are known and the matrix temperatures for the first column are also known. The calculation begins with the first element in the first column, but from the finite temperature difference equations it is seen that, in order to solve it for the matrix outlet temperature for a particular element, it is necessary to know the matrix temperature of the next element. An estimate of these temperatures can be made by determining the temperature distribution for zero conduction [10], setting the constants (R8), (R12), (S8), and (S12) to zero. And it is necessary to know the air relative humidity for the next element to evaluate the average matrix temperature using Eq. (36). An estimate of this temperature can be made by assuming it to be equal to the first element temperature, then the absolute humidity for the second row calculated from Eq. (11). Then the matrix temperature for the next element which is assumed will be calculated from Eq. (12). Now the result should be compared with the first value, if the difference is nearly zero, then it is satisfied and calculation can be continued for next element and so on. Otherwise the first matrix temperature value that is assumed should be replaced by the new value, which is calculated form Eq. (12), and the calculations repeated. After the calculations are completed for this side the average temperature and the average relative humidity should be calculated and compared with the first values. If the differences are nearly zero, then the calculation with conduction can be carried out. Otherwise, the first values should be replaced by the new values and the calculations repeated. The problem is solved for no conduction case to obtain the initial estimate of matrix temperature for the problem with conduction. Now with this initial estimate of all element temperatures the calculations are carried out. Notably, the next element matrix temperature, which is used to calculate the average matrix temperature (see Eq. (36)) has been taken from the calculation with no conduction. Therefore, the next element matrix temperature which will be calculated from Eq. (12) should be compared with the first value. If the difference is nearly zero, then the calculation can be continued. Otherwise, it should be replaced by the new value and the calculation repeated. After several iterations, an energy balance will be made. Same calculation procedures mentioned above can be used for Λ_c.

The condensed water vapor begins to evaporate on the hot-fluid side as soon as the matrix surface temperature exceeds the $d_{pt,h}$.

The evaporation on the hot side is limited by [8]

$$w_h(i+1,j)=w_{h,i} \tag{38}$$

On the other hand, if the matrix temperature still includes some points lower than $d_{pt,h}$ (dew point temp.), these points will follow the matrix to the cold side and moisture from them will begin to evaporate. We assume that all the moisture deposited during the matrix heating period will completely evaporate on the cooling period. Or in other words, the amount of moisture deposited during a particular time interval in the hot period will evaporate during the corresponding time interval in the cold period. Thus [8],

$$\frac{\dot{m}_c}{N_c}\sum_{g=1}^{N_c}[w_c(f+1,g)-w_c(f,g)]=\frac{\dot{m}_h}{N_h}\sum_{j=1}^{N_h}[w_h(i,j)-w_h(i+1,j)] \tag{39}$$

where

$$f=1,2\ldots N_r$$

$$i=N_r+1-f$$

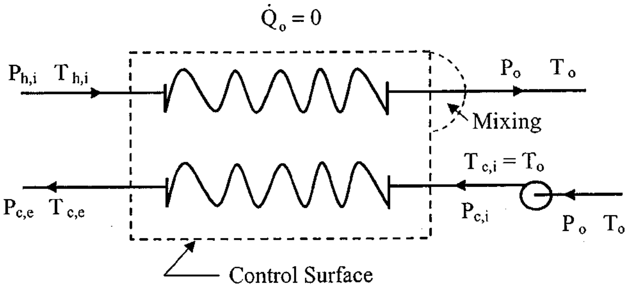

Fig. 2 Control surface used in the analysis of the regenerator

Exergy Analysis

A rotary regenerator used in an air-conditioning system is optimized using the unit cost of the energy of the warm air delivered as the objective function.

Objective Function. It is common practice in thermoeconomics to select the unit cost of the product $c^{\varepsilon}_{\mathrm{PROD}}$, as the objective function. The unit cost of the product is obtained by dividing the cost rate of operating of the regenerator by the output. The cost rate of operation consists principally of the cost of investment and the running cost. Because of lack of cost data, the cost of investment is excluded. Consequently, the unit cost of the product will be expressed as

$$c^{\varepsilon}_{\mathrm{PROD}}=\frac{\dot{C}_R}{\dot{E}_{\mathrm{out}}} \tag{40}$$

where $\dot{C}_R$ is the running cost rate, and $\dot{E}_{\mathrm{out}}$ is the exergy flow rate of the heated air.

Consider now the exergy balance for the control region, shown in Fig. 2, which comprises the matrix and the part of immediate environment where the waste gas rejected from the regenerator mixes with ambient air temperature.

$$\dot{E}^{\Delta T}_{h,i}+\dot{E}^{\Delta P}_{h,i}+\dot{E}^{\Delta T}_{c,i}+\dot{E}^{\Delta P}_{c,i}-[\dot{E}^{\Delta T}_{c,e}+\dot{E}^{\Delta P}_{c,e}+\dot{E}^{\Delta T}_{h,e}+\dot{E}^{\Delta P}_{h,e}]=\dot{I} \tag{41}$$

In this expression each exergy flux is split into the pressure component $\dot{E}^{\Delta P}$ and the thermal component $\dot{E}^{\Delta T}$. These are, respectively, zero when the stream pressure $P=P_o$ or temperature $T=T_o$. In this paper, P_o is considered as the exhaust pressure of both streams, and T_o as the exit temperature of the hot stream.

One of the LHS of Eq. (41) can now be identified as desired output and those remaining as the input. These are:

$$\dot{E}_{\mathrm{out}}=\dot{E}^{\Delta T}_{c,e} \tag{42}$$

and

$$\dot{E}_{in}=\dot{E}^{\Delta T}_{h,i}+\dot{E}^{\Delta T}_{c,i}+\dot{E}^{\Delta P}_{h,i}+\dot{E}^{\Delta P}_{c,i} \tag{43}$$

The idealization of the input and output terms carried out above is based on the same principles used in the formulation of the exergetic efficiency of a heat exchanger.

Since the input consists of both forms of exergy, $\dot{E}^{\Delta T}$ and $\dot{E}^{\Delta P}$, they will be allocated the appropriate unit costs $c^{\epsilon}_{\Delta T}$ and $c^{\epsilon}_{\Delta P}$, respectively. Hence, we get the cost rate of the input in the following form:

$$\dot{C}_{in}=c^{\epsilon}_{\Delta T}(\dot{E}^{\Delta T}_{h,i}+\dot{E}^{\Delta T}_{c,i})+c^{\epsilon}_{\Delta P}(\dot{E}^{\Delta P}_{h,i}+\dot{E}^{\Delta P}_{c,i}) \tag{44}$$

If the running cost $\dot{C}_R$ is considered equal to $\dot{C}_{in}$, the objective function may be written in a dimensionless form as a cost ratio.

$$R_c=\frac{c^{\epsilon}_{\mathrm{PROD}}}{c^{\epsilon}_{\Delta T}}=\frac{\dot{E}^{\Delta T}_{h,i}+\dot{E}^{\Delta T}_{c,i}+F_w(\dot{E}^{\Delta P}_{h,i}+\dot{E}^{\Delta P}_{c,i})}{\dot{E}^{\Delta T}_{c,e}} \tag{45}$$

where

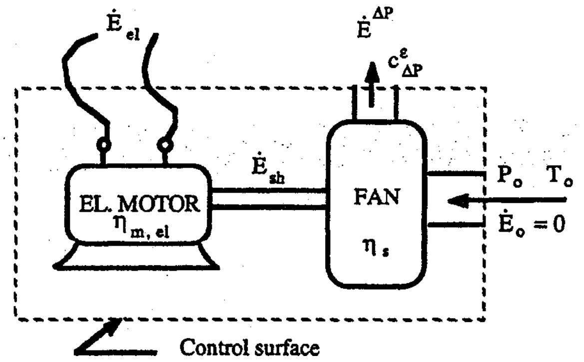

Fig. 3 The motor-fan assembly for generating the pressure component of exergy $\dot{E}^{\Delta P}$

$$F_w = \frac{c^{\epsilon}_{\Delta P}}{c^{\epsilon}_{\Delta T}} \tag{46}$$

Introducing the physical exergy relations of a perfect gas into Eq. (45), we get

$$R_c = \frac{t_{h,i} - T_o - T_o \ln\left(\frac{t_{h,i}}{T_o}\right) + t_{c,i} - T_o - T_o \ln\left(\frac{t_{c,i}}{T_o}\right)}{\overline{t_{c,e}} - T_o - T_o \ln\left(\frac{\overline{t_{c,e}}}{T_o}\right)} + \frac{F_w\left(\frac{\gamma-1}{\gamma}\right) T_o\left[\ln\left(1+\frac{\Delta P_h}{P_o}\right) + \ln\left(1+\frac{\Delta P_c}{P_o}\right)\right]}{\overline{t_{c,e}} - T_o - T_o \ln\left(\frac{\overline{t_{c,e}}}{T_o}\right)} \tag{47}$$

where $\Delta P_h = P_{h,i} - P_o$ and $\Delta P_c = P_{c,i} - P_o$.

Note that the exit temperature $\overline{t_{c,e}}$ is an average temperature, owing to the fact that the matrix temperature varies with angular coordinate.

To evaluate R_c, it is necessary to obtain the values of $\overline{t_{c,e}}$ and the pressure drops ΔP_h and ΔP_c. The value of $\overline{t_{c,e}}$ is evaluated using the presented finite difference technique, while the values of ΔP_h and ΔP_c are evaluated as the inlet pressure minus the exhaust pressure (P_o) for hot and cold sides.

Weighting Factor

As defined by Eq. (46), the weighting factor is a ratio of the unit cost of the pressure component of exergy, $c^{\varepsilon}_{\Delta P}$, to that the thermal component of exergy $c^{\varepsilon}_{\Delta T}$.

The weighting factor is calculated for an air-conditioning application in which the rotary regenerator is used. Expressions will be obtained in the following sub-sections for the two unit costs in terms of unit cost of electricity, c_{el}.

Determination of the Unit Cost of Exergy of Waste Air From an Air Conditioning System

A—The Unit Cost of the Pressure Component of Exergy, $c^{\varepsilon}_{\Delta P}$ The pressure component of exergy, which is delivered to the regenerator with the gas streams is generated, in the case of application considered here, in a motor-driven fan, as shown in Fig. 3. Consequently it can be obtained without a reference to the plant in which the regenerator is used. The exergetic efficiency of the fan is

$$\Psi = \frac{\dot{E}^{\Delta P}}{\dot{E}_{sh}} \tag{48}$$

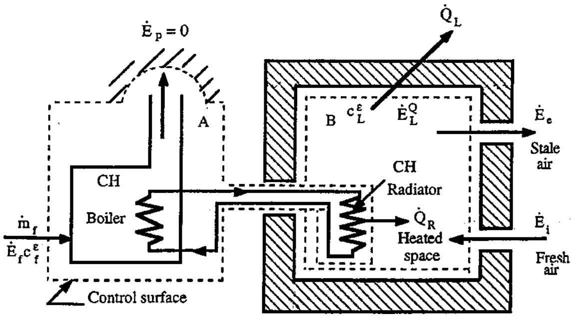

Fig. 4 Control surface of the air conditioning for determining the unit cost of waste air

This process takes place at near-environment temperature and therefore, as shown by Kotas [12], its exergetic efficiency is equal here to the fan isentropic efficiency. Hence,

$$\eta_s = \frac{\dot{E}^{\Delta P}}{\dot{E}_{sh}} \tag{49}$$

The mechanical-electrical efficiency of the motor is defined as follows:

$$\eta_{m,el} = \frac{\dot{E}_{sh}}{\dot{E}_{el}} \tag{50}$$

From Eqs. (49) and (50)

$$\dot{E}^{\Delta P} = \eta_s \eta_{m,el} \dot{E}_{el} \tag{51}$$

The exergy cost equation for motor-fan sub-assembly is

$$\dot{E}^{\Delta P} c^{\epsilon}_{\Delta P} = \dot{E}_{el} c_{el} + \dot{Z}_{M,F} \tag{52}$$

where $\dot{Z}_{M,F}$ is the investment cost rate for the motor-fan sub-assembly.

As shown by Tsatsaronis and Winhold [11] the magnitude of the capital investment rate of such fans is typically about 15% of the cost of electric input $\dot{E}_{el} c_{el}$, i.e.,

$$\dot{Z}_{M,F} = 0.15 \dot{E}_{el} c_{el} \tag{53}$$

Combining Eqs. (52) and (53)

$$c^{\epsilon}_{\Delta P} = 1.15 \frac{\dot{E}_{el}}{\dot{E}^{\Delta P}} c_{el} \tag{54}$$

Using Eq. (51), we get

$$c^{\epsilon}_{\Delta P} = \frac{1.15}{\eta_s \eta_{m,el}} c_{el} \tag{55}$$

Taking $\eta_{m,el} = 0.85$ and $\eta_s = 0.82$, we get

$$c^{\varepsilon}_{\Delta P} = 1.65 \ c_{el} \tag{56}$$

B—The Unit Cost of the Temperature Component of Exergy, $c^{\varepsilon}_{\Delta T}$. For the purpose of this analysis, the total system consisting of a central heating boiler and the heat space (a building), as shown in Fig. 4 is divided into two subregions,

- *Subregion A* consisting of the boiler and part of the heated space adjoining the CH radiator.
- *Subregion B* consisting of the interior of the heated building.

It is assumed that

1. $\dot{Q}_R$ crosses the central surface between subregions A and B at the temperature of the room T_R.

2. The temperature of the room varies negligibly and viscous dissipation due to air movement in the room also negligible. Hence, there are no irreversibilities taking place in subregion B.

Subregion A. Applying the exergetic cost balance to subregion A, we have

$$\dot{E}_R^Q c_R^\epsilon = \dot{E}_f c_f^\epsilon + \dot{Z}_A \tag{57}$$

At this stage it is necessary to consider the investment cost rate $\dot{Z}_A$. Then the capital investment rate is given by Kotas [12].

$$\dot{Z}_A = \frac{a^c C_A}{t_{op}} \tag{58}$$

where

a^c=capital-recovery factor

$$= \frac{i_r(1+i_r)^{\mathrm{NY}}}{[(1+i_r)^{\mathrm{NY}}-1]} \tag{59}$$

C_A=capital cost of boiler
t_{op}=time of operation
and
i_r=interest rate on the capital
NY=period of operation (years)
Assume

$$C_A = \mathrm{GBP1500}$$

$$t_{op} = 4000 \ \ \mathrm{h}$$

$$i_r = 15\%$$

$$\mathrm{NY} = 20 \ \ \mathrm{years}$$

Then, the investment rate $\dot{Z}_A$ can be obtained

$$\dot{Z}_A = \mathrm{GBP} \ \ 239.6 \ \ \mathrm{per\ \ year}$$

Assume also

$\dot{E}_f c_f^\epsilon$=GBP800 per year

$$\frac{\dot{Z}_A}{\dot{E}_f c_f^\epsilon} = \frac{239.6}{800} = 0.3 \tag{60}$$

Hence,

$$\dot{E}_R^Q c_R^\epsilon = 1.3 \dot{E}_f c_f^\epsilon \tag{61}$$

$$\dot{E}_R^Q c_R^\epsilon = 1.3 \dot{E}_f c_f^\epsilon \tag{62}$$

From the thermodynamic considerations,

$$c_R^\epsilon = 1.3 \frac{\dot{m}_f (NCV) \varphi}{\dot{E}_R^Q} c_f^\epsilon \tag{63}$$

The exergy flow associated with heat transfer is

$$\dot{E}_R^Q = \frac{\dot{Q}_R (T_R - T_o)}{T_R} \tag{64}$$

$$\eta_{\mathrm{comb}} = \frac{\dot{Q}_R}{\dot{m}_f (NCV)} \tag{65}$$

Substituting Eqs. (65) and (64) into (63), we get

$$c_R^\epsilon = 1.3 \frac{T_R \varphi}{\eta_{\mathrm{comb}} (T_R - T_o)} c_f^\varepsilon \tag{66}$$

If we let $T_R = 294.15$ K, $T_o = 273.15$ K, $\eta_{\mathrm{comb}} = 0.75$ and $\varphi = 1.04$, then,

$$c_R^\epsilon = 25.25 c_f^\epsilon \tag{67}$$

The unit price of fuel used in a power station $c_f^{\epsilon'}$, is lower than c_f^ϵ used in a boiler. Therefore, if it is 50% lower, then,

$$c_f^\epsilon = 1.5 c_f^{\epsilon'} \tag{68}$$

The unit cost $c_f^{\epsilon'}$ can be related to c_{el} by the fact that the cost of fuel is regarded as a proportion of total cost of electric generation. Kotas and Jassim [7] have shown the relation between $c_f^{\epsilon'}$ and c_{el} as

$$c_f^{\epsilon'} = 0.1467 c_{el} \tag{69}$$

Substituting Eqs. (68) and (69) into (67), then

$$c_R^\varepsilon = 25.25 \times 1.5 \times 0.1467 c_{el} = 5.556 c_{el} \tag{70}$$

Subregion B. If an exergetic cost balance is applied to subregion B, it can be shown that

$$\dot{E}_A c_A^\epsilon + \dot{E}_L^Q c_L^\epsilon = \dot{E}_R^Q c_R^\epsilon$$

Since

$$\dot{E}_A + \dot{E}_L^Q = \dot{E}_R^Q \quad (\dot{I}_R) = 0$$

and

$$c_A^\epsilon + c_L^\epsilon = c_R^\epsilon = c_{\Delta T}^\epsilon$$

Then

$$c_{\Delta T}^\epsilon = 5.556 c_{el} \tag{71}$$

Substituting Eqs. (56) and (71) into Eq. (46), we get

$$F_w = \frac{1.65 c_{el}}{5.556 c_{el}} = 0.3 \tag{72}$$

Numerical Example

In order to study how mass transfer and thermal conductivity in the fluid flow direction influence heat transfer, the temperature distribution has been calculated with and without mass transfer and thermal conductivity for the following parameter values and inlet air conditions which are typical to an air conditioning application.

Mass flow rate=$\dot{m}_h = \dot{m}_c = 40$ kg/s
Wheel diameter=$D_w = 4$ m
Regenerator length=$L = 0.666$ m

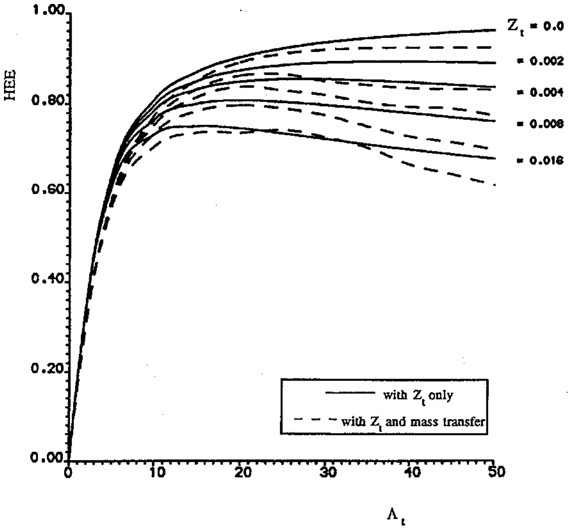

Fig. 5 Longitudinal heat conduction and mass transfer effect ($\Pi_t = 5$, $t_{h,i} = 293.15$ K, $t_{c,i} = 263.15$ K, $C^* = (hA)^* = (A_s)^* = 1$, $\Phi_h = 0.4$, and $\Phi_c = 0.8$)

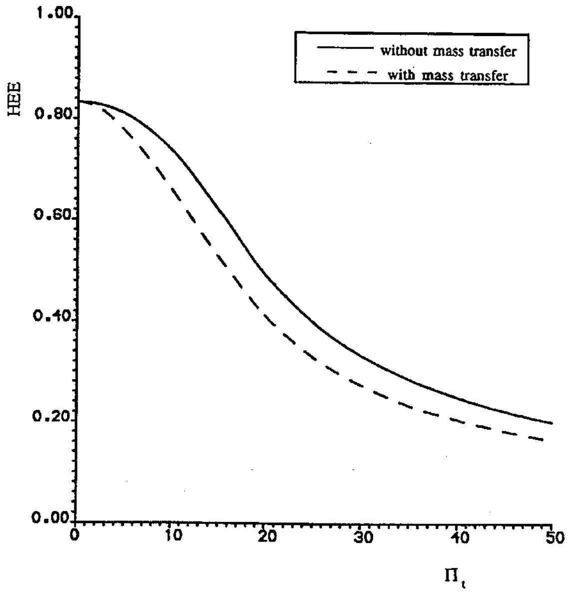

Fig. 6 Mass transfer effect ($\Lambda_t=10$, $t_{h,i}=293.15$ K, $t_{c,i}=263.15$ K, $C^*=(hA)^*=(A_s)^*=1$, $\Phi_h=0.4$, $\Phi_c=0.8$ and $Z_t=0$)

Matrix porosity$=\sigma=0.8$
Weighting factor$=F_w=0.3$
Inlet waste gas temperature$=t_{h,i}=293.15$ K
Inlet fresh air temperature$=t_{c,i}=263.15$ K
Atmospheric temperature$=T_o=273.15$ K
Hot side relative humidity$=\Phi_h=0.4$
Cold side relative humidity$=\Phi_c=0.8$
Material=mild steel

From the numerical example the inlet fresh air temperature is lower than the atmospheric temperature, then the thermal component of energy $\dot{E}^{\Delta T}_{c,i}$ has been considered.

Results and Discussion

The results were obtained using the finite difference technique that presented in this paper. From the results which were obtained, several general observations can be made.

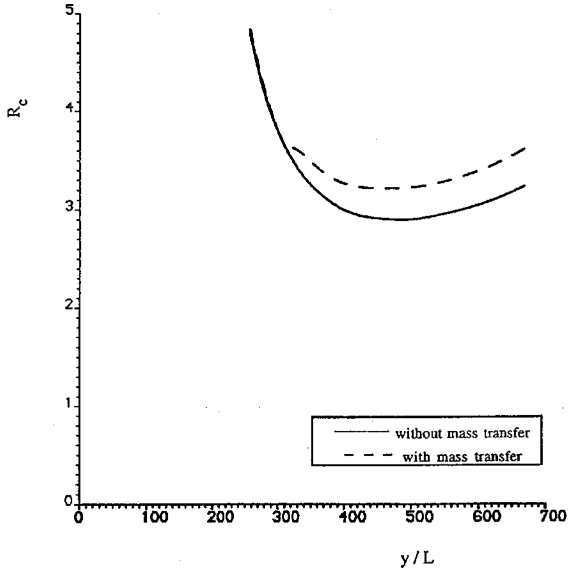

Fig. 7 Dependence of R_c on L/d

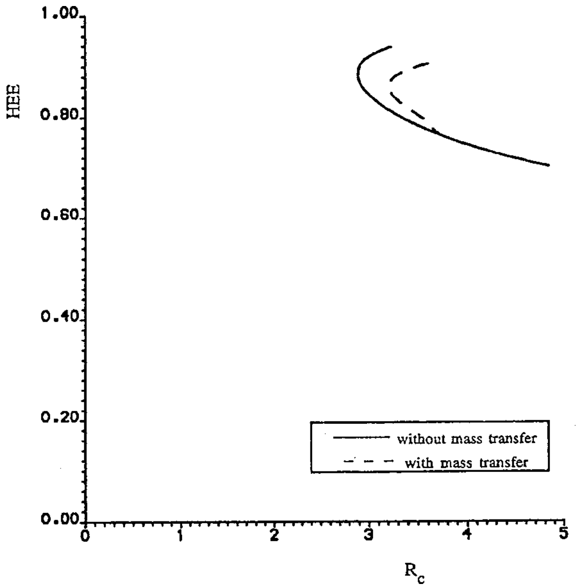

Fig. 8 Relationship between HEE and R_c

Figure 5 shows the effect of mass transfer and thermal conductivity at the same time for fixed values of all parameters. Clearly this figure shows that an increase in the conduction parameter Z_t will produce a reduction in the effectiveness. It also shows the effect of mass transfer on the regenerator performance. The effect of mass transfer is diminishing while the overall reduced length Λ_t is approaching zero.

Figure 6 shows that, for particular values of Λ_t and Z_t ($\Lambda_t=10$ and $Z_t=0$) with increasing the overall reduced period Π_t the

Table 1 The values of $(L/d)_{\mathrm{op}}$ $(\mathrm{HEE})_{op}$ and $(R_c)_{\min}$

$Z_t=0$					
without mass transfer			with mass transfer		
$(L/d)_{op}$	$(\mathrm{HEE})_{op}$	$(R_c)_{\min}$	$(L/d)_{op}$	$(\mathrm{HEE})_{op}$	$(R_c)_{\min}$
450.0	0.8843	2.891	450.0	0.8556	3.2129

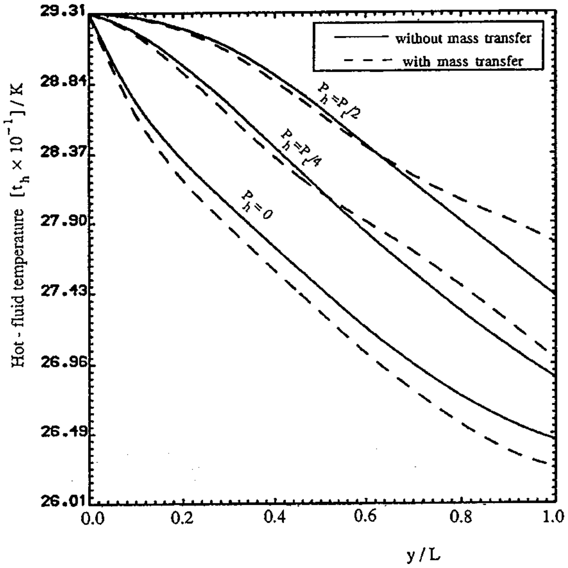

Fig. 9 The effect of moisture transfer on hot-fluid temperature distribution for ($\Lambda_t=10$, $\Pi_t=5$, $Z_t=0$)

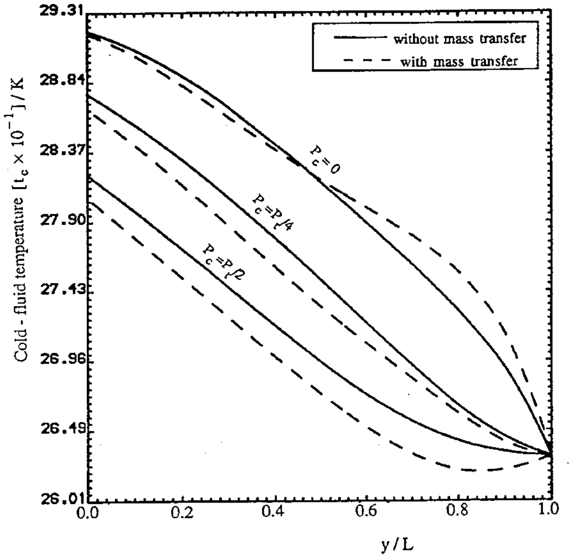

Fig. 10 The effect of moisture transfer on cold-fluid temperature distribution for ($\Lambda_t=10$, $\Pi_t=5$, $Z_t=0$)

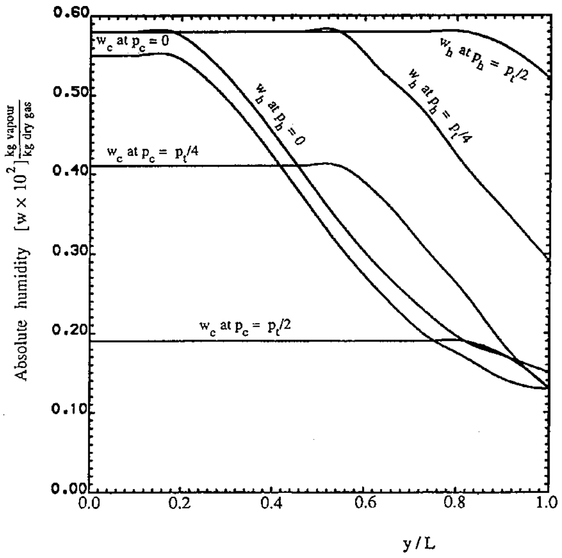

Fig. 11 Absolute humidity distribution in fluid flow direction for ($\Lambda_t=10$, $\Pi_t=5$, $Z_t=0$)

regenerator effectiveness HEE decreases rapidly. The effect of mass transfer is diminishing while the overall reduced period is approaching zero.

Figures 7 and 8 show the effect of the ratio L/d and effectiveness on the regenerator performance criteria. From these figures the following conclusions can be drawn.

1. The effect of mass transfer on the performance criteria for the numerical example given in previous section is about 10%.
2. When L/d is less than 320 the effect of mass transfer is diminishing for reasons which have been explained above.

In terms of the objective function, R_c, the optimum hydraulic diameter for the two cases (without mass transfer and with mass transfer) are shown in Table 1. Figures 9 and 10 show the temperature distribution of the fluid streams in the flow direction is shown against the dimensionless flow length y/L. The curves have been plotted both for the case without condensation and with condensation. As will be noted the effect of mass transfer is playing sufficient effect on the fluids temperature distribution. The curves have been plotted for three positions of the duct under consideration during each half revolution for the hot and cold periods.

Also Figs. 9 and 10 show the regenerator matrix transfer the sensible heat and latent heat from one side to the other, this understood by the fact that the latent heat, which is released on condensation on hot side, is picked up by the matrix and is transferred to the cold side, where it is expended in evaporating the condensate. Thus, the matrix must not only transfer the sensible heat but also the latent heat.

Figure 11 shows the points along the matrix path where condensation starts. The condensation occurs when the matrix temperature falls below the dew point temperature. These points occur at the following values of y/L for the periods stated [8]

y/L	p
0.2	0
0.5	$p_h/2$
0.8	p_h

Table 2 gives a comparison between the experimental results obtained from reference [4] and the results of the analysis presented in this paper and shows good agreement. It also shows the regenerator humidity effectiveness (see Eq. (3))

Conclusions

As will be seen from the above example, the cost ratio is made up of the costs of compensation for the destruction of the two components of exergy $\dot{E}^{\Delta T}$ and $\dot{E}^{\Delta P}$. Since the compensation for exergy destroyed in the heat transfer process has to come from the earth's natural resources, the objective function used in this paper may be directly relevant to the problem of conservation of natural resources.

One of the features of the optimization technique that presented in this work is the use of the weighting factor, F_w, which reflects

Table 2 A comparison between presented analysis results and van Leersum and Ambrose results [4]

Λ_t	Π_t	$t_{h,i}$ K	$t_{c,i}$ K	$W_{h,i}$ ($kg_{\text{vap}}/kg_{d.a.}$)	$W_{c,i}$ ($kg_{\text{vap}}/kg_{\text{d.a.}}$)	Ref. [4] results HEE	Presented analysis results HEE	Presented analysis results HEE_{hu}
10.00	2.00	293.15	273.15	0.0058	0.0029	0.8200	0.82251	0.318
10.00	5.00	293.15	273.15	0.0058	0.0029	0.7800	0.78630	0.250
10.00	2.00	297.15	273.15	0.0075	0.0029	0.8100	0.81652	0.492
13.66	3.2065	308.10	287.58	0.0306	0.0054	0.7610	0.76674	0.585
13.46	3.1820	318.44	289.33	0.0259	0.0069	0.7962	0.80591	0.415
13.28	3.1544	324.84	290.86	0.0189	0.0060	0.8476	0.84789	0.116
13.24	3.1600	324.60	291.61	0.0209	0.0074	0.8383	0.84001	0.167

the different values of the unit costs of the two components of exergy. Although in the present work the value of F_w was determined from thermoeconomic considerations of the exergy conservation processes in the plant in which the regenerator is used. Clearly, the use of the weighting factor can be extended to other types of heat exchangers.

A numerical method used to calculate the temperatures and absolute humidity distributions in a periodic regenerator with non hygroscopic material, using finite temperature difference, is general and can be used for other application of rotary regenerator. Furthermore, the technique developed for optimizing finite difference mesh size leads to a high degree of precision in the results and shorter computing processing times. The finite difference mesh size is obtained from equations that are given in reference [6].

Nomenclature

A = heat transfer area (according to subscript), (m^2)
A_s = solid area available for longitudinal heat conduction (according to subscript), (m^2)
$(A_s)_t$ = total available conduction, $(A_s)_c+(A_s)_h$, (m^2)
$(A_s)^*$ = conduction area ratio, $(A_s)_c/(A_s)_h$, (m^2)
c_p = fluid specific heat capacity, (J/kg K)
c_w = regenerator matrix specific heat capacity, (J/kg K)
c^ϵ = unit cost of exergy (according to subscript)
C^* = heat capacity rate ratio, $(\dot{m}c_p)_c/(\dot{m}c_p)_h$
d = matrix element diameter, m
$d_{pt,h}$ = dew-point temperature of the exhaust air.
F_w = weighting factor
h = heat transfer coefficient, (W/m^2 K)
h_m = mass transfer coefficient, (m/s)
h_v = enthalpy of evaporation of air-vapor mixture, (J/kg)
$(hA)_t$ = total heat transfer coefficient times heat transfer area, $(hA)_c+(hA)_h$
$(hA)^*$ = convection conductance ratio, $(hA)_c/(hA)_h$
HEE = heat exchanger effectiveness (according to subscript)
i = irreversibility rate, (W)
k = regenerator matrix thermal conductivity, (W/m K)
k_t = total thermal conductivity, (k_c+k_h)
k^* = matrix thermal conductivity ratio, (k_c/k_h)
L = matrix length, (m)
Le = lewis relation, $h/h_m\rho c_p$
$\dot{m}$ = mass flow rate (kg/s)
M_w = regenerator matrix mass (kg)
N_c = finite difference cold side period intervals
NCV = net calorific value, (J/kg)
N_h = finite difference hot side period intervals
N_r = finite difference regenerator length intervals
p = period of operation (according to subscript), (s)
Rc = cost ratio, defined by Eq. (47)
R1-R12 = dimensionless, see Appendix A
S1-S12 = dimensionless, see Appendix A
t = gas temperature (according to subscript), (K)
T_w = regenerator matrix temperature (according to subscript), (K)
y = flow length coordinate measured from fluid inlet, (m)
$\dot{Z}$ = investment cost rate (GBP/y)
Z_t = thermal conductivity parameter, $k_t(A_s)_t/L(hA)_t$
w = absolute humidity

Greek Symbols

ρ = fluid density, (kg/m^3)
γ = ratio of principal specific heat capacities
E, ε = exergy, specific exergy (W, J/kg)
$\dot{E}_{\text{out}}$ = The exergy flow rate of the heated air
$\dot{E}_{c,i}^{\Delta P}$ = cold side inlet pressure component of exergy
$\dot{E}_{c,e}^{\Delta P}$ = cold side outlet pressure component of exergy
$\dot{E}_{h,i}^{\Delta P}$ = hot side inlet pressure component of exergy
$\dot{E}_{h,e}^{\Delta P}$ = hot side outlet pressure component of exergy
$\dot{E}_{c,i}^{\Delta T}$ = cold side inlet thermal component of exergy
$\dot{E}_{c,e}^{\Delta T}$ = cold side outlet thermal component of exergy
$\dot{E}_{h,i}^{\Delta T}$ = hot side inlet thermal component of exergy
$\dot{E}_{h,e}^{\Delta T}$ = hot side outlet thermal component of exergy
σ = porosity
η = efficiency (according to subscript)
Λ = reduced length, $hA/\dot{m}c_p$ (according to subscript)
Π = reduced length, $hA\,p/M_w c_w$ (according to subscript)
$\dot{\Pi}$ = product cost rate
φ = fuel exergy factor, ε_f/NCV
Φ = relative humidity (according to subscript)
ψ = exergetic efficiency

Subscripts

a = dry air
$av,-$ = average
c = cold side
el = electrical
f = cold side row number in finite difference grid, fuel
g = cold side column number in finite difference grid
h = hot side, humidity (according to subscript)
hu,c = humidity for cold side
hu,h = humidity for hot side
i = hot side row number in finite difference grid, inlet
j = hot side column number in finite difference grid.
m = mechanical
min = minimum
op = optimum
ov = overall
p = product of combustion
r = finite difference mesh size for regenerator length.
R = room (space to be air conditioned)
s = isentropic
sa = saturation
t = total
v = water vapor
ΔP = pressure component
ΔT = thermal component

Superscripts

ΔP = pressure component
ΔT = thermal component

Appendix A

Hot Side (Λ_h).

$$R1=\frac{2N_r-\Lambda_h}{2N_r+\Lambda_h},\quad R2=\frac{\Lambda_h}{2N_r+\Lambda_h},\quad R3=\frac{2N_r\text{Le}-\Lambda_h}{2N_r\text{Le}+\Lambda_h}$$

$$R4=\frac{\Lambda_h}{2N_r\text{Le}+\Lambda_h},\quad R5=\frac{1-R1}{R2+2H1+H3},$$

$$R6=\frac{H2}{R2+2H1+H3}$$

$$R7=\frac{R2+2H1-H3}{R2+2H1+H3},\quad R8=\frac{H1}{R2+2H1+H3},$$

$$R9=\frac{1-R1}{R2+H1+H3}$$

$$R10=\frac{R2+H1-H3}{R2+H1+H3},\quad R11=\frac{H2}{R2+H1+H3},$$

$$R12 = \frac{H1}{R2 + H1 + H3}$$

where

$$H1 = \frac{k_h (A_s)_h N_r}{2L(hA)_h}, \quad H2 = \frac{h_{v,h} \dot{m}_h \Lambda_h}{(hA)_h}, \quad H3 = \frac{N_h \Lambda_h}{\Pi_h N_r}$$

Cold Side (Λ_c).

$$S1 = \frac{2N_r - \Lambda_c}{2N_r + \Lambda_c}, \quad S2 = \frac{\Lambda_c}{2N_r + \Lambda_c}, \quad S3 = \frac{2N_r \mathrm{Le} - \Lambda_c}{2N_r \mathrm{Le} + \Lambda_c}$$

$$S4 = \frac{\Lambda_c}{2N_r \mathrm{Le} + \Lambda_c}, \quad S5 = \frac{1 - S1}{S2 + 2E1 + E3},$$

$$S6 = \frac{E2}{S2 + 2E1 + E3}$$

$$S7 = \frac{S2 + 2E1 - E3}{S2 + 2E1 + E3}, \quad S8 = \frac{E1}{S2 + 2E1 + E3},$$

$$S9 = \frac{1 - S1}{S2 + E1 + E3}$$

$$S10 = \frac{S2 + E1 - E3}{S2 + E1 + E3}, \quad S11 = \frac{E2}{S2 + E1 + E3},$$

$$S12 = \frac{E1}{S2 + E1 + E3}$$

where

$$E1 = \frac{k_c (A_s)_c N_r}{2L(hA)_c}, \quad E2 = \frac{h_{v,c} \dot{m}_c \Lambda_c}{(hA)_c}, \quad E3 = \frac{N_c \Lambda_c}{\Pi_c N_r}$$

References

[1] Chung-hsinh, Li, 1983, ‘‘A Numerical Finite Difference Method for Performance Evaluation of a Periodic-Flow Heat Exchanger,’’ ASME J. Heat Transfer, **105**, pp. 611–617.

[2] Hausen, H., 1983, *Heat Transfer in Counterflow, Paralleflow and Crossflow*, McGraw Hill NY.

[3] Jassim, R. K., 2002, ‘‘Evaluation of Matrix Thermal Conductivity Effect on the Thermoeconomic Optimization of an Air-Conditioning Rotary Regenerator’’ ECOS 2002, **1**, Berlin, Germany, pp. 285–296.

[4] van-Leersum, J. G., and Ambrose, C. W., 1981, ‘‘Comparisons Between Experiments and Theoretical Model of Heat and Mass Transfer in Regenerators With Non-Sorbing Matrices,’’ ASME J. Heat Transfer, **103**, pp. 189–195.

[5] van-Leersum, J. G., 1986, ‘‘A Numerical Description of Condensation in Non-Hygroscopic Regenerator Matrices,’’ Numer. Heat Transfer, **9**, pp. 365–379.

[6] Jassim, R. K., 1992, ‘‘Thermoeconomic Optimization of Periodic Flow Heat Exchangers,’’ Ph.D. thesis, Dept of Mechanical Engineering Q.M.W. College, University of London.

[7] Kotas, T. J., and Jassim, R. K., 1993, ‘‘The Costing of Exergy Flows in the Thermoeconomic Optimization of the Geometry of Rotary Regenerators,’’ ENSEC 93, pp. 313–322.

[8] Holmberg, R. B., 1977, ‘‘Heat and Mass Transfer in Rotary Heat Exchanger With Non-Hygroscopic Rotor Materials,’’ ASME J. Heat Transfer, **99**, pp. 196–202.

[9] *ASHRAE Fundamentals*, 1997, ASHRAE, Atlanta, GA, Chpt. 5 and 6.

[10] Bahnke, G. D., and Howard, C. P., 1964, ‘‘The Effect of Longitudinal Heat Conduction on Periodic-Flow Heat Exchanger Performance,’’ ASME J. Eng. Power, **86**, pp. 105–120.

[11] Tsatsaronis, G., and Winhold, M., 1984, ‘‘Thermoeconomic Analysis of Power Plant,’’ Desert Research Institute, AP—3651, Research Project 2029-8.

[12] Kotas, T. J., 1995, *The Exergy Analysis Method of Thermal Plant Analysis*, Second Edition Krieger, Melbourne, Australia.

Journal of
Heat Transfer

Technical Notes

This section contains shorter technical papers. These shorter papers will be subjected to the same review process as that for full papers.

On Natural Convective Heat Transfer in Vertical Channels With a Single Surface Mounted Heat-Flux Module

G. Desrayaud
e-mail: gilles.desrayaud@insset.u-picardie.fr
LETEM/INSSET, Université de Picardie, 48 rue Raspail
BP 422, 02109 Saint-Quentin, France

A. Fichera
DIIM, Università di Catania, Viale A.
Doria 6 95125 Catania, Italy

This paper presents the numerical predictions of heat transfer and fluid flow characteristics for natural convection in a vertical channel with two-dimensional protruding heat-flux module as applied to the cooling of electronic components. The investigation is for a configuration consisting of a single module mounted on a vertical adiabatic wall. An attempt was made to combine the temperature of the module for all the dimensions of the module into a single composite correlation, along with the numerical data.

Keywords: Channel Flow, Electronics, Heat Transfer, Natural Convection

Introduction

The problem of heat transfer convective cooling in electronic equipment packages and particularly in the packaging of computer systems has gained considerable attention during the past two decades, because of the reduction in the component size, which increases the heat flux per unit volume and consequently the temperature level [1]. Packaging constraints and electronic considerations as well as system cooling modes lead to a wide variety of cooling systems. These methods include natural and forced convection in duct flows, impingement cooling, and phase change heat transfer. Natural convective cooling of electronic devices has recently received a renewal of interest owing to the proliferation of office and home computing, i.e., the use of low cost personal computers. This results in a preference for air-cooled systems whenever the application requirements allow it.

Attention is here focused on the printed circuit boards (PCBs) usually found inside computers. As pointed out by Young and Vafai [2] the problem of cooling electronic devices has often been idealized to the thermal analysis of heat generating rectangular obstacles within parallel plate channels, which allows general behavior to be obtained. This led to composite correlations for heat transfer being proposed for forced convection on an isolated heated module [2,3] or arrays of modules [4,5] in ducts, taking into account the module geometry and possibly its thermal conductivity. The aspect ratio of the channel and location of the module are obviously not relevant parameters as they would be in natural convection. On the other hand, for natural convection in a vertical channel only global correlations are given for a single heated module [6] or arrays of modules [7,8].

Numerical experiments are reported here for laminar natural convective airflow in a channel containing a single two-dimensional rectangular transverse element located along one channel wall. A planar source of uniform heat flux input is positioned at the base of the protruding element. The geometry is intended to represent an individual electronic flat-pack module. As pockets of recirculating flow appear within the channel, the terms in the equations that give an elliptic character to the model are retained. A composite correlation of the module temperature is presented as a function of all the parametric variables.

Numerical Solution

Governing Equations. In this paper, a laminar flow inside a vertical adiabatic channel originating from the uniform surface heat flux input q_s'' at the base of a surface-mounted rectangular element is considered. The flow under consideration is shown in Fig. 1, along with the coordinate systems employed. The protruding heat source is of width w and of height h. Its axial position on the vertical plate, x_c, is at the mid-height of the module. The transverse dimension is taken large enough for a two-dimensional flow to be assumed. The PCBs are treated as adiabatic, and the essential features of the natural convection were studied.

The full elliptic equations governing the flow are solved numerically, using the control volume method under the Boussinesq-fluid assumption. The dimensionless equations are written in strong conservative form,

$$\frac{\partial U}{\partial X}+\frac{\partial V}{\partial Y}=0 \tag{1}$$

$$\frac{\partial(UU)}{\partial X}+\frac{\partial(VU)}{\partial Y}+KU=-\frac{\partial P_m}{\partial X}+\Pr\left(\frac{\partial^2 U}{\partial X^2}+\frac{\partial^2 U}{\partial Y^2}\right)+\mathrm{Ra}\Pr\theta \tag{2a}$$

$$\frac{\partial(UV)}{\partial X}+\frac{\partial(VV)}{\partial Y}+KV=-\frac{\partial P_m}{\partial Y}+\Pr\left(\frac{\partial^2 V}{\partial X^2}+\frac{\partial^2 V}{\partial Y^2}\right) \tag{2b}$$

$$\frac{\partial(U\theta)}{\partial X}+\frac{\partial(V\theta)}{\partial y}=\Lambda\left(\frac{\partial^2\theta}{\partial X^2}+\frac{\partial^2\theta}{\partial Y^2}\right) \tag{3}$$

Contributed by the Heat Transfer Division for publication in the JOURNAL OF HEAT TRANSFER. Manuscript received by the Heat Transfer Division January 4, 2001; revision received October 8, 2002. Associate Editor: T. Y. Chu.

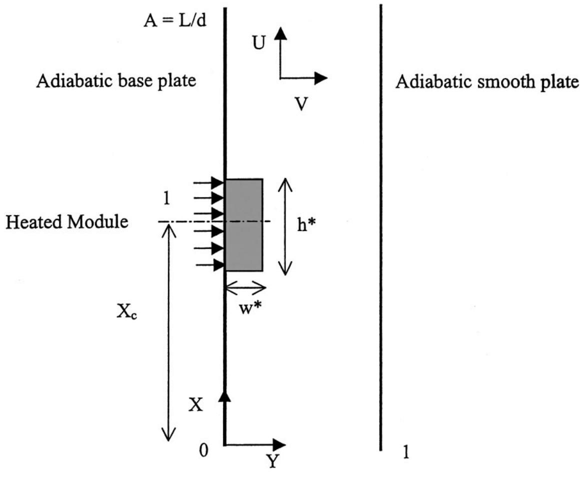

Fig. 1 Computational domain and coordinate system

The geometric dimensions, velocity and temperature difference were adimensionalized by d, α/d and $\Delta T = q_s'' d/k_a$. In the following, we considered that the conductivity ratio Λ is that of the solid-fluid conductivity ($\Lambda = k_m/k_a$) in the solid part and $\Lambda = 1$ in the fluid region. The solid and fluid parts are taken into account through the use of the purely numerical K-parameter, $K \to \infty$ for the solid part and $K \to 0$ for the fluid part.

The governing parameters are the Rayleigh number and the Prandtl number, K being a control parameter used to distinguish solid and fluid regions.

$$\mathrm{Ra} = g\beta q_s'' d^4/k_a \nu\alpha \qquad \mathrm{Pr} = \nu/\alpha = 0.71$$

The computational domain can be restricted to the space between plates, excluding the entrance and exit regions outside the channel for large enough values of the Rayleigh number. It is assumed that there is no transport of heat by conduction through the boundary at $X = 0$, and that the fluid enters the channel at the ambient temperature with parabolic velocity profiles. The entrance pressure is calculated using Bernoulli's equation. No-slip boundary conditions are imposed at the channel walls. They are insulated except at the base of the solid obstacle which receives a prescribed heat flux, q_s''.

$$0 \le Y \le 1 \qquad \text{at} \quad X = 0: \left\{ \begin{array}{c} V = 0, \dfrac{\partial U}{\partial X} = 0 \\ \theta = 0 \\ P_m = -0.5\dot{M}^2 \end{array} \right\} \qquad \text{Inlet} \qquad (4)$$

$$0 \le X \le X_C - 0.5h^* \qquad \text{and} \qquad X_C + 0.5h^* \le X \le A$$

$$\text{at} \quad Y = 0: \left\{ \begin{array}{c} \dfrac{\partial \theta}{\partial Y} = 0 \\ U = V = 0 \end{array} \right\}$$

$$X_C - 0.5h^* < X < X_C + 0.5h^*$$

$$\text{at} \quad Y = 0: \left\{ \begin{array}{c} -\Lambda \dfrac{\partial \theta}{\partial Y} = 1 \\ U = V = 0 \end{array} \right\} \qquad \text{Left wall} \qquad (5a)$$

Table 1 Effect of grid refinement on various local and global variables, Ra=10^6, w^*=0.125, h^*=0.5, A=5

Meshes (N_y, N_x)	$\dot{M}$	$\Psi_{\max}$	$\overline{\theta}_m$
(32, 100)	40.22	45.75	0.0822
(32, 150)	39.84	45.53	0.0812
(22, 200)	38.16	44.67	0.0886
(32, 200)	39.17	45.20	0.0809
(42, 200)	41.14	46.30	0.0804

$$0 \le X \le A \qquad \text{at} \quad Y = 1: \left\{ \begin{array}{c} \dfrac{\partial \theta}{\partial Y} = 0 \\ U = V = 0 \end{array} \right\} \qquad (\text{Right wall}) \quad (5b)$$

$$0 \le Y \le 1$$

$$\text{at} \quad X = A: \left\{ \begin{array}{c} \dfrac{\partial \theta}{\partial X} = 0 \quad \text{or} \quad \theta = 0 \\ \dfrac{\partial V}{\partial X} = 0; \dfrac{\partial U}{\partial X} = -\dfrac{\partial V}{\partial Y}; P_m = 0 \end{array} \right\} \qquad \text{Outlet} \qquad (6)$$

The dimensionless mass flow rate was calculated at any horizontal location X by $\dot{M} = \int_0^1 U dY$.

Numerical Method. The control volume procedure is utilized to discretize on a staggered, non-uniform Cartesian grid the nonlinear system of governing equations and boundary conditions with the second order centered scheme for the convective terms. The SIMPLER algorithm proposed by Patankar [9] is employed to solve the coupling between continuity and momentum equations through pressure. The conservation equations were cast in transient form and have been solved by implementing the alternating direction implicit (ADI) method, which transforms the discretized partial differential equations into tridiagonal systems of algebraic equations that are solved by a vectorized version of the Thomas algorithm.

Validation of the Numerical Method. The grid structure for computations was optimized by performing a systematic grid independence study. The grids were non-uniform in nature and distributed over the fluid and solid (module) regions to adequately capture steep velocity, pressure and temperature gradients arising from to the presence of the isolated heat flux module. The computations were done on increasingly finer grid size distributions for a Rayleigh number Ra=10^6 and a module size, $w^* = 0.125$ and $h^* = 0.5$. The parameters used to check the grid independence of the computational results were the mass flow rate ($\dot{M}$), maximum of the stream-function ($\Psi_{\max}$) and mean temperature of the module ($\overline{\theta}_m$), and are given in Table 1 for various grid arrangements. It is noted that the differences in the mean temperature, mass flow rate and maximum of the stream function between the (42,200) grid and the (32,150) grid or the (32,100) grid are less than 3 percent. Accordingly, the (32,100) seems to be a good

Table 2 Range of independent parameters

Parameters	Range
Ra	5 10^3, 5 10^4, 10^5, 2.5 10^5, 5 10^5, 10^6
Pr	0.71
Λ	5627
w^*	0.125, 0.25, 0.5
h^*	0.25, 0.5, 1
A	5, 8, 10, 12
X_c	Inlet (0.5+h^*/2), Center (A/2), Outlet (A−0.5−h^*/2)

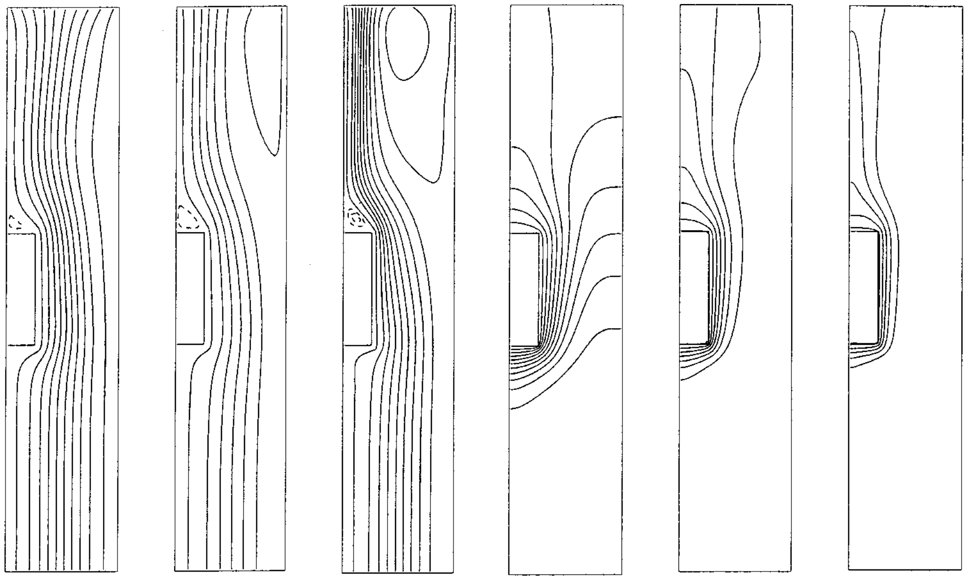

(a) Ra=10^4 **(b)** Ra = 10^5 **(c)** Ra = 10^6 **(d)** Ra = 10^4 **(e)** Ra = 10^5 **(f)** Ra = 10^6

[0.2, 1:9(1)] [1:31(5)] [1:51(5)] [from 0.01 (outside isoline) in 0.02 steps]

$\dot{M} = 9.33$ $\dot{M} = 31.17$ $\dot{M} = 45.83$ $\bar{\theta}_m = 0.210$ $\bar{\theta}_m = 0.132$ $\bar{\theta}_m = 0.097$

Fig. 2 Streamlines (*a*, *b*, *c*) and isotherms (*d*, *e*, *f*) for three different Rayleigh numbers, $h^* = 1$, $w^* = 0.25$, $A = 5$, Pr = 0.71

compromise between accuracy and reasonable CPU computing time and is considered to be suitable for the present study.

To check the adequacy of the modelisation of the solid and fluid parts (*K*-parameter in Eq. (2)), our results are compared with those of Said and Krane [10] who performed a numerical and experimental investigation of natural convection in an isothermal channel with a single rounded obstacle. These results are in qualitative agreement.

Results and Discussion

Examination of the governing equations (1–3) reveals that the independent parameters are the Rayleigh number (Ra), the Prandtl number (Pr), the conductivity ratio of the module to the fluid (Λ), and geometrical parameters. From Fig. 1, the latter are the reduced height and width of the module, its position on the base plate, and the aspect ratio of the channel.

In order to calculate dimensionless parameters for numerical computation, air at ambient conditions ($k_a = 0.0263$ W/mK) was taken as the cooling fluid and silicon ($k_m = 148$ W/mK) as the material of the protruding module. Thus, the fixed input parameters utilized in the simulations were Pr = 0.71 and $\Lambda = 5627$ in the solid part so that we can consider that the module acts as a perfect fin ($\Lambda \rightarrow \infty$). A very high ratio of the module conductivity to air is used to focus on heat transfer and fluid flow characteristics inside the channel. Numerical simulations were first conducted to determine the heat transfer and flow rates for various sizes (height and width) of a module located in the center part (at $X_c = A/2$) of the left wall of a channel of aspect ratio $A = 5$. Table 2 shows the parametric range adopted for this study. Air was selected for its generality as the cooling fluid.

Effect of the Rayleigh Number. Figure 2 displays the contours of the stream function and isotherms for three different values of the Rayleigh number 10^4, 10^5, and 10^6, and a fixed dimension of the heat module ($w^* = 0.25, h^* = 1$). Isovalues of the solid lines are given in square brackets in the legend with characteristic values. Three different regions can be distinguished inside the channel.

In the region just below the module, the fluid is heated by conduction only and the heating extends slightly further upstream (see Figs. 2(*d–f*)). A stagnant zone exists in the lower base corner of the module but no eddy was detected. The shear force of the main stream is unable to promote an anti-clockwise eddy and the main flow streamlines are closer and closer to the inside corner for increasing Ra number (Figs. 2(*a–c*)). It appears that this is attributable not to mesh coarseness but to the boundary layer which develops on the bottom face of the module and becomes thinner when the input heat flux increases. The buoyancy flow along the horizontal surface, upwardly oriented, inhibits the formation of a separated eddy at the inside lower corner. It should be recalled that the base plate is adiabatic and consequently, no thermal boundary layer can develop along its surface, upstream of the module.

In the second region, the flow is redirected into the by-pass zone and accelerates. The crowding of the streamlines near the vertical surface of the heated module clearly indicates that the buoyancy boundary layer is more and more vigorous. Although the formation of *vena contracta* at the module is evident, the flow never separates at the leading edge of the module (lower front corner) along its vertical surface, owing to the weak velocity of natural convective flows.

At the upper front corner of the module, a flow separation takes place, even at moderate values of Ra, and an anti-clockwise eddy develops along the horizontal downstream face of the module. This eddy has a triangular shape due to reattachment of the main flow on the vertical adiabatic base plate.

In the third zone, downstream of the module, a wall plume-like behavior near the channel base plate develops as can be seen in Fig. 2(*d-f*), which presents the isotherms. This figure shows that the plume occupies less and less space as the Ra number increases. A large recirculating zone downstream of the module,

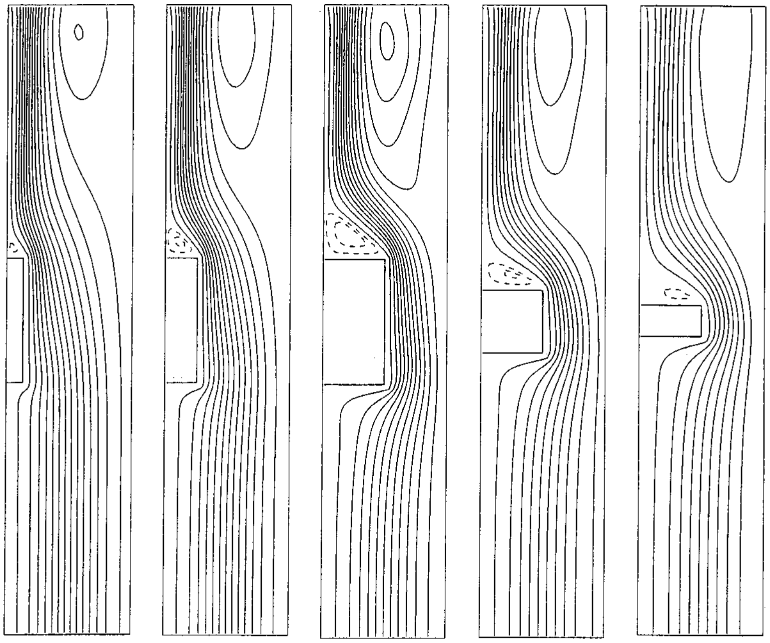

a) $w^* = 0.125$, $h^* = 1$ [1,46(3)]; **b)** $w^* = 0.25$, $h^* = 1$ [1,45(3)]; **c)** $w^* = 0.5$, $h^* = 1$ [1,43(3)]; **d)** $w^* = 0.5$, $h^* = 0.5$ [1,36(3)]; **e)** $w^* = 0.5$, $h^* = 0.25$ [1,30(3)]

$\dot{M} = 40.56$ 38.27 32.44 28.51 27.25

$\bar{\theta}_m = 0.116$ 0.107 0.096 0.067 0.043

Fig. 3 Streamlines for various sizes of the heated module, Ra=5 10^5, Pr =0.71, A=5

located along the smooth adiabatic plate, then supplies additional ambient airflow coming from the outlet (Figs. 2(*b–c*)). The deep penetration of this recirculation zone is substantial, constraining the area of the anti-clockwise eddy to be small, although increasing in strength with the Ra number. The width of the outlet-recirculating zone also increases with the Ra number while the wall plume becomes thinner. The outlet recirculation originates from the stagnant zone situated near the adiabatic smooth plate. Looking at Fig. 2(*a*), Ra=10^4, it can be noticed that the streamlines close to the plate are distorted. This leads to the onset of a pocket of recirculating flow within the channel for such a moderate value of the Rayleigh number. Nevertheless, such recirculation does not substantially modify the heat transfer inside the channel because it is located along an adiabatic plate.

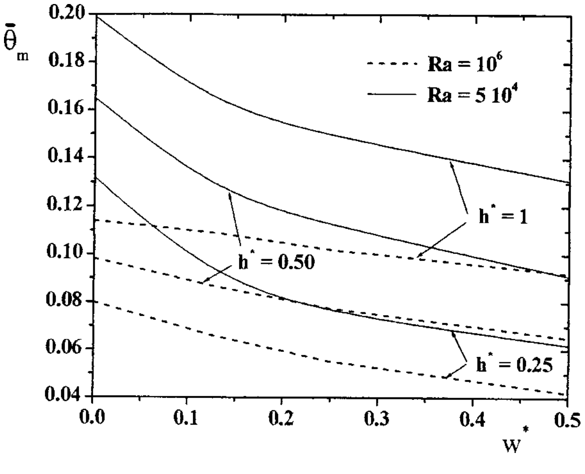

Fig. 4 Temperature variation of the heat flux module versus its width for two Rayleigh numbers, A=5, Pr=0.71

Effect of the Module Geometry. The effects of varying the module width are demonstrated in Figs. 3(*a–c*) for three different widths, the height being fixed. The input heat flux is then kept constant and for the same geometrical dimension of the channel, the Rayleigh number is also unchanged. The values of the main flow characteristics are given in the legend of the figure. At such a high Rayleigh number, Ra=5 10^5, an anti-clockwise eddy always occurs at the downstream horizontal face of the module, even for small widths. Increasing the width increases the size of this eddy but the presence of an outside recirculation inhibits its expansion largely downstream of the module. The outside recirculation zone increases in size but only slightly in strength with increasing w^* owing to the mass flow rate $\dot{M}$ which decreases. This reduction is of 6 percent order for an increase in w^* from 0.125 to 0.25 while a 20 percent diminution is observed when w^* increases from 0.125 to 0.50. It should be noticed that at the upstream bottom face, no eddy was ever detected at the lower base corner whatever the computational grid used.

Streamlines of Figs. 3(*e–c*) show that as the height of the module increases the downstream eddy extends its size downstream and increases in strength. It can be noticed that the total heat injected inside the channel is proportional to the height of the module although the Rayleigh number is the same owing to the way in which it is constructed (using the width of the channel as the dimension reference and $q_s'' \, d/k_a$ as the temperature refer-

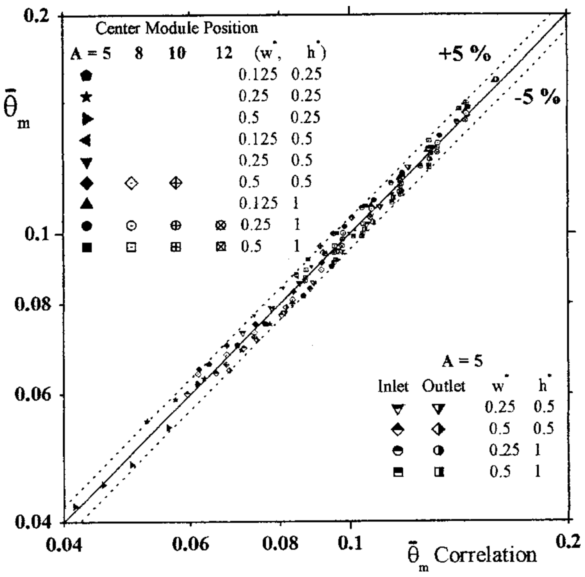

Fig. 5 Numerical versus predicted module temperature for the correlation (7). The straight line is the line of equality between prediction and numerical experiments, and the broken lines are +/−5 percent

ence). The wall-plume like flow being more vigorous, more fluid has to be supplied to the plume and the outside recirculation through the outlet is greater and greater. This constrains the eddy in the downstream direction and inhibits its growth in size but not in strength. This is readily seen on Figs. 3(*e–c*) on which the streamlines are equally spaced (by step 3). Due to lack of space, isotherms are not presented here because there are very similar to those shown in Fig. 2(*f*).

A knowledge of the module temperature is of crucial importance in the design of the PCB for the reliability and useful life to electronic components. Figure 4 gives the variation of the module temperature versus the width of the module for three different heights and two Rayleigh numbers. It must be recalled that the module temperature is uniform, its thermal conductivity being very large. The curves are shifted down when the module height decreases whatever the Rayleigh number. It can be observed that for the lowest value of Ra and a given height, corresponding to the same input heat flux, the temperature of the module decreases with a greater slope for the lowest width. The highest temperature is always reached for a flush-mounted source, $w^*=0$. When the Rayleigh number is high, the decrease in the temperature is almost monotonic.

Composite Data Correlation. One of the goals of this study was to develop a composite correlation for all the parameters. The correlation is presented so as to illustrate more clearly the trends in the data and can be used to support the qualitative observations made about the dependence of the module temperature on the problem parameters. Numerical simulations were performed over a broad range of the geometric parameters (Table 2).

The height of the module strongly influences its temperature, the input heat flux being proportional to the base surface area of the module. Hence, the parameter h^* was taken into account to construct the correlation. The peripheral surface of the heated module $(2w^*+h^*)$ was also chosen as a parameter, the horizontal areas of the module being non-negligible compare to its vertical surface. The flow constriction $(1-w^*)$ presented by the protruding heater was also included in the correlation. It should be recalled that the behavior of the module has been studied for a perfectly conducting encapsulant $(\Lambda\rightarrow\infty)$. Thus, a single composite correlation of the form was determined.

$$\overline{\theta}_m=0.687\ \mathrm{Ra}^{-0.131}h^{*0.706}(2w^*+h^*)^{-0.517}(1-w^*)^{-0.075}[1-(X_c+0.5h^*)/A]^{-0.064} \tag{7}$$

The empirical correlation predicts the numerical data with an average error of 2.5 percent and a maximum individual error of 5 percent. The strong dependence on the height of the heated module is evident in Eq. (7) while only slight dependence is noted on the unheated length above the module and on the flow constriction. These findings agree qualitatively with some previous work of Hung and Shiau [6]. The correlation is illustrated with the numerical data and the +/−5 percent error-lines in Fig. 5. Although some grouping of the data is evident and was found elsewhere, the low error of Eq. (7) in representing over 85 numerical experiments attests to its accuracy. Note that the correlation is not valid for flush-mounted heaters.

Extra computations (20 for each of the 2 cases) have also been carried out for two different locations of the module, designated as the inlet (at $X_c=0.5+h^*/2$) and outlet (at $X_c=A-0.5-h^*/2$) location. For this reason, a "chimney effect" has been introduced into the correlation through the use of the length of the unheated channel above the heated module, $[A-(X_c+0.5h^*)]$. Nevertheless, care must be taken using this correlation for locations of the module near the inlet. Indeed, Naylor et al. [11] showed that for isothermal smooth channel a separation bubble forms at the channel entrance for high values of the Rayleigh numbers. This separation bubble can reach the module, modifying the overall module heat transfer and thus the module temperature.

The last group of Eq. (7), the chimney effect group, is normalized by A so that the correlation could extend over various channel aspect ratios. It should be noticed that some computations were carried out with $A=8,10,12$ for a centered module of various sizes. Only slight variation of the module temperature was noticed when increasing A, the other geometrical parameters being kept fixed. These calculations are illustrated in Fig. 5 as open symbols for the same range of the Rayleigh numbers as before. The lower value of the new average error, i.e., 2.34 percent, obtained for all of the 125 numerical experiments indicates that the new data fit very well with correlation (7).

Conclusion

This work represents an investigation of the natural convective cooling of a single, two-dimensional heated element located on one wall of a vertical insulated channel. Numerical experiments were performed to investigate the effect of heat source protrusion on the flow field and heat transfer characteristics. A composite correlation of the numerical temperature data of the module for all module sizes and position, Rayleigh numbers, and channel aspect ratios was formulated, and was found to agree with the numerical data with an average error of less than 2.5 percent, all individual errors being lower than 5 percent.

Acknowledgments

The authors acknowledge the help of D. Mea with some of the computational work. This work was supported by research grant No. 991182 from the IDRIS-Computer Center (French National Institute for Advances in Scientific Computations).

Nomenclature

A = aspect ratio of the channel (L/d)
d = width of the channel, m
g = gravitational acceleration, $\mathrm{m.s}^{-2}$

h = height of the module, m
k = thermal conductivity, W.m^{-1}.K^{-1}
K = control parameter
L = height of the channel, m
$\dot{M}$ = dimensionless mass flow rate
N_y, N_x = number of cells in the y and x-direction
P = dimensionless motion pressure
Pr = Prandtl number
q_s'' = uniform heat flux input at the base of the module, W.m^{-2}
Ra = Rayleigh number based on d
T = temperature, K
T_0 = ambient temperature, K
X, Y = dimensionless cartesian coordinates
X_c = position of the mid-height of the module
U, V = dimensionless velocity components in x and y directions
w = width of the module, m

Greek Symbols

α = thermal diffusivity of the fluid, m^2.s^{-1}
β = thermal expansion coefficient of fluid, K^{-1}
ν = kinematic viscosity of fluid, m^2.s^{-1}
θ = dimensionless temperature
$\overline{\theta_m}$ = dimensionless mean temperature of the module
Ψ = dimensionless stream function
ΔT = reference temperature difference ($q_s''d/k_a$), K

Subscript

0 = at reference temperature
a = relative to the air
s = relative to the module

Superscript

* = dimensionless variables

References

[1] Sathe, S., and Sammakia, B., 1998, "A Review of Recent Developments in Some Practical Aspects of Air-Cooled Electronic Packages," ASME J. Heat Transfer, **120**, pp. 830–839.
[2] Young, T. J., and Vafai, K., 1998, "Convective Cooling of a Heated Obstacle in Channel," Int. J. Heat Mass Transf., **41**, pp. 3131–3148.
[3] Roeller, P. T., and Webb, B. W., 1992, "A Composite Correlation for Heat Transfer From Isolated Two and Three-Dimensional Protrusions in Channel," Int. J. Heat Mass Transf., **35**(4), pp. 987–990.
[4] Kim, S. H., and Anand, N. K., 1994, "Laminar Developing Flow and Heat Transfer Between a Series of Parallel Plates With Surface Mounted Discrete Heat Sources," Int. J. Heat Mass Transf., **37**(15), pp. 2231–2244.
[5] Gupta, A., and Jaluria, Y., 1988, "Forced Convective Liquid Cooling of Arrays of Protruding Heated Elements Mounted in a Rectangular Duct," ASME J. Electron. Packag., **120**, pp. 243–252.
[6] Hung, Y. H., and Shiau, W. M., 1988, "Local Steady-State Natural Convection Heat Transfer in Vertical Parallel Plates With a Two-Dimensional Rectangular Rib," Int. J. Heat Mass Transf., **31**, pp. 1279–1288.
[7] Lin, T.-Y., and Hsieh, S.-S., 1990, "Natural Convection of Opposing/Assisting Flows in Vertical Channels With Asymmetrically Discrete Heated Ribs," Int. J. Heat Mass Transf., **33**, pp. 2295–2309.
[8] Tanda, G., 1997, "Natural Convection Heat Transfer in Vertical Channels With and Without Transverse Square Ribs," Int. J. Heat Mass Transf., **40**, pp. 2173–2185.
[9] Patankar, S. V., 1980, *Numerical Heat Transfer and Fluid Flow*, Hemisphere Publishing, Washington, DC.
[10] Said, S. A. M., and Krane, R. J., 1990, "An Analytical and Experimental Investigation of Natural Convection Heat Transfer in Vertical Channels With a Single Obstruction," Int. J. Heat Mass Transf., **33**, pp. 1121–1134.
[11] Naylor, D., Floryan, J. M., and Tarasuk, J. D., 1991, "A Numerical Study of Developing Free Convection Between Isothermal Vertical Plates," ASME J. Heat Transfer, **113**, pp. 620–626.

The Synthetic Kernel (SK_N) Method Applied to Thermal Radiative Transfer in Absorbing, Emitting, and Isotropically Scattering Homogeneous and Inhomogeneous Solid Spherical Medium

Zekeriya Altaç
Professor
e-mail: zaltac@ogu.edu.tr

Mesut Tekkalmaz
Graduate Student
e-mail: tmesut@ogu.edu.tr

Osmangazi University, School of Engineering
and Architecture, Mechanical Engineering Department,
26480 Batı Meşelik, Eskişehir, Turkey

The SK_N method is proposed for solving radiative transfer problems in solid spherical participating medium. The method relies on approximating the integral transfer kernels by a sum of synthetic kernels. Then the transfer equation is reducible to a set of N-coupled second-order differential equations. The method is benchmarked against the exact and the discrete-ordinates method solutions for various optical radius and scattering albedos. Spatially varying scattering albedos are used to test the performance of the method in inhomogeneous media. Three quadrature sets are proposed for use with this method, and their convergence to the exact solution is investigated. It is demonstrated that the SK_N method possess the capability of solving radiative transfer problems yielding excellent solutions in solid spherical media.
[DOI: 10.1115/1.1561454]

Keywords: Absorption, Computational, Emitting, Heat Transfer, Participating Media, Radiation

1 Introduction

There are numerous engineering applications which involve heat generating gray gas radiation and the analysis of heat transfer through fibrous and foam insulating materials, molten glass and glassy material in spherical geometries. The problem of an arbitrary distribution of interior and exterior sources is also of great interest in astrophysical applications. Similar problems arise in neutron transport theory.

Solving radiative transfer problems in a participating medium requires solution of the radiative transfer equation (RTE) or the radiative integral transfer equation (RITE). Though, a number of methods were developed over the years, in the last decade, the discrete ordinates method (DOM) has become the dominant means for obtaining numerical solutions of the RTE. It should be noted that the DOM yields results of sufficient accuracy for most engineering problems, however, the DOM even in one-dimensional cylindrical and spherical media exhibits the "ray effect," which manifests itself as non-physical oscillations of intensity around the correct value [1]. To mitigate the ray effect, which is a direct result of angular discretization of the RTE, one has to

---

Contributed by the Heat Transfer Division for publication in the JOURNAL OF HEAT TRANSFER. Manuscript received by the Heat Transfer Division May 26, 2002; revision received November 6, 2002. Associate Editor: R. Skocypec.

increase the number of discrete directions, but the ray effect is still persistent [1]. Additionally, in curved geometries a great deal of difficulties are to be overcome due to RTE streaming term which involves the directional derivative of the intensity. On the other hand, RITE completely eliminates the angular dependence of the incident radiation by integrating the radiative transfer equation over all solid angles. Since the angular variable is completely removed, the integral method is dimensionally simpler than the RTE. However, the solution of RITE, which provides the exact solution of thermal radiative transfer problems, leads to dense matrices in multi-dimensional geometries which result in severe limitations on the number of grid points that can be treated without incurring prohibitive requirements for the computational memory and execution time.

The Synthetic Kernel (SK_N) method deals with the exact integral equation and involves an exponential approximation to its transfer kernels. Then, the integral equation for the incident energy can be reduced to a set of coupled second-order differential equations for which proper boundary conditions can be found. The method was first proposed and applied to the integral neutron transport equation for homogeneous and inhomogeneous problems [2–5]. The results for homogeneous media were excellent yielding 3 to 4 significant digit accuracy while for the inhomogeneous systems which included problems of stepwise varying medium properties agreed remarkably well with the numerical solutions of the integral equation, DOM, and spherical harmonics. It was also shown that the method did not exhibit the ray effect [3–5]. The method was first successfully applied in thermal radiative transfer field by solving the radiation-conduction problem in plane-parallel medium by Altaç [6] where the SK_N equations were coupled with the energy equation. The method was later applied to an absorbing, emitting, and isotropically scattering homogeneous rectangular medium [7]. It was shown that with the proposed "corrected" boundary conditions the accuracy is enhanced yielding errors of a few percent. However, the foregoing studies used the Gauss quadrature set in the half range, referred to as Set-1 in this paper. The SK_N method was recently extended to homogeneous, inhomogeneous and linearly, anisotropically-scattering, participating, plane-parallel media, and two new quadrature sets were proposed to obtain solutions with greater accuracy at low order SK_N approximations [8,9]. The solutions were compared with high order spherical harmonics (P_N), DOM (S_N) and integral equation solutions. It was demonstrated that the performance of Set-2 was superior at low order approximations such as SK_1 and SK_2 yielding better or comparable solutions to S_{128} and P_{11} approximations.

In this paper, the SK_N method is employed to solve radiative transfer in isotropically scattering participating one-dimensional solid spherical media and the performance of the quadrature sets, Set-1, 2, and 3, which were proposed in Ref. [8] are explored by comparison of the test problems with the exact and DOM S_8 solutions.

2 The Radiative Integral Transfer Equation

The radiative integral transfer equations (RITEs) for the incident energy and the net heat flux for a spherical shell were derived by Viskanta et al. [10]. To save space, the derivation will be skipped here and the integral equations in the zero limit of the inner shell radius will be considered. The medium is absorbing, emitting and isotropically scattering. Then the dimensionless monochromatic RITEs for one-dimensional solid sphere can be written as

$$G(\tau)=f_1(\tau)+\int_{\tau'=0}^{\tau_0} S(\tau')[E_1(|\tau-\tau'|)-E_1(\tau+\tau')]\,\frac{\tau' d\tau'}{2\tau} \tag{1}$$

$$q(\tau)=f_2(\tau)+\int_{\tau'=0}^{\tau_0} S(\tau')\left[\frac{(\tau-\tau')}{|\tau-\tau'|}\tau E_2(|\tau-\tau'|)-\tau E_2(\tau+\tau')\right.$$
$$\left.+E_3(|\tau-\tau'|)-E_3(\tau+\tau')\right]\frac{\tau' d\tau'}{2\tau^2} \tag{2}$$

where τ_0 is the optical radius, and $S(\tau)$ is the isotropic source function which is defined as

$$S(\tau)=4\pi[1-\Omega_0(\tau)]\theta^4(\tau)+\Omega_0(\tau)G(\tau) \tag{3}$$

where $\Omega_0(\tau)$ is the space-dependent scattering albedo given by $\sigma(\tau)/\beta$, where $\beta=\sigma(\tau)+\kappa(\tau)$ is the extinction coefficient while $\sigma(\tau)$ and $\kappa(\tau)$ are the space-dependent scattering and absorption coefficients, respectively and $[1-\Omega_0(\tau)]\theta^4(\tau)$ is the dimensionless blackbody radiation intensity. For the isotropic incidence of radiation intensity, I_w, on the surface of the sphere, the boundary integrals become

$$f_1(\tau)=\frac{I_w}{2\tau}\{\tau_0 E_2(\tau_0-\tau)-\tau_0 E_2(\tau_0+\tau)$$
$$+E_3(\tau_0-\tau)-E_3(\tau_0+\tau)\} \tag{4}$$

and

$$f_2(\tau)=\frac{I_w}{2\tau^2}\left\{\begin{array}{l}-\tau\tau_0 E_3(\tau_0-\tau)-\tau\tau_0 E_3(\tau_0+\tau)-(\tau_0+\tau)E_4(\tau_0+\tau)+(\tau_0-\tau)E_4(\tau_0-\tau)\\ \quad +E_5(\tau_0-\tau)-E_5(\tau_0+\tau)\end{array}\right\} \tag{5}$$

3 The Derivation of the SK_N Equations

To introduce the SK_N approximation, the m^{th} order exponential integral function, $E_m(x)$, is replaced with the following finite sum obtained by the N-point Gaussian summation over interval (0,1):

$$E_m(x)=\int_0^I \mu^{m-2}e^{-x/\mu}d\mu \doteq \sum_{n=1}^{N} w_n\mu_n^{m-2}e^{-x/\mu_n} \tag{6}$$

where w_n and μ_n are the appropriate Gauss quadrature weights and abscissas, respectively. These quadratures which are for various N values tabulated in Ref. [11] are referred to as Set-1. Using the format of the exponential approximation to $E_m(x)$, various quadrature sets can be generated by matching the spatial moments of the real and approximate $E_1(x)$ as discussed in Ref. [8]. However, this technique provides an approximation for only $E_1(x)$, approximations for $m>1$ can be obtained through successive integrations using the $dE_{m+1}(x)/dx=-E_m(x)$, recursive property of the exponential integral functions which also yields the same form of Eq. (6). But these approximations do not necessarily satisfy the real spatial moments of the exponential integral functions for $m>1$.

To begin the derivation of the SK_N equations, the approximations for the m^{th} order exponential integral functions given by Eq. (6) are substituted into Eqs. (1) and (2). Upon defining

$$G_n(\tau)=\frac{1}{2\tau\mu_n}\int_{\tau'=0}^{\tau_0} S(\tau')\{e^{-|\tau-\tau'|/\mu_n}-e^{-(\tau+\tau')/\mu_n}\}\tau' d\tau' \tag{7}$$

and

$$q_n(\tau)=\frac{1}{2\tau^2}\int_{\tau'=0}^{\tau_0}S(\tau')\left\{\tau\frac{\tau-\tau'}{|\tau-\tau'|}e^{-|\tau-\tau'|/\mu_n}-\tau e^{-(\tau+\tau')/\mu_n}+\mu_n e^{-|\tau-\tau'|/\mu_n}-\mu_n e^{-(\tau+\tau')/\mu_n}\right\}\tau'\,d\tau' \tag{8}$$

the incident radiation and the radiative heat flux can be recast as

$$G(\tau)=f_1(\tau)+\sum_{n=1}^{N}w_nG_n(\tau) \tag{9}$$

$$q(\tau)=f_2(\tau)+\sum_{n=1}^{N}w_nq_n(\tau) \tag{10}$$

Taking the derivative of Eq. (7) with respect to τ and with the inspection of Eq. (8), one obtains the following relation between $q_n(\tau)$ and $dG_n(\tau)/d\tau$:

$$q_n(\tau)=-\mu_n^2\frac{dG_n(\tau)}{d\tau} \tag{11}$$

On the other hand, by taking the derivative of Eq. (8) with respect to τ and observing Eq. (7) and rearranging, the following equation is obtained:

$$\frac{1}{\tau^2}\frac{d}{d\tau}[\tau^2q_n(\tau)]=-G_n(\tau)+S(\tau) \tag{12}$$

Eliminating $q_n(\tau)$ from Eq. (12), using Eq. (11) and Eq. (3), and rearranging yields the SK_N equations for the spherical geometry:

$$-\mu_n^2\frac{1}{\tau^2}\frac{d}{d\tau}\left[\tau^2\frac{dG_n(\tau)}{d\tau}\right]+G_n(\tau)=4\pi[1-\Omega_0(\tau)]\theta^4(\tau)+\Omega_0(\tau)G(\tau),\quad n=1,2,\ldots,N \tag{13}$$

Equation (13) with Eq. (9) constitute coupled second-order differential equations subject to boundary conditions; at the center

$$\frac{dG_n(0)}{d\tau}=0 \tag{14}$$

and at the surface

$$\frac{dG_n(\tau_0)}{d\tau}+\left(\frac{1}{\tau_0}+\frac{1}{\mu_n}\right)G_n(\tau_0)=0 \tag{15}$$

Equation (14) is the natural symmetry boundary condition while Eq. (15) is obtained by inspecting $G_n(\tau)$ and $dG_n(\tau)/d\tau$ at $\tau=\tau_0$. These boundary conditions are mathematical boundary conditions in nature, and are used regardless of the physical boundary conditions since the physical boundary conditions are already embedded in the boundary terms $f_1(\tau)$ and $f_2(\tau)$.

Substitution of Eq. (11) into Eq. (10) gives an expression for the net radiative heat flux as

$$q(\tau)=f_2(\tau)-\sum_{n=1}^{N}w_n\mu_n^2\frac{dG_n(\tau)}{d\tau} \tag{16}$$

which requires the knowledge of only $G_n(\tau)$.

4 Results and Discussion

The following benchmark problems have been set for the comparison of the SK_N solutions using quadrature Set-1, 2, and 3 [8] with the exact integral and DOM S_8 solutions.

Benchmark Problem 1. The problem of radiative transfer in a cold solid spherical medium ($\theta(\tau)=0$) with a constant scattering albedo (homogeneous medium) and transparent surface is considered. Scattering is isotropic. The only source in the medium is due to the externally isotropic unit incidence of radiation at the surface of the sphere $\tau=\tau_0$; that is, $I_w=1$. The hemispherical reflectivity for optical radiuses ranging from $\tau_0=0.1$ to $\tau_0=10$ are determined for scattering albedos from $\Omega_0=0.2$ to $\Omega_0=0.995$. The reflectivity is defined as $R=q^+(\tau_0)/\pi$, where $q^+(\tau_0)$ is computed from $q^+(\tau_0)=\pi+q(\tau_0)$.

Benchmark Problem 2. A cold solid spherical medium ($\theta(\tau)=0$) with linear and quadratic variations of scattering albedo which was solved by Tsai et al. [12] using DOM S_8 is considered. Scattering is isotropic. Additionally, exponential and cosine growing/damped oscillations, which were used in plane-parallel medium problems [8,9] are also considered to severely test the approximation and its effects with respect to spatially varying source term not only in the medium but also near the walls. The medium is also subject to the externally isotropic unit incidence of radiation on the surface of the sphere, $I_w=1$, and has a constant optical path $\tau_0=1$. The average value $\Omega_0(\tau)$ over the medium is equal to 0.5 in all cases.

The relative per cent error of the reflectivity is computed as follows:

$$R\%=\left(\frac{R_{\mathrm{exact}}-R_{\mathrm{approx}}}{R_{\mathrm{exact}}}\right)\times 100 \tag{17}$$

Thus, the term ''error'' throughout this paper will be used to imply the relative per cent error computed by Eq. (17).

The integral and SK_N equations are solved using the techniques described in Ref. [8]. From the solution of the integral equations, we generated the same solutions in five-decimal places as cited in Ref. [12] for $\Omega_0=0.5$, linearly and quadratically varying albedo cases. Thus, our solutions and those of provided in Ref. [12] were identical. The S_8 solutions for exponential and cosine-varying scattering albedo cases are obtained using the quadratures and numerical procedure provided in Ref. [12].

The memory requirement for the SK_N approximation for one-dimensional geometries is approximately the same as that of plane-parallel geometries [8]. However, the computation time is affected by the nature of the physical problem under consideration. For instance, if the boundary is diffuse and/or specularly reflecting, then the solution algorithm has to be an iterative one, since the boundary terms $f_1(\tau)$ and $f_2(\tau)$ will now contain the intensity and/or partial heat fluxes which converges as the solution for the incident radiation and heat flux converges. Also, the convergence the SK_N equations using an iterative algorithm, even for isotropic diffuse boundary condition, depends on the magnitude of the scattering albedo. It is our experience that the solutions are obtained for absorbing-dominant medium within 5–10 iterations while for scattering-dominant medium solutions iterations are about 15–25.

This study was carried out on a Pentium III 667 MHz processor with 128 Mb RAM. Several cases of grids ranging from 50 to 800 intervals are considered to ensure grid independence of the presented solutions. In Table 1, a comparison of the computed reflectivity and computational times (cpu time) obtained with the exact and SK_N approximations using Set-2 are given for the $\tau_0=1$ and $\Omega_0=0.5$ case of benchmark problem 1. The optimum number of grids is 200 for the present case; however, for optically thicker ($\tau_0\geqslant 5$) geometries 400 grids are used. The computational time with 800 grid elements is 18.48, 0.017, 0.131, 0.281, 0.502 and 0.505 seconds for the exact, and SK_1 through SK_5 approximations, respectively. The computational advantage of the method even for high order approximations is clear.

4.1 The SK_N Approximation Solutions in Homogeneous Medium. The exact solutions and the errors using the SK_N approximation of orders up to 3 with all three quadrature sets are tabulated in Table 2. The errors from SK_1 approximation with all three sets increase with increasing scattering albedo. For Set-1, the errors are high for optically thin systems; for $\tau_0=0.1$ the errors change from 0.03 percent for $\Omega_0=0.2$ to 0.7 percent for

Table 1 Comparisons of grid sensitivity and computational time (cpu) for case $\tau_0=1$ and $\Omega_0=0.5$ case

	Number of grids used									
	50		*100*		*200*		*400*		*800*	
Method	R	CPU (sec)	R	CPU (sec)	R	CPU (sec)	R	CPU (sec)	R	CPU (sec)
Exact	0.54230	0.020	0.54227	0.218	0.54226	0.704	0.54226	3.414	0.54226	18.48
SK_1	0.53225	0.001	0.53221	0.002	0.53220	0.004	0.53220	0.008	0.53220	0.017
SK_2	0.54229	0.005	0.54225	0.009	0.54223	0.020	0.54223	0.039	0.54223	0.131
SK_3	0.54228	0.009	0.54223	0.018	0.54222	0.036	0.54222	0.102	0.54222	0.281
SK_4	0.54230	0.014	0.54225	0.028	0.54224	0.087	0.54224	0.209	0.54224	0.502
SK_5	0.54232	0.019	0.54227	0.049	0.54226	0.163	0.54226	0.331	0.54226	0.505

Table 2 Comparison of the exact reflectivity solutions with those of SK_N method for various scattering albedo and optical thickness (Benchmark Problem 1)

		τ_0					
Method	Ω_0	0.1	0.5	1	2	5	10
Exact	0.200	0.89950[‡]	0.59961	0.38060	0.18909	0.07833	0.05715
	0.500	0.93580	0.72417	0.54226	0.34893	0.20521	0.17038
	0.800	0.97374	0.87698	0.77496	0.62840	0.45319	0.39165
	0.995	0.99923	0.99667	0.99337	0.98682	0.96805	0.94118
SK_1	0.200	0.03[§] −0.01 0.02	0.25 −0.06 0.13	0.32 −0.06 0.39	0.35 0.13 0.83	0.57 0.64 2.08	0.82 0.82 3.03
	0.500	0.18 −0.05 0.13	1.53 −0.40 1.12	1.86 −0.43 2.29	1.54 0.40 4.09	2.11 1.99 7.23	2.28 2.28 9.17
	0.800	0.47 −0.13 0.32	3.87 −1.10 2.87	4.78 −1.42 5.87	3.18 −0.02 10.08	3.37 3.12 15.21	3.57 3.57 18.40
	0.995	0.70 −0.22 0.48	5.98 −1.82 4.48	7.71 −2.72 9.42	4.61 −1.92 17.33	0.34 −0.13 28.72	0.18 0.18 34.31
SK_2	0.200	0.02 0** 0	0.03 −0.02 0.01	0.01 −0.03 0.01	0.03 −0.01 0.02	0.05 0.04 0.09	0.07 0.07 0.17
	0.500	0.12 −0.01 0.02	0.16 −0.11 0.07	0.01 −0.16 0.06	0.11 −0.07 0.06	0.14 0.08 0.24	0.14 0.13 0.39
	0.800	0.31 −0.03 0.04	0.41 −0.30 0.19	−0.11 −0.44 0.16	0.07 −0.26 0.08	0.12 0.05 0.26	0.11 0.11 0.42
	0.995	0.47 −0.06 0.06	0.63 −0.48 0.31	−0.35 −0.74 0.26	−0.20 −0.57 0.03	−0.03 −0.08 −0.07	−0.05 −0.05 −0.08
SK_3	0.200	0.01 0 0	0 −0.01 0	0 −0.01 0	0.01 0 0.01	0 0 0	0 0 0.02
	0.500	0.06 0 0.01	−0.02 −0.03 0.02	0.01 −0.05 0.02	0.01 −0.03 0.01	0.01 0 0.01	0 0 0.01
	0.800	0.16 −0.01 0.01	−0.08 −0.09 0.06	−0.01 −0.13 0.06	0.01 −0.08 0.01	0.01 0 0	−0.01 −0.01 0
	0.995	0.24 −0.02 0.01	−0.14 −0.14 0.10	−0.04 −0.22 0.10	0.01 −0.16 0.03	−0.01 −0.02 −0.01	−0.03 −0.03 −0.03

[‡] Reflectivity values at the surface of the sphere.

[§] In each box, the values from top to bottom are the percent relative errors for Set-1, Set-2 and 3, respectively.

**The truncated error value in two decimal places is zero.

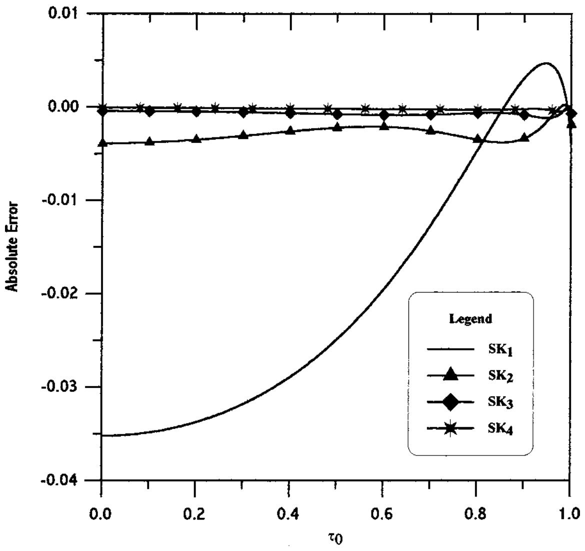

Fig. 1 Absolute error of the incident energy as a function of space for $\Omega_0=0.5$ and $\tau_0=1$ mfp with the SK_N approximation

$\Omega_0=0.995$. Similarly, for $\tau_0=0.5$ the errors range from 0.25 percent for $\Omega_0=0.2$ to 5.98 percent for $\Omega_0=0.995$, and for $\tau_0=1$ these errors range from 0.32 percent for $\Omega_0=0.2$ to 7.71 percent for $\Omega_0=0.995$. The best solutions for all optical configurations are achieved with quadrature Set-2, in SK_1 approximation yielding the maximum errors of -0.22, -1.82, -2.72, -1.92, -0.13, and 0.18 percent for $\tau_0=0.1$ to $\tau_0=10$, respectively for $\Omega_0=0.995$. The errors are much less as the scattering albedo decreases yielding the exact solutions for absorbing medium while the errors with Set-3 are worse than those with Set-1. As the order of approximation is increased, the errors are reduced for all optical configurations, but the maximum errors are generally observed in optically thin medium. In SK_2 approximation using Set-3, the solutions for optically thin systems are better than those of Set-1 and Set-2, for $\Omega_0=0.995$, yielding the errors of 0.06, 0.31, 0.26, 0.03, -0.07, and -0.08 percent for $\tau_0=0.1$ to $\tau_0=10$, respectively. In SK_3 approximation, the maximum errors of -0.24 percent, -0.22 percent, and 0.10 percent are observed for $\tau_0<2$ and $\Omega_0=0.995$ with Set-1, 2 and 3, respectively. The errors in magnitude are further reduced as the order of the SK_N approximation is increased and convergence to the exact solution is achieved. For high order approximations, $N\geqslant 4$, the performance of all three quadrature sets become identical. It should also be noted that in all the cases presented here the ray effect was not observed in the solutions for the incident energy and/or the heat flux.

In Fig. 1, the absolute error of the incident energy as a function of space $(=G_{\text{exact}}(\tau)-G_{SKN}(\tau))$ is depicted for $\Omega_0=0.5$ and $\tau_0=1$ mfp for the SK_N approximations of order 1 thru 4 using Set-2 to illustrate the convergence of the solutions throughout the medium. As the order of approximation is increased, the SK_N solutions converge the exact value, but, for low order approximations, solutions for the incident energy or heat flux may oscillate around zero horizontal line. This behavior is analyzed in detail in Ref. [6], and it is closely related with the accuracy of the synthetic kernels. However, in any case, for any medium properties, the solutions to the exact values within the solution domain are assured.

4.2 The SK_N Approximation Solutions in Inhomogeneous Medium. The solutions for linearly varying scattering albedo cases with the SK_N approximation of orders up to 4 with Set 1, 2, and 3 are tabulated comparatively with the exact and S_8 [12] solutions in Table 3. The cases considered are $\Omega_0(\tau)=2\tau/3$, $0.2+2\tau/5$, $0.4+2\tau/15$, $0.6-2\tau/15$, $0.8-2\tau/5$, and $1-2\tau/3$. In the first three cases, the scattering albedo increases towards the surface of the sphere. The SK_1 approximation for $\Omega_0(\tau)=2\tau/3$ case yields the errors of 2.26, 0.07, and 2.67 percent for Set-1, 2, and 3, respectively. These error values for SK_2 and SK_3 approximations are 0.26, -0.15, and 0.07; and 0.03, -0.05, and 0.02 percent, for Set-1, 2, and 3, respectively. While the error of S_8 approximation is -0.06 percent, and the SK_4 approximation with all three sets yields errors less than 0.02 percent. In $\Omega_0(\tau)=0.2+2\tau/5$ case, the errors for SK_1 through SK_3 approximations are 2.05, -0.14, and 2.46 percent; 1.96, -0.15, and 0.07 percent; and 0.02, -0.05, and 0.02 percent, for Set-1, 2, and 3, respectively. The error with S_8 approximation is -0.08 percent. The SK_4 approximation using all three sets yields errors less than 0.01 percent yielding solutions better than S_8. In $\Omega_0(\tau)=0.4+2\tau/15$ case, the errors for SK_1 through SK_3 approximations are 1.91, -0.33, and 2.32 percent; 0.05, -0.16, and 0.07 percent; and 0.01, -0.05, and 0.02 percent, for Set-1, 2, and 3, respectively. While the error with S_8 is -0.09 percent, with SK_4 approximation using all three sets are reduced below 0.01 percent. In the next group, the scattering at the core of the sphere is highest. In $\Omega_0(\tau)=0.6-2\tau/15$ case, the error with S_8 becomes -0.10 percent, and the SK_1 approximation errors using Set-1 are smaller when compared to the first three albedo alternatives while the order of errors using Set-3 remains the

Table 3 Reflectivities of the benchmark problem 2 for linearly varying scattering albedo cases

	Scattering Albedo, $\Omega_0(\tau)$					
Method	$2\tau/3$	$0.2+2\tau/5$	$0.4+2\tau/15$	$0.6-2\tau/15$	$0.8-2\tau/5$	$1-2\tau/3$
Exact	0.55957	0.55205	0.54532	0.53941	0.53441	0.53038
S_8	0.55990	0.55247	0.54581	0.53997	0.53502	0.53103
SK_1	0.54690[††] 0.55919 0.54464	0.54074 0.55281 0.53848	0.53493 0.54713 0.53265	0.52955 0.54641 0.52717	0.52456 0.53808 0.52205	0.52000 0.53487 0.51732
SK_2	0.55814 0.56042 0.55918	0.54122 0.55290 0.55168	0.54503 0.54617 0.54496	0.53964 0.54028 0.53907	0.53511 0.53528 0.53409	0.53154 0.53126 0.53010
SK_3	0.55938 0.55985 0.55946	0.55192 0.55233 0.55194	0.54524 0.54558 0.54520	0.53941 0.53967 0.53930	0.53448 0.53466 0.53429	0.53055 0.53065 0.53026
SK_4	0.55957 0.55967 0.55953	0.55205 0.55215 0.55203	0.54530 0.54541 0.54528	0.53939 0.53950 0.53937	0.53438 0.53449 0.53437	0.53035 0.53046 0.53034

[††] In each column, the values from the top to bottom are for Set-1, Set-2, and Set-3, respectively.

Table 4 Reflectivities of the benchmark problem 2 for quadratically varying scattering albedo cases

Method	Scattering Albedo, $\Omega_0(\tau)$			
	$4\tau/15+0.5\tau^2$	$0.4-4\tau/15+0.5\tau^2$	$0.6-8\tau/15+0.5\tau^2$	$1-16\tau/15+0.5\rho^2$
Exact	0.56871	0.55292	0.54619	0.53534
S_8	0.56882	0.55321	0.54656	0.53582
SK_1	0.55431[‡‡]	0.54165	0.53587	0.52552
	0.56694	0.55358	0.54793	0.53898
	0.55203	0.53940	0.53358	0.52302
SK_2	0.56648	0.55197	0.54581	0.53598
	0.56954	0.55376	0.54703	0.53620
	0.56821	0.55247	0.54576	0.53497
SK_3	0.56837	0.55271	0.54605	0.53537
	0.56901	0.55320	0.54646	0.53559
	0.56861	0.55281	0.54608	0.53522
SK_4	0.56870	0.55289	0.54616	0.53530
	0.56882	0.55301	0.54628	0.53542
	0.56867	0.55288	0.54615	0.53530

[‡‡] In each column, the values from the top to bottom are for Set-1, Set-2, and Set-3, respectively.

same. The errors with Set-2 slightly increase. The errors for SK_1 through SK_3 approximations are 1.83, 1.30, and 2.32 percent; -0.04, -0.16, and 0.06 percent; and 0.0, -0.05, and 0.02 percent, for Set-1, 2, and 3, respectively. In $\Omega_0(\tau)=0.8-2\tau/5$ and $\Omega_0(\tau)=1-2\tau/3$ cases, the error with S_8 approximation is -0.12 percent while the SK_1 approximation errors are 1.84, -0.69, and 2.31; and 1.96, -0.85, and 2.56 percent for Set-1, 2, and 3, respectively. The SK_2 approximation errors are -0.13, -0.16, and 0.06; and -0.22, -0.17, and 0.05 percent for Set-1, 2 and 3, respectively. While the maximum errors with SK_3 approximation are 0.05 percent, the errors with SK_4 approximation are reduced to less than 0.02 percent in both scattering albedo cases. Overall assessment reveals that, the SK_1 approximation using Set-2 yields much better solutions than the other two sets; however, in the SK_2 approximation using Set-3 is better. As the order of approximation is increased all three quadrature sets yield smaller errors and also the performance of the quadratures become nearly identical.

The solutions for quadratically varying scattering albedo cases with the SK_N approximation of orders up to 4 with the three quadrature sets are tabulated comparatively with the exact and S_8 [12] solutions in Table 4. The following cases are considered: $\Omega_0(\tau)=4\tau/15+0.5\tau^2$, $\Omega_0(\tau)=0.4-4\tau/15+0.5\tau^2$, $\Omega_0(\tau)=0.6-8\tau/15+0.5\tau^2$ and $\Omega_0(\tau)=1-16\tau/15+0.5\tau^2$. The SK_1 approximation for $\Omega_0(\tau)=4\tau/15+0.5\tau^2$ and $\Omega_0(\tau)=0.4-4\tau/15+0.5\tau^2$ cases, which scattering albedo is greater near the surface of the sphere, yields errors of 2.53, 0.31 and 2.93 percent, and 2.04, -0.12 and 2.45 percent, for the cases and for Set-1, 2 and 3, respectively. These error values for SK_2 approximation are 0.39, -0.15 and 0.09; and 0.17, -0.15 and 0.08, and for SK_3 the errors are reduced to 0.06, -0.05 and 0.02 percent, for Set-1, 2 and 3, respectively. The S_8 approximation errors for $\Omega_0(\tau)=4\tau/15+0.5\tau^2$ and $\Omega_0(\tau)=0.4-4\tau/15+0.5\tau^2$ are -0.02 and -0.05 percent, respectively. On the other hand, the SK_1 approximation for $\Omega_0(\tau)=0.6-8\tau/15+0.5\tau^2$ and $\Omega_0(\tau)=1-16\tau/15+0.5\tau^2$ cases, which scattering albedo is higher at the core of the sphere, yield errors of 1.89, -0.32 and 2.31 percent, and 1.83, -0.68 and 2.30 percent, for the given cases and for Set-1, 2 and 3, respectively. These error values for SK_2 approximation are 0.07, -0.15 and 0.08 and -0.12, -0.16 and 0.07, and for SK_3 the errors are further reduced to 0.03, -0.05 and 0.02 percent, for Set-1 through 3, respectively. The errors for SK_4 approximation are less than 0.02 percent for all cases considered. The S_8 approximation errors for $\Omega_0(\tau)=0.6-8\tau/15+0.5\tau^2$ and $\Omega_0(\tau)=1-16\tau/15+0.5\tau^2$ are -0.07 and -0.09 percent, respectively. The SK_1 approximation using Set-2 is again superior to the other two sets; but in the SK_2 approximation with Set-3 yields solutions better than Set-2. As the order of approximation is increased all three quadrature sets yields smaller errors and they also have converge the same solutions.

The solutions for exponential and cosine variation of scattering albedo cases with the SK_N approximation of orders up to 4 with the three quadrature sets are tabulated comparatively with the exact and S_8 solutions in Table 5. The following exponential and cosine variation of scattering albedo cases are considered: $\Omega_0(\tau)=0.790988e^{-\tau}$, $\Omega_0(\tau)=0.790988e^{-(1-\tau)}$, $\Omega_0(\tau)=0.5+0.5\tau\cos 12\pi\tau$ and $\Omega_0(\tau)=0.5+0.5(1-\tau)\cos 12\pi(1-\tau)$. In $\Omega_0(\tau)=0.790988e^{-\tau}$ and $\Omega_0(\tau)=0.790988e^{-(1-\tau)}$ cases, the SK_1 approximation yields errors of 1.07, -0.41 and 1.35 percent, and 3.21, -0.18 and 3.83 percent, for Set-1, 2 and 3, respectively. These error values for SK_2 approximation become -0.09, -0.09 and 0.03; and 0.26, -0.24 and 0.11, for Set-1, 2 and 3, respectively. On the other hand, while the errors with S_8 approximation are -0.12 and 0.07 percent, for the exponential cases, respectively, in SK_3 approximation, the errors are reduced to -0.01, -0.03 and 0.01; and 0.05, -0.08, and 0.03, for Set-1, 2, and 3, respectively. In cosine growing/damped albedo cases, the SK_1 approximation yields errors of 2.1, -0.16 and 2.53 percent, and 1.89, -0.39 and 2.32 percent, for Set-1, 2 and 3 and $\Omega_0(\tau)=0.5+0.5\tau\cos 12\pi\tau$ and $\Omega_0(\tau)=0.5+0.5(1-\tau)\cos 12\pi(1-\tau)$, respectively. The SK_2 approximation yields the errors of 0.27, 0.01 and 0.3 percent; and 0.04, -0.14 and 0.09, for Set-1, 2, and 3, respectively while the errors with S_8 approximation are -0.07 and 0.09 percent, respectively. The errors with the SK_3 approximation are below 0.07 percent with all three sets. The performance of the quadrature sets are the same; as previously mentioned scattering albedo cases where Set-2 is better with SK_1 and Set-3 with SK_2 approximations.

4.3 Error Assessment at Low Orders. The argument presented in Refs. [8], [9] on the accuracy of the synthetic kernels and the quadrature sets is also valid here. The solutions of the cases of benchmark problem 2 with scattering albedos decreasing towards the surface are less than those of increasing towards the surface of the sphere. This outcome is the opposite of that of the plane-parallel medium since $E_1(|\tau-\tau'|)$ term of the integral kernel at $\tau=\tau'$ has a singularity. However, the integral kernel of the plane-parallel medium consists of only $E_1(|\tau-\tau'|)$ [8] whereas the integral kernel for the incident radiation in spherical medium

Table 5 Reflectivities of the benchmark problem 2 for exponential and cosine varying scattering albedo cases

Method	Scattering Albedo, $\Omega_0(\tau)$			
	$0.790988e^{-\tau}$	$0.790988e^{-(1-\tau)}$	$0.5+0.5\tau\cos 12\pi\tau$	$0.5+0.5(1-\tau)\cos 12\pi(1-\tau)$
Exact	0.46360	0.64401	0.54935	0.54165
S_8	0.46416	0.64443	0.54973	0.54214
SK_1	0.45862[§§]	0.62335	0.53781	0.53141
	0.46551	0.64517	0.55021	0.54376
	0.45732	0.61935	0.53546	0.52908
SK_2	0.46400	0.64232	0.54787	0.54144
	0.46403	0.64557	0.54928	0.54241
	0.46344	0.64329	0.54772	0.54116
SK_3	0.46364	0.64372	0.54823	0.54147
	0.46373	0.64452	0.54958	0.54192
	0.46354	0.64381	0.54892	0.54151
SK_4	0.46359	0.64400	0.54839	0.54153
	0.46364	0.64418	0.54948	0.54174
	0.46358	0.64393	0.54937	0.54162

[§§] In each column, the values from the top to bottom are Set-1, Set-2, and Set-3, respectively.

is a combination of $E_1(|\tau-\tau'|)$ and $E_1(\tau+\tau')$. Thus, the errors associated by each exponential integral function compensate for each other and since the number of exponential integral functions of order 1 and 3 are encountered in the transfer kernels—Eqs. (1) and (2)—a different trend from the plane-parallel geometry is to be expected. On the other hand, the success of Set-3 for $N\geqslant 2$ is due to Set-3 satisfying also the first spatial moment of $E_2(x)$ which is demonstrated in Ref. [9]. Yet the convergence of the SK_N approximation to the integral equation solution is not affected by the number and/or the order of exponential integrals of the transfer kernels, and as the order of approximation is increased the SK_N solutions yield the exact RITE solutions.

5 Conclusions

The SK_N approximation is applied to RITEs in one-dimensional spherical isotropically scattering participating homogeneous and inhomogeneous medium, and the SK_N equations along with the proper mathematical boundary conditions are derived. The benchmark problems consisting of a wide range of optical configurations and spatially varying scattering albedos are used to compare the SK_N solutions with those of the exact and DOM S_8. Based on the results presented, the following conclusions have been drawn:

1) The method is computationally very cheap and memory efficient. The cpu time with 800 grids for the exact, SK_2 and SK_5 are on the order of 18, 0.13 and 0.5 seconds, respectively, which makes even high order approximations, such as SK_5, very attractive to be used.

2) Since the method is derived from the RITE rather than RTE, the ray affect, which is a problem associated with the angular discretization, is not observed in the solutions.

3) The solutions with increasing orders converge the exact solution regardless of the optical thickness and scattering albedo variations. Even in the presence of a highly oscillating source in the medium, such as cosine variation of albedo cases, the results even with the SK_3 approximation are in excellent agreement with the exact solutions.

4) The performance of the quadratures are as follows: in SK_1 approximation Set-2 is better than the others yielding maximum errors of 2.72 percent in highly scattering medium and $\tau_0=1$ whereas the errors for absorbing medium is less than 1 percent occurring in optically thick medium; in SK_2 approximation Set-3 in optically thin and moderate medium is better, however, in optically thick medium Set-1 and Set-2 yield identical solutions. The SK_3 approximation with Set-3 is slightly better than the other two sets for optically thin systems; however, for optically thick systems, all three quadrature sets yield the same order of magnitude errors.

Nomenclature

$E_n(x)$ = n^{th} order exponential integral function
$G(\tau)$ = dimensionless incident radiation $(=2\pi\int_{-1}^{1}I(\tau,\mu)d\mu)$
$G_n(\tau)$ = functions defined by Eq. (7)
I = dimensionless radiative intensity
I_w = incident isotropic radiation intensity on the surface of sphere
R = reflectivity
S = dimensionless isotropic source function defined by Eq. (3)
T = temperature
$f_1(\tau)$, $f_2(\tau)$ = boundary terms defined by Eqs. (4) and (5)
$q(\tau)$ = dimensionless radiative heat flux $(=2\pi\int_{-1}^{1}I(\tau,\mu)\mu d\mu)$
$q_n(\tau)$ = functions defined by Eq. (8)
r = radial variable
r_0 = radius
w_n = quadrature weights

Greek Symbols

Ω_0 = scattering albedo $(=\kappa/\beta)$
β = extinction coefficient
κ = absorption coefficient
μ = angular cosine
μ_n = quadrature abscissas
σ = scattering coefficient
θ = dimensionless temperature $(=T/T_{\text{ref}})$
τ = dimensionless optical variable $(=\beta r)$
τ_0 = optical radius $(=\beta r_0)$

Subscripts

n = n^{th} component of the SK_N equation
$+$ = outgoing
$-$ = incoming

Superscript

$'$ = dummy integration variable

References

[1] Lewis, E. E., and Miller, W. F., 1984, *Computational Methods of Neutron Transport*, John Wiley & Sons, Inc.
[2] Spinrad, B. I., and Sterbentz, J. S., 1985, "Approximations to Neutron Transport Problems in Complex Geometries: I," Nucl. Sci. Eng., **90**, pp. 431–440.
[3] Altaç, Z., and Spinrad, B. I., 1990, "The SK_N Method I: A High Order Transport Approximation to Neutron Transport Problems," Nucl. Sci. Eng., **106**, pp. 471–479.
[4] Spinrad, B. I., and Altaç, Z., 1990, "The SK_N Method II: Heterogeneous Problems," Nucl. Sci. Eng., **106**, pp. 480–488.
[5] Altaç, Z., 1989, "The SK_N approximation: A New Method for Solving the Integral Transport Equations," Ph.D. thesis, Iowa State University, Ames, IA.
[6] Altaç, Z., 1997, "The SK_N approximation for solving Radiation Transport Problems In Absorbing, Emitting, and Scattering Media," DOGA Turk. Eng. Environ. Sci., **21**, pp. 51–58.
[7] Altaç, Z., and Tekkalmaz, M., 2002, "The SK_N approximation for Solving Radiation Transport Problems in Absorbing, Emitting, and Scattering Rectangular Geometries," J. Quant. Spectrosc. Radiat. Transf., **73**, pp. 219–230.
[8] Altaç, Z., 2002, "The SK_N approximation for Solving Radiative Transfer Problems In Absorbing, Emitting, and Isotropically Scattering Plane-Parallel Medium: Part 1," ASME J. Heat Transfer, **124**(4), pp. 674–684.
[9] Altaç, Z., 2002, "The SK_N approximation for Solving Radiative Transfer Problems In Absorbing, Emitting, and Linearly Anisotropically Scattering Plane-Parallel Medium: Part 2," ASME J. Heat Transfer, **124**(4), pp. 685–695.
[10] Viskanta, R., and Crosbie, A. L., 1967, "Radiative Transfer Through a Spherical Shell of an Absorbing-Emitting Gas Medium," J. Quant. Spectrosc. Radiat. Transf., **7**, pp. 871–889.
[11] Abramowitz, M., and Stegun, I. A., 1964, *Handbook of Mathematical Functions*, Dover Publications Inc.
[12] Tsai, J. R., Özişik, M. N., and Santarelli, F., 1989, "Radiation in Spherical Symmetry With Anisotropic Scattering and Variable Properties," J. Quant. Spectrosc. Radiat. Transf., **42**, pp. 187–199.

The Performances of Internal Helical-Rib Roughness Tubes Under Fouling Conditions: Practical Cooling Tower Water Fouling and Accelerated Particulate Fouling

---

Wei Li
e-mail: weili96@hotmail.com
Mem. ASME
Consultant
2 Breezy Tree Ct., Apt. H, Timonium, MD 21093

This paper addresses fouling in a family of seven copper helically ribbed tubes. Series of semi-theoretical linear fouling correlations for long term combined precipitation and particulate fouling (PPF) in cooling tower systems and for accelerated particulate fouling were developed. [DOI: 10.1115/1.1571090]

Keywords: Cooling Towers, Fouling, Heat Transfer, Heat Recovery

Introduction

The two subject areas of fouling and enhancement have been developed mainly independently for many years. Watkinson [1] had attempted to bring the two areas together in an early paper. Rabas et al. [2] monitored the fouling characteristics of helically corrugated (indented) steam condenser tubes in an electric utility plant for 15 months. Bott [3] and Epstein [4] described information on particle deposition.

Bergles and Somerscales [5] suggested a method to measure the fouling thermal resistance in condenser tubes by supplying the cooling water that flows through the tubes in a separate testing condenser, from the same source as the main condenser. The method was used in this study. The fouling in cooling tower water systems is the combination of precipitation fouling and particulate fouling (PPF). Seven helical rib roughened tubes and one plain tube were tested for their susceptibility to PPF in one cooling season [6]. In order to provide further data, accelerated particulate fouling tests were performed [7]. Little information exists on the differences between modeling of practical long-term PPF data and modeling of accelerated particulate fouling data in enhanced tubes. The purpose of this paper is to provide correlations of the experimental results [6,7]. The comparison of the PPF and the accelerated particulate fouling correlations is used to explain the apparent differences between the in-lab and the in-plant results.

Tube Geometries and Experimental Method

The tube geometries and test procedures were fully described [6,7]. One of the tubes (Tube 1) is a plain copper tube and is used to compare to the other seven helically ribbed copper tubes. The ranges of geometric parameters were number of rib starts (18 to 45), helix angle (25 to 45 deg), and height (0.33 to 0.55 mm). All fins were of a trapezoidal cross-section shape with a 41 deg included angle. All eight tubes have the same inside diameter of 15.54 mm.

The apparatus for long term practical fouling tests [6], a fouling test condenser, was connected in parallel with the condenser of a 880 kW water chiller. The cooling tower water supplied to the main refrigerant condenser was also supplied to the tubes in the fouling condenser. It contains sixteen 3.66 m long tubes, installed as eight pairs of identical tubes (seven pairs of enhanced tubes and one pair of plain tube geometry). The cooling tower water is circulated through the condenser in a one-pass arrangement at 1.07 m/s tube side velocity ($\mathrm{Re}=16{,}000$)-about half of the commonly used velocity for refrigerant condenser applications. System water has 800 ppm ($\pm 20\%$) calcium hardness and 8.5 pH. The water mass flow rate in each tube was determined by measuring the water pressure drop in the tube. Typical operating conditions for water pressure drop and temperature difference are 6.8 kPa and 2.5°C, respectively. The absolute errors in pressure and temperature measurement are ± 0.03 kPa and ± 0.1°C, respectively. The estimated uncertainty in fouling measurement is 6.2%.

The apparatus for accelerated particulate fouling tests [7] was capable of testing four 19 mm O.D. tubes simultaneously. Heat is transferred to the 3.05 m long test sections by condensing R-114 on the annulus side of the test section. Condensed R-114 is returned to electric heated boilers. Plain tube 1 and helical-rib tubes 2, 3, 4, 5 and 8 in Table 1 were tested at 1300 ppm concentration and at $\mathrm{Re}=16{,}000$. The tests were conducted using aluminum oxide particles (3.0 μm average particle diameter) suspended in 8.0 pH city water. The fouling resistance has an uncertainty of 11.8%.

Table 1 $R_f^{\mathrm{Part}}/R_{fp}^{\mathrm{Part}}$ **at the end of the testing period and** $R_f^{\mathrm{PPF}}/R_{fp}^{\mathrm{PPF}}$ **at the end of one cooling season**

Tube	$R_f^{\mathrm{PPF}}/R_{fp}^{\mathrm{PPF}}$	$R_f^{\mathrm{Part}}/R_{fp}^{\mathrm{Part}}$	$\beta\eta$	η	p/e
2	5.15	8.71	1.96	1.18	2.81
5	3.40	5.42	1.82	1.04	3.31
3	2.26	5.34	1.64	1.05	3.50
6	1.57	n/a	1.54	1.01	5.02
7	1.51	n/a	1.60	1.05	7.05
8	1.25	4.40	1.37	0.98	9.77
4	1.13	3.76	1.18	0.95	9.88
1	1.0	1.0	1.0	1.0	n/a

Contributed by the Heat Transfer Division for publication in the JOURNAL OF HEAT TRANSFER. Manuscript received by the Heat Transfer Division July 26, 2002; revision received February 11, 2003. Associate Editor: J. N. Chung.

Fouling Data Analysis and Discussion

Li et al. [7] have shown:

$$\frac{R_f^*}{R_{fp}^*}=C\eta \qquad (1)$$

where $\eta=(j/j_p)/(f/f_p)$ is the efficiency index and subscript "p" indicates a plain surface. C is a constant, which is determined from the fouling tests. In principle, Eq. (1) can embrace all fouling mechanisms providing the fouling is asymptotic [7].

Table 1 lists the fouling factor ratios $R_f^{\text{Part}}/R_{fp}^{\text{Part}}$ at the end of the testing period and $R_f^{\text{PPF}}/R_{fp}^{\text{PPF}}$ at the end of the cooling season. Figure 1 shows the $R_f^{\text{Part}}/R_{fp}^{\text{Part}}$ and the $R_f^{\text{PPF}}/R_{fp}^{\text{PPF}}$ versus the clean tube η in Table 1. The $R_f^{\text{Part}}/R_{fp}^{\text{Part}}$ ratio linearly increases with increasing η:

$$\frac{R_f^{\text{Part}}}{R_{fp}^{\text{Part}}}=21.36\eta-16.70 \qquad (2)$$

Equation (2) has an average deviation of 4.1%. Figure 1 also shows that the $R_f^{\text{PPF}}/R_{fp}^{\text{PPF}}$ is not able to be correlated as a function of η. Since Eq. (1) is based on the heat-mass transfer analogy, it is automatically assumed that the fouling deposit is formed by a large amount of individual particles [7]. The effect of cohesion between the particles and the tube surface is not included. This is valid for particulate fouling instead of PPF. Inverse solubility salts (mostly $CaCO_3$ and $MgCO_3$ in cooling tower water) exhibit decreasing saturation concentration beyond certain temperature. As a consequence, crystalline deposits start to form if such solutions contact heated surfaces. The particulate fouling deposits primarily on the surfaces between the ribs and on rib tip surfaces. The nominal internal surface area (A) based on a plain tube, the reference surface in above Eqs. (1) and (2), has been use widely in particulate fouling data analysis of enhanced tubes [7]. Figure 2 shows that significant physical PPF deposits cover the total internal surface of a tested tube 5 after the completion of tests in one cooling season. The PPF deposits on the total internal surface (A_w) including the surfaces between ribs, rib tip surfaces, and side surfaces of ribs, due to the deposit cohesion. This is the reason why the $R_f^{\text{PPF}}/R_{fp}^{\text{PPF}}$ is not able to be correlated as a function of η. In order to including the difference between A_w and A, we introduced an area index, $\beta=(A_w/A)/(A_c/A_{cp})$ into equation (1): $R_f^{\text{PPF}}/R_{fp}^{\text{PPF}}\propto\beta\eta$. No information exits of the physical meaning of $\beta\eta$. The helical rib roughened tubes probably provide some of the attributes of a rough tube (local flow separations), which is reflected in η, and some of an internally finned tube (large surface area increase), which is reflected in β.

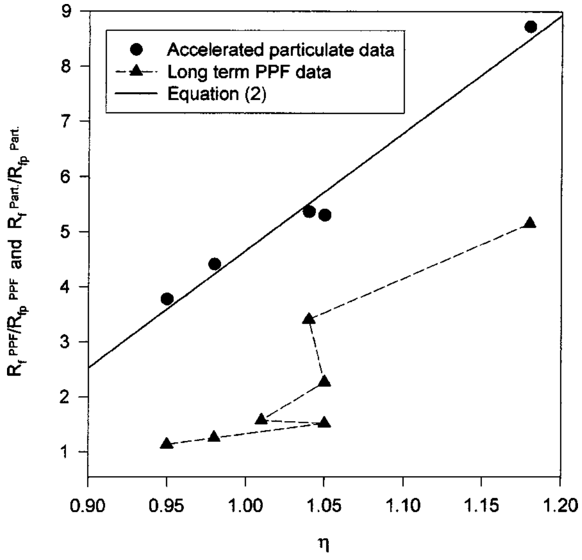

Fig. 1 $R_f^{\text{PPF}}/R_{fp}^{\text{PPF}}$ **and** $R_f^{\text{Part}}/R_{fp}^{\text{Part}}$ **versus** η

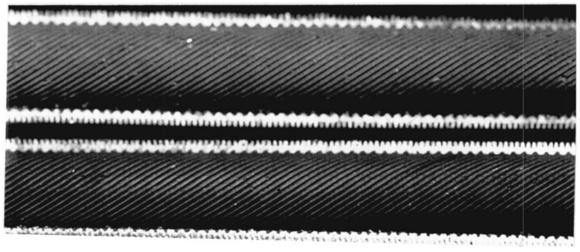

Fig. 2 A photo of fouled (upper photo) and unfouled (lower photo) tube 5 after completion of tests

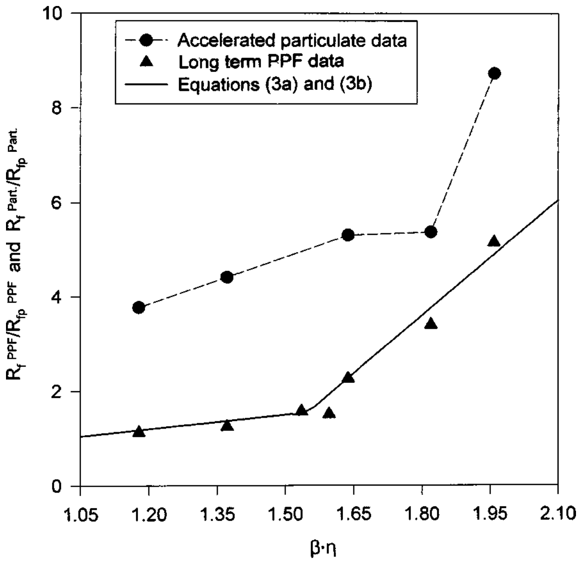

Fig. 3 $R_f^{\text{PPF}}/R_{fp}^{\text{PPF}}$ **and** $R_f^{\text{Part}}/R_{fp}^{\text{Part}}$ **versus** $\beta\eta$

Figure 3 shows $R_f^{\text{Part}}/R_{fp}^{\text{Part}}$ and $R_f^{\text{PPF}}/R_{fp}^{\text{PPF}}$ versus the clean tube $\beta\eta$ in Table 1. As we expected, the $R_f^{\text{Part}}/R_{fp}^{\text{Part}}$ is not able to be correlated as a function of $\beta\eta$. On the other hand, the $R_f^{\text{PPF}}/R_{fp}^{\text{PPF}}$ ratio linearly increases with increasing $\beta\eta$:

$$\frac{R_f^{\text{PPF}}}{R_{fp}^{\text{PPF}}}=\beta\eta \qquad 10.0>p/e\geqslant 5.0 \qquad (3a)$$

$$\frac{R_f^{\text{PPF}}}{R_{fp}^{\text{PPF}}}=8.18\beta\eta-11.11 \qquad p/e<5.0 \qquad (3b)$$

Equation 3(a) and 3(b) have an average deviation of 5.8%. For transverse ribs ($\alpha=90$ deg), reattachment will occur, when the pitch of roughness is larger than approximately five rib heights [7]. For helical rib roughness tubes, when $e/D_i<0.04$ in this study, the fouling process is mainly determined by the separated flow caused by the pitch of ribs. It is interesting to know that there is only one linear range for $R_f^{\text{Part}}/R_{fp}^{\text{Part}}$ in Fig. 1. This is another hint of the difference between particulate fouling deposition and PPF deposition. The particulate fouling deposits mainly exist in the interfin region of the test tube. The actual p/e increases as the fouling deposits continue to fill in the interfin region. When the fouling resistance reaches asymptotic value, the p/e of each helical rib roughness tube will be larger than five. Figure 2(a) in Li et al. [7] shows that the $R_f^{\text{Part}}/R_{fp}^{\text{Part}}$ in Table 1 is close to asymptotic value. On the other hand, PPF deposits exist on the total heat transfer surfaces of the tubes. The actual p/e values remain closed to the p/e values of clean tubes as the fouling deposits increase, which is confirmed by Fig. 2. Therefore, there are two ranges in Fig. 3 corresponding to $p/e \geqslant 5.0$ and $p/e < 5.0$, respectively.

Conclusions

The fouling resistances of helical rib roughened tubes were higher than that of plain tube at low Re (16,000) for both practical long-term PPF and accelerated particulate fouling.

With respect to PPF, the $R_f^{\text{PPF}}/R_{fp}^{\text{PPF}}$ ratio linearly increases with increasing $\beta \cdot \eta$; There are two linear ranges of fouling characteristics corresponding to $p/e < 5.0$ and $p/e \geqslant 5.0$. With respect to accelerated particulate fouling, the ratio of $R_f^{\text{Part}}/R_{fp}^{\text{Part}}$ linearly increases with increasing η; There is one range of fouling characteristics.

Acknowledgment

The author would like to thank Prof. Ralph L. Webb at Penn State and Prof. Arthur E. Bergles at RPI for their valuable contributions.

Nomenclature

A = nominal internal surface area based on plain tube, m^2
A_c = cross sectional area, m^2
A_w = inside wetted surface area, m^2
e = internal rib height (average value), m
f = fanning friction factor, dimensionless
j = Colburn j-factor ($= \text{StPr}^{2/3}$), dimensionless
p = axial element pitch, m
R_f = fouling resistance, m$^2 \cdot$K/W
R_f^* = asymptotic fouling resistance, m$^2 \cdot$K/W

Greek Letters

β = area index, $(A_w/A_{wp})/(A_c/A_{cp})$, dimensionless
η = efficiency index, $(j/j_p)/(f/f_p)$, dimensionless

References

[1] Watkinson, A. P., 1990, "Fouling of Augmented Heat Transfer Tubes," Heat Transfer Eng., **11**(3), p. 57.
[2] Rabas, T. J., et al., 1993, "Comparison of Power-Plant Condenser Cooling-Water Fouling Rates for Spirally-indented and Plain Tubes," Heat Transfer Eng., **14**(4), p. 58.
[3] Bott, T. R., 1995, *Fouling of Heat Excangers*, Elsevier Science, New York.
[4] Epstein, N., 1997, "Elements of Particle Deposition Onto Nonporous Solid Surface Parallel to Suspension Flows," Exp. Therm. Fluid Sci., **14**, pp. 323–334.
[5] Bergles, A. E., and Somerscales, E. F. C., 1995, "The Effect of Fouling on Enhanced Heat Transfer Equipment," J. Enhanced Heat Transfer, **2**(1–2), pp. 157–166.
[6] Webb, R. L., and Li, W., 2000, "Fouling in Enhanced Tubes Using Cooling Tower Water Part I: Long Term Fouling Data," Int. J. Heat Mass Transf., **43**, pp. 3567.
[7] Li, W., Webb, R. L., and Bergles, A. E., 2002, "Particulate Fouling of Water in Internal Helical-rib Roughness Tubes," Proc. 12th International Conference of Heat Transfer at Grenoble in France, editor: Jean Taine, Société française des thermiciens (SFT), Elsevier, Paris in France.

Monte Carlo Simulation of Radiative Heat Transfer in Coarse Fibrous Media

Eugen Nisipeanu
Fluent, Inc., Evanston, IL

Peter D. Jones
Mechanical Engineering Department, Auburn University, AL 36849

Direct Geometric Monte Carlo modeling of a fibrous medium is undertaken. The medium is represented as a monodisperse array, with known solidity, of randomly oriented cylinders of known index of refraction. This technique has the advantage that further radiative properties of the medium (absorption coefficient, scattering albedo, scattering phase function) are not required, and the drawback that its' Snell- and Fresnel-generated dynamics suggest a limitation to large, smooth fibers. It is found that radiative heat flux results are highly dependent on bias in the polar orientation angle (relative to the boundary planes) of the fibers. Randomly oriented fiber results compare well to both the large (specular radiosity method) and small (radiative transfer equation) limits, while the results of previous experiments lie within the range of simulation results generated using varying degrees of orientation bias. [DOI: 10.1115/1.1571092]

Keywords: Heat Transfer, Insulation, Monte Carlo, Porous Media, Radiation

Introduction

In studies of radiative transfer through fibrous materials, the medium is usually represented as spatially continuous and the Radiative Transfer Equation (RTE) is applied, using radiative properties determined from experiment or by applying electromagnetic theory. In the present note fibrous media are represented as discrete arrays of randomly located and oriented cylindrical surfaces. Bundles of radiation intensity are released from the boundaries of the medium in a Geometric Monte Carlo (GMC) simulation. The bundles interact as surface reflections and absorptions with the fibers in their path. By more detailed representation of the fibrous medium morphology, this method avoids breakdown of radiative continuum near the boundaries of the medium, and allows bias in the fiber orientation direction to be conveniently considered. Snell's laws are used for fiber-surface reflection directions, and Fresnel's equations are used to derive surface radiation properties. Hence the method applies only to smooth-surfaced fibers in the geometric limit. However, the method has the advantage that the only radiative property required is the complex index of refraction for the fiber material, and there is no uncertainty over the form of the scattering phase function. The technique is similar to that employed by Nisipeanu and Jones [1] in a study of spherical particle suspensions. This note reports an extension of the technique into the geometry of a dispersion of cylindrical particles, which require a different geometrical development, and admit the complication of non-random fiber orientation.

Contributed by the Heat Transfer Division for publication in the JOURNAL OF HEAT TRANSFER. Manuscript received by the Heat Transfer Division January 24, 2002; revision received February 13, 2003. Associate Editor: R. Skocypec.

Analysis

The fibers are randomly oriented, infinitely long, straight cylinders. The fibers are limited in axial extent only by the rectangular boundaries of the medium. Bent fibers could be represented by two or more of these cylinders. Fiber intersection volumes are ignored.

Randomly oriented cylinders are generated in a three-dimensional rectangular control domain of variable size. One of the control domain corners is the origin of the global coordinate system. Randomly oriented position vectors $\hat{\mathbf{v}}$ are generated having a length S (Fig. 1).

$$S=\lambda x+\mu y+\nu z \tag{1}$$

is the equation of a plane PP normal to $\hat{\mathbf{v}}$ at a distance S from the origin, where $\{x, y, z\}$ is the global coordinate system and $\{\lambda,\mu,\nu\}$ are the direction cosines of $\hat{\mathbf{v}}$. A local coordinate system $\{x_l, y_l, z_l\}$ is constructed with one axis $\hat{\mathbf{t}}_\mathbf{n}$ normal to plane PP, and the other two included in the plane (Fig. 1):

$$\begin{aligned}\hat{\mathbf{t}}_\mathbf{n}&=\lambda\hat{\mathbf{i}}+\mu\hat{\mathbf{j}}+\nu\hat{\mathbf{k}}\\ \hat{\mathbf{t}}_\mathbf{1}&=\frac{\hat{\mathbf{i}}\times\hat{\mathbf{t}}_\mathbf{n}}{|\hat{i}|\times\hat{\mathbf{t}}_\mathbf{n}}=\frac{-\nu\hat{\mathbf{j}}+\mu\hat{\mathbf{k}}}{\sqrt{\mu^2+\nu^2}}\\ \hat{\mathbf{t}}_\mathbf{2}&=\frac{\hat{\mathbf{t}}_\mathbf{n}\times\hat{\mathbf{t}}_\mathbf{1}}{|\hat{\mathbf{t}}_n\times\hat{\mathbf{t}}_\mathbf{1}|}=\frac{\sqrt{\mu^2+\nu^2}\hat{\mathbf{i}}-\lambda\mu\hat{j}+\lambda\nu\hat{\mathbf{k}}}{\sqrt{\mu^2+\nu^2}}.\end{aligned} \tag{2}$$

If

$$\mathbf{A}=\begin{bmatrix}0 & \frac{-\nu}{\sqrt{\mu^2+\nu}} & \frac{\mu}{\sqrt{\mu^2+\nu}}\\ \sqrt{\mu^2+\nu} & \frac{-\lambda\mu}{\sqrt{\mu^2+\nu}} & \frac{-\lambda\nu}{\sqrt{\mu^2+\nu}}\\ \lambda & \mu & \nu\end{bmatrix}, \tag{3}$$

then

$$x_l\hat{\mathbf{t}}_\mathbf{1}+y_l\hat{\mathbf{t}}_\mathbf{2}+z_l\hat{\mathbf{t}}_\mathbf{n}=x\hat{\mathbf{i}}+y\hat{\mathbf{j}}+z\hat{\mathbf{k}}\Rightarrow\begin{Bmatrix}x_l\\ y_l\\ z_l\end{Bmatrix}=\mathbf{A}\begin{Bmatrix}x\\ y\\ z\end{Bmatrix} \tag{4}$$

relates the local to the global coordinate system.

The equations of a cylinder normal to plane PP in the local coordinate system are

$$\begin{gathered}R^2=(x_l-x_{lo})^2+(y_l-y_{lo})^2\\ z_l\in\Re\end{gathered} \tag{5}$$

where x_{lo} and y_{lo} are the coordinates of a point arbitrarily chosen on plane PP, and R is the fiber radius. The local coordinate system is used in order to construct cylinders that are not necessarily centered around the position vector $\hat{\mathbf{v}}$. By applying Eq. (4), the infinite cylinder equation in the global coordinate system becomes

$$R^2=\frac{[(\mu^2+\nu^2)(x-x_o)-\lambda\mu(y-y_o)-\lambda\nu(z-z_o)]^2+[\mu(z-z_o)-\nu(y-y_o)]^2}{\mu^2+\nu^2}. \tag{6}$$

Randomly oriented cylinders with random offsets from the position vector are generated until the desired volume fraction is obtained. A representation of just a few randomly oriented and positioned fibers is shown in Fig. 2, along with a representative intensity bundle path.

The bottom boundary of the control domain is taken to be hot and black, emitting radiative flux simulated as energy bundles released from random positions and directions. The top boundary is taken to be black, cold in some cases, and cooler than the bottom boundary (though still emitting) in others. The coordinates of an energy bundle after it travels a distance P are

$$\begin{aligned}x&=x_{st}+l_1P\\ y&=y_{st}+l_2P\\ z&=z_{st}+l_3P\end{aligned} \tag{7}$$

where $\{x_{st}, y_{st}, z_{st}\}$ initially represent the starting position of the bundle (x_{st} and y_{st} are random, and z_{st} corresponds to the top or bottom boundary), and $\{l_1, l_2, l_3\}$ are the direction cosines of the

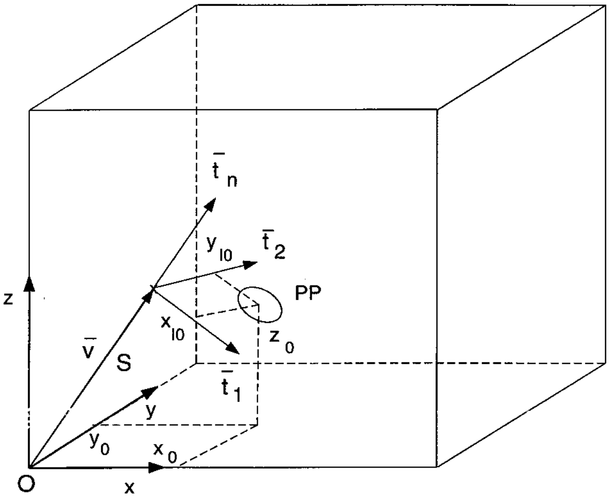

Fig. 1 Generation of randomly oriented cylindrical fibers

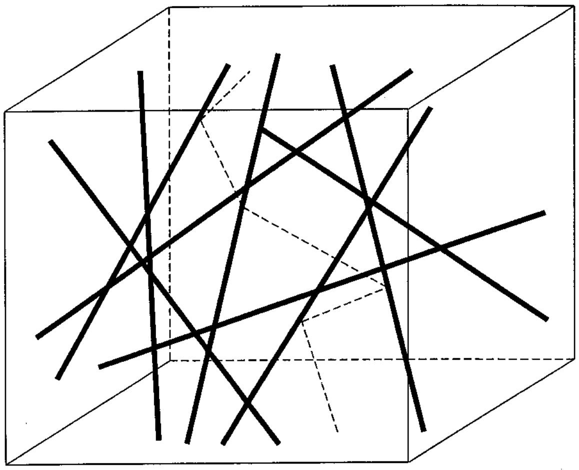

Fig. 2 Three dimensional view of a fibrous medium

bundle's random direction. Writing Eqs. (7) into Eqs. (6) yields a relation where P defines a point of intersection between the bundle and a cylinder. The discriminant of this second order equation in P is computed. If this discriminant is positive, the equation has real roots and there is an impact at the smaller of the two [2], the other impact point being impossible for opaque fibers. The incident polar and azimuthal angles relative to the fiber surface are computed from the direction of the in-coming ray and the surface normal at the intersection point.

At the point of impact with the fiber's surface, the energy bundle is absorbed or reflected depending on the absorptivity or reflectivity of the fiber. The surface radiative properties are predicted by Fresnel's equations, which are functions of the fiber material complex index of refraction $m=n-ik$. Reflections by individual fibers may be taken as specular without loss of accuracy [1]. The direction of a reflected ray is determined using Snell's law:

$$\hat{\mathbf{s}}_{\mathbf{r}}=\hat{\mathbf{s}}_{\mathbf{i}}+2|\hat{\mathbf{s}}_{\mathbf{i}}\cdot\hat{\mathbf{n}}|\hat{\mathbf{n}} \tag{8}$$

in which the unit surface normal $\hat{\mathbf{n}}(n_1,n_2,n_3)$ is

$$\hat{\mathbf{n}}=\frac{\nabla g}{|\nabla g|} \tag{9}$$

and g is the right-hand side of the surface equation of the cylinder given by Eq. (6). The bundle is followed in its new (reflected) direction, from (x_{st},y_{st},z_{st}) at the impact point until it either strikes another fiber, reflects off the (perfectly specular) sides of the medium, or exits the medium through its top or bottom surfaces. For each reflection of each bundle, each fiber is checked for possible impact. If more than one fiber shows a possible impact, then the closest is taken as the true impact.

If the energy bundle is absorbed by an interaction with a point on the fiber surface, and then re-emitted from the interaction point (a consequence of radiative equilibrium), then its direction is taken to satisfy an overall diffuse directional distribution. A local coordinate system is chosen with one unit vector $\hat{\mathbf{t}}_{\mathbf{n}}$ at the impact point on the fiber surface and axially directed, and the other defined by

$$\hat{\mathbf{t}}_{\mathbf{t}}=\hat{\mathbf{t}}_{\mathbf{n}}\times\hat{\mathbf{n}}. \tag{10}$$

The direction of the emitted ray is given by

$$\begin{aligned}\hat{\mathbf{s}}_{\mathbf{e}}&=l_{l1}\hat{\mathbf{t}}_{\mathbf{t}}+l_{l2}\hat{\mathbf{t}}_{\mathbf{n}}+l_{l3}\hat{\mathbf{n}}=(\lambda l_{l2}+l_{l3}n_1-\nu l_{l1}n_2+\mu l_{l1}n_3)\hat{\mathbf{i}}+(\mu l_{l2}\\&\quad+\nu l_{l1}n_1+l_{l3}n_2-\lambda l_{l1}n_3)\hat{\mathbf{j}}+(\nu l_{l2}-\mu l_{l1}n_1+\lambda l_{l1}n_2+l_{l3}n_3)\hat{\mathbf{k}}\\&=l_1\hat{\mathbf{i}}+l_2\hat{\mathbf{j}}+l_3\hat{\mathbf{k}}\end{aligned} \tag{11}$$

where the local direction cosines result from a random local azimuth, and a local polar angle whose probability density function corresponds to a diffuse distribution.

If Eqs. (6) and (7) with unknown P have no real solution, then the energy bundle strikes one of the bounding surfaces. The side walls are considered to be perfect specular reflectors in order to account for contributions to radiative transfer from the regions beyond the computational domain. The energy bundles undergo multiple reflections, absorptions, and/or re-emissions until they eventually get to the top or bottom boundaries. The total number of bundles that pass through the top boundary determines the transmitted flux.

Energy bundles are released until the transmittance of the medium becomes stationary to within at most 3%, which requires as many as 10^5 bundles for higher optical thicknesses (representing over 200 hours of run time on a 200 MHz UltraSPARC processor). For lower optical thickness, stationarity within 0.1% is achieved with a few as 10^4 bundles (20 to 30 hours). No results are reported that use fewer than 10^4 bundles.

In the discontinuous limit, GMC results were checked against the cases of a single fiber, placed both horizontally and vertically in the medium. These cases are readily solved using a radiosity method with specular view factors. GMC results agreed to within 3% with the radiosity method for a horizontal cylinder and 10^4 bundles. GMC results are essentially identical to radiosity results for a vertical cylinder and 10^4 bundles.

In the continuous limit, GMC results were checked against Monte Carlo simulations of a radiative continuum (Continuous Monte Carlo, CMC, as derived from Modest, [3], by Nisipeanu, [4]). The CMC simulations use both Linearly Anisotropic Scattering (LAS, with specified angular distribution coefficient) as well as an embedded Scattering-on-Cone (SC) method [4]. In the later, the scattering direction compliments an incoming ray's polar angle from the axis of a randomly oriented scattering fiber, but it is assumed that in the small fiber limit, the azimuthal scattering angle about the fiber axis is uniformly distributed. Comparison of GMC results to CMC is described in the Results section. CMC with LAS was itself verified against an exact integral solution of the RTE [3], agreeing within 1% for 10^4 bundles.

Results

Test case parameters are chosen in order to allow qualitative comparison to the experimental results of Tong et al. [5], concerning fiberglass insulation material 2.54×10^{-2} m thick with a solidity of 0.0033 and a mean (though not uniform) fiber diameter of 6.9 μm. The directional bias of the fibers, if any, is unknown. These parameters represent a practical engineering example of the application of disperse fibrous media, and are considered here even though the ratio of fiber diameter to wavelength (at low ends of the diameter distribution and for longer radiatively significant wavelengths) is very near the accepted limit of applicability of geometric scattering. Tong et al. measured the total heat flux under vacuum conditions (radiation plus a small amount of fiber-to-fiber conduction) between black boundary plates at varying hot boundary temperatures and a fixed cold boundary temperature (308 K); results are reproduced in Fig. 3.

Figure 3 shows CMC radiative heat flux results of both LAS and SC for the physical conditions of Tong et al.'s experiment. Tong et al. derived theoretical radiative properties for these conditions using a random fiber orientation, yielding a wavelength-averaged extinction coefficient (825 m^{-1}), scattering albedo (0.605), and angular distribution coefficient for LAS (0.804). These properties were used in the gray CMC simulations. The

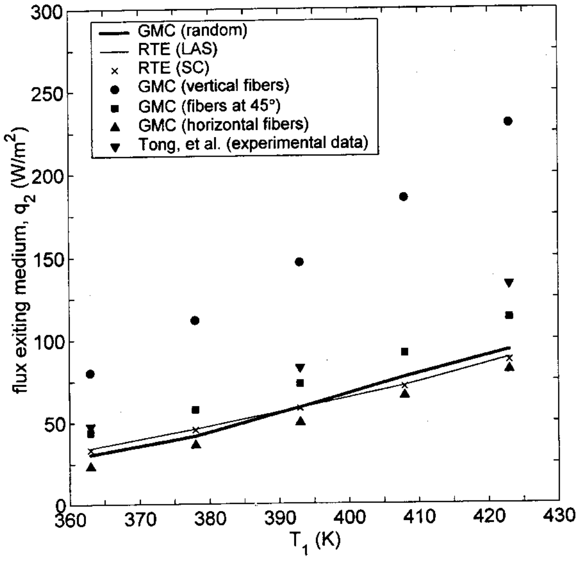

Fig. 3 Comparison between Monte Carlo solutions for continuous media with various fiber orientations, and the experimental data of Tong et al. (1983)

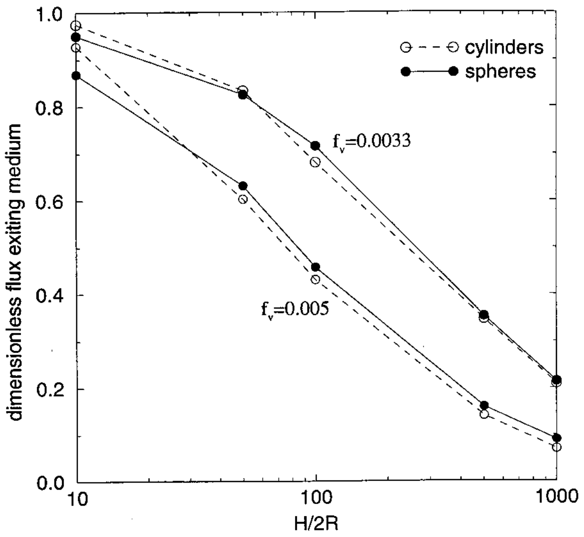

Fig. 4 Comparison of Monte Carlo solutions for fibers modeled as infinitely long, randomly oriented cylinders, and suspended spheres

LAS and SC results agree well, indicating that use of SC might allow CMC simulation without explicit knowledge of the angular distribution coefficient.

Figure 3 also shows GMC results for the boundary conditions and solidity of Tong et al.'s experiment, modeling a monodisperse medium with a fiber diameter of 6.9 μm and a wavelength-averaged index of refraction for glass of $1.49+i1\times10^{-4}$ (derived from the data of Hsieh and Su, [6]). Agreement between GMC and CMC results is quite good, though this should be regarded as somewhat fortuitous since the GMC results did not consider fiber diameter variations, while the radiative properties derived by Tong et al. are integrated over a particular fiber radius distribution. Also, the index of refraction itself was averaged for the GMC simulations, instead of more properly averaging the heat flux results over a range of spectral simulations. This was done because of the extreme run times required by present GMC simulations, and because the intent of the present results is to serve as a general illustration, as follows.

Primarily, Fig. 3 shows GMC results under varying conditions of fiber orientation bias. Practical fibrous media might not be accurately represented by randomly oriented fibers, especially in mat applications. Figure 3 shows GMC results in which the fiber orientation azimuthal angle is random, but the polar angle (relative to the boundary planes) is fixed at 0, 45 deg, and 90 deg. Figure 3 shows a significant dependence of the GMC results on fiber orientation. Radiation is mostly back-scattered by horizontal fibers, and the best transmittance is for vertical fibers. Results both from randomly oriented fibers and from Tong et al.'s experiment lie within the range of the orientation bias results. Clearly, quantitative comparison between GMC and experimental results will require knowledge of the fiber orientation bias in the experimental test article.

The issue of the applicability of the radiative continuum assumption to discontinuous media is addressed for spherical particles by Nisipeanu and Jones [1], with the conclusion that the assumption is not valid for solidities greater than about 0.1 (depending on the particle reflectance and the desired accuracy). By way of extending this conclusion to cylindrical particles (fibers), Fig. 4 shows the ratio of radiative flux at a cold boundary to hot boundary emissive power for a variety of finenesses (ratio of medium thickness to particle diameter—indicative of number density of scatterers, correlated with optical thickness) at different solidities for both spherical particles and randomly oriented cylindrical fibers. The results are very similar, suggesting that as long as the particle orientation is random, the particle shape (varying from spherical to cylindrical) may be relatively unimportant. This suggestion holds only for randomly oriented scatterers.

Confidence in the applicability of GMC to fibrous media would certainly benefit from future research in such areas as: sensitivity to index of refraction variations; non-smooth (non-specular) fiber surfaces; and less idealized descriptions of the fibrous medium geometry. The present computational implementation of GMC is rather cumbersome, though future improvements should make a wider variety of results more readily available.

Conclusions

A Geometric Monte Carlo (GMC) model is developed for radiation in discrete (non-continuum) fibrous media. Unlike continuous medium (RTE) models, GMC requires only volume fraction, fiber diameter, fiber orientation, and fiber material complex index of refraction as parameters; independent computation of an extinction coefficient, scattering albedo, and scattering phase function are not necessary. However, applicability of GMC to fibrous media in small diameter, long wavelength situations remains to be demonstrated. GMC results for fibrous media suggest that:

1. The distribution of polar orientation direction of the fibers is very important to radiative flux; comparison between the GMC results and experimental results cannot be meaningful without knowledge of the orientation distribution in the experiment.
2. In the geometric limit, the shape of randomly-oriented scattering particles in a discontinuous medium or solid matrix may be relatively less important, as indicated by the similarity of fibrous medium and spherical suspension results for equal volume fraction and fineness parameter.

Nomenclature

A = transformation matrix: global to local coordinates
f_v = volume fraction (solidity)
g = left-hand side for the surface equation of a cylinder
H = plane-parallel medium depth, m
$\hat{\mathbf{i}}, \hat{\mathbf{j}}, \hat{\mathbf{k}}$ = unit vectors in x, y, z directions
l_1, l_2, l_3 = direction cosines
$\hat{\mathbf{n}}$ = unit surface normal
P = dimensionless pathlength
PP = plane perpendicular on the position vector
R = fiber radius, m
$\Re$ = real numbers domain
S = distance from origin to plane PP
$\hat{\mathbf{s}}, \hat{\mathbf{s}}'$ = original and scattered ray direction vectors
$\hat{\mathbf{s}}_\mathbf{i}, \hat{\mathbf{s}}_\mathbf{r}$ = incident and reflected ray direction vectors
$\hat{\mathbf{t}}_1, \hat{\mathbf{t}}_2$ = unit vectors included in plane PP
$\hat{\mathbf{t}}_\mathbf{n}$ = unit vector parallel to direction of cylinder
T = boundary temperature, K
$\hat{\mathbf{v}}$ = position vector
x, y, z = position coordinates
λ, μ, ν = direction cosines of cylinders

subscripts

e = emitted
i, r = incident, reflected
l = local
st = starting point
1,2 = hot, cold boundary
1,2,3 = perpendicular directions in local coordinate system

References

[1] Nisipeanu, E., and Jones, P. D., 2000, ''Comparison of Monte Carlo Surface Exchange With Radiative Continuum Results in Large Particle Dispersions,'' ASME J. Heat Transfer, **122**, pp. 503–508.
[2] Chan, C. K., and Tien, C. L., 1974, ''Radiative Transfer with Dependent Scattering by Particles: Part 1—Theoretical Investigation,'' ASME J. Heat Transfer, **96**, pp. 52–58.
[3] Modest, M. F., 1993, *Radiative Heat Transfer*, McGraw-Hill.
[4] Nisipeanu, E., 1998, *Limits on the Continuum Assumption for Radiative Transfer Through Particulate Media*, Ph.D. thesis, Auburn University.
[5] Tong, T. W., Yang, Q. S., and Tien, C. L., 1983, ''Radiative Heat Transfer in Fibrous Insulations—Part II: Experimental Study,'' ASME J. Heat Transfer, **105**, pp. 76–81.
[6] Hsieh, C. K., and Su, K. C., 1979, ''Thermal Radiative Properties of Glass from 0.32 to 206 μm,'' Sol. Energy, **22**, pp. 37–43.

Unified Wilson Plot Method for Determining Heat Transfer Correlations for Heat Exchangers

Teresa B. Styrylska

Agnieszka A. Lechowska
e-mail: alechowska@ptys.wis.pk.edu.pl

Cracow University of Technology, Institute of Thermal Engineering, ul. Warszawska 24, 31-155 Kraków,
Poland

The paper deals with the unified Wilson plot method used for obtaining heat transfer correlations for finned heat exchangers. In this approach, the direct nonlinear regression is implemented. The numerical example with uncertainty analysis is included as well. [DOI: 10.1115/1.1576810]

Keywords: Convection, Data Analysis, Energy, Finned Surfaces, Heat Transfer, Heat Exchangers, Parameter Estimation

1 Introduction

For design and analysis of heat exchangers, it is necessary to evaluate the average heat transfer coefficients, if not available, for one or both fluid side surfaces. If they are to be determined for both fluid sides of a heat exchanger or for the case when the thermal resistances on both fluid sides are of the same order of magnitude and we want to determine an accurate heat transfer correlation on the unknown fluid side, the Wilson method appears to be very useful. The main idea of Wilson technique is to split the overall thermal resistance, previously determined, into individual thermal resistances. In order to obtain the overall thermal resistance, inlet and outlet flow rates and temperatures on both sides of the heat exchanger and heat transfer rate have to be measured. Afterwards, we need to make the precise energy balance of the heat exchanger, and to apply a suitable statistical procedure of data analysis. When the modified Wilson plot techniques are applied, the linear regression is used as a statistical procedure. Due to the fact that only linear regression is used to estimate the unknowns, the number of unknowns cannot be greater than 2 in the modified Wilson method. One of the modifications of Wilson method, which allows us to estimate 3 unknown parameters is based on the double use of the linear regression scheme connected with an iterative procedure [1–4]. If the number of unknowns is greater than 3, the required evaluations are more complicated and the estimation results are less accurate. Moreover, when using linearization by means of taking the natural logarithm, heat transfer correlations may have the form of monomials only, which additionally limits possible applications of the modified method. Furthermore, it changes the original equation for the overall heat transfer coefficient and can lead to unsatisfactory estimates. It is worth mentioning that the fin efficiency can be taken into account only by an additional, internal iterative scheme. In the modified techniques, the issue of experimental uncertainty is not addressed at all. For these reasons the unified method has been suggested.

2 The Unified Wilson Plot Method

For any two-fluid heat exchanger, the overall heat transfer coefficient is given by:

$$\frac{1}{U}=\frac{1}{h_i}+\sum_l R_l+\frac{1}{h_o}\frac{A_i}{A_o}\quad l=1,2,\ldots,q. \tag{1}$$

If, additionally, the finned cooler is considered, the above equation takes the form:

$$\frac{1}{U}=\frac{1}{h_i}+\sum_l R_l+\frac{A_i}{\chi h_o(\eta_f A_f+A_{tn})}, \tag{2}$$

where χ is a coefficient connected with condensation of air moisture, which is equal:

$$\chi=\frac{\Delta X\dot{m}_{da}i+\dot{Q}}{\dot{Q}} \tag{3}$$

and η_f is the fin efficiency for the straight fins, defined by:

$$\eta_f=\frac{\tanh(\gamma h_e)}{\gamma h_e}. \tag{4}$$

The value γ in formula (4) is the fin efficiency parameter given by:

$$\gamma=\sqrt{\frac{2\chi h_o}{k_f\delta_f}}. \tag{5}$$

The unified Wilson plot technique allows us to consider different flow regimes, but requires all test data on one side of the exchanger to be in one flow regime and no phase changes in the fluid streams flowing through the exchanger. Other limitations given by Shah [1] are relaxed.

Let us assume the following heat transfer correlations for the outside and inside of the exchanger (respectively) [2]:

$$\mathrm{Nu}_o=\frac{h_o d_e}{k_o}=C_o\,\mathrm{Re}_o^p\,\mathrm{Pr}_o^{1/3}, \tag{6}$$

$$\mathrm{Nu}_i=\frac{h_i d}{k_i}=C_i\,\mathrm{Re}_i^m\,\mathrm{Pr}_i^{0.4}. \tag{7}$$

The finned exchanger belongs to the group of highly effective heat exchangers with high values of overall heat transfer coefficients. In that case the left-hand side of Eq. (2) has very small values. It may cause some numerical problems, that is why Eq. (2) is being inversed in the adjustment procedure. Assume four unknowns: C_o, p, C_i, m in Eqs. (6) and (7), and take into account the following notations for indirectly measured quantities:

$$x_1=\frac{d}{k_i\mathrm{Pr}_i^{0.4}},\quad x_2=\mathrm{Re}_i, \tag{8}$$

Contributed by the Heat Transfer Division for publication in the JOURNAL OF HEAT TRANSFER. Manuscript received by the Heat Transfer Division May 16, 2001; revision received February 24, 2003. Associate Editor: G. Dulikravich.

$$x_3=\frac{\sqrt{\chi\frac{k_o}{d_e}\mathrm{Pr}_o^{1/3}}}{\sqrt{\frac{2}{k_f\delta_f}h_e\frac{A_i}{A_f}}},\quad x_4=\mathrm{Re}_o, \tag{9}$$

$$x_5=\sqrt{\frac{2\chi k_o\mathrm{Pr}_o^{1/3}}{d_e\delta_f k_f}}h_e,\quad x_6=\chi\frac{k_o}{d_e}\mathrm{Pr}_o^{1/3}\frac{A_{tn}}{A_i}. \tag{10}$$

Equations (2) for all data points take the form:

$$y_j\left\{\left[\sum_l R_l+\frac{x_{1j}}{\mathbf{C}_i x_{2j}^m}+\frac{1}{\sqrt{\mathbf{C}_o}x_{3j}x_{4j}^{p/2}\tanh(\sqrt{\mathbf{C}_o}x_{4j}^{p/2}x_{5j})+\mathbf{C}_o x_{4j}^p x_{6j}}\right]^{-1}-U_j\right\}=0,\quad j=1,2,\ldots,r. \tag{11}$$

Let us arrange the constraint equations (11) into the form:

$$y_j(\alpha_1,\alpha_2,\ldots,\alpha_s,\beta_1,\beta_2,\ldots,\beta_n)=0, \tag{12}$$

where: $\alpha_t\,(t=1,2,\ldots,s)$ is the indirect measurements, that is overall heat transfer coefficient U and expressions $x_1,\ldots,x_6$, which are functions of direct measurements, it means inlet and outlet mass flow rates, temperatures and heat transfer rate, and $\beta_k\,(k=1,2,\ldots,n)$ are the values to be determined, in the paper: constants C_o, C_i, and exponents p, m in Nusselt correlations.

When indirectly measured quantities, denoted by $\boldsymbol{l}^T=[U_j^\circ,x_{1j}^\circ,\ldots,x_{6j}^\circ]$ and preliminary values of unknowns, denoted by $\mathbf{z}^T=[C_o^\circ,p^\circ,C_i^\circ,m^\circ]$, are inserted into Eqs. (12), they are not satisfied. The residuals of those equations are calculated as:

$$y_j(l_1,l_2,\ldots,l_s,z_1,z_2,\ldots,z_n)=-w_j. \tag{13}$$

To ensure that Eqs. (12) are satisfied, corrections to measurements $\mathbf{v}_t\,(t=1,2,\ldots,s)$ and corrections to preliminary values of unknowns $\mathbf{u}_k\,(k=1,2,\ldots,n)$, need to be added as follows:

$$y_j(l_1+v_1,l_2+v_2,\ldots,l_s+v_s,z_1+u_1,z_2+u_2,\ldots,z_n+u_n)=0. \tag{14}$$

Functions y_j are extended into Taylor's series in the vicinity (**l**,**z**), as follows (the powers higher than the first one are neglected):

$$\left(\frac{\partial y_j}{\partial\alpha_1}\right)_{l_1}v_1+\ldots+\left(\frac{\partial y_j}{\partial\alpha_s}\right)_{l_s}v_s+\left(\frac{\partial y_j}{\partial\beta_1}\right)_{z_1}u_1+\ldots+\left(\frac{\partial y_j}{\partial\beta_n}\right)_{z_n}u_n=-y_j(l_1,l_2,\ldots,l_s,z_1,z_2,\ldots,z_n),\quad j=1,2,\ldots,r \tag{15}$$

what can be expressed in matrix notation as:

$$\mathbf{Av}+\mathbf{Bu}=\mathbf{w}, \tag{16}$$

where **A** and **B** are the $r\times s$ and $r\times n$ matrices of coefficients of the measured quantities and unknowns, (respectively):

$$\mathbf{A}=\begin{bmatrix}\left(\frac{\partial y_1}{\partial\alpha_1}\right)_{l_1} & & \left(\frac{\partial y_1}{\partial\alpha_s}\right)_{l_s}\\ \vdots & & \vdots\\ \left(\frac{\partial y_j}{\partial\alpha_1}\right)_{l_1} & \ddots & \left(\frac{\partial y_j}{\partial\alpha_s}\right)_{l_s}\\ \vdots & & \vdots\\ \left(\frac{\partial y_r}{\partial\alpha_1}\right)_{l_1} & & \left(\frac{\partial y_r}{\partial\alpha_s}\right)_{l_s}\end{bmatrix},$$

$$\mathbf{B}=\begin{bmatrix}\left(\frac{\partial y_1}{\partial\beta_1}\right)_{z_1} & & \left(\frac{\partial y_1}{\partial\beta_n}\right)_{z_n}\\ \vdots & & \vdots\\ \left(\frac{\partial y_j}{\partial\beta_1}\right)_{z_1} & \ddots & \left(\frac{\partial y_j}{\partial\beta_n}\right)_{z_n}\\ \vdots & & \vdots\\ \left(\frac{\partial y_r}{\partial\beta_1}\right)_{z_1} & & \left(\frac{\partial y_r}{\partial\beta_n}\right)_{z_n}\end{bmatrix}. \tag{17}$$

The vector of corrections to the measurements, **v**, the vector of corrections to the unknowns, **u**, and the vector of residuals of the constraint equations, **w**, have *s*, *n*, and *r* elements, (respectively).

In steady-state heat transfer in a heat exchanger, the overall heat transfer coefficient U is equal:

$$U=\frac{\dot{Q}}{AF\Delta T_m}, \tag{18}$$

where ΔT_m is the log-mean temperature difference.

The preliminary calculations and the error propagation rule show that among all indirectly measured quantities, the overall heat transfer coefficient U has the highest measurement uncertainty. The other quantities, that is $x_1,\ldots,x_6$ can be treated as exact values. In that case, the number of measurements *s* equals the number of constraint equations *r*. The matrix **A** becomes a unit one $\mathbf{A}=-\mathbf{I}$ and constraint equations (16) take the form:

$$\mathbf{Bu}-\mathbf{v}=\mathbf{w}. \tag{19}$$

In accordance with the error propagation rule, the uncertainty of U equals:

$$\delta U=\sqrt{\left(\frac{\partial U}{\partial\dot{Q}}\right)^2\delta\dot{Q}^2+\left(\frac{\partial U}{\partial\Delta T_m}\right)^2\delta(\Delta T_m)^2}, \tag{20}$$

where $\delta(\Delta T_m)$ is the uncertainty of log-mean temperature difference calculated according to the error propagation rule, as well. The uncertainty of heat transfer area has been neglected.

The basis of the unified approach is the assumption that all quantities of the problem (measurements and unknowns) are treated as observations, as it has been suggested by Mikhail [5] and applied to the Wilson plot method by the authors of this paper. Observations are those variables, for which covariance matrix is known a priori. In this procedure, the extension of the covariance matrix a priori of the measurements $\mathbf{F}_l$ by the additional covariance matrix of the preliminary values of unknowns $\mathbf{F}_z$ is needed. The extended covariance matrix a priori is given by:

$$\overline{\mathbf{F}}=\begin{bmatrix}\mathbf{F}_l & \mathbf{0}\\ \mathbf{0} & \mathbf{F}_z\end{bmatrix}. \tag{21}$$

The covariance matrices a priori of the real data $\mathbf{F}_l$ and of preliminary values of unknowns $\mathbf{F}_z$ have the forms:

$$\mathbf{F}_l=\begin{bmatrix}\frac{1}{(\delta U_1)^2} & & \\ & \ddots & \\ & & \frac{1}{(\delta U_s)^2}\end{bmatrix},$$

$$\mathbf{F}_z=\begin{bmatrix} \frac{1}{(\delta C_o^\circ)^2} & & & \\ & \frac{1}{(\delta p^\circ)^2} & & \\ & & \frac{1}{(\delta C_i^\circ)^2} & \\ & & & \frac{1}{(\delta m^\circ)^2} \end{bmatrix}. \tag{22}$$

The covariance matrix $\mathbf{F}_l$ has elements, which are determined by Eq. (20), while the covariance matrix of the preliminary values of unknowns $\mathbf{F}_z$ has to be assumed by the researcher. Due to the fact, that the unknowns have uncertainties approaching infinity in classical sense, the elements of covariance matrix $\mathbf{F}_z$ should be much greater than the elements of covariance matrix $\mathbf{F}_l$. The preliminary calculations show that the uncertainties of unknowns can be assumed to be as high as ±200% of the preliminary values of unknowns.

We need to introduce the block matrix of coefficients of measurements and unknowns, treated as observations, as well. Now, the constraint Eq. (19) take the form:

$$\overline{\mathbf{A}}\overline{\mathbf{v}}=\mathbf{w}, \tag{23}$$

where:

$$\overline{\mathbf{A}}=[-\mathbf{I}\ \ \mathbf{B}], \quad \overline{\mathbf{v}}=\begin{bmatrix}\mathbf{v}\\ \mathbf{u}\end{bmatrix}. \tag{24}$$

The matrix $\overline{\mathbf{A}}$ has $r\times(s+n)$ dimension and the extended vector $\overline{\mathbf{v}}$ contains the correction vector of measured quantities $\mathbf{v}$ and the correction vector of preliminary values of unknowns $\mathbf{u}$, and has $(s+n)$ elements.

The solution of so formulated adjustment problem is expressed by [5,6]: the vector of corrections to measurements and unknowns:

$$\overline{\mathbf{v}}=\overline{\mathbf{F}}\overline{\mathbf{A}}^T(\overline{\mathbf{A}}\overline{\mathbf{F}}\overline{\mathbf{A}}^T)^{-1}\mathbf{w}, \tag{25}$$

and the *a posteriori* covariance matrix of measurements and unknowns:

$$\mathbf{G}_{\overline{\alpha}}=\overline{\mathbf{F}}-\overline{\mathbf{F}}\overline{\mathbf{A}}^T(\overline{\mathbf{A}}\overline{\mathbf{F}}\overline{\mathbf{A}}^T)^{-1}\overline{\mathbf{A}}\overline{\mathbf{F}}. \tag{26}$$

Estimates of the measurements and unknowns are given by:

$$\overline{\alpha}=\begin{bmatrix}\tilde{\alpha}\\ \tilde{\beta}\end{bmatrix}=\begin{bmatrix}\mathbf{l}\\ \mathbf{z}\end{bmatrix}+\begin{bmatrix}\mathbf{v}\\ \mathbf{u}\end{bmatrix}. \tag{27}$$

3 Example

In this section, the tube-fin air cooler having plain fins on an array of tubes was tested. Water was passed through the tube-side and air—through the shell-side. For this exchanger, 27 data points were tested. Table 1 shows the values of directly measured quantities of inlet and outlet mass flow rates, temperatures, heat transfer rate and humidity of air, which are subject to uncertainties as follows: $\delta\dot{m}_o=\delta\dot{m}_i=0.01\,[\mathrm{kg/s}]$, $\delta T_{1o}=\delta T_{2o}=\delta T_{1i}=\delta T_{2i}=0.1\,[\mathrm{K}]$, $\delta\dot{Q}=30\,[\mathrm{W}]$, $\delta X=0.1\,[\mathrm{g/kg}]$.

The directly measured quantities of inlet and outlet mass flow rates, temperatures, heat transfer rate and humidity of air allow us to calculate the values given in Table 2, that is: values of Reynolds and Prandtl numbers and overall heat transfer coefficients. Based on geometrical information and the data from Table 2 we can evaluate the vector $\mathbf{l}^T=[U_j^\circ,x_{1j}^\circ,\ldots,x_{6j}^\circ]$, $j=1,2,\ldots,s$. The quantities $x_1,\ldots,x_6$ are treated as exact values. In this way the vector $\mathbf{l}$ is reduced to the form $\mathbf{l}^T=[U_1^\circ,\ldots,U_j^\circ,\ldots,U_r^\circ]$.

Table 1 Directly measured quantities

No.	$\dot{m}_o$ [kg/s]	T_{1o} [°C]	T_{2o} [°C]	$\dot{m}_i$ [kg/s]	T_{1i} [°C]	T_{2i} [°C]	$\dot{Q}$ [W]	X_1 [g/kg]	X_2 [g/kg]
1	0.57	27.8	14.3	0.85	7.6	10.2	9650	11.0	9.7
2	0.93	27.9	16.0	0.85	7.6	10.8	11750	10.9	10.6
3	0.57	28.1	13.9	1.22	7.6	9.6	10550	11.4	9.7
4	0.93	27.9	15.9	1.22	7.6	10.1	12900	11.2	10.5
5	0.58	28.1	18.2	0.81	7.4	12.0	15750	20.8	13.7
6	0.93	28.3	20.9	0.82	7.5	13.0	19300	20.7	15.3
7	0.58	28.0	17.4	1.22	7.5	10.9	17350	20.6	13.0
8	0.57	31.4	14.9	0.82	4.1	8.6	16300	16.7	11.5
9	0.93	30.8	17.9	0.82	4.1	9.5	19200	16.4	13.2
10	0.57	31.4	14.1	1.28	4.0	7.3	18200	16.8	10.9
11	0.92	31.1	17.1	1.22	3.9	8.1	22000	16.5	12.5
12	0.39	28.5	12.0	1.01	5.1	7.8	11550	13.9	8.7
13	1.12	28.7	17.6	1.02	5.0	9.3	18750	14.0	11.8
14	0.75	28.8	14.7	1.41	5.0	7.9	17150	13.9	10.5
15	0.74	28.2	18.8	1.02	10.1	13.3	13700	17.6	13.9
16	0.75	35.2	14.7	1.01	4.1	7.8	16050	9.5	9.0
17	0.76	28.6	19.9	1.02	4.5	10.3	25650	25.9	15.7
18	0.74	28.8	14.8	1.02	5.1	8.5	14900	12.6	10.1
19	0.75	28.5	15.3	1.02	5.1	8.7	15650	13.6	10.5
20	0.75	28.4	15.4	1.01	5.1	8.7	15550	13.9	10.8
21	0.76	28.8	15.7	1.01	5.0	8.8	16500	14.2	10.8
22	0.74	28.7	15.2	1.02	5.1	8.6	15500	13.7	10.6
23	0.76	28.7	15.4	1.02	4.9	8.5	15700	13.8	10.8
24	0.74	28.6	15.1	1.02	5.1	8.5	15250	13.6	10.5
25	0.74	34.8	21.8	1.41	4.2	10.0	35050	31.5	17.8
26	0.90	35.2	26.2	0.61	4.1	15.3	28950	31.2	21.9
27	0.91	35.6	28.1	0.61	10.2	19.5	23950	31.7	24.4

Table 2 Values of Reynolds and Prandtl numbers and overall heat transfer coefficients

No.	Re_o	Pr_o	Re_i	Pr_i	U [W/m^{2}K]
1	16943	0.694	14295	9.79	868
2	27580	0.694	14433	9.69	976
3	16947	0.694	20297	9.90	947
4	27585	0.694	20451	9.81	1054
5	17147	0.693	13963	9.51	1208
6	27394	0.693	14428	9.32	1371
7	17168	0.694	20672	9.69	1341
8	16850	0.693	12833	10.69	1031
9	27410	0.693	12990	10.53	1130
10	16869	0.694	19517	10.94	1150
11	27133	0.693	18797	10.82	1268
12	11619	0.694	15750	10.66	935
13	33112	0.693	16256	10.41	1211
14	22255	0.694	21981	10.66	1197
15	21858	0.693	18771	8.83	1210
16	22072	0.693	15542	10.84	922
17	22406	0.693	16429	10.32	1554
18	21954	0.694	16085	10.53	1056
19	22245	0.694	16127	10.50	1100
20	22245	0.694	15972	10.50	1091
21	22521	0.694	15980	10.50	1129
22	21945	0.694	16119	10.51	1084
23	22533	0.694	16035	10.57	1077
24	21951	0.694	16105	10.53	1071
25	21602	0.693	22442	10.43	1701
26	26129	0.692	10574	9.51	1405
27	26352	0.692	12650	7.77	1436

The preliminary values of unknowns are assumed as in literature [2]: $\mathbf{z}^T=[C_o^\circ,p^\circ,C_i^\circ,m^\circ]=[1.0,0.5,0.023,0.8]$, while the preliminary values of measurements, it means U_j°, are given in Table 2. The uncertainties of unknowns have been assumed to be as high as about ±200% of the preliminary values of unknowns, i.e.,

$$\mathbf{F}_z=\begin{bmatrix} \frac{1}{2.0^2} & & & \\ & \frac{1}{1.0^2} & & \\ & & \frac{1}{0.05^2} & \\ & & & \frac{1}{2.0^2} \end{bmatrix}, \tag{28}$$

while the uncertainties of overall heat transfer coefficients δU_j° are determined by Eq. (20).

The matrix **B**, in the considered example, is expressed by:

$$\mathbf{B}=\begin{bmatrix} \left(\frac{\partial y_1}{\partial C_o}\right)_{c_o^\circ} & \left(\frac{\partial y_1}{\partial p}\right)_{p^\circ} & \left(\frac{\partial y_1}{\partial C_i}\right)_{c_i^\circ} & \left(\frac{\partial y_1}{\partial m}\right)_{m^\circ} \\ \vdots & \vdots & \vdots & \vdots \\ \left(\frac{\partial y_j}{\partial C_o}\right)_{c_o^\circ} & \left(\frac{\partial y_j}{\partial p}\right)_{p^\circ} & \left(\frac{\partial y_j}{\partial C_i}\right)_{c_i^\circ} & \left(\frac{\partial y_j}{\partial m}\right)_{m^\circ} \\ \vdots & \vdots & \vdots & \vdots \\ \left(\frac{\partial y_r}{\partial C_o}\right)_{c_o^\circ} & \left(\frac{\partial y_r}{\partial p}\right)_{p^\circ} & \left(\frac{\partial y_r}{\partial C_i}\right)_{c_i^\circ} & \left(\frac{\partial y_r}{\partial m}\right)_{m^\circ} \end{bmatrix},$$

$$j=1,2,\ldots,r. \qquad (29)$$

The computer program (written in Fortran 95) has been written to estimate the unknowns and their uncertainties. The program consists of three parts. First, all required geometrical information and measurement data are provided and indirectly measured quantities, i.e., overall heat transfer coefficients, are calculated. The dimensions of vector, **l**, **z**, **w**, $\overline{\mathbf{v}}$ and of matrices $\overline{\mathbf{F}}$, $\overline{\mathbf{A}}$, $\overline{\mathbf{G}}_{\bar{\alpha}}$ have to be given. Then, uncertainties of indirect measurements and assumed preliminary values of uncertainties of unknowns have to be provided to create the covariance matrices a priori $\mathbf{F}_l$ and $\mathbf{F}_z$. Finally, the matrix **A** is created, using matrix **B** (Eq. (17)). The second part of the program implements iterative scheme suitable to nonlinear problems. At each of the iterations the extended vector of corrections to indirect measurements and unknowns $\overline{\mathbf{v}}$ is evaluated (Eq. (25)). The corrections are added to the current values of measurements and unknowns. The corrected values from the current step are the base of iteration in the next step. The iteration procedure is continued until the corrections do not change within the desired accuracy. In the last part, the estimates of measurements and unknowns $\bar{\alpha}$ (Eq. (27)) and the covariance matrix *a posteriori* $\overline{\mathbf{G}}_{\bar{\alpha}}$ (Eq. (26)) are evaluated. The uncertainties of the estimates are the square roots of diagonal elements of the matrix $\overline{\mathbf{G}}_{\bar{\alpha}}$.

The estimation procedure was convergent to the following results:

$$\left.\begin{aligned} C_o&=2.000\pm0.097\\ p&=0.5200\pm0.0091\\ C_i&=0.0400\pm0.0039\\ m&=0.740\pm0.016 \end{aligned}\right\}. \qquad (30)$$

Finally, the following heat transfer correlations were obtained:

$$\mathrm{Nu}_o=\frac{h_o d_e}{k_o}=2.0\,\mathrm{Re}_o^{0.52}\,\mathrm{Pr}_o^{1/3}, \quad 11600\leqslant \mathrm{Re}_o\leqslant 33100 \quad (31)$$

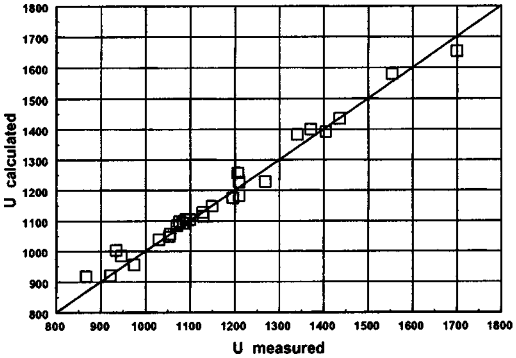

Fig. 1 The comparison of measured and estimated values of *U* using the unified Wilson plot method

$$\mathrm{Nu}_i=\frac{h_i d}{k_i}=0.04\,\mathrm{Re}_i^{0.74}\,\mathrm{Pr}_i^{0.4}. \quad 10500\leqslant \mathrm{Re}_i\leqslant 22500 \quad (32)$$

The quality of fit of the derived correlations with experimental data is shown in Fig. 1. The relative error of U is not higher than 7.5%, what indicates a high quality of fit. Furthermore, it should be noticed that the fin efficiency was directly taken into account without any additional iterative scheme.

4 Conclusions

We have presented that the unified Wilson plot method is an useful tool for determining heat transfer correlations for heat exchangers, if only we are able to write one Nusselt correlation for one side of the exchanger and there are no phase changes in the fluid streams. This approach has no other limitations of modified methods and allows one to determine any number of unknowns for arbitrary chosen heat transfer correlations, if the number of supplementary data is large enough. It is worth to mention that the heat transfer correlations may have any form, not only the form of monomials. When we apply the unified method—it means we treat the unknowns as observations with covariance matrix a priori—the solution is more stable than in the classical approach, i.e., when the constraint equations have the form of Eqs. (16) or (19). Moreover, the fin efficiency can be taken into account in a direct way, what is the main advantage of the suggested unified plot technique.

Acknowledgments

We thank Dr A. Guzik for access to his computer programs and help during the course of this research.

Nomenclature

A = heat transfer area [m^2]
A_{tn} = tube outside primary surface area (without the area of fins) [m^2]
C = constant in heat transfer correlations
d = inside tube diameter [m]
d_e = equivalent diameter [m]
F = log-mean temperature difference correction factor
h = heat transfer coefficient [W/(m^{2}K)]
h_e = fin height [m]
i = evaporation enthalpy of air [J/kg]
k = thermal conductivity [W/(mK)]
m = tube-side Reynolds number exponent
$\dot{m}$ = fluid mass flow rate [kg/s]
$\dot{m}_{da}$ = dry air mass flow rate [kg/s]
n = number of unknowns
Nu = Nusselt number
p = shell-side Reynolds number exponent
Pr = Prandtl number
q = number of resistances
$\dot{Q}$ = heat transfer rate [W]
R = heat conduction resistance [m^{2}K/W]
r = number of constraint equations
Re = Reynolds number
s = number of measurements
T = temperature [K]
U = overall heat transfer coefficient [W/(m^{2}K)]
X = humidity of air [kg/kg]

Greek Letters

$\tilde{\alpha}$ = vector of estimates of measurements
$\tilde{\beta}$ = vector of estimates of unknowns
χ = coefficient defined by Eq. (3)
δ_f = fin thickness [m]
$\Delta\mathrm{T}_\mathrm{m}$ = log-mean temperature difference [K]
γ = fin efficiency parameter [1/m]
η_f = fin efficiency

Matrices

A = matrix of coefficients of measurements
B = matrix of coefficients of unknowns
$\mathbf{F}_l$ = covariance matrix *a priori* of measurements
$\mathbf{F}_z$ = covariance matrix *a priori* of unknowns
l = vector of measurements
u = vector of corrections to unknowns
v = vector of corrections to measurements
w = vector of residuals of constraint equations
z = vector of preliminary values of unknowns

Subscripts

1 = inlet
2 = outlet
f = fin
i = inside
o = outside

References

[1] Shah, R. K., 1990, ''Assessment of Modified Wilson Plot Techniques for Obtaining Heat Exchanger Design Data,'' *Heat Transfer 1990*, Proc. 9th Int. Heat Transfer Conf., **5**, pp. 51–56.
[2] Shah, R. K., and Sekulić, D. P., 1998, ''Heat Exchangers'' in *Handbook of Heat Transfer*, Third Edition, W. M. Rohsenow, J. P. Hartnett, and C. Young, eds., McGraw-Hill, New York, Chap. 17.
[3] Briggs, D. E., and Young, E. H., 1969, ''Modified Wilson Plot Techniques for Obtaining Heat Transfer Correlations for Shell and Tube Heat Exchangers,'' Chem. Eng. Prog., Symp. Ser., **65**, No. 92, p. 35.
[4] Khartabil, H. F., Christensen, R. N., and Richards, D. E., 1988, ''A Modified Wilson Plot Technique for Determining Heat Transfer Correlations,'' 2nd UK National Conference on Heat Transfer, Glasgow, Vol. II, pp. 1331–1357.
[5] Mikhail, E., and Ackermann, F., 1976, *Observations and Least Squares*, IEP-A Dun-Donnaley Publisher, New York.
[6] Brandt, S., 1997, *Statistical and Computational Methods in Data Analysis*, Third Edition, Springer Verlag, New York.

Correction for Exponential Dependence of Viscosity on Temperature for Natural Convection by an Integral Method

Louis C. Burmeister
e-mail: kume@mecheng.me.ukans.edu
ASME Mem.,
Department of Mechanical Engineering, University of Kansas, Lawrence, KS 66045

It is common to correct for the effect of exponential dependence on inverse absolute temperature of the viscosity on the Nusselt number for laminar natural convection by multiplying the correlation for constant properties by a factor $(\mu_\infty/\mu_w)^n$ *to obtain* $\mathrm{Nu}=\mathrm{C\,Ra}^{1/4}(\mu_\infty/\mu_w)^n$*. That there is a sound basis for the functional form of this corrective term is newly shown by employing an integral method to obtain closed-form solutions to the laminar boundary-layer equations for the case of a vertical plate of specified temperature immersed in such a liquid. The basis for the alternative means of correction by using the correlation for constant properties with viscosity evaluated at a special reference temperature is also shown.* [DOI: 10.1115/1.1573228]

Keywords: Boundary Layer, Convection, Heat Transfer, Natural Convection

Introduction

Kakac et al. [1], in their survey of the influence of variable properties on natural convection, report that a special correction for Nusselt number-versus-Rayleigh-number correlations is suggested for a fluid, such as an oil or water, whose viscosity varies exponentially with inverse absolute temperature. This correction, apparently first suggested by Akagi [2] to correlate his numerical solutions to similarity formulations, for this effect for the laminar state is to multiply the correlation for constant properties by a factor $(\mu_\infty/\mu_w)^n$ to obtain $\mathrm{Nu}=\mathrm{C\,Ra}^{1/4}(\mu_\infty/\mu_w)^n$. Fujii et al. [3,4] successfully correlated their measurements for an electrically heated vertical cylinder in this way, finding $n=0.21$ for a constant temperature boundary condition and $n=0.17$ for a constant heat flux boundary condition. They also found that evaluation of all properties at a reference temperature $T_r=T_w-(1/4)(T_w-T_\infty)$ enables the correlation for constant properties to be accurate without any other correction. Ito et al. [5] later applied the integral method to the same problem without additional recommendation. Later, Chu and Hickox [6] showed that evaluation of all properties at the film temperature enabled their measurements of natural convection from a horizontal plate at the bottom of a rectangular enclosure, cooled at the top and filled with corn syrup, to be correlated with $n=0.035$, a much smaller value of the exponent.

According to Kakac et al. [1], the only known basis for the multiplicative viscosity correction, other than its success in correlating measurements and calculated results, is the procedure set forth earlier by Sieder and Tate [7] to correlate measurements of heat transfer coefficients for fully developed laminar flow of oils in tubes. The Sieder-Tate viscosity correction exponent is $n=0.14$, close to the values found for natural convection. Oskay and Kakac [8,9] demonstrated that the exponent of the viscosity correction depends upon the conditions of the application, finding the best value of the exponent to be 0.152 for mineral oils in laminar flow in tubes.

In the following, an analytical basis for the $(\mu_\infty/\mu_w)^n$ form of the viscosity corrective term for the Nusselt-Rayleigh number correlation for constant properties will be developed. Closed-form solutions will be obtained to the integral form of the laminar boundary layer equations for natural convection from a vertical plate to a liquid whose viscosity has an exponential dependence on inverse absolute temperature. The functional form of the viscosity correction and the numerical value of its exponent will be discerned from these solutions. The basis for selecting a reference temperature at which viscosity can be evaluated to enable the correlation for constant properties to be used without other correction will also be shown.

Formulation and Solution

The physical configuration for the problem of natural convection from a vertical plate under consideration is illustrated in Fig. 1. The wall temperature is taken to be less than the environmental temperature so that flow is downward. The integral forms [10] of the x-motion and energy equations, respectively, are

$$-\frac{\partial(\delta u_1^2 i_4)}{\partial x}+g\beta\int_0^\delta (T-T_\infty)\,dy=\nu\frac{\partial u(y=0)}{\partial y} \tag{1}$$

and

$$\frac{\partial[\delta u_1(T_w-T_\infty)i]}{\partial x}=-\alpha\frac{\partial T(y=0)}{\partial y} \tag{2}$$

where

$$i=\int_0^1 \frac{u}{u_1}\theta\, d\eta \tag{3a}$$

and

Contributed by the Heat Transfer Division for publication in the JOURNAL OF HEAT TRANSFER. Manuscript received by the Heat Transfer Division March 11, 2002; revision received December 11, 2002. Associate Editor: V. Prasad.

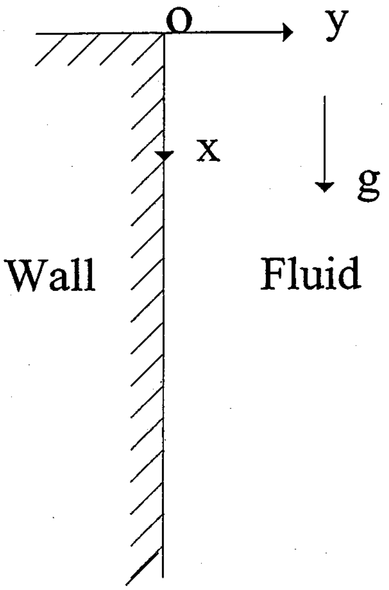

Fig. 1 The physical situation and coordinate system

$$i_4=\int_0^1\left(\frac{u}{u_1}\right)^2 d\eta \tag{3b}$$

Except for the temperature dependence of density that is taken into account only in the buoyancy term of the x-motion equation, all properties other than viscosity are taken to be constant.

Similarity solutions [1] reveal that the viscosity variation primarily affects the velocity distribution, having much less effect on the temperature distribution. Therefore, a temperature distribution for Eqs. (1) and (2) can be obtained by requiring a polynomial to satisfy the five conditions of known temperature at the wall and at the edge of the boundary layer, local energy equation at the wall and at the edge of the boundary layer, and vanishing heat flux at the outer edge of the boundary layer

$$T(y=0)=T_w,\quad T(y=\delta)=T_\infty,\quad \partial^2T(y=0)/\partial y^2=0,\quad \partial^2T(y=\delta)/\partial y^2=0,\quad \partial T(y=\delta)/\partial y=0$$

So doing results in, with $\eta=y/\delta$,

$$\theta=(T-T_\infty)/(T_w-T_\infty)=(1-\eta)^2 \tag{4}$$

A velocity distribution for the same service is obtained in a different way in order to incorporate the influence of variable viscosity. Because of the slow motion of the fluid, the body and shear forces are expected to be nearly in equilibrium so that

$$\frac{d(\mu\partial u/\partial y)}{dy}\approx -g\beta(T-T_\infty)$$

Two integrations with respect to y give an approximate velocity distribution to be

$$u=u_1[I(\eta)+C_1I_1(\eta)+C_2] \tag{5}$$

where

$$I(\eta)=\int_0^\eta\left(\frac{\mu_\infty}{\mu}\int_0^\eta \theta d\eta\right) \tag{6}$$

and

$$I_1(\eta)=\int_0^\eta\frac{\mu_\infty}{\mu}d\eta \tag{7}$$

As has been done by others [[10], p. 393], the lead coefficient on the right-hand side of Eq. (5) is taken to be u_1 so that there are two parameters, u_1 and δ, to be determined in the course of solving Eqs. (1) and (2). So doing is analogous to taking the velocity boundary layer and the thermal boundary layer thickness to be different. Thus, δ and u_1 are parameters whose values best enable the *x*-motion and energy equations to be satisfied on the average over the boundary layer for the profiles used. Setting $u(y=0)=0=u(y=\delta)$ gives the constants of integration as

$$C_2=0\qquad\text{and}\qquad C_1=-\int_0^1\left(\frac{\mu_\infty}{\mu}\int_0^\eta\theta d\eta\right)d\eta\Big/\int_0^1\frac{\mu_\infty}{\mu}d\eta$$

The viscosity depends upon the inverse absolute temperature as

$$\frac{\mu_\infty}{\mu}=\exp\left[B\left(\frac{1}{T_\infty}-\frac{1}{T}\right)\right] \tag{8}$$

Under the assumption that the absolute temperature T does not vary greatly from the film temperature $T_f=T_w-(1/2)(T_w-T_\infty)$ the viscosity ratio is taken to be

$$\frac{\mu_\infty}{\mu}=\exp[\pm b\theta] \tag{9}$$

in which

$$b=\frac{B|T_w-T_\infty|}{T_fT_\infty}$$

The plus sign is used if the wall temperature T_w exceeds the ambient temperature T_∞, while the negative sign is used if T_w is less than T_∞. For mathematical convenience, the case of $T_w<T_\infty$ is pursued in this study.

After substitution of the temperature distribution of Eq. (4) and the viscosity ratio of Eq. (9) into Eqs. (6) and (7), the integrals are evaluated with the aid of Maple [11] to be

$$6b^2I=b^{3/2}\pi^{1/2}[\mathrm{erf}(b^{1/2})-\mathrm{erf}(z)]+(b+1)\exp(-b)-(z^2+1)\exp(-z^2) \tag{10a}$$

$$2b^{1/2}I_1=\pi^{1/2}[\mathrm{erf}(b^{1/2})-\mathrm{erf}(z)] \tag{10b}$$

and

$$3C_1=1+[(b+1)\exp(-b)-1]/[\pi^{1/2}b^{3/2}\mathrm{erf}(b)] \tag{10c}$$

with $z=b^{1/2}(1-\eta)$. The velocity distribution follows substitution of Eq. (10) into Eq. (5) as

$$6b^2\frac{u}{u_1}=-(b+1)\exp(-b)+(z^2+1)\exp(-z^2)+\frac{(b+1)\exp(-b)-1}{\mathrm{erf}(b^{1/2})}[\mathrm{erf}(b^{1/2})-\mathrm{erf}(z)] \tag{11}$$

Use of the temperature distribution of Eq. (4) and the velocity distribution of Eq. (6) in the two integrals of Eq. (3) leads, with the aid of Maple [11], to

$$3b^{7/2}i=\frac{5\pi^{1/2}}{16}\mathrm{erf}(b^{1/2})-\frac{[1-(b+1)\exp(-b)]^2}{6\pi^{1/2}\mathrm{erf}(b^{1/2})}-\frac{b^{1/2}[b(b+1)/3+b/2+5/4]\exp(-b)}{2} \tag{12}$$

and

$$
\begin{aligned}
36b^{9/2}i_4 = & \left\{ -\left(\frac{2}{\pi}\right)^{1/2}\left[\frac{1-(b+1)\exp(-b)}{\mathrm{erf}(b^{1/2})}\right]^2 \right. \\
& \left. +\frac{27}{32}\left(\frac{\pi}{2}\right)^{1/2}\right\}\mathrm{erf}[(2b)^{1/2}] \\
& +\frac{2}{\pi^{1/2}}\frac{1-(b+1)\exp(-b)}{\mathrm{erf}(b^{1/2})}\left[\frac{5}{4}-\left(b+\frac{5}{4}\right)\exp(-2b)\right] \\
& +b^{1/2}\left(\frac{21}{16}+\frac{11}{4}b+b^2\right)\exp(-2b)-\frac{3\pi^{1/2}}{4}[(b+1) \\
& \times\exp(-b)+1]\mathrm{erf}(b^{1/2}) \qquad (13)
\end{aligned}
$$

If the wall temperature exceeds the temperature of the ambient fluid the familiar error function erf(z) [12] in the solutions is then replaced by the less familiar Dawson's integral dawson(z) [12], both functions that are recognized by Maple [11]. However, the conclusions that flow from that case are the same as those that follow.

Use of these distributions in Eqs. (1) and (2) enables them to be rewritten as

$$
-\frac{d(\delta u_1^2 i_4)}{dx}+\frac{g\beta\delta|T_w-T_\infty|}{3}=\nu_\infty\frac{u_1}{\delta}C_1 \qquad (14)
$$

and

$$
\frac{d(\delta u_1 i)}{dx}=\frac{2\alpha}{\delta} \qquad (15)
$$

The functional forms of u_1 and δ are assumed to be

$$
\delta=K_2x^p \qquad (16a)
$$

and

$$
u_1=K_1x^s \qquad (16b)
$$

as done in the constant-property case [[10], p. 393]. Use of these assumed forms in Eqs. (14) and (15) results in, for the x-motion equation,

$$
\begin{aligned}
& -i_4(K_1K_2)^2(2s+p)x^{2s+2p-1}+(g\beta|T_w-T_\infty|/3)K_2^2x^{2p} \\
& =K_1C_1\nu_\infty x^s
\end{aligned}
$$

and, for the energy equation,

$$
iK_1K_2^2(s+p)x^{s+2p-1}=2\alpha
$$

Since these two relationships hold for all x, the exponents must all be the same in each. Thus,

$$
2s+2p-1=2p=\mathrm{s} \quad \text{and} \quad s+2p-1=0
$$

from which it is found that

$$
s=1/2 \qquad (17a)
$$

and

$$
p=1/4 \qquad (17b)
$$

With these values for p and s in hand, it is next found that

$$
\mathrm{K}_1=8\alpha/(3\mathrm{iK}_2^2) \qquad (18a)
$$

and

$$
\mathrm{K}_2^4=\frac{8\alpha\nu_\infty\mathrm{C}_1}{\mathrm{i}g\beta|\mathrm{T_w}-\mathrm{T}_\infty|}\left(1+\frac{10\mathrm{i}_4}{3\mathrm{iC}_1\mathrm{Pr}_\infty}\right) \qquad (18b)
$$

Discussion

The Nusselt number can be obtained from the foregoing results. The heat flux q_w at the plate is related to the temperature difference and to the temperature gradient as

$$
q_w=h(T_w-T_\infty)=-k\partial T(y=0)/\partial y
$$

The local heat transfer coefficient h follows from this as

$$
h=-\frac{k}{\delta}\frac{\partial\theta(\eta=0)}{\partial\eta}
$$

Use of Eqs. (16)–(18) in this relationship then gives

$$
\frac{h}{k}=2\left[\frac{i}{8C_1}\frac{g\beta|T_w-T_\infty|}{\alpha\nu_\infty}\frac{\mathrm{Pr}_\infty}{\mathrm{Pr}_\infty+\dfrac{10i_4}{3C_1i}}\right]^{1/4}x^{-1/4}
$$

The average heat transfer coefficient $\bar{h}$ being $4h/3$, the average Nusselt number Nu–Rayleigh number Ra relationship is

$$
\frac{\mathrm{Nu}}{\mathrm{Ra}_\infty^{1/4}}=\frac{8}{3}\left[\frac{i}{8C_1}\frac{\mathrm{Pr}_\infty}{\mathrm{Pr}_\infty+\dfrac{10i_4}{3C_1i}}\right]^{1/4} \qquad (19)
$$

In the case of small viscosity variation for which $b\rightarrow 0$, it is found with the aid of Maple [11] that

$$
\begin{aligned}
& i=\frac{1}{112}\left(1-\frac{49}{81}b+\ldots\right), \quad C_1=\frac{1}{4}\left(1+\frac{1}{9}b+\ldots\right), \quad i_4 \\
& =\frac{1}{1296}\left(1-\frac{229}{220}b+\ldots\right)
\end{aligned}
$$

The average Nusselt number for $b=0$ is

$$
\frac{\mathrm{Nu}}{\mathrm{Ra}_\infty^{1/4}}=\frac{4}{3}\left[\frac{1}{14}\frac{\mathrm{Pr}_\infty}{\mathrm{Pr}_\infty+\dfrac{280}{243}}\right]^{1/4}
$$

For $\mathrm{Pr}_\infty=0.73$ as it is for air, this becomes

$$
\frac{\mathrm{Nu}}{\mathrm{Ra}_\infty^{1/4}}=0.544
$$

which is only 2% below the recommended [13] value of 0.555 on the right-hand side. For small values of b, the Nusselt number dependence upon the parameter b is

$$
\frac{\mathrm{Nu}(b)}{\mathrm{Nu}(b=0)}=1-\frac{29}{162}\left(1-\frac{2983}{4640}\frac{1}{\mathrm{Pr}_\infty+\dfrac{280}{243}}\right)b+\ldots
$$

Comparison of this result with the series

$$
e^{-nb}=1-nb+\ldots
$$

for the expansion of an exponential justifies the approximation that

$$
\frac{\mathrm{Nu}(b)}{\mathrm{Nu}(b=0)}\approx(e^{-b})^n=\left(\frac{\mu_\infty}{\mu_w}\right)^n \qquad (20)
$$

in which

$$
n=\frac{29}{162}\left(1-\frac{2983}{4640}\frac{1}{\mathrm{Pr}_\infty+\dfrac{280}{243}}\right)=0.179\frac{\mathrm{Pr}_\infty+0.5094}{\mathrm{Pr}_\infty+1.152} \qquad (21)
$$

The ratio in Eq. (20) ameliorates the consequences of inaccuracies in the assumed profiles.

Equation (20) is the functional form of the correction that is sought. The variation of the Nusselt number ratio versus the viscosity ratio predicted by Eqs. (19) and (20) is shown in Fig. 2. There it can be seen that Eq. (20) with $n=0.167$ is a good approximation for the moderate Prandtl number, $\mathrm{Pr}_\infty\approx 10$, that is characteristic of water; it can be shown that $n=0.176$ is a good approximation for the large Prandtl number, $\mathrm{Pr}_\infty\approx 10^3$, that is

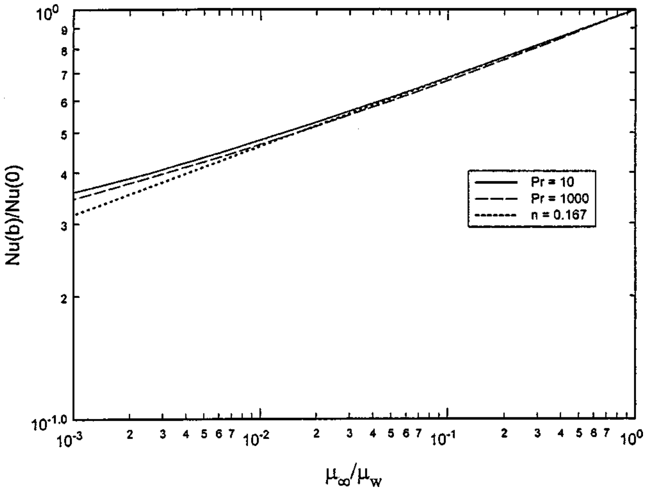

Fig. 2 The ratio of Nusselt number with temperature-dependent viscosity to Nusselt number with constant properties versus the ratio of ambient viscosity to wall viscosity

characteristic of oils. These values differ slightly from the findings by Fujii et al. [3], partly due to the fact that effects of curvature result in velocity and temperature distributions that differ from those used in this analysis [14].

To see that evaluation of the viscosity at the film temperature T_f reduces the exponent of the viscosity correction, note that the Nusselt number is then given by

$$\frac{\mathrm{Nu}}{\mathrm{CR}a_f^{1/4}}=\left(\frac{\mu_\mathrm{f}}{\mu_\infty}\right)^{1/4}\left(\frac{\mu_\infty}{\mu_w}\right)^n \tag{22}$$

Appealing to the temperature dependence of Eq. (8), this relationship can be rewritten as

$$\frac{\mathrm{Nu}}{\mathrm{CR}a_f^{1/4}}=\exp\left\{\mathrm{B}\left(\frac{1}{T_\infty}-\frac{1}{T_w}\right)\left[n-\frac{T_\mathrm{w}}{4(T_\infty+T_w)}\right]\right\}=\left(\frac{\mu_\infty}{\mu_w}\right)^m$$

It is seen that the new exponent m of the viscosity correction term is less than the value n as

$$m=n-\frac{T_w}{4(T_\infty+T_w)} \tag{23}$$

This result can be compared with that of Chu and Hickox [6] for which the temperature T_w of the heated strip was 315.7 to 347.6°K and the temperature T_∞ of the top was 277.1°K to 323.1°K. With the averages of these values it is predicted that

$$m\approx 0.167-\frac{330}{4(300+330)}=0.036$$

This result is in fair agreement with their finding that $m=0.035$.

The reference temperature T_r at which to evaluate the viscosity so that the constant property correlation can be employed can be ascertained in a similar way. For this reference temperature

$$\frac{\mathrm{Nu}}{\mathrm{CR}a_r^{1/4}}=\left(\frac{\mu_r}{\mu_\infty}\right)^{1/4}\left(\frac{\mu_\infty}{\mu_w}\right)^n$$

In parallel with the previous manipulation, it is found that

$$\frac{\mathrm{Nu}}{\mathrm{CR}a_f^{1/4}}=\exp\left\{\frac{\mathrm{B}}{4}\left[\frac{1}{T_r}-\frac{1}{T_\infty}+4n\left(\frac{1}{T_\infty}-\frac{1}{T_w}\right)\right]\right\}$$

Setting the exponent on the right-hand side equal to zero leads to

$$T_r=T_w-\left[\frac{T_w}{T_w+4n(T_\infty-T_w)}(1-4n)\right](T_w-T_\infty) \tag{24}$$

If $n=0.179$ as shown by Eq. (21), Eq. (24) gives $T_r=T_w-0.284(T_w-T_\infty)$; if $n=0.167$ to fit the complete solution plotted in Fig. 2, Eq. (24) gives $T_r=T_w-0.333(T_w-T_\infty)$. For the conditions of Fujii et al. [3] for oils in which $56°\mathrm{C}<T_w<152°\mathrm{C}$ and $21°\mathrm{C}<T_\infty<62°\mathrm{C}$, use of the average values with $n=0.176$ gives $T_r=T_w-0.334(T_w-T_\infty)$. Although the 0.284, 0.333, and 0.334 values of the coefficient of the temperature difference are above the 1/4 value recommended by Akagi [2] and Fujii et al. [3], there is agreement that the reference temperature is closer to the wall temperature than is the film temperature.

Nomenclature

b = dimensionless form of B, see Eq. (9)
B = constant in the viscosity-temperature relationship, see Eq. (8)
C = constant
C_1 = constant of integration, see Eq. (5)
C_2 = constant of integration, see Eq. (5)
C_p = specific heat at constant pressure, J/kg°K
dawson (z) = Dawson's integral, $=\exp(-z^2)\int_0^z \exp(\eta^2)d\eta$
e = natural number, $e=2.71828\ldots$
erf(z) = error function, $=\int_0^z \exp(-\eta^2)d\eta$
g = gravitational acceleration, m/s^2
h = local heat transfer coefficient, W/m^2°K
$\overline{h}$ = average heat transfer coefficient, $=(1/x)\int_0^x h\,dx'$
i = integral, see Eq. (3a)
i_4 = integral, see Eq. (3b)
I = velocity distribution integral, see Eq. (6)
I_1 = velocity distribution integral, see Eq. (7)
k = thermal conductivity, W/m°K
K_1 = constant, see Eq. (18a)
K_2 = constant, see Eq. (18b)
m = constant exponent, see Eq. (23)
n = exponent of the viscosity ratio, see Eqs. (20) and (21)
Nu = Nusselt number, $=\overline{h}x/k$, dimensionless
p = constant exponent, see Eq. (16a)
Pr = Prandtl number, $=\nu/\alpha$, dimensionless
q = heat flux, W/m^2
Ra = Rayleigh number, $=g\beta|T_w-T_\infty|x^3/\alpha\nu$, dimensionless
s = constant exponent, see Eq. (16b)
T = absolute temperature, °K
u = x-component of velocity
u_1 = parameter, see Eq. (5)
x = distance along the wall from the boundary layer origin, m
y = distance normal to the wall, m

Greek

α = thermal diffusivity, $=k/\rho C_p$, m^2/s
β = coefficient of thermal expansion, °K^{-1}
δ = boundary layer thickness
η = dimensionless distance normal to the wall, $=y/\delta$
θ = dimensionless temperature, see Eq. (4)
μ = dynamic viscosity, kg/m s
ν = momentum diffusivity, $=\mu/\rho$, m^2/s
π = natural number, $\pi=3.14159\ldots$
ρ = density, kg/m^3

Subscripts

f = evaluated at the film temperature
r = evaluated at the reference temperature
w = evaluated at the wall temperature
∞ = evaluated at the ambient temperature

References

[1] Kakac, S., Atesoglu, O., and Yener, J., 1985, "The Effects of the Temperature Dependent Fluid Properties on Natural Convection—Summary and Review," *Natural Convection Fundamentals And Applications*, S. Kakac, W. Aung, and R. Viskanta, eds., Hemisphere, pp. 729–771.

[2] Akagi, S., 1967, "Free Convective Heat Transfer in Viscous Oil," Trans. Jpn. Soc. Mech. Eng., **30**, pp. 624–635.

[3] Fujii, T., Takeuchi, M., Fujii, M., Suzaki, K., and Uehara, H., 1970, "Experi-

ments on Natural-Convection Heat Transfer From the Outer Surface of a Vertical Cylinder to Liquids,'' Int. J. Heat Mass Transf., **13**, pp. 753–787.
[4] Fujii, T., 1958, ''Heat Transfer From a Vertical Flat Surface by Laminar Free-Convection—the Cases Where the Physical Constants of Fluids Depend on the Temperatures and the Surface has an Arbitrary Temperature Distribution in the Vertical Direction,'' Trans. Jpn. Soc. Mech. Eng., **24**, pp. 964–972.
[5] Ito, T., Yamashita, H., and Nishikawa, K., 1974, ''Investigation of Variable Property Problem Concerning Natural Convection From Vertical Plate With Prescribed Uniform Heat Flux,'' *Proc. Of the Fifth Int. Heat Transfer Conference*, JSME/SCEJ, Japan, **3**, pp. 49–53.
[6] Chu, T., and Hickox, C., 1990, ''Thermal Convection With Large Viscosity Variation in an Enclosure With Localized Heating,'' ASME J. Heat Transfer, **112**, pp. 388–395.
[7] Sieder, E., and Tate, G., 1936, ''Heat Transfer and Pressure Drop of Liquids in Tubes,'' Ind. Eng. Chem., **28**, pp. 1429–1436.
[8] Kakac, S., and Oskay, R., 1972, ''Effect of Property Variations on Forced Convection Heat Transfer in Pipe Flow,'' *4th International Congress*, Czechoslovakia.
[9] Oskay, R., and Kakac, S., 1973, ''Effect of Viscosity Variation on Forced Convection Heat Transfer in Pipe Flow,'' Middle East Technical University J. Pure Appl. Sci., **6**(2), pp. 211–230.
[10] Burmeister, L., 1993, *Convective Heat Transfer*, 2nd ed., Wiley-Interscience.
[11] Heal, K., Hansen, M., and Rickard, K., 1998, *Maple V Learning Guide*, Springer.
[12] Abramowitz, M., and Stegun, I., 1965, *Handbook of Mathematical Functions*, National Bureau of Standards Applied Mathematics Series 55, Superintendent of Documents, U.S. Government Printing Office, Washington, DC, pp. 298, 319.
[13] Gryzagoridis, J., 1971, ''Natural Convection From a Vertical Flat Plate in the Low Grashof Number Range,'' Int. J. Heat Mass Transf., **14**, pp. 162–164.
[14] Le Fevre, E., and Ede, A., 1957, ''Laminar Free Convection From the Outer Surface of a Vertical Circular Cylinder,'' *Proc. 9th International Congress on Applied Mechanics Brussels*, **4**, pp. 175–183.

Numerical Study of EHD-Enhanced Forced Convection Using Two-Way Coupling

M. Huang
Graduate Research Assistant

F. C. Lai
Associate Professor

School of Aerospace and Mechanical Engineering,
University of Oklahoma, Norman, OK 73019

Numerical results are presented for heat transfer enhancement using electric field in forced convection in a horizontal channel. The main objective of the present study is to verify the assumption that is commonly used in the numerical study of this kind of problem, which assumes that the electric field can modify the flow field but not vice versa (i.e., the so-called one-way coupling). To this end, numerical solutions are obtained for a wide range of governing parameters ($V_0=10$, 12.5, 15 and 17.5 kV as well as $u_i=0.0759$ to 1.2144 m/s) using both one-way and two-way couplings. The results obtained, in terms of the flow, temperature, and electric fields as well as the heat transfer enhancement, are thoroughly examined. Since the difference in the results obtained by two approaches is insignificant, it is concluded that the assumption of one-way coupling is valid for the problem considered. [DOI: 10.1115/1.1578505]

Keywords: Computational, Electric Fields, Enhancement, Forced Convection, Heat Transfer

Introduction

Heat transfer between a surface and ambient air can be significantly increased through the application of electric field. When a high voltage is applied to a fine wire or a sharp needle, air in its vicinity is ionized and the ions are drawn towards the electrical ground. The collisions between the ions and the neutral air molecules during the transit produce a jet stream of corona wind that impinges the grounded surface. The impingement disturbs the boundary layer developed from the grounded surface and thus enhances the heat transfer between the surface and its ambient air.

Due to the complicated interactions among the electric, flow, and temperature fields, studies of heat transfer enhancement by electric fields are mostly accomplished by experiments. Numerical solutions are possible but usually subject to some simplification of these complicated interactions [1–6]. One of the most common assumptions employed is the one-way coupling between the electric and flow fields, which is valid only when the velocity of corona wind is much higher than that of the bulk flow. Under this assumption, an electric field can have influences over the flow field, but not vice versa. Although the assumption may seem reasonable (and deemed necessary in some cases), it has never been verified. One of the difficulties to verify this assumption is associated with the accurate measurement of corona wind velocity. Even with the nonintrusive measurement technique like laser Doppler anemometry, the seeding particles become charged in the presence of electric field. As such, the measured (particle) velocity is a function of both corona wind and electrostatic precipitation [7]. It is the purpose of this study to verify the assumption through a comparison of the results obtained from both one-way and two-way couplings as they were applied to the problem of EHD-enhanced forced convection in a horizontal channel.

Formulation and Numerical Method

The geometry considered is a two-dimensional channel with a length of 21 cm and a height of 6 cm (Fig. 1). This channel has exactly the same dimensions as that used by Yamamoto and Velkoff [8] so that their experimental data of electric field can be used for comparison in the present study. The walls are electrically grounded and maintained at a constant temperature of T_w. Air with a uniform velocity u_i and temperature T_i is introduced to the channel. A fine wire is suspended in the center of the channel and is charged with a direct current at a high positive voltage to generate the electric field. Four applied voltages (10, 12.5, 15, and 17.5 kV) are considered in this study. Due to the symmetry of the problem, only half the channel is used for computations.

The governing equations for the electric field are derived from Maxwell equations and are given by [9]

$$\nabla^2 V = -\frac{\rho_c}{\varepsilon_0}, \tag{1}$$

and

$$-\nabla\rho_c\cdot\nabla V+\frac{\rho_c^2}{\varepsilon_0}+\frac{1}{b}\nabla\rho_c\cdot\vec{u}=0. \tag{2}$$

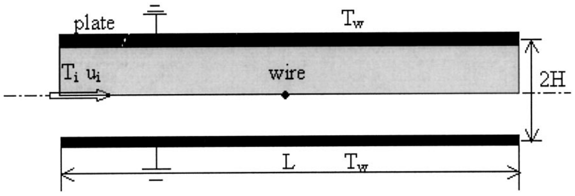

Fig. 1 A two-dimensional channel with constant wall temperature and one electrode wire located at the center (the shaded area represents the computational domain)

Contributed by the Heat Transfer Division for publication in the JOURNAL OF HEAT TRANSFER. Manuscript received by the Heat Transfer Division July 11, 2002; revision received March 17, 2003. Associate Editor: C. Amon.

Clearly, it is the third term in the above equation that provides the coupling from flow field to electric field. If one-way coupling is assumed, Eq. (2) is simplified to give

$$\nabla \rho_c \cdot \nabla \mathrm{V} = \frac{\rho_c^2}{\varepsilon_0}. \tag{3}$$

The corresponding boundary conditions for the electric field are:

$$V = V_0, \quad \text{at the wire} \tag{4a}$$

$$\frac{\partial V}{\partial x} = 0, \quad \text{at the channel inlet and outlet } (x = 0, L) \tag{4b}$$

$$V = 0, \quad \text{along the grounded wall } (y = H) \tag{4c}$$

$$\frac{\partial V}{\partial y} = 0, \quad \text{along the centerline } (y = 0) \tag{4d}$$

The governing equations for the flow and temperature fields are:

$$\frac{\partial u}{\partial x} + \frac{\partial v}{\partial y} = 0, \tag{5}$$

$$\frac{\partial u}{\partial t} + u\frac{\partial u}{\partial x} + v\frac{\partial u}{\partial y} = -\frac{1}{\rho}\frac{\partial p}{\partial x} + \nu\left(\frac{\partial^2 u}{\partial x^2} + \frac{\partial^2 u}{\partial y^2}\right) - \frac{\rho_c}{\rho}\frac{\partial V}{\partial x}, \tag{6}$$

$$\frac{\partial v}{\partial t} + u\frac{\partial v}{\partial x} + v\frac{\partial v}{\partial y} = -\frac{1}{\rho}\frac{\partial p}{\partial y} + \nu\left(\frac{\partial^2 v}{\partial x^2} + \frac{\partial^2 v}{\partial y^2}\right) - \frac{\rho_c}{\rho}\frac{\partial V}{\partial y}, \tag{7}$$

$$\frac{\partial T}{\partial t} + u\frac{\partial T}{\partial x} + v\frac{\partial T}{\partial y} = \alpha\left(\frac{\partial^2 T}{\partial x^2} + \frac{\partial^2 T}{\partial y^2}\right). \tag{8}$$

The last term in the momentum equations, Eqs. (6) and (7), represents the electric body force, which provides the coupling from electric field to flow field. The effects of Joule heating have been shown negligible for most heat transfer applications [10].

The dimensionless governing equations in terms of the stream function and vorticity are given by

$$\frac{\partial^2 \Psi}{\partial X^2} + \frac{\partial^2 \Psi}{\partial Y^2} = -\Omega, \tag{9}$$

$$\frac{\partial \Omega}{\partial \tau} + \frac{\partial \Psi}{\partial Y}\frac{\partial \Omega}{\partial X} - \frac{\partial \Psi}{\partial X}\frac{\partial \Omega}{\partial Y} = \frac{1}{\mathrm{Re}}\left(\frac{\partial^2 \Omega}{\partial X^2} + \frac{\partial^2 \Omega}{\partial Y^2}\right) + \frac{u_e^2}{u_i^2}\left(\frac{\partial \overline{\rho_c}}{\partial Y}\frac{\partial \overline{V}}{\partial X} - \frac{\partial \overline{\rho_c}}{\partial X}\frac{\partial \overline{V}}{\partial Y}\right), \tag{10}$$

$$\frac{\partial \theta}{\partial \tau} + \frac{\partial \Psi}{\partial Y}\frac{\partial \theta}{\partial X} - \frac{\partial \Psi}{\partial X}\frac{\partial \theta}{\partial Y} = \frac{1}{\mathrm{Pe}}\left(\frac{\partial^2 \theta}{\partial X^2} + \frac{\partial^2 \theta}{\partial Y^2}\right). \tag{11}$$

Since the electric characteristic velocity u_e is no longer a constant in the two-way coupling approach, we use the inlet velocity u_i as the reference velocity. This is different from most studies based on one-way coupling [1–6].

The corresponding boundary conditions for the flow and temperature fields are:

$$X = 0, \quad \Omega = 0, \quad \Psi = Y, \quad \theta = 1. \tag{12a}$$

$$X = \frac{L}{H}, \quad \frac{\partial \Omega}{\partial X} = 0, \quad \frac{\partial \Psi}{\partial X} = 0, \quad \frac{\partial \theta}{\partial X} = 0. \tag{12b}$$

$$Y = 0, \quad \Omega = 0, \quad \Psi = 0, \quad \frac{\partial \theta}{\partial Y} = 0. \tag{12c}$$

$$Y = 1, \quad \Omega = -\frac{\partial^2 \Psi}{\partial Y^2}, \quad \Psi = 1, \quad \theta = 0. \tag{12d}$$

For one-way coupling, the algorithm used to calculate the electric field is the same as that proposed by Yamamoto and Velkoff [8]. In this approach, the electric field can be determined independently of the flow field following the steps outlined below.

1. The potential distribution is first calculated by solving Eq. (1) with the assumption of no charge density.
2. After the potential distribution is known, the charge density can be determined by solving Eq. (2) with an initial guess of the charge density at the wire.
3. Given the charge density, the potential distribution can be recalculated using Eq. (1).
4. With the newly available potentials, the charge density can be updated by solving Eq. (2).
5. The process is repeated until both potential and charge density converge. When converged, the current density on the ground surface is calculated using

$$I = -\int_0^L \rho_c b\left(\frac{\partial \mathrm{V}}{\partial x}\right) L_w dx. \tag{13}$$

If this value agrees well with the experimental data [8], then the electric field is determined. Otherwise, a new charge density at the wire is assumed and the process is repeated from step (2).

For two-way coupling, the electric field has to be determined simultaneously with the flow field. At each time step, the electric field is first calculated, followed by the flow field. After the flow field is determined, the electric field is recalculated using the most recently available velocity data. As such, the numerical approach based on the two-way coupling is more computationally intensive (and thus more time consuming) than that of one-way coupling.

To evaluate the heat transfer results, the local Nusselt number at the wall is calculated by

$$\mathrm{Nu}_X = \frac{D_h}{L}\frac{T_i - T_w}{T_w - T_m}\left(\frac{\partial \theta}{\partial Y}\right)_{Y=1}. \tag{14}$$

The average Nusselt number can then be obtained from the local Nusselt number by

$$\mathrm{Nu} = \frac{1}{A}\int_0^A \mathrm{Nu}_x dX. \tag{15}$$

For periodic flows, the time-averaged Nusselt number is determined by averaging the Nusselt number over a period of oscillation and is given by

$$\overline{\mathrm{Nu}} = \frac{1}{\tau_P}\int_\tau^{\tau+\tau_P} \mathrm{Nu}\, d\tau \tag{16}$$

where τ_P is the period of oscillation, and Nu is determined from Eq. (15) at each time step.

A finite difference method based on the control volume approach [11] was used to solve the governing equations (Eqs. 9–11) subject to the boundary conditions imposed (Eq. 12). A uniform grid (225×33) has been shown to produce satisfactory results [12]. A time step of 5×10^{-4} was used in the present calculations. To ensure that the oscillation in flow and temperature fields is not induced by numerical stability, the time step has been reduced to 10^{-5} and 5×10^{-5} and nearly identical results were obtained.

To validate the code, heat transfer by forced convection without electric field in the same conditions were calculated and compared with the empirical correlation (Eq. 17) available in the literature [13].

$$\mathrm{Nu}_0 = 7.55 + \frac{0.024(x^*)^{-1.14}}{1 + 0.0358(x^*)^{-0.64}\mathrm{Pr}^{0.17}}, \quad x^* = \frac{x}{D_h \,\mathrm{Re}\,\mathrm{Pr}}. \tag{17}$$

The discrepancy found varies from one to six percent, depending on the Reynolds number, which is acceptable in the consideration of the uncertainty involved in the correlation itself.

Results and Discussion

It has been reported that the flow field under the influence of corona wind can develop into steady or oscillatory modes depending on the strength of flow inertia and electric body force [12]. The same phenomena were observed in the present study. The relative magnitude of flow inertia and electric body force can be quantified by the EHD number, which is defined below,

$$N_{\mathrm{EHD}}=\frac{HI}{b\rho u_i^2 A_p}. \tag{18}$$

It is the ratio of the electric body force to inertial force and is expressed in terms of the measurable quantities [12]. When the value is zero, it represents pure forced convection. When the value approaches infinity, it becomes the corona wind dominated flow. As reported by Lai et al. [12], oscillatory flows usually occur when $N_{\mathrm{EHD}}>1$.

When the flow and temperature fields are steady, the results obtained from one-way and two-way coupling are exactly the same. Both show that a secondary flow (i.e., recirculating cell) appears directly above the wire as the result of the interaction between the corona wind and the primary flow. As the Reynolds number increases, the strength of the recirculating cell decreases. The impingement of the corona wind on the wall perturbs the thermal boundary layer. It increases the local heat flux at the region directly above the wire. However, the perturbation of thermal boundary layer by the corona wind is suppressed when the Reynolds number increases.

When the flow and temperature fields become oscillatory, which usually occurs at a low Reynolds number and a high applied voltage, the results obtained from one-way and two-way coupling are still quite similar but there exist slight differences between them. Figures 2–5 show the variation of flow and temperature fields (in terms of streamlines and isotherms, respectively) through a complete cycle of oscillation. The semicircle in the center of the lower boundary indicates the location of the wire. For this particular case, $V_0=15\,\mathrm{kV}$ and $\mathrm{Re}=450\,(u_i=0.057\,\mathrm{m/s})$, one notices that there is a small difference in the oscillating period despite the similarity in the flow and temperature profiles. Also there is a small phase shift between these two results. Nevertheless, both results have captured the nature of the flow oscillation. When no flow is introduced to the channel, the

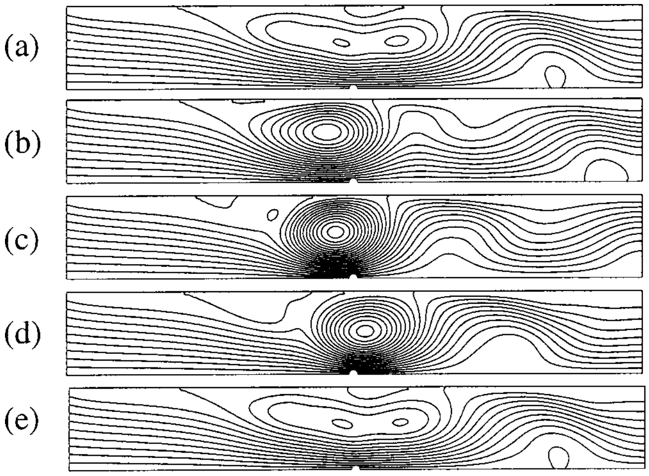

Fig. 3 Flow fields at $V_0=15\,\mathrm{kV}$ and $\mathrm{Re}=450$, (a) $\tau=57.9$, (b) $\tau=58.5$, (c) $\tau=59.1$, (d) $\tau=59.7$, and (e) $\tau=60.2$, (two-way coupling, $\Delta\Psi=0.2$)

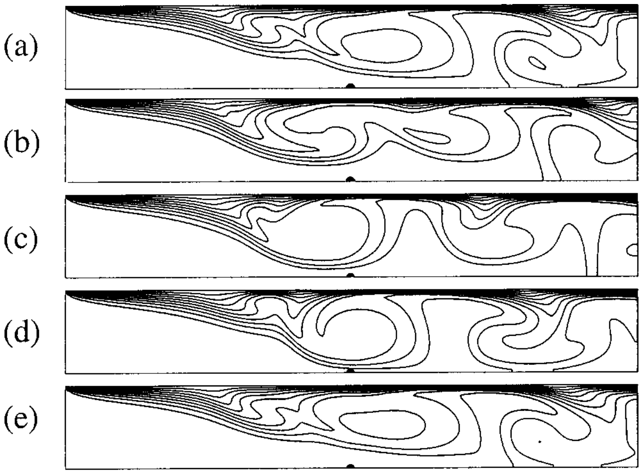

Fig. 4 Temperature fields at $V_0=15\,\mathrm{kV}$ and $\mathrm{Re}=450$, (a) $\tau=55.8$, (b) $\tau=56.4$, (c) $\tau=57.0$, (d) $\tau=57.6$, and (e) $\tau=58.2$, (one-way coupling, $\Delta\theta=0.1$)

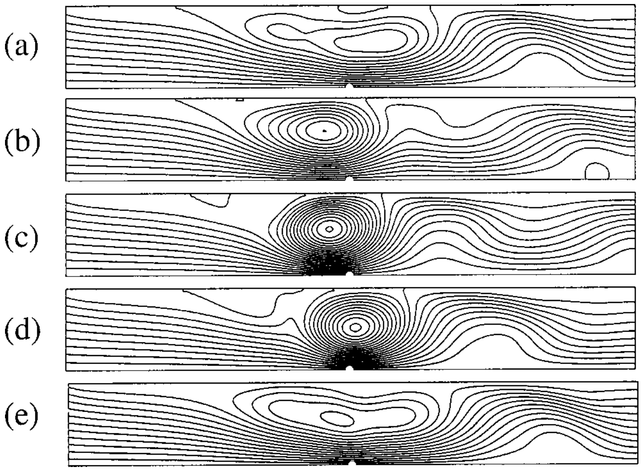

Fig. 2 Flow fields at $V_0=15\,\mathrm{kV}$ and $\mathrm{Re}=450$, (a) $\tau=55.8$, (b) $\tau=56.4$, (c) $\tau=57.0$, (d) $\tau=57.6$, and (e) $\tau=58.2$, (one-way coupling, $\Delta\Psi=0.2$)

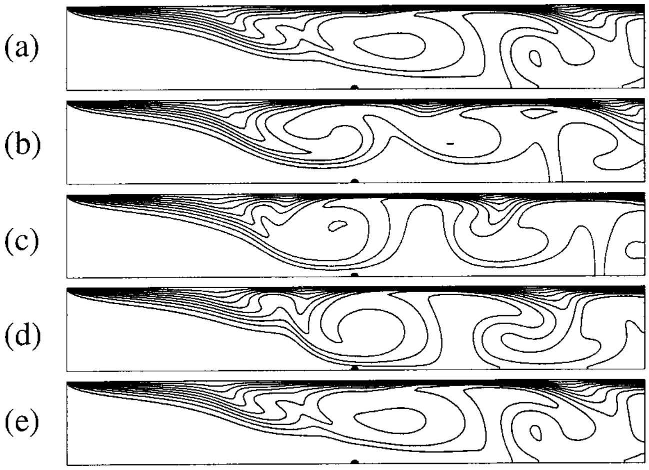

Fig. 5 Temperature fields at $V_0=15\,\mathrm{kV}$ and $\mathrm{Re}=450$, (a) $\tau=57.9$, (b) $\tau=58.5$, (c) $\tau=59.1$, (d) $\tau=59.7$, and (e) $\tau=60.2$, (two-way coupling, $\Delta\theta=0.1$)

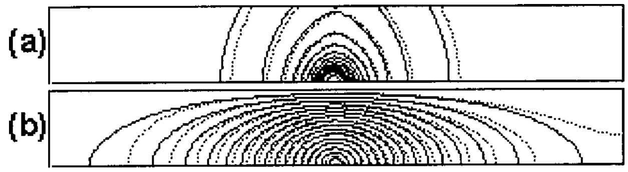

Fig. 6 Modification of electric field by air flow, $V_0 = 15$ kV and $u_i = 5$ m/s: (a) charge density, and (b) potential (one-way coupling—solid line, two-way coupling—dashed line)

flow field is induced by the electric field alone and remains stable. Four recirculating cells produced by the corona wind locate symmetrically about the center of the channel. When an external flow is introduced to the channel, the symmetry of corona-induced flow is destroyed. As a result, one can clearly observe the regeneration and destruction of the secondary cells in the flow field, which in turn produces a wave-like isotherm pattern in the temperature field. The periods of oscillation as predicted by one-way coupling and two-way coupling are mostly the same. For the cases in which they are different, the difference is usually small (less than 0.1 dimensionless time).

The reason why the prediction of flow and temperature fields using one-way and two-way coupling agrees so well is attributed to the small change of the electric field by the bulk airflow. For the range of inlet velocities considered in the present study, it is found that the modification of electric field by air flow is quite negligible. To produce a noticeable change in the electric field by convective air, one needs to increase the inlet velocity substantially (for example, $u_i = 5$ m/s, which is about four times of the maximum velocity considered in the present study). From Fig. 6, it is clear that most changes in the potential and charge density takes place at a location far away from the wire. Also, the magnitude of these changes is observed to be proportional to the distance from the wire. The charge density at the wire is found to be 9.62×10^{-4} C/m^3 when one-way coupling approach is used while it is 9.71×10^{-4} C/m^3 when two-way coupling approach is applied. The ion velocity is found to vary from -160 to 160 m/s, which is more than 30 times of the inlet air velocity. As a result, the modification of the electric field by convective air is minimal. However, it is interesting to observe that the electric field also becomes oscillatory when the flow and temperature fields are oscillatory, which is something cannot be revealed using the one-way approach.

For the present study, the heat transfer enhancement is defined as the ratio of the Nusselt number resulted from the application of electric field to that without the electric field. The heat transfer enhancement is shown in Fig. 7 as a function of the EHD number. For oscillatory flows, the time-averaged Nusselt numbers along with its maximum and minimum values are presented. As observed, oscillatory flows usually occur at a large EHD number (i.e., a low Reynolds number at a given electric field) and normally lead to a higher heat transfer enhancement. For oscillatory flows, the average Nusselt numbers predicted by both approaches are nearly the same. But, there are slight differences in the maximum and minimum values. From the figure, one also observes that heat transfer enhancement increases with the applied voltage and is negligible when the EHD number is less than 0.1. The maximum heat transfer enhancement can be as high as 3.5 times of that without electric field. Although the applied voltage may seem high in the present application, the current involved is considerably low. As such, the power required is very small, which make this an effective heat transfer enhancement technique.

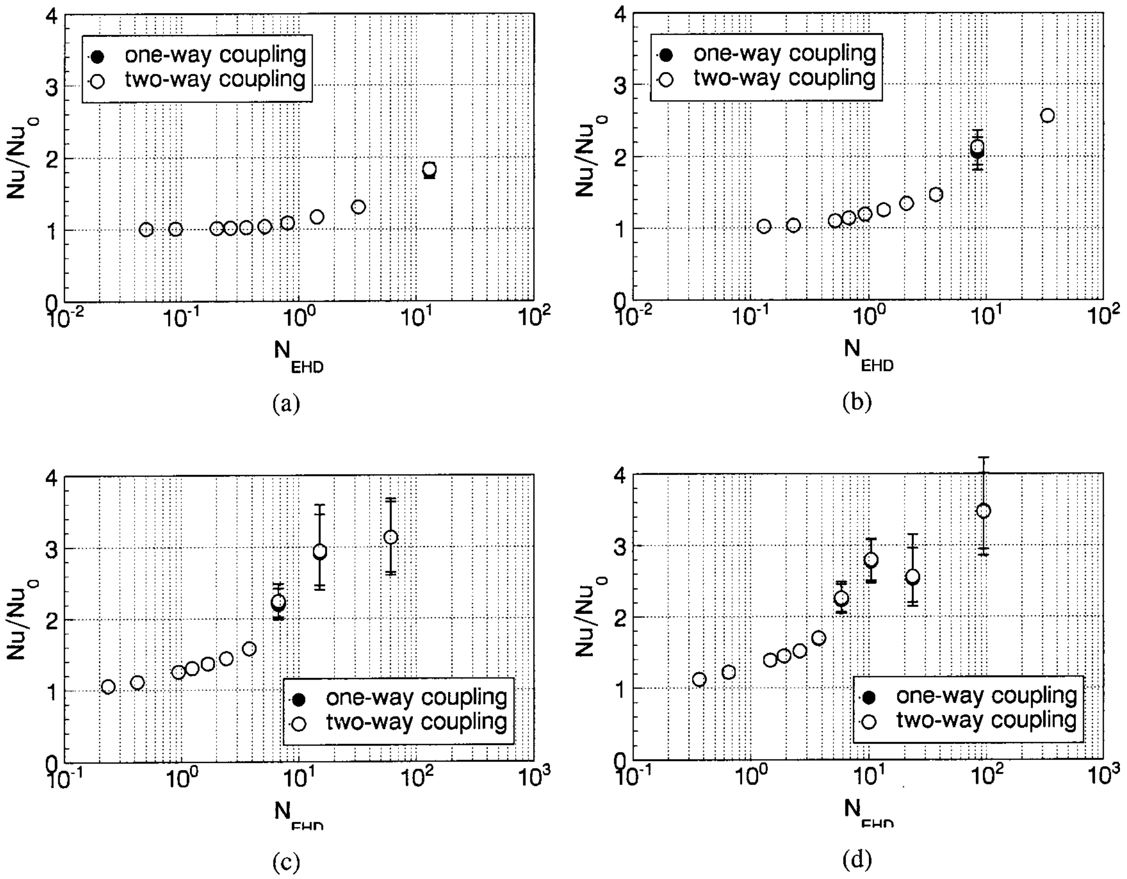

(a)

(b)

(c)

(d)

Fig. 7 Heat transfer enhancement as a function of EHD number: (a) $V_0 = 10.0$ kV, (b) $V_0 = 12.5$ kV, (c) $V_0 = 15.0$ kV, (d) $V_0 = 17.5$ kV

Conclusions

Numerical results have been presented for heat transfer enhancement in forced convection by electric fields. Although two different approaches (one-way and two-way coupling) were used to determine the interactions between the electric and flow fields, their differences are usually negligible. The results thus justify the use of one-way coupling in earlier studies. Further analysis shows that the ion velocity driven by charge mobility is typically two-order of magnitude larger than the inlet air velocity, which also lends the support of formulation based on one-way coupling. In summary, corona discharge is found to be an effective way in heat transfer enhancement. The enhancement increases with the applied voltage and can be as high as 350% from the present study. Both numerical approaches predict the existence of oscillatory flows, which is the main mechanism for the high heat transfer enhancement.

Nomenclature

A = aspect ratio of the computational domain, L/H
A_p = surface area of the wall, $[\mathrm{m}^2]$
b = ion mobility, $b = 1.4311 \times 10^{-4}\ \mathrm{m}^2/\mathrm{V \cdot s}$ for positive ions in air
D_h = hydraulic diameter of the channel, [m]
H = distance between wire and plate, [m]
h = convective heat transfer coefficient, $[\mathrm{W/m^2 \cdot K}]$
I = total current, [A]
k = thermal conductivity, $[\mathrm{W/m \cdot K}]$
L = length of the channel, [m]
L_w = length of the wire, [m]
Nu = average Nusselt number, hL/k
Nu_x = average Nusselt number, hx/k
$\overline{\mathrm{Nu}}$ = time-averaged Nusselt number
Pe = Peclet number, $u_i H/\alpha$
Pr = Prandtl number, ν/α
p = pressure, [Pa]
Re = Reynolds number, $u_i H/\nu$
t = time, [s]
T = temperature, [K]
T_w = wall temperature, [K]
T_i = temperature of fluid at inlet, [K]
$\vec{u}$ = velocity vector, [m/s]
u = velocity in x-direction, [m/s]
$\mathrm{u_e}$ = characteristic velocity of ionic wind, $\sqrt{\rho_{c0} V_0/\rho}$,
v = velocity in the y-direction, [m/s]
V = electric potential, [V]
$\mathrm{V_0}$ = electric potential at the wire, [V]
$\bar{\mathrm{v}}$ = dimensionless electric potential, V/V_0
x, y = Cartesian coordinate, [m]
X, Y = dimensionless Cartesian coordinates, $X = x/H$, $Y = y/H$
α = thermal diffusivity, $[\mathrm{m^2/s}]$
ε_0 = permitivity of free space, $\varepsilon_0 = 8.854 \times 10^{-12}$ F/m
ν = kinematic viscosity, $[\mathrm{m^2/s}]$
θ = dimensionless temperature, $(T - T_w)/(T_i - T_w)$
ρ = fluid density, $[\mathrm{kg/m^3}]$
ρ_c = space charge density, $[\mathrm{C/m^3}]$
ρ_c0 = space charge density at the wire, $[\mathrm{C/m^3}]$
$\bar{\rho}_\mathrm{c}$ = dimensionless space charge density, ρ_c/ρ_{c0}
τ = dimensionless time, $u_i t/H$
Ψ = dimensionless stream function
Ω = dimensionless vorticity

References

[1] Yabe, A., Mori, Y., and Hijikata, K., 1978, "EHD Study of the Corona Wind Between Wire and Plate Electrodes," AIAA J., **16**, pp. 340–345.
[2] Takimoto, A., Tada, Y., Yamada, K., and Hayashi, Y., 1988, "Heat Transfer Enhancement in a Convective Field With a Corona Discharge," Trans. Jpn. Soc. Mech. Eng., Ser. B, **54**(449), pp. 695–703.
[3] Kulkarni, S. S., and Lai, F. C., 1995, "Effects of Electric Field on Mixed Convection in a Vertical Channel," *Proceedings of the 1995 National Heat Transfer Conferences*, **8**, pp. 59–67.
[4] Mathew, J., and Lai, F. C., 1995, "Enhanced Heat Transfer in a Horizontal Channel With Double Electrodes," *Conference Record of the 1995 IEEE Industry Applications Society 30th Annual Meeting*, **2**, pp. 1472–1479.
[5] Owsenek, B. L., and Seyed-Yagoobi, J., 1997, "Theoretical and Experimental Study of Electrohydrodynamic Heat Transfer Enhancement Through Wire-Plate Corona Discharge," ASME J. Heat Transfer, **119**, pp. 604–610.
[6] Lai, F. C., 1998, "Effects of Buoyancy on EHD-Enhanced Forced Convection in a Horizontal Channel," J. Thermophys. Heat Transfer, **12**, pp. 431–436.
[7] Lamb, D. W., and Woolsey, G. A., 1995, "Characterization and Use of an Optical-Fiber Interferometer for Measurement of the Electric Wind," Appl. Opt., **34**, pp. 1608–1616.
[8] Yamamoto, T., and Velkoff, H. R., 1981, "Electrohydrodynamics in an Electrostatic Precipitator," J. Fluid Mech., **108**, pp. 1–18.
[9] Davidson, J. H., Kulacki, F. A., and Dunn, P. F., 1987, "Convective Heat Transfer With Electric and Magnetic Field," *Handbook of Single-Phase Convective Heat Transfer*, edited by S. Kakac et al., Wiley, New York, Chap. 9.
[10] Huang, M., and Lai, F. C., 2002, "Effects of Joule Heating on EHD-Enhanced Natural Convection in an Enclosure," AIAA Paper 2002–3318.
[11] Roache, P. J., 1998, *Fundamentals of Computational Fluid Dynamics*, Hermosa, Albuquerque, New Mexico.
[12] Lai, F. C., McKinney, P. J., and Davidson, J. H., 1995, "Oscillatory Electrohydrodynamic Gas Flows," J. Fluid Eng., **117**, pp. 491–497.
[13] Shah, R. K., and London, A. L., 1978, "Laminar Flow Forced Convection in Ducts," Adv. Heat Transfer, **1**, pp. 189–191.